frontiers | Research Topics

Brain imaging and stimulation editor's pick 2021

Edited by
Mingzhou Ding

Published in
Frontiers in Human Neuroscience

ISSN 1664-8714
ISBN 978-2-83251-931-8
DOI 10.3389/978-2-83251-931-8

About Frontiers

Frontiers is more than just an open access publisher of scholarly articles: it is a pioneering approach to the world of academia, radically improving the way scholarly research is managed. The grand vision of Frontiers is a world where all people have an equal opportunity to seek, share and generate knowledge. Frontiers provides immediate and permanent online open access to all its publications, but this alone is not enough to realize our grand goals.

Frontiers journal series

The Frontiers journal series is a multi-tier and interdisciplinary set of open-access, online journals, promising a paradigm shift from the current review, selection and dissemination processes in academic publishing. All Frontiers journals are driven by researchers for researchers; therefore, they constitute a service to the scholarly community. At the same time, the *Frontiers journal series* operates on a revolutionary invention, the tiered publishing system, initially addressing specific communities of scholars, and gradually climbing up to broader public understanding, thus serving the interests of the lay society, too.

Dedication to quality

Each Frontiers article is a landmark of the highest quality, thanks to genuinely collaborative interactions between authors and review editors, who include some of the world's best academicians. Research must be certified by peers before entering a stream of knowledge that may eventually reach the public - and shape society; therefore, Frontiers only applies the most rigorous and unbiased reviews. Frontiers revolutionizes research publishing by freely delivering the most outstanding research, evaluated with no bias from both the academic and social point of view. By applying the most advanced information technologies, Frontiers is catapulting scholarly publishing into a new generation.

What are Frontiers Research Topics?

Frontiers Research Topics are very popular trademarks of the *Frontiers journals series*: they are collections of at least ten articles, all centered on a particular subject. With their unique mix of varied contributions from Original Research to Review Articles, Frontiers Research Topics unify the most influential researchers, the latest key findings and historical advances in a hot research area.

Find out more on how to host your own Frontiers Research Topic or contribute to one as an author by contacting the Frontiers editorial office: frontiersin.org/about/contact

Brain imaging and stimulation editor's pick 2021

Topic editor
Mingzhou Ding — University of Florida, United States

Citation
Ding, M., ed. (2023). *Brain imaging and stimulation editor's pick 2021*. Lausanne: Frontiers Media SA. doi: 10.3389/978-2-83251-931-8

Table of contents

frontiers in Human Neuroscience

REVIEW
published: 09 January 2019
doi: 10.3389/fnhum.2018.00521

EEG Frequency Bands in Psychiatric Disorders: A Review of Resting State Studies

*Jennifer J. Newson and Tara C. Thiagarajan**

Sapien Labs, Arlington, VA, United States

A significant proportion of the electroencephalography (EEG) literature focuses on differences in historically pre-defined frequency bands in the power spectrum that are typically referred to as alpha, beta, gamma, theta and delta waves. Here, we review 184 EEG studies that report differences in frequency bands in the resting state condition (eyes open and closed) across a spectrum of psychiatric disorders including depression, attention deficit-hyperactivity disorder (ADHD), autism, addiction, bipolar disorder, anxiety, panic disorder, post-traumatic stress disorder (PTSD), obsessive compulsive disorder (OCD) and schizophrenia to determine patterns across disorders. Aggregating across all reported results we demonstrate that characteristic patterns of power change within specific frequency bands are not necessarily unique to any one disorder but show substantial overlap across disorders as well as variability within disorders. In particular, we show that the most dominant pattern of change, across several disorder types including ADHD, schizophrenia and OCD, is power increases across lower frequencies (delta and theta) and decreases across higher frequencies (alpha, beta and gamma). However, a considerable number of disorders, such as PTSD, addiction and autism show no dominant trend for spectral change in any direction. We report consistency and validation scores across the disorders and conditions showing that the dominant result across all disorders is typically only 2.2 times as likely to occur in the literature as alternate results, and typically with less than 250 study participants when summed across all studies reporting this result. Furthermore, the magnitudes of the results were infrequently reported and were typically small at between 20% and 30% and correlated weakly with symptom severity scores. Finally, we discuss the many methodological challenges and limitations relating to such frequency band analysis across the literature. These results caution any interpretation of results from studies that consider only one disorder in isolation, and for the overall potential of this approach for delivering valuable insights in the field of mental health.

Keywords: EEG, electroencephalography, resting-state, power spectrum, psychiatric, ADHD, schizophrenia, depression

OPEN ACCESS

Edited by:
Tamer Demiralp,
Istanbul University, Turkey

Reviewed by:
Madhavi Rangaswamy,
Christ University, India
Antonio Ivano Triggiani,
University of Foggia, Italy

***Correspondence:**
Tara C. Thiagarajan
tara@sapienlabs.org

Received: *05 September 2018*
Accepted: *11 December 2018*
Published: *09 January 2019*

Citation:
Newson JJ and Thiagarajan TC (2019) EEG Frequency Bands in Psychiatric Disorders: A Review of Resting State Studies. Front. Hum. Neurosci. 12:521. doi: 10.3389/fnhum.2018.00521

INTRODUCTION

In 2001 the World Health Organization[1] (WHO) reported that about 450 million people worldwide suffer from some form of mental disorder or brain condition, and that 1 in 4 people will meet this criteria at some point in their life (Sayers, 2001). More recent statistics[2] suggest that globally, 300 million people are affected by depression, 60 million people suffer from bipolar disorder, 23 million people are affected by schizophrenia, 1 in 160 children has autism spectrum disorder[3] and between 5% and 7% of children and adolescents suffer from attention deficit-hyperactivity disorder (ADHD; Polanczyk et al., 2007). Diagnosis of these psychiatric disorders is typically carried out using clinical interviews structured around the diagnosis classification systems of DSM-5 and ICD-11. These diagnostic criteria are based on self-reported symptom clusters, with each disorder type having its own group of symptoms which can include behavioral, cognitive, affective or physical disturbances. For example, ADHD diagnosis primarily focuses on cognitive and behavioral complaints by the child or adult, whilst diagnosis of depressive disorders typically focuses on disruptions to an individual's affective and physical functioning.

However, the reliance on a subjective assessment approach which can be prone to patient and expert bias means that researchers have been trying to develop new ways to inform clinical diagnosis and treatment effectiveness using objective symptom biomarkers, with electroencephalography (EEG) being one method of interest (McLoughlin et al., 2014; Jeste et al., 2015; Olbrich et al., 2015). The approach that dominates the literature focuses on analyzing broad frequency bands in the EEG power spectrum termed delta, theta, alpha, beta, and gamma (Berger, 1929; Jasper and Andrews, 1936; Hoagland et al., 1937a,b; Dustman et al., 1962). This interpretation of the EEG signal in terms of spectral bands has its origins in the technical limitations of the pre-computer era of the 1930s and '40s when few other analytical options were available. However, this approach results in a reduction in the rich temporal information available within the EEG and was, even at that time, acknowledged to be sub-optimal (Walter, 1938). Yet, despite the tremendous progress in computing power and available algorithms, the spectral band approach continues to persist as the dominant approach to EEG analysis, including in the development of clinical biomarkers. A recent example of this is the approval by the FDA[4] of the use of the theta/beta ratio as a biomarker for ADHD diagnosis (Saad et al., 2015; Gloss et al., 2016) whilst others are exploring the application of alpha-asymmetry as a potential marker for depression (van der Vinne et al., 2017; Kaiser et al., 2018). One question, therefore, is whether the approach of splicing the power spectrum into bands has persisted because it offers a superior approach in terms of research insight, methodological standardization, and reliability of results across studies, or whether it is because researchers have simply kept with the status quo of 80 years ago.

To explore the degree to which spectral band analysis of the EEG offers a reliable and useful approach for understanding different psychiatric disorders, we have reviewed the methods and results from 184 resting-state EEG studies across a host of psychiatric disorders that report differences (or lack thereof) in the various frequency bands within the power spectrum. The objectives of this review are therefore threefold. First, to determine the dominant patterns of results and reveal similarities and dissimilarities in the spectral trends both between and within different brain disorders during resting-state; second, to report the reliability and consistency of results across disorder types to determine the validity of applying power spectral analyses to inform on individual psychiatric disorders; and thirdly to review the methodological and analytical approaches across all studies to determine the degree to which they can be compared and contrasted to draw reliable conclusions within the field. In this respect, we provide an objective view of the literature along numerous methodological dimensions from sample size and choice of demographic (e.g., age, gender) to method of clinical diagnosis and parameters of EEG recording (e.g., reference type) and analysis (e.g., artifact removal, Fourier transform algorithm) used both within and across disorder types. We note that we restrict our focus to analysis of frequency bands at the level of single channels or averaged across channels and do not cover derivative analysis of these spectral bands such as their spatial coherence or asymmetry.

Such a cross disorder view is particularly warranted since the majority of clinical resting-state EEG studies focus primarily on one clinical disorder at a time, and do not offer a perspective across a broader range of psychiatric disorders. Therefore, whilst a study may report changes in particular frequency bands for one disorder type, it is not always obvious whether this is unique to this particular disorder, or whether similar patterns of change are found across other psychiatric disorders. In other words, are there unique EEG signatures which differentiate one disorder from another, or do the macro-level changes observed in studies employing a frequency band approach overlap with other disorders, therefore being more limited in their clinical diagnosis potential.

MATERIALS AND METHODS

Studies Identified and Reporting Characteristics

We present a review of studies published over the last 25 years that report spectral power in different bands during resting state conditions (eyes open and/or closed) across 10 mental health disorders. These include depression, bipolar disorder, addiction, autism, ADHD, anxiety, panic disorder, obsessive compulsive disorder (OCD), post-traumatic stress disorder (PTSD) and schizophrenia, allowing us to compare both within and across disorders. We limit our review to studies with an N of at least 20 participants that reported

[1] http://www.who.int/

[2] http://www.who.int/en/news-room/fact-sheets/detail/mental-disorders

[3] http://www.who.int/en/news-room/fact-sheets/detail/autism-spectrum-disorders

[4] https://www.accessdata.fda.gov/cdrh_docs/reviews/K112711.pdf

quantifiable results in at least one frequency band. Our intention was not to perform a full-scale meta-analysis but rather a comprehensive review of the state of recent literature. To do so we conducted a search of PubMed[5] in May 2018 using combinations of the following keywords in the title or abstract: quantitative OR qEEG OR ongoing/on-going OR spontaneous OR resting/rest, combined with EEG and the key terms for each of the disorders of interest. Only studies that examined EEG spectral differences in at least one frequency band (exclusively or alongside other EEG metrics) between a clinical and a control group were included. Studies whose research focus was on other aspects of mental health or cognition, or whose analysis focused exclusively on other EEG metrics (e.g., asymmetry, coherence, microstates, entropy etc.) were excluded. No study was excluded due to methodological limitations, but rather because it missed the proposed research topic. This enabled a comprehensive review of the variability of experimental and clinical parameters across the published literature, rather than restricting it to a particular subset of studies.

As a next step, various methodological parameters were collated including sampling characteristics, EEG recording parameters and power spectrum computation. Sampling characteristics included sample size, demographic data (age, gender), medication status and diagnostic screening method. Key EEG parameters (where available) included referencing style, and recording length, and power spectrum computation included FFT method (windowing function, overlap, epoch length), frequency bands (and frequency window) and whether absolute and/or relative power differences were analyzed within each band. We then noted any reported significant difference (increase or decrease) or lack of significant difference in power/amplitude across each spectral band (delta, theta, alpha, beta, gamma where analyzed) for each study. In addition, to standardize across studies, frequency bands which had been split into sub-bands (e.g., beta1/beta2) were collapsed for all analyses, and where results differed across sub bands (e.g., beta1 showed significance, beta2 showed no significance) we considered the significant finding as the primary result. In addition, in one study (Hong et al., 2012) the theta and alpha bands were collapsed together and in this instance we allocated the result to both bands individually.

Where reported in text or figures, the magnitude of change was also calculated (as a % increase or decrease). Any reported correlations between individual spectral bands and clinical symptoms were also recorded when reported. All collected data were consolidated in a spreadsheet for review and analysis.

Consistency and Reliability Scores

To determine the dominant result for each band within each disorder group and recording condition we first identified the most frequently occurring (i.e., dominant) result (significant increase, significant decrease or no significant difference). For example, for ADHD in children in the eyes closed condition there were 13 studies reporting a significant increase in the absolute power of the delta band, one study reporting no difference and three studies reporting a significant decrease. In this case the dominant result is a significant increase. When the number of studies showing either a significant increase or decrease was the same as the number showing no difference, the dominant result was considered no difference. When an equal number of studies showed an increase and a decrease (and the number was higher than those showing no significant difference) the result was marked as "opposing."

We then created a consistency score computed as the ratio of the number of studies reporting the dominant result (e.g., no significant difference) to the number of studies reporting a different result (e.g., significant increase or decrease); essentially how much more frequently the dominant result was reported in the literature compared to some other result. When all studies agreed (i.e., the divisor was zero) we used the number of studies as the consistency score. When the studies were evenly divided between any two results, we computed the consistency score as 1.

We next created a validation score by first computing the average N for the studies showing the dominant result in each band and multiplying this by the number of studies showing the dominant result. We then averaged these values across all the bands (excluding the gamma band which was sparsely reported). The validation score is therefore an indication of the size of the population from which the dominant result was obtained.

RESULTS

A total of 184 publications published between 1993 and 2018, found using the above search criteria in PubMed, matched our inclusion criteria. A detailed list of studies with key study parameters can be found in **Supplementary Table S1**. while trends in results are summarized below.

Overview of Studies

Sample Characteristics

A summary of the number of studies across disorders and their corresponding sample characteristics is shown in **Table 1**. Some disorders such as ADHD and schizophrenia were widely studied (65 and 37 articles, respectively) while others such as depression and autism were also popular, though less so (18 and 16 studies respectively). In contrast, some disorders such as bipolar, generalized anxiety and panic disorder were very poorly represented in the literature (six or fewer studies each). The median sample size across the studies was 60, with roughly equal numbers of patients and controls in the majority of studies. Seventy-three percent of studies had sample sizes less than 100 whilst only 10 studies (Clarke et al., 2001d; Wuebben and Winterer, 2001; Rangaswamy et al., 2002, 2006; Magee et al., 2005; McFarlane et al., 2005; Grin-Yatsenko et al., 2009; Kam et al., 2013; Narayanan et al., 2014; Arns et al., 2015) had sample sizes greater than 250 and only one of these (Arns et al., 2015) had a sample size greater than 1,000 ($N = 1{,}344$; depression; **Figure 1**). Participants were generally adults with an average age between 30 and 40 except for ADHD and autism where studies largely focused on children and the average age ranged from 5 to 11 years

[5]https://www.ncbi.nlm.nih.gov/pubmed/

TABLE 1 | Overview of studies.

	No. of studies*	Median N	% Controls	Average age (years)	% Females	% Eyes closed[$]
ADHD (children)	56[#]	76	45	11	25	75
ADHD (adults)	14[#]	55.5	50	33	43	54
Schizophrenia	37	63	54	31	33	92
ASD/Autism[&]	16	56	52	8.5	21	33
Depression	18	55	44	39	57	86
OCD	10	61.5	49	32	56	100
PTSD	13	74	50	40	37	67
Addiction	16	45	49	33	30	88
Panic disorder	4	79	44	35	69	50
Bipolar disorder	6	99.5	55	30	55	50
Anxiety	3	50	50	31	76	50

**Includes five joint studies: (1) depression/post-traumatic stress disorder (PTSD); (2) schizophrenia/bipolar; and (3) schizophrenia/depression. [$]Includes studies which had only eyes closed as well as studies which included both eyes closed and eyes open. [&]Excludes the one adult ASD/autism study. [#]Includes five studies with both children and adult participant groups.*

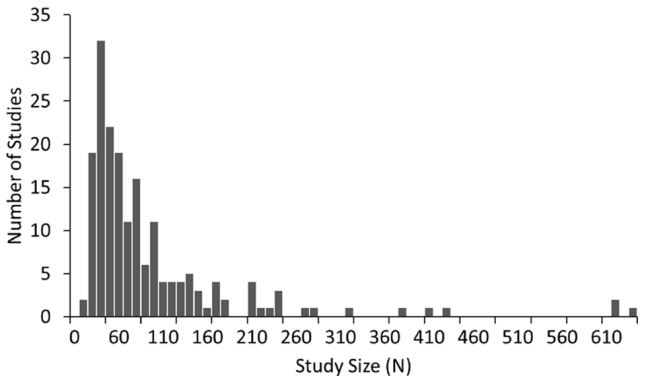

FIGURE 1 | Distribution of sample size across 184 studies in this review. Sample size includes both patients and controls. Median sample size was 60. One study, with a sample size of 1,344, was beyond the scale of this graph.

old. Furthermore, samples were typically skewed towards male subjects (64%).

Each study compared a group with a diagnosed disorder to a control group. The majority of studies report on only one disorder, although a minority compare two disorders, e.g., bipolar disorder and schizophrenia (Clementz et al., 1994; Kam et al., 2013; Narayanan et al., 2014), depression and schizophrenia (Begić et al., 2011), depression and PTSD (Kemp et al., 2010), alcohol and internet addiction (Son et al., 2015). In each case, the disorder group(s) were determined using common psychiatric questionnaires as described in **Supplementary Table S2**. In the majority of studies (70%), patients were unmedicated which was defined as being medication naive or having abstained from taking medication for a predefined period of time (ranging from 12 h to 3 months).

Reported Metrics

The majority of studies reported resting state EEG with eyes closed recordings (66% of studies). However, a minority of studies reported results for eyes open (19% of studies) or both eyes open and closed (15%), analyzed either combined or separately. While some studies reported all frequency bands, many were selective in reporting only one or two bands. Across the studies, the alpha and theta bands were the most frequently reported (in 85/84% of studies), followed by beta (80%) and delta (70%). Gamma is the least frequently reported (only 18% of studies). Given this pattern of reporting, it is sometimes unclear when a study reported on only one or two bands, whether it was because the other bands were not analyzed, or whether they were excluded on account of negative or null results. Underreporting of negative or null results may therefore bias this review towards the positive results. It is also important to note that while most studies followed a typical definition for the theta and alpha bands, there was wide variation in the definitions of other bands (see "Methodological Challenges and Limitations" section).

For each band, studies most often reported differences in the absolute power between control and disorder groups (61% of studies). Some of these studies additionally reported relative power (28%) while a few reported differences in relative power only (10%). Relative power is typically calculated by computing the power of each given band divided by the sum of power across all bands. Surprisingly, 29% of studies did not explicitly indicate the method of reporting and required some inference. Where a study did not mention whether it reported absolute or relative data, it was generally assumed that it was absolute in the absence of any evidence to the contrary. Most studies reported aggregated results for broad cortical or source localized regions (60%) while others reported results for individual channels (32%). A small minority provided results aggregated across all recorded channels (8%). Given these differences in reporting we computed the magnitude of difference between the control and disorder groups as percentages, where the information was available (in 40% of cases), averaging across broad regions in all studies. Where there was a regional split between increases and decreases across the scalp (e.g., frontal increases and posterior decreases) the regional magnitudes were allocated to their respective increase and decrease groupings (rather than being averaged together). Finally, a proportion of studies (27%) additionally reported correlations (significant or non-significant) between individual bands and disorder severity.

It is also important to note that although some of the studies reported here exclusively focused on the analysis of the power spectrum, many of them additionally reported on other metrics

including coherence analysis and asymmetries which are not reported here.

Aggregate Trends Across Frequency Bands and Disorders

A trend analysis was performed for both absolute and relative power differences reported between the disorder and control group in each band (definitional and other methodological differences notwithstanding) for each disorder. To standardize across studies, we collapsed across any bands which had been split into sub-bands (e.g., beta1/beta2). Where results differed across bands (e.g., beta1 showed significance, beta2 showed no significance) we considered the significant result as the primary result. Furthermore, results are shown separately for the eyes closed and eyes open conditions. A small number of studies that combined eyes open and closed (for opioid addiction, depression, panic disorder, anxiety) are excluded from the trend analysis but displayed in the tables for completeness. In addition, in the minority of cases where there was only a single study condition (i.e., eye open/closed, absolute/relative) for a particular disorder, the study was not included in the summary table or trend analysis.

Dominant Results Across Disorders

The number of studies reporting either a significant increase, a significant decrease, or no significant difference in the power in each of the frequency bands relative to control for each disorder are shown in **Supplementary Tables S3, S4** for absolute and relative power respectively. The dominant result for each band within each disorder group and recording condition (significant increase, significant decrease or no significant difference) was determined based on the result reported by the greatest number of studies as described in the methods section "Consistency and Reliability Scores."

Altogether we found that the most common result across all disorders and bands combined was an absence of any significant difference in both the eyes closed (53% absolute power, 63% relative power) and relative eyes open conditions (83%), whilst there were similar levels of significant increase (46%) and no significant difference (39%) for absolute eyes open. The dominant results for each band aggregated across all distinct disorders and conditions are shown in **Figure 2** for absolute power (**Figure 2A**) and relative power (**Figure 2B**).

When restricting our view to the smaller proportion of disorders/conditions where the dominant result was a significant increase or decrease, the general pattern that emerged was that increases dominated in the lower frequency delta and theta bands (86% for absolute and relative power) while decreases dominated in the alpha band (67% absolute, 100% relative). In contrast decreases were roughly as likely as increases in the beta band depending on the condition (37.5% absolute, 50% relative). The gamma band was excluded from analysis due to the small number of studies, although here again, decreases were more common.

Examining this general effect at the level of the individual disorder types, the results showed that there was an increase in absolute power for both delta and theta in the eyes closed condition for ADHD (in children), schizophrenia, OCD and depression, while ADHD (in adults) and alcohol addiction showed an increase only in the theta band (**Figure 3A**). In

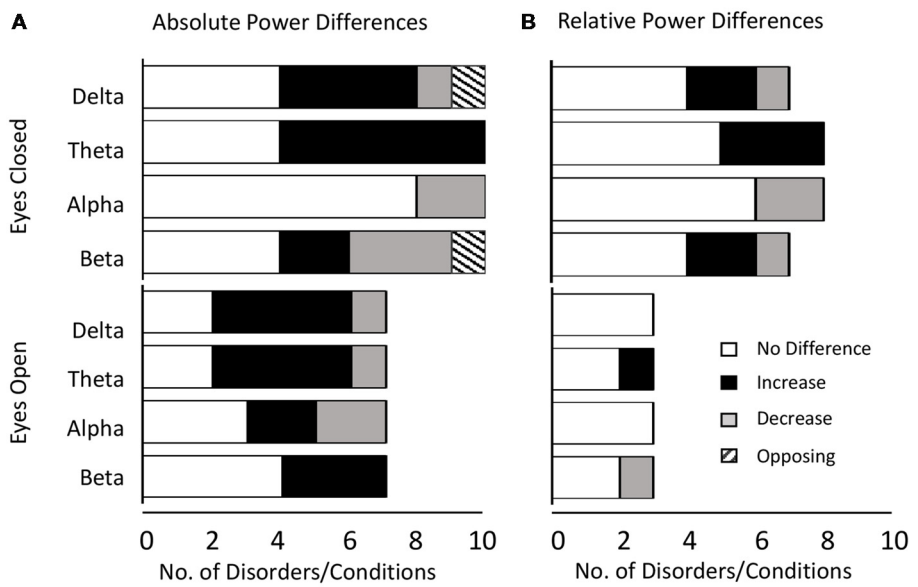

FIGURE 2 | Dominant result aggregated across all disorders and bands. **(A)** Number of disorders with no difference in absolute power relative to controls (white), an increase (black), a decrease (gray) or opposing results (hashed) for eyes closed (top) and eyes open (bottom) conditions. Increases are more common for lower frequency bands (delta and theta) whilst decreases or no significant difference are more common for higher frequency bands (alpha and beta). **(B)** Same as **(A)** for relative power. Legends and axis labels are common.

the eyes open condition, an increase was dominant in both delta and theta for depression, ADHD (in children) and bipolar disorder but only in the delta band for ADHD (adults) and only in the theta band for schizophrenia. However, even across those disorders where an increase dominated these bands, there were nonetheless a minority of studies reporting the opposite effect (e.g., three studies of ADHD in children, Dupuy et al., 2014a; Giertuga et al., 2017; Shephard et al., 2018, two studies of schizophrenia Pascual-Marqui et al., 1999; Knyazeva et al., 2008 and one of OCD, Bucci et al., 2004). The only cases in the lower frequency bands where the dominant result was a decrease, rather than an increase, was in the delta band for autism (eyes closed, Coben et al., 2008) and in the theta and delta bands for PTSD/early life stress (eyes open, McFarlane et al., 2005; Veltmeyer et al., 2006).

Significant decreases in absolute power were dominant in the alpha band for schizophrenia and OCD (eyes closed), autism and PTSD (eyes open), and in the beta band for ADHD (children), autism and internet addiction (all eyes closed; **Figure 3A**). In contrast, significant increases were dominant in a handful of disorders, most frequently when participants had their eyes open, including depression (beta, eyes open and closed), bipolar (alpha and beta, eyes open), schizophrenia (alpha and beta, eyes open) and alcohol addiction (beta, eyes closed).

In two cases (OCD, eyes closed beta band and alcohol addiction, eyes closed delta band) there was no dominant result but rather an equal number of studies showing increases and decreases. These are shown as hash marked in **Figure 3A**.

In **Figure 3B** we show the differences between the dominant result for absolute and relative power differences. Overall the dominant result for relative power was the same as for absolute power in 62% of experimental comparisons (white squares) where each comparison is one band within one disorder and condition. Results were most similar across relative and absolute for the theta band (73% of disorders/conditions). Cases where there was a significant difference in one method but not the other are indicated as gray (36% of disorders/conditions), which, when examined in more detail, was the case for 50% of the disorders and conditions in the beta band and 40% in the delta band. There was a greater proportion of disorders/conditions with no significant difference for relative power compared to absolute power. This was particularly true for the delta band. The only case where the dominant result was diametrically opposed for absolute power vs. relative power was in the delta band for ADHD in children (eyes closed) where there was an increase in the absolute power and decrease in the relative power (**Figure 3B**, hashed box).

Given the overall pattern of a greater likelihood of increases in the lower frequencies and no change or decreases in higher frequencies, it is important to note that, with the exception of ADHD, the same disorders that were dominated by increases in theta were not the ones dominated by decreases in beta. However, the overall trend across disorders would be for a decreased theta/beta ratio either due to an increase in theta and decrease in beta, an increase in theta and no change in beta, or no change in theta and a decrease in beta.

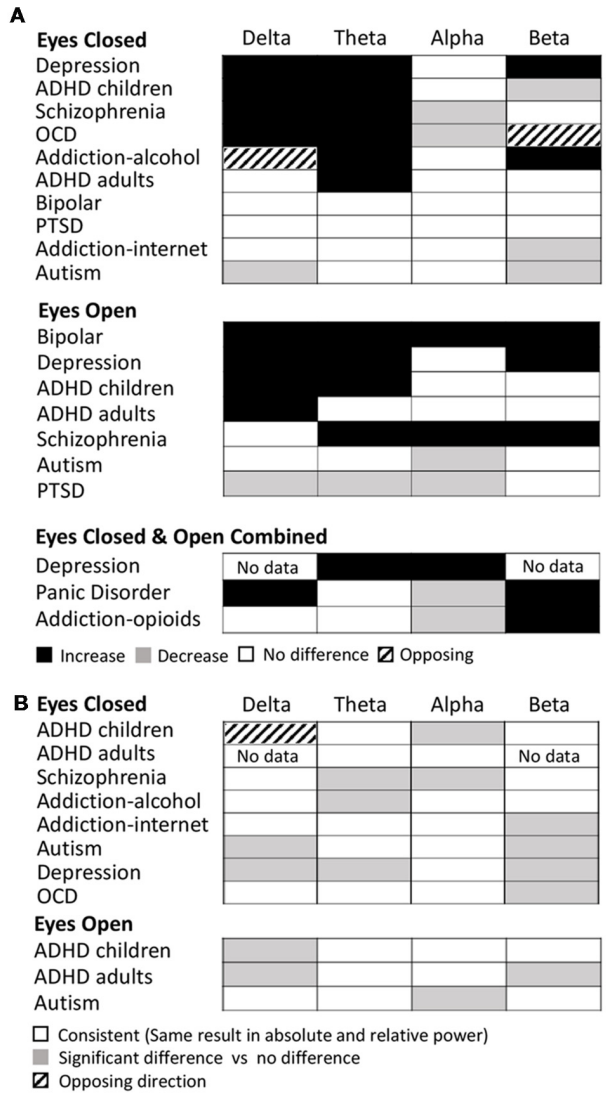

FIGURE 3 | Dominant results for each individual disorder and band. **(A)** Differences in absolute power for each disorder (relative to control) for eyes closed condition (top), eyes open (middle) and eyes open and closed combined (bottom). White boxes indicate no change, black indicates an increase, and gray indicates a decrease. Opposing results are shown by hashed boxes. **(B)** Difference in results between absolute power and relative power for the same disorders. White indicates no difference, gray indicates a significant increase or decrease in one but no significant difference in the other, while a hashed box indicates opposite results.

Consistency of Results

We next report analysis of consistency of the results for those disorders/conditions where there were at least two studies reporting on any particular band (**Figures 4**, **5**). Consistency scores were calculated as described in methods section "Consistency and Reliability Scores" and can be read as how much more frequently the dominant result occurred in the literature compared to any other result.

Figure 4 shows the average consistency scores across all disorders for each band for the eyes closed (solid bars) and eyes

open conditions (hashed bars), for both absolute and relative power (gray and black bars respectively). Overall, the highest consistency score, aggregated across all disorders and bands was for relative power with eyes closed (3.0) followed by absolute power with eyes closed (2.2). Eyes open had lower consistency with 2.0 and 1.5 for absolute and relative power respectively. When calculated separately for each band, a similar pattern was observed, though scores were slightly lower overall for delta and alpha. Taken together this suggests that eyes open is a much more variable condition and that relative power estimates are more reliable.

Analysis of individual disorders/conditions, aggregated across bands (**Figure 5A**), revealed that the highest consistency score was for relative power comparisons of controls to ADHD in children with eyes closed (7.0) followed by internet addiction with eyes closed (4). The highest consistency scores for absolute power with eyes closed was for OCD (3.3), internet addiction (2.8) and ADHD in children (2.8). Autism and ADHD in adults had generally the lowest consistency across all conditions. It is significant, however, that the literature for two disorders with the highest consistency scores, ADHD in children and internet addiction, were each dominated by a single research group (47% of the articles for ADHD, 100% for internet addiction) which was not the case for other disorders with multiple studies. This has the advantage of a consistent methodology but also risks bias. We thus point out the consistency score for ADHD in children when the dominant group is removed with an asterisk (**Figure 5A**).

We next report validation scores, computed as described in methods sections "Consistency and Reliability Scores," that are essentially the total number (N) of study participants across all the studies reporting the dominant result (**Figure 5B**). ADHD in children with eyes closed had the highest number of studies showing the dominant result (8–25 per band) and with an average N of 129 the validation scores were the highest with 2,516 for relative power (beyond the scale of the graph) and 1,563 for absolute power. We note however that this more than halves for relative power when the dominant research group is excluded. Also high was schizophrenia with 1,446 for absolute power followed by depression (absolute, eyes closed) with 880.

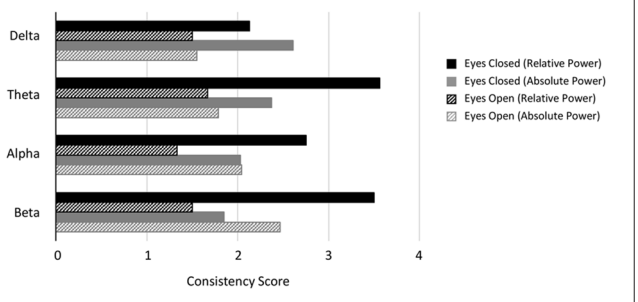

FIGURE 4 | Consistency scores aggregated across disorders for each band and condition. Consistency scores (frequency of dominant result relative to other results) were between 2 and 3 for absolute power in the eyes closed condition for all bands (gray bars), between 2 and 4 for relative power eyes closed (black bars) and typically between 1 and 2 for eyes open (absolute and relative, gray and black hashed bars, except beta eyes open absolute power).

Nineteen percentage of disorders/conditions had scores less than 100 and 47% had less than 200 indicating that they involved few studies and participants and therefore cannot be considered to be sufficiently validated results.

Magnitude of Results

We next considered the reported magnitudes of difference (in %) for absolute and relative power, averaged across only those studies where a significant difference was reported, and where accurate information was available in the text, tables or figures of the publication (shown in detail in **Supplementary Table S5**). On average, 40% of study comparisons reported magnitude data, although this varied across disorder types and ranged from 68%, 67% and 58% for ADHD (adults), ASD/Autism and bipolar disorder respectively at the upper end, through to 26% for ADHD (children) and 29% for OCD at the lower end (in addition, no anxiety studies identified for this review included magnitude data).

Across all disorders/conditions, the reported magnitude of difference (mean ± SD) was 34 ± 13% for absolute power and 26 ± 14% for relative power, irrespective of whether the reported result was the dominant one or not. The distribution of magnitudes is shown in **Figure 6A**. Overall the magnitude of increases (vs. decreases) were higher on average for absolute power (gray bars) but not relative power (black bars). Given that magnitude data was not consistently reported across bands and conditions, no disorder or band specific trend can be reliably inferred. We therefore do not report any trends. However, we do note that reported magnitudes were highest for schizophrenia, depression and bipolar disorder (∼44% on average for eyes closed and ∼48% on average for eyes open across all bands) and lowest for opioid, internet addiction, ADHD in children with eyes open and PTSD with eyes open (all 21%–22%). Overall magnitudes were also highest for the alpha band, particularly for decreases reported with eyes closed (46% on average) while other bands were similarly lower.

We note that in many cases where different studies reported opposing results, the magnitudes reported were not very different. For example, although the dominant result for schizophrenia was a decrease in alpha (on average 58%), those studies that reported an increase in alpha (Hong et al., 2012; Kim et al., 2015) reported a similar magnitude (64%).

Correlation With Disorder Severity

We also looked at reported correlations between individual bands and disorder severity, as rated by the clinical diagnosis and symptom questionnaire (**Supplementary Table S6**). Twenty-seven percent of studies reported multiple such correlations for different bands and brain regions. We included all reported correlations regardless of the specific brain region or band or symptom subset for which the correlation was reported. The distribution of these correlations is shown in **Figure 6B**. The correlations generally ranged from 0.2 to 0.5 with an average around 0.4 (positive or negative) while a fraction of instances reported no significant correlation (shown as 0). It is highly likely that the nonsignificant correlations are underreported. Higher correlations of 0.6–0.8 were reported in some studies showing a second peak in the distribution. However, these

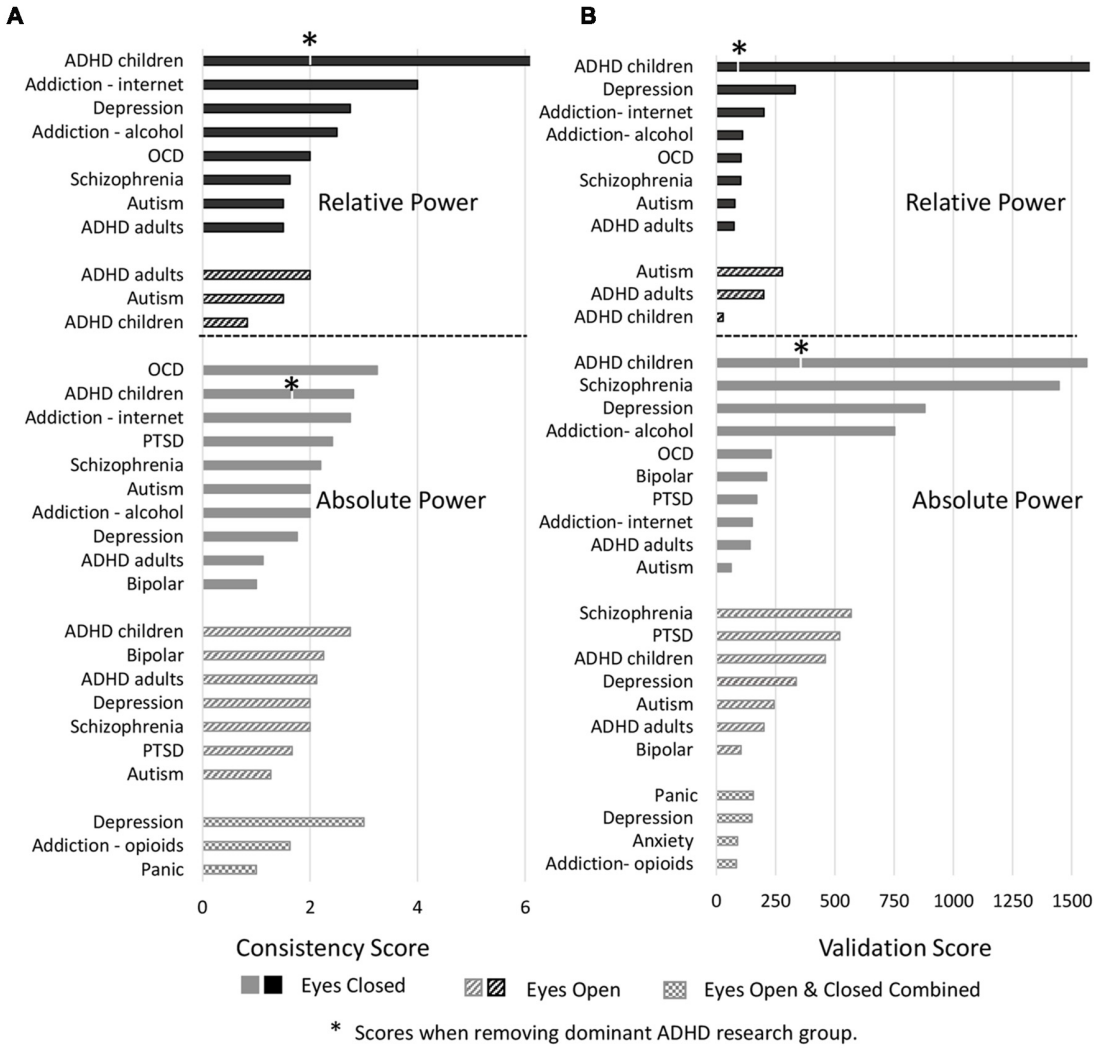

FIGURE 5 | Consistency and validation scores by disorders. **(A)** Consistency scores for each disorder for relative power (top) with eyes closed (black bars) and eyes open (black hashed bars) and absolute power (bottom) with eyes closed (gray bars), eyes open (gray hashed bars) and eyes closed and open combined (hatched bars). Asterisk marks for attention deficit-hyperactivity disorder (ADHD) indicate consistency scores when the dominant research group is excluded. **(B)** Validation scores for each disorder. Order and legend are as in **(A)**. Validation score for ADHD in children, relative power with eyes closed goes beyond the scale of this graph (2,516).

were disproportionately from two studies (Pogarell et al., 2006; Roh et al., 2015) with a very small number of participants (less than 40). When these were excluded, the peak at 0.7 was much reduced (shown by the dotted line). Further, there were no notable differences in the correlations for any individual disorder or band. In addition, some studies reported regression coefficients rather than correlations which were generally lower (between 0.2 and 0.3) and are not included in the distribution. Thus, as an overall conclusion, it appears that correlations of band power to symptom scores are generally weak and not specific to any band or disorder.

We note that some studies included correlations to other factors such as a particular task performance, demographic variables or age of onset that are not reported here. In addition, a handful of studies performed other types of diagnosis classification modeling to distinguish and predict differences between the two study groups (Kim et al., 2015: schizophrenia; Knott et al., 2001b; Deldin and Chiu, 2005: depression; Chan and Leung, 2006; Chan et al., 2007; Sheikhani et al., 2012: autism; Kim et al., 2017: internet addiction; Ogrim et al., 2012; Buyck and Wiersema, 2014a; Poil et al., 2014; Markovska-Simoska and Pop-Jordanova, 2017: ADHD). Again, these are not reported here.

Individual Psychiatric Disorders

ADHD

This review identified 65 ADHD studies with a median sample size of 76 (children) and 55.5 (adults; range 23–378). Of these, 56 studied children and adolescents (average age of

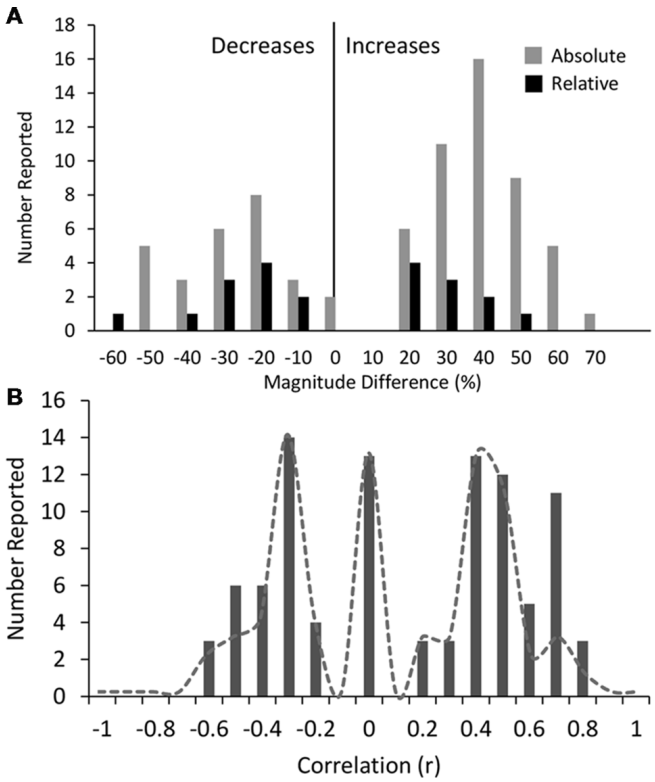

FIGURE 6 | Histograms of magnitudes of differences and correlations. **(A)** All reported magnitudes for differences between disorder groups and controls across all bands for absolute (gray bars) and relative power (black bars). Increases are shown as positive and decreases are negative. Reported increases for absolute power outnumbered reported decreases, although were similar in magnitude (35% and 34% respectively). Relative power was relatively symmetric with average magnitude increases of 22% and decreases of 31%. **(B)** Histogram of all reported correlations of band increases or decreases with symptom severity scores (all results were included even if not the dominant result). Reports of "no significant correlation" are shown as 0. Positive and negative correlations were typically between 0.2 and 0.5 although positive correlations were higher on average. High correlations (>0.6) were only found in two small studies ($N < 40$). Dotted line shows histogram excluding these two studies.

11 years; Kuperman et al., 1996; Clarke et al., 1998, 2001a,b,c,d, 2002a,b,c,d,e,f, 2003, 2006, 2007, 2008b, 2011, 2013, 2016; Bresnahan et al., 1999; Swartwood et al., 2003; Hermens et al., 2005a,b,c; Magee et al., 2005; Hobbs et al., 2007; Fonseca et al., 2008, 2013; Barry et al., 2009a,b, 2010; Sohn et al., 2010; Dupuy et al., 2011, 2013, 2014a,b; Lansbergen et al., 2011; Ogrim et al., 2012; Shi et al., 2012; Liechti et al., 2013; Buyck and Wiersema, 2014a,b, 2015; Poil et al., 2014; Tye et al., 2014; Kitsune et al., 2015; Roh et al., 2015; Kamida et al., 2016; Kim et al., 2016; Thomas and Viljoen, 2016; Giertuga et al., 2017; Jarrett et al., 2017; Markovska-Simoska and Pop-Jordanova, 2017; Park et al., 2017; Rommel et al., 2017; Shephard et al., 2018) and 14 studied adults (average age of 33 years; Bresnahan et al., 1999, 2006; Bresnahan and Barry, 2002; Hermens et al., 2004; Clarke et al., 2008a; Koehler et al., 2009; van Dongen-Boomsma et al., 2010; Woltering et al., 2012; Liechti et al., 2013; Buyck and Wiersema, 2014a; Poil et al., 2014; Rommel et al., 2016; Markovska-Simoska and Pop-Jordanova, 2017; Tombor et al., 2018). Five of these studies included both adults and children as participant groups (Bresnahan et al., 1999; Liechti et al., 2013; Buyck and Wiersema, 2014a; Poil et al., 2014; Markovska-Simoska and Pop-Jordanova, 2017). Above and beyond DSM or ICD in these studies, diagnosis for ADHD was most typically performed using the Conners' Parent Rating Scale (CPRS; Conners et al., 1998), the Child Behavior Checklist (CBCL; Achenbach and Rescorla, 2001), the Wender Utah Rating Scale (WURS; Ward et al., 1993), Conners' Adult ADHD Rating Scales (CAARS; Conners and Sparrow, 1999) and Barkley's Semi-structured Interview for Adults with ADHD (Barkley, 2011; **Supplementary Table S2**).

The dominant results for all age groups and conditions are shown in **Figure 7A**. Overall as described above, the results for relative power in ADHD in children with eyes closed had very high consistency (7.0) and validation (2,516) scores. Absolute power for eyes closed was still reliable but less so, with a consistency score of 2.8 and validation score of 1,563. The eyes open condition had a consistency score of 2.8 and validation score of 460. On the other hand, studies in adults were substantially less consistent (consistency scores of 2.1 for eyes open and 1.1 for eyes closed for absolute power, and 2 for eyes open and 1.5 for eyes closed for relative power) and poorly validated (75–201 depending on condition). However, given that nearly half the studies reported for ADHD, particularly for children, came from a single research group (31 out of 65), we also show here the results when excluding this group

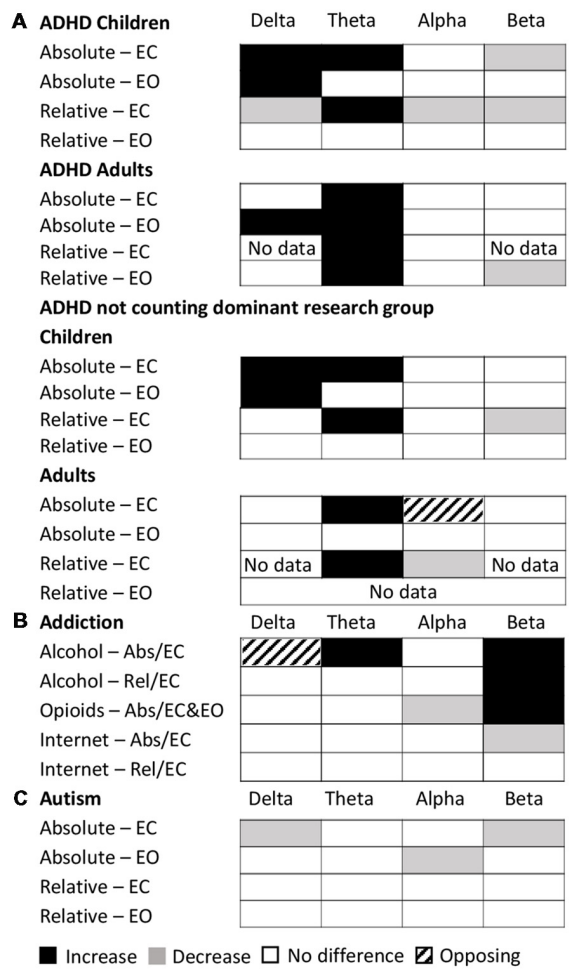

FIGURE 7 | Dominant results across conditions for specific disorders. **(A)** Dominant result for each band for ADHD for each of various conditions and age groups for both relative (rel) and absolute (abs) power and for eyes closed (EC) and eyes open (EO), including all studies (top) and excluding the dominant research group (bottom). White boxes indicate no change, black indicates an increase, and gray indicates a decrease. Opposing results are shown by hashed boxes. **(B)** Dominant result for each band for each type of addiction and condition. Legend as in **(A)**. **(C)** Dominant result for each band for autism for each condition. Legend as in **(A)**.

(**Figure 7A**, bottom). As can be seen, in the absence of this group the dominant result for both delta and theta increases for children remains, as does the decrease in beta activity for relative eyes closed for children, but there is a greater number of "no-significant difference" results overall for children. For adults, theta increases persist for absolute and relative eyes closed, but differences are observed for the other conditions and bands.

The following nine ADHD studies in children (absolute power; eyes closed) failed to see the decrease in the beta band (Clarke et al., 2001d; Hobbs et al., 2007; Fonseca et al., 2008; Liechti et al., 2013; Buyck and Wiersema, 2014b, 2015; Dupuy et al., 2014a; Kamida et al., 2016; Kim et al., 2016) whilst three further ADHD studies reported a decrease in beta in posterior regions but an increase in frontal regions (Clarke et al., 2002a, 2011; Hermens et al., 2005a). These inconsistencies could be due to differences in the methodological approach (see below) or demographic or clinical differences within the participant groups.

Overall, considering all studies, there is a reasonable confidence in the general trend reported in the results for children but not adults, particularly for relative power eyes closed. However, in all cases the magnitudes of difference were modest (∼28% for both absolute and relative power) and correlations with symptom severity were typically in the order of 0.3–0.4 for all bands (with the exception of Roh et al., 2015) which reported correlations between 0.6 and 0.7 across all bands and brain regions for a very small sample set). This indicates that overall results pertaining to frequency bands are not sufficiently discriminatory nor predictive of symptoms.

Given the reliable increase in theta and concomitant decrease in beta reported in children under the eyes closed condition, the theta/beta ratio had been proposed and approved by the FDA as a diagnostic biomarker for ADHD. However, the lack of consistency in adults suggests that these findings are likely age dependent and can perhaps not be extrapolated beyond the narrow age group studied. Furthermore, the general pattern of either an increase in theta or a decrease in beta is shared by a number of other disorders including OCD, schizophrenia and internet addiction suggesting that a reduced theta/beta ratio is a general marker for shared symptoms across a number of disorders rather than specific to the diagnosis of ADHD. However, we acknowledge that there are some studies which specifically examine the theta/beta ratio, without reporting results from individual spectral bands and therefore did not meet the inclusion criteria for this review (e.g., see Arns et al., 2013). Reported results relating to the theta/beta ratio may therefore be underreported in this review. For this we point the reader to a number of recent reviews and meta-analyses of EEG and ADHD, which have tried to detangle the pattern of EEG frequency band changes across studies (Barry et al., 2003; Snyder and Hall, 2006; Loo and Makeig, 2012).

Schizophrenia

A number of resting-state EEG studies have been conducted on patients with schizophrenia (vs. healthy controls) most often with eyes closed (although see Venables et al., 2009; Hanslmayr et al., 2013; Narayanan et al., 2014 for three eyes open studies). In total, 37 schizophrenia studies were identified for this review (Clementz et al., 1994; Sponheim et al., 1994; Wada et al., 1994; Omori et al., 1995; Pascual-Marqui et al., 1999; Begić et al., 2000; Harris et al., 2001; Knott et al., 2001a; Wuebben and Winterer, 2001; Mientus et al., 2002; Veiga et al., 2003; Kirino, 2004; Harris et al., 2006; Kirino, 2007; Knyazeva et al., 2008; Tislerova et al., 2008; John et al., 2009; Venables et al., 2009; Bandyopadhyaya et al., 2011; Begić et al., 2011; Itoh et al., 2011; Schug et al., 2011; Hong et al., 2012; Hanslmayr et al., 2013; Kam et al., 2013; Narayanan et al., 2014; Ranlund et al., 2014; Tikka et al., 2014; Andreou et al., 2015; Garakh et al., 2015; Goldstein et al., 2015; Kim et al., 2015; Mitra et al., 2015; Shreekantiah Umesh et al., 2016; Mitra et al., 2017; Moeini et al., 2017; Baradits et al., 2018). The median sample size was 63 (range 26–425),

with the average age of participants being 31 years old. As well as more conventional DSM/ICD measures, schizophrenia diagnosis and severity was typically assessed using the Positive and Negative Syndrome Scale (PANSS; Kay et al., 1987) and the Brief Psychiatric Rating Scale (BPRS; Overall and Gorham, 1962).

Schizophrenia showed consistent and reliable increases in the absolute delta and theta band power and decreases in the absolute alpha band power compared to controls with eyes closed (consistency scores of 2.2, reliability score 1,446). Furthermore, these differences were higher in magnitude relative to differences reported for other disorders (average theta increase of 50%, alpha decrease of 58%). The net result would be a higher theta/beta ratio compared to controls, very similar to ADHD in children. However, the three eyes open studies (Venables et al., 2009; Hanslmayr et al., 2013; Narayanan et al., 2014) showed a completely different pattern—an increase in theta, alpha and beta activity. Regional differences were also observed in a handful of studies in the delta (Begić et al., 2000) and alpha (Omori et al., 1995; Kim et al., 2015) bands where there was a frontal-posterior split with frontal increases and posterior decreases for alpha and the opposite pattern in the delta band. In addition, we found only three studies (Kirino, 2004, 2007; John et al., 2009) which measured relative changes in spectral power, the majority of which showed non-significant differences across all bands (although see John et al., 2009).

Depression

Eighteen depression studies were identified for this review (Kwon et al., 1996; Bruder et al., 1997; Bell et al., 1998; Debener et al., 2000; Knott et al., 2001b; Pizzagalli et al., 2002; Deldin and Chiu, 2005; Morgan et al., 2005; Bruder et al., 2008; Korb et al., 2008; Price et al., 2008; Grin-Yatsenko et al., 2009; Kemp et al., 2010; Begić et al., 2011; Jaworska et al., 2012; Cook et al., 2014; Arns et al., 2015; Slobodskoy-Plusnin, 2018). The median sample size was 55 (range 21–1344) with the average age of participants being 39 years old. Beyond more conventional DSM/ICD measures, depression diagnosis and severity was most typically measured using the Hamilton Rating Scale for Depression (HAM-D; Hamilton, 1960).

The dominant result for depression was an increase in the absolute power in both theta and beta bands for both eyes open and eyes closed conditions (eyes closed consistency 1.8, validation 880; eyes open consistency 2.0, validation 337) with average magnitudes of 48%. However, these increases were no longer visible when considering relative power where most studies failed to find any significant differences across any band (Knott et al., 2001b; Morgan et al., 2005; Korb et al., 2008; Cook et al., 2014). The largest study (Arns et al., 2015) consisting of 1,344 participants showed increases in theta power across frontal regions of the brain using the eLORETA source localized signal which is methodologically different from most other depression studies identified for this review which perform their analysis in electrode space.

Addiction

Here, we focus on three major types of addiction: opioids, alcohol and the internet and identified 16 addiction studies in this review. The median sample size was 45 (range 28–614), with the average age of participants being 33 years old. Beyond more conventional DSM/ICD measures, diagnosis and severity of internet addiction was most typically performed using the Young's Internet Addiction Test (IAT; Young, 1998), whilst alcohol and opioid addiction were assessed using a variable set of questionnaires depending on the study.

Surprisingly, despite the enormous attention to opioid addiction by both media and government, particularly in the United States, only four resting-state EEG studies (Wang et al., 2015b, 2016; Motlagh et al., 2017; Zhao et al., 2017) were identified for this review based on our inclusion criteria (for other reviews, see Wang et al., 2015a; Ieong and Yuan, 2017). In addition, nine alcohol addiction (Günther et al., 1997; Bauer, 2001; Rangaswamy et al., 2002, 2006; Saletu-Zyhlarz et al., 2004; Fein and Allen, 2006; Andrew and Fein, 2010; Son et al., 2015; Herrera-Díaz et al., 2016) and four internet addiction (Choi et al., 2013; Lee et al., 2014; Son et al., 2015; Kim et al., 2017) studies were identified for this review (includes one publication which examined both alcohol and internet addiction in the same study). It is important to acknowledge that addiction is a heterogeneous label encompassing multiple "types" of addictive disorder, and that the similarities and differences in the underlying etiologies between substance addiction and internet addiction are still not well defined. However, with the recent inclusion of gaming addiction in the 11th Revision of the International Classification of Diseases (ICD-11)[6], we have included internet addiction alongside substance addiction disorders for interest and comparison.

The dominant result across all addictions and conditions was one of no significant difference in all bands of the power spectrum except beta which showed an increase for opioid and alcohol addiction and a decrease for internet addiction (**Figure 7B**). In addition, there was an increase in theta power for alcohol addiction, and a decrease in alpha power for opioid addiction. Even where significant differences were reported, the magnitudes were small (15%–27%). While internet addiction had a high consistency score of 4, all four studies came from the same research group. Alcohol addiction had a consistency score of 2.25 while the studies for opioid addiction were too few in each condition to calculate a consistency score. Overall, across all addictions, the validation scores ranged (from 35 to 753 depending on addiction type and condition). Given the small number of studies and high methodological variability, dependable conclusions cannot yet be drawn. However, as it stands, other than for the beta band, the power spectrum appears essentially unaffected in any consistent and reliable way by addiction.

OCD

Ten OCD studies were identified (all eyes closed) for this review (Molina et al., 1995; Tot et al., 2002; Karadag et al., 2003; Bucci et al., 2004; Pogarell et al., 2006; Velikova et al., 2010; Kopřivová et al., 2011, 2013; Olbrich et al., 2013; Kamaradova et al., 2016) with an median sample size of 61.5 (range 26–100).

[6]http://www.who.int/features/qa/gaming-disorder/en/

The average age of participants was 32 years old. Five of these studies analyzed spectral power in the source localized signal (Velikova et al., 2010; Kopřivová et al., 2011, 2013; Olbrich et al., 2013; Kamaradova et al., 2016), however source localized results were not substantially different from non-source localized studies. Beyond more conventional DSM/ICD measures, OCD diagnosis and severity was typically performed using the Yale-Brown Obsessive Compulsive Scale (Y-BOCS; Goodman et al., 1989).

Like ADHD (in children) and schizophrenia, the dominant pattern was an increase in the delta and theta bands (average increases of ∼27 and 36% for absolute and relative power respectively) and a decrease in the alpha band (average decrease of 41%). Further this pattern had a high consistency score of 3.3 and a validation score of 231 for absolute power. On the other hand, relative power was highly inconsistent (score 2) and poorly validated (score 104).

OCD is often comorbid with other mental disorders and therefore the pattern of EEG frequency band differences is unlikely to reflect changes that are purely attributable to OCD. There may also be overlap in symptoms with ADHD (Abramovitch et al., 2015) and schizophrenia (Cunill et al., 2009).

PTSD

Thirteen studies with patients with PTSD (Begić et al., 2001; Jokić-Begić and Begić, 2003; Ehlers et al., 2006; Rabe et al., 2006; Veltmeyer et al., 2006; Falconer et al., 2008; Shankman et al., 2008; Kemp et al., 2010; Todder et al., 2012; Wahbeh and Oken, 2013; Imperatori et al., 2014; Clancy et al., 2017), and with individuals who have suffered significant early life stress (McFarlane et al., 2005), were identified for this review. The median sample size was 74 (range 20–407), with the average age of participants being 40 years old. In addition to conventional DSM/ICD measures, PTSD diagnosis and severity was most typically performed using the Clinician-Administered PTSD Scale (CAPS; Blake et al., 1995).

The majority of eyes closed studies indicate no significant differences in spectral bands between PTSD patients and controls with a reasonable consistency score of 2.4 for absolute power. When differences were reported, they suggest a decrease in all bands in the disorder group for eyes open conditions, and both increases and decreases for eyes closed conditions. However, in most of these studies while "significant" effects are stated, specific numbers pertaining to the magnitude are not reported making it difficult to evaluate.

Autism

Seventeen studies with patients with autism or ASD were identified for this review (Dawson et al., 1995; Sutton et al., 2004; Chan and Leung, 2006; Chan et al., 2007; Orekhova et al., 2007; Stroganova et al., 2007; Coben et al., 2008; Burnette et al., 2011; Mathewson et al., 2012; Sheikhani et al., 2012; Tierney et al., 2012; Machado et al., 2015; Maxwell et al., 2015; van Diessen et al., 2015; Jaime et al., 2016; Kozhushko et al., 2018; Lefebvre et al., 2018). These have primarily been conducted with children with the average age of participants (children) being 8.5 years old (but see Mathewson et al., 2012 for an example of a study with adults, and not included in the trend analysis). The median sample size was 56 (range 25–156). Beyond more conventional DSM/ICD measures, autism diagnosis and severity was typically performed using Autism Diagnostic Interview-Revised (ADI-R; Lord et al., 1994), the Autism Diagnostic Observation Schedule (ADOS; Lord et al., 1989) and the Social Communication Questionnaire (SCQ; Rutter and Lord, 2003).

Overall autism showed little or no significant difference in the majority of bands (with the exception of delta and beta eyes closed and alpha eyes open; **Figure 7C**). However, the results for autism are highly inconsistent (consistency scores all below 2), and no general pattern can be inferred.

Other Disorders

Other disorders such as bipolar disorder (Clementz et al., 1994; El-Badri et al., 2001; Başar et al., 2012; Kam et al., 2013; Narayanan et al., 2014; Moeini et al., 2015), anxiety (Sachs et al., 2004; Oathes et al., 2008; Xing et al., 2017) and panic disorder (Knott et al., 1996; Gordeev, 2008; Wise et al., 2011; de Carvalho et al., 2015) are included here for completeness. However generally there was no more than one or two studies for any one condition (eyes closed, eyes open, relative power, absolute power), which was too few for the inference of any trends or for the calculation of consistency scores. Nonetheless we show these results as part of our table with the caveat that they are generally poorly validated.

Summary

In summary, differences reported for ADHD in children stood out as being the most consistent and validated, although published results were dominated by a single research group. The trends for schizophrenia could be considered as the next most reliable with a trend similar to ADHD in children. Others such as OCD, depression and internet addiction are moderately reliable while the results for other disorders or conditions are either too sparse or inconsistent to be considered reliable.

Methodological Challenges and Limitations

One considerable challenge when reviewing the literature is the range of methodologies employed that result in difficulties comparing one study to another. Here, we outline the differences in participant selection, EEG recording and analysis that could impact the results reported in this review.

Several sets of EEG guidelines have been published over the years, including guidelines from the American Clinical Neurophysiological Society[7] as well as from other published studies (e.g., Pivik et al., 1993; Roach and Mathalon, 2008; Keil et al., 2013; Webb et al., 2015). These discuss the various factors that need to be considered when choosing which EEG parameters to use. For example, Keil et al. (2013), emphasize the multitude of parameters which can influence the transformation of the power spectrum and highlight the importance of noting the parameters that influence the final reported outcome. For example, in relation to the Fourier transform, they state that "Researchers... should indicate the

[7] https://www.acns.org/practice/guidelines

type, size, and overlap of the window functions used," reminding researchers that "When using commercial software, it is not sufficient to indicate that the spectrum was calculated using a particular software package." However, when looking across the 184 resting-state EEG studies identified for this review it is apparent that there is very poor compliance to many of these standardization recommendations. For example, several studies in this review, simply state that the data was transformed by FFT without providing any further details of the parameters used. This lack of standards presents a general confound for the field that extends beyond the implications for this particular review.

Study Size, Composition and Controls

The sample size of studies varies between n = 20 and n = 1,344 with three quarters of studies based on less than 100 participants. The median is 60 (**Figure 1**) with similar numbers of controls and patients in the majority of studies. For most studies the age of participants were adults in the range of 25–45.

Interestingly most of the studies in this review were skewed towards male participants (64% compared to 36% female). This pattern is found for all disorders except for depression, bipolar disorder, panic disorder, anxiety and OCD (where the % of females ranged from 55% to 68%). The largest gender disparity is seen for ADHD (72% M/28% F), schizophrenia (67% M/33% F), autism (78% M/22% F) and addiction (70% M/30% F). In addition, it was more common to study all-male participant groups (20% of studies) compared to all-female participants (4% of studies). In some instances, the ratio of males to females was intentionally designed to reflect the relative proportions of sufferers in the general population, but at other times was a reflection of participant availability, limiting the generalizability of these results, especially towards the female population.

There is substantial variability in the EEG both across and within normal individuals that has been reported in the literature (Haegens et al., 2014) that can relate to various factors from task performance (Arazi et al., 2017a,b) to age (Voytek et al., 2015; Hashemi et al., 2016) and socioeconomic factors (Parameshwaran and Thiagarajan, 2017a,b,c). Furthermore, there is a great deal of intra person variability that can arise both naturally and with ingestion of common substances such as caffeine (Kelly et al., 2008; Foxe et al., 2012; Gonen-Yaacovi et al., 2016) and alcohol (Korucuoglu et al., 2016). Only a handful of studies considered inter person variability, relationship to age or intra person variability in their analysis (e.g., see Debener et al., 2000; Chan and Leung, 2006). One study (autism) which did monitor intrapersonal variability by conducting two testing sessions 3 months apart found that amplitudes of theta, alpha and beta significantly differed for patients (but not controls) between the two sessions, although only alpha, and the theta/beta ratio remained significantly different after correction for familywise errors (Chan and Leung, 2006). In addition, the small sample sizes make it challenging to tease out effects of age and normal individual variability from those related to psychiatric symptoms.

ADHD provides an example of studies focused separately on adults and children. The stark difference between the results of these two groups points to changes over the lifespan and it is conceivable that similar studies in the elderly may produce different results still. Without controlling for normal variability and change across the lifespan, it is difficult to know whether these changes are due to the clinical evolution of ADHD, or reflect independent age-related maturation of the EEG.

Clinical Groups and Assessment

Ten different disorder types were included in this review. These were selected as being the most dominant mental health disorders in the population. Due to the wide scope of our review, we acknowledge that we may have missed some studies for the disorder types of interest. Age-related disorders such as dementia were not included in this review as they were considered to reflect a different aspect of brain health.

From a clinical perspective, participants were typically recruited based on screening with DSM or ICD criteria for diagnosis, complemented by additional screening questionnaires. However, a handful of studies relied purely on screening questionnaires. The study participants also varied according to whether the clinical group was unmedicated (70%), defined as naïve or temporarily abstaining from taking medication for a variable length of time (12 h to 3 months) depending on the type of drug, medicated (5%) or included a mix of medicated and unmedicated patients (25%). Furthermore, although the majority of studies had specific inclusion and exclusion criteria, only a minority of studies specifically mention that they excluded patients with comorbidities, or specifically outlined the comorbidities in their patient group. The results from a particular disorder may therefore be influenced by other clinical comorbidities. Finally, the studies typically only report on spectral differences between groups and only 27% of studies provide insight into the relationship between the severity of the symptom score from the diagnosis questionnaires and the spectral bands.

Recording Configuration

A significant confound in the EEG space is the lack of standardization of hardware configurations and, in particular, the wide variety of different reference types used. Most common are linked ears (34%), average referencing (23%) and mastoids (15%). However, earlobes (14%), Cz (4%) and the nose (4%) are also used. The type of referencing used has a significant impact on the reported results, from the PSD and source localization (Trujillo et al., 2017) to functional connectivity (Huang et al., 2017) and various other aspects (e.g., Qin et al., 2010; Lei and Liao, 2017).

In addition, although the majority of studies covered the entire scalp, some studies chose to focus on midline sites. Only a proportion of studies reported results from individual electrodes (32%), with the majority choosing to focus on broad scalp regions (60%). In addition, some studies calculated the power spectrum using source localization techniques (e.g., LORETA) which may have resulted in a different regional profile from those studies focusing on the location of the electrodes on the scalp.

TABLE 2 | Summary of frequency band parameters.

	% of Publications	Typical range (Hz)	Minimum start value (Hz)	Maximum end value (Hz)
Delta	70	1.3–3.5	0	6
Theta	84	4–7.5	2.5	8
Alpha	85	8–13	6	14
Beta	80	12.5–30	12	50
Gamma	18	30–40	20	100

Processing of the Signal

The length of recordings was fairly consistent with a median of 5 min. However, often this entire recording window is not used but is divided up into artifact free segments that are epoched before the FFT computation is applied. The epoch length used for the FFT transform displays considerable variability (from 0.5 s to 600 s) with a median of 2.5 s. This variability is of concern as this can impact the window length utilized in the FFT algorithm and therefore the spreading or leakage across frequencies.

There are also inconsistencies in the methods used for identification of artifacts. This is sometimes done with methods such as Independent Component Analysis (ICA; Makeig et al., 1996; Vigário, 1997; Vigário et al., 2000; Jung et al., 2003) but many other techniques exist and many still use a manual or visually determined approach which can be highly inconsistent from "expert" to "expert" (see Urigüen and Garcia-Zapirain, 2015; Islam et al., 2016). These can result in substantial differences in the signal and therefore the spectral results.

The method used to determine the spectrum and different normalizations are another aspect of variability that can impact the magnitude of differences. There are presently a wide variety of software packages, algorithms and parameters used for computing the power spectrum. Software packages and functions include MATLAB/EEGLab Brainwave, Cadwell, sLORETA, eLORETA, RHYTHM, Neuroscan, Neuroguide, NXLink, Brain Vision Analyzer, Neurospeed, Persyst. While the FFT functions in these packages are roughly similar they do have differences in their default settings, and in some software the parameters used in the algorithm are not exposed and therefore not reported. Each function (for example spectrogram; pwelch algorithm; psd function; FFT function in MATLAB) further differ in their default settings with respect to the way the window length is selected, the overlap (here the studies range from 0 to 80%) and averaging (e.g., Bartlett or Welch method), and the windowing function used (e.g., Hamming or Hanning Window). All of these can make the difference between a small "significant" difference vs. a negative result (Keil et al., 2013). In addition, several studies did not provide any details about the parameters used, making it difficult to make a complete assessment of the consistency of methods in the field.

Finally, some studies report the differences in the absolute power and others report relative power which can also result in different outcomes, as we have seen above. However, as not all studies specifically mentioned whether they used absolute or relative power, for 29% of studies we had to infer which one was used.

Frequency Band Definition

Last, and perhaps most significant, there is a great deal of variability and confusion as to the specific frequency range that defines each band (**Table 2**). We show the more frequently used range as well as the entire range of definitions found in the reviewed literature in **Figure 8**. While alpha and theta were more consistent, delta could start anywhere from 0 Hz to 2 Hz and end anywhere from 3.5 Hz to 6 Hz. Meanwhile, beta could begin anywhere between 12 Hz and 15 Hz and end anywhere between 20 Hz and 50 Hz. Across all bands the most frequently used range was found in only 30- 50% of studies depending on the particular band. What one publication means by "delta," or "beta" (etc.) is therefore not necessarily the same as what another publication means by the same terminology.

Some of these differences arise on account of hardware configurations which apply different band pass filtering of the signal during preprocessing, forcibly defining the ranges and definition of the delta and gamma bands. Filters applied to resting state EEG data typically vary from 0.1 Hz to 1 Hz at the lower end to 40–100 Hz at the upper end. In addition, notch filters are often applied at 50 Hz and/or 60 Hz to filter out AC line noise.

Such differences in definition have enormous consequences for interpretation. Indeed, it's conceivable that differences reported may disappear when moving the band windows slightly. Thus, the considerable variability and overlapping definitions across studies greatly diminishes the value of using the terminology of macro bands.

Reporting Omissions

One limitation of the literature was the possible bias towards positive results. For example, some studies did not include results for all bands specified in the methods. This could result in a number of unreported non-significant results that skew our

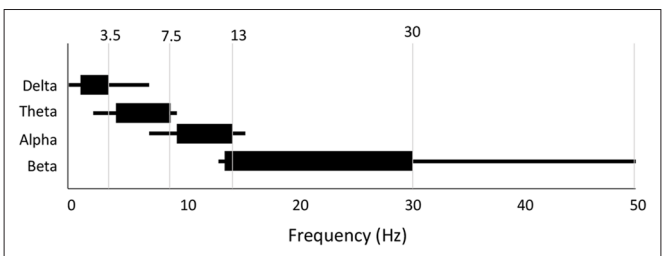

FIGURE 8 | Variability in frequency band definition. Range of frequencies used for each band across all 184 studies. Thick line indicates most commonly used range.

analysis, particularly in the less frequently reported delta and beta bands.

Another inadequacy of this review relates to the sparse reporting of magnitudes of power change. Magnitude changes were calculated where the information was readily available, which was only in 40% of studies. The consequence of this is that the magnitude estimations are only based on a subset of studies, and do not necessarily reflect the complete picture. This is especially the case for ADHD (children) and OCD where the availability of magnitude data was considerably lower. In addition, this incomplete reporting of magnitudes across studies, and across individual electrodes also makes it challenging to study regional differences in spectral power in a consistent manner.

In summary, there are a number of dimensions of methodological variability and omissions that form limitations for this review and the field in general.

DISCUSSION

Our review describes reported differences in bands of the EEG power spectrum between controls and those with various psychiatric disorders including ADHD, schizophrenia, depression, bipolar disorder, anxiety, panic disorder, autism, PTSD, OCD and addiction. Across all disorders and conditions however, there was a wide range of often contradictory results for each frequency band (delta, theta, alpha, beta, gamma), although one result typically dominated. When considering the dominant results, the pattern that emerged is a tendency for higher levels in the low frequency bands (delta and theta) coupled with lower levels in the higher frequency bands (alpha, beta, gamma) across one group of disorders (ADHD, schizophrenia and OCD) relative to controls, and little to no difference in the power spectrum for others (addiction, PTSD and autism). Significant differences in this second set, when reported, were most often decreases in the higher frequency bands. Depression stood out as having a different pattern—an increase across the entire spectrum.

Across all disorders and conditions, the number of studies reporting the dominant result was on average 2.2 times the number of studies reporting other results and was similar across bands. In general, the eyes closed condition delivered more consistent results than the eyes open. Furthermore, while absolute power was most commonly reported, results were more consistent across studies for relative power. Across disorders and conditions, the validation score, a measure of how many participants and studies, on average, delivered the dominant result, was less than 250 for the majority of disorders. ADHD in children with eyes closed stood out as being by far the most studied and consistent in result, while schizophrenia, alcohol addiction, depression and PTSD with eyes closed followed by a substantial lag in being the next most reported and consistent in the literature. However, it is important to note that the majority of the ADHD (children) studies identified for this review were generated from a relatively small group of researchers (from the University of Wollongong) and the results from other research groups for ADHD are more variable. Other disorders and conditions were either too inconsistent or sparsely reported. The magnitude of significant results, when reported, was on average 34% across all bands and disorders for absolute power, and somewhat lower for relative power differences. Interestingly the magnitude of reported results was highest for schizophrenia (46%–53%) and lower than average for ADHD (11%–36%) and autism (11%–33%). Finally, the correlations between symptom severity and the power in any particular band was low for any brain regions reported and generally in the range of 0.3–0.5.

Implications of These Results

The extreme lack of standardization across the field raises a strong caution to any clinical interpretation or application of current findings. From a purely methodological perspective, it is important that standards are imposed and adhered to in the research community. Particularly, we emphasize the need to use a standardized definition for each frequency band, based on the most commonly used non-overlapping frequencies: (delta: <4 Hz; theta: 4–7.5 Hz; alpha: 7.5–12.5 Hz; beta: 12.5–30 Hz; gamma: 30–40 Hz). Standardization of power spectrum computation, and the comparison of relative as well as absolute power are also essential. Absolute power, which relates to amplitude or magnitude of the signal, is more influenced by factors such as skull thickness and head geometry which vary considerably across people (Hagemann et al., 2008). These factors may be mitigated by the normalization used for relative power. Second, the eyes open paradigm is highly variable as visual input and attention can vary across subjects during the course of the experiment, pointing to eyes closed as a more uniform condition.

However, the generally common pattern across multiple disorders is an indication that individual frequency bands or even a pattern across frequency bands does not serve as a useful measure of distinction between disorders. It also strongly makes the case that studying individual disorders in isolation can be very misleading. For instance, a higher theta/beta ratio is considered an indicator of ADHD in children and even approved as a diagnostic marker by the FDA[8]. However, a similarly higher theta/beta ratio would be likely for schizophrenia and OCD as well. Psychiatric disorders are generally a loose set of symptoms that may overlap across disorders and there may be additional symptom comorbidities that are not accounted for in studies. Consequently, analysis based on specific symptoms and symptom clusters may yield more specific insights. This is particularly important to consider in the context of biomarkers based on the power spectrum.

It is also important to note that the patterns described across disorders are at a group level. For example, theta power was on average 27% higher in children diagnosed with ADHD vs. a control group. However, there was still substantial overlap in values between the groups. Further, the correlation values between symptom severity and power were typically around 0.4. This means that differences in frequency bands are not particularly useful for diagnosis at an individual level. With the wide variation in the power spectrum across normal populations

[8]https://www.accessdata.fda.gov/cdrh_docs/reviews/K112711.pdf

and the lifespan (Haegens et al., 2014; Voytek et al., 2015; Hashemi et al., 2016; Arazi et al., 2017a,b; Parameshwaran and Thiagarajan, 2017a,b,c), it would be essential to look at larger sample sizes across multiple disorders, and with repeated recording sessions to control for both inter and intra person variability and parse out relationships to particular symptoms.

That said, in our view, these results along with the associated methodological concerns and limitations call for a new approach that goes beyond frequency bands to take into consideration new advances in our understanding of the power spectrum and new tools available for analysis.

From Frequency Bands to Integrated Views: A Way Forward?

The Fourier transform which is used to describe the power spectrum was invented as a method of resolving sinusoids of different frequencies—an application of tremendous value in radio transmission. The EEG however is not a simple superposition of sinusoids of various frequencies. The power spectrum therefore should not be interpreted as such.

The dominant structure of the EEG power spectrum has been shown to be a decreasing function with lower power at higher frequencies that approximates a $1/f^{\gamma}$ pattern (Pritchard, 1992; Voytek et al., 2015). This is seen at various levels from surface measurements with microelectrodes (local field potentials or LFPs; Thiagarajan et al., 2010) and surface electrocorticographs or ECoG (Gao, 2016). The implication is that there is an inverse relationship between frequency and power across the measurable range and as the frequency increases, the power decreases. The steepness with which the power drops off as the frequency gets higher is represented by the exponent γ. This $1/f^{\gamma}$ structure has an important implication—that there is an underlying relationship or temporal correlations between the frequencies such that individual frequencies are not independent of one another (Milotti, 2002). We note however, that the origin and mechanisms of this structure is still very much a subject of debate as a frequency dependent filtering effect arising from the measurement cannot be ruled out (Bédard et al., 2006, 2017). Thus, if the spectrum best fits a 1/f function, the power of any individual frequency or range of frequency can be estimated if the exponent of the decay is known.

That said, there can be deviations from the 1/f spectrum. The most common such deviation are peaks that rises above the 1/f envelope, particularly with the eyes closed. The harmonic around 10 Hz (in the alpha range) is most commonly encountered, although it can sometimes occur at other frequencies and can be visualized in the autocorrelation of the signal. The presence of an alpha oscillation or harmonic peak is a feature that is distinct from the underlying 1/f envelope and should therefore be considered separately from the underlying envelope.

Specifically, we suggest reporting of metrics relating to the power spectrum in its entirety and identifying ways of identifying and separating periodicity from the 1/f background. There are a number of ways in which this can be done. The most obviously useful metric is estimation of the 1/f exponent γ (Voytek et al., 2015). This provides a consolidated view of the differences across bands and can be used to compute the difference between any two frequencies if desired. The 1/f decay exponent is best estimated in the range of 2–30 Hz where baseline drifts, line noise and distortions introduced by band pass filters have the least impact. Second, goodness of fit or other metrics that provide insight into deviations from the 1/f structure would also be informative. Recently new metrics have been proposed to provide a view into the degree of periodicity in different bands (Haller et al., 2018) and the harmonic component of the alpha band separately from the background envelope (Parameshwaran and Thiagarajan, 2017c). However, even while deeper views of the power spectrum could potentially provide better discrimination between disorders, this does not negate the impact of a lack of standardization in EEG measurement and methods used for signal preprocessing and computation of the power spectrum itself.

Beyond the Power Spectrum

While there are ways to substantially improve our understanding of spectral properties in the context of psychiatric disorders, it is important to acknowledge that the power spectrum itself is a very general feature of the signal with few degrees of freedom. As we have seen it does not show significant difference across several disorders (autism, addiction, PTSD) and is not a reliable predictor of outcomes on an individual level (as shown by similarities of change across multiple disorders). Thus, on its own, it is not likely to provide fundamental discriminatory power between disorder types. Spatial views such as spectral coherence and hemispheric asymmetry can extend the scope of the spectral approach. However, spectral decomposition and spectral filtering by definition disregard relative phase information which may provide important discriminatory perspective.

The power spectrum might be thought of as analogous to describing a picture in terms of its color spectrum, or the relative distribution of red, blue and green pixels. While the color spectrum of an image can provide some general suggestion of the content of a picture (for example, higher blue on average means more sky, an increase in green means more nature), it loses all the relative spatial information that tells you what the picture actually is. The EEG power spectrum similarly loses relative temporal information, which at a more general level is one of the main advantages of EEG signal processing over other methods such as fMRI. Further, given that spectral decomposition is not instantaneous and utilized blocks of signal, and spectral filtering can distort the signal (Vanrullen, 2011; Acunzo et al., 2012; Rousselet, 2012; Widmann and Schröger, 2012), views such as spatial coherence are also limited in terms of their temporal resolution and insight into relative phase information. Using the same analogy of color, one might think of coherence, for example, as analogous to comparing the spatial positions of pixels in one narrow range of colors between successive image frames after some spatial blurring, while disregarding all the others.

We therefore suggest that more discriminating insights into differences between disorders are likely to be found in metrics that probe the temporal structure of the EEG signal as well as in novel connectivity measures. Numerous metrics have been proposed including various methods of assessing the entropy of

the signal (Sabeti et al., 2009; Liang et al., 2015) and temporal memory (Jospin et al., 2007; Hardstone et al., 2012; Márton et al., 2014). However, this is a continually evolving field where new analytical tools are regularly being trialed. These should be increasingly embraced by EEG researchers involved in resting-state research who are looking to shift their approach away from spectral bands towards other potential methods which may offer greater clinical opportunities, applying these tools to their future and past datasets.

A Call for Data Sharing and Sharable Analytical Pipelines

Finally, whether performing spectral analysis or exploring the signal using other methodologies, the primary issues are common. First, a lack of standardization of preprocessing steps and parameter choices within algorithms can result in a diversity of results that preclude easy comparison, and even appear contradictory. Second, small datasets limit the ability to determine meaningful results given the large diversity of human EEG dynamics. Consequently, we call for a concerted effort by the field to participate in open data efforts by sharing their raw data, and for those with analytical toolkits and analysis pipelines to make them available for the community. We emphasize the importance of sharing raw rather than preprocessed data given the numerous differences in preprocessing methodologies. We also emphasize the need for providing clear descriptions of the recording parameters such as the referencing, sampling rate and electrode characteristics.

While well-established databases specific for EEG are not yet available as they are for fMRI (e.g., openNeuro) some options presently exist and new ones are in development. For example, data can be shared in public repositories such as the National Institute of Mental Health Data Archive (NDA)[9], Physionet[10] and Zenodo[11] or in the open EEG-specific database Brainbase which is presently in development (Thiagarajan, 2017). Similarly, open toolkits such as EEGLAB (MATLAB) and MNE (Python) are already available but complete pipelines are only now being established or are in development. In the meantime, tools can be shared on Github and other repositories and this should be made known through clear referencing in publications.

AUTHOR CONTRIBUTIONS

JN performed the literature search and discussed the results with TT. TT drafted the manuscript. TT and JN revised the manuscript, approved the final version, and agreed to be accountable for all aspects of the work.

FUNDING

This work was supported by internal funding from Sapien Labs.

SUPPLEMENTARY MATERIAL

The Supplementary Material for this article can be found online at: https://www.frontiersin.org/articles/10.3389/fnhum.2018.00521/full#supplementary-material

[9]https://data-archive.nimh.nih.gov/
[10]https://www.physionet.org/
[11]https://zenodo.org/

REFERENCES

Abramovitch, A., Dar, R., Mittelman, A., and Wilhelm, S. (2015). Comorbidity between attention deficit/hyperactivity disorder and obsessive-compulsive disorder across the lifespan: a systematic and critical review. *Harv. Rev. Psychiatry* 23, 245–262. doi: 10.1097/HRP.0000000000000050

Achenbach, T. M., and Rescorla, L. A. (2001). *Manual for the ASEBA School-Age Forms and Profiles: An Integrated System of Mult-Informant Assessment.* Burlington: University of Vermont, Research Center for Children, Youth and Families.

Acunzo, D. J., MacKenzie, G., and van Rossum, M. C. W. (2012). Systematic biases in early ERP and ERF components as a result of high-pass filtering. *J. Neurosci. Methods* 209, 212–218. doi: 10.1016/j.jneumeth.2012.06.011

Andreou, C., Nolte, G., Leicht, G., Polomac, N., Hanganu-Opatz, I. L., Lambert, M., et al. (2015). Increased resting-state Gamma-band connectivity in first-episode schizophrenia. *Schizophr. Bull.* 41, 930–939. doi: 10.1093/schbul/sbu121

Andrew, C., and Fein, G. (2010). Induced theta oscillations as biomarkers for alcoholism. *Clin. Neurophysiol.* 121, 350–358. doi: 10.1016/j.clinph.2009.11.080

Arazi, A., Censor, N., and Dinstein, I. (2017a). Neural variability quenching predicts individual perceptual abilities. *J. Neurosci.* 37, 97–109. doi: 10.1523/JNEUROSCI.1671-16.2016

Arazi, A., Gonen-Yaacovi, G., and Dinstein, I. (2017b). The magnitude of trial-by-trial neural variability is reproducible over time and across tasks in humans. *eneuro* 4:ENEURO.0292-17.2017. doi: 10.1523/ENEURO.0292-17.2017

Arns, M., Conners, C. K., and Kraemer, H. C. (2013). A decade of EEG theta/Beta ratio research in ADHD: a meta-analysis. *J. Atten. Disord.* 17, 374–383. doi: 10.1177/1087054712460087

Arns, M., Etkin, A., Hegerl, U., Williams, L. M., DeBattista, C., Palmer, D. M., et al. (2015). Frontal and rostral anterior cingulate (rACC) theta EEG in depression: implications for treatment outcome? *Eur. Neuropsychopharmacol.* 25, 1190–1200. doi: 10.1016/j.euroneuro.2015.03.007

Bandyopadhyaya, D., Nizamie, S. H., Pradhan, N., and Bandyopadhyaya, A. (2011). Spontaneous γ coherence as a possible trait marker of schizophrenia—An explorative study. *Asian J. Psychiatr.* 4, 172–177. doi: 10.1016/j.ajp.2011.06.006

Baradits, M., Kakuszi, B., Bálint, S., Fullajtár, M., Mód, L., Bitter, I., et al. (2018). Alterations in resting-state γ activity in patients with schizophrenia: a high-density EEG study. *Eur. Arch. Psychiatry Clin. Neurosci.* doi: 10.1007/s00406-018-0889-z [Epub ahead of print].

Barkley, R. A. (2011). *Barkley Adult ADHD Rating Scale-IV (BAARS-IV).* New York, NY: Guilford Press.

Barry, R. J., Clarke, A. R., Hajos, M., McCarthy, R., Selikowitz, M., and Bruggemann, J. M. (2009a). Acute atomoxetine effects on the EEG of children with Attention-Deficit/Hyperactivity Disorder. *Neuropharmacology* 57, 702–707. doi: 10.1016/j.neuropharm.2009.08.003

Barry, R. J., Clarke, A. R., Johnstone, S. J., McCarthy, R., and Selikowitz, M. (2009b). Electroencephalogram θ/β ratio and arousal in attention-deficit/hyperactivity disorder: evidence of independent processes. *Biol. Psychiatry* 66, 398–401. doi: 10.1016/j.biopsych.2009.04.027

Barry, R. J., Clarke, A. R., Hajos, M., McCarthy, R., Selikowitz, M., and Dupuy, F. E. (2010). Resting-state EEG gamma activity in children with Attention-Deficit/Hyperactivity Disorder. *Clin. Neurophysiol.* 121, 1871–1877. doi: 10.1016/j.clinph.2010.04.022

Barry, R. J., Clarke, A. R., and Johnstone, S. J. (2003). A review of electrophysiology in attention-deficit/hyperactivity disorder: I. Qualitative and quantitative

electroencephalography. *Clin. Neurophysiol.* 114, 171–183. doi: 10.1016/s1388-2457(02)00362-0

Başar, E., Güntekin, B., Atagün, İ., Turp Gölbaşı, B., Tülay, E., and Özerdem, A. (2012). Brain's alpha activity is highly reduced in euthymic bipolar disorder patients. *Cogn. Neurodyn.* 6, 11–20. doi: 10.1007/s11571-011-9172-y

Bauer, L. (2001). Predicting relapse to alcohol and drug abuse via quantitative electroencephalography. *Neuropsychopharmacology* 25, 332–340. doi: 10.1016/S0893-133X(01)00236-6

Bédard, C., Gomes, J.-M., Bal, T., and Destexhe, A. (2017). A framework to reconcile frequency scaling measurements, from intracellular recordings, local-field potentials, up to EEG and MEG signals. *J. Integr. Neurosci.* 16, 3–18. doi: 10.3233/JIN-160001

Bédard, C., Kröger, H., and Destexhe, A. (2006). Does the 1/f frequency scaling of brain signals reflect self-organized critical states? *Phys. Rev. Lett.* 97:118102. doi: 10.1103/PhysRevLett.97.118102

Begić, D., Hotujac, L., and Jokić-Begić, N. (2000). Quantitative EEG in "positive" and "negative" schizophrenia. *Acta Psychiatr. Scand.* 101, 307–311. doi: 10.1111/j.1600-0447.2000.tb10930.x

Begić, D., Hotujac, L., and Jokić-Begić, N. (2001). Electroencephalographic comparison of veterans with combat-related post-traumatic stress disorder and healthy subjects. *Int. J. Psychophysiol.* 40, 167–172. doi: 10.1016/s0167-8760(00)00153-7

Begić, D., Popović-Knapić, V., Grubišin, J., Kosanović-Rajačić, B., Filipčić, I., Telarović, I., et al. (2011). Quantitative electroencephalography in schizophrenia and depression. *Psychiatr. Danub.* 23, 355–362.

Bell, I. R., Schwartz, G. E., Hardin, E. E., Baldwin, C. M., and Kline, J. P. (1998). Differential resting quantitative electroencephalographic—patterns in women with environmental chemical intolerance, depressives and normals. *Biol. Psychiatry* 43, 376–388. doi: 10.1016/s0006-3223(97)00245-x

Berger, H. (1929). Über das elektrenkephalogramm des menschen. *Arch. F. Psychiat.* 87, 527–570. doi: 10.1007/BF01797193

Blake, D. D., Weathers, F. W., Nagy, L. M., Kaloupek, D. G., Gusman, F. D., Charney, D. S., et al. (1995). The development of a clinician-administered PTSD scale. *J. Trauma. Stress* 8, 75–90. doi: 10.1002/jts.2490080106

Bresnahan, S. M., and Barry, R. J. (2002). Specificity of quantitative EEG analysis in adults with attention deficit hyperactivity disorder. *Psychiatry Res.* 112, 133–144. doi: 10.1016/s0165-1781(02)00190-7

Bresnahan, S. M., Anderson, J. W., and Barry, R. J. (1999). Age-related changes in quantitative EEG in attention- deficit/hyperactivity disorder. *Biol. Psychiatry* 46, 1690–1697. doi: 10.1016/s0006-3223(99)00042-6

Bresnahan, S. M., Barry, R. J., Clarke, A. R., and Johnstone, S. J. (2006). Quantitative EEG analysis in dexamphetamine-responsive adults with attention-deficit/hyperactivity disorder. *Psychiatry Res.* 141, 151–159. doi: 10.1016/j.psychres.2005.09.002

Bruder, G. E., Fong, R., Tenke, C. E., Leite, P., Towey, J. P., Stewart, J. E., et al. (1997). Regional brain asymmetries in major depression with or without an anxiety disorder: a quantitative electroencephalographic study. *Biol. Psychiatry* 41, 939–948. doi: 10.1016/S0006-3223(96)00260-0

Bruder, G. E., Sedoruk, J. P., Stewart, J. W., McGrath, P. J., Quitkin, F. M., and Tenke, C. E. (2008). Electroencephalographic alpha measures predict therapeutic response to a selective serotonin reuptake inhibitor antidepressant: pre- and post-treatment findings. *Biol. Psychiatry* 63, 1171–1177. doi: 10.1016/j.biopsych.2007.10.009

Bucci, P., Mucci, A., Volpe, U., Merlotti, E., Galderisi, S., and Maj, M. (2004). Executive hypercontrol in obsessive-compulsive disorder: electrophysiological and neuropsychological indices. *Clin. Neurophysiol.* 115, 1340–1348. doi: 10.1016/j.clinph.2003.12.031

Burnette, C. P., Henderson, H. A., Inge, A. P., Zahka, N. E., Schwartz, C. B., and Mundy, P. C. (2011). Anterior EEG asymmetry and the modifier model of autism. *J. Autism Dev. Disord.* 41, 1113–1124. doi: 10.1007/s10803-010-1138-0

Buyck, I., and Wiersema, J. R. (2014a). Resting electroencephalogram in attention deficit hyperactivity disorder: developmental course and diagnostic value. *Psychiatry Res.* 216, 391–397. doi: 10.1016/j.psychres.2013.12.055

Buyck, I., and Wiersema, J. R. (2014b). State-related electroencephalographic deviances in attention deficit hyperactivity disorder. *Res. Dev. Disabil.* 35, 3217–3225. doi: 10.1016/j.ridd.2014.08.003

Buyck, I., and Wiersema, J. R. (2015). Electroencephalographic activity before and after cognitive effort in children with attention deficit/hyperactivity disorder. *Clin. EEG Neurosci.* 46, 88–93. doi: 10.1177/1550059414553244

Chan, A. S., and Leung, W. W. M. (2006). Differentiating autistic children with quantitative encephalography: a 3-month longitudinal study. *J. Child Neurol.* 21, 391–399. doi: 10.1177/08830738060210050501

Chan, A. S., Sze, S. L., and Cheung, M.-C. (2007). Quantitative electroencephalographic profiles for children with autistic spectrum disorder. *Neuropsychology* 21, 74–81. doi: 10.1037/0894-4105.21.1.74

Choi, J.-S., Park, S. M., Lee, J., Hwang, J. Y., Jung, H. Y., Choi, S.-W., et al. (2013). Resting-state beta and gamma activity in Internet addiction. *Int. J. Psychophysiol.* 89, 328–333. doi: 10.1016/j.ijpsycho.2013.06.007

Clancy, K., Ding, M., Bernat, E., Schmidt, N. B., and Li, W. (2017). Restless 'rest': intrinsic sensory hyperactivity and disinhibition in post-traumatic stress disorder. *Brain* 140, 2041–2050. doi: 10.1093/brain/awx116

Clarke, A. R., Barry, R. J., Baker, I. E., McCarthy, R., and Selikowitz, M. (2016). An investigation of stimulant effects on the EEG of children with attention-deficit/hyperactivity disorder. *Clin. EEG Neurosci.* 48, 235–242. doi: 10.1177/1550059416664657

Clarke, A., Barry, R., Bond, D., McCarthy, R., and Selikowitz, M. (2002a). Effects of stimulant medications on the EEG of children with attention-deficit/hyperactivity disorder. *Psychopharmacology* 164, 277–284. doi: 10.1007/s00213-002-1205-0

Clarke, A. R., Barry, R. J., McCarthy, R., and Selikowitz, M. (2002b). Children with attention-deficit/hyperactivity disorder and comorbid oppositional defiant disorder: an EEG analysis. *Psychiatry Res.* 111, 181–190. doi: 10.1016/s0165-1781(02)00137-3

Clarke, A. R., Barry, R. J., McCarthy, R., and Selikowitz, M. (2002c). EEG analysis of children with attention-deficit/hyperactivity disorder and comorbid reading disabilities. *J. Learn. Disabil.* 35, 276–285. doi: 10.1177/002221940203500309

Clarke, A. R., Barry, R. J., McCarthy, R., and Selikowitz, M. (2002d). EEG differences between good and poor responders to methylphenidate and dexamphetamine in children with attention-deficit/hyperactivity disorder. *Clinical Neurophysiol.* 113, 194–205. doi: 10.1016/s1388-2457(01)00736-2

Clarke, A., Barry, R. J., McCarthy, R., Selikowitz, M., and Brown, C. R. (2002e). EEG evidence for a new conceptualisation of attention deficit hyperactivity disorder. *Clin. Neurophysiol.* 113, 1036–1044. doi: 10.1016/s1388-2457(02)00115-3

Clarke, A. R., Barry, R. J., McCarthy, R., Selikowitz, M., and Croft, R. J. (2002f). EEG differences between good and poor responders to methylphenidate in boys with the inattentive type of attention-deficit/hyperactivity disorder. *Clinical Neurophysiol.* 113, 1191–1198. doi: 10.1016/s1388-2457(02)00147-5

Clarke, A., Barry, R., Dupuy, F., McCarthy, R., Selikowitz, M., and Johnstone, S. (2013). Excess beta activity in the EEG of children with attention-deficit/hyperactivity disorder: a disorder of arousal? *Int. J. Psychophysiol.* 89, 314–319. doi: 10.1016/j.ijpsycho.2013.04.009

Clarke, A. R., Barry, R. J., Dupuy, F. E., McCarthy, R., Selikowitz, M., and Heaven, P. C. L. (2011). Childhood EEG as a predictor of adult attention-deficit/hyperactivity disorder. *Clin. Neurophysiol.* 122, 73–80. doi: 10.1016/j.clinph.2010.05.032

Clarke, A. R., Barry, R. J., Heaven, P. C. L., McCarthy, R., Selikowitz, M., and Byrne, M. K. (2008a). EEG in adults with Attention-Deficit/Hyperactivity Disorder. *Int. J. Psychophysiol.* 70, 176–183. doi: 10.1016/j.ijpsycho.2008.07.001

Clarke, A. R., Barry, R. J., McCarthy, R., Selikowitz, M., and Johnstone, S. J. (2008b). Effects of imipramine hydrochloride on the EEG of children with Attention-Deficit/Hyperactivity Disorder who are non-responsive to stimulants. *Int. J. Psychophysiol.* 68, 186–192. doi: 10.1016/j.ijpsycho.2008.01.007

Clarke, A. R., Barry, R. J., McCarthy, R., and Selikowitz, M. (1998). EEG analysis in Attention-deficit/Hyperactivity Disorder: a comparative study of two subtypes. *Psychiatry Res.* 81, 19–29. doi: 10.1016/s0165-1781(98)00072-9

Clarke, A. R., Barry, R. J., McCarthy, R., and Selikowitz, M. (2001a). Age and sex effects in the EEG: differences in two subtypes of attention-deficit/hyperactivity disorder. *Clin. Neurophysiol.* 112, 815–826. doi: 10.1016/s1388-2457(01)00487-4

Clarke, A. R., Barry, R. J., McCarthy, R., and Selikowitz, M. (2001b). EEG-defined subtypes of children with attention-deficit/hyperactivity disorder. *Clin. Neurophysiol.* 112, 2098–2105. doi: 10.1016/s1388-2457(01)00668-x

Clarke, A. R., Barry, R. J., McCarthy, R., and Selikowitz, M. (2001c). Electroencephalogram differences in two subtypes of Attention-Deficit/Hyperactivity Disorder. *Psychophysiology* 38, 212–221. doi: 10.1111/1469-8986.3820212

Clarke, A. R., Barry, R. J., McCarthy, R., and Selikowitz, M. (2001d). Excess beta activity in children with attention-deficit/hyperactivity disorder: an atypical electrophysiological group. *Psychiatry Res.* 103, 205–218. doi: 10.1016/s0165-1781(01)00277-3

Clarke, A. R., Barry, R. J., McCarthy, R., Selikowitz, M., Clarke, D. C., and Croft, R. J. (2003). EEG activity in girls with attention-deficit/hyperactivity disorder. *Clin. Neurophysiol.* 114, 319–328. doi: 10.1016/s1388-2457(02)00364-4

Clarke, A. R., Barry, R. J., McCarthy, R., Selikowitz, M., and Johnstone, S. J. (2007). Effects of stimulant medications on the EEG of girls with Attention-Deficit/Hyperactivity Disorder. *Clin. Neurophysiol.* 118, 2700–2708. doi: 10.1016/j.clinph.2007.08.020

Clarke, A. R., Barry, R. J., McCarthy, R., Selikowitz, M., Magee, C. A., Johnstone, S. J., et al. (2006). Quantitative EEG in low-IQ children with attention-deficit/hyperactivity disorder. *Clin. Neurophysiol.* 117, 1708–1714. doi: 10.1016/j.clinph.2006.04.015

Clementz, B. A., Sponheim, S. R., Iacono, W. G., and Beiser, M. (1994). Resting EEG in first-episode schizophrenia patients, bipolar psychosis patients and their first-degree relatives. *Psychophysiology* 31, 486–494. doi: 10.1111/j.1469-8986.1994.tb01052.x

Coben, R., Clarke, A. R., Hudspeth, W., and Barry, R. J. (2008). EEG power and coherence in autistic spectrum disorder. *Clin. Neurophysiol.* 119, 1002–1009. doi: 10.1016/j.clinph.2008.01.013

Conners, C. K., Sitarenios, G., and Parker, J. D. (1998). The revised conners' parent rating scale (CPRS-R): factor structure, reliability, and criterion Validity. *J. Abnorm. Child Psychol.* 26, 257–268. doi: 10.1023/A:1022602400621

Conners, C. K. E., and Sparrow, M. A. (1999). *Conners' Adult ADHD Rating Scales (CAARS).* New York, NY: Multihealth Systems, Inc.

Cook, I. A., Hunter, A. M., Korb, A. S., and Leuchter, A. F. (2014). Do prefrontal midline electrodes provide unique neurophysiologic information in Major Depressive Disorder? *J. Psychiatr. Res.* 53, 69–75. doi: 10.1016/j.jpsychires.2014.01.018

Cunill, R., Castells, X., and Simeon, D. (2009). Relationships between obsessive-compulsive symptomatology and severity of psychosis in schizophrenia: a systematic review and meta-analysis. *J. Clin. Psychiatry* 70, 70–82. doi: 10.4088/jcp.07r03618

Dawson, G., Klinger, L. G., Panagiotides, H., Lewy, A., and Castelloe, P. (1995). Subgroups of autistic children based on social behavior display distinct patterns of brain activity. *J. Abnorm. Child Psychol.* 23, 569–583. doi: 10.1007/bf01447662

de Carvalho, M. R., Velasques, B. B., Freire, R. C., Cagy, M., Marques, J. B., Teixeira, S., et al. (2015). Frontal cortex absolute beta power measurement in Panic Disorder with Agoraphobia patients. *J. Affect. Disord.* 184, 176–181. doi: 10.1016/j.jad.2015.05.055

Debener, S., Beauducel, A., Nessler, D., Brocke, B., Heilemann, H., and Kayser, J. (2000). Is resting anterior EEG 003B1 asymmetry a trait marker for depression? *Neuropsychobiology* 41, 31–37. doi: 10.1159/000026630

Deldin, P. J., and Chiu, P. (2005). Cognitive restructuring and EEG in major depression. *Biol. Psychol.* 70, 141–151. doi: 10.1016/j.biopsycho.2005.01.003

Dupuy, F. E., Clarke, A. R., Barry, R. J., McCarthy, R., and Selikowitz, M. (2014a). EEG differences between the combined and inattentive types of attention-deficit/hyperactivity disorder in girls: a further investigation. *Clin. EEG Neurosci.* 45, 231–237. doi: 10.1177/1550059413501162

Dupuy, F. E., Clarke, A. R., Barry, R. J., Selikowitz, M., and McCarthy, R. (2014b). EEG and electrodermal activity in girls with Attention-Deficit/Hyperactivity Disorder. *Clin. Neurophysiol.* 125, 491–499. doi: 10.1016/j.clinph.2013.09.007

Dupuy, F. E., Barry, R. J., Clarke, A. R., McCarthy, R., and Selikowitz, M. (2013). Sex differences between the combined and inattentive types of attention-deficit/hyperactivity disorder: an EEG perspective. *Int. J. Psychophysiol.* 89, 320–327. doi: 10.1016/j.ijpsycho.2013.04.004

Dupuy, F. E., Clarke, A. R., Barry, R. J., McCarthy, R., and Selikowitz, M. (2011). Girls with attention-deficit/hyperactivity disorder: EEG differences between DSM-IV types. *Clin. EEG Neurosci.* 42, 1–5. doi: 10.1177/155005941104200104

Dustman, R. E., Boswell, R. S., and Porter, P. B. (1962). Beta brain waves as an index of alertness. *Science* 137, 533–534. doi: 10.1126/science.137.3529.533

Ehlers, C. L., Hurst, S., Phillips, E., Gilder, D. A., Dixon, M., Gross, A., et al. (2006). Electrophysiological responses to affective stimuli in american indians experiencing trauma with and without PTSD. *Ann. N Y Acad. Sci.* 1071, 125–136. doi: 10.1196/annals.1364.011

El-Badri, S. M., Ashton, C. H., Moore, P. B., Marsh, V. R., and Ferrier, I. N. (2001). Electrophysiological and cognitive function in young euthymic patients with bipolar affective disorder. *Bipolar Disord.* 3, 79–87. doi: 10.1034/j.1399-5618.2001.030206.x

Falconer, E. M., Felmingham, K. L., Allen, A., Clark, C. R., McFarlane, A. C., Williams, L. M., et al. (2008). Developing an integrated brain, behavior and biological response profile in posttraumatic stress disorder (PTSD). *J. Integr. Neurosci.* 7, 439–456. doi: 10.1142/s0219635208001873

Fein, G., and Allen, J. (2006). EEG spectral changes in treatment-naive, actively drinking alcoholics. *Alcohol. Clin. Exp. Res.* 29, 538–546. doi: 10.1097/01.alc.0000159107.08471.97

Fonseca, L. C., Tedrus, G. M., Bianchini, M. C., and Silva, T. F. (2013). Electroencephalographic α reactivity on opening the eyes in children with attention-deficit hyperactivity disorder. *Clin. EEG Neurosci.* 44, 53–57. doi: 10.1177/1550059412445659

Fonseca, L. C., Tedrus, G. M. A. S., de Moraes, C., de Vicente Machado, A., de Almeida, M. P., and de Oliveira, D. O. F. (2008). Epileptiform abnormalities and quantitative EEG in children with attention-deficit/hyperactivity disorder. *Arquivos de Neuro-Psiquiatria* 66, 462–467. doi: 10.1590/s0004-282x2008000400004

Foxe, J. J., Morie, K. P., Laud, P. J., Rowson, M. J., de Bruin, E. A., and Kelly, S. P. (2012). Assessing the effects of caffeine and theanine on the maintenance of vigilance during a sustained attention task. *Neuropharmacology* 62, 2320–2327. doi: 10.1016/j.neuropharm.2012.01.020

Gao, R. (2016). Interpreting the electrophysiological power spectrum. *J. Neurophysiol.* 115, 628–630. doi: 10.1152/jn.00722.2015

Garakh, Z., Zaytseva, Y., Kapranova, A., Fiala, O., Horacek, J., Shmukler, A., et al. (2015). EEG correlates of a mental arithmetic task in patients with first episode schizophrenia and schizoaffective disorder. *Clin. Neurophysiol.* 126, 2090–2098. doi: 10.1016/j.clinph.2014.12.031

Giertuga, K., Zakrzewska, M. Z., Bielecki, M., Racicka-Pawlukiewicz, E., Kossut, M., and Cybulska-Klosowicz, A. (2017). Age-related changes in resting-state EEG activity in attention deficit/hyperactivity disorder: a cross-sectional study. *Front. Hum. Neurosci.* 11:285. doi: 10.3389/fnhum.2017.00285

Gloss, D., Varma, J. K., Pringsheim, T., and Nuwer, M. R. (2016). Practice advisory: the utility of EEG theta/beta power ratio in ADHD diagnosis: report of the guideline development, dissemination, and implementation subcommittee of the american academy of neurology. *Neurology* 87, 2375–2379. doi: 10.1212/WNL.0000000000003265

Goldstein, M. R., Peterson, M. J., Sanguinetti, J. L., Tononi, G., and Ferrarelli, F. (2015). Topographic deficits in α-range resting EEG activity and steady state visual evoked responses in schizophrenia. *Schizophr. Res.* 168, 145–152. doi: 10.1016/j.schres.2015.06.012

Gonen-Yaacovi, G., Arazi, A., Shahar, N., Karmon, A., Haar, S., Meiran, N., et al. (2016). Increased ongoing neural variability in ADHD. *Cortex* 81, 50–63. doi: 10.1016/j.cortex.2016.04.010

Goodman, W. K., Price, L. H., Rasmussen, S. A., Mazure, C., Fleischmann, R. L., Hill, C. L., et al. (1989). The yale-brown obsessive compulsive scale: I. development, use, and reliability. *Arch. Gen. Psychiatry* 46, 1006–1011. doi: 10.1001/archpsyc.1989.01810110048007

Gordeev, S. A. (2008). Clinical-psychophysiological studies of patients with panic attacks with and without agoraphobic disorders. *Neurosci. Behav. Physiol.* 38, 633–637. doi: 10.1007/s11055-008-9016-3

Grin-Yatsenko, V. A., Baas, I., Ponomarev, V. A., and Kropotov, J. D. (2009). EEG power spectra at early stages of depressive disorders. *J. Clin. Neurophysiol.* 26, 401–406. doi: 10.1097/WNP.0b013e3181c298fe

Günther, W., Müller, N., Knesewitsch, P., Haag, C., Trapp, W., Banquet, J.-P., et al. (1997). Functional EEG mapping and SPECT in detoxified male alcoholics.

Eur. Arch. Psychiatry Clin. Neurosci. 247, 128–136. doi: 10.1007/bf03033066

Haegens, S., Cousijn, H., Wallis, G., Harrison, P. J., and Nobre, A. C. (2014). Inter- and intra-individual variability in alpha peak frequency. *Neuroimage* 92, 46–55. doi: 10.1016/j.neuroimage.2014.01.049

Hagemann, D., Hewig, J., Walter, C., and Naumann, E. (2008). Skull thickness and magnitude of EEG alpha activity. *Clin. Neurophysiol.* 119, 1271–1280. doi: 10.1016/j.clinph.2008.02.010

Haller, M., Donoghue, T., Peterson, E., Varma, P., Sebastian, P., Gao, R., et al. (2018). Parameterizing neural power spectra. *bioRxiv [Preprint]*. doi: 10.1101/299859

Hamilton, M. (1960). A rating scale for depression. *J. Neurol. Neurosurg. Psychiatry* 23:56. doi: 10.1136/jnnp.23.1.56

Hanslmayr, S., Backes, H., Straub, S., Popov, T., Langguth, B., Hajak, G., et al. (2013). Enhanced resting-state oscillations in schizophrenia are associated with decreased synchronization during inattentional blindness: schizophrenia and abnormal resting-state activity. *Hum. Brain Mapp.* 34, 2266–2275. doi: 10.1002/hbm.22064

Hardstone, R., Poil, S.-S., Schiavone, G., Jansen, R., Nikulin, V., Mansvelder, H., et al. (2012). Detrended fluctuation analysis: a scale-free view on neuronal oscillations. *Front. Physiol.* 3:450. doi: 10.3389/fphys.2012.00450

Harris, A. W. F., Bahramali, H., Slewa-Younan, S., Gordon, E., Williams, L., and Li, W. M. (2001). The topography of quantified electroencephalography in three syndromes of schizophrenia. *Int. J. Neurosci.* 107, 265–278. doi: 10.3109/00207450109150689

Harris, A., Melkonian, D., Williams, L., and Gordon, E. (2006). Dynamic spectral analysis findings in first episode and chronic schizophrenia. *Int. J. Neurosci.* 116, 223–246. doi: 10.1080/00207450500402977

Hashemi, A., Pino, L. J., Moffat, G., Mathewson, K. J., Aimone, C., Bennett, P. J., et al. (2016). Characterizing population EEG dynamics throughout adulthood. *eNeuro* 3:ENEURO.0275-16.2016. doi: 10.1523/ENEURO.0275-16.2016

Hermens, D. F., Kohn, M. R., Clarke, S. D., Gordon, E., and Williams, L. M. (2005a). Sex differences in adolescent ADHD: findings from concurrent EEG and EDA. *Clin. Neurophysiol.* 116, 1455–1463. doi: 10.1016/j.clinph.2005.02.012

Hermens, D. F., Soei, E. X. C., Clarke, S. D., Kohn, M. R., Gordon, E., and Williams, L. M. (2005b). Resting EEG theta activity predicts cognitive performance in attention-deficit hyperactivity disorder. *Pediatr. Neurol.* 32, 248–256. doi: 10.1016/j.pediatrneurol.2004.11.009

Hermens, D. F., Williams, L. M., Clarke, S., Kohn, M., Cooper, N., and Gordon, E. (2005c). Responses to methylphenidate in adolescent AD/HD: evidence from concurrently recorded autonomic (EDA) and central (EEG and ERP) measures. *Int. J. Psychophysiol.* 58, 21–33. doi: 10.1016/j.ijpsycho.2005.03.006

Hermens, D. F., Williams, L. M., Lazzaro, I., Whitmont, S., Melkonian, D., and Gordon, E. (2004). Sex differences in adult ADHD: a double dissociation in brain activity and autonomic arousal. *Biol. Psychol.* 66, 221–233. doi: 10.1016/j.biopsycho.2003.10.006

Herrera-Díaz, A., Mendoza-Quiiñones, R., Melie-Garcia, L., Martínez-Montes, E., Sanabria-Diaz, G., Romero-Quintana, Y., et al. (2016). Functional connectivity and quantitative EEG in women with alcohol use disorders: a resting-state study. *Brain Topogr.* 29, 368–381. doi: 10.1007/s10548-015-0467-x

Hoagland, H., Cameron, D. E., and Rubin, M. A. (1937a). The "delta index" of the electrencephalogram in relation to insulin treatments of Schizophrenia. *Psychol. Rec.* 1, 196–202.doi: 10.1007/bf03393201

Hoagland, H., Rubin, M. A., and Cameron, D. E. (1937b). Electrical brain waves in schizophrenics during insulin treatments. *J. Psychol.* 3, 513–519. doi: 10.1080/00223980.1937.9917518

Hobbs, M. J., Clarke, A. R., Barry, R. J., McCarthy, R., and Selikowitz, M. (2007). EEG abnormalities in adolescent males with AD/HD. *Clin. Neurophysiol.* 118, 363–371. doi: 10.1016/j.clinph.2006.10.013

Hong, L. E., Summerfelt, A., Mitchell, B. D., O'Donnell, P., and Thaker, G. K. (2012). A shared low-frequency oscillatory rhythm abnormality in resting and sensory gating in schizophrenia. *Clin. Neurophysiol.* 123, 285–292. doi: 10.1016/j.clinph.2011.07.025

Huang, Y., Zhang, J., Cui, Y., Yang, G., He, L., Liu, Q., et al. (2017). How different EEG references influence sensor level functional connectivity graphs. *Front. Neurosci.* 11:368. doi: 10.3389/fnins.2017.00368

Ieong, H. F.-H., and Yuan, Z. (2017). Resting-state neuroimaging and neuropsychological findings in opioid use disorder during abstinence: a review. *Front. Hum. Neurosci.* 11:169. doi: 10.3389/fnhum.2017.00169

Imperatori, C., Farina, B., Quintiliani, M. I., Onofri, A., Castelli Gattinara, P., Lepore, M., et al. (2014). Aberrant EEG functional connectivity and EEG power spectra in resting state post-traumatic stress disorder: a sLORETA study. *Biol. Psychol.* 102, 10–17. doi: 10.1016/j.biopsycho.2014.07.011

Islam, M. K., Rastegarnia, A., and Yang, Z. (2016). Methods for artifact detection and removal from scalp EEG: a review. *Neurophysiol. Clin.* 46, 287–305. doi: 10.1016/j.neucli.2016.07.002

Itoh, T., Sumiyoshi, T., Higuchi, Y., Suzuki, M., and Kawasaki, Y. (2011). LORETA analysis of three-dimensional distribution of delta band activity in schizophrenia: relation to negative symptoms. *Neurosci. Res.* 70, 442–448. doi: 10.1016/j.neures.2011.05.003

Jaime, M., McMahon, C. M., Davidson, B. C., Newell, L. C., Mundy, P. C., and Henderson, H. A. (2016). Brief report: reduced temporal-central EEG alpha coherence during joint attention perception in adolescents with autism spectrum disorder. *J. Autism Dev. Disord.* 46, 1477–1489. doi: 10.1007/s10803-015-2667-3

Jarrett, M., Gable, P., Rondon, A., Neal, L., Price, L., and Hilton, D. (2017). An EEG study of children with and without ADHD symptoms: between-group differences and associations with sluggish cognitive tempo symptoms. *J. Atten. Disord.* doi: 10.1177/1087054717723986 [Epub ahead of print].

Jasper, H. H., and Andrews, H. L. (1936). Human brain rhythms: I. Recording techniques and preliminary results. *J. Gen. Psychol.* 14, 98–126. doi: 10.1080/00221309.1936.9713141

Jaworska, N., Blier, P., Fusee, W., and Knott, V. (2012). Alpha power, alpha asymmetry and anterior cingulate cortex activity in depressed males and females. *J. Psychiatr. Res.* 46, 1483–1491. doi: 10.1016/j.jpsychires.2012.08.003

Jeste, S. S., Frohlich, J., and Loo, S. K. (2015). Electrophysiological biomarkers of diagnosis and outcome in neurodevelopmental disorders. *Curr. Opin. Neurol.* 28, 110–116. doi: 10.1097/WCO.0000000000000181

John, J. P., Rangaswamy, M., Thennarasu, K., Khanna, S., Nagaraj, R. B., Mukundan, C. R., et al. (2009). EEG power spectra differentiate positive and negative subgroups in neuroleptic-naive schizophrenia patients. *J. Neuropsychiatry Clin. Neurosci.* 21, 160–172. doi: 10.1176/appi.neuropsych.21.2.160

Jokić-Begić, N., and Begić, D. (2003). Quantitative electroencephalogram (qEEG) in combat veterans with post-traumatic stress disorder (PTSD). *Nord. J. Psychiatry* 57, 351–355. doi: 10.1080/08039480310002688

Jospin, M., Caminal, P., Jensen, E. W., Litvan, H., Vallverdü, M., Struys, M. M. R. F., et al. (2007). Detrended fluctuation analysis of EEG as a measure of depth of anesthesia. *IEEE Trans. Biomed. Eng.* 54, 840–846. doi: 10.1109/tbme.2007.893453

Jung, T.-P., Makeig, S., Humphries, C., Lee, T.-W., McKeown, M. J., Iragui, V., et al. (2003). Removing electroencephalographic artifacts by blind source separation. *Psychophysiology* 37, 163–178. doi: 10.1111/1469-8986.3720163

Kaiser, A. K., Gnjezda, M. T., Knasmüller, S., and Aichhorn, W. (2018). Electroencephalogram alpha asymmetry in patients with depressive disorders: current perspectives. *Neuropsychiatr. Dis. Treat.* 14, 1493–1504. doi: 10.2147/NDT.S137776

Kam, J. W. Y., Bolbecker, A. R., O'Donnell, B. F., Hetrick, W. P., and Brenner, C. A. (2013). Resting state EEG power and coherence abnormalities in bipolar disorder and schizophrenia. *J. Psychiatr. Res.* 47, 1893–1901. doi: 10.1016/j.jpsychires.2013.09.009

Kamaradova, D., Prasko, J., Taborsky, J., Grambal, A., Latalova, K., Hajda, M., et al. (2016). Cognitive deficits in patients with obsessive–compulsive disorder–electroencephalography correlates. *Neuropsychiatr. Dis. Treat.* 12, 1119–1125. doi: 10.2147/NDT.S93040

Kamida, A., Shimabayashi, K., Oguri, M., Takamori, T., Ueda, N., Koyanagi, Y., et al. (2016). EEG power spectrum analysis in children with ADHD. *Yonago Acta Med.* 59, 169–173.

Karadag, F., Oguzhanoglu, N. K., Kurt, T., Oguzhanoglu, A., Atesci, F., and öZdel, O. (2003). Quantitative EEG analysis in obsessive compulsive disorder. *Int. J. Neurosci.* 113, 833–847. doi: 10.1080/00207450390200963

Kay, S. R., Fiszbein, A., and Opler, L. A. (1987). The positive and negative syndrome scale (PANSS) for schizophrenia. *Schizophr. Bull.* 13, 261–276. doi: 10.1093/schbul/13.2.261

Keil, A., Debener, S., Gratton, G., Junghöfer, M., Kappenman, E. S., Luck, S. J., et al. (2013). Committee report: publication guidelines and recommendations for studies using electroencephalography and magnetoencephalography. *Psychophysiology* 51, 1–21. doi: 10.1111/psyp.12147

Kelly, S. P., Gomez-Ramirez, M., Montesi, J. L., and Foxe, J. J. (2008). L-theanine and caffeine in combination affect human cognition as evidenced by oscillatory α-band activity and attention task performance. *J. Nutr.* 138, 1572S–1577S. doi: 10.1093/jn/138.8.1572S

Kemp, A. H., Griffiths, K., Felmingham, K. L., Shankman, S. A., Drinkenburg, W., Arns, M., et al. (2010). Disorder specificity despite comorbidity: resting EEG α asymmetry in major depressive disorder and post-traumatic stress disorder. *Biol. Psychol.* 85, 350–354. doi: 10.1016/j.biopsycho.2010.08.001

Kim, J. W., Kim, B.-N., Lee, J., Na, C., Kee, B. S., Min, K. J., et al. (2016). Desynchronization of theta-phase gamma-amplitude coupling during a mental arithmetic task in children with attention deficit/hyperactivity disorder. *PLoS One* 11:e0145288. doi: 10.1371/journal.pone.0145288

Kim, J. W., Lee, Y. S., Han, D. H., Min, K. J., Lee, J., and Lee, K. (2015). Diagnostic utility of quantitative EEG in un-medicated schizophrenia. *Neurosci. Lett.* 589, 126–131. doi: 10.1016/j.neulet.2014.12.064

Kim, Y. J., Lee, J.-Y., Oh, S., Park, M., Jung, H. Y., Sohn, B. K., et al. (2017). Associations between prospective symptom changes and slow-wave activity in patients with Internet gaming disorder: a resting-state EEG study. *Medicine* 96:e6178. doi: 10.1097/MD.0000000000006178

Kirino, E. (2004). Correlation between P300 and EEG rhythm in schizophrenia. *Clin. EEG Neurosci.* 35, 137–146. doi: 10.1177/155005940403500306

Kirino, E. (2007). Mismatch negativity correlates with delta and theta EEG power in schizophrenia. *Int. J. Neurosci.* 117, 1257–1279. doi: 10.1080/00207450600936635

Kitsune, G. L., Cheung, C. H. M., Brandeis, D., Banaschewski, T., Asherson, P., McLoughlin, G., et al. (2015). A matter of time: the influence of recording context on EEG spectral power in adolescents and young adults with ADHD. *Brain Topogr.* 28, 580–590. doi: 10.1007/s10548-014-0395-1

Knott, V. J., Bakish, D., Lusk, S., Barkely, J., and Perugini, M. (1996). Quantitative EEG correlates of panic disorder. *Psychiatry Res.* 68, 31–39. doi: 10.1016/s0925-4927(96)02962-9

Knott, V., Labelle, A., Jones, B., and Mahoney, C. (2001a). Quantitative EEG in schizophrenia and in response to acute and chronic clozapine treatment. *Schizophr. Res.* 50, 41–53. doi: 10.1016/s0920-9964(00)00165-1

Knott, V., Mahoney, C., Kennedy, S., and Evans, K. (2001b). EEG power, frequency, asymmetry and coherence in male depression. *Psychiatry Res.* 106, 123–140. doi: 10.1016/s0925-4927(00)00080-9

Knyazeva, M. G., Jalili, M., Meuli, R., Hasler, M., De Feo, O., and Do, K. Q. (2008). Alpha rhythm and hypofrontality in schizophrenia. *Acta Psychiatr. Scand.* 118, 188–199. doi: 10.1111/j.1600-0447.2008.01227.x

Koehler, S., Lauer, P., Schreppel, T., Jacob, C., Heine, M., Boreatti-Hümmer, A., et al. (2009). Increased EEG power density in alpha and theta bands in adult ADHD patients. *J. Neural Transm.* 116, 97–104. doi: 10.1007/s00702-008-0157-x

Kopřivová, J., Congedo, M., Horáček, J., Praško, J., Raszka, M., Brunovský, M., et al. (2011). EEG source analysis in obsessive-compulsive disorder. *Clin. Neurophysiol.* 122, 1735–1743. doi: 10.1016/j.clinph.2011.01.051

Kopřivová, J., Horáček, J., Raszka, M., Brunovský, M., and Praško, J. (2013). Standardized low-resolution electromagnetic tomography in obsessive-compulsive disorder—a replication study. *Neurosci. Lett.* 548, 185–189. doi: 10.1016/j.neulet.2013.05.015

Korb, A. S., Cook, I. A., Hunter, A. M., and Leuchter, A. F. (2008). Brain electrical source differences between depressed subjects and healthy controls. *Brain Topogr.* 21, 138–146. doi: 10.1007/s10548-008-0070-5

Korucuoglu, O., Gladwin, T. E., and Wiers, R. W. (2016). The effect of acute alcohol on motor-related EEG asymmetries during preparation of approach or avoid alcohol responses. *Biol. Psychol.* 114, 81–92. doi: 10.1016/j.biopsycho.2015.12.012

Kozhushko, N. J., Nagornova, Z. V., Evdokimov, S. A., Shemyakina, N. V., Ponomarev, V. A., Tereshchenko, E. P., et al. (2018). Specificity of spontaneous EEG associated with different levels of cognitive and communicative dysfunctions in children. *Int. J. Psychophysiol.* 128, 22–30. doi: 10.1016/j.ijpsycho.2018.03.013

Kuperman, S., Johnson, B., Arndt, S., Lindgren, S., and Wolraich, M. (1996). Quantitative EEG differences in a nonclinical sample of children with ADHD and undifferentiated ADD. *J. Am. Acad. Child Adolesc. Psychiatry* 35, 1009–1017. doi: 10.1097/00004583-199608000-00011

Kwon, J. S., Youn, T., and Jung, H. Y. (1996). Right hemisphere abnormalities in major depression: quantitative electroencephalographic findings before and after treatment. *J. Affect. Disord.* 40, 169–173. doi: 10.1016/0165-0327(96)00057-2

Lansbergen, M. M., Arns, M., van Dongen-Boomsma, M., Spronk, D., and Buitelaar, J. K. (2011). The increase in theta/beta ratio on resting-state EEG in boys with attention-deficit/hyperactivity disorder is mediated by slow alpha peak frequency. *Prog. Neuropsychopharmacol. Biol. Psychiatry* 35, 47–52. doi: 10.1016/j.pnpbp.2010.08.004

Lee, J., Hwang, J. Y., Park, S. M., Jung, H. Y., Choi, S.-W., Kim, D. J., et al. (2014). Differential resting-state EEG patterns associated with comorbid depression in Internet addiction. *Prog. Neuropsychopharmacol. Biol. Psychiatry* 50, 21–26. doi: 10.1016/j.pnpbp.2013.11.016

Lefebvre, A., Delorme, R., Delanoë, C., Amsellem, F., Beggiato, A., Germanaud, D., et al. (2018). Alpha waves as a neuromarker of autism spectrum disorder: the challenge of reproducibility and heterogeneity. *Front. Neurosci.* 12:662. doi: 10.3389/fnins.2018.00662

Lei, X., and Liao, K. (2017). Understanding the influences of EEG reference: a large-scale brain network perspective. *Front. Neurosci.* 11:205. doi: 10.3389/fnins.2017.00205

Liang, Z., Wang, Y., Sun, X., Li, D., Voss, L. J., Sleigh, J. W., et al. (2015). EEG entropy measures in anesthesia. *Front. Comput. Neurosci.* 9:16. doi: 10.3389/fncom.2015.00016

Liechti, M. D., Valko, L., Müller, U. C., Döhnert, M., Drechsler, R., Steinhausen, H.-C., et al. (2013). Diagnostic value of resting electroencephalogram in attention-deficit/hyperactivity disorder across the lifespan. *Brain Topogr.* 26, 135–151. doi: 10.1007/s10548-012-0258-6

Loo, S. K., and Makeig, S. (2012). Clinical utility of EEG in attention-deficit/hyperactivity disorder: a research update. *Neurotherapeutics* 9, 569–587. doi: 10.1007/s13311-012-0131-z

Lord, C., Rutter, M., and Couteur, L. A. (1994). Autism diagnostic interview-revised: a revised version of a diagnostic interview for caregivers of individuals with possible pervasive developmental disorders. *J. Autism Dev. Disord.* 24, 659–685. doi: 10.1007/bf02172145

Lord, C., Rutter, M., and Goode, S. (1989). Austism diagnostic observation schedule: a standardized observation of communicative and social behavior. *J. Autism Dev. Disord.* 19, 185–212. doi: 10.1007/bf02211841

Machado, C., Estévez, M., Leisman, G., Melillo, R., Rodríguez, R., DeFina, P., et al. (2015). QEEG spectral and coherence assessment of autistic children in three different experimental conditions. *J. Autism Dev. Disord.* 45, 406–424. doi: 10.1007/s10803-013-1909-5

Magee, C. A., Clarke, A. R., Barry, R. J., McCarthy, R., and Selikowitz, M. (2005). Examining the diagnostic utility of EEG power measures in children with attention deficit/hyperactivity disorder. *Clin. Neurophysiol.* 116, 1033–1040. doi: 10.1016/j.clinph.2004.12.007

Makeig, S., Bell, A. J., Jung, T.-P., and Sejnowski, T. J. (1996). "Advances in neural information processing systems 8," in *Independent Component Analysis of Electroencephalographic Data,* eds D. Touretzky, M. Mozer and M. Hasselmo (Cambridge, MA: MIT Press), 145–151.

Markovska-Simoska, S., and Pop-Jordanova, N. (2017). Quantitative EEG in children and adults with attention deficit hyperactivity disorder: comparison of absolute and relative power spectra and theta/Beta ratio. *Clin. EEG Neurosci.* 48, 20–32. doi: 10.1177/1550059416643824

Márton, L. F., Brassai, S. T., Bakó, L., and Losonczi, L. (2014). Detrended fluctuation analysis of EEG signals. *Procedia Technol.* 12, 125–132. doi: 10.1016/j.protcy.2013.12.465

Mathewson, K. J., Jetha, M. K., Drmic, I. E., Bryson, S. E., Goldberg, J. O., and Schmidt, L. A. (2012). Regional EEG alpha power, coherence, and behavioral symptomatology in autism spectrum disorder. *Clin. Neurophysiol.* 123, 1798–1809. doi: 10.1016/j.clinph.2012.02.061

Maxwell, C. R., Villalobos, M. E., Schultz, R. T., Herpertz-Dahlmann, B., Konrad, K., and Kohls, G. (2015). Atypical laterality of resting gamma

oscillations in autism spectrum disorders. *J. Autism Dev. Disord.* 45, 292–297. doi: 10.1007/s10803-013-1842-7

McFarlane, A., Clark, C. R., Bryant, R. A., Williams, L. M., Niaura, R., Paul, R. H., et al. (2005). The impact of early life stress on psycholphysiological, personality and behavoral measure in 740 non-clinical subjects. *J. Integr. Neurosci.* 4, 27–40. doi: 10.1142/s0219635205000689

McLoughlin, G., Makeig, S., and Tsuang, M. T. (2014). In search of biomarkers in psychiatry: EEG-based measures of brain function. *Am. J. Med. Genet. B Neuropsychiatr. Genet.* 165, 111–121. doi: 10.1002/ajmg.b.32208

Mientus, S., Gallinat, J., Wuebben, Y., Pascual-Marqui, R. D., Mulert, C., Frick, K., et al. (2002). Cortical hypoactivation during resting EEG in schizophrenics but not in depressives and schizotypal subjects as revealed by low resolution electromagnetic tomography (LORETA). *Psychiatry Res.* 116, 95–111. doi: 10.1016/s0925-4927(02)00043-4

Milotti, E. (2002). 1/f noise: a pedagogical review. *arXiv:physics/0204033 [physics.class-ph] [Preprint]*.

Mitra, S., Nizamie, S. H., Goyal, N., and Tikka, S. K. (2015). Evaluation of resting state gamma power as a response marker in schizophrenia. *Psychiatry Clin. Neurosci.* 69, 630–639. doi: 10.1111/pcn.12301

Mitra, S., Nizamie, S. H., Goyal, N., and Tikka, S. K. (2017). Electroencephalogram alpha-to-theta ratio over left fronto-temporal region correlates with negative symptoms in schizophrenia. *Asian J. Psychiatr.* 26, 70–76. doi: 10.1016/j.ajp.2017.01.013

Moeini, M., Khaleghi, A., and Mohammadi, M. R. (2015). Characteristics of alpha band frequency in adolescents with bipolar II disorder: a resting-state QEEG study. *Iran. J. Psychiatry* 10, 8–12.

Moeini, M., Khaleghi, A., Mohammadi, M. R., Zarafshan, H., Fazio, R. L., and Majidi, H. (2017). Cortical alpha activity in schizoaffective patients. *Iran. J. Psychiatry* 12, 1–7.

Molina, V., Montz, R., Pérez-Castejón, M. J., Martín-Loeches, M., Carreras, J. L., Calcedo, A., et al. (1995). Cerebral perfusion, electrical activity and effects of serotonergic treatment in obsessive-compulsive disorder. A preliminary study. *Neuropsychobiology* 32, 139–148. doi: 10.1159/000119227

Morgan, M. L., Witte, E. A., Cook, I. A., Leuchter, A. F., Abrams, M., and Siegman, B. (2005). Influence of age, gender, health status, and depression on quantitative EEG. *Neuropsychobiology* 52, 71–76. doi: 10.1159/000086608

Motlagh, F., Ibrahim, F., Rashid, R., Seghatoleslam, T., and Habil, H. (2017). Investigation of brain electrophysiological properties among heroin addicts: quantitative EEG and event-related potentials. *J. Neurosci. Res.* 95, 1633–1646. doi: 10.1002/jnr.23988

Narayanan, B., O'Neil, K., Berwise, C., Stevens, M. C., Calhoun, V. D., Clementz, B. A., et al. (2014). Resting state electroencephalogram oscillatory abnormalities in schizophrenia and psychotic bipolar patients and their relatives from the bipolar and schizophrenia network on intermediate phenotypes study. *Biol. Psychiatry* 76, 456–465. doi: 10.1016/j.biopsych.2013.12.008

Oathes, D. J., Ray, W. J., Yamasaki, A. S., Borkovec, T. D., Castonguay, L. G., Newman, M. G., et al. (2008). Worry, generalized anxiety disorder, and emotion: evidence from the EEG gamma band. *Biol. Psychol.* 79, 165–170. doi: 10.1016/j.biopsycho.2008.04.005

Ogrim, G., Kropotov, J., and Hestad, K. (2012). The quantitative EEG theta/beta ratio in attention deficit/hyperactivity disorder and normal controls: sensitivity, specificity, and behavioral correlates. *Psychiatry Res.* 198, 482–488. doi: 10.1016/j.psychres.2011.12.041

Olbrich, S., Olbrich, H., Adamaszek, M., Jahn, I., Hegerl, U., and Stengler, K. (2013). Altered EEG lagged coherence during rest in obsessive-compulsive disorder. *Clin. Neurophysiol.* 124, 2421–2430. doi: 10.1016/j.clinph.2013.05.031

Olbrich, S., van Dinteren, R., and Arns, M. (2015). Personalized medicine: review and perspectives of promising baseline EEG biomarkers in major depressive disorder and attention deficit hyperactivity disorder. *Neuropsychobiology* 72, 229–240. doi: 10.1159/000437435

Omori, M., Koshino, Y., Murata, T., Murata, I., Nishio, M., Sakamoto, K., et al. (1995). Quantitative EEG in never-treated schizophrenic patients. *Biol. Psychiatry* 38, 303–309. doi: 10.1016/0006-3223(95)00300-6

Orekhova, E. V., Stroganova, T. A., Nygren, G., Tsetlin, M. M., Posikera, I. N., Gillberg, C., et al. (2007). Excess of high frequency electroencephalogram oscillations in boys with autism. *Biol. Psychiatry* 62, 1022–1029. doi: 10.1016/j.biopsych.2006.12.029

Overall, J. E., and Gorham, D. R. (1962). The brief psychiatric rating scale. *Psychol. Rep.* 10, 799–812. doi: 10.2466/pr0.10.3.799-812

Parameshwaran, D., and Thiagarajan, T. C. (2017a). Complexity of EEG reflects socioeconomic context and geofootprint. *bioRxiv [Preprint]*. doi: 10.1101/125872

Parameshwaran, D., and Thiagarajan, T. C. (2017b). Dynamical features of human EEG scale systematically with life context. *bioRxiv [Preprint]*. doi: 10.1101/125906

Parameshwaran, D., and Thiagarajan, T. C. (2017c). Modernization, wealth and the emergence of strong α oscillations in the human EEG. *bioRxiv [Preprint]*. doi: 10.1101/125898

Park, J. H., Hong, J. S., Han, D. H., Min, K. J., Lee, Y. S., Kee, B. S., et al. (2017). Comparison of QEEG findings between adolescents with attention deficit hyperactivity disorder (ADHD) without comorbidity and ADHD comorbid with internet gaming disorder. *J. Korean Med. Sci.* 32, 514–521. doi: 10.3346/jkms.2017.32.3.514

Pascual-Marqui, R. D., Lehmann, D., Koenig, T., Kochi, K., Merlo, M. C. G., Hell, D., et al. (1999). Low resolution brain electromagnetic tomography (LORETA) functional imaging in acute, neuroleptic-naive, first-episode, productive schizophrenia. *Psychiatry Res.* 90, 169–179. doi: 10.1016/s0925-4927(99)00013-x

Pivik, R. T., Broughton, R. J., Coppola, R., Davidson, R. J., Fox, N., and Nuwer, M. R. (1993). Guidelines for the recording and quantitative analysis of electroencephalographic activity in research contexts. *Psychophysiology* 30, 547–558. doi: 10.1111/j.1469-8986.1993.tb02081.x

Pizzagalli, D. A., Nitschke, J. B., Oakes, T. R., Hendrick, A. M., Horras, K. A., Larson, C. L., et al. (2002). Brain electrical tomography in depression: the importance of symptom severity, anxiety, and melancholic features. *Biol. Psychiatry* 52, 73–85. doi: 10.1016/s0006-3223(02)01313-6

Pogarell, O., Juckel, G., Mavrogiorgou, P., Mulert, C., Folkerts, M., Hauke, W., et al. (2006). Symptom-specific EEG power correlations in patients with obsessive-compulsive disorder. *Int. J. Psychophysiol.* 62, 87–92. doi: 10.1016/j.ijpsycho.2006.02.002

Poil, S. S., Bollmann, S., Ghisleni, C., O'Gorman, R. L., Klaver, P., Ball, J., et al. (2014). Age dependent electroencephalographic changes in attention-deficit/hyperactivity disorder (ADHD). *Clin. Neurophysiol.* 125, 1626–1638. doi: 10.1016/j.clinph.2013.12.118

Polanczyk, G., de Lima, M. S., Horta, B. L., Biederman, J., and Rohde, L. A. (2007). The worldwide prevalence of ADHD: a systematic review and metaregression analysis. *Am. J. Psychiatry* 164, 942–948. doi: 10.1176/ajp.2007.164.6.942

Price, G. W., Lee, J. W., Garvey, C., and Gibson, N. (2008). Appraisal of sessional EEG features as a correlate of clinical changes in an rTMS treatment of depression. *Clin. EEG Neurosci.* 39, 131–138. doi: 10.1177/155005940803900307

Pritchard, W. S. (1992). The brain in fractal time: 1/f-like power spectrum scaling of the human electroencephalogram. *Int. J. Neurosci.* 66, 119–129. doi: 10.3109/00207459208999796

Qin, Y., Xu, P., and Yao, D. (2010). A comparative study of different references for EEG default mode network: the use of the infinity reference. *Clin. Neurophysiol.* 121, 1981–1991. doi: 10.1016/j.clinph.2010.03.056

Rabe, S., Beauducel, A., Zöllner, T., Maercker, A., and Karl, A. (2006). Regional brain electrical activity in posttraumatic stress disorder after motor vehicle accident. *J. Abnorm. Psychol.* 115, 687–698. doi: 10.1037/0021-843X.115.4.687

Rangaswamy, M., Porjesz, B., Chorlian, D. B., Choi, K., Jones, K. A., Wang, K., et al. (2006). Theta power in the EEG of alcoholics. *Alcohol. Clin. Exp. Res.* 27, 607–615. doi: 10.1097/01.ALC.0000060523.95470.8F

Rangaswamy, M., Porjesz, B., Chorlian, D. B., Wang, K., Jones, K. A., Bauer, L. O., et al. (2002). Beta power in the EEG of alcoholics. *Biol. Psychiatry* 52, 831–842. doi: 10.1016/s0006-3223(02)01362-8

Ranlund, S., Nottage, J., Shaikh, M., Dutt, A., Constante, M., Walshe, M., et al. (2014). Resting EEG in psychosis and at-risk populations—a possible endophenotype? *Schizophr. Res.* 153, 96–102. doi: 10.1016/j.schres.2013.12.017

Roach, B. J., and Mathalon, D. H. (2008). Event-related EEG time-frequency analysis: an overview of measures and an analysis of early gamma band phase

locking in schizophrenia. *Schizophr. Bull.* 34, 907–926. doi: 10.1093/schbul/sbn093

Roh, S.-C., Park, E.-J., Park, Y.-C., Yoon, S.-K., Kang, J.-G., Kim, D.-W., et al. (2015). Quantitative electroencephalography reflects inattention, visual error responses and reaction times in male patients with attention deficit hyperactivity disorder. *Clin. Psychopharmacol. Neurosci.* 13, 180–187. doi: 10.9758/cpn.2015.13.2.180

Rommel, A.-S., James, S.-N., McLoughlin, G., Brandeis, D., Banaschewski, T., Asherson, P., et al. (2017). Altered EEG spectral power during rest and cognitive performance: a comparison of preterm-born adolescents to adolescents with ADHD. *Eur. Child Adolesc. Psychiatry* 26, 1511–1522. doi: 10.1007/s00787-017-1010-2

Rommel, A.-S., Kitsune, G. L., Michelini, G., Hosang, G. M., Asherson, P., McLoughlin, G., et al. (2016). Commonalities in EEG spectral power abnormalities between women with ADHD and women with bipolar disorder during rest and cognitive performance. *Brain Topogr.* 29, 856–866. doi: 10.1007/s10548-016-0508-0

Rousselet, G. (2012). Does filtering preclude us from studying ERP time-courses? *Front. Psychol.* 3:131. doi: 10.3389/fpsyg.2012.00131

Rutter, M. B. A., and Lord, C. (2003). *The Social Communication Questionnaire: Manual.* Los Angeles, CA: Western Psychological Services.

Saad, J. F., Kohn, M. R., Clarke, S., Lagopoulos, J., and Hermens, D. F. (2015). Is the theta/β EEG Marker for ADHD inherently flawed? *J. Atten. Disord.* 22, 815–826. doi: 10.1177/1087054715578270

Sabeti, M., Katebi, S., and Boostani, R. (2009). Entropy and complexity measures for EEG signal classification of schizophrenic and control participants. *Artif. Intell. Med.* 47, 263–274. doi: 10.1016/j.artmed.2009.03.003

Sachs, G., Anderer, P., Dantendorfer, K., and Saletu, B. (2004). EEG mapping in patients with social phobia. *Psychiatry Res.* 131, 237–247. doi: 10.1016/j.pscychresns.2003.08.007

Saletu-Zyhlarz, G. M., Arnold, O., Anderer, P., Oberndorfer, S., Walter, H., Lesch, O. M., et al. (2004). Differences in brain function between relapsing and abstaining alcohol-dependent patients, evaluated by EEG mapping. *Alcohol Alcohol.* 39, 233–240. doi: 10.1093/alcalc/agh041

Sayers, J. (2001). The world health report 2001—Mental health: new understanding, new hope. *Bull. World Health Organ.* 79, 1085–1085.

Schug, R. A., Yang, Y., Raine, A., Han, C., Liu, J., and Li, L. (2011). Resting EEG deficits in accused murderers with schizophrenia. *Psychiatry Res.* 194, 85–94. doi: 10.1016/j.pscychresns.2010.12.017

Shankman, S. A., Silverstein, S. M., Williams, L. M., Hopkinson, P. J., Kemp, A. H., Felmingham, K. L., et al. (2008). Resting electroencephalogram asymmetry and posttraumatic stress disorder. *J. Trauma. Stress* 21, 190–198. doi: 10.1002/jts.20319

Sheikhani, A., Behnam, H., Mohammadi, M. R., Noroozian, M., and Mohammadi, M. (2012). Detection of abnormalities for diagnosing of children with autism disorders using of quantitative electroencephalography analysis. *J. Med. Syst.* 36, 957–963. doi: 10.1007/s10916-010-9560-6

Shephard, E., Tye, C., Ashwood, K. L., Azadi, B., Asherson, P., Bolton, P. F., et al. (2018). Resting-state neurophysiological activity patterns in young people with ASD, ADHD and ASD + ADHD. *J. Autism Dev. Disord.* 48, 110–122. doi: 10.1007/s10803-017-3300-4

Shi, T., Li, X., Song, J., Zhao, N., Sun, C., Xia, W., et al. (2012). EEG characteristics and visual cognitive function of children with attention deficit hyperactivity disorder (ADHD). *Brain Dev.* 34, 806–811. doi: 10.1016/j.braindev.2012.02.013

Shreekantiah Umesh, D., Tikka, S. K., Goyal, N., Nizamie, S. H., and Sinha, V. K. (2016). Resting state theta band source distribution and functional connectivity in remitted schizophrenia. *Neurosci. Lett.* 630, 199–202. doi: 10.1016/j.neulet.2016.07.055

Slobodskoy-Plusnin, J. (2018). Behavioral and brain oscillatory correlates of affective processing in subclinical depression. *J. Clin. Exp. Neuropsychol.* 40, 437–448. doi: 10.1080/13803395.2017.1371281

Snyder, S. M., and Hall, J. R. (2006). A meta-analysis of quantitative EEG power associated with attention-deficit hyperactivity disorder. *J. Clin. Neurophysiol.* 23, 441–456. doi: 10.1097/01.wnp.0000221363.12503.78

Sohn, H., Kim, I., Lee, W., Peterson, B. S., Hong, H., Chae, J.-H., et al. (2010). Linear and non-linear EEG analysis of adolescents with attention-deficit/hyperactivity disorder during a cognitive task. *Clin. Neurophysiol.* 121, 1863–1870. doi: 10.1016/j.clinph.2010.04.007

Son, K.-L., Choi, J.-S., Lee, J., Park, S. M., Lim, J.-A., Lee, J. Y., et al. (2015). Neurophysiological features of Internet gaming disorder and alcohol use disorder: a resting-state EEG study. *Transl. Psychiatry* 5:e628. doi: 10.1038/tp.2015.124

Sponheim, S. R. C., Clementz, B. A., Iacono, W. G., and Beiser, M. (1994). Resting EEG in first-episode and chronic schizophrenia. *Psychophysiology* 31, 37–43. doi: 10.1111/j.1469-8986.1994.tb01023.x

Stroganova, T. A., Nygren, G., Tsetlin, M. M., Posikera, I. N., Gillberg, C., Elam, M., et al. (2007). Abnormal EEG lateralization in boys with autism. *Clin. Neurophysiol.* 118, 1842–1854. doi: 10.1016/j.clinph.2007.05.005

Sutton, S. K., Burnette, C. P., Mundy, P. C., Meyer, J., Vaughan, A., Sanders, C., et al. (2004). Resting cortical brain activity and social behavior in higher functioning children with autism. *J. Child Psychol. Psychiatry* 46, 211–222. doi: 10.1111/j.1469-7610.2004.00341.x

Swartwood, J. N., Swartwood, M. O., Lubar, J. F., and Timmermann, D. L. (2003). EEG differences in ADHD-combined type during baseline and cognitive tasks. *Pediatr. Neurol.* 28, 199–204. doi: 10.1016/s0887-8994(02)00514-3

Thiagarajan, T. (2017). "Brainbase: a research and data management platform for human EEG," in *2017 IEEE Signal Processing in Medicine and Biology Symposium (SPMB)* (Philadelphia, PA: IEEE), 1–5.

Thiagarajan, T. C., Lebedev, M. A., Nicolelis, M. A., and Plenz, D. (2010). Coherence potentials: loss-less, all-or-none network events in the cortex. *PLoS Biol.* 8:e1000278. doi: 10.1371/journal.pbio.1000278

Thomas, B. L., and Viljoen, M. (2016). EEG brain wave activity at rest and during evoked attention in children with attention-deficit/hyperactivity disorder and effects of methylphenidate. *Neuropsychobiology* 73, 16–22. doi: 10.1159/000441523

Tierney, A. L., Gabard-Durnam, L., Vogel-Farley, V., Tager-Flusberg, H., and Nelson, C. A. (2012). Developmental trajectories of resting EEG power: an endophenotype of autism spectrum disorder. *PLoS One* 7:e39127. doi: 10.1371/journal.pone.0039127

Tikka, S. K., Yadav, S., Nizamie, S. H., Das, B., Tikka, D. L., and Goyal, N. (2014). Schneiderian first rank symptoms and gamma oscillatory activity in neuroleptic naïve first episode schizophrenia: a 192 channel EEG study. *Psychiatry Investig.* 11:467. doi: 10.4306/pi.2014.11.4.467

Tislerova, B., Brunovsky, M., Horacek, J., Novak, T., Kopecek, M., Mohr, P., et al. (2008). LORETA functional imaging in antipsychotic-naive and olanzapine-, clozapine- and risperidone-treated patients with schizophrenia. *Neuropsychobiology* 58, 1–10. doi: 10.1159/000154474

Todder, D., Levine, J., Abujumah, A., Mater, M., Cohen, H., and Kaplan, Z. (2012). The quantitative electroencephalogram and the low-resolution electrical tomographic analysis in posttraumatic stress disorder. *Clin. EEG Neurosci.* 43, 48–53. doi: 10.1177/1550059411428716

Tombor, L., Kakuszi, B., Papp, S., Réthelyi, J., Bitter, I., and Czobor, P. (2018). Decreased resting gamma activity in adult attention deficit/hyperactivity disorder. *World J. Biol. Psychiatry* doi: 10.1080/15622975.2018.1441547 [Epub ahead of print].

Tot, Ş., Özge, A., Çömelekoğlu, Ü., Yazici, K., and Bal, N. (2002). Association of QEEG findings with clinical characteristics of OCD: evidence of left frontotemporal dysfunction. *Can. J. Psychiatry* 47, 538–545. doi: 10.1177/070674370204700605

Trujillo, L. T., Stanfield, C. T., and Vela, R. D. (2017). The effect of electroencephalogram (EEG) reference choice on information-theoretic measures of the complexity and integration of EEG signals. *Front. Neurosci.* 11:425. doi: 10.3389/fnins.2017.00425

Tye, C., Rijsdijk, F., and McLoughlin, G. (2014). Genetic overlap between ADHD symptoms and EEG theta power. *Brain Cogn.* 87, 168–172. doi: 10.1016/j.bandc.2014.03.010

Urigüen, J. A., and Garcia-Zapirain, B. (2015). EEG artifact removal-state-of-the-art and guidelines. *J. Neural Eng.* 12:031001. doi: 10.1088/1741-2560/12/3/031001

van der Vinne, N., Vollebregt, M. A., van Putten, M. J. A. M., and Arns, M. (2017). Frontal α asymmetry as a diagnostic marker in depression: fact or fiction? A meta-analysis. *Neuroimage Clin.* 16, 79–87. doi: 10.1016/j.nicl.2017.07.006

van Diessen, E., Senders, J., Jansen, F. E., Boersma, M., and Bruining, H. (2015). Increased power of resting-state gamma oscillations in autism spectrum disorder detected by routine electroencephalography. *Eur. Arch. Psychiatry Clin. Neurosci.* 265, 537–540. doi: 10.1007/s00406-014-0527-3

van Dongen-Boomsma, M., Lansbergen, M. M., Bekker, E. M., Sandra Kooij, J. J., van der Molen, M., Kenemans, J. L., et al. (2010). Relation between resting EEG to cognitive performance and clinical symptoms in adults with attention-deficit/hyperactivity disorder. *Neurosci. Lett.* 469, 102–106. doi: 10.1016/j.neulet.2009.11.053

Vanrullen, R. (2011). Four common conceptual fallacies in mapping the time course of recognition. *Front. Psychol.* 2:365. doi: 10.3389/fpsyg.2011.00365

Veiga, H., Deslandes, A., Cagy, M., Fiszman, A., Piedade, R. A. M., and Ribeiro, P. (2003). Neurocortical electrical activity tomography in chronic schizophrenics. *Arq. Neuropsiquiatr.* 61, 712–717. doi: 10.1590/s0004-282x2003000500002

Velikova, S., Locatelli, M., Insacco, C., Smeraldi, E., Comi, G., and Leocani, L. (2010). Dysfunctional brain circuitry in obsessive-compulsive disorder: source and coherence analysis of EEG rhythms. *Neuroimage* 49, 977–983. doi: 10.1016/j.neuroimage.2009.08.015

Veltmeyer, M. D., McFarlane, A. C., Bryant, R. A., Mayo, T., Gordon, E., and Clark, C. R. (2006). Integrative assessment of brain function in PTSD: brain stability and working memory. *J. Integr. Neurosci.* 5, 123–138. doi: 10.1142/s0219635206001057

Venables, N. C., Bernat, E. M., and Sponheim, S. R. (2009). Genetic and disorder-specific aspects of resting state EEG abnormalities in schizophrenia. *Schizophr. Bull.* 35, 826–839. doi: 10.1093/schbul/sbn021

Vigário, R. N. (1997). Extraction of ocular artefacts from EEG using independent component analysis. *Electroencephalogr. Clin. Neurophysiol.* 103, 395–404. doi: 10.1016/s0013-4694(97)00042-8

Vigário, R., Särelä, J., Jousmäki, V., Hämäläinen, M., and Oja, E. (2000). Independent component approach to the analysis of EEG and MEG recordings. *IEEE Trans. Biomed. Eng.* 47, 589–593. doi: 10.1109/10.841330

Voytek, B., Kramer, M. A., Case, J., Lepage, K. Q., Tempesta, Z. R., Knight, R. T., et al. (2015). Age-related changes in 1/f neural electrophysiological noise. *J. Neurosci.* 35, 13257–13265. doi: 10.1523/JNEUROSCI.2332-14.2015

Wada, Y., Takizawa, Y., Kitazawa, S., Zheng-Yan, J., and Yamaguchi, N. (1994). Quantitative EEG analysis at rest and during photic stimulation in drug-naive patients with first-episode paranoid schizophrenia. *Eur. Arch. Psychiatry Clin. Neurosci.* 244, 247–251. doi: 10.1007/bf02190377

Wahbeh, H., and Oken, B. S. (2013). Peak high-frequency HRV and peak α frequency higher in PTSD. *Appl. Psychophysiol. Biofeedback* 38, 57–69. doi: 10.1007/s10484-012-9208-z

Walter, W. G. (1938). Critical review: the technique and application of electro-encephalography. *J. Neurol. Psychiatry* 1, 359–385. doi: 10.1136/jnnp.1.4.359

Wang, G. Y., Kydd, R., and Russell, B. R. (2015a). Resting EEG and ERPs findings in methadone-substituted opiate users: a review. *Acta Neurol. Belg.* 115, 539–546. doi: 10.1007/s13760-015-0476-2

Wang, G. Y., Kydd, R., Wouldes, T. A., Jensen, M., and Russell, B. R. (2015b). Changes in resting EEG following methadone treatment in opiate addicts. *Clin. Neurophysiol.* 126, 943–950. doi: 10.1016/j.clinph.2014.08.021

Wang, G. Y., Kydd, R. R., and Russell, B. R. (2016). Quantitative EEG and low-resolution electromagnetic tomography (LORETA) imaging of patients undergoing methadone treatment for opiate addiction. *Clin. EEG Neurosci.* 47, 180–187. doi: 10.1177/1550059415586705

Ward, M. F., Wender, P. H., and Reimherr, F. W. (1993). The wender utah rating scale: an aid in the retrospective diagnosis of childhood attention deficit hyperactivity disorder [published erratum appears in Am J Psychiatry 1993 Aug;150(8):1280] . *Am. J. Psychiatry* 150, 885–890. doi: 10.1176/ajp.150.6.885

Webb, S. J., Bernier, R., Henderson, H. A., Johnson, M. H., Jones, E. J. H., Lerner, M. D., et al. (2015). Guidelines and best practices for electrophysiological data collection, analysis and reporting in autism. *J. Autism Dev. Disord.* 45, 425–443. doi: 10.1007/s10803-013-1916-6

Widmann, A., and Schröger, E. (2012). Filter effects and filter artifacts in the analysis of electrophysiological data. *Front. Psychol.* 3:233. doi: 10.3389/fpsyg.2012.00233

Wise, V., McFarlane, A. C., Clark, C. R., and Battersby, M. (2011). An integrative assessment of brain and body function 'at rest' in panic disorder: a combined quantitative EEG/autonomic function study. *Int. J. Psychophysiol.* 79, 155–165. doi: 10.1016/j.ijpsycho.2010.10.002

Woltering, S., Jung, J., Liu, Z., and Tannock, R. (2012). Resting state EEG oscillatory power differences in ADHD college students and their peers. *Behav. Brain Funct.* 8:60. doi: 10.1186/1744-9081-8-60

Wuebben, Y., and Winterer, G. (2001). Hypofrontality—a risk-marker related to schizophrenia? *Schizophr. Res.* 48, 207–217. doi: 10.1016/s0920-9964(00)00047-5

Xing, M., Tadayonnejad, R., MacNamara, A., Ajilore, O., DiGangi, J., Phan, K. L., et al. (2017). Resting-state theta band connectivity and graph analysis in generalized social anxiety disorder. *Neuroimage Clin.* 13, 24–32. doi: 10.1016/j.nicl.2016.11.009

Young, K. S. (1998). Internet Addiction: the emergence of a new clinical disorder. *CyberPsychol. Behav.* 1, 237–244. doi: 10.1089/cpb.1998.1.237

Zhao, Q., Jiang, H., Hu, B., Li, Y., Zhong, N., Li, M., et al. (2017). Nonlinear dynamic complexity and sources of resting-state EEG in abstinent heroin addicts. *IEEE Trans. Nanobioscience* 16, 349–355. doi: 10.1109/TNB.2017.2705689

Conflict of Interest Statement: The authors declare that the research was conducted in the absence of any commercial or financial relationships that could be construed as a potential conflict of interest.

frontiers in Human Neuroscience

ORIGINAL RESEARCH
published: 11 January 2019
doi: 10.3389/fnhum.2018.00505

Current Status and Issues Regarding Pre-processing of fNIRS Neuroimaging Data: An Investigation of Diverse Signal Filtering Methods Within a General Linear Model Framework

Paola Pinti[1,2]*, *Felix Scholkmann*[3], *Antonia Hamilton*[2], *Paul Burgess*[2] *and Ilias Tachtsidis*[1]

[1] Department of Medical Physics and Biomedical Engineering, University College London, London, United Kingdom, [2] Institute of Cognitive Neuroscience, University College London, London, United Kingdom, [3] Department of Neonatology, Biomedical Optics Research Laboratory, University Hospital Zurich, University of Zurich, Zurich, Switzerland

Functional near-infrared spectroscopy (fNIRS) research articles show a large heterogeneity in the analysis approaches and pre-processing procedures. Additionally, there is often a lack of a complete description of the methods applied, necessary for study replication or for results comparison. The aims of this paper were (i) to review and investigate which information is generally included in published fNIRS papers, and (ii) to define a signal pre-processing procedure to set a common ground for standardization guidelines. To this goal, we have reviewed 110 fNIRS articles published in 2016 in the field of cognitive neuroscience, and performed a simulation analysis with synthetic fNIRS data to optimize the signal filtering step before applying the GLM method for statistical inference. Our results highlight the fact that many papers lack important information, and there is a large variability in the filtering methods used. Our simulations demonstrated that the optimal approach to remove noise and recover the hemodynamic response from fNIRS data in a GLM framework is to use a 1000th order band-pass Finite Impulse Response filter. Based on these results, we give preliminary recommendations as to the first step toward improving the analysis of fNIRS data and dissemination of the results.

Keywords: functional near infrared spectroscopy, digital filter, general linear model, pre-processing standardization, functional data analysis, pre-processing guidelines

OPEN ACCESS

Edited by:
Stephane Perrey,
Université de Montpellier, France

Reviewed by:
Abdul Rauf Anwar,
University of Engineering and Technology, Lahore, Pakistan
Noman Naseer,
Air University, Pakistan

***Correspondence:**
Paola Pinti
p.pinti@ucl.ac.uk

Received: *24 September 2018*
Accepted: *03 December 2018*
Published: *11 January 2019*

Citation:
Pinti P, Scholkmann F, Hamilton A, Burgess P and Tachtsidis I (2019) Current Status and Issues Regarding Pre-processing of fNIRS Neuroimaging Data: An Investigation of Diverse Signal Filtering Methods Within a General Linear Model Framework. Front. Hum. Neurosci. 12:505. doi: 10.3389/fnhum.2018.00505

INTRODUCTION

The last few years have seen a rapid (almost exponential) growth in the number of functional neuroimaging studies performed and published with functional near-infrared spectroscopy (fNIRS) (Yücel et al., 2017). fNIRS has provided neuroscientists and clinicians with a novel and invaluable tool to study and monitor tissue oxygenation changes in the brain non-invasively. Based on neurovascular coupling, fNIRS measures the brain tissue concentration changes in oxyhemoglobin (HbO_2) and deoxyhemoglobin (HbR) associated with an increased metabolic demand of the brain during neuronal activity, and an increased tissue perfusion

(Scholkmann et al., 2014). To date, one of the major fields of application of fNIRS is cognitive neuroscience, where the mechanisms underlying brain functioning are typically investigated by monitoring the task or stimulus-evoked changes in the brain during the execution of cognitive tasks (see Pinti et al., 2018 for review). fNIRS is well-suited to this application since it allows the study of cognition with very few physical constraints, allowing brain monitoring in a wide range of cognitive tasks, e.g., those including bodily movements, and in a variety of populations, e.g., infants, healthy adults, clinical patients. A typical sequence of steps performed in a neuroscience with fNIRS is shown in **Figure 1**, usually comprising 4 main steps.

Step 1: The first step is the design and implementation of the experimental protocol. Block or event-related designs are usually employed, in which the stimuli are presented several times to increase the statistical power, and experimental task periods are typically interspersed with contrast conditions or stimuli (or in some cases rest periods) to better assess the presence of hemodynamic responses. fNIRS data are then collected during the execution of the designed experiment. A mixed block/event-related design can be also employed (Petersen and Dubis, 2012).

Step 2: The data acquisition step comprises the placement of a certain number of light sources and detectors (i.e., "optodes") on the participants' head by means of fiber optics, and at a light source-detector distance of 3 cm in case of studies with adults. The raw fNIRS signal measured by the detector, e.g., the raw light intensity signal, originates from the tissue volume located below the source and detector having a maximal depth a bit less than half the source-detector distance [i.e., this is called "channel" (Patil et al., 2011)]. The number of channels and the sampling frequency of the acquisition depend on the particular fNIRS instrument used.

Step 3: During the pre-processing phase, the raw intensity data are usually visually inspected to assess signals' quality (e.g., the presence of large motion artifacts, and of heart beat oscillations indicating a good optical coupling between the optodes and the scalp). Intensity time-series are converted into changes in attenuation (or optical density, ΔOD) and then into concentration changes of HbO_2 and HbR (ΔHbO_2 and ΔHbR), usually by means of the modified Beer-Lambert law (Delpy et al., 1988). In order to extract useful information from fNIRS data, any source of variability in the ΔHbO_2 and ΔHbR signals not related to the task-evoked hemodynamic activity needs to be removed, or at least minimized. For a review on the structures and the statistical properties of the noises that are often present in fNIRS data, we advise the reader to see the publication of Huppert (2016). One typically experienced source of noise is that due to head movements. In fact, although fNIRS is more robust to motion artifacts than other modalities [e.g., functional magnetic resonance imaging (fMRI), electroencephalography/magnetoencephalography (EEG/MEG)], signals can be corrupted by head movements, causing fast spikes or shifts from the baseline values. The most common practice to deal with these motion errors is to include the identification and correction of such artifacts as a step in the signal pre-processing stream. Several techniques have been proposed so far and have been reviewed elsewhere (Brigadoi et al., 2014). In addition, fNIRS data are also contaminated by physiological noises not directly related to cortical brain activity that can deteriorate the Signal-to-Noise Ratio (SNR), and mask and/or mimic the presence of brain hemodynamic responses (Tachtsidis and Scholkmann, 2016). The origin of these components and the methods developed so far to reduce their impact on the estimation of brain activity by fNIRS have been reviewed by Scholkmann et al. (2014). Briefly, such physiological changes contribute a large amount of variance to the fNIRS signals and can be elicited both (i) by the execution of the cognitive task, and (ii) spontaneously. In the first case, the execution of particularly complex or stressful tasks can affect the psychophysiological state of the participant, resulting in changes in heart rate, breathing rate, blood pressure, carbon dioxide (CO_2) concentration of the blood and autonomic regulatory activity happening both at the intra- and extra-cerebral levels (Rowley et al., 2006; Kirilina et al., 2012; Scholkmann et al., 2013; Holper et al., 2014; Tachtsidis and Scholkmann, 2016); the second case refers to the spontaneous hemodynamic oscillations related to physiological vasomotor regulations and breathing-related fluctuations (Tachtsidis et al., 2004; Tong et al., 2012). These spontaneous components are characterized by signals at specific frequencies associated with the heart rate ($\sim$1 Hz), breathing rate ($\sim$0.3 Hz), Mayer waves ($\sim$0.1 Hz), and very low frequency (< 0.04, VLF) oscillations. One of the most common and more straightforward approaches used by the

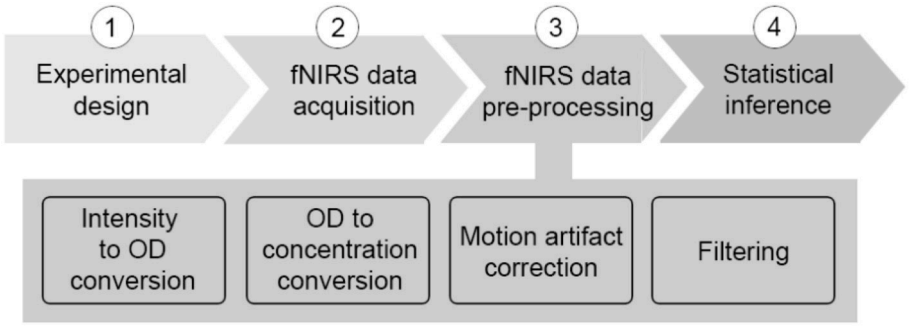

FIGURE 1 | Typical neuroscience experiment pipeline with fNIRS.

scientific community to reduce the impact of these components, is to remove specific frequency bands in fNIRS signals by means of digital filters. Digital filtering is a mathematical procedure applied to discrete time-series to reduce or enhance certain properties of the input signals (e.g., frequency ranges). Filters are divided into three classes: (i) *high-pass filters*, which remove high frequency components above the cut-off frequency; (ii) *low-pass filters*, which remove low frequency components below the cut-off frequency; (iii) *band-pass filters*, which preserve the frequency range between a lower and a higher cut-off frequency. Some research groups apply filters on ΔOD data prior the conversion into concentration changes; others apply the filter on the ΔHbO_2 and ΔHbR signals. However, in both cases, the frequency range to include needs to be chosen carefully in order to preserve the stimulus frequency and to preserve the task-evoked response.

Step 4: Once the data are pre-processed, statistical analyses are performed, and the pre-processed ΔHbO_2 and ΔHbR signals are used to make inference about task-evoked functional brain activity (see Tak and Ye, 2014 for a review). One of the most common statistical frameworks employed by the community is the General Linear Model (GLM). This approach has more statistical power than other methods commonly used for fNIRS (e.g., block averaging). In fact, the GLM considers the entire fNIRS time series taking advantage of the high temporal resolution of fNIRS. It also provides good flexibility as it allows to test specific hypothesis by comparing combinations of the experimental conditions with different statistical testing approaches (e.g., t-tests, F-tests, ANOVAs, ANCOVAs; Monti, 2011). In addition, it permits the inclusion of other covariates within the model or design matrix [e.g., behavioral performance, head movement, physiological signals, short-separation fNIRS channels (Tachtsidis and Scholkmann, 2016)] to improve the inference accuracy. However, the GLM has the disadvantage that it assumes a specific pre-defined hemodynamic response function, which e.g., to a great extent is still unknown for neonates or might be different across brain regions.

It is important to highlight how the experiment pipeline described above (**Figure 1**) is not made of stand-alone steps. Each phase influences the other and, more importantly, they influence the outcome of the statistical analyses and the study results. For instance, if the experimental protocol is not carefully designed and, for example, a task block duration of $\sim$10 s is chosen, the task frequency ($\sim$0.1 Hz) overlaps with the Mayer wave oscillation, leading to inflated statistics. Additionally, the pre-processing stream has a major impact also on the comparison of results among different studies and research groups, and on study replication, because the statistical analyses depend on the data content. It is therefore extremely important and good practice to always report detailed information about each individual step of the experiment pipeline (**Figure 1**), from the protocol specification (type of stimuli, structure, durations, presentation software), the device features (model, sampling frequency, wavelengths), signal pre-processing (algorithm to compute ΔHbO_2 and ΔHbR, motion artifact correction algorithm, filter parameters), to the statistical analyses (hypotheses, statistical test).

Whilst all these procedures are almost standardized for other neuroimaging modalities such as fMRI, this is not the case for fNIRS yet. As recently highlighted by Hocke et al. (2018), fNIRS publications often lack useful information, and there is a huge variability in the analysis procedures and in the way methods are described. For instance, the absence of standardization of input parameters for fNIRS pre-processing and analysis methods can lead to suboptimal papers or irreproducible studies and results. In addition, the authors demonstrated how the use and the combination of different methods (e.g., criteria for identifying noisy channels, motion artifact correction, signals' filtering, etc.) can lead to different results, influencing the neuroscientific conclusions. Another relevant issue is related to the best fNIRS-derived signal to infer functional brain activity, as fNIRS provides measurements of both HbO_2 and HbR. For example, some papers draw neuroscientific conclusions based only on ΔHbO_2. But, others report total hemoglobin (ΔHbO_2 +ΔHbR), and yet others describe both ΔHbO_2 and ΔHbR. Therefore, there is an urgent need to move toward a standardization of the experimental procedures, right through from the study design phase to the presentation of results. The aim of the current report is to start tackling this standardization issue and to set the ground for the development of toward common guidelines. More precisely, in this work we focus (i) on the filtering step of the pre-processing phase and (ii) on the assessment of the completeness of the information reported in the published research articles. To this end, we first review the papers published in 2016 in the field of functional neuroimaging with fNIRS to analyse information on (i) the latest most used filtering approaches and (ii) the data inclusiveness. Then, we test the identified filter specifications on synthetic fNIRS data generated from 18 subjects resting state data with a superimposed task-related component simulating a block-design experiment, and explore the effect of filters and their application to ΔOD or ΔHbO_2 and ΔHbR on the outcome of statistical analyses in order to optimize the inference procedure in a GLM-based framework.

LITERATURE REVIEW

A literature review of fNIRS articles published in the field of cognitive neuroscience was performed as first step with the aim of identifying the most common filtering approaches adopted by the community, and of evaluating the completeness of the information reported in research papers. To this end, we used the PubMed database, plus a manual search from articles, references, and the publication surveys made available by the Society for functional Near Infrared Spectroscopy (http://fnirs.org/publications/nirs-niri-publications/). Articles were selected on the basis of the following criteria:

1. Papers published in 2016, in order to review the most updated and advanced pre-processing approaches as a representative sample of the fNIRS field
2. Original research articles published on peer-reviewed journals. Conference proceedings and review papers were excluded from further analyses

3. Studies conducted on adults, as infants' fNIRS data have different spectral characteristics [e.g., a higher heart rate frequency band (von Siebenthal et al., 1999)] and thus different filtering specifications must be used
4. Papers that included task-evoked functional activation experiments, as fNIRS is by far mostly used for monitoring task-related brain activity in response to cognitive tasks
5. Our analysis included only continuous-wave (CW) fNIRS studies looking at concentration changes of oxy- and deoxy-hemoglobin due to the popularity of CW-fNIRS in current fNIRS research and neuroscience applications.

A total of 110 papers were selected (see **Supplementary Material 4** for a complete list). From each full-text, we collected the following information (**Figure 2**):

1. the sampling frequency (F_s) of the fNIRS acquisition
2. the inclusion of the filtering step in the pre-processing stream
3. the type of filtered signal (ΔOD or ΔHbO_2 and ΔHbR)
4. the type of filter applied (e.g., Butterworth, finite impulse response (FIR), Moving Average)
5. the filter characteristic (low-pass (LP), high-pass (HP), band-pass (BP) filtering)
6. the filter order, where applicable
7. the cut-off frequencies (F_c)

Note: If the authors stated in the paper that they used the Homer2 software package (http://homer-fnirs.org/) for their analysis and did not report any information about the filter type, we automatically considered they used a 3rd order Butterworth filter as this is the default option in the software. Papers including more than one functional experiment within the same work were considered as separate studies.

Out of the 110 papers, 75.5% of the articles reported the F_s of the fNIRS acquisition (**Figure 2A**).

This result suggests that not all the papers report all the relevant information necessary for replicating or comparing the study results. Indeed, the F_s is an important parameter to evaluate the frequency bandwidth of the fNIRS signals or for assessing the filter stability within a certain frequency range. Additionally, as **Figure 2C** shows, there is not a clear agreement about whether it is a better practice to filter the optical density data or concentration data, and the fNIRS community is divided between the two approaches. In fact, for the papers we analyzed, the filter is applied on ΔOD signals in 32.5% of the studies and on ΔHbO_2 and ΔHbR in 65%. The remaining 2.5% of the papers did not include this information.

Concerning the use of filters, the 72.7% of the papers included a filtering step in the pre-processing pipeline (**Figure 2B**). **Figure 2D** shows the distribution of the filter types across these papers. With "Generic" (**Figure 2D**) we refer to those filters for which the authors did not mention the particular filter type (e.g., '…data were band-pass filtered…'). The filter types shown in **Figure 2D** were both used individually or in combination with each other (e.g., W-MDL together with HRF). Within the majority of the papers (36.3%), the filter type was not properly described (i.e., Generic), further proving that not all the articles provide the most salient information, hence making it difficult for others to replicate the same procedure.

For the following analyses, we focused on the filter types being used in more than 3 papers (1.8%, **Figure 2D**, red rectangle), these are the Generic, Butterworth (BW), Moving Average (MovAvg) and Finite Impulse Response (FIR) filters. Among these filters, we determined how many articles included information about:

- the type of filter (LP/HP/BP, where applicable, i.e., Generic, BW, FIR)
- the filter order (where applicable, i.e., Generic, BW, FIR)
- the cut-off frequency ranges (where applicable, i.e., Generic, BW, MovAvg, FIR)

Results are presented in **Figures 2E–H**. Encouragingly enough only 1.6% of the papers did not include information about the type of filters (**Figure 2E**). **Figure 2E** also illustrates the distribution of the filter characteristics, showing that BP and LP are more often used rather than HP filters. However, concerning the filter orders (**Figure 2F**), the majority of the papers (59.7%) did not provide information about this parameter, which is really important for filters design. For our further analyses (see section Data Analysis), we have focused on BP and LP filters (**Figure 2E** red rectangle) since they are the most popular; and on all the filter orders (3, 4, 5, 20, **Figure 2F** red rectangle). Regarding the cut-off frequencies (**Figures 2G,H**), authors usually reports these except for the lower F_c for one BP filter (**Figure 2G**) and for 8.1% of the LP filters (**Figure 2H**). For our tests (see section Data Analysis), we used the F_c adopted by at least 3 papers (1.8%) and we indicated those with red rectangles in **Figures 2G,H**.

MATERIALS AND METHODS

Participants

In order to investigate the effects of the filters on the outcome of statistical analyses, resting-state fNIRS data were collected on a cohort of healthy adults. Sixteen individuals (9 females, 7 males; age = 26.9 ± 2.9 years) were recruited and 18 sessions were performed. Prior the experiment, participants acclimated for about 15 min within the testing room. During the experiment, they were asked to keep their eyes closed for the entire session while being awake. The study was approved by the UCL ethics committee (Reference 1133/001) and participants gave informed consent prior to the experimental session.

fNIRS Data Acquisition

Spontaneous changes in prefrontal cortex hemodynamics were measured using the Wearable Optical Tomography (WOT, Hitachi High-technologies Corporation, Japan) fNIRS device. The system is made of a portable box, containing the recording unit, and a headset, containing the optical components (**Figure 3A**). The headset is equipped with 6 laser diodes emitting light at 705 and 830 nm, and 6 silicon photodiodes (Atsumori et al., 2009), arranged in an alternating geometry creating 16 measurement channels (**Figure 3B**; source-detector separation: 3 cm). Raw fNIRS data were recorded at 5 Hz. In order to place

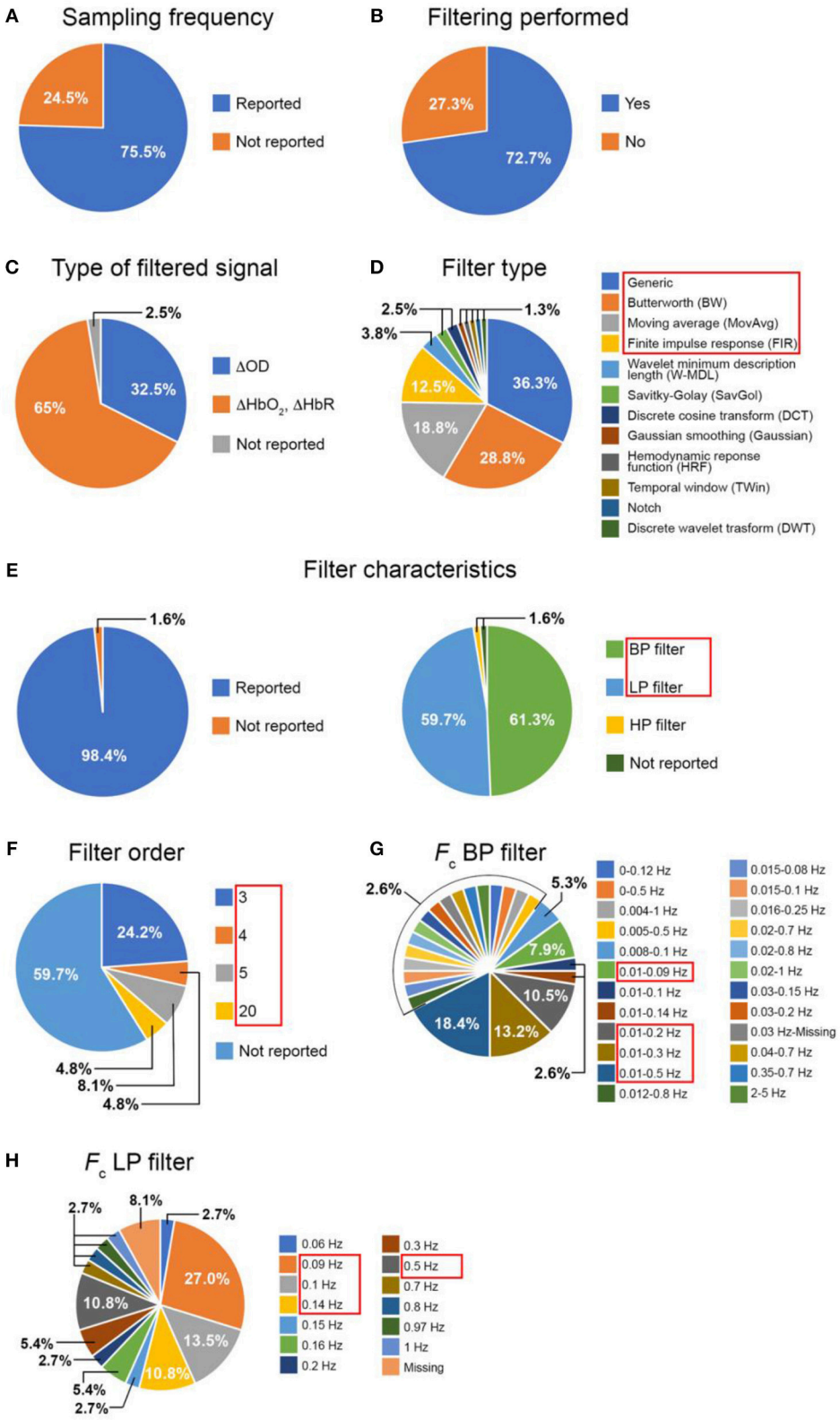

FIGURE 2 | Summary of the literature review results: inclusion of **(A)** the F_S and of **(B)** a filtering step in the studies; proportion of the filtered signals **(C)**, filter type **(D)**, filter characteristics **(E)**, filter order **(F)**, F_C of band-pass **(G)** and low-pass **(H)** filters across the papers that included a filtering step. (BP, band-pass; LP, low-pass).

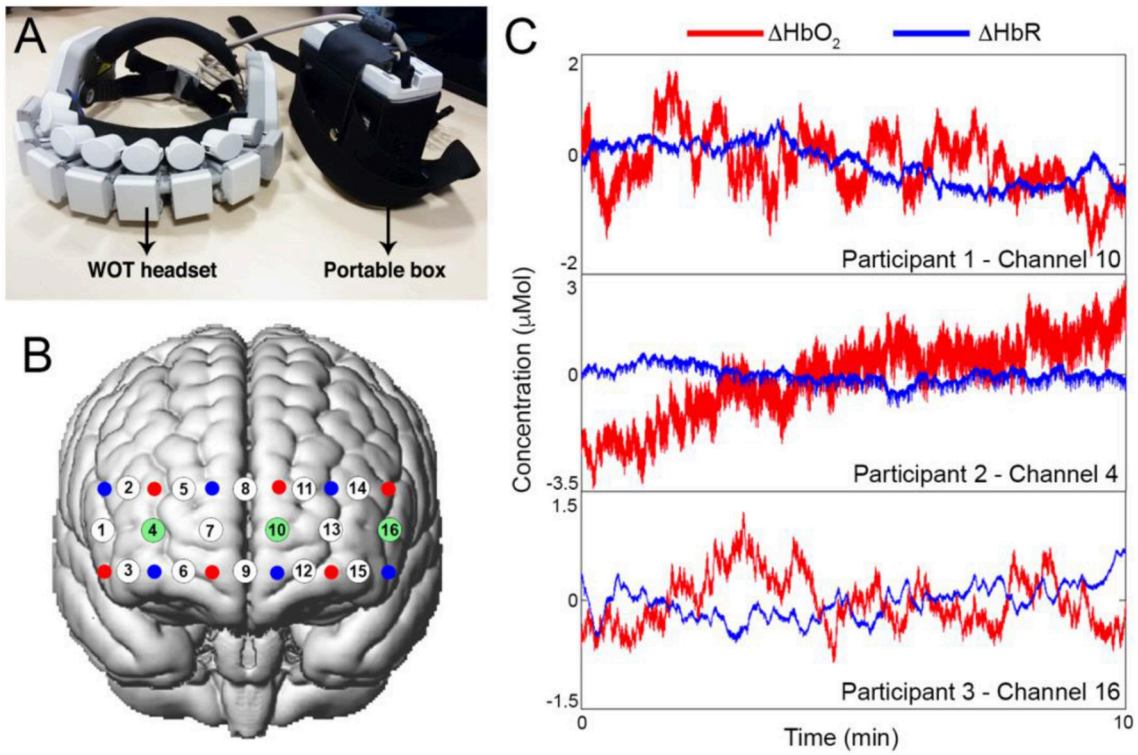

FIGURE 3 | (A) Hitachi Wearable Optical Tomography fNIRS device, and corresponding channels configuration onto the prefrontal cortex **(B)**. Sources are represented as red dots, detectors as blue dots and channels as white dots. Highlighted in green are the channels for which the corresponding time-series are presented in **(C)**. **(C)** shows examples of raw ΔHbO_2 and ΔHbR resting-state signals for one channel for each of three participants.

the WOT headset in a reliable way across all the participants, we used the 10/20 electrode positioning system (Okamoto et al., 2004) and placed channel 8 in correspondence of the Fpz point and channel 8 and 9 were aligned to the Nasion-Inion line. Resting-state data were collected for ∼10 min while participants were comfortably sitting on a chair with their eyes closed. Examples of resting-state data for one channel from three subjects are shown in **Figure 3C**.

Data Analysis

Single-subject's data analysis flowchart is presented in **Figure 4**.

Raw time-series were visually inspected to detect noisy channels (e.g., due to large motion errors, sudden amplitude changes, poor coupling) and channels with a poor optical coupling [e.g., absence of the ∼1 Hz heartbeat oscillations in raw signals (Pinti et al., 2015)] were excluded from further analyses. Raw resting-state fNIRS data were first converted into optical density data and then into changes in concentration through the modified Beer-Lambert law, using a differential pathlength factor of 6 (Yücel et al., 2016). For all channels, a synthetic task-related component (the same for all 16 channels) simulating a block-design experiment was added to both ΔHbO_2 and ΔHbR signals. This was created by convolving a Hemodynamic Response Function (HRF) with a boxcar function reflecting the simulated experimental protocol. The HRF was composed of two gamma functions, the positive one modeling the response and the negative one modeling the undershoot (peak: 6 s and undershoot: 16 s after the onset); the boxcar included 14 task blocks of 20 s spaced out by 20 s rest periods. This resulted in a stimulation frequency (F_{stim}) of 0.025 Hz (F_{stim} = 1/(20+20) Hz). We used different amplitudes for the HbO_2 and HbR task-related components, with the HbR one being ∼-1/3 of the HbO_2 component, as HbR has smaller changes than HbO_2 (Gagnon et al., 2012). More precisely, in order to generate signals with different SNR, we considered the following amplitudes:

1. Amplitude 1: 0.8 μMol for ΔHbO_2 and −0.27 μMol for ΔHbR
2. Amplitude 2: 0.5 μMol for ΔHbO_2 and −0.17 μMol for ΔHbR
3. Amplitude 3: 0.3 μMol for ΔHbO_2 and −0.1 μMol for ΔHbR

Three different synthetic datasets were thus generated for each of the 18 resting-state data.

Synthetic ΔHbO_2 and ΔHbR signals were re-converted into ΔOD data and motion artifacts were identified and corrected (**Figure 4**) using the targeted principal component analysis (tPCA Yücel et al., 2014) implemented in the Homer2 software package, as it acts only on corrupted data segments, thus not altering the frequency content of the signals (function: *hmrMotionCorrectPCArecurse*; input parameters: $tMotion = 0.5$, $tMask = 1$, $STDthresh = 10$, $AMPthresh = 5$, $nSV = 0.97$, *maxIter*

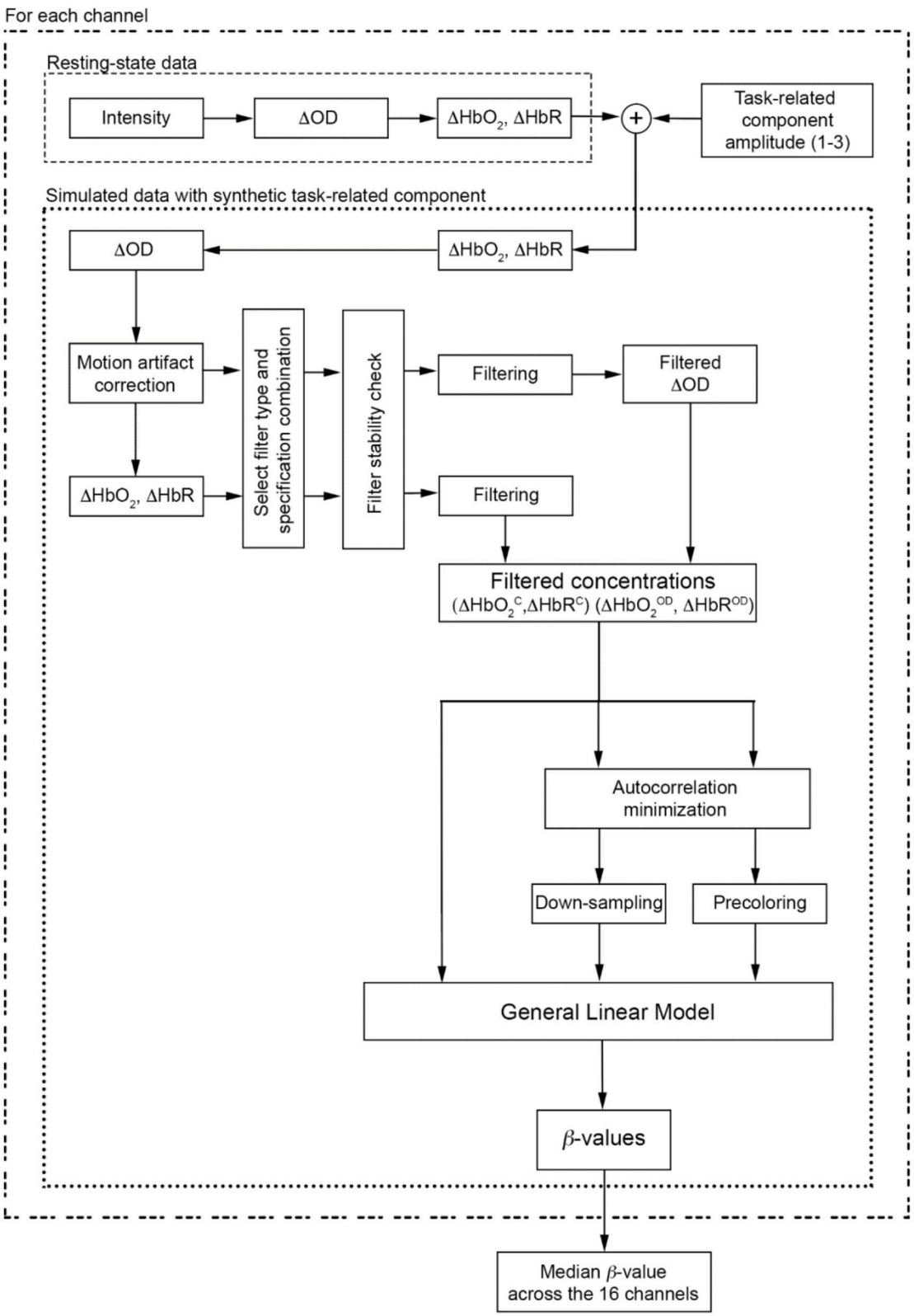

FIGURE 4 | Data analysis flow chart applied to each participant and to each task-related component amplitude. The procedure is also applied for each filter type and specification combinations.

= 5). Optical density data corrected for motion errors were converted into ΔHbO_2 and ΔHbR.

Based on the literature review (see section Literature Review), we filtered both synthetic ΔOD and, ΔHbO_2 and ΔHbR signals using the filter specifications summarized in **Table 1**. All the F_c ranges include our F_{stim} (0.025 Hz). Filter orders of 100, 500, 1000 were also included in addition to the ones found in the literature, as FIR filters require higher orders than IIR filters (i.e., Butterworth) to achieve a good level of performance. More precisely, for each type of filter, we used all the combinations of filter type, filtered signals, filter order, and F_c.

Whilst FIR filters are always stable (i.e., for a finite input, the output is always finite, and the region of convergence of the transfer function of the filter includes the unit circle), IIR filters can be unstable for a given order and F_c (Ifeachor and Jervis, 2002). In fact, considering the transfer function of the filters, FIR filters have as many poles as zeros but they are all located at the origin of the *z*-plane, thus being always stable; by contrast, IIR filters are stable only if the poles are inside the unitary circle in the *z*-plane. Moving average filters operate by averaging the input signal within a certain window to produce the output signal. They are a particular type of low-pass FIR filters where the output signal is not multiplied by filter coefficients, but it is only scaled by 1/(window length). MovAvg are thus also always stable. Therefore, we first checked the stability of BP and LP Butterworth filters since they are IIR, for all the F_c and orders, using the zero-pole analysis, i.e., looking at the location of poles in the *z*-plane (for this procedure we used the Matlab functions *butter*, *isstable,* and *zplane*). Once the stability was assessed, we applied the type of filter with all the possible combination of specifications to synthetic ΔOD and, ΔHbO_2 and ΔHbR signals. Filtered ΔOD were then converted into concentration changes. We will refer to ΔHbO_2^C and ΔHbR^C if the filter was applied directly to concentration data, and to ΔHbO_2^{OD} and ΔHbR^{OD} if the filter was applied to optical density data and then converted into concentration changes. In addition to the filters' stability, the phase delay introduced by the filter needs to be taken into account. In fact, the filtered signal can be shifted in time respect to the original unfiltered signal. In case of a FIR filter, the phase delay is constant, i.e., the same across the whole frequency range, and can be corrected by shifting back in time the filtered signal of the delay amount. With IIR filters (i.e., Butterworth), the phase delay is frequency-dependent, i.e., the shift is different for the different frequencies. This phenomenon is known as phase distortion and can be compensated using a zero-phase filter that we performed in Matlab with the *filtfilt* function.

Filtered concentration data were used to carry out statistical analyses and to establish the best filtering approach. The procedure described below was applied for each task-related component amplitude, to each channel of each participant's filtered signal (ΔHbO_2^C, ΔHbR^C, ΔHbO_2^{OD}, ΔHbR^{OD}), each type of filter (BP and LP), and each filter specification combination (**Table 1**). Statistical analyses were performed using the GLM approach (**Figure 4**). This method consists of regressing fNIRS data with a linear combination of explanatory variables (or regressors) and an error term. Regressors are computed through the convolution of the boxcar function describing the experimental protocol with the HRF (Friston et al., 1994). In our case, the design matrix was composed of the task-related regressor modeling the hemodynamic response to the simulated block-design experiment, plus the constant term. β-values were estimated through the least square estimation. These parameters are indicators of the strength of the relationship between a regressor and the experimental fNIRS data, and represent the contribution of each regressor to the fNIRS signal. However, fNIRS data are affected by serial autocorrelations due to the oscillating nature of the fNIRS signals (Barker et al., 2016) that impact on the accuracy of GLM-based analyses (Ye et al., 2009). Autocorrelations originate from the high sampling rate of fNIRS acquisition and from the physiological noises and motion errors present in the signals (Barker et al., 2016; Huppert, 2016). To account for serial autocorrelations and to minimize their impact on the GLM, we used two approaches: (i) down-sampling, and (ii) precoloring. In the first approach, we down-sampled the filtered concentration data to 1 Hz using a spline interpolation to reduce the sampling rate. Down-sampling the signal before the filter is applied can introduce a form of distortion in the data called aliasing, especially at the high-frequencies and when the new sampling rate is smaller than twice the highest frequency of interest in the signal (Nyquist frequency). To avoid this issue, low-pass filters (i.e., anti-aliasing filter) are typically used to remove the components above the new Nyquist frequency. In the second approach, we applied the precoloring method, i.e., smoothing the fNIRS data and the design matrix with a low-pass filter shaped like the HRF (Worsley and Friston, 1995; Huppert, 2016), which is a common method for analyzing fMRI and fNIRS data (Worsley and Friston, 1995; Ye et al., 2009). In order to test the impact of serial autocorrelations, we applied the GLM also to the filtered concentration data without any of these corrections (**Figure 4**). For each participant's data, the GLM was applied to each channel and each chromophore individually. β-values were then estimated for each channel and the median β-value across the 16 channels was computed for each participant. Median β-values for all the subjects were used to run statistical analyses at group-level. More precisely, we first checked for (i) the normality of the distribution of the group median β-values using the Shapiro-Wilk test as recommended for small sample sizes (Shapiro et al., 1968; Ghasemi and Zahediasl, 2012; < 50), and (ii)

TABLE 1 | Type of filter and filer specifications resulting from the literature review process.

FILTER CHARACTERISTIC: BP	
Filter type	BW, FIR
Filtered signals	ΔOD, ΔHbO_2, ΔHbR
Filter order	3, 4, 5, 20, 100*, 500*, 1000*
F_C [Hz]	0.01–0.09, 0.01–0.2, 0.01–0.3, 0.01–0.5
FILTER CHARACTERISTIC: LP	
Filter type	BW, FIR, MovAvg
Filtered signals	ΔOD, ΔHbO_2, ΔHbR
Filter order	3, 4, 5, 20, 100*, 500*, 1000*
F_C [Hz]	0.09, 0.1, 0.14, 0.5

Asterisks indicate filter orders that were further added.

the presence of outliers. We considered as outliers when the β-values are below Q1 $-$ 1.5 $\times$ IQR or above Q3 + 1.5 $\times$ IQR (Q1: 1st quartile; Q3: 3rd quartile; IQR: interquartile range). Amplitude 1, Amplitude 2 and Amplitude 3 of the imposed task-related components constitute the reference β-values and represent the metric to assess filters' performance. In fact, the closer are the estimated β-values to the reference β, the better the filter, i.e., less task-related information and more physiological noise were removed. Therefore, in order to establish the best type of filter, we used one sample *t*-tests to test the null hypothesis that the estimated group median β-values are equal to the reference β at a significance level $\alpha = 0.05$. The closer the *p*-value to α, the more the group β-values are similar to the reference β, and thus the better the filter performance.

Additionally, we tested whether the filter performs better if applied to optical density or concentration data. To this goal, we used paired sample *t*-tests to compare the group β-values estimated on ΔHbO_2^C and ΔHbR^C with the group β-values estimated on ΔHbO_2^{OD} and ΔHbR^{OD}, for a given type of filter and specification combinations.

All the analyses were carried out using Matlab (The MathWorks Inc., Natick, Massachusetts; v. R2014a) and the Homer2 software package.

RESULTS

Examples of synthetic iconcentration data for a representative participant and channel generated using task-related components with Amplitude 1, Amplitude 2, and Amplitude 3 are shown in **Figure 5**.

Due to the poor coupling between the fNIRS headset and the head, channel 11 was excluded from further analyses for participant 11, and channel 14 and 16 were excluded for participant 18. Synthetic datasets simulating a block-design experiment with 20 s task blocks were used to test the performance of filters in reducing the unwanted noise components in the fNIRS signals and in preserving the task-evoked hemodynamic response. To achieve this, we applied the type of filters and filter specifications summarized in **Table 1** to the synthetic datasets. More precisely, we filtered both the ΔOD and, ΔHbO_2 and ΔHbR time-series to determine the best signal to filter to obtain correct statistics. Prior the application of these filters, we tested the stability of BW filters for data sampled at 5 Hz using the zero-pole analysis, i.e., looking at the location of the poles of the filter transfer function with respect to the unitary circle in the *z*-plane. Filters with poles located within the unitary circles were considered stable. The procedure was applied to all the combinations of orders and F_c and to both BP and LP BW filters. Results for BP and LP filters are summarized in **Figures 6A,B** respectively. Green squares indicate stable filters, red elements indicate unstable filters.

For instance, a BW BP filter for data sampled at 5 Hz with order 5 and F_c = [0.01 0.2] Hz results stable as all the poles of the transfer function are inside the unitary circle (**Figure 6C**), whereas the same BW with order 20 is unstable (**Figure 6D**).

Figure 7 shows an example of filtered ΔHbO_2^C and ΔHbR^C signals using a BW BP filter (5th order, F_c: 0.01–0.2 Hz, **Figures 7A,B**), FIR BP filters (5th order, F_c: 0.01–0.2 Hz, **Figures 7C,D**) and FIR BP filters (1000th order, F_c: 0.01–0.2 Hz, **Figures 7E,F**) to synthetic ΔHbO_2 and ΔHbR, demonstrating the need for higher orders for FIR filters respect to IIR filters. The corresponding estimated β-values are reported as well.

Whilst the 5th order BW BP filter was able to remove the slow drifts in the unfiltered ΔHbO_2 and ΔHbR signals (**Figures 7A,B**), a FIR filter with order 5 is not effective enough (**Figures 7C,D**). In fact, very low frequency modulations in the filtered ΔHbO_2 signal can still be observed as well as a slow trend in the filtered ΔHbR (**Figures 7C,D**) and both signals are not centered around the zero-level. This results in an overestimation of the β-values (9.28×10^{-7} for ΔHbO_2 and of -3.38×10^{-7} for ΔHbR). As a property of FIR filters, they require much higher orders than IIR filters to achieve comparable performance. As expected, with a 1000th order FIR filter, slow trends are effectively removed (**Figures 7E,F**), the signal mean is reported to be around the zero-level and a similar performance of the 5th order BW filter is achieved (light green and cyan signals in **Figures 7E,F**). The improvement in filters' performance is also reflected in the estimated β-values. The 1000th order FIR filter corresponds to a β-value of 7.51×10^{-7} for ΔHbO_2^C and of -2.27×10^{-7} for ΔHbR^C that are more similar to the reference β (8×10^{-7} for ΔHbO_2 and of -2.7×10^{-7} for ΔHbR) than the estimated β-values for the 5th order FIR filter (β-value = 9.28×10^{-7} for ΔHbO_2^C; β-value = -3.38×10^{-7} for ΔHbR^C). More precisely, the β-values for the 5th order FIR filter are higher than the reference β because the slow trends of the signals were not removed effectively, worsening the GLM-fitting. The 1000th order FIR filter also performs similarly to the 5th order BW BP filter for which the β-values are 7.58×10^{-7} for ΔHbO_2^C and of -2.26×10^{-7} for ΔHbR^C, demonstrating that FIR filters require higher orders than IIR to achieve comparable performance.

For each task-related component amplitude, and each type of filter and filter specification, ΔHbO_2^C and ΔHbR^C, and ΔHbO_2^{OD} and ΔHbR^{OD} were used to run statistical analyses by means of the GLM approach. Since GLM-based analyses of fNIRS data can be influenced by serial autocorrelations, β-values were estimated (i) with no correction for serial correlations, (ii) down-sampling to 1 Hz the filtered data, (iii) using the precoloring method. The corresponding median β-values computed for each participant across the 16 measurement channels were used to assess filters performance. To achieve this, we first checked for the normality of the group β-values distribution using the Shapiro-Wilk test, testing the null hypothesis that median β-values are normal at significance level $\alpha = 0.05$. Results referring to BP filters, Amplitude 1 and ΔHbO_2^C obtained using the precoloring method are shown in **Table 2** and in **Table 3** for ΔHbR^C. The corresponding normality test results for LP and BP filters, all amplitudes, ΔHbO_2^{OD} and ΔHbR^{OD} are included in **Supplementary Material 1**.

Median β-values were normally distributed for BW filters ($p > \alpha$) according to the Shapiro-Wilk normality test. By contrast, for ΔHbO_2^C the null hypothesis of normal distribution was rejected ($p < \alpha$) for all the FIR filters with an order $<$ 500

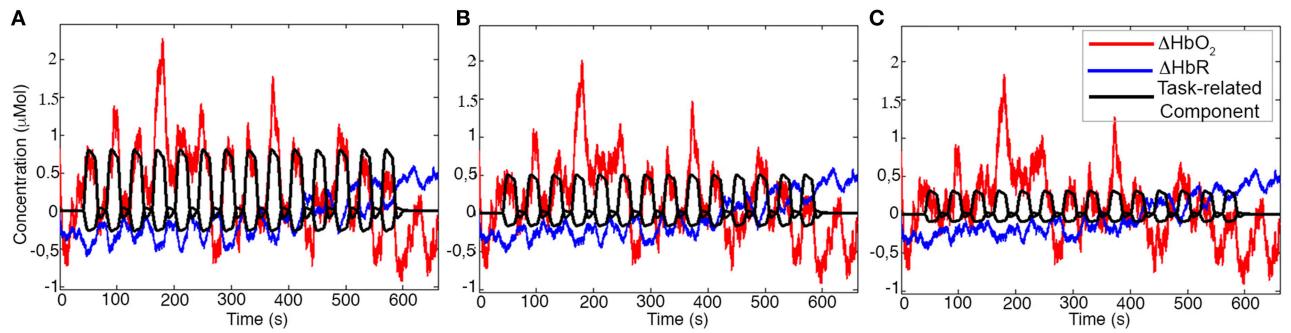

FIGURE 5 | Examples of synthetic ΔHbO_2 (red) and ΔHbR (blue) signals for one channel of a representative participant. The black signal represents the task-related component with Amplitude 1 **(A)**, Amplitude 2 **(B)**, and Amplitude 3 **(C)** added to the concentration data.

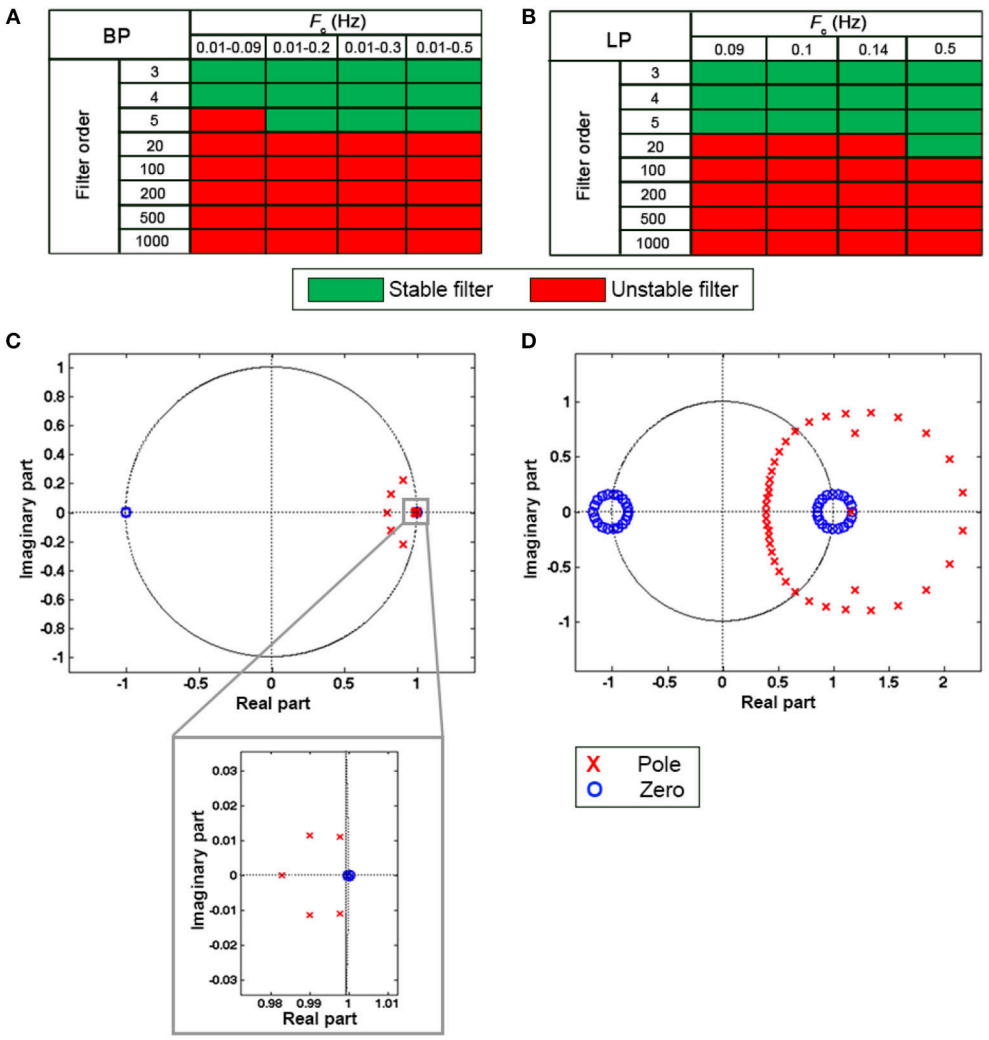

FIGURE 6 | Results of the filter stability for the BP BW filters **(A)** and LP BW filters **(B)** for all the combination of orders and F_C. Green and red squares indicate stable and unstable filters, respectively. **(C,D)** show examples of filter stability analysis considering a BW BP filter with F_C = [0.01 0.2] Hz. The filter results stable for a filter order 5 **(C)**, as the poles are inside the unitary circle as shown in the zoom. By contrast, with an order: 20 **(D)** the filter becomes unstable. Zeros are indicated by blue circles and poles by red crosses.

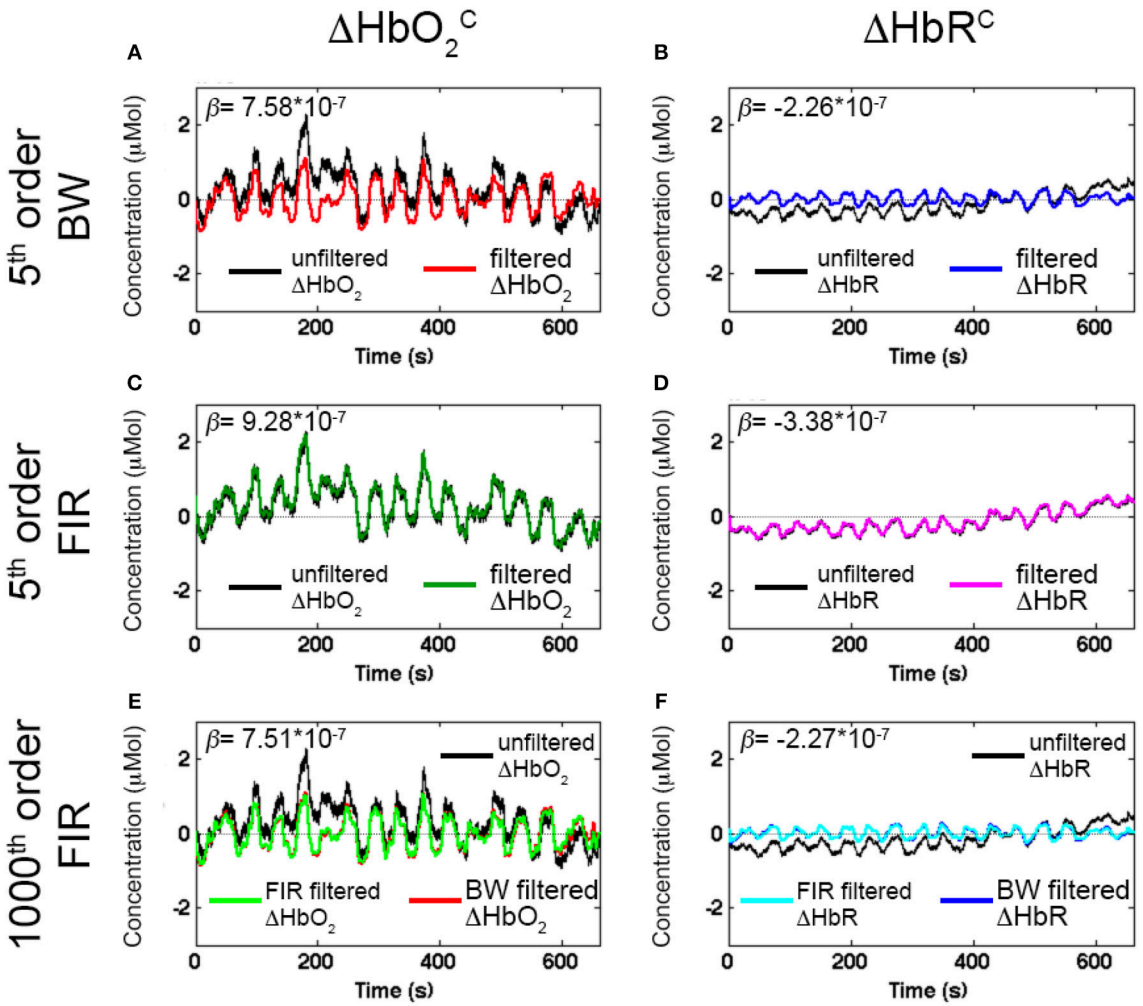

FIGURE 7 | Examples of filtered ΔHbO_2^C and ΔHbR^C signals with Amplitude 1 for one channel of a representative participant using a 5th order BW BP filter (**A,B**, red and blue signals), a 5th order FIR BP filter (**C** and **D**, green and magenta signals), and a 1000th order FIR BP filter (**E,F**, light green and cyan signals) within the range [0.01, 0.2] Hz. The estimated β-values from the GLM fitting of the filtered ΔHbO_2^C and ΔHbR^C are included. The reference β are 8×10^{-7} for ΔHbO_2 and of -2.7×10^{-7} for ΔHbR.

(**Table 2**) and with an order < 200 for ΔHbR^C (**Table 3**). In fact, as also shown in **Figure 7**, FIR filters require higher orders to effectively remove unwanted noise. For instance, with lower orders, slow trends in the signals related to e.g., instrumental noise or spontaneous physiological fluctuations are not properly filtered, introducing variability in the group β-values, since these types of noise can differ from subject to subject. As ΔHbR is less influenced by physiological interferences (Kirilina et al., 2012; Zhang et al., 2016) and there is thus less inter-subject variability, FIR filters with orders > 200 for are effective enough for ΔHbR. This variability results in outliers that alter the β-values distribution, as it can be observed in the box-plots in **Supplementary Figures 9**, **10** (Supplementary Material 2) referring to the data in **Tables 2** and **3**, respectively. The normality assumption is not violated when an order > 500 for ΔHbO_2 and order > 200 for ΔHbR is used for FIR filters and no outliers are present (**Supplementary Figures 9**, **10** in Supplementary Material 2), further demonstrating the need of high orders.

The same is true for LP filters (**Table 4** for ΔHbO_2^C, and **Table 5** for ΔHbR^C), where median β-values never follow a normal distribution for any filter. In fact, especially in this case, slower signal modulations related to instrumental noise and slow vascular regulations are not filtered out since LP filters only attenuate noise with higher frequency content than the F_c reported in **Table 1**.

In fact, outliers can be found for all the three filter types (**Supplementary Figures 11**, **12** in Supplementary Material 2). This also results in an overestimation of the β-values since the noise amplifies the signal amplitude and change its dynamics. This applies for all amplitudes and filtered signals (**Supplementary Materials 1, 2**). The use of LP filters on their

TABLE 2 | Shapiro-Wilk test results computed on ΔHbO_2^C BP filtered data, with Amplitude 1.

Order/F_c	0.01–0.09 Hz		0.01–0.2 Hz		0.01–0.3 Hz		0.01–0.5 Hz	
	$W_{(18)}$	p	$W_{(18)}$	p	$W_{(18)}$	p	$W_{(18)}$	p
BW								
3	0.91	0.10	0.91	0.07	0.91	0.07	0.90	0.07
4	0.92	0.14	0.91	0.08	0.91	0.08	0.91	0.08
5	-	-	0.93	0.21	0.93	0.20	0.93	0.19
20	-	-	-	-	-	-	-	-
100	-	-	-	-	-	-	-	-
200	-	-	-	-	-	-	-	-
500	-	-	-	-	-	-	-	-
1000	-	-	-	-	-	-	-	-
FIR								
3	0.77	1.04E-03	0.77	1.04E-03	0.77	1.04E-03	0.77	1.04E-03
4	0.77	1.04E-03	0.77	1.04E-03	0.77	1.04E-03	0.77	1.04E-03
5	0.77	1.03E-03	0.77	1.03E-03	0.77	1.03E-03	0.77	1.03E-03
20	0.77	9.85E-04	0.77	9.96E-04	0.77	1.01E-03	0.77	1.04E-03
100	0.77	1.09E-03	0.78	1.44E-03	0.78	1.43E-03	0.78	1.43E-03
200	0.85	1.14E-02	0.85	1.18E-02	0.85	1.17E-02	0.85	1.16E-02
500	0.92	1.09E-01	0.91	9.55E-02	0.91	9.23E-02	0.91	9.11E-02
1000	0.91	8.16E-02	0.91	7.44E-02	0.91	7.34E-02	0.91	7.34E-02

W-values and corresponding p-values are reported. $p < 0.05$ are underlined, meaning that the null hypothesis that the β-values are normally distributed is rejected at significance level $\alpha = 0.05$. Results are not reported in case of unstable filters. '-' indicates unstable filters for which the Shapiro-Wilk test was not carried out.

TABLE 3 | Shapiro-Wilk test results computed on ΔHbR^C BP filtered data, with Amplitude 1.

Order/F_c	0.01–0.09 Hz		0.01–0.2 Hz		0.01–0.3 Hz		0.01–0.5 Hz	
	$W_{(18)}$	p	$W_{(18)}$	p	$W_{(18)}$	p	$W_{(18)}$	p
BW								
3	0.95	0.48	0.95	0.50	0.95	0.50	0.95	0.48
4	0.95	0.51	0.95	0.44	0.95	0.47	0.95	0.48
5	-	-	0.95	0.50	0.95	0.47	0.95	0.47
20	-	-	-	-	-	-	-	-
100	-	-	-	-	-	-	-	-
200	-	-	-	-	-	-	-	-
500	-	-	-	-	-	-	-	-
1000	-	-	-	-	-	-	-	-
FIR								
3	0.81	3.33E-03	0.81	3.33E-03	0.81	3.33E-03	0.81	3.33E-03
4	0.81	3.33E-03	0.81	3.33E-03	0.81	3.33E-03	0.81	3.33E-03
5	0.81	3.32E-03	0.81	3.32E-03	0.81	3.32E-03	0.81	3.33E-03
20	0.81	3.11E-03	0.81	3.16E-03	0.81	3.23E-03	0.81	3.35E-03
100	0.82	4.25E-03	0.83	6.28E-03	0.83	6.25E-03	0.83	6.13E-03
200	0.94	2.97E-01	0.94	3.01E-01	0.94	3.01E-01	0.94	2.97E-01
500	0.93	1.76E-01	0.93	2.06E-01	0.93	2.09E-01	0.93	2.10E-01
1000	0.96	6.04E-01	0.96	6.04E-01	0.96	6.03E-01	0.96	6.01E-01

W-values and corresponding p-values are reported. $p < 0.05$ are underlined, meaning that the null hypothesis that the β-values are normally distributed is rejected at significance level $\alpha = 0.05$. Results are not reported in case of unstable filters. '-' indicates unstable filters for which the Shapiro-Wilk test was not carried out.

TABLE 4 | Shapiro-Wilk test results computed on ΔHbO_2^C LP filtered data, with Amplitude 1.

Order/F_c	0.09 Hz		0.1 Hz		0.14 Hz		0.5 Hz	
	$W_{(18)}$	p	$W_{(18)}$	p	$W_{(18)}$	p	$W_{(18)}$	p
BW								
3	0.77	1.04E-03	0.77	1.04E-03	0.77	1.03E-03	0.77	1.04E-03
4	0.77	1.05E-03	0.77	1.05E-03	0.77	1.03E-03	0.77	1.04E-03
5	0.77	1.08E-03	0.77	1.06E-03	0.77	1.04E-03	0.77	1.04E-03
20	-	-	-	-	-	-	0.77	1.04E-03
100	-	-	-	-	-	-	-	-
200	-	-	-	-	-	-	-	-
500	-	-	-	-	-	-	-	-
1000	-	-	-	-	-	-	-	-
FIR								
3	0.77	1.04E-03	0.77	1.04E-03	0.77	1.04E-03	0.77	1.04E-03
4	0.77	1.04E-03	0.77	1.04E-03	0.77	1.04E-03	0.77	1.04E-03
5	0.77	1.03E-03	0.77	1.03E-03	0.77	1.03E-03	0.77	1.03E-03
20	0.77	9.84E-04	0.77	9.85E-04	0.77	9.88E-04	0.77	1.03E-03
100	0.76	8.65E-04	0.77	9.39E-04	0.77	1.03E-03	0.77	1.05E-03
200	0.77	1.02E-03	0.77	1.05E-03	0.77	1.04E-03	0.77	1.05E-03
500	0.77	1.02E-03	0.77	1.05E-03	0.77	1.04E-03	0.77	1.04E-03
1000	0.77	1.04E-03	0.77	1.05E-03	0.77	1.04E-03	0.77	1.04E-03
MovAvg								
	0.77	1.03E-03	0.77	1.03E-03	0.77	1.04E-03	-	-

W-values and corresponding p-values are reported. $p < 0.05$ are underlined, meaning that the null hypothesis that the β-values are normally distributed is rejected at significance level $\alpha = 0.05$. Results are not reported in case of unstable filters and $F_c = 0.5$ Hz that corresponds to a null window length for the MovAvg filter. '-' indicates unstable filters for which the Shapiro-Wilk test was not carried out.

own has thus not enough performance for denoising fNIRS data so that LP filters were excluded from further analyses.

Concerning the filter performance, we used one-sample t-tests to compare the group β-values to the reference β for each amplitude, filtered signals, type of filter and filter specifications. In addition, this was done for data not corrected for serial correlations, corrected through down-sampling and precoloring (**Supplementary Material 3**). In **Table 6** and **Table 7** we report the results referring to the β-values computed on ΔHbO_2^C and ΔHbR^C data corrected through the precoloring method, for Amplitude 1.

For our experimental design with the F_{stim} of 0.025 Hz, we found that the best compromise across the three amplitudes, filtered signals, and in terms of outliers (**Tables 2** and **3**) is to use a BP FIR filter with order 1000 and F_c = [0.01, 0.09] Hz (**Supplementary Material 3**). In fact, the F_c range is more centered and narrower around the F_{stim} than the other F_c ranges (**Table 1**), and includes both the F_{stim} and the following two harmonics ($2 \times F_{stim}$ and $3 \times F_{stim}$), maximizing the hemodynamic content and removing unnecessary frequency components. These filter specifications generally correspond to smallest t-value that means more similarity to the reference β, i.e., a better recovery of the hemodynamic response. Concerning the correction for serial autocorrelations, we found that the best results were obtained using the precoloring method (Ye et al., 2009), as the median β-values are more similar to the reference β for all the three amplitudes respect to the median β-values computed with no correction and down-sampling (**Supplementary Material 3**). This further establishes the precoloring as an effective way of accounting for autocorrelation in fNIRS signal and a fundamental step for GLM analyses (Ye et al., 2009).

We did not find statistically significant differences ($p > 0.05$) between corresponding β-values computed on $\Delta HbO_2^{OD}/\Delta HbR^{OD}$ and $\Delta HbO_2^C/\Delta HbR^C$, suggesting that it does not make any difference if the filter is applied to ΔOD data prior the conversion in concentration changes or to ΔHbO_2 and ΔHbR (**Supplementary Material 3**).

DISCUSSION

Since fNIRS is one of the most recent neuroimaging modalities, there is no agreement yet about the way of analyzing data and describing the methodological details in research articles. We have identified 110 papers published in 2016 which reported task-related investigation of brain activity with fNIRS to identify the most common missing information that is critical for any study replication or comparison. More precisely, we found that nearly ¼ of the papers did not report the sampling frequency of the fNIRS acquisition, which is important for defining some preprocessing parameters (e.g., filters' cut-off frequencies). More than a half of the reviewed papers used BP filters to denoise fNIRS data and nearly half employed LP filters. Among the articles using BP filters, 24 different F_c were proposed with the most common

TABLE 5 | Shapiro-Wilk test results computed on ΔHbR^C LP filtered data, with Amplitude 1.

Order/F_c	0.09 Hz		0.1 Hz		0.14 Hz		0.5 Hz	
	$W_{(18)}$	p	$W_{(18)}$	p	$W_{(18)}$	p	$W_{(18)}$	p
BW								
3	0.81	3.38E-03	0.81	3.38E-03	0.81	3.38E-03	0.81	3.34E-03
4	0.81	3.36E-03	0.81	3.37E-03	0.81	3.38E-03	0.81	3.34E-03
5	0.81	3.37E-03	0.81	3.37E-03	0.81	3.38E-03	0.81	3.34E-03
20	-	-	-	-	-	-	0.81	3.34E-03
100	-	-	-	-	-	-	-	-
200	-	-	-	-	-	-	-	-
500	-	-	-	-	-	-	-	-
1000	-	-	-	-	-	-	-	-
FIR								
3	0.81	3.33E-03	0.81	3.33E-03	0.81	3.33E-03	0.81	3.33E-03
4	0.81	3.33E-03	0.81	3.33E-03	0.81	3.33E-03	0.81	3.33E-03
5	0.81	3.32E-03	0.81	3.32E-03	0.81	3.32E-03	0.81	3.33E-03
20	0.81	3.11E-03	0.81	3.11E-03	0.81	3.13E-03	0.81	3.34E-03
100	0.80	2.60E-03	0.81	3.05E-03	0.81	3.42E-03	0.81	3.40E-03
200	0.82	3.65E-03	0.82	3.72E-03	0.81	3.47E-03	0.81	3.41E-03
500	0.81	3.48E-03	0.81	3.51E-03	0.81	3.43E-03	0.81	3.36E-03
1000	0.81	3.58E-03	0.81	3.49E-03	0.81	3.42E-03	0.81	3.35E-03
MovAvg								
	0.81	3.31E-03	0.81	3.32E-03	0.81	3.33E-03	-	-

W-values and corresponding p-values are reported. $p < 0.05$ are underlined, meaning that the null hypothesis that the β-values are normally distributed is rejected at significance level $\alpha = 0.05$. Results are not reported in case of unstable filters and $F_c = 0.5$ Hz that corresponds to a null window length for the MovAvg filter. '-' indicates unstable filters for which the Shapiro-Wilk test was not carried out.

being [0.01, 0.5] Hz (18.4% of the papers), and the most employed filter type was not defined (i.e. Generic, 36.3%) followed by Butterworth filters (28.8%). In terms of LP filters, a F_c of 0.09 Hz was most often used. However, important filtering parameters are very often missing in articles (see section Literature Review), especially the filter type (36.3%, **Figure 2D**) and the filter order (59.7%, **Figure 2F**). These are extremely important information that must be explicitly included in research papers to allow their full replication and understanding. In addition, there is not an agreement either on the filter type (**Figure 2D**) and the best signal to filter (**Figure 2C**).

In order to clarify these aspects and to start setting the ground for common practice in filtering and analyzing fNIRS data, we investigated the performance of the most frequently used band-pass and low-pass filters in terms of their influence on the outcome of the statistical inference step (**Figure 1**) in a GLM framework. The main findings of our simulation analysis using synthetic fNIRS data were:

(1) there is no difference in outcome of the statistical analyses in terms of filtered signals (optical density or concentration, **Supplementary Material 3**)
(2) low-pass filters and FIR filters with low orders (<500) are not effective in removing the physiological VLF components and slow trends in the fNIRS signals, resulting in higher inter-subjects variability that impacts on group-level statistical analyses (section Materials and Methods, **Supplementary Materials 1, 2, 3**). LP filters should thus be combined with HP filters or detrending approaches (e.g., linear detrending) to remove very slow trends and VLF from fNIRS data
(3) the best signal denoising is achieved using a BP FIR filter with high orders (e.g., >1000)
(4) better results and more suitable statistics are obtained when correcting the GLM-analysis for serial correlations by means of the precoloring method (**Supplementary Material 3**).

Here, we have only tested three different types of filters with some specifications based on the most common practices adopted by the community. Further studies are needed that explore additional filtering methods in case of e.g., event-related design and block-design experiments with variable durations, and using additional parameter specifications. In the following section, we provide some recommendations and guidelines that we believe could help users in designing an appropriate filter for fNIRS data and in disseminating the research procedures in articles.

RECOMMENDATIONS FOR FILTER DESIGN AND THE WAY FORWARD

Figure 8 shows the flow-chart of practical steps (A-E) that we advise to follow to design an effective filter for

TABLE 6 | One sample *t*-test results computed on ΔHbO_2^C BP filtered data, with Amplitude 1, comparing the group median β-values to the reference β, in case of precoloring correction.

Order/F_c	0.01–0.09 Hz		0.01–0.2 Hz		0.01–0.3 Hz		0.01–0.5 Hz	
	$t_{(17)}$	p	$t_{(17)}$	p	$t_{(17)}$	p	$t_{(17)}$	p
BW								
3	−5.12	8.59E-05	−5.10	8.98E-05	−5.09	9.04E-05	−5.11	8.69E-05
4	−5.32	5.62E-05	−5.22	6.87E-05	−5.22	6.93E-05	−5.25	6.49E-05
5	-	-	−5.09	9.04E-05	−5.20	7.25E-05	−5.20	7.27E-05
20	-	-	-	-	-	-	-	-
100	-	-	-	-	-	-	-	-
200	-	-	-	-	-	-	-	-
500	-	-	-	-	-	-	-	-
1000	-	-	-	-	-	-	-	-
FIR								
3	0.80	4.32E-01	0.88	3.91E-01	0.99	3.36E-01	1.32	2.04E-01
4	0.82	4.25E-01	0.95	3.57E-01	1.14	2.71E-01	1.68	1.12E-01
5	0.83	4.17E-01	1.03	3.18E-01	1.31	2.09E-01	2.05	5.58E-02
20	1.38	1.85E-01	3.11	6.32E-03	3.94	1.05E-03	2.35	3.13E-02
100	1.43	1.72E-01	−5.95	1.59E-05	−5.99	1.45E-05	−5.98	1.48E-05
200	−10.37	9.04E-09	−10.63	6.29E-09	−10.67	5.90E-09	−10.74	5.41E-09
500	−5.76	2.32E-05	−5.93	1.66E-05	−5.93	1.66E-05	−5.93	1.66E-05
1000	−4.73	1.93E-04	−4.93	1.27E-04	−4.92	1.28E-04	−4.92	1.29E-04

Underlined is the highest negative t-value obtained for a 1000th order BP FIR filter. The t-value is negative as the reference β (0.8) is higher than the group median β-values (0.7). '-' indicates unstable filters for which the t-test was not carried out.

TABLE 7 | One sample *t*-test results computed on ΔHbR^C BP filtered data, with Amplitude 1, comparing the group median β-values to the reference β, in case of precoloring correction.

Order/F_c	0.01–0.09 Hz		0.01–0.2 Hz		0.01–0.3 Hz		0.01–0.5 Hz	
	$t_{(17)}$	p	$t_{(17)}$	p	$t_{(17)}$	p	$t_{(17)}$	p
BW								
3	4.94	1.23E-04	4.82	1.61E-04	4.85	1.49E-04	4.88	1.41E-04
4	5.15	8.06E-05	5.06	9.67E-05	5.05	9.95E-05	5.01	1.07E-04
5	-	-	4.96	1.19E-04	4.98	1.13E-04	4.94	1.25E-04
20	-	-	-	-	-	-	-	-
100	-	-	-	-	-	-	-	-
200	-	-	-	-	-	-	-	-
500	-	-	-	-	-	-	-	-
1000	-	-	-	-	-	-	-	-
FIR								
3	−3.05	7.31E-03	−3.12	6.24E-03	−3.23	4.94E-03	−3.55	2.45E-03
4	−3.06	7.12E-03	−3.18	5.42E-03	−3.37	3.63E-03	−3.90	1.16E-03
5	−3.07	6.90E-03	−3.26	4.58E-03	−3.54	2.54E-03	−4.27	5.22E-04
20	−3.59	2.26E-03	−5.28	6.12E-05	−6.10	1.19E-05	−4.55	2.81E-04
100	−3.65	1.99E-03	3.71	1.76E-03	3.75	1.59E-03	3.74	1.64E-03
200	10.09	1.35E-08	10.48	7.79E-09	10.52	7.33E-09	10.59	6.65E-09
500	5.36	5.23E-05	5.56	3.49E-05	5.55	3.54E-05	5.55	3.54E-05
1000	4.01	9.05E-04	4.24	5.49E-04	4.23	5.61E-04	4.22	5.71E-04

Underlined is the lowest positive t-value obtained for a 1000th order BP FIR filter. The t-value is positive as the reference β (-0.27) is smaller than the group median β-values (−0.24). '-' indicates unstable filters for which the t-test was not carried out.

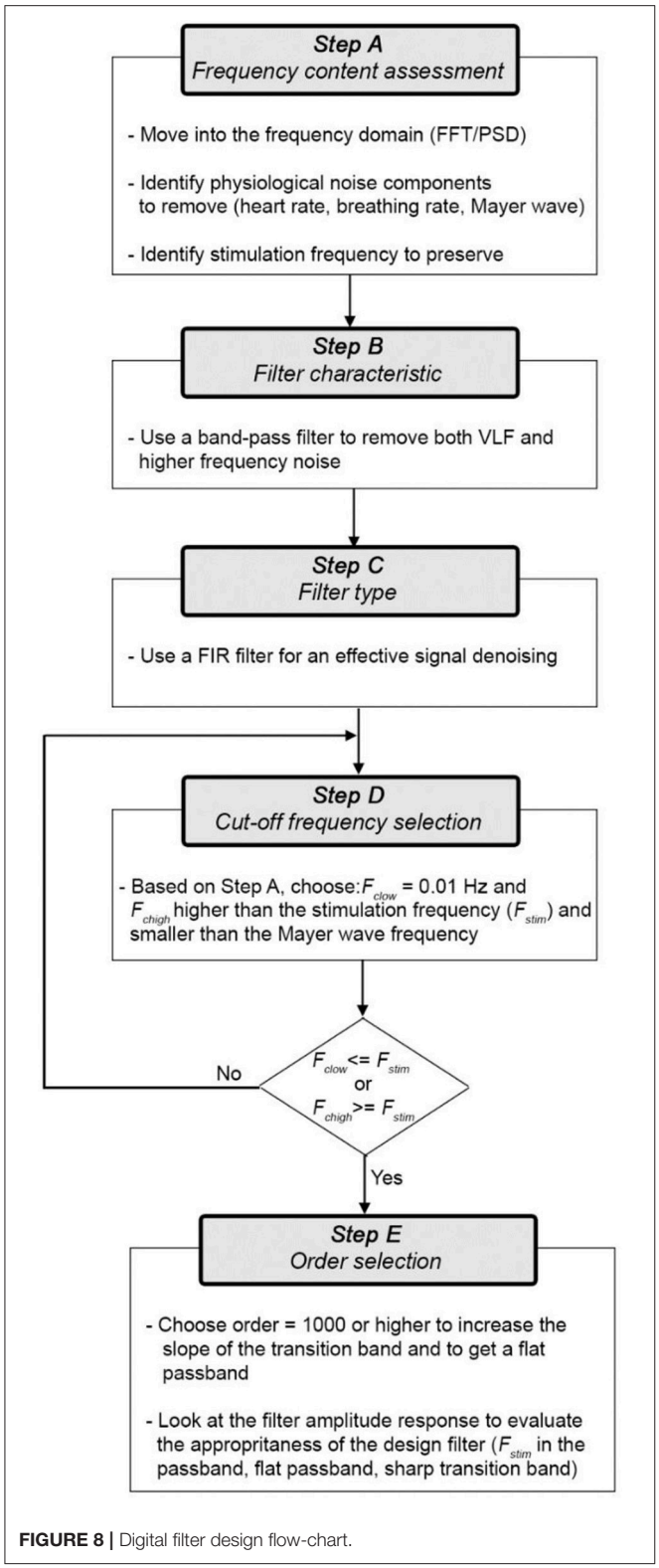

FIGURE 8 | Digital filter design flow-chart.

fNIRS data. Here, we consider ΔHbO_2 and ΔHbR as the signals to filter, but the same flow-chart applies to ΔOD.

More precisely, the steps are the follows:

Step A) Frequency content assessment: the first step we advise to perform is to evaluate the frequency content of fNIRS signals. This will allow the identification of the stimulus frequency band to preserve and of the physiological noise components (e.g., heart rate, respiration, Mayer waves) to remove. To this goal, there are different algorithms that can be used to e.g., compute the Fast Fourier Transform (FFT) of the signal or the Power Spectral Density (PSD). For instance, in **Figure 9** we used the Welch's estimation method to compute the PSD (function: *pwelch*; window length: 120 s; overlap: 50%) of the synthetic ΔHbO_2 and ΔHbR signals to assess the physiological noises frequency ranges to remove. The PSD shows how the power of a signal is distributed as a function of frequency. From the PSD of the fNIRS signals of a representative participant (**Figure 9**), we can identify the heart rate component (∼1.3 Hz), the respiration component (∼0.25 Hz), and the Mayer wave component (∼0.09 Hz); these are frequencies that we want to remove. We can also identify the stimulation frequency (F_{stim} = 1/40 s = ∼0.025 Hz in our case) that we want to preserve; and that guides the choice of the F_c of the filter.

Step B) Filter characteristic: the first choice to make prior to designing a filter is the filter characteristic (BP/LP/HP). Based on the literature review (see section Literature Review) and our results, a BP filter achieves the highest performances in the outcome of statistical analyses. In fact, a LP filter alone is not enough as it does not remove the VLF frequencies corresponding to the very low vasomotion regulations and instrumental noise (e.g., low trends) (see section Materials and Methods).

Step C) Filter type: Different BP filters are available (e.g., FIR or IIR). Based on our results (see Section Materials and Methods), we recommend the use of BP FIR filters as they are (i) more stable and hence easier to control than IIR filters (i.e., the output is always finite), and (ii) do not introduce phase distortions and phase shift across the whole frequency band.

Step D) Cut-off frequencies selection: For BP filters, two cut-off frequencies must be selected. The lowest F_c ($F_{c,\,low}$) will allow the frequencies higher than $F_{c,\,low}$ to pass. The highest F_c ($F_{c,\,high}$) will allow the frequencies lower than $F_{c,\,high}$ to pass. In this way, $F_{c,\,low}$ and $F_{c,\,high}$ define the passband of the BP filter, i.e. the frequency range that can pass through the filter (**Figure 10A**).

The cut-off frequency choice is a compromise between noise reduction and hemodynamic signal maximization. In fact, whilst it is relatively easy to remove e.g., the heart rate component and the VLF such as those related to vascular endothelial regulations [<0.01 (Yücel et al., 2016)], other components [e.g., Mayer waves or vascular neurogenic regulations (∼0.04 Hz Yücel et al., 2016)] might overlap or be very close to the stimulation frequency. This must be taken into consideration when designing the experimental protocol, e.g., avoiding 10 s blocks overlapping the Mayer waves frequency and using variable rest durations. We also have to consider that it is impossible to design ideal digital filters (**Figure 10A**) where the filter amplitude response is rectangular with very sharp passband edges that allow an exact separation between passband and stopband and e.g., a precise separation between stimulation and noise frequencies. In reality, one also has to consider the transition band (which will

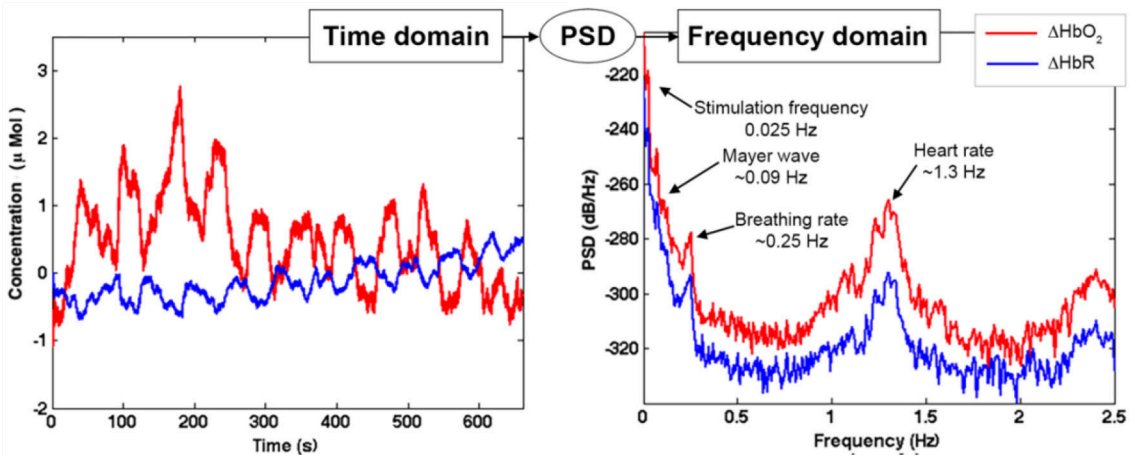

FIGURE 9 | Example of ΔHbO_2 and ΔHbR signals with Amplitude 1 for one channel of a representative participant in the time domain (left panel) and frequency domain (right panel). The PSD transforms the fNIRS signal from the time domain into the frequency domain. This allows the identification of the noise components (heart rate, breathing rate, Mayer waves) and the stimulation component, as shown in the left panel.

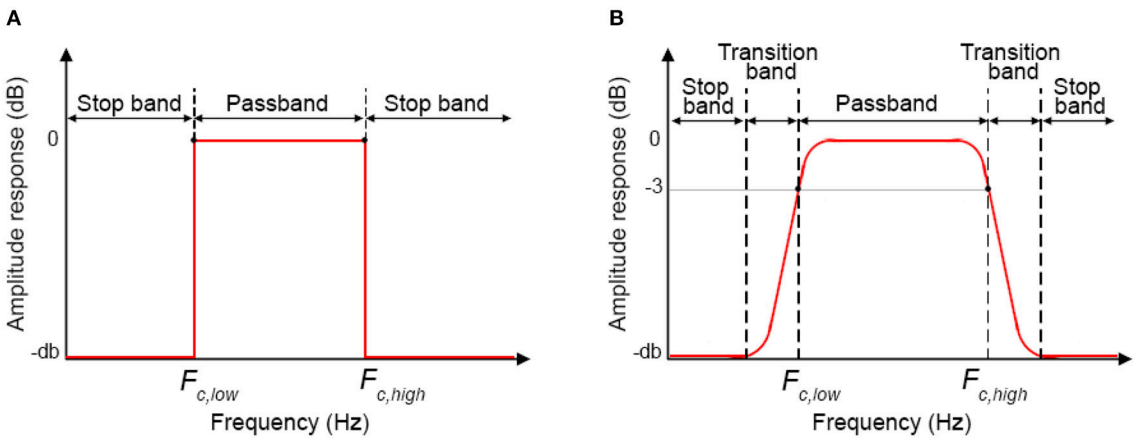

FIGURE 10 | Filter amplitude response for ideal filters **(A)** and real filters **(B)**.

depend on the filter order and type, see *Step E* and **Figure 10B**), which includes the frequency components that are progressively attenuated from −3 dB (i.e., the F_c) to the total attenuation of the filter. Therefore, some of the signal's frequencies outside the passband will be attenuated and will still pass through the filter.

In our case with 20 s task-rest periods, the stimulation frequency (0.025 Hz) does not overlap with the Mayer wave component (∼0.09 Hz). In this way, based on **Figure 9**, we can set $F_{c,\,high} = 0.09$ Hz so that the Mayer wave, breathing rate, heart rate components can be filtered out, and we include also the second and third harmonic of the fundamental stimulation frequency (i.e., $2 \times F_{stim}$ and $3 \times F_{stim}$) that still have substantial information. In terms of $F_{c,\,low}$, $F_{c,\,low} = 0.01$ Hz is typically used (**Figure 2**). It allows to effectively remove very slow trends and vascular endothelial regulations (Yücel et al., 2016) in fNIRS signals, as slow as 100 s, and to preserve the stimulation frequency as task block/event durations smaller than 100 s are typically used. In case of stimulation protocols in which brain activity is expected to be sustained for periods longer than 100 s, then a smaller $F_{c,\,low}$ should be used. Neurogenic regulations (∼0.04 Hz) can be difficult to remove as they are really close to our stimulation frequency (0.025 Hz). By choosing a passband in the range [0.01, 0.09] Hz (**Figure 11A**), we can ensure that the stimulation frequency falls within the flat passband region (0 dB attenuation; **Figure 10B**) and is not attenuated, and that additional unnecessary components are not preserved. For instance, if higher $F_{c,\,high}$ is used such as 0.6 Hz (**Figure 11B**) and 1.2 Hz (**Figure 11C**), higher frequency oscillations in the signals are included, worsening the GLM-fitting as shown by the estimated β-values that are more dissimilar to the reference β (8×10^{-7} for ΔHbO_2 and of -2.7×10^{-7} for ΔHbR) than the ones obtained with the range [0.01, 0.09] Hz (**Figure 11A**).

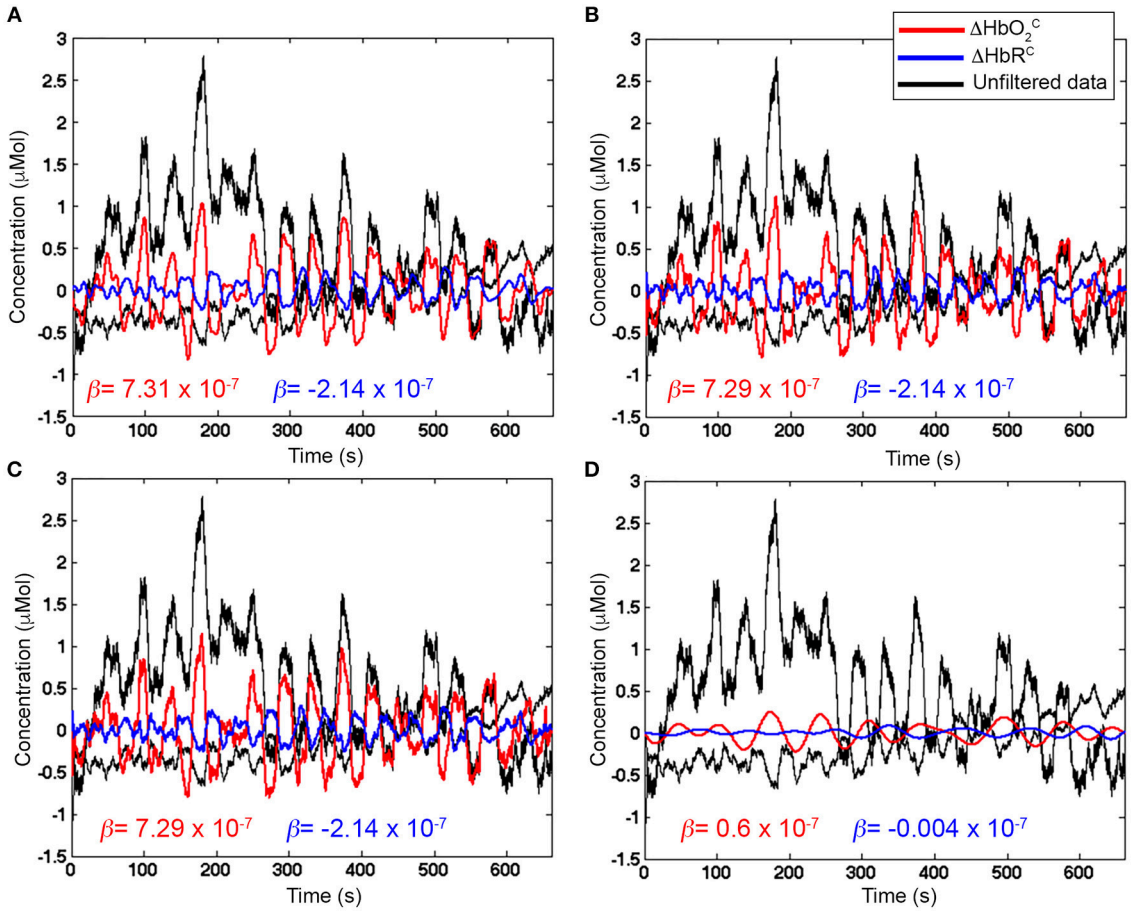

FIGURE 11 | Examples of filtered ΔHbO_2 (red) and ΔHbR (blue) signals with Amplitude 1 for one channel of a representative participant. Unfiltered ΔHbO_2 and ΔHbR are presented in black. β-values (in red for ΔHbO_2 and in blue for ΔHbR) are included as well. **(A)** shows properly filtered ΔHbO_2 and ΔHbR data (BP FIR filter, order = 1,000, F_C = [0.01, 0.09] Hz) where the stimulation frequency (0.025 Hz) is correctly included in the F_C range, so that the hemodynamic response component is preserved and the β-values are the closest to the reference (8×10^{-7} for ΔHbO_2 and of -2.7×10^{-7} for ΔHbR). **(B,C)** present filtered ΔHbO_2 and ΔHbR (BP FIR filter, order = 1,000) with wider passband ranges (F_C = [0.01, 0.6] Hz and F_C = [0.01, 1.2] Hz, respectively) that let pass also unnecessary higher frequency noise (i.e., faster oscillations in the signals) that worsen the fit with the GLM approach. **(D)**, wrongly filtered ΔHbO_2 and ΔHbR data (BP FIR filter, order = 1,000, F_C = [0.01 0.015] Hz) are presented, where the stimulation frequency (0.025 Hz) is not included in the F_C range, and the hemodynamic response component is strongly attenuated.

Including the stimulation frequency in the flat passband—and in the passband in general—is extremely important to avoid removing the hemodynamic responses that can correctly pass through the filter (**Figure 11A**). If the $F_{c,\,high}$ is lower than the stimulation frequency, for instance $F_{c,\,high} = 0.015$ Hz as shown in **Figure 11D**, the task-related component is strongly attenuated and can lead to false negatives in the statistical inference step, as proven by the very small β-values compared to the reference β.

In case the stimulation protocol has different task-rest durations, a stimulation frequency range [F_{stim_min} F_{stim_max}] must be identified and preserved. F_{stim_min} is the inverse of the maximum block duration (e.g., the maximum rest duration + the maximum task duration); F_{stim_max} is the inverse of the minimum block duration (e.g., the minimum rest duration + the minimum task duration);

Step E) Order selection: In order to minimize the transition band (**Figure 10B**) and make the filter response more similar to the response of an ideal filter (**Figure 10A**), high filter orders should be used. This is not always possible with IIR filters because, as demonstrated in **Figure 6**, they can become unstable with higher orders in certain passband ranges. On the contrary, FIR filters are always stable and high orders can be used to maximize the performance. Based on our analyses, effective filtering can be achieved with order = 1000. Through the use of a high order and a passband with a range of [0.01, 0.09] Hz, we obtain a filter that has a flat passband region (0 dB attenuation) including the stimulation frequency and a narrow transition band (**Figure 12**; for illustration purposes, the frequency axis limit is set at 0.2 Hz).

For an effective filter design and to choose appropriate filters parameters, a useful tool is to look at the amplitude response of the filter [e.g., using the Matlab function *freqz* or the filter visualization tool (*FVtool*)] to optimize the passband based on the task design and the transition band. For instance, a sharper transition band can be achieved increasing the filter order (i.e., the higher the order, the higher the slope of the

response in the transition band). Different formulas have been proposed for the estimation of the optimal FIR filter order to meet the design specification. The two oldest ones are the Kaiser's (Kaiser, 1974) and the Hermann-Rabiner-Chan's (Herrmann et al., 1973) formulas. The Kaiser's formula is the simplest and expresses the filter order as inversely proportional to the transition bandwidth (function *kaiserord* in Matlab). The estimation accuracy can decrease when the band ripples are not equal and the passband and stopband are very narrow respect to the transition band. Hermann-Rabiner-Chan's formula provides a solution for equiripple filters with either very narrow or very wide bandwidth. However, both formulas were optimized for filter orders smaller than ∼150 and only for FIR filters with odd orders or length. New estimation methods were later proposed, e.g., Ichige et al. (2000) (Ichige et al., 2000), to overcome the abovementioned limitations.

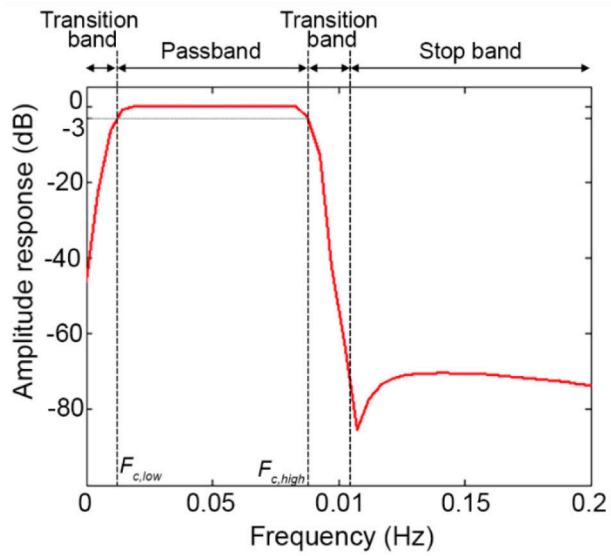

FIGURE 12 | Filter amplitude response considering a BP FIR filter with order = 1000 and F_C = [0.01, 0.09] Hz.

Besides the optimization of fNIRS signals preprocessing, there are other aspects that have to be taken into consideration to improve the information communicated within the fNIRS papers. Following the experimental stream in **Figure 1**, we summarized in **Figure 13** the workflow that we think should be applied when conducting a typical neuroscience experiment with fNIRS. More importantly, for each stage of the process, we have indicated in red the information that we recommend to use and report in the methods section of any fNIRS research article.

Our recommendations refer to basic procedures and the workflows shown in **Figures 12**, **13** can be expanded with further improvements, such as integrating fNIRS measurements with simultaneous systemic physiology recordings or using short-separation channels to allow a better interpretation of fNIRS neuroimaging data and to formulate more accurate neuroscientific conclusions (Tachtsidis and Scholkmann, 2016). For instance, these measurements can be easily integrated in the GLM framework as additional regressors in the design matrix, making this approach even more powerful and versatile. Moreover, other approaches can be included as an additional step between phase 3 and phase 4 of the workflow in **Figure 13**, such as the principal component spatial filter developed by Zhang and

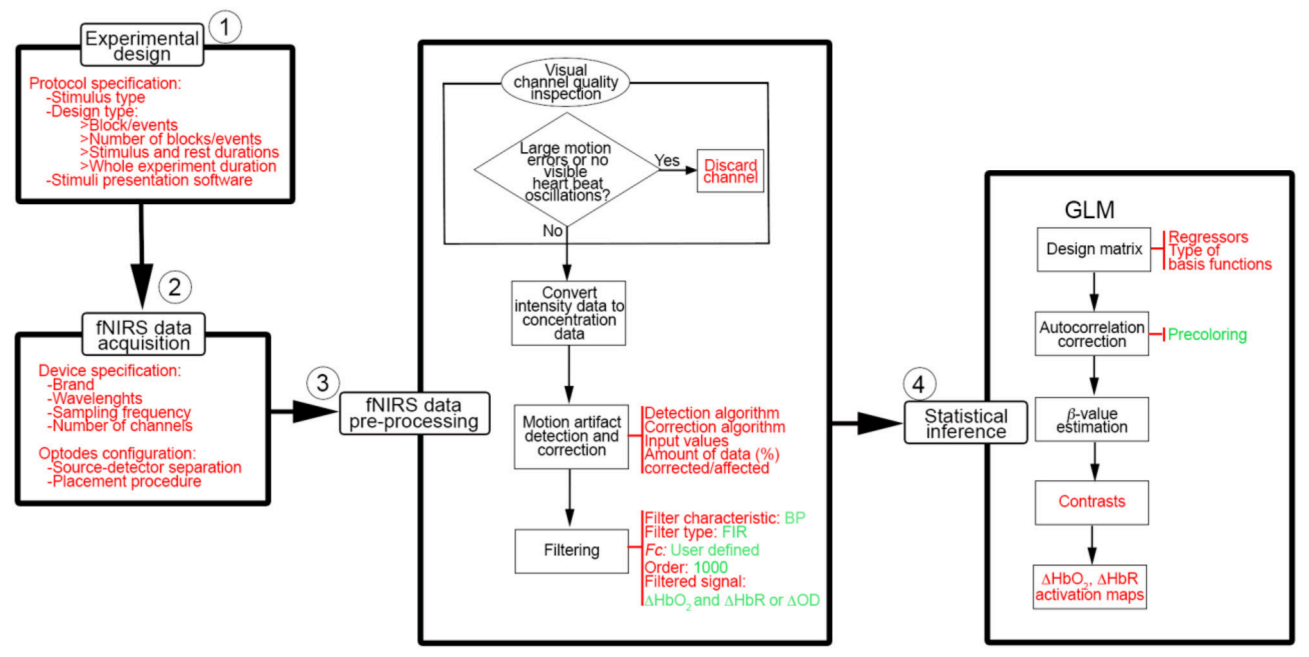

FIGURE 13 | Basic workflow to conduct a typical neuroscience experiment with fNIRS. Information and parameters that we advise to report in research papers are indicated in red and the ones we recommend to use are presented in green.

colleagues (Zhang et al., 2016) to remove the global systemic effects from fNIRS data, or combining the HbO_2 and HbR signals in e.g., the activation signal [through the correlation-based signal improvement (Cui et al., 2010)], total hemoglobin ($HbT = HbO_2 + HbR$) or hemoglobin difference [$Hb_{diff} = HbO_2 - HbR$ (Tachtsidis et al., 2009)] and use the combined signal to carry out the statistical inference. However, the present workflows (**Figures 12**, **13**) represent the starting point toward an improvement and standardization of fNIRS studies that could guide the community through all the phases of a neuroscience experiment with fNIRS.

AUTHOR CONTRIBUTIONS

PP, FS, and IT conceived and designed the study. PP carried out the data acquisition. PP and FS analyzed the data. PP, FS, IT, AH, and PB contributed to the interpretation of the results and to the manuscript writing. All authors provided critical feedback and helped shape the research, analysis, and manuscript.

ACKNOWLEDGMENTS

IT and PP are supported by the Wellcome Trust (104580/Z/14/Z). We would like to thank David Perpetuini for useful support with data collection.

SUPPLEMENTARY MATERIAL

The Supplementary Material for this article can be found online at: https://www.frontiersin.org/articles/10.3389/fnhum.2018.00505/full#supplementary-material

REFERENCES

Atsumori, H., Kiguchi, M., Obata, A., Sato, H., Katura, T., Funane, T., et al. (2009). Development of wearable optical topography system for mapping the prefrontal cortex activation. *Rev. Sci. Instrum.* 80:043704. doi: 10.1063/1.3115207

Barker, J. W., Rosso, A. L., Sparto, P. J., and Huppert, T. J. (2016). Correction of motion artifacts and serial correlations for real-time functional near-infrared spectroscopy. *Neurophotonics* 3:031410. doi: 10.1117/1.NPh.3.3.031410

Brigadoi, S., Ceccherini, L., Cutini, S., Scarpa, F., Scatturin, P., Selb, J., et al. (2014). Motion artifacts in functional near-infrared spectroscopy: a comparison of motion correction techniques applied to real cognitive data. *Neuroimage* 85, 181–191. doi: 10.1016/j.neuroimage.2013.04.082

Cui, X., Bray, S., and Reiss, A. L. (2010). Functional near infrared spectroscopy (NIRS) signal improvement based on negative correlation between oxygenated and deoxygenated hemoglobin dynamics. *Neuroimage* 49, 3039–3046. doi: 10.1016/j.neuroimage.2009.11.050

Delpy, D. T., Cope, M., van der Zee, P., Arridge, S. R., Wray, S., and Wyatt, J. (1988). Estimation of optical pathlength through tissue from direct time of flight measurement. *Phys. Med. Biol.* 33:1433. doi: 10.1088/0031-9155/33/12/008

Friston, K. J., Holmes, A. P., Worsley, K. J., Poline, J. P., Frith, C. D., and Frackowiak, R. S. (1994). Statistical parametric maps in functional imaging: a general linear approach. *Hum. Brain Mapp.* 2, 189–210. doi: 10.1002/hbm.460020402

Gagnon, L., Cooper, R. J., Yücel, M. A., Perdue, K. L., Greve, D. N., and Boas, D. A. (2012). Short separation channel location impacts the performance of short channel regression in NIRS. *Neuroimage* 59, 2518–2528. doi: 10.1016/j.neuroimage.2011.08.095

Ghasemi, A., and Zahediasl, S. (2012). Normality tests for statistical analysis: a guide for non-statisticians. *Int. J. Endocrinol. Metab.* 10:486. doi: 10.5812/ijem.3505

Herrmann, O., Rabiner, L. R., and Chan, D. S. K. (1973). Practical design rules for optimum finite impulse response low-pass digital filters. *Bell Syst. Tech. J.* 52, 769–799. doi: 10.1002/j.1538-7305.1973.tb01990.x

Hocke, L. M., Oni, I. K., Duszynski, C. C., and Corrigan, A. V. (2018). Automated Processing of fNIRS Data—a visual guide to the pitfalls and consequences. *Algorithms* 11:67. doi: 10.3390/a11050067

Holper, L., Scholkmann, F., and Wolf, M. (2014). The relationship between sympathetic nervous activity and cerebral hemodynamics and oxygenation: a study using skin conductance measurement and functional near-infrared spectroscopy. *Behav. Brain Res.* 270, 95–107. doi: 10.1016/j.bbr.2014.04.056

Huppert, T. J. (2016). Commentary on the statistical properties of noise and its implication on general linear models in functional near-infrared spectroscopy. *Neurophotonics* 3:010401. doi: 10.1117/1.NPh.3.1.010401

Ichige, K., Iwaki, M., and Ishii, R. (2000). Accurate estimation of minimum filter length for optimum FIR digital filters. *IEEE Trans. Circ. Syst. II* 47, 1008–1016. doi: 10.1109/82.877143

Ifeachor, E. C., and Jervis, B. W. (2002). *Digital Signal Processing: a Practical Approach*. Harlow; New York, NY: Pearson Education; Prentice Hall.

Kaiser, J. F. (1974). "Nonrecursive digital filter design using the I_0-sinh window function," in *Proceedings of the 1974 IEEE International Symposium on Circuits and Systems* (San Francisco, DA).

Kirilina, E., Jelzow, A., Heine, A., Niessing, M., Wabnitz, H., Brühl, R., et al. (2012). The physiological origin of task-evoked systemic artefacts in functional near infrared spectroscopy. *Neuroimage* 61, 70–81. doi: 10.1016/j.neuroimage.2012.02.074

Monti, M. M. (2011). Statistical analysis of fMRI time-series: a critical review of the GLM approach. *Front. Hum. Neurosci.* 5:28. doi: 10.3389/fnhum.2011.00028

Okamoto, M., Dan, H., Sakamoto, K., Takeo, K., Shimizu, K., Kohno, S., et al. (2004). Three-dimensional probabilistic anatomical cranio-cerebral correlation via the international 10–20 system oriented for transcranial functional brain mapping. *Neuroimage* 21, 99–111. doi: 10.1016/j.neuroimage.2003.08.026

Patil, A. V., Safaie, J., Moghaddam, H. A., Wallois, F., and Grebe, R. (2011). Experimental investigation of NIRS spatial sensitivity. *Biomed. Opt. Express* 2, 1478–1493. doi: 10.1364/BOE.2.001478

Petersen, S. E., and Dubis, J. W. (2012). The mixed block/event-related design. *Neuroimage* 62, 1177–1184. doi: 10.1016/j.neuroimage.2011.09.084

Pinti, P., Aichelburg, C., Lind, F., Power, S., Swingler, E., Merla, A., et al. (2015). Using fiberless, wearable fNIRS to monitor brain activity in real-world cognitive tasks. *J. Vis. Exp.* 106:5366. doi: 10.3791/53336

Pinti, P., Tachtsidis, I., Hamilton, A., Hirsch, J., Aichelburg, C., Gilbert, S., et al. (2018). The present and future use of functional near-infrared spectroscopy (fNIRS) for cognitive neuroscience. *Ann. NY. Acad. Sci.* doi: 10.1111/nyas.13948. [Epub ahead of print].

Rowley, A. B., Payne, S. J., Tachtsidis, I., Ebden, M. J., Whiteley, J. P., Gavaghan, D. J., et al. (2006). Synchronization between arterial blood pressure and cerebral oxyhaemoglobin concentration investigated by wavelet cross-correlation. *Physiol. Meas.* 28:161. doi: 10.1088/0967-3334/28/2/005

Scholkmann, F., Gerber, U., Wolf, M., and Wolf, U. (2013). End-tidal CO_2: an important parameter for a correct interpretation in functional brain studies using speech tasks. *Neuroimage* 66, 71–79. doi: 10.1016/j.neuroimage.2012.10.025

Scholkmann, F., Kleiser, S., Metz, A. J., Zimmermann, R., Mata Pavia, J., Wolf, U., et al. (2014). A review on continuous wave functional near-infrared spectroscopy and imaging instrumentation and methodology. *Neuroimage* 85, 6–27. doi: 10.1016/j.neuroimage.2013.05.004

Shapiro, S. S., Wilk, M. B., and Chen, H. J. (1968). A comparative study of various tests for normality. *J. Am. Stat. Assoc.* 63, 1343–1372. doi: 10.1080/01621459.1968.10480932

Tachtsidis, I., Elwell, C. E., Leung, T. S., Lee, C. W., Smith, M., and Delpy, D. T. (2004). Investigation of cerebral haemodynamics by near-infrared spectroscopy in young healthy volunteers reveals posture-dependent spontaneous oscillations. *Physiol. Meas.* 25:437. doi: 10.1088/0967-3334/25/2/003

Tachtsidis, I., and Scholkmann, F. (2016). False positives and false negatives in functional near-infrared spectroscopy: issues, challenges, and the way forward. *Neurophotonics* 3:031405. doi: 10.1117/1.NPh.3.3.031405

Tachtsidis, I., Tisdall, M. M., Leung, T. S., Pritchard, C., Cooper, C. E., Smith, M., et al. (2009). "Relationship between brain tissue haemodynamics, oxygenation and metabolism in the healthy human adult brain during hyperoxia and hypercapnea," in *Oxygen Transport to Tissue XXX* (Boston, MA: Springer), 315–320.

Tak, S., and Ye, J. C. (2014). Statistical analysis of fNIRS data: a comprehensive review. *Neuroimage* 85, 72–91. doi: 10.1016/j.neuroimage.2013.06.016

Tong, Y., Hocke, L. M., and Licata, S. C. (2012). Low-frequency oscillations measured in the periphery with near-infrared spectroscopy are strongly correlated with blood oxygen level-dependent functional magnetic resonance imaging signals. *J. Biomed. Opt.* 17, 1060041–10600410. doi: 10.1117/1.JBO.17.10.106004

von Siebenthal, K., Beran, J., Wolf, M., Keel, M., Dietz, V., Kundu, S., et al. (1999). Cyclical fluctuations in blood pressure, heart rate and cerebral blood volume in preterm infants. *Brain Dev.* 21, 529–534. doi: 10.1016/S0387-7604(99)00062-5

Worsley, K. J., and Friston, K. J. (1995). Analysis of fMRI time-series revisited—again. *Neuroimage* 2, 173–181. doi: 10.1006/nimg.1995.1023

Ye, J. C., Tak, S., Jang, K. E., Jung, J., and Jang, J. (2009). NIRS-SPM: statistical parametric mapping for near-infrared spectroscopy. *Neuroimage* 44, 428–447. doi: 10.1016/j.neuroimage.2008.08.036

Yücel, M. A., Selb, J., Aasted, C. M., Lin, P. Y., Borsook, D., Becerra, L., et al. (2016). Mayer waves reduce the accuracy of estimated hemodynamic response functions in functional near-infrared spectroscopy. *Biomed. Opt. Express* 7, 3078–3088. doi: 10.1364/BOE.7.003078

Yücel, M. A., Selb, J., Cooper, R. J., and Boas, D. A. (2014). Targeted principle component analysis: a new motion artifact correction approach for near-infrared spectroscopy. *J. Innov. Opt. Health Sci.* 7:1350066. doi: 10.1142/S1793545813500661

Yücel, M. A., Selb, J. J., Huppert, T. J., Franceschini, M. A., and Boas, D. A. (2017). Functional near infrared spectroscopy: enabling routine functional brain imaging. *Curr. Opin. Biomed. Eng.* 4, 78–86. doi: 10.1016/j.cobme.2017.09.011

Zhang, X., Noah, J. A., and Hirsch, J. (2016). Separation of the global and local components in functional near-infrared spectroscopy signals using principal component spatial filtering. *Neurophotonics* 3:015004. doi: 10.1117/1.NPh.3.1.015004

Conflict of Interest Statement: The authors declare that the research was conducted in the absence of any commercial or financial relationships that could be construed as a potential conflict of interest.

frontiers in Human Neuroscience

TECHNOLOGY REPORT
published: 12 March 2019
doi: 10.3389/fnhum.2019.00076

Automatic Analysis of EEGs Using Big Data and Hybrid Deep Learning Architectures

*Meysam Golmohammadi, Amir Hossein Harati Nejad Torbati, Silvia Lopez de Diego, Iyad Obeid and Joseph Picone**

The Neural Engineering Data Consortium, Temple University, Philadelphia, PA, United States

Brain monitoring combined with automatic analysis of EEGs provides a clinical decision support tool that can reduce time to diagnosis and assist clinicians in real-time monitoring applications (e.g., neurological intensive care units). Clinicians have indicated that a sensitivity of 95% with specificity below 5% was the minimum requirement for clinical acceptance. In this study, a high-performance automated EEG analysis system based on principles of machine learning and big data is proposed. This hybrid architecture integrates hidden Markov models (HMMs) for sequential decoding of EEG events with deep learning-based post-processing that incorporates temporal and spatial context. These algorithms are trained and evaluated using the Temple University Hospital EEG, which is the largest publicly available corpus of clinical EEG recordings in the world. This system automatically processes EEG records and classifies three patterns of clinical interest in brain activity that might be useful in diagnosing brain disorders: (1) spike and/or sharp waves, (2) generalized periodic epileptiform discharges, (3) periodic lateralized epileptiform discharges. It also classifies three patterns used to model the background EEG activity: (1) eye movement, (2) artifacts, and (3) background. Our approach delivers a sensitivity above 90% while maintaining a specificity below 5%. We also demonstrate that this system delivers a low false alarm rate, which is critical for any spike detection application.

Keywords: electroencephalography, EEG, hidden markov models, HMM, deep learning, stochastic denoising autoencoders, SdA, automatic detection

OPEN ACCESS

Edited by:
Mikhail Lebedev,
Duke University, United States

Reviewed by:
Pierre Mégevand,
Université de Genève, Switzerland
Jose Manuel Ferrandez,
Universidad Politécnica de Cartagena, Spain
Sebastian Stober,
Otto-von-Guericke Universität Magdeburg, Germany

***Correspondence:**
Joseph Picone
joseph.picone@gmail.com

Received: *27 April 2018*
Accepted: *13 February 2019*
Published: *12 March 2019*

Citation:
Golmohammadi M, Harati Nejad Torbati AH, Lopez de Diego S, Obeid I and Picone J (2019) Automatic Analysis of EEGs Using Big Data and Hybrid Deep Learning Architectures. Front. Hum. Neurosci. 13:76. doi: 10.3389/fnhum.2019.00076

INTRODUCTION

Electroencephalograms (EEGs) are used in a broad range of health care institutions to monitor and record electrical activity in the brain using electrodes placed on the scalp. EEGs are essential in diagnosis of clinical conditions such as epilepsy, depth of anesthesia, coma, encephalopathy, and brain death (Yamada and Meng, 2017). Manual scanning and interpretation of EEGs is time-consuming since these recordings may last hours or days. It is also an expensive process as it requires highly trained experts. Therefore, high performance automated analysis of EEGs can reduce time to diagnosis and enhance real-time applications by flagging sections of the signal that need further review. Many methods have been developed over the years (Ney et al., 2016) including time-frequency digital signal processing techniques (Osorio et al., 1998; Gotman, 1999), wavelet analysis (Sartoretto and Ermani, 1999), multivariate techniques based on simulated leaky integrate-and-fire

neurons (Schindler et al., 2001; Schad et al., 2008), non-linear dynamical analysis of EEG(Stam, 2005), expert systems that attempt to mimic a human observer (Deburchgraeve et al., 2008) and autoregressive spectral analysis of scalp EEG (Khamis et al., 2009). In spite of recent research progress in this field, the transition of current EEG analysis methodologies to the real-life usage in clinical settings like ICUs has been limited, mainly because of unacceptably high false detection rates (Varsavsky and Mareels, 2006; Hopfengärtner et al., 2007).

Machine learning has made tremendous progress over the past three decades due to rapid advances in low-cost highly-parallel computational infrastructure, powerful machine learning algorithms, and, most importantly, big data. Although contemporary approaches for automatic interpretation of EEGs have employed more modern machine learning approaches such as neural networks (Ramgopal, 2014) and support vector machines (Alotaiby et al., 2014), state of the art machine learning algorithms that employ high dimensional models have not previously been utilized in EEG analysis because there has been a lack of large databases that incorporate sufficient real-world variability to adequately train these systems. In fact, what has been lacking in many bioengineering fields including automatic interpretation of EEGs are the big data resources required to support the application of advanced machine learning approaches. A significant big data resource, known as the TUH EEG Corpus (Obeid and Picone, 2016), has recently become available creating a unique opportunity to evaluate high performance deep learning models that require large amounts of training data. This database includes detailed physician reports and patient medical histories, which are critical to the application of deep learning. But, transforming physicians' reports into a deep learning paradigm is proving to be challenging because the mapping of reports to underlying EEG events is non-trivial. Our experiments suggest that a hybrid structure based on hidden Markov models and deep learning can approach clinically acceptable levels of performance.

Spike and seizure detection software is widely used in many countries around the world. Industry leaders such as Persyst (Persyst Development Corporation, 2017) provide a wide variety of tools to automatically detect and classify various EEG events. The limitations of the performance of such systems on tasks such as seizure detection is a widely discussed topic within the clinical and research communities. In fact, in collaboration with IBM, we are hosting a Kaggle-style challenge (see https://www.kaggle.com/) focused on the problem of seizure detection. More details on this challenge will follow in Spring 2019.

METHODS

An overview of our proposed system is shown in **Figure 1**. In order to classify data, N independent feature streams are extracted from the multichannel EEG signal using a standard cepstral coefficient-based feature extraction approach. A sequential modeler analyzes each channel and produces event hypotheses. Three passes of post-processing are performed to produce the final output. In this section, we discuss the various components of this system, including development of the statistical models using a supervised training approach. We begin with a discussion of the data used to train and evaluate the system.

Data: The TUH EEG Corpus

Our system was developed using the TUH EEG Corpus (TUH-EEG) (Obeid and Picone, 2016), which is the largest publicly available corpus of clinical EEG recordings in the world. The most recent release, v1.1.0, includes data from 2002 to 2015. It contains over 23,000 sessions from over 13,500 patients (over 1.8 years of multichannel signal data in total). This dataset was collected at the Department of Neurology at Temple University Hospital. The data includes sessions taken from outpatient treatments, Intensive Care Units (ICU) and Epilepsy Monitoring Units (EMU), Emergency Rooms (ER) as well as several other locations within the hospital. Since TUH-EEG consists entirely of clinical data, it contains many real-world artifacts (e.g., eye blinking, muscle artifacts, head movements). This makes it an extremely challenging task for machine learning systems and differentiates from most research corpora currently available in this area. Each of the sessions contains at least one EDF file and one physician report. These reports are generated by a board-certified neurologist and are the official hospital record. These reports are comprised of unstructured text that describes the patient, relevant history, medications, and clinical impression. The corpus is publicly available from the Neural Engineering Data Consortium (www.nedcdata.org).

EEG signals in TUH-EEG were recorded using several generations of Natus Medical Incorporated's Nicolet^{TM} EEG recording technology. The raw signals consist of multichannel recordings in which the number of channels varies between 20 and 128 channels (Harati et al., 2014). A 16-bit A/D converter was used to digitize the data. The sample frequency varies from 250 to 1024 Hz. In our work, we resample all EEGs to a sample frequency of 250 Hz. The Natus system stores the data in a proprietary format that has been exported to EDF with the use of NicVue v5.71.4.2530. The original EEG records are split into multiple EDF files depending on how the session was annotated by the attending technician. Some statistics about the corpus are shown in **Figure 2**. For our studies, we use the 22 channels associated with a standard 10/20 EEG configuration (American Clinical Neurophysiology Society, 2006).

A portion of TUH-EEG was annotated manually during a study conducted with Temple University Hospital neurologists (Harati et al., 2014). We selected the data based more on the presence of the events of interest described below than the type of EEG since it is difficult to locate examples of spikes. We have analyzed performance as a function of the type/location of the EEG recording for a specific application, seizure detection, using similar technology to that presented in this paper, and not found a significant correlation. The error profiles are similar for EEGs collected in the ICU and EMU from a machine learning perspective.

The annotations we developed comprise six patterns of clinical interest. The first three patterns that might be useful in diagnosing brain disorders are:

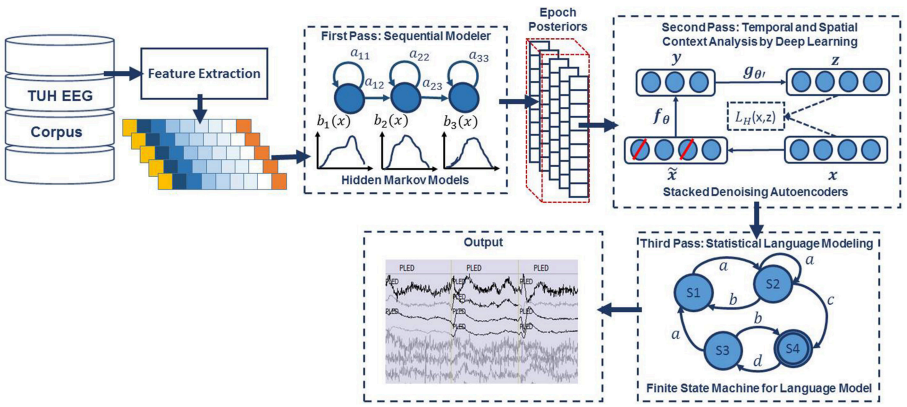

FIGURE 1 | A three-pass architecture for automatic interpretation of EEGs that integrates hidden Markov models for sequential decoding of EEG events with deep learning for decision-making based on temporal and spatial context.

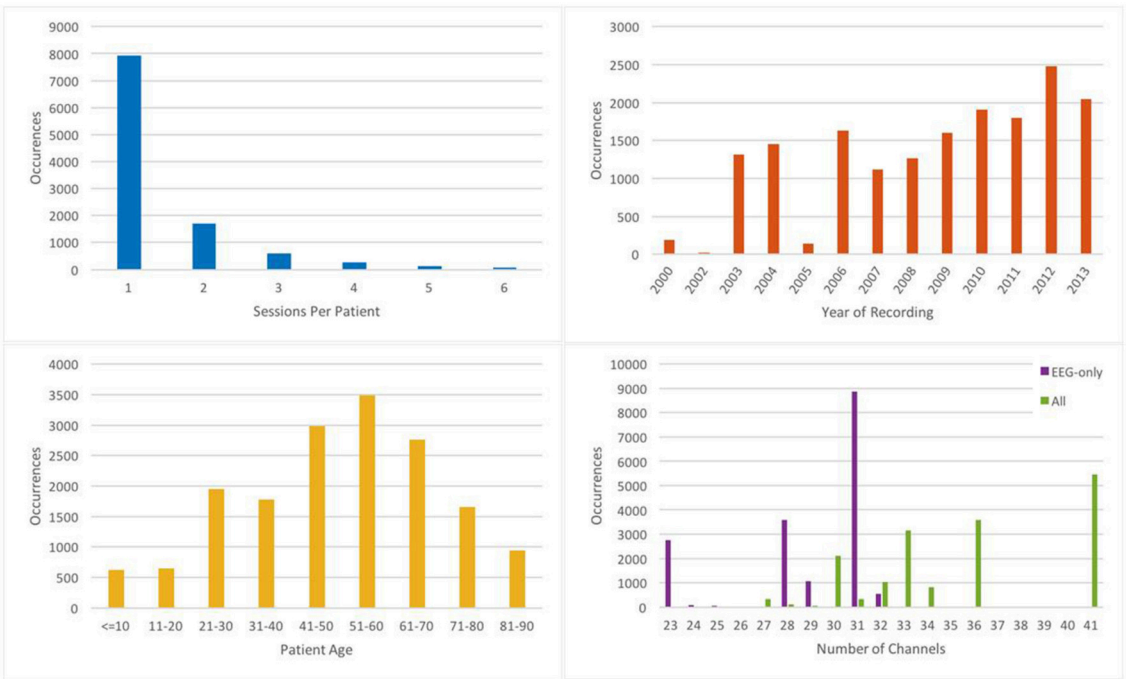

FIGURE 2 | Some relevant statistics demonstrating the variety of data in TUH-EEG.

(1) *spike and/or sharp waves (SPSW):* patterns of EEGs observed during epileptic seizures.
(2) *periodic lateralized epileptiform discharges (PLED)*: patterns observed in the context of destructive structural lesions of the cortex. PLED events manifest themselves by presence of a pattern of repetitive periodic, focal, or hemispheric epileptiform discharges like sharp waves, spikes, spike and waves and polyspikes, at intervals of between 0.5 and 3 s.
(3) *generalized periodic epileptiform discharges (GPED)*: manifest themselves as periodic short-interval diffuse discharges, periodic long-interval diffuse discharges and suppression-burst patterns. GPEDs are encountered in metabolic encephalopathy and cerebral hypoxia and ischemia. They are similar to PLEDs. In fact, if periodic complexes are limited to a focal brain area they are called as PLEDs, but if periodic complexes are observed over both hemispheres in a symmetric, diffuse and synchronized manner, they are defined as GPEDs.

The other three patterns were used by our machine learning technology to model background noise:

(4) *eye movement (EYEM)*: spike-like signals that occur during patient eye movement.

(5) *artifacts (ARTF)*: recorded electrical activity that is not of cerebral origin including physiologic artifacts generated from sources other than brain. This class also includes extraphysiologic artifacts arising from outside the body such as noise generated from the recording equipment.
(6) *background (BCKG)*: a class used to denote all other data that does not fall in the five classes above. This class usually plays an instrumental role in machine learning systems and needs to include a rich variety of artifacts that are not events of clinical interest.

Note that standard terminology in this field has changed somewhat. PLEDs are now referred to as lateralized periodic discharges (LPDs), GPEDs are now referred to as generalized periodic discharges (GPDs) and spike and sharp waves are referred to as spike and wave (SW) (American Clinical Neurophysiology Society, 2012). However, we will retain the older terminology because this aligns with the way the corpus was annotated and is what was used in our machine learning experiments.

There are over 10 different electrode configurations and over 40 channel configurations represented in the corpus. This poses a serious challenge for machine learning systems since for a system to be practical it must be able to adapt to the specific type of EEG being administered. However, for this initial study, we focused on a subset of the data in which signals were recorded using the Averaged Reference (AR) electrode configuration (Lopez et al., 2016). This data is publicly available at https://www.isip.piconepress.com/projects/tuh_eeg/html/downloads.shtml.

In this paper we focus on the problem of six-way event classification. We have also recently worked on seizure detection using technology that was based on the technology presented here. The work presented here represents our first attempts at doing machine learning on EEG signals and forms the basis for our subsequent work on a wide range of EEG challenges (see https://www.isip.piconepress.com/publications/_index.shtml).

Data: The TUH-EEG Event Short Set

We collaborated with several neurologists and a team of undergraduate annotators (Shah et al., 2018) to manually label a subset of TUH-EEG for the six different kinds of EEG patterns described in Section Data: The TUH EEG Corpus. This subset, known as the TUH EEG Events Corpus (TUH-EEG-ESS), is available from our project web site: https://www.isip.piconepress.com/projects/tuh_eeg/html/downloads.shtml. The training set is designed to include segments from 359 sessions and the evaluation dataset contains segments from 159 sessions. This data is designed in a way that every patient appears just once in the dataset.

Note that the annotations were created on a channel basis—the specific channels on which an event was observed were annotated. This is in contrast to many open source databases that we have observed which only mark events in time and do not annotate the specific channels on which the events occurred. In general, with EEG signals, events such as SPSW do not appear on all channels. The subset of channels on which the event appears is relevant diagnostic information. Our annotations are demonstrated in **Figure 3**.

A summary of the TU-EEG-ESS dataset is presented in **Table 1**. The dataset is divided into a training and evaluation

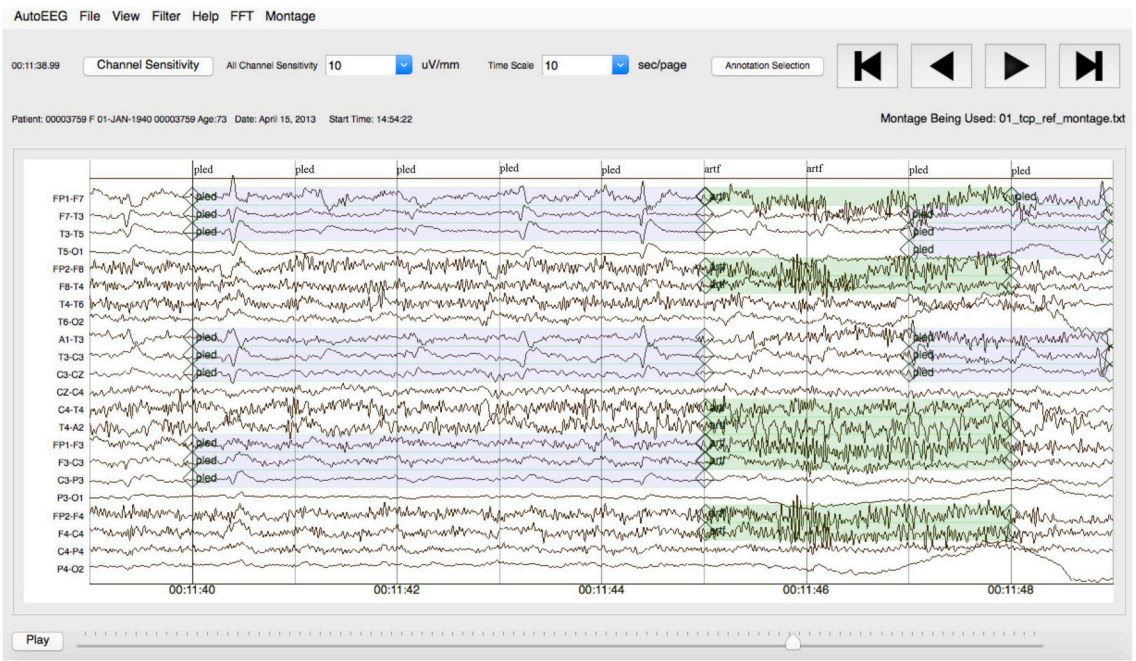

FIGURE 3 | An example demonstrating that the reference data is annotated on a per-channel basis.

TABLE 1 | An overview of the distribution of events in the subset of the TUH EEG Corpus used in our experiments.

Event	Train	Train % (CDF)	Eval	Eval % (CDF)
SPSW	645	0.8% (1%)	567	1.9% (2%)
GPED	6,184	7.4% (8%)	1,998	6.8% (9%)
PLED	11,254	13.4% (22%)	4,677	15.9% (25%)
EYEM	1,170	1.4% (23%)	329	1.1% (26%)
ARTF	11,053	13.2% (36%)	2,204	7.5% (33%)
BCKG	53,726	63.9% (100%)	19,646	66.8% (100%)
Total:	84,032	100.0% (100%)	29,421	100.0% (100%)

set in a way that it includes sufficient number of observations to train machine learning models such as HMMs and evaluate these models on unseen examples from new patients. An overview of the distribution of six types of events for both of training and evaluation set demonstrates that some events occur much less frequently in the actual corpus than other common events. For example, while just <1%of the subset is assigned to SPSW more than 60% is assigned to BCKG. Also notice that 99% of the TU-EEG-ESS data composed of three classes for modeling background which are EYEM, ARTF and BCKG. This distribution of data makes the design of robust classifiers for the detection of non-background classes even more challenging. High performance automatic analysis of EEGs requires dealing with infrequently occurring events since much of the data is uninformative. This is often referred to as an unbalanced data problem, and it is quite common in many biomedical applications. Hence, the evaluation set was designed to contain a reasonable representation of all classes. All of EEGs in this subset were recorded using standard 10–20 system and processed using a TCP montage (Lopez et al., 2016), resulting in 22 channels of signal data per EEG.

Pre-processing: Feature Extraction

The first step in EEG processing in **Figure 1** consists of converting the signal to a sequence of feature vectors (Picone, 1990). Common EEG feature extraction methods include temporal, spatial and spectral analysis (Mirowski et al., 2009; Thodoroff et al., 2016). A variety of methodologies have been broadly applied for extracting features from EEG signals including wavelet transform, independent component analysis and autoregressive modeling (Jahankhani et al., 2006; Subasi, 2007). In this study, we use a methodology based on mel-frequency cepstral coefficients (MFCC) which have been successfully applied to many signal processing applications including speech recognition (Picone, 1993). In our systems, we use linear frequency cepstral coefficients (LFCCs) since a linear frequency scale provides some slight advantages over the mel scale for EEG signals (Harati et al., 2015). A block diagram summarizing the feature extraction process used in this work for automatic classification of EEG signals is presented in **Figure 4**. Recent experiments with different types of features (Da Rocha Garrit et al., 2015) or with using sampled data directly (Xiong et al., 2017) have not shown a significant improvement in performance by eliminating the feature extraction process and using sampled data directly.

The first step to derive cepstral coefficients using LFCC feature extraction method is to divide raw EEG signals into shorter frames. The second step is to take a high resolution discreet fast Fourier Transform of each frame. Next, the spectrum is downsampled with a filter bank composed of an array of overlapping bandpass filters. Finally, the cepstral coefficients are derived by computing a discrete cosine transform of the filter bank's output (Picone, 1993). In our experiments, we discarded the zeroth-order cepstral coefficient. Instead of this term we use a frequency domain energy term which is calculated by adding the output of the oversampled filter bank after they are downsampled:

$$E_f = log\left(\sum_{k=0}^{N-1} \left|X(k)\right|^2\right) \tag{1}$$

In our experiments, we found adding a new feature that is able to model the long-term differentiation in energy can improve the results of spike detection significantly. We call this new feature as differential energy term which can differentiate between transient pulse shape patterns and stationary background noise. To compute differential energy term, we compute the energy of frames inside a window of a channel of EEG. Differential energy equals to maximum energy minus minimum energy over this interval:

$$E_d = \max_{\mathrm{m}}\left(E_f\,(m)\right) - \min_{\mathrm{m}}\left(E_f\,(m)\right) \tag{2}$$

We have used a window with length of a 0.9 s to calculate differential energy term. Even though this term is a simple feature, our experiments showed that it results in a statistically significant improvement in performance (Harati et al., 2015).

Our experiments have also shown that using derivatives of features based on a regression approach, which is a popular method in speech recognition (Picone, 1993), are effective in the classification of EEG events. We use the following definition for the derivative:

$$d_t = \frac{\sum_{n=1}^{N} n\,(c_{t+n} - c_{t-n})}{2\sum_{n=1}^{N} n^2} \tag{3}$$

Equation (3) is applied to the cepstral coefficients, c_t, to compute the first derivatives, referred to as delta coefficients. Equation (3) is then reapplied to the first derivatives to compute the second derivatives, which are referred to as delta-delta coefficients. We use a window with length of 9 ($N = 9$) for the first derivative and a window with length of 3 ($N = 3$) for the second derivative. The introduction of derivatives helps the system discriminate between steady-state behavior, such as that found in a PLED event, and impulsive or non-stationary signals, such as that found in spikes (SPSW) and eye movements (EYEM).

In this work, through experiments designed to optimize feature extraction, we found best performance can be achieved using a feature vector length of 26. This vector includes nine

absolute features consisting of seven cepstral coefficients, one frequency-domain energy term, and one differential energy term. Nine deltas are added for these nine absolute features. Eight delta-deltas are added because we exclude the delta-delta term for differential energy (Harati et al., 2015).

First Pass: Sequential Decoding Using Hidden Markov Models

Hidden Markov Models (HMMs) are one of the most important machine learning models available today for sequential machine learning problems that require both temporal and spectral modeling (Picone, 1990; Juang and Rabiner, 1991). HMMs can be considered as a class of doubly stochastic processes that are able to model discrete state sequences as Markov chains. HMMs have been used broadly in speech recognition where a speech signal can be decomposed into an energy and frequency profile in which particular events in the frequency domain can be used to identify the sound spoken.

The challenge of interpreting and finding patterns in EEG signal data is very similar to that of speech related projects. There is one distinct difference, however. In a typical speech signal, speech comprises about 50% of the signal and speech events occur frequently. In EEG signals, key events such as seizures occur <1% of the time. This disparity in prior probabilities of these events makes training somewhat of a challenge, since there is overwhelming pressure for the system to simply ignore the events of interest.

For automatic analysis of EEGs, we consider EEG signals to bare composed of a chain of encoded messages as a sequence of one or more symbols. We model an EEG as a sequence of one of six symbols: SPSW, PLED, GPED, EYEM, ARTF, and BCKG. We assume that each one of these patterns is represented by a sequence of feature vectors or observations O, defined as:

$$O = o_1, o_2, \ \ldots, o_T \tag{4}$$

Here o_T is the feature vector observed at time t. If we define S_i as the ith event in our dictionary of K events, and S as a sequence of events from this dictionary, then the EEG pattern recognition problem can be considered as finding the most probable sequence of events that maximize the posterior probability P (O | S). We train one HMM model for each event in our dictionary using manually annotated data.

A simple left-to-right GMM-HMM, illustrated in **Figure 5**, was used for sequential decoding of EEG signals. A GMM-HMM is characterized by N states where each state consists of an L-component Gaussian mixture model. The transition probability matrix which describes how the states are interconnected consists of a set of probabilities a_{ij} which denotes the probability of a transition from state i to j. Considering $\alpha(i,t)$ as the forward probability where (i = 1, 2,…,N; t = 1, 2, …, T) , $\beta(j,t)$ as the

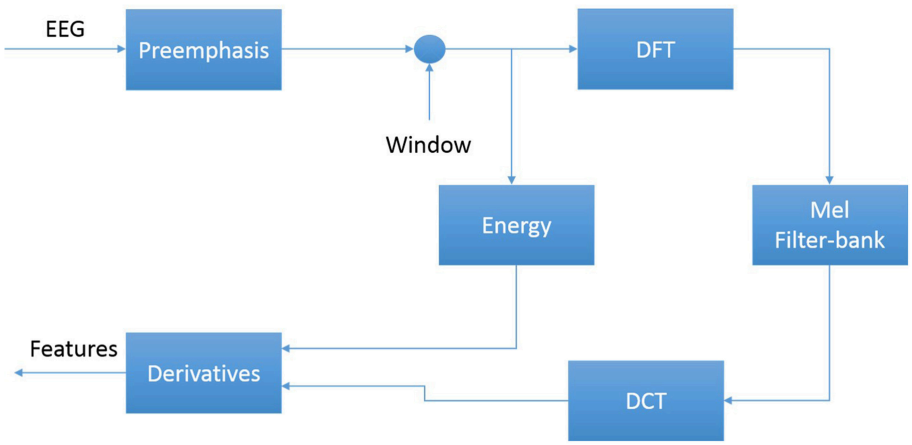

FIGURE 4 | An overview of the feature extraction algorithm.

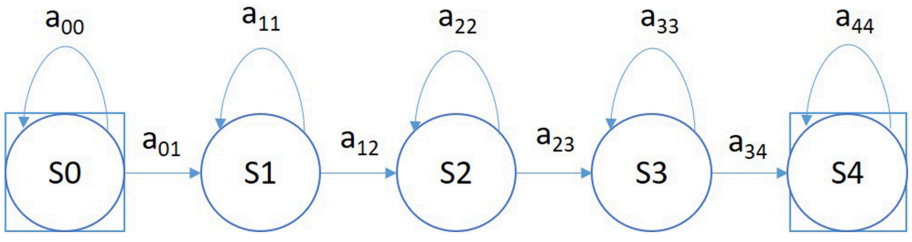

FIGURE 5 | A left-to-right HMM is used for sequential decoding in the first pass of processing.

backward probability where (j = 1, 2, …, N; t = T-1, …,0), and P(O|M) as the probability that model M generates symbol series O, the probability that there will be a transition from state i to state j at time t can be defined as:

$$\gamma_i(i,j) = \frac{\alpha(i,t-1)\, a_{ij} b_{ij}(O_t, \mu_{ij}, \Sigma_{ij}) \beta(j,t)}{P(O|M)} \quad (5)$$

The reestimation formulae for the transition probabilities are:

$$a_{ij} = \frac{\sum_t \gamma_i(i,j)}{\sum_t \sum_j \gamma_i(i,j)} \quad (6)$$

We can calculate the output density function using the output vector, O_t, if it follows an n-dimensional normal distribution as:

$$b_{ij}(o_t, \mu_{ij}, \Sigma_{ij}) = \frac{exp\{-(o_t - \mu_{ij})^t \sum_{ij}^{-1} (o_t - \mu_{ij})/2}{(2\pi)^{n/2} |\Sigma_{ij}|^{1/2}} \quad (7)$$

where μ_{ij} is the mean and Σ_{ij} is the covariance matrix. The mean and covariance for each Gaussian mixture component can be estimated by:

$$\mu_{ij} = \frac{\sum_t \gamma_i(i,j)\, o_t}{\sum_t \gamma_i(i,j)} \quad (8)$$

$$\Sigma_{ij} = \frac{\sum_t \gamma_i(i,j)\, (o_t - \mu_{ij})(o_t - \mu_{ij})^t}{\sum_t \gamma_i(i,j)} \quad (9)$$

In the first pass of signal modeling shown in **Figure 1**, we divide each channel of the EEG signal into epochs. Each epoch is represented by a sequence of frames where each frame is represented by a feature vector. During training, we estimate the parameters of the K models ($\{a_{ij}\}$, $\{b_{ij}\}$, $\{\mu_{ij}\}$ and $\{\Sigma_{ij}\}$) from the training dataset by iterating over all epochs using Equations (5–9). To determine these parameters in an iterative fashion, it is first necessary to initialize them with a carefully chosen value (Picone, 1990). Once this is done, more accurate parameters, in the maximum likelihood sense, can be found by applying the so-called Baum-Welch reestimation algorithm (Picone, 1990). Decoding is typically performed using the Viterbi algorithm (Alphonso and Picone, 2004). Using one HMM model per label, we generate one posterior probability for each model and we select the label that corresponds to the highest probability. Rather than use the best overall output from the HMM system, we let the HMM system output probabilities for each event for each epoch for each channel, and we postprocess these probabilities using a second pass consisting of a deep learning-based system.

Second Pass: Temporal and Spatial Context Analysis Based on Deep Learning

The goal of the second pass of processing in **Figure 1** is to integrate spatial and temporal context to improve decision-making. Therefore, the output of the first pass of processing, which is a vector of six posterior probabilities for every epoch of each channel, is postprocessed by a deep learning system. This system extracts knowledge in a data-driven manner and learn representations of data that involve multiple levels of abstraction (LeCun et al., 2015).

In the second pass of processing, we are using a specific type of deep leaning network known as a Stacked denoising Autoencoder (SdA) (Vincent et al., 2010). SdAs have proven to perform well for applications where we need to emulate human knowledge (Bengio et al., 2007). Since interrater agreement for annotation of seizures tends to be relatively low and somewhat ambiguous, we need a deep learning structure that can deal with noisy inputs. From a structural point of view, SdAs are composed of multiple layers of denoising autoencoders in a way that the input to each layer is the latent representation of the denoising autoencoder found in the layer below. The most important feature of denoising autoencoders that make them appropriate for automatic analysis of EEGs is their ability in reconstructing a repaired input from a corrupted version of it.

Denoising Autoencoders are themselves an extension of a classical autoencoder (Vincent et al., 2008). The input vector to an autoencoder is $x \in [0,1]^d$. Then using a deterministic mapping, autoencoder maps the input to a hidden representation $y \in [0,1]^{d'}$ as:

$$y = f_\theta(x) = s(Wx + b) \quad (10)$$

where W is a $d' \times d$ weight matrix, b is a bias vector, s is a non-linearity such as sigmoid function and $\theta = \{W, b\}$.

A decoder maps this latent representation y to a reconstruction z of the same shape as x:

$$z = g_{\theta'}(y) = s\left(W' y + b'\right) \quad (11)$$

It is common to constrain this mapping using a technique by applying a constraint on these equations such as . This particular constraint is known as tied weights. The parameters of this model are optimized to minimize the average reconstruction error using a loss function, L, such as reconstruction cross-entropy:

$$\theta^*, \theta'^* = \arg \min_{\theta, \theta'} \frac{1}{n} \sum_{i=1}^{n} L(x^{(i)}, g_{\theta'}(f_\theta(x^{(i)}))) \quad (12)$$

To implement a denoising autoencoder, we train an autoencoder on partially corrupted and destroyed input data in a way that it learns to reconstruct a repaired version of the input. To implement this methodology, we use a stochastic mapping function as $\tilde{x} = q_D(\tilde{x}|x)$ for mapping the input x to a partially destroyed version $\tilde{x}$. We use the corrupted data $\tilde{x}$ as the input of a typical autoencoder to calculate the latent representation by means of $y = f_\theta(\tilde{x}) = s(W\tilde{x} + b)$. We reconstruct a repaired version of the input using $y = f_\theta(\tilde{x}) = s(W\tilde{x} + b)$. The schematic representation of the process is presented in **Figure 6**. In the training process, the goal is to find parameters that minimize the loss function which in this case is the average reconstruction error on the training dataset. Note that in these equations, unlike basic autoencoders, reconstruction of z is not a function of x but it is a deterministic function of $\tilde{x}$ and thereby the result of a stochastic mapping of x.

The application of deep learning networks like SdAs generally involves three steps: design, training and implementation. In the design step, the number of inputs and outputs, the number of layers, and the function of nodes are defined. During training, the weights of the nodes are determined through a deep learning process. In the last step, the statistical model is implemented using the fixed parameters of the network determined during training. Pre-processing of the input data is an additional step that is extremely important to various aspects of the deep learning training process.

The block diagram of the second stage of processing is depicted in **Figure 7**. This stage consists of three parallel SdAs designed to integrate spatial and temporal context to improve decision-making. These SdAs are implemented with varying window sizes to effectively perform a multi-time-scale analysis of the signal and map event labels onto a single composite epoch label vector. A first SdA, referred to as an SPSW-SdA, is responsible for mapping labels into one of two classes: epileptiform and non-epileptiform. A second SdA, EYEM-SdA, maps labels onto the background (BCKG) and eye movement (EYEM) classes. A third SdA, 6W-SdA, maps labels to any one of the six possible classes. The first two SdAs use a relatively short window context because SPSW and EYEM are localized events and can only be detected when we have adequate temporal resolution.

Training of these three SdA networks is done in two steps: pre-training and fine-tuning. SdAs are deep learning networks that are composed of multiple layers of denoising autoencoders. Pre-training is an unsupervised approach that minimizes the reconstruction error. During pre-training, we train each layer of the SdA separately using an unsupervised approach in which we train the first level of a denoising autoencoder to minimize the error in reconstructing of its input. Next, using the output code of the first layer, we train the second layer denoising autoencoder to learn a second level encoding function. This process is repeated for all layers.

Following completion of pre-training, we perform fine-tuning using a supervised training procedure. In fine-tuning the goal is to minimize a loss function that represents the classification error. First, we compose a network with just the encoding parts of each denoising auto-encoder and then we add a logistic regression layer as the last layer of a SdA deep learning network. We initialize this network using weights that we obtained during pre-training and train the entire network to minimize the prediction error (Hinton et al., 2006; Bengio et al., 2007).

As shown in **Figure 7**, we also preprocess the data using a global principal components analysis (PCA) to reduce dimensionality before application of these SdAs (van der Maaten et al., 2009). PCA is applied to each individual epoch by concatenating each channel output into a supervector and then reducing its dimensionality. For rare and localized events (e.g., SPSW and EYEM), we use an out-of-sample technique to increase the number of training samples (van der Maaten et al., 2009).

Finally, using a block called an enhancer (Vincent et al., 2010), the outputs of these three SdAs are then combined to obtain the final decision. To add the three outputs together, we initialize our final probability output with the output of the 6-way classifier. For each epoch, if the other two classifiers detect epileptiform or eye movement and the 6-way classifier was not in agreement with this, we update the output probability based on the output of 2-way classifiers. The overall result of the second stage is a probability vector of dimension six containing a likelihood that each label could have occurred in the epoch. It should also be noted that the outputs of these SdAs are a probability vector. A soft decision paradigm is used because this output will be smoothed in the third stage of processing.

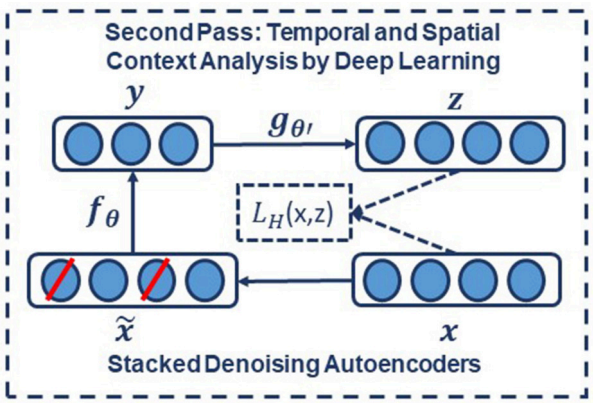

FIGURE 6 | In a stacked denoising autoencoder the input, x, is corrupted to $\tilde{x}$. The autoencoder then maps it to y and attempts to reconstruct x.

Third Pass: Statistical Language Modeling

Neurologists generally impose certain restrictions on events when interpreting an EEG. For example, PLEDs and GPEDs don't happen in the same session. None of the previous

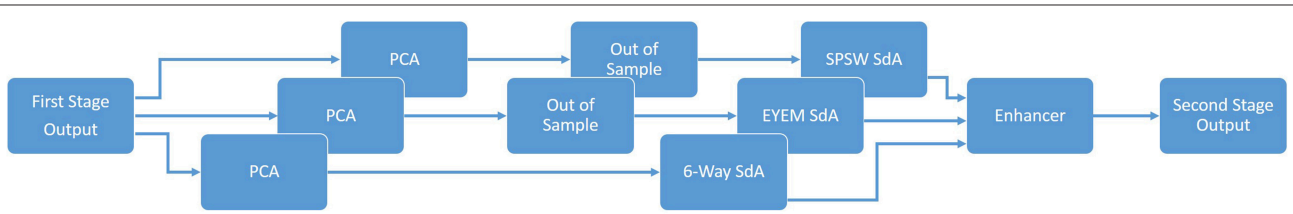

FIGURE 7 | An overview of the second pass of processing.

stages of processing address this problem. Even the output of the second stage accounts mostly for channel context and is not extremely effective at modeling long-term temporal context. The third pass of processing addresses this issue and improves the overall detection performance by using a finite state machine based on a statistical language model. In general, for problems such as EEG event detection in which infrequently occurring events play a significant role, post-processing based on domain knowledge tends to provide large gains in performance. Automatic this using deep learning is not trivial.

As is shown in **Figure 1**, the third stage of post-processing is designed to impose some contextual restrictions on the output of the second stage. These contextual relationships involve long-term behavior of the signal and are learned in a data-driven fashion. This approach is also borrowed from speech recognition where a probabilistic grammar is used that combines the left and right contexts with the labels (Levinson, 2005). This is done using a finite state machine that imposes specific syntactic constraints.

In this study, a bigram probabilistic language model that provides the probability of transiting from one type of epoch to another (e.g., PLED to PLED) is prepared using the training dataset and also in consultation with neurologists in Temple Hospital University. The bigram probabilities for each of the six classes are shown in **Table 2**, which models all possible transitions from one label to the next. The remaining columns alternate between the class label being transitioned to and its associated probability. The probabilities in this table are optimized on a training database that is a subset of TUH-EEG. For example, since PLEDs are long-term events, the probability of transitioning from one PLED to the next is high ∼0.9. However, since spikes that occur in groups are PLEDs or GPEDs, and not SPSWs, the probability of transitioning from a PLED to SPSW is 0.0. Therefore, these transition probabilities emulate the contextual knowledge used by neurologists.

After compiling the probability table, a long window is centered on each epoch and the posterior probability vector for that epoch is updated by considering left and right context as a prior (essentially predicting the current epoch from its left and right context). A Bayesian framework is used to update the probabilities of this grammar for a single iteration of the algorithm:

$$P_{gprior} = \frac{\sum_{i=1}^{L} P_i + \epsilon_{prior} M}{L + M} \tag{13}$$

$$RPP(k) = \frac{\beta_R \sum_{i=1}^{N} \exp(-i\lambda) P_{k+i} + \alpha P_{gprior}}{1 + \alpha} \tag{14}$$

$$LPP(k) = \frac{\beta_L \sum_{i=1}^{N} \exp(-i\lambda) P_{k-i} + \alpha P_{gprior}}{1 + \alpha} \tag{15}$$

$$P_{C_k|LR} = \beta_C P_{C_k} \Big(\sum_{i=1}^{k} \sum_{j=1}^{k} LPP(i)\, RPP(j)\, Prob(i,k)\, Prob(k,j) \Big)^{\frac{\gamma}{n}} \tag{16}$$

In these equations, k = 1, 2… K where K is the total number of classes (in this study K = 6), L is number of epochs in a file, ϵ_{prior} is the prior probability for an epoch (a vector of length K) and M is the weight. LPP and RPP are left and right context probabilities, respectively. λ is the decaying weight for window, α is the weight associated with P_{gprior} and β_R and β_L are normalization factors. P_{C_k} is the prior probability, $P_{C_k|LR}$ is the posterior probability of epoch C for class k given the left and right contexts, y is the grammar weight, n is the iteration number (starting from 1) and β_C is the normalization factor. Prob (i, j) is a representation of the probability table shown in **Table 2**. The algorithm iterates until the label assignments, which are decoded based on a probability vector, converge. The output of this stage is the final output and what was used in the evaluations described in Section Results.

RESULTS

In this section, we present results on a series of experiments designed to optimize and evaluate each stage of processing.

Pre-processing: Feature Extraction

Features from each epoch are identified using a feature extraction technique described in Section Data: The TUH-EEG Event Short Set. Neurologists review EEGs in 10 s windows. Pattern recognition systems often subdivide the signal into small segments during which the signal can be considered quasi-stationary. HMM systems need further subdivision so that there are enough observations to allow the system to develop a strong sense of the correct choice. A simple set of preliminary experiments determined that a reasonable tradeoff between computational complexity and performance was to split the 10 s window into 1 s epochs, and to further subdivide these into 0.1 s frames. Hence, features were computed every 0.1 s using a 0.2 s overlapping analysis window. The output of the feature extraction system is 22 channels of data, where in each channel, a feature vector of dimension 26 corresponds to every 0.1 s. These parameters were optimized experimentally in a previous study (Harati et al., 2015).

First Pass: Sequential Decoding Using Hidden Markov Models

A 6-way classification experiment was conducted using the models described in **Figure 5**. Each state uses 8 Gaussian mixture components and a diagonal covariance assumption (drawing on our experience with speech recognition systems and balancing dimensionality of the models with the size of the training data). Models were trained using all events on all channels resulting in what we refer to as channel independent models. Channel dependent models have not proven to provide a boost in performance and add considerable complexity to the system.

The results for the first pass of processing are shown in **Table 3**, in the first pass section. A more informative performance analysis can be constructed by collapsing the three background classes into one category. We refer to this second evaluation paradigm as a 4-way classification task: SPSW, GPED, PLED and BACKG. The latter class contains an enumeration of the three background classes. The 4-way classification results for the first pass of processing are presented in **Table 4**, in the first pass section. Finally, in order that we can produce a detection error

TABLE 2 | A bigram probabilistic language model for the third pass of processing which models all possible transitions from one of the six classes to the next.

i	j	P(i, j)	j	P(i, j)	j	P(i, j)	j	P(i, j)	j	P(i, j)	j	P(i, j)
SPSW	SPSW	0.40	PLED	0.00	GPED	0.00	EYEM	0.10	ARTF	0.20	BCKG	0.30
PLED	SPSW	0.00	PLED	0.90	GPED	0.00	EYEM	0.00	ARTF	0.05	BCKG	0.05
GPED	SPSW	0.00	PLED	0.00	GPED	0.60	EYEM	0.00	ARTF	0.20	BCKG	0.20
EYEM	SPSW	0.10	PLED	0.00	GPED	0.00	EYEM	0.40	ARTF	0.10	BCKG	0.40
ARTF	SPSW	0.23	PLED	0.05	GPED	0.05	EYEM	0.23	ARTF	0.23	BCKG	0.23
BCKG	SPSW	0.33	PLED	0.05	GPED	0.05	EYEM	0.23	ARTF	0.13	BCKG	0.23

TABLE 3 | The 6-way classification results for the three passes of processing.

Pass	Event	ARTF	BCKG	EYEM	GPED	PLED	SPSW
First	ARTF	41.24	45.19	2.18	3.81	2.77	4.81
	BCKG	7.02	71.93	2.59	7.37	2.28	8.81
	EYEM	2.13	0.61	82.37	2.13	8.51	4.26
	GPED	7.46	4.85	2.39	53.32	20.42	11.55
	PLED	0.70	1.85	4.70	17.62	54.80	20.32
	SPSW	4.41	8.29	9.17	33.33	4.59	40.21
Second	ARTF	27.49	61.73	7.28	0.00	1.08	2.43
	BCKG	7.00	82.03	5.79	0.97	0.36	3.86
	EYEM	4.21	16.84	77.89	0.00	0.00	1.05
	GPED	0.60	14.69	0.00	59.96	10.26	14.49
	PLED	1.40	22.65	0.80	13.83	52.30	9.02
	SPSW	7.69	35.90	2.56	28.21	0.00	25.64
Third	ARTF	14.04	72.98	10.18	0.00	0.00	2.81
	BCKG	3.42	81.40	8.93	0.30	0.00	5.95
	EYEM	2.30	17.24	79.31	0.00	0.00	1.15
	GPED	0.30	3.65	0.00	65.05	13.37	17.63
	PLED	0.00	10.76	0.49	9.78	65.28	13.69
	SPSW	10.00	33.33	13.33	10.00	0.00	33.33

TABLE 4 | The 4-way classification results for the three passes of processing.

Pass	Event	BCKG	SPSW	GPED	PLED
First	BCKG	82.30	8.35	6.94	2.42
	SPSW	21.87	40.21	33.33	4.59
	GPED	14.71	11.55	53.32	20.42
	PLED	7.26	20.32	17.62	54.80
Second	BCKG	95.60	3.24	0.62	0.54
	SPSW	46.15	25.64	28.21	0.00
	GPED	15.29	14.49	59.96	10.26
	PLED	24.85	9.02	13.83	52.30
Third	BCKG	95.11	4.69	0.19	0.00
	SPSW	56.67	33.33	10.00	0.00
	GPED	3.95	17.63	65.05	13.37
	PLED	11.25	13.69	9.78	65.28

TABLE 5 | The 2-way classification results for the three passes of processing.

Pass	Event	TARG	BCKG
First	TARG	86.92	13.08
	BCKG	18.20	81.80
Second	TARG	78.94	21.06
	BCKG	4.40	95.60
Third	TARG	90.10	9.90
	BCKG	4.89	95.11

tradeoff (DET) curve (Martin et al., 1997) we also report a 2-way classification result in which we collapse the data into a target class (TARG) and a background class (BCKG). The 2-way classification results for the first pass of processing are presented in **Table 5**, in the first pass section. Note that the classification results for all these tables are measured by counting each epoch for each channel as an independent event. We refer to this as forced-choice event-based scoring because every epoch for every channel is assigned a score based on its class label.

Second Pass: Temporal and Spatial Context Analysis Based on Deep Learning

The output of the first stage of processing is a vector of six scores, or likelihoods, for each channel at each epoch. Therefore, if we have 22 channels and six classes, we will have a vector of dimension $6 \times 22 = 132$ scores for each epoch. This 132-dimension epoch vector is computed without considering similar vectors from epochs adjacent in time. Information available from other channels within the same epoch is referred to as "spatial" context since each channel corresponds to a specific electrode location on the skull. Information available from other epochs is referred to as "temporal" context. The goal of this level of processing is to integrate spatial and temporal context to improve decision-making.

To integrate context, the input to the second pass deep learning system is a vector of dimension 6 x 22 x window length, where we aggregate 132-dimension vectors in time. If we consider a 41-second window, then we will have a 5,412-dimension input to the second pass of processing. This input dimensionality is high even though we have a considerable amount of manually labeled training. To deal with this problem we follow a standard approach of using Principal Components Analysis (PCA) (Fukunaga, 1990) before every SdA. The output of PCA is a vector of dimension 13 for SdA detectors that look for SPSW and EYEM and 20 for 6-way SdA classifier.

Further, since we do not have enough SPSW and EYEM events in the training dataset, we must use an out-of-sample technique (van der Maaten et al., 2009) to train SdA. Three consecutive outputs are averaged, so the output is further reduced from 3

× 13 to just 13, using a sliding window approach to averaging. Therefore, the input for SPSW SdA and EYEM SdA decreases to 13 x window length and 20 x window length for 6-way SdA.

We used an open source toolkit, Theano (Bergstra et al., 2010; Bastien et al., 2012), to implement the SdAs. The parameters of the models are optimized to minimize the average reconstruction error using a cross-entropy loss function. In the optimization process, a variant of stochastic gradient descent is used, referred to as minibatches. Minibatch stochastic gradient descent is similar to stochastic gradient descent, but we use more than one training example to calculate each estimate of the gradient. Using this optimization method, we will have less variance in the estimate of the gradient. Additionally, this framework makes better use of the hierarchical memory organization in modern computers.

SPSW SdA uses a window length of 3 which means it has 39 inputs and 2 outputs. It has three hidden layers with corruption levels of 0.3 for each layer. The number of nodes per layer are: first layer = 100, second layer = 100, third layer = 100. The parameters for pre-training are: learning rate = 0.5, number of epochs = 200, batch size = 300. The parameters for fine-tuning are: learning rate = 0.2, number of epochs = 800 and batch size = 100.

EYEM SdA uses a window length of 3 which means it has 39 inputs and 2 outputs. It has three hidden layers with corruption levels of 0.3 for each layer. The number of nodes per layer are: first layer = 100, second layer = 100, third layer = 100. The parameters for pre-training are: learning rate = 0.5, number of epochs = 200, batch size = 300. The parameters for fine-tuning are: learning rate = 0.2, number of epochs = 100 and batch size = 100.

Six-way SdA uses a window length of 41 which means it has 820 inputs and 6 outputs. It has three hidden layers with corruption levels of 0.3 for each layer. The number of nodes per layer are: first layer = 800, second layer = 500, third layer = 300. The parameters for pre-training are: learning rate = 0.5, number of epochs = 150 and batch size = 300. The parameters for fine-tuning are: learning rate = 0.1, number of epochs = 300 and batch size = 100.

The 6-way, 4-way and 2-way classification results for the second stage of processing are presented in **Tables 3–5**, in the second pass section, respectively. Note that unlike the tables for the first pass of processing, the classification results in each of these tables are measured once per epoch—they are not per-channel results. We refer to these results as epoch-based.

Third Pass: Statistical Language Modeling

The output of the second stage of processing is a vector of six scores, or likelihoods, per epoch. This serves as the input for the third stage of processing. The optimized parameters for the third pass of processing are: prior probability for an epoch, ϵ_{prior}, is 0.1; the weight, M, is 1; the decaying weight, λ, is 0.2; the weight associated with P_{gprior},α, is 0.1; the grammar weight, y, is 1; the number of iterations, n, is 20, and the window length to calculate the left and right prior probabilities is 10.

The 6-way, 4-way and 2-way classification results are presented in **Tables 3–5**, in the third pass section, respectively. Note that these results are also epoch-based.

DISCUSSION

The 6-way classification task can be structured into several subtasks. Of course, due to the high probability of the signal being background, the system is heavily biased toward choosing the background model. Therefore, in **Table 4** in the first pass section, we see that performance on BACKG is fairly high. Not surprisingly, BCKG is most often confused with SPSW. SPSW events are short in duration and there are many transient events in BCKG that resemble an SPSW event. This is one reason we added ARTF and EYEM models, so that we can reduce the confusions of all classes with the short impulsive SPSW events. As we annotate background data in more detail, and identify more commonly occurring artifacts, we can expand on our ability to model BCKG events explicitly.

GPEDs are, not surprisingly, most often confused with PLED events. Both events have a longer duration than SPSWs and artifacts. From the first pass section of **Table 4**, we see that performance on these two classes is generally high. The main difference between GPED and PLED is duration, so we designed the post-processing to learn this as a discriminator. For example, in the second pass of processing, we implemented a window duration of 41 s so that the SdA system would be exposed to long-term temporal context. We also designed three separate SdA networks to differentiate between short-term and long-term context. In **Table 4** in the second pass section, we see that the performance of GPEDs and PLEDs improves with the second pass of post-processing. More significantly, the confusions between GPEDs and PLEDs also decreased. Note that also in **Table 4** in the second pass section, performance of BCKG increased significantly. Confusions with GPEDs and PLEDs dropped dramatically to below 1%.

While performance across the board increased, performance for SPSW dropped by adding the second pass of post-processing. This is a reflection on the imbalance of the data. Less than one percent of data is annotated as SPSWs, while we have ten times more training samples for GPEDs and PLEDs. Note that we used an out-of-sample technique to increase the number of training samples for SPSWs, but even this technique could not solve the problem of a lack of annotated SPSW data. By comparing the first pass results of **Tables 3–5** we saw a similar behavior with the EYEM class because there are also fewer EYEM events.

A summary of the results for different stages of processing is shown in **Table 6**. The overall performance of the multi-pass

TABLE 6 | Specificity and sensitivity for each pass of processing.

Pass	Sensitivity	Specificity
1 (HMM)	86.78	17.70
2 (SdA)	78.93	4.40
3 (SLM)	90.10	4.88

hybrid HMM/deep learning classification system is promising: more than 90% sensitivity and <5% specificity.

Because the false alarm rate in these types of applications varies significantly with sensitivity, it is important to examine performance using a DET curve. A DET curve for the first, second, and third stage of processing is given in **Figure 8**. Note that the tables previously presented use the unprocessed likelihoods output from the system. They essentially correspond to the point on the DET curve where a penalty of 0 is applied. This operating point is identified on each of the curves in **Figure 8**. We see that the raw likelihoods of the system correspond to different operating points in the DET curve space. From **Figure 8** it is readily apparent that post-processing significantly improves our ability to maintain a low false alarm rate as we increase the detection rate. In virtually all cases, the trends shown in **Tables 3–6** hold up for the full range of the DET curve. This study demonstrates that a significant amount of contextual processing is required to achieve a specificity of 5%.

CONCLUSION

Virtually all previous R&D efforts involving EEG, including seizure detection, have been conducted on small databases (Akareddy et al., 2014). Often these databases are not good representations of the type of data observed in clinical environments. Transient artifacts, not common in databases collected under research conditions, can significantly degrade performance. Not surprisingly, despite high accuracies presented in the research literature, the performance of commercially available systems has been lacking in clinical settings. There is still great demand for an automated system that achieves a low false alarm rate in clinical applications.

We have presented a three-pass system that can achieve high performance classifying EEG events of clinical relevance. The system uses a combination of HMMs for accurate temporal segmentation and deep learning for high performance classification. In the first pass, the signal is converted to EEG events using an HMM-based system that models the temporal evolution of the signal. In the second pass, three stacked denoising autoencoders (SDAs) with different window durations are used to map event labels onto a single composite epoch label vector. We demonstrated that both temporal and spatial context analysis based on deep learning can improve the performance of sequential decoding using HMMs. In the third pass, a probabilistic grammar is applied that combines left and right context with the current label vector to produce a final decision for an epoch.

Our hybrid HMM/deep learning system delivered a sensitivity above 90% while maintaining a specificity below 5%, making automated analysis a viable option for clinicians. This framework for automatic analysis of EEGs can be applied in other classification tasks such as seizure detection or abnormal detection. There are many straightforward extensions of this system that can include more powerful deep learning networks such as Long Short-Term Memory Networks or Convolutional Neural Networks. This is the subject of our ongoing research.

This project is part of a long-term collaboration with the Department of Neurology at Temple University Hospital that has produced several valuable outputs including a large corpus (TUH-EEG), a subset of the corpus annotated for clinically relevant events (TUH-EEG-ESS), and technology to automatically interpret EEGs. In related work, we are also making the corpus searchable using multimodal queries that integrate metadata, information extracted from EEG reports and the signal event data described here (Obeid and Picone, 2016). The resulting system can be used to retrieve many different types of cohorts and will be a valuable tool for clinical work, research and teaching.

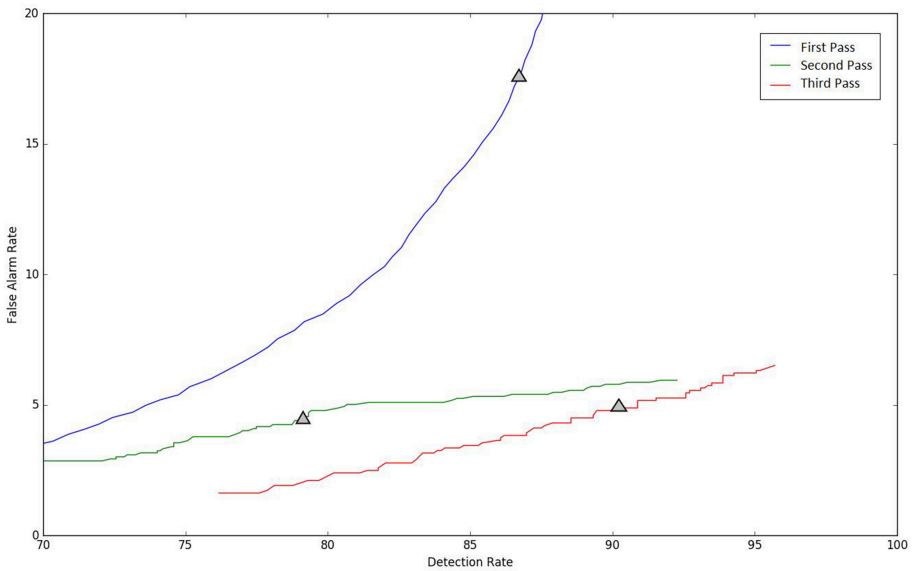

FIGURE 8 | DET curves are shown for each pass of processing. The "zero penalty" operating point is also shown since this was used in **Tables 3–5**.

AUTHOR CONTRIBUTIONS

MG and AH: algorithm design, programmer; SL: data collection; IO: data collection, CO-PI; JP: data collection, algorithm design, PI.

FUNDING

The primary funder of this research was the QED Proof of Concept program of the University City Science Center (Grant No. S1313). Research reported in this publication was also supported by the National Human Genome Research Institute of the National Institutes of Health under Award Number U01HG008468 and the National Science Foundation through Major Research Instrumentation Grant No. CNS-09-58854. The TUH-EEG database work was funded by (1) the Defense Advanced Research Projects Agency (DARPA) MTO under the auspices of Dr. Doug Weber through the Contract No. D13AP00065, (2) Temple University's College of Engineering and (3) Temple University's Office of the Senior Vice-Provost for Research.

ACKNOWLEDGMENTS

We are also grateful to Dr. Mercedes Jacobson, Dr. Steven Tobochnik and David Jungries of the Temple University School of Medicine for their assistance in developing the classification paradigm used in this study and for preparing the manually annotated data.

REFERENCES

Akareddy, S. M., Akareddy, S. M., and Kulkarni, P. K. (2014). EEG signal classification for epilepsy seizure detection using improved approximate entropy. *Int. J. Publ. Health Sci. 2*, 23–32. doi: 10.11591/ijphs.v2i1.1836

Alotaiby, T., Alshebeili, S., Alshawi, T., Ahmad, I., and Abd El-Samie, F. (2014). EEG seizure detection and prediction algorithms: a survey. *EURASIP. J. Adv. Signal Process.* 2014, 1–21. doi: 10.1186/1687-6180-2014-183

Alphonso, I., and Picone, J. (2004). "Network training for continuous speech recognition," in *Proceedings of the European Signal Processing Conference* (Vienna), 553–556.

American Clinical Neurophysiology Society. (2006). *Guideline 6: A Proposal for Standard Montages to be Used in Clinical EEG*. Milwaukee. Available online at: http://www.acns.org/pdf/guidelines/Guideline-6.pdf

American Clinical Neurophysiology Society. (2012). *ACNS Standardized ICU EEG Nomenclature v.* Milwaukee. Available online at: https://www.acns.org/pdf/guidelines/Guideline-14-pocket-version.pdf

Bastien, F., Lamblin, P., Pascanu, R., Bergstra, J., Goodfellow, I., Bergeron, A., et al. (2012). *Theano: New Features and Speed Improvements. arXiv.* Available online at: http://arxiv.org/abs/1211.5590

Bengio, Y., Lamblin, P., Popovici, D., and Larochelle, H. (2007). "Greedy layer-wise training of deep networks," in *Advances in Neural Information Processing System* (Vancouver, BC), 153–160.

Bergstra, J., Breuleux, O., Bastien, F., Lamblin, P., Pascanu, R., Desjardins, G., et al. (2010). "Theano: a CPU and GPU math expression compiler," in *Proceedings of the Python for Scientific Computing Conference (SciPy)*, 1–7. Available online at: http://conference.scipy.org/proceedings/scipy2010/bergstra.html

Da Rocha Garrit, P. H., Guimaraes Moura, A., Obeid, I., and Picone, J. (2015). "Wavelet analysis for feature extraction on EEG Signals," *Presented at the NEDC Summer Research Experience for Undergraduates.* Philadelphia, PA*:* Department of Electrical and Computer Engineering, Temple University. Available online at: http://www.isip.piconepress.com/publications/unpublished/conferences/2015/summer_of_code/wavelets/

Deburchgraeve, W., Cherian, P. J., De Vos, M., Swarte, R. M., Blok, J. H., Visser, G. H., et al. (2008). Automated neonatal seizure detection mimicking a human observer reading EEG. *Clin. Neurophysiol.* 119, 2447–2454. doi: 10.1016/j.clinph.2008.07.281

Fukunaga, K. (1990). *Introduction to Statistical Pattern Recognition. Computer Science and Scientific Computing. 2nd Edn*. San Diego, CA: Academic Press, Inc. Available online at: https://www.elsevier.com/books/introduction-to-statistical-pattern-recognition/fukunaga/978-0-08-047865-4

Gotman, J. (1999). Automatic detection of seizures and spikes. *J. Clin. Neurophysiol.* 6, 130–140.

Harati, A., Golmohammadi, M., Lopez, S., Obeid, I., and Picone, J. (2015). "Improved EEG event classification using differential energy," *Proceedings of the IEEE Signal Processing in Medicine and Biology Symposium*. (Philadelphia, PA), 1–4.

Harati, A., Lopez, S., Obeid, I., Jacobson, M., Tobochnik, S., and Picone, J. (2014). "The TUH EEG corpus: a big data resource for automated EEG interpretation," in *Proceedings of the IEEE Signal Processing in Medicine and Biology Symposium*. (Philadelphia, PA), 1–5.

Hinton, G. E., Osindero, S., and Teh, Y.-W. (2006). A fast learning algorithm for deep belief nets. *Neural Comput.* 18, 1527–1554. doi: 10.1162/neco.2006.18.7.1527

Hopfengärtner, R., Kerling, F., Bauer, V., and Stefan, H. (2007). An efficient, robust and fast method for the offline detection of epileptic seizures in long-term scalp EEG recordings. *Clin. Neurophysiol.* 118, 2332–2343. doi: 10.1016/j.clinph.2007.07.017

Jahankhani, P., Kodogiannis, V., and Revett, K. (2006). "EEG signal classification using wavelet feature extraction and neural networks," in *IEEE John Vincent Atanasoff 2006 International Symposium on Modern Computing (JVA'06)*, 120–124.

Juang, B.-H., and Rabiner, L. (1991). Hidden markov models for speech recognition. *Technometrics* 33, 251–272.

Khamis, H., Mohamed, A., and Simpson, S. (2009). Seizure state detection of temporal lobe seizures by autoregressive spectral analysis of scalp EEG. *Clin. Neurophysiol.* 120, 1479–1488. doi: 10.1016/j.clinph.2009.05.016

LeCun, Y., Bengio, Y., and Hinton, G. (2015). Deep learning. *Nature* 521, 436–444. doi: 10.1038/nature14539%5Cn10.1038/nature14539

Levinson, S. E. (2005). "Syntactic Analysis," in *Mathematical Models for Speech Technology*, John Wiley & Sons, Ltd, 119–135. Available online at: https://onlinelibrary.wiley.com/doi/book/10.1002/0470020911

Lopez, S., Golmohammadi, M., Obeid, I., and Picone, J. (2016). "An analysis of two common reference points for EEGs," in *Proceedings of the IEEE Signal Processing in Medicine and Biology Symposium* (Philadelphia, PA), 1–4

Martin, A., Doddington, G., Kamm, T., Ordowski, M., and Przybocki, M. (1997). "The DET curve in assessment of detection task performance," in *Proceedings of Eurospeech*. (Rhodes), 1895–1898.

Mirowski, P., Madhavan, D., Lecun, Y., and Kuzniecky, R. (2009). Classification of patterns of EEG synchronization for seizure prediction. *Clin. Neurophysiol.* 120, 1927–1940. doi: 10.1016/j.clinph.2009.09.002

Ney, J. P., van der Goes, D. N., Nuwer, M. R., and Nelson, L. (2016). Continuous and routine EEG in intensive care: utilization and outcomes, United States 2005-2009. *Neurology* 81, 2002–2008. doi: 10.1212/01.wnl.0000436948.93399.2a

Obeid, I., and Picone, J. (2016). The temple university hospital EEG data corpus. *Front. Neurosci.* 10:196. doi: 10.3389/fnins.2016.00196

Osorio, I., Frei, M. G., and Wilkinson, S. B. (1998). Real-time automated detection and quantitative analysis of seizures and short-term prediction of clinical onset. *Epilepsia* 39, 615–627.

Persyst Development Corporation. (2017). *Seizure Detection (P13 rev*. B). Available online at: https://www.persyst.com/~technology/seizure-detection/.

Picone, J. (1990). Continuous speech recognition using hidden markov models. *IEEE ASSP Mag. 7*, 26–41. doi: 10.1109/53.54527

Picone, J. (1993). Signal modeling techniques in speech recognition. *Proc. IEEE.* 81, 1215–1247. doi: 10.1109/5.237532

Ramgopal, S. (2014). Seizure detection, seizure prediction, and closed-loop warning systems in epilepsy. *Epilepsy Behav.* 37, 291–307. doi: 10.1016/j.yebeh.2014.06.023

Sartoretto, F., and Ermani, M. (1999). Automatic detection of epileptiform activity by single-level wavelet analysis. *Clin. Neurophysiol.* 110, 239–249.

Schad, A., Schindler, K., Schelter, B., Maiwald, T., Brandt, A., Timmer, J., and Schulze-Bonhage, A. (2008). Application of a multivariate seizure detection and prediction method to non-invasive and intracranial long-term EEG recordings. *Clin. Neurophysiol.* 119, 197–211. doi: 10.1016/j.clinph.2007.09.130

Schindler, K., Wiest, R., Kollar, M., and Donati, F. (2001). Using simulated neuronal cell models for detection of epileptic seizures in foramen ovale and scalp EEG. *Clin. Neurophysiol.* 112, 1006–1017. doi: 10.1016/S1388-2457(01)00522-3

Shah, V., von Weltin, E., Lopez, S., McHugh, J. R., Veloso, L., Golmohammadi, M., et al. (2018). The temple university hospital seizure detection corpus. *Front. Neuroinform.* 12:83. doi: 10.3389/fninf.2018.00083

Stam, C. J. (2005). Nonlinear dynamical analysis of EEG and MEG: review of an emerging field. *Clin. Neurophysiol.* 116, 2266–2301. doi: 10.1016/j.clinph.2005.06.011

Subasi, A. (2007). EEG signal classification using wavelet feature extraction and a mixture of expert model. *Expert Syst. Appl.* 32, 1084–1093. doi: 10.1016/j.eswa.2006.02.005

Thodoroff, P., Pineau, J., and Lim, A. (2016). Learning robust features using deep learning for automatic seizure detection. *Proc. Mach. Learn. Res. 56*, 178–190. Available online at: http://proceedings.mlr.press/v56/Thodoroff16.html

van der Maaten, L., Postma, E., and van den Herik, J. (2009). Dimensionality reduction: a comparative review. *J. Mach. Learn. Res. 10*, 1–41. doi: 10.1080/13506280444000102

Varsavsky, A., and Mareels, I. (2006). "Patient un-specific detection of epileptic seizures through changes in variance," in *Proceedings of the Annual International Conference of the IEEE Engineering in Medicine and Biology Society*. (New York, NY: IEEE), 3747–3750. Available online at: *http://ieeexplore.ieee.org/xpls/abs_all.jsp?arnumber=4462614*

Vincent, P., Larochelle, H., Bengio, Y., and Manzagol, P.-A. (2008). "Extracting and composing robust features with denoising autoencoders," in *Proceedings of the 25th International Conference on Machine Learning*. (New York, NY), 1096–1103

Vincent, P., Larochelle, H., Lajoie, I., Bengio, Y., and Manzagol, P.-A. (2010). Stacked denoising autoencoders: learning useful representations in a deep network with a local denoising criterion pierre-antoine manzagol. *J. Mach. Learn. Res.* 11, 3371–3408. doi: 10.1111/1467-8535.00290

Xiong, W., Wu, L., Alleva, F., Droppo, J., Huang, X., and Stolcke, A. (2017). *The Microsoft 2017 Conversational Speech Recognition System*. Available online at: https://doi.org/https://arxiv.org/abs/1708.06073

Yamada, T., and Meng, E. (2017). *Practical Guide for Clinical Neurophysiologic Testing: EEG*. Philadelphia, PA: Lippincott Williams & Wilkins. Available online at: https://shop.lww.com/Practical-Guide-for-Clinical-Neurophysiologic-Testing--EEG/p/9781496383020

Conflict of Interest Statement: The authors declare that the research was conducted in the absence of any commercial or financial relationships that could be construed as a potential conflict of interest.

frontiers in Human Neuroscience

ORIGINAL RESEARCH
published: 05 April 2019
doi: 10.3389/fnhum.2019.00103

Effects of Transcranial Direct Current Stimulation of Primary Motor Cortex on Reaction Time and Tapping Performance: A Comparison Between Athletes and Non-athletes

Oliver Seidel[1,2] *and Patrick Ragert*[1,2]*

[1]*Institute for General Kinesiology and Exercise Science, Faculty of Sport Science, University of Leipzig, Leipzig, Germany,*
[2]*Department of Neurology, Max Planck Institute for Human Cognitive and Brain Sciences, Leipzig, Germany*

Recent studies provided compelling evidence that physical activity leads to specific changes on a functional and structural level of brain organization. The observed neural adaptions are specific to the sport and manifested in those brain regions which are associated with neuronal processing of sport-specific skills. Techniques of non-invasive brain stimulation have been shown to induce neuroplastic changes and thereby also facilitate task performance. In the present study, we investigated the influence of transcranial direct current stimulation (tDCS) over the leg area of the primary motor cortex (M1) on simple reaction time tasks (RTT) and tapping tasks (TT) as a comparison between trained football (FB) and handball players (HB) and non-athletes (NA). We hypothesized that anodal tDCS over M1 (leg area) would lead to specific behavioral gains in RTT and TT performance of the lower extremity as compared to sham condition. On an exploratory level, we aimed at revealing if trained athletes would show stronger tDCS-induced behavioral gains as compared to NA, and, furthermore, if there are any differential effects between FB and HB. A total number of 46 participants were enrolled in a sham-controlled, double-blinded, cross-over study. A test block consisting of RTT and TT was performed before, during, after as well as 30 min after a 20-min tDCS application. Additionally, the specificity of tDCS-induced changes was examined by testing upper extremity using the same experimental design as a control condition. Our data showed no group- or sport-specific tDCS-induced effects (online and offline) on RTT and TT neither for lower nor upper extremities. These findings indicate that neither athletes nor NA seems to benefit from a brief period of tDCS application in speed-related motor tasks. However, more knowledge on neuronal processing of RTT and TT performance in trained athletes, the influence of tDCS parameters including stimulation sites, and the effect of inter-individual differences are required in order to draw a comprehensive picture of whether tDCS can help to enhance motor abilities on a high-performance level.

Keywords: tDCS, reaction time, tapping, primary motor cortex, athletes

OPEN ACCESS

Edited by:
Stephane Perrey,
Université de Montpellier, France

Reviewed by:
Antonio Ivano Triggiani,
University of Foggia, Italy
Paul Sauseng,
Ludwig Maximilian University of Munich, Germany

***Correspondence:**
Patrick Ragert
patrick.ragert@uni-leipzig.de

Received: *19 December 2018*
Accepted: *07 March 2019*
Published: *05 April 2019*

Citation:
Seidel O and Ragert P (2019) Effects of Transcranial Direct Current Stimulation of Primary Motor Cortex on Reaction Time and Tapping Performance: A Comparison Between Athletes and Non-athletes. Front. Hum. Neurosci. 13:103. doi: 10.3389/fnhum.2019.00103

INTRODUCTION

A variety of studies suggest that physical exercise leads to specific changes on a functional and structural level of brain organization (Colcombe et al., 2006; Bullitt et al., 2009; Voss et al., 2010; Erickson et al., 2012). In addition, it has been shown that this neuroplasticity seems to be specific to the individual exercise regime or sport (Jäncke et al., 2009; Park et al., 2009; Schlaffke et al., 2014). On a functional level, the findings of Lulic et al. (2017), using transcranial magnetic stimulation (TMS), indicate that the propensity for exercise-induced functional plasticity is different in high vs. low physically active individuals. In this study, a single session of moderate intensity aerobic exercise increased the amplitude of corticospinal output in the HIGH (physically active) group, and, in contrast, did not alter corticospinal output in the LOW (physically active) group. Apart from the physical activity itself, also the exercise regime leads to specific brain alterations and influences the amount of structural plasticity (Schlaffke et al., 2014). Concerning brain structure, a study by Meier et al. (2016), for example, showed that handball players have an increased volume of gray matter (GM) in the hand area of the primary motor cortex (M1), while ballet dancers are characterized by an increased GM volume in the foot area of M1. These results indicate that the observed functional and structural adaptions are sport-specific/ physical activity-dependent and seem to manifest in those brain regions that are involved in the neural processing of sport-specific skills.

It is well known that M1 is a key region involved in motor control and functions in terms of precision, speed, strength, endurance and execution of daily motor tasks (Levasseur-Moreau et al., 2013). One opportunity to explore the function of certain brain areas can be found in non-invasive brain stimulation methods such as transcranial magnetic (TMS) and/or direct current stimulation (tDCS). To investigate the role of motor-related brain regions during the execution of motor tasks, tDCS is a common method to modulate brain function specifically and thereby induce a possible behavioral change.

tDCS is a non-invasive method for modulating the excitability of certain brain regions by applying a weak direct current to the scalp. It has been proposed that tDCS modulates neural firing rates during stimulation and synaptic strength following long-term stimulation (Stagg and Nitsche, 2011). Using this method, either an increase (by means of anodal tDCS) or a reduction (by means of cathodal tDCS) of the area-specific excitability is possible (Nitsche and Paulus, 2000), as demonstrated by changes in the motor evoked potential (MEP) elicited *via* TMS.

Although tDCS has been mainly used for patients with neurologic disorders (Flöel, 2014; Lattari et al., 2017b) and psychiatric disorders (Aparício et al., 2016), it has also been highlighted as a valuable tool to enhance physical performance in healthy individuals. Current reviews including studies investigating healthy adults provided evidence that anodal tDCS over motor-related brain regions can lead to positive behavioral effects (Banissy and Muggleton, 2013; Machado et al., 2018). For example, a tDCS-induced increase of isometric muscle force has been found in both lower (Tanaka et al., 2009) and upper extremities (Boggio et al., 2006; Hummel et al., 2006; Stagg et al., 2011; Salimpour and Shadmehr, 2014). Further studies have shown that endurance performance (Angius et al., 2018) and both static and dynamic balance regulation (Dutta et al., 2014; Kaminski et al., 2016) can be improved by anodal tDCS. However, concerning anodal tDCS effects in speed-related motor tasks, the current literature is inconsistent. Positive effects have been demonstrated especially in serial and choice reaction time tasks (RTT) with upper extremities (Nitsche et al., 2003b; Verissimo et al., 2016; Drummond et al., 2017; Hupfeld et al., 2017). In studies using simple RTT, the findings are rather contradictory, since both improved reaction times (Carlsen et al., 2015; Devanathan and Madhavan, 2016; Hupfeld et al., 2017) and no effects (Tanaka et al., 2009; Stagg et al., 2011; Horvath et al., 2016) are reported. Only a small number of studies investigated the influence of anodal tDCS on tapping tasks (TT), focusing mainly on (serial) finger TT. The results showed either positive (Tecchio et al., 2010; Saimpont et al., 2016) or null effects (Boehringer et al., 2013), while one reported a significant impairment following anodal tDCS (Stagg et al., 2011). However, concerning tDCS effects on frequency-oriented hand or even foot TT, there is a clear lack of evidence in the current literature.

More recently, there has been great interest in the use of tDCS to enhance sports performance (Davis, 2013; Reardon, 2016) and to facilitate neuroplasticity and training adaptations (Bolognini et al., 2009) in athletes. First, approaches can be found in recent studies showing a tDCS-induced increase of isometric strength of shoulder rotators muscles in handball players (Hazime et al., 2017) and an increased isometric quadriceps strength after stimulation in soccer players (Vargas et al., 2018). Similar results were found by Lattari et al. (2017a) examining tDCS-induced effects on muscle power in individuals with advanced resistance training experience. Furthermore, anodal tDCS is capable to have positive effects on the time of exhaustion in trained individuals performing a cycling task (Vitor-Costa et al., 2015). Beyond that, Okano et al. (2015) studied the effects of 20 min of tDCS with the anode over the left temporal cortex on trained cyclists during an incremental cycling test and found significantly improved peak power, as well as reduced heart rate and perception of effort at submaximal workloads. These findings suggest that tDCS can potentially facilitate the athlete's performance under laboratory conditions. However, there is no evidence that this could lead to positive transfer effects under field conditions or even during competition. Further risks, opportunities and potential approaches concerning the use of tDCS at an elite sports level have already been discussed by Banissy and Muggleton (2013) and Edwards et al. (2017). It seems clear that more research is needed to clarify the usefulness of tDCS in highly trained individuals (Colzato et al., 2017; Edwards et al., 2017). As maximum performance in fine motor control could not be further improved in elite pianists (Furuya et al., 2013), it needs to be investigated whether similar ceiling effects might apply to the performance of elite athletes as well.

The primary aim of the present study was to investigate the influence of a 20-min anodal tDCS over leg area of the M1 on the performance of trained athletes in simple speed-related motor tasks, using simple reaction time and TT for both upper and lower extremities. According to a systematic review and meta-analysis by Machado et al. (2018) that assessed the effect of tDCS on exercise performance enhancement in healthy adults, no effect was found for cathodal tDCS for any tasks (performance in isometric, isokinetic or dynamic strength exercise and whole-body exercise). Similarly, Tanaka et al. (2009) found no effect of cathodal tDCS over M1 leg area on simple RTT for lower extremities. Hence, the application of cathodal tDCS was waived in the present study. Therefore, the focus was on the question of whether athletes would show stronger anodal tDCS-induced performance gains compared to non-athletes and if sport-specific differences could be determined. In general, we first hypothesized that anodal tDCS over M1 (leg area) would lead to specific behavioral gains in simple reaction time and tapping performance of the foot (not hand, since this can be considered as a kind of control condition) as compared to sham condition (in accordance with Devanathan and Madhavan, 2016; Saimpont et al., 2016). To demonstrate that potential performance gains are in fact related to tDCS, we tested a control group (CG) of participants performing exactly the same procedure but without brain stimulation. Concerning athletes, we expected football and handball players to show superior initial performances as compared to non-athletes. This hypothesis is based on previous studies showing better initial performances in athletes in several motor abilities (Verburgh et al., 2016; Seidel et al., 2017). On an exploratory level, we aimed at revealing if athletes would show stronger tDCS-induced behavioral gains as compared to non-athletes, and, furthermore, if there are any differential effects between football and handball players. Since there is barely evidence concerning tDCS-effects at an elite sports level in speed-related motor tasks, we cannot make direct inferences about the directionality of tDCS-induced behavioral effects.

MATERIALS AND METHODS

Ethics Statement

The study was approved by the local ethics-committee of the Medical Faculty at the University of Leipzig. All participants gave written informed consent to participate in the experiments according to the Declaration of Helsinki, and were compensated for participation.

Participants

In the present study, a total of 46 healthy, young adults were recruited, divided into three groups of football players (FB), handball players (HB) and non-athletes (NA). To exclude the presence of any neurological disease and/or contraindications, all participants underwent a detailed neurological examination prior to the testing phase. Inclusion criteria for FB and HB consisted of an individual training history of at least 2 years as well as regular practice and regular participation in competitions/matches in their respective sports discipline. NA were not allowed to do more than 2 h of combined sports activities per week. The investigated sample of this study consisted of 13 FB (three females, mean age = 24.00 ± 3.89 years), 12 HB (five females, mean age = 22.50 ± 4.32 years) and 21 NA (11 females, mean age = 26.95 ± 3.43 years). On average, FB trained for 16.31 ± 5.02 years and currently 5.65 ± 2.15 h/week, whereas HB trained for 13.17 ± 4.49 years and currently 8.54 ± 3.84 h/week in their respective sports disciplines. On the other hand, NA performed an average of less than 2 h of combined sports activities per week (1.41 ± 1.32 h/week). Additionally, all participants (FB, HB and NA) with regular practice of musical instruments were excluded from participation in this study. This was motivated by the fact that recent studies have shown that musical training induces functional and structural plasticity in motor-related brain regions (Steele et al., 2013; Vollmann et al., 2014) which in turn might affect the amount of tDCS effect. As assessed by the Edinburgh Handedness Inventory (Oldfield, 1971), all participants were right-handed [mean laterality quotient (LQ) of FB: 84.02 ± 16.45; HB: 95.83 ± 8.14; NA: 90.15 ± 14.15].

Furthermore, a CG was tested to ensure that potential behavioral changes in simple reaction time and tapping frequency are in fact tDCS related and not a mere effect of fatigue or learning. A total of six male and six female right-handed (mean LQ: 80.4 ± 17.1) participants (n = 12) in this group with an mean age of 21.25 ± 1.14 years and sports-related activities of 4.85 ± 3.86 h/week had to perform the whole procedure (see "Experimental Design" section for further details) but without tDCS.

Experimental Design

A sham-controlled, double-blinded, cross-over design was carried out. The study was compromised of two sessions that were separated by at least 24 h in order to avoid task-related impacts of cognitive or muscular fatigue. Study procedure for both sessions was identical (see **Figure 1A**), starting with an initial run of a test block consisting of RTT and TT for upper and lower extremities (see "Motor Tasks" section for further details). Afterward, tDCS was applied over the leg area of the (M1 leg area) for a period of 20 min. Participants received either the anodal tDCS condition or the control condition, where sham tDCS was applied [see "Transcranial Direct Current Stimulation (tDCS)" section for further details]. For each participant, the type of stimulation was randomly assigned to either session 1 or 2. Another run of the aforementioned test block was performed after 10 min of stimulation (during tDCS, online) as well as directly after and 30 min after stimulation has ended (offline). The second test block was performed after 10 min of stimulation because previous studies have demonstrated that a time of 9–13 min is required to obtain an increase in cortical excitability for up to 1.5 h (Nitsche and Paulus, 2000). Participants were instructed to avoid alcohol and caffeine 24 h prior to each session because of their well-known influences on motor control and central nervous system (CNS) functioning (Pesta et al., 2013). Additionally, participants were asked to report their daily activities 48 h before both sessions, their current levels of attention, fatigue and discomfort on a visual analog scale (pre and

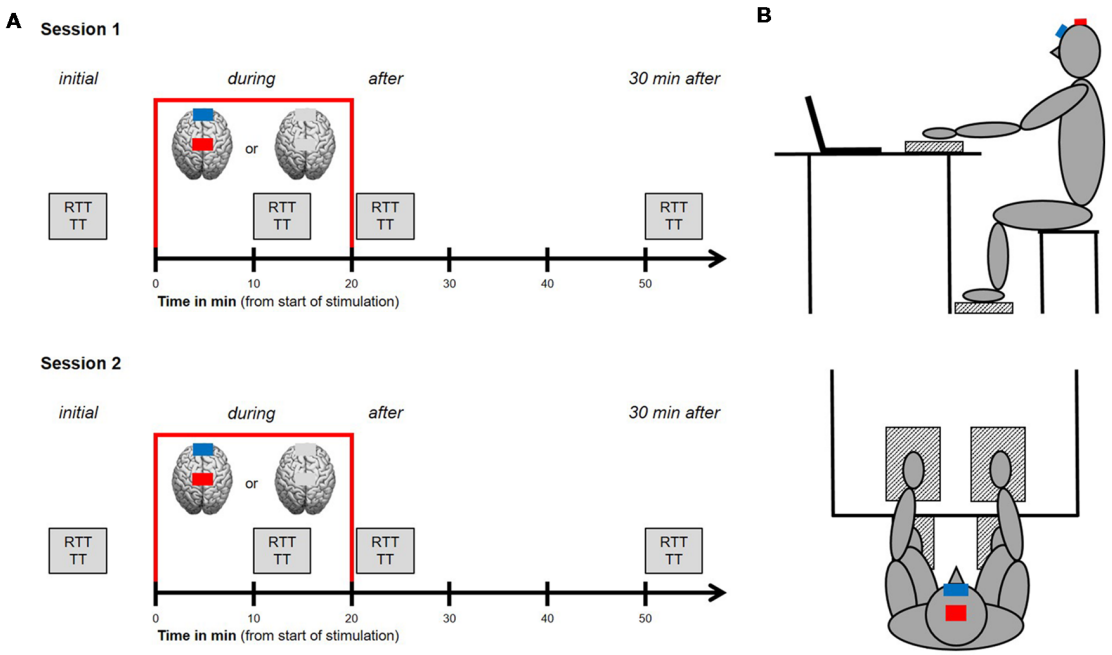

FIGURE 1 | Study design and experimental setup. **(A)** Procedures for session 1 and 2. Study procedure for both sessions was identical, starting with an initial run of a test block consisting of reaction time tasks (RTT) and tapping tasks (TT) for upper and lower extremities. Afterwards, transcranial direct current stimulation (tDCS) was applied over the leg area of the primary motor cortex (M1 leg area) for a period of 20 min (indicated by the red frame). Participants received either the anodal tDCS condition or the control condition, where sham tDCS was applied. Another run of the aforementioned test block was performed after 10 min of stimulation (during tDCS, online) as well as directly after and 30 min after stimulation has ended (offline). **(B)** Experimental setup. Participants were seated 1 m away from a computer monitor, upright on a stool (hips and knees at 90°) with their hands resting on and their feet resting under a table in front of them. Next to each hand and foot, with a defined distance of 10 cm, a custom made force plate (indicated as patterned boxes) was installed. Indicated by the red (anode) and blue (cathode) boxes, the anode was placed over the M1 leg area target region, the cathode (reference electrode) was placed over the middle of the forehead.

post), as well as their individual amount of sleep the night before the experimental sessions, to sufficiently control for this matter.

Transcranial Direct Current Stimulation (tDCS)

For tDCS, a weak direct current of 2 mA was delivered for 20 min by means of two surface electrodes using a battery driven-stimulator (neuroConn GmbH, Ilmenau, Germany). For each session, either anodal tDCS or sham tDCS was applied to the bilateral M1 leg area. While the anode (7 cm × 5 cm) was placed over the M1 leg area target region, the cathode (10 cm × 10 cm, reference electrode) was placed over the middle of the forehead. The anatomical landmark for M1 leg area was chosen according to the 10–20 system and the anode was placed over the vertex (Cz) on the mid-sagittal line (Madhavan and Stinear, 2010; Laczó et al., 2014). Cz was determined over the intersection of the courses nasion to inion and left preauricular point to right preauricular point according to Jurcak et al. (2007). tDCS was applied using two saline-soaked (0.9% NaCl) sponges and flexible elastic straps were used to fixate the electrodes on the head. The current was ramped up for 30 s at the beginning of tDCS eliciting a transient tingling sensation on the scalp that faded over seconds (Nitsche et al., 2003a; Gandiga et al., 2006) and also ramped down for 30 s. During sham tDCS, the current was increased, maintained and decreased for 30 s each. According to Gandiga et al. (2006), this is enough time to identify the presence of the current with no effective brain stimulation. The electrical resistance was constantly monitored on the stimulator's display within a range between 5 and 10 kΩ. The adverse effects were evaluated after each application through spontaneous reports of any unpleasant sensations such as burning, tingling, headache or nausea.

Motor Tasks

During each session, participants were seated 1 m away from a computer monitor, upright on a stool (hips and knees at 90°) with their hands resting on and their feet resting under a table in front of them (see **Figure 1B**). Next to each hand and foot, with a defined distance of 10 cm, a custom made force plate was installed. Participants were instructed to rest and relax their inactive extremities in this position. Facing the computer monitor, participants performed four runs of a test block (initial, during, after and 30 min after tDCS) consisting of speed-related motor tasks. Each block consisted of two runs of a simple RTT and two runs of a TT for each hand and foot separately. Therefore, a total amount of eight RTTs and eight TTs had to be performed with a total duration of approx. 8 min. The order of these tasks was randomized for each block and the software avoided two or more tasks for the same extremity in a row. Between each task was a short

rest period of 3 s when the upcoming task appeared on the computer monitor.

Simple Reaction Time Task (RTT)

For simple RTT, participants had to place their active hand (respectively foot) at the defined spot 10 cm away from the respective force plate. In this position, they were instructed to face the computer monitor and read the upcoming task carefully. After a countdown of 3 s, indicating the start of the run, participants were asked to press the respective force plate as quickly as possible in response to the appearance of a visual stimulus (cross) on the computer monitor. During one RTT, a total of 15 trials had to be responded in this manner with a randomized inter-trial interval of 0.5–2.0 s to avoid anticipation of trial onsets. Between each trial, the active hand (respectively foot) had to be placed back to the defined spot. For each trial, the time interval (ms) between the onset of the trial (cross) and the response was recorded as an outcome measure.

Tapping Task (TT)

For TT, participants were asked to take the same position as previously described for RTT. After a countdown of 3 s, participants started the run on their own with their first touch of the respective force plate. Subsequently, they had to press the force plate as often as possible over a period of 20 s. Concerning upper extremity TT, participants were instructed to tap in the center of the force plate with a flat hand. For the lower extremity counterpart, they were asked to keep the heel up in the air and to tap with their forefoot. As an outcome measure, tapping frequency (Hz) was recorded.

Analysis

For each test block, two runs of 15 trials were recorded for the left hand (HL), right hand (HR), left foot (FL) and right foot (FR), respectively. Afterward, these 30 reaction times of one block were averaged for each extremity separately. Outliers were defined as values <100 ms and >1,000 ms (Geiger et al., 2018) of each participant and were excluded from the averages. The lower limit was determined since all reaction times <100 ms are considered to be unphysiological and only in very few cases have been measured so far for the much faster auditory reaction times (Pain and Hibbs, 2007). After averaging all valid reaction times, this resulted in one value for RTT before (*initial*), *during*, *after* and 30 min *after* tDCS stimulation. Baseline differences were tested using a univariate ANOVA and revealed significant differences between groups (see "Results" section for further details). Hence, all values were normalized to *initial* (= 100%).

Concerning TT, two runs of 20 s were recorded for each test block for HL, HR, FL and FR, respectively. First, the total amount of taps during one run resulted in an average tapping frequency over 20 s that was averaged for both runs for each extremity (TT_{20}). Second, the total amount of taps during the first 3 s was considered, extracting the tapping frequency of the fastest second (TT_{max}). According to RTT, this resulted in one value for TT_{20} and TT_{max} before (*initial*), *during*, *after* and 30 min *after* tDCS stimulation. Due to baseline differences (see "Results" section for further details), values were also normalized to *initial* (= 100%).

All statistical analyses were performed with the software SPSS 22 (IBM, Armonk, NY, USA) using parametric tests since Shapiro-Wilk test revealed that RTT and TT data were normally distributed. As already described above, baseline differences were examined using an univariate ANOVA with factor group (FB vs. HB vs. NA) using Gabriel and Games-Howell *post hoc* tests, respectively to analyze the differences if necessary. A 2 × 3 × 3 repeated measures ANOVA was conducted to analyze the mean normalized values of RTT, TT_{max} and TT_{20} of each group and each extremity for three test blocks of the tasks (first within-subject factor), including stimulation condition (anodal vs. sham) as second within-subject factor and group (FB vs. HB vs. NA) as between-subject factor. Regarding the first within-subject factor, *initial* was not included since data were normalized and level *initial* would not have any variance across participants since all of them would have a value of 100%.

For the CG (without tDCS), a repeated measures ANOVA with factor test block (within-subjects factor) was conducted. Additionally, we computed the test-retest reliability using an intraclass correlation coefficient (ICC) to examine whether potential performance gains are in fact tDCS related or an effect of fatigue or learning.

When the respective interactions were significant, also Gabriel and Games-Howell *post hoc* tests, respectively were applied to analyze the differences. The critical level of significance for RTT and TT differences in all tests was set to $p < 0.05$ and Bonferroni adjusted for multiple comparisons. If necessary, data were corrected for sphericity using Greenhouse-Geisser correction. Partial eta-squared (η_p^2) for ANOVAs are provided as measures of effect size and used to aid in the interpretation of inferential statistics. As a rule of thumb, introduced by Miles and Shevlin (2000), $\eta_p^2 \geq 0.01$ is considered to be a small, $\eta_p^2 \geq 0.06$ a medium, and $\eta_p^2 \geq 0.14$ a large effect. Additionally, as recommended for tDCS studies by Biel and Friedrich (2018), Bayes factors (BF), a useful tool for evaluating evidence both for the research hypothesis and for the null hypothesis (Dienes, 2011; Kruschke, 2011), are reported for repeated measures ANOVAs using JASP (Jeffreys's Amazing Statistics Program, Marsman and Wagenmakers, 2017). BFs above 1 indicate evidence for H1 over H0, whereas BFs below 1 suggest the exact opposite. If BFs are above 3 or below 0.33, the strength of evidence for one hypothesis compared to its competing hypothesis is regarded as noteworthy (Jeffreys, 1961; Lee and Wagenmakers, 2013). Thus, BFs between 0.33 and 3 are considered as inconclusive, or only anecdotal evidence for any hypothesis.

RESULTS

Test-Retest Reliability of RTT and TT

To exclude that the pure repetition of RTT and TT would lead to significant behavioral alterations, we performed a test-retest analysis using a CG (n = 12). We found no statistically significant alterations neither in RTT performance

(rmANOVA, main effect of test block, HL: $F_{(3,33)} = 0.363$, $p = 0.780$, $\eta_p^2 = 0.032$; HR: $F_{(3,33)} = 0.215$, $p = 0.886$, $\eta_p^2 = 0.019$; FL: $F_{(2.139,23.531)} = 2.002$, $p = 0.155$, $\eta_p^2 = 0.154$; FR: $F_{(3,33)} = 0.290$, $p = 0.832$, $\eta_p^2 = 0.026$) nor in TT performance (rmANOVA, main effect of test block, HL: $F_{(1.914,21.055)} = 2.227$, $p = 0.134$, $\eta_p^2 = 0.168$; HR: $F_{(1.379,15.172)} = 2.622$, $p = 0.118$, $\eta_p^2 = 0.192$; FL: $F_{(1.600,17.598)} = 1.695$, $p = 0.214$, $\eta_p^2 = 0.133$; FR: $F_{(1.525,16.770)} = 2.103$, $p = 0.160$, $\eta_p^2 = 0.160$) performance. These findings were confirmed by good intrasession reliabilities according to Larsson et al. (1999) for RTT (ICC_{HL} (33,11) = 0.908; ICC_{HR} (33,11) = 0.884; ICC_{FL} (33,11) = 0.845; ICC_{FR} (33,11) = 0.897) and TT (ICC_{HL} (33,11) = 0.974; ICC_{HR} (33,11) = 0.952; ICC_{FL} (33,11) = 0.947; ICC_{FR} (33,11) = 0.940).

Initial Group Comparisons of RTT and TT

Initial RTT Performance

Initial RTT values differed significantly between groups indicating superior RTT performances in FB and HB as compared to NA (see **Figure 2A**). uANOVA revealed a significant main effect of group in HL ($F_{(2,43)} = 4.752$, $p = 0.014$, $\eta_p^2 = 0.181$), HR ($F_{(2,43)} = 7.910$, $p = 0.001$, $\eta_p^2 = 0.269$), FL ($F_{(2,43)} = 9.272$, $p = 0.000$, $\eta_p^2 = 0.301$) and FR ($F_{(2,43)} = 6.863$, $p = 0.003$, $\eta_p^2 = 0.242$). *Post hoc* analyses showed significant differences between FB and NA in HR ($p_{adjusted} = 0.018$), FL ($p_{adjusted} = 0.004$) and FR ($p_{adjusted} = 0.040$) as well as between HB and NA in HL ($p_{adjusted} = 0.023$), HR ($p_{adjusted} = 0.002$), FL ($p_{adjusted} = 0.002$) and FR ($p_{adjusted} = 0.003$). However, there were no significant differences between FB and HB (HL: $p_{adjusted} = 0.950$; HR: $p_{adjusted} = 0.839$; FL: $p_{adjusted} = 0.983$; FR: $p_{adjusted} = 0.770$).

Initial TT_{max} Performance

Initial maximum tapping frequency (TT_{max}) differed significantly between groups indicating superior TT_{max} performances in FB and HB as compared to NA (see **Figure 2B**). uANOVA revealed a significant main effect of group in HL ($F_{(2,43)} = 10.729$, $p = 0.000$, $\eta_p^2 = 0.333$), HR ($F_{(2,43)} = 8.525$, $p = 0.001$, $\eta_p^2 = 0.284$), FL ($F_{(2,43)} = 14.231$, $p = 0.000$, $\eta_p^2 = 0.398$) and FR ($F_{(2,43)} = 7.501$, $p = 0.002$, $\eta_p^2 = 0.259$). *Post hoc* analyses showed significant differences between FB and NA in HL ($p_{adjusted} = 0.002$), HR ($p_{adjusted} = 0.001$), FL ($p_{adjusted} = 0.000$) and FR ($p_{adjusted} = 0.008$) as well as between HB and NA in HL ($p_{adjusted} = 0.001$), FL ($p_{adjusted} = 0.003$) and FR ($p_{adjusted} = 0.006$). However, there were no significant differences between FB and HB (HL: $p_{adjusted} = 0.973$; HR: $p_{adjusted} = 0.292$; FL: $p_{adjusted} = 0.536$; FR: $p_{adjusted} = 0.999$).

Initial TT_{20} Performance

Initial average tapping frequency over 20 s (TT_{20}) differed significantly between groups indicating superior TT_{20} performances in FB and HB as compared to NA (see **Figure 2C**). uANOVA revealed a significant main effect of group in HL ($F_{(2,43)} = 13.081$, $p = 0.000$, $\eta_p^2 = 0.378$), HR ($F_{(2,43)} = 9.995$, $p = 0.000$, $\eta_p^2 = 0.317$), FL ($F_{(2,43)} = 15.682$, $p = 0.000$, $\eta_p^2 = 0.422$) and FR ($F_{(2,43)} = 11.426$, $p = 0.000$, $\eta_p^2 = 0.347$). *Post hoc* analyses showed significant differences between FB and NA in HL ($p_{adjusted} = 0.000$), HR ($p_{adjusted} = 0.000$), FL ($p_{adjusted} = 0.000$) and FR ($p_{adjusted} = 0.000$) as well as between HB and NA in HL ($p_{adjusted} = 0.001$), FL ($p_{adjusted} = 0.000$) and FR ($p_{adjusted} = 0.004$). However, there were no significant differences between FB and HB (HL: $p_{adjusted} = 0.988$; HR: $p_{adjusted} = 0.282$; FL: $p_{adjusted} = 0.963$; FR: $p_{adjusted} = 0.815$).

tDCS-Induced Effects on RTT and TT Performance

tDCS-Induced Effects on RTT Performance

Regarding tDCS-induced effects on RTT performance in the upper extremities (see **Figure 3**), rmANOVA revealed a non-significant time × group × condition interaction (HL: $F_{(4,86)} = 0.741$, $p = 0.566$, $\eta_p^2 = 0.033$, BF = 0.077; HR: $F_{(4,86)} = 0.321$, $p = 0.863$, $\eta_p^2 = 0.015$, BF = 0.064). Only factor time showed a significant influence on RTT performance (HL: $F_{(2,86)} = 9.228$, $p = 0.000$, $\eta_p^2 = 0.177$; HR: $F_{(2,86)} = 4.622$, $p = 0.012$, $\eta_p^2 = 0.097$). Moreover, *post hoc* tests revealed a significant influence of factor group in HR directly after tDCS ($F_{(2,43)} = 4.267$, $p_{adjusted} = 0.020$, $\eta_p^2 = 0.166$).

For FL, rmANOVA examined a significant influence of factor group ($F_{(2,43)} = 3.564$, $p = 0.037$, $\eta_p^2 = 0.142$) indicating significant differences between HB and NA ($p_{adjusted} = 0.045$), although

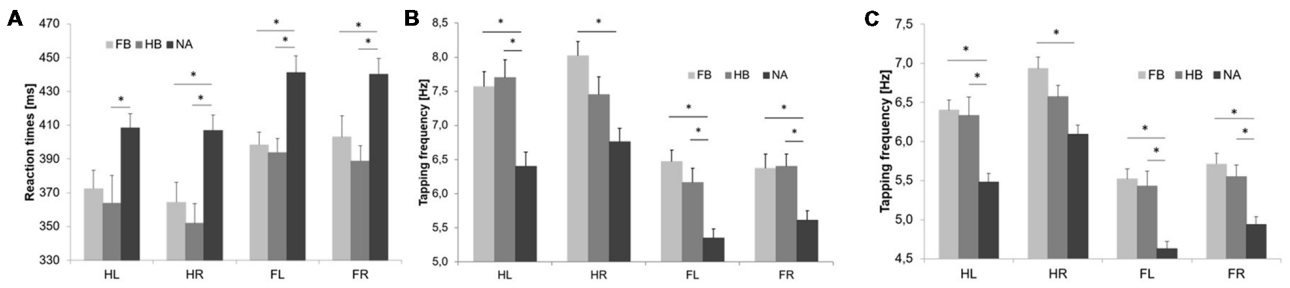

FIGURE 2 | Initial RTT and TT results. Values are mean ± SE of left hand (HL), right hand (HR), left foot (FL) and right foot (FR), respectively. Light gray bars represent football players (FB), medium gray bars represent handball players (HB) and dark gray bars represent non-athletes (NA). *($p < 0.05$) indicates significant differences between groups in their initial performances. Initial simple RTT values **(A)**, TT_{max} values **(B)** and TT_{20} values **(C)** differed significantly between groups indicating superior performances in FB and HB as compared to NA.

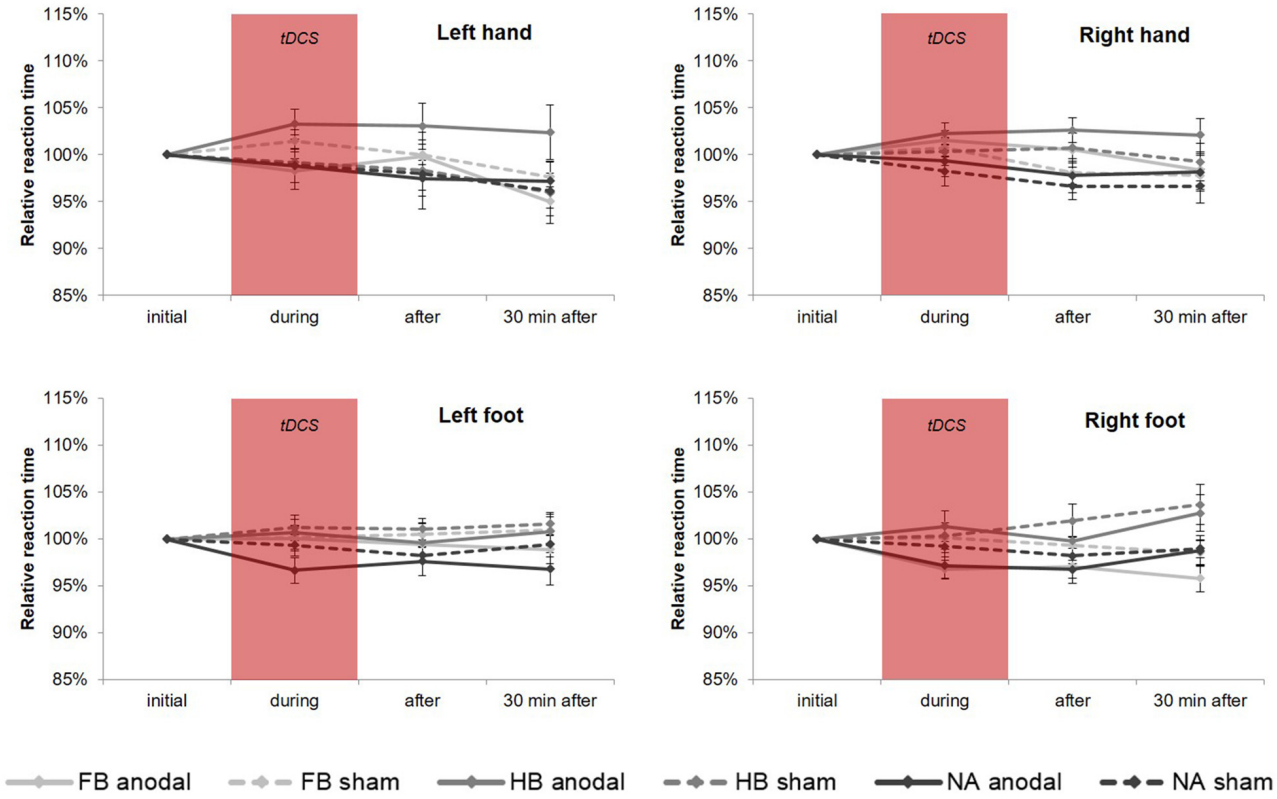

FIGURE 3 | tDCS-induced effects on simple RTT performance. Diagrams include normalized (% of initial values) simple reaction time values (mean ± SE) of left hand (HL), right hand (HR), left foot (FL) and right foot (FR), respectively for before (initial), during, after as well as 30 min after a 20-min tDCS which is indicated by the red box. Light gray lines represent football players (FB), medium gray lines represent handball players (HB) and dark gray lines represent non-athletes (NA). The solid lines define values for anodal tDCS and the corresponding dashed lines indicate values for sham tDCS.

there was no significant time × group × condition interaction ($F_{(3.311,71.190)}$ = 0.788, p = 0.516, η_p^2 = 0.035, BF = 0.078). For FR, results showed a significant time × group interaction ($F_{(4,86)}$ = 2.504, p = 0.048, η_p^2 = 0.104) and a significant influence of factor group ($F_{(2,43)}$ = 4.434, p = 0.018, η_p^2 = 0.171) indicating differences between FB vs. HB ($p_{adjusted}$ = 0.037) and HB vs. NA ($p_{adjusted}$ = 0.029). The highest influence of factor group has been found 30 min after tDCS ($p_{adjusted}$ = 0.001). However, there was no significant influence of tDCS condition (time × group × condition: $F_{(4,86)}$ = 1.061, p = 0.381, η_p^2 = 0.047, BF = 0.088). On a group level, RTT performance in FB differed significantly between anodal and sham ($p_{adjusted}$ = 0.022) indicating a tDCS-induced RTT performance gain of 3.21%.

tDCS-Induced Effects on TT_{max} Performance

rmANOVA revealed no significant time × group × condition interaction for TT_{max} performance (see **Figure 4**), neither in upper (HL: $F_{(3.272,70.351)}$ = 1.114, p = 0.352, η_p^2 = 0.049, BF = 0.091; HR: $F_{(4,86)}$ = 1.485, p = 0.214, η_p^2 = 0.065, BF = 0.123) nor in lower extremities (FL: $F_{(3.334,71.682)}$ = 2.039, p = 0.110, η_p^2 = 0.087, BF = 0.153; FR: $F_{(3.009,64.689)}$ = 1.553, p = 0.209, η_p^2 = 0.067, BF = 0.210). The same applies to all *post hoc* tests, which also showed no significant results.

tDCS-Induced Effects on TT_{20} Performance

Regarding the upper extremities, rmANOVA revealed a non-significant time × group × condition interaction for TT_{20} performance (see **Figure 5**) in HL ($F_{(4,86)}$ = 0.672, p = 0.613, η_p^2 = 0.030, BF = 0.070) and HR ($F_{(4,86)}$ = 0.945, p = 0.442, η_p^2 = 0.042, BF = 0.095). However, findings in HL showed a significant time × condition interaction ($F_{(2,86)}$ = 4.540, p = 0.013, η_p^2 = 0.095) indicating a significant influence of tDCS condition directly after stimulation (*post hoc* test: $p_{adjusted}$ = 0.011). Moreover, subsequent comparisons on group level for HL revealed a significant difference between anodal and sham condition in FB ($p_{adjusted}$ = 0.033) indicating a tDCS-induced performance gain of 4.06% in TT_{20}.

However, regarding the lower extremities, TT_{20} findings showed no significant results (see also **Figure 5**) neither in rmANOVA (FL: $F_{(3.090,66.440)}$ = 1.019, p = 0.392, η_p^2 = 0.045, BF = 0.097; FR: $F_{(3.239,69.633)}$ = 1.061, p = 0.375, η_p^2 = 0.047, BF = 0.120) nor in all *post hoc* tests.

DISCUSSION

The present study aimed to investigate whether 20 min of anodal tDCS over the leg area of the M1 is capable to affect motor

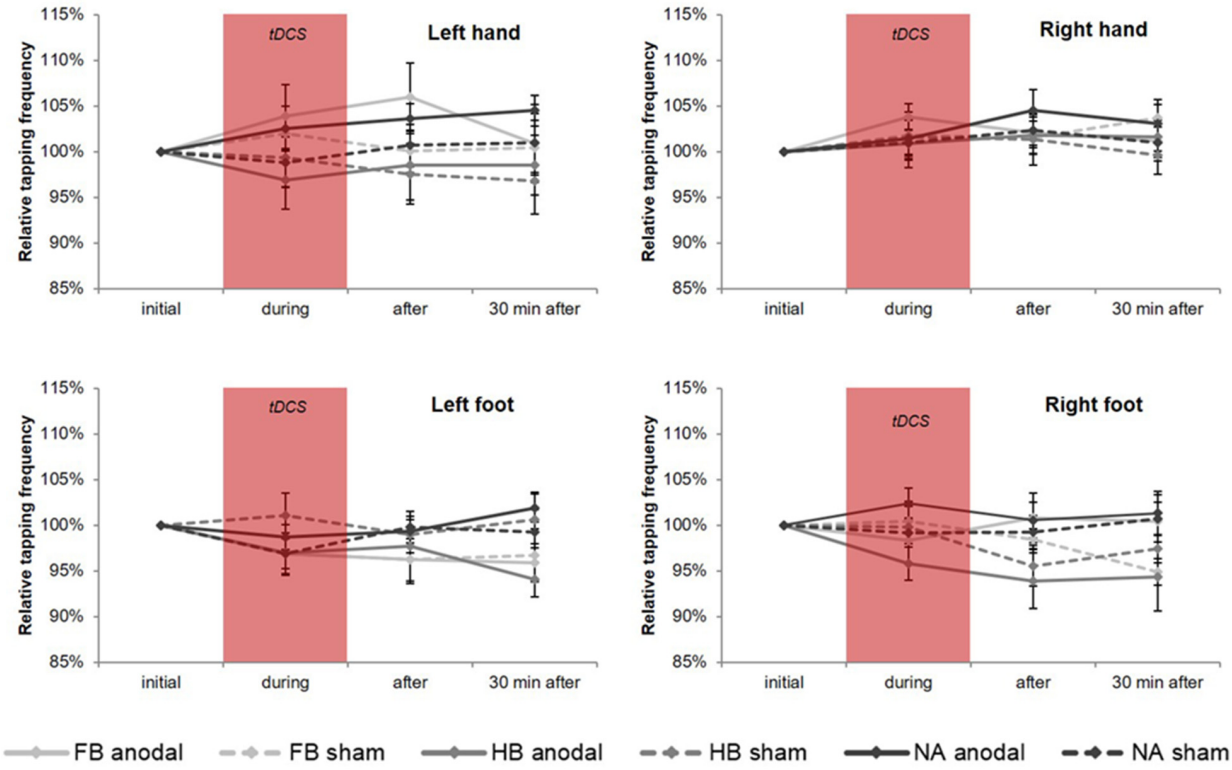

FIGURE 4 | tDCS-induced effects on maximum tapping frequency (TT_{max}). Diagrams include normalized (% of initial values) TT_{max} values (mean ± SE) of left hand (HL), right hand (HR), left foot (FL) and right foot (FR), respectively for before (initial), during, after as well as 30 min after a 20-min tDCS which is indicated by the red box. Light gray lines represent football players (FB), medium gray lines represent handball players (HB) and dark gray lines represent non-athletes (NA). The solid lines define values for anodal tDCS and the corresponding dashed lines indicate values for sham tDCS.

performance in a simple reaction time (RTT) and tapping task (TT) for both upper and lower extremities. Here, trained athletes of different sports disciplines [football players (FB) and handball players (HB)] were tested to investigate possible tDCS-induced behavioral gains using speed-related motor tasks. The study focused on the question of whether athletes would differ in their behavioral response to tDCS compared to non-athletes (NA) and if sport-specific differences could be determined. In line with previous findings, we revealed no differences between anodal and sham tDCS conditions neither on RTT (Tanaka et al., 2009; Stagg et al., 2011; Horvath et al., 2016) nor on TT (Boehringer et al., 2013) performance. Thus, our results indicate that the application of tDCS over M1 leg area did not elicit performance enhancement neither in athletes nor in NA. Future studies can use this knowledge to identify valid and suitable conditions that could lead to tDCS-induced performance gains on speed-related motor tasks with regard to different sports and other responsible brain regions such as cerebellum.

Superior Initial Performances in Athletes Compared to Non-athletes

We hypothesized that athletes would show better RTT and TT performances as compared to NA which was confirmed in both tasks. As well known, physical training has a positive effect on both reaction time (Davranche et al., 2006) and speed (Little and Williams, 2005). Since FB and HB usually integrate speed-related tasks for upper and lower extremities into their practice routine, it is reasonable to assume that this translates into superior performance in RTT and TT compared to performance of NA. Even an acute short-term physical exercise is capable to improve motor time in a simple and choice RTT as it has been shown by Davranche et al. (2006) and Kashihara and Nakahara (2005). Furthermore, it has been reported by several studies that the dynamic visual acuity of athletes was superior to that of NA (Ishigaki and Miyao, 1993) and that athletes were faster in RTTs than NA (Yandell and Spirduso, 1981; Ando et al., 2001; Akarsu et al., 2009; Atan and Akyol, 2014; Kuan et al., 2018). These findings can be explained by the fact that hand-eye coordination plays an important role especially in sports that require high motor hand skills such as team sports and racket sports (Paul et al., 2011; Laby et al., 2018). Moreover, this is also reasonable for sports depending on high motor foot skills such as football. In a recent study by Atan and Akyol (2014), a large number of athletes from different sports branches (football, basketball, judo, track and field, taekwondo) performed a simple RTT of left and right hand in comparison to NA. As a conclusion they found that NA's reaction time parameters were worse than the most branch athletes. In addition to that, reaction time parameters of athletes did not differ between sports branches (except judokas) which could be confirmed by the present study.

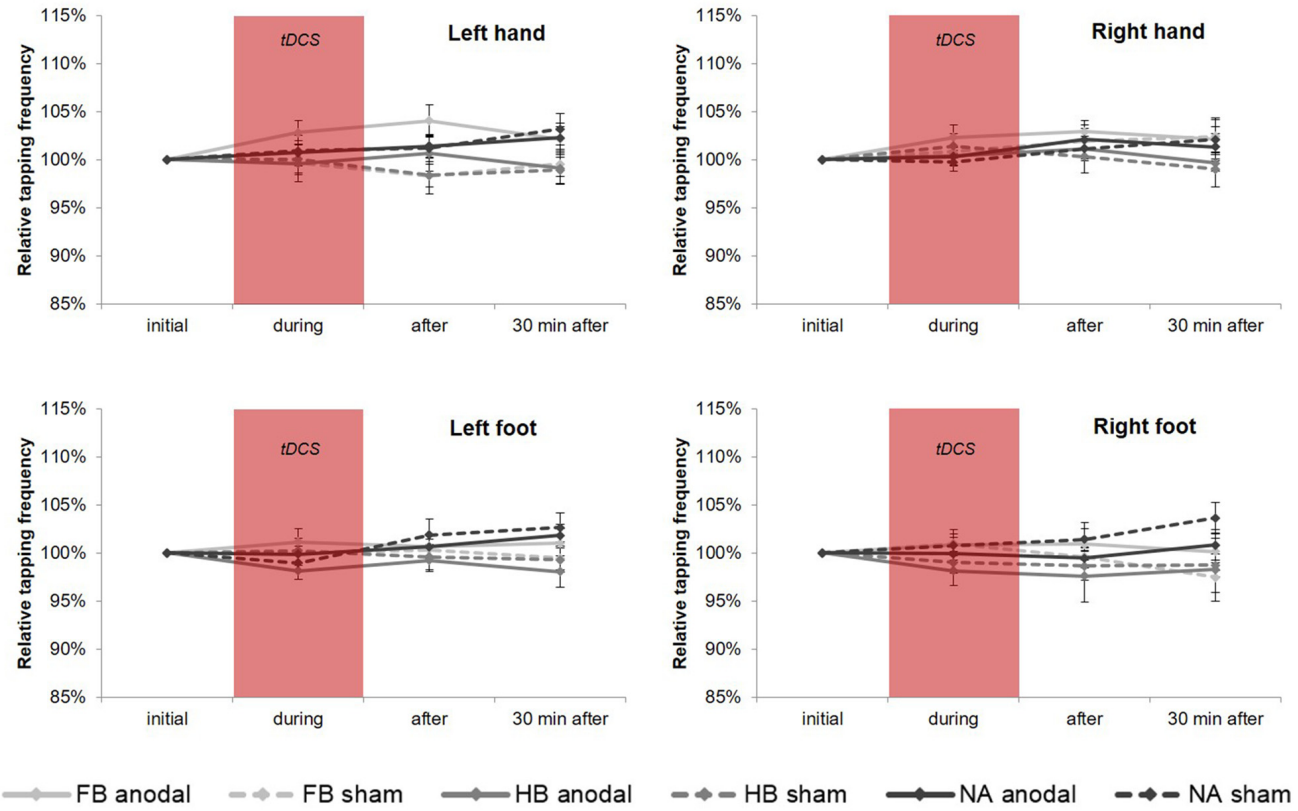

FIGURE 5 | tDCS-induced effects on average tapping frequency over 20 s (TT_{20}). Diagrams include normalized (% of initial values) TT_{20} values (mean ± SE) of left hand (HL), right hand (HR), left foot (FL) and right foot (FR), respectively for before (initial), during, after as well as 30 min after a 20-min tDCS which is indicated by the red box. Light gray lines represent football players (FB), medium gray lines represent handball players (HB) and dark gray lines represent non-athletes (NA). The solid lines define values for anodal tDCS and the corresponding dashed lines indicate values for sham tDCS.

No Effect of tDCS on RTT and TT Performance

We further hypothesized that anodal tDCS over M1 leg area would lead to specific behavioral gains in simple reaction time and tapping performance of the foot as compared to sham condition. Using common tDCS parameters [see "Transcranial Direct Current Stimulation (tDCS)" section for further details], our results showed no effect of anodal tDCS on RTT and TT performance neither as online gains nor offline.

Concerning RTT results, our findings go in line with a previous study by Tanaka et al. (2009). In this cross-over study, a total number of 10 participants performed hand and foot RTTs before and during as well as 10, 30 and 60 min after anodal, cathodal or sham tDCS, respectively. Stimulation was applied for 10 min over the left leg representation of the right motor cortex with an intensity of 2 mA (for anodal and cathodal condition). The authors stated that the anodal tDCS over the leg motor cortex did not change the leg RTT performance contralateral to the stimulation. From their point of view, that might be due to performance ceiling, task sensitivity or stimulation strength and/or duration. With regard to our results, we could show that even doubling the stimulation duration did not lead to a significant enhancement on the behavioral level. Concerning task sensitivity, some studies suggest that tDCS effects depend upon task-difficulty and individual level of task performance (Kwon et al., 2015; Mizuguchi et al., 2018). Hence, the complexity and sensitivity of simple speed-related motor tasks that were used in the present study might be too low to induce a modulatory tDCS effect on a behavioral level. Using a choice RTT as a more complex task, Drummond et al. (2017) were able to demonstrate enhanced choice reaction times in left and right hand after stimulating M1 for 10 min with an intensity of 1 mA. Furthermore, Hupfeld et al. (2017) provide evidence that a choice RTT is more sensitive to benefit from tDCS.

In contrast, the simple reaction time in hand motor tasks has been reported to be facilitated by anodal tDCS (Hummel and Cohen, 2005; Hummel et al., 2006). Tanaka et al. (2009) assume that, because of low spatial focality of tDCS, anodal tDCS in the previous studies stimulated not only the hand motor cortex but also parts of the premotor cortex. Since this specific brain region is responsible for externally triggered movements (Goldberg, 1985; Wessel et al., 1997; Crosson et al., 2001), it would be reasonable to suppose that RTT performance might be facilitated by tDCS over this area. This clearly elucidates that M1 is only one of several brain regions that is eligible to induce behavioral changes by tDCS in a huge variety of motor

tasks. Several studies show that also the cerebellum might play an important role in speed-related motor tasks. In a study by Martin et al. (2006), magnetoencephalography (MEG) was used to measure brain activity while participants performed a simple RTT. The cerebellar results may reflect a number of possible factors, including a role in timing, response readiness, prediction and attention. This is confirmed by an investigation by Théoret et al. (2001), showing no effect of repetitive TMS (rTMS) of the lateral cerebellum or motor cortex, and sham stimulation, on performance of a paced-finger-tapping task (PFT) but following a 5 min train of 1 Hz rTMS to the medial cerebellum.

Concerning TT performance, we hypothesized to elucidate tDCS-induced effects at least on tapping frequency over 20 s since this task is mainly influenced by neuromuscular fatigue (Arias et al., 2012). There is compelling evidence that neuromuscular fatigue, that is defined as the exercise-dependent decrease in the ability of muscle fibers to generate force, occurs due to both central and peripheral factors (Gandevia, 2001). In a previous study, Cogiamanian et al. (2007) investigated whether tDCS delivered over motor cortex would have any effect on fatigue in normal volunteers assessing the endurance time for a submaximal isometric contraction of left elbow flexors. Their findings indicate that anodal stimulation had effects consistent with a reduction in fatigue in comparison to both no stimulation and cathodal stimulation. According to Banissy and Muggleton (2013), these results lead to the assumption that it is possible to modulate fatigue to a large degree with tDCS stimulation. Contrarily, in our case, neither tapping performance over 20 s nor maximum tapping frequency were influenced by anodal tDCS. Therefore, it is absolutely essential to reveal the underlying neural mechanisms of maximum fast movements and movements that are influenced by neuromuscular fatigue in order to use possible tDCS benefits in any sports training.

Taken together, we showed that tDCS is not capable of evoking enhanced performance in speed-related motor tasks. As argued above, the outcome of tDCS seems to be affected by multiple factors involving task characteristics and individual determinants (Ridding and Ziemann, 2010). Furthermore, little is known about neuronal correlates of RTT and TT performance. Therefore, more research is needed to draw a comprehensive picture on speed-related motor abilities in healthy adults and how non-invasive brain stimulation techniques may interact with such complex coordinative behavior.

tDCS-Effects in Athletes

On an exploratory level, we hypothesized that athletes would show stronger tDCS-induced behavioral gains as compared to NA, and, furthermore, if there are any differential effects between FB and HB. This is based on the assumption that tDCS is capable to broadly modulate brain activity, but, as pointed out by Edwards et al. (2017), it remains to be conclusively determined whether it can improve sports performance at an elite level. Our results indicate that athletes also did not benefit from tDCS stimulation on a behavioral level as did NA. This is partly due to the ceiling effect that may have occurred in RTT and TT, but is also due to the high specificity of the brain of trained athletes. According to the "neural efficiency" hypothesis (Dunst et al., 2014), the athlete's brain works differently when performing a task compared to NA. More precisely, it consumes less neural resources for the same task. Another peculiarity is based on the concept of "homeostatic plasticity" in human subjects, suggesting that homeostatic mechanisms operating across hemispheric boundaries contribute to regulating motor cortical function in the M1 as previously shown by Ragert et al. (2009). In terms of the present study, this means that a high level of performance in a specific task in combination with an external stimulation can lead to a decline in physical performance. Consequently, anodal tDCS over M1 can induce inhibition of cortical excitability or a null effect on a behavioral level in trained athletes.

However, it is not legitimate to claim that tDCS has no effect on trained athletes *per se*. The reviews of Banissy and Muggleton (2013) and Edwards et al. (2017) include a number of studies showing positive tDCS-induced effects on motor abilities like muscle power and endurance in athletes. Nevertheless, Banissy and Muggleton (2013) draw attention to the point that currently much of the evidence supporting this is theoretical, having been obtained from individuals not involved in a high standard of sport. While this does not apply to the present study, the investigation of more homogeneous groups of athletes might also lead to different results. Although the level of FB and HB was high, they differed quite in their individual training history or in their current training effort.

Study Limitations

In the present study, we used anodal tDCS to induce a possible behavioral change in the performance of athletes and NA in speed-related motor tasks. To get a better understanding of the neuronal correlates of RTT and TT performance and potential tDCS effects on neuronal networks, further studies that combine neurophysiological assessments of brain activation with behavioral outcome measures are needed. Our findings indicate that the target region (M1 leg area) seems to be less responsible for RTT and TT performance in the lower extremities. Therefore, in future studies, the role of other key regions such as cerebellum or supplementary motor area (SMA) needs to be further investigated. Even though we did not detect any tDCS-induced effects on RTT and TT performance in our study population, it has been previously shown that tDCS affects other motor abilities in athletes. Additionally, we did not investigate the role of multiple tDCS-sessions on RTT and TT performance and did not test for any long-term effects. It is worth considering that multiple tDCS application sessions may have induced stronger behavioral effects that could be more persistent. Following up on this, future studies should also address the problem of optimal stimulation duration and intensity. Concerning polarity, the chance to obtain a different result using cathodal tDCS over M1 leg area is very little since previous findings suggest that it is more difficult to suppress the excitability of the leg motor cortex with cathodal tDCS than the hand area of the motor cortex (Jeffery et al., 2007). This might be due to the leg motor cortex having fewer inhibitory circuits than the hand motor cortex, or

cathodal current might be less effective in M1 leg area because of the different orientation and position of the leg motor cortex relative to the scalp (Jeffery et al., 2007; Tanaka et al., 2009). However, this study was the first step in understanding the effect of a single tDCS session on the performance in simple speed-related motor tasks in trained athletes. For future studies, it is conceivable that a more sensitive motor task, as well as a homogeneous study group at a high performance level, can nevertheless lead to a positive tDCS-induced effect in athletes.

CONCLUSION

Previous research provides evidence that the application of tDCS is capable to affect the performance in various motor abilities. This is not only true for patients or healthy adults, but also for trained athletes who represent a highly specific group of experts regarding their neuronal adaptions on long-term physical activity. The present study contributes to current approaches to increase sports performance using non-invasive stimulation methods. Our results provide novel quantitative evidence that neither athletes nor NA seems to benefit from a brief period of tDCS application in speed-related motor tasks. However, it is not legitimate to claim that tDCS has no effect on trained athletes *per se*. More knowledge on neuronal processing of RTT and TT performance in trained athletes, the influence of tDCS parameters, and the effect of inter-individual differences are required in order to draw a comprehensive picture of whether tDCS can help to enhance motor abilities on a high performance level.

AUTHOR CONTRIBUTIONS

All experiments were conducted at the Max Planck Institute for Human Cognitive and Brain Sciences Leipzig. OS and PR designed the study and experimental set-up. Participants were recruited and tested by OS. OS analyzed the data. All authors interpreted the data, contributed to the manuscript, reviewed it, approved the final version content and agree to be accountable for all aspects of the work. All persons designated as authors qualify for authorship, and all those who qualified for authorship are listed.

FUNDING

This work was supported by the Max Planck Society.

ACKNOWLEDGMENTS

We acknowledge all participants of this study for their contribution. We also thank Ramona Menger, Christin Ihle, Fabian Piecha, Rouven Kenville, Tom Maudrich, Nobuaki Mizuguchi, Dennis Maudrich and Hartmut Domröse for their organizational and technical support.

REFERENCES

Akarsu, S., Caliskan, E., and Dane, S. (2009). Athletes have faster eye-hand visual reaction times and higher scores on visuospatial intelligence than nonathletes. *Turk. J. Med. Sci.* 39, 871–874.doi: 10.3906/sag-0809-44

Ando, S., Kida, N., and Oda, S. (2001). Central and peripheral visual reaction time of soccer players and nonathletes. *Percept. Mot. Skills* 92, 786–794. doi: 10.2466/pms.92.3.786-794

Angius, L., Mauger, A. R., Hopker, J., Pascual-Leone, A., Santarnecchi, E., and Marcora, S. M. (2018). Bilateral extracephalic transcranial direct current stimulation improves endurance performance in healthy individuals. *Brain Stimul.* 11, 108–117. doi: 10.1016/j.brs.2017.09.017

Aparício, L. V. M., Guarienti, F., Razza, L. B., Carvalho, A. F., Fregni, F., and Brunoni, A. R. (2016). A systematic review on the acceptability and tolerability of transcranial direct current stimulation treatment in neuropsychiatry trials. *Brain Stimul.* 9, 671–681. doi: 10.1016/j.brs.2016.05.004

Arias, P., Robles-García, V., Espinosa, N., Corral, Y., and Cudeiro, J. (2012). Validity of the finger tapping test in Parkinson's disease, elderly and young healthy subjects: is there a role for central fatigue? *Clin. Neurophysiol.* 123, 2034–2041. doi: 10.1016/j.clinph.2012.04.001

Atan, T., and Akyol, P. (2014). Reaction times of different branch athletes and correlation between reaction time parameters. *Proc. Soc. Behav. Sci.* 116, 2886–2889. doi: 10.1016/j.sbspro.2014.01.674

Banissy, M. J., and Muggleton, N. G. (2013). Transcranial direct current stimulation in sports training: potential approaches. *Front. Hum. Neurosci.* 7:129. doi: 10.3389/fnhum.2013.00129

Biel, A. L., and Friedrich, E. V. C. (2018). Why you should report bayes factors in your transcranial brain stimulation studies. *Front. Psychol.* 9:1125. doi: 10.3389/fpsyg.2018.01125

Boehringer, A., Macher, K., Dukart, J., Villringer, A., and Pleger, B. (2013). Cerebellar transcranial direct current stimulation modulates verbal working memory. *Brain Stimul.* 6, 649–653. doi: 10.1016/j.brs.2012.10.001

Boggio, P. S., Castro, L. O., Savagim, E. A., Braite, R., Cruz, V. C., Rocha, R. R., et al. (2006). Enhancement of non-dominant hand motor function by anodal transcranial direct current stimulation. *Neurosci. Lett.* 404, 232–236. doi: 10.1016/j.neulet.2006.05.051

Bolognini, N., Pascual-Leone, A., and Fregni, F. (2009). Using non-invasive brain stimulation to augment motor training-induced plasticity. *J. Neuroeng. Rehabil.* 6:8. doi: 10.1186/1743-0003-6-8

Bullitt, E., Rahman, F. N., Smith, J. K., Kim, E., Zeng, D., Katz, L. M., et al. (2009). The effect of exercise on the cerebral vasculature of healthy aged subjects as visualized by MR angiography. *Am. J. Neuroradiol.* 30, 1857–1863. doi: 10.3174/ajnr.a1695

Carlsen, A. N., Eagles, J. S., and MacKinnon, C. D. (2015). Transcranial direct current stimulation over the supplementary motor area modulates the preparatory activation level in the human motor system. *Behav. Brain Res.* 279, 68–75. doi: 10.1016/j.bbr.2014.11.009

Cogiamanian, F., Marceglia, S., Ardolino, G., Barbieri, S., and Priori, A. (2007). Improved isometric force endurance after transcranial direct current stimulation over the human motor cortical areas. *Eur. J. Neurosci.* 26, 242–249. doi: 10.1111/j.1460-9568.2007.05633.x

Colcombe, S. J., Erickson, K. I., Scalf, P. E., Kim, J. S., Prakash, R., McAuley, E., et al. (2006). Aerobic exercise training increases brain volume in aging humans. *J. Gerontol. A Biol. Sci. Med. Sci.* 61, 1166–1170. doi: 10.1093/gerona/61.11.1166

Colzato, L. S., Nitsche, M. A., and Kibele, A. (2017). Noninvasive brain stimulation and neural entrainment enhance athletic performance—a review. *J. Cogn. Enhanc.* 1, 73–79. doi: 10.1007/s41465-016-0003-2

Crosson, B., Sadek, J. R., Maron, L., Gökçay, D., Mohr, C. M., Auerbach, E. J., et al. (2001). Relative shift in activity from medial to lateral frontal cortex during internally versus externally guided word generation. *J. Cogn. Neurosci.* 13, 272–283. doi: 10.1162/089892901564225

Davis, N. J. (2013). Neurodoping: brain stimulation as a performance-enhancing measure. *Sports Med.* 43, 649–653. doi: 10.1007/s40279-013-0027-z

Davranche, K., Burle, B., Audiffren, M., and Hasbroucq, T. (2006). Physical exercise facilitates motor processes in simple reaction time performance: an electromyographic analysis. *Neurosci. Lett.* 396, 54–56. doi: 10.1016/j.neulet.2005.11.008

Devanathan, D., and Madhavan, S. (2016). Effects of anodal tDCS of the lower limb M1 on ankle reaction time in young adults. *Exp. Brain Res.* 234, 377–385. doi: 10.1007/s00221-015-4470-y

Dienes, Z. (2011). Bayesian versus orthodox statistics: which side are you on? *Perspect. Psychol. Sci.* 6, 274–290. doi: 10.1177/1745691611406920

Drummond, N. M., Hayduk-Costa, G., Leguerrier, A., and Carlsen, A. N. (2017). Effector-independent reduction in choice reaction time following bi-hemispheric transcranial direct current stimulation over motor cortex. *PLoS One* 12:e0172714. doi: 10.1371/journal.pone.0172714

Dunst, B., Benedek, M., Jauk, E., Bergner, S., Koschutnig, K., Sommer, M., et al. (2014). Neural efficiency as a function of task demands. *Intelligence* 42, 22–30. doi: 10.1016/j.intell.2013.09.005

Dutta, A., Chugh, S., Banerjee, A., and Dutta, A. (2014). Point-of-care-testing of standing posture with Wii balance board and Microsoft Kinect during transcranial direct current stimulation: a feasibility study. *NeuroRehabilitation* 34, 789–798. doi: 10.3233/NRE-141077

Edwards, D. J., Cortes, M., Wortman-Jutt, S., Putrino, D., Bikson, M., Thickbroom, G., et al. (2017). Transcranial direct current stimulation and sports performance. *Front. Hum. Neurosci.* 11:243. doi: 10.3389/fnhum.2017.00243

Erickson, K. I., Weinstein, A. M., Sutton, B. P., Prakash, R. S., Voss, M. W., Chaddock, L., et al. (2012). Beyond vascularization: aerobic fitness is associated with N-acetylaspartate and working memory. *Brain Behav.* 2, 32–41. doi: 10.1002/brb3.30

Flöel, A. (2014). tDCS-enhanced motor and cognitive function in neurological diseases. *Neuroimage* 85, 934–947. doi: 10.1016/j.neuroimage.2013.05.098

Furuya, S., Nitsche, M. A., Paulus, W., and Altenmüller, E. (2013). Early optimization in finger dexterity of skilled pianists: implication of transcranial stimulation. *BMC Neurosci.* 14:35. doi: 10.1186/1471-2202-14-35

Gandevia, S. C. (2001). Spinal and supraspinal factors in human muscle fatigue. *Physiol. Rev.* 81, 1725–1789. doi: 10.1152/physrev.2001.81.4.1725

Gandiga, P. C., Hummel, F. C., and Cohen, L. G. (2006). Transcranial DC stimulation (tDCS): a tool for double-blind sham-controlled clinical studies in brain stimulation. *Clin. Neurophysiol.* 117, 845–850. doi: 10.1016/j.clinph.2005.12.003

Geiger, A., Cleeremans, A., Bente, G., and Vogeley, K. (2018). Social cues alter implicit motor learning in a serial reaction time task. *Front. Hum. Neurosci.* 12:197. doi: 10.3389/fnhum.2018.00197

Goldberg, G. (1985). Supplementary motor area structure and function: review and hypotheses. *Behav. Brain Sci.* 8:567. doi: 10.1017/s0140525x00045167

Hazime, F. A., da Cunha, R. A., Soliaman, R. R., Romancini, A. C. B., Pochini, A. D. C., Ejnisman, B., et al. (2017). Anodal transcranial direct current stimulation (TDCS) increases isometric strength of shoulder rotators muscles in handball players. *Int. J. Sports Phys. Ther.* 12, 402–407.

Horvath, J. C., Carter, O., and Forte, J. D. (2016). No significant effect of transcranial direct current stimulation (tDCS) found on simple motor reaction time comparing 15 different simulation protocols. *Neuropsychologia* 91, 544–552. doi: 10.1016/j.neuropsychologia.2016.09.017

Hummel, F., and Cohen, L. G. (2005). Improvement of motor function with noninvasive cortical stimulation in a patient with chronic stroke. *Neurorehabil. Neural Repair* 19, 14–19. doi: 10.1177/1545968304272698

Hummel, F. C., Voller, B., Celnik, P., Floel, A., Giraux, P., Gerloff, C., et al. (2006). Effects of brain polarization on reaction times and pinch force in chronic stroke. *BMC Neurosci.* 7:73. doi: 10.1186/1471-2202-7-73

Hupfeld, K. E., Ketcham, C. J., and Schneider, H. D. (2017). Transcranial direct current stimulation (tDCS) to the supplementary motor area (SMA) influences performance on motor tasks. *Exp. Brain Res.* 235, 851–859. doi: 10.1007/s00221-016-4848-5

Ishigaki, H., and Miyao, M. (1993). Differences in dynamic visual acuity between athletes and nonathletes. *Percept. Mot. Skills* 77, 835–839. doi: 10.2466/pms.1993.77.3.835

Jäncke, L., Koeneke, S., Hoppe, A., Rominger, C., and Hänggi, J. (2009). The architecture of the golfer's brain. *PLoS One* 4:e4785. doi: 10.1371/journal.pone.0004785

Jeffery, D. T., Norton, J. A., Roy, F. D., and Gorassini, M. A. (2007). Effects of transcranial direct current stimulation on the excitability of the leg motor cortex. *Exp. Brain Res.* 182, 281–287. doi: 10.1007/s00221-007-1093-y

Jeffreys, H. (1961). *The Theory of Probability*, 3rd ed. *Oxford Classic Texts in the Physical Sciences* Oxford: Oxford University Press.

Jurcak, V., Tsuzuki, D., and Dan, I. (2007). 10/20, 10/10, and 10/5 systems revisited: their validity as relative head-surface-based positioning systems. *Neuroimage* 34, 1600–1611. doi: 10.1016/j.neuroimage.2006.09.024

Kaminski, E., Steele, C. J., Hoff, M., Gundlach, C., Rjosk, V., Sehm, B., et al. (2016). Transcranial direct current stimulation (tDCS) over primary motor cortex leg area promotes dynamic balance task performance. *Clin. Neurophysiol.* 127, 2455–2462. doi: 10.1016/j.clinph.2016.03.018

Kashihara, K., and Nakahara, Y. (2005). Short-term effect of physical exercise at lactate threshold on choice reaction time. *Percept. Mot. Skills* 100, 275–291. doi: 10.2466/pms.100.2.275-291

Kruschke, J. K. (2011). Bayesian assessment of null values via parameter estimation and model comparison. *Perspect. Psychol. Sci.* 6, 299–312. doi: 10.1177/1745691611406925

Kuan, Y. M., Zuhairi, N. A., Manan, F. A., Knight, V. F., and Omar, R. (2018). Visual reaction time and visual anticipation time between athletes and non-athletes. *Malaysian J. Public Health Med.*, 1, 135–141.

Kwon, Y. H., Kang, K. W., Son, S. M., and Lee, N. K. (2015). Is effect of transcranial direct current stimulation on visuomotor coordination dependent on task difficulty? *Neural Regen. Res.* 10, 463–466. doi: 10.4103/1673-5374.153697

Laby, D. M., Kirschen, D. G., Govindarajulu, U., and DeLand, P. (2018). The hand-eye coordination of professional baseball players: the relationship to batting. *Optom. Vis. Sci.* 95, 557–567. doi: 10.1097/opx.0000000000001239

Laczó, B., Antal, A., Rothkegel, H., and Paulus, W. (2014). Increasing human leg motor cortex excitability by transcranial high frequency random noise stimulation. *Restor. Neurol. Neurosci.* 32, 403–410. doi: 10.3233/RNN-130367

Larsson, B., Månsson, B., Karlberg, C., Syvertsson, P., Elert, J., and Gerdle, B. (1999). Reproducibility of surface EMG variables and peak torque during three sets of ten dynamic contractions. *J. Electromyogr. Kinesiol.* 9, 351–357. doi: 10.1016/s1050-6411(99)00006-1

Lattari, E., Campos, C., Lamego, M. K., Passos de Souza, S. L., Neto, G. M., Rocha, N. B., et al. (2017a). Can transcranial direct current stimulation improve muscle power in individuals with advanced resistance training experience? *J. Strength Cond. Res.* doi: 10.1519/jsc.0000000000001956 [Epub ahead of print].

Lattari, E., Costa, S. S., Campos, C., de Oliveira, A. J., Machado, S., and Maranhao Neto, G. A. (2017b). Can transcranial direct current stimulation on the dorsolateral prefrontal cortex improves balance and functional mobility in Parkinson's disease? *Neurosci. Lett.* 636, 165–169. doi: 10.1016/j.neulet.2016.11.019

Lee, M. D., and Wagenmakers, E.-J. (2013). *Bayesian Cognitive Modeling: A Practical Course*. New York, NY: Cambridge University Press.

Levasseur-Moreau, J., Brunelin, J., and Fecteau, S. (2013). Non-invasive brain stimulation can induce paradoxical facilitation. Are these neuroenhancements transferable and meaningful to security services? *Front. Hum. Neurosci.* 7:449. doi: 10.3389/fnhum.2013.00449

Little, T., and Williams, A. G. (2005). Specificity of acceleration, maximum speed, and agility in professional soccer players. *J. Strength Cond. Res.* 19, 76–78. doi: 10.1519/00124278-200502000-00013

Lulic, T., El-Sayes, J., Fassett, H. J., and Nelson, A. J. (2017). Physical activity levels determine exercise-induced changes in brain excitability. *PLoS One* 12:e0173672. doi: 10.1371/journal.pone.0173672

Machado, D. G. D. S., Unal, G., Andrade, S. M., Moreira, A., Altimari, L. R., Brunoni, A. R., et al. (2018). Effect of transcranial direct current stimulation on exercise performance: a systematic review and meta-analysis. *Brain Stimul.* doi: 10.1016/j.brs.2018.12.227 [Epub ahead of print].

Madhavan, S., and Stinear, J. W. (2010). Focal and bi-directional modulation of lower limb motor cortex using anodal transcranial direct current stimulation. *Brain Stimul.* 3:42. doi: 10.1016/j.brs.2009.06.005

Marsman, M., and Wagenmakers, E.-J. (2017). Bayesian benefits with JASP. *Eur. J. Dev. Psychol.* 14, 545–555. doi: 10.1080/17405629.2016.1259614

Martin, T., Houck, J. M., Bish, J. P., Kicić, D., Woodruff, C. C., Moses, S. N., et al. (2006). MEG reveals different contributions of somatomotor cortex and cerebellum to simple reaction time after temporally structured cues. *Hum. Brain Mapp.* 27, 552–561. doi: 10.1002/hbm.20200

Meier, J., Topka, M. S., and Hänggi, J. (2016). Differences in cortical representation and structural connectivity of hands and feet between professional handball players and ballet dancers. *Neural Plast.* 2016:6817397. doi: 10.1155/2016/6817397

Miles, J. and Shevlin, M. (2000). *Applying Regression and Correlation: A Guide for Students and Researchers*. London, UK; CA, USA; New Delhi, India: Sage publications Ltd.

Mizuguchi, N., Katayama, T., and Kanosue, K. (2018). The effect of cerebellar transcranial direct current stimulation on a throwing task depends on individual level of task performance. *Neuroscience* 371, 119–125. doi: 10.1016/j.neuroscience.2017.11.048

Nitsche, M. A., Liebetanz, D., Lang, N., Antal, A., Tergau, F., and Paulus, W. (2003a). Safety criteria for transcranial direct current stimulation (tDCS) in humans. *Clin. Neurophysiol.* 114, 2220–2222; author reply 2222–2223. doi: 10.1016/s1388-2457(03)00235-9

Nitsche, M. A., Schauenburg, A., Lang, N., Liebetanz, D., Exner, C., Paulus, W., et al. (2003b). Facilitation of implicit motor learning by weak transcranial direct current stimulation of the primary motor cortex in the human. *J. Cogn. Neurosci.* 15, 619–626. doi: 10.1162/089892903321662994

Nitsche, M. A., and Paulus, W. (2000). Excitability changes induced in the human motor cortex by weak transcranial direct current stimulation. *J. Physiol.* 527, 633–639. doi: 10.1111/j.1469-7793.2000.t01-1-00633.x

Okano, A. H., Fontes, E. B., Montenegro, R. A., Farinatti Pde, T. V., Cyrino, E. S., Li, L. M., et al. (2015). Brain stimulation modulates the autonomic nervous system, rating of perceived exertion and performance during maximal exercise. *Br. J. Sports Med.* 49, 1213–1218. doi: 10.1136/bjsports-2012-091658

Oldfield, R. C. (1971). The assessment and analysis of handedness: the Edinburgh inventory. *Neuropsychologia* 9, 97–113. doi: 10.1016/0028-3932(71)90067-4

Pain, M. T. G., and Hibbs, A. (2007). Sprint starts and the minimum auditory reaction time. *J. Sports Sci.* 25, 79–86. doi: 10.1080/02640410600718004

Park, I. S., Lee, K. J., Han, J. W., Lee, N. J., Lee, W. T., Park, K. A., et al. (2009). Experience-dependent plasticity of cerebellar vermis in basketball players. *Cerebellum* 8, 334–339. doi: 10.1007/s12311-009-0100-1

Paul, M., Biswas, S. K., and Sandhu, S. J. (2011). Role of sports vision and eye hand coordination training in performance of table tennis players. *Braz. J. Biomot.* 5, 106–116.

Pesta, D. H., Angadi, S. S., Burtscher, M., and Roberts, C. K. (2013). The effects of caffeine, nicotine, ethanol, and tetrahydrocannabinol on exercise performance. *Nutr. Metab.* 10:71. doi: 10.1186/1743-7075-10-71

Ragert, P., Camus, M., Vandermeeren, Y., Dimyan, M. A., and Cohen, L. G. (2009). Modulation of effects of intermittent theta burst stimulation applied over primary motor cortex (M1) by conditioning stimulation of the opposite M1. *J. Neurophysiol.* 102, 766–773. doi: 10.1152/jn.00274.2009

Reardon, S. (2016). 'Brain doping' may improve athletes' performance. *Nature* 531, 283–284. doi: 10.1038/nature.2016.19534

Ridding, M. C., and Ziemann, U. (2010). Determinants of the induction of cortical plasticity by non-invasive brain stimulation in healthy subjects. *J. Physiol.* 588, 2291–2304. doi: 10.1113/jphysiol.2010.190314

Saimpont, A., Mercier, C., Malouin, F., Guillot, A., Collet, C., Doyon, J., et al. (2016). Anodal transcranial direct current stimulation enhances the effects of motor imagery training in a finger tapping task. *Eur. J. Neurosci.* 43, 113–119. doi: 10.1111/ejn.13122

Salimpour, Y., and Shadmehr, R. (2014). Motor costs and the coordination of the two arms. *J. Neurosci.* 34, 1806–1818. doi: 10.1523/JNEUROSCI.3095-13.2014

Schlaffke, L., Lissek, S., Lenz, M., Brüne, M., Juckel, G., Hinrichs, T., et al. (2014). Sports and brain morphology—a voxel-based morphometry study with endurance athletes and martial artists. *Neuroscience* 259, 35–42. doi: 10.1016/j.neuroscience.2013.11.046

Seidel, O., Carius, D., Kenville, R., and Ragert, P. (2017). Motor learning in a complex balance task and associated neuroplasticity: a comparison between endurance athletes and nonathletes. *J. Neurophysiol.* 118, 1849–1860. doi: 10.1152/jn.00419.2017

Stagg, C. J., Jayaram, G., Pastor, D., Kincses, Z. T., Matthews, P. M., and Johansen-Berg, H. (2011). Polarity and timing-dependent effects of transcranial direct current stimulation in explicit motor learning. *Neuropsychologia* 49, 800–804. doi: 10.1016/j.neuropsychologia.2011.02.009

Stagg, C. J., and Nitsche, M. A. (2011). Physiological basis of transcranial direct current stimulation. *Neuroscientist* 17, 37–53. doi: 10.1177/1073858410386614

Steele, C. J., Bailey, J. A., Zatorre, R. J., and Penhune, V. B. (2013). Early musical training and white-matter plasticity in the corpus callosum: evidence for a sensitive period. *J. Neurosci.* 33, 1282–1290. doi: 10.1523/JNEUROSCI.3578-12.2013

Tanaka, S., Hanakawa, T., Honda, M., and Watanabe, K. (2009). Enhancement of pinch force in the lower leg by anodal transcranial direct current stimulation. *Exp. Brain Res.* 196, 459–465. doi: 10.1007/s00221-009-1863-9

Tecchio, F., Zappasodi, F., Assenza, G., Tombini, M., Vollaro, S., Barbati, G., et al. (2010). Anodal transcranial direct current stimulation enhances procedural consolidation. *J. Neurophysiol.* 104, 1134–1140. doi: 10.1152/jn.00661.2009

Théoret, H., Haque, J., and Pascual-Leone, A. (2001). Increased variability of paced finger tapping accuracy following repetitive magnetic stimulation of the cerebellum in humans. *Neurosci. Lett.* 306, 29–32. doi: 10.1016/s0304-3940(01)01860-2

Vargas, V. Z., Baptista, A. F., Pereira, G. O. C., Pochini, A. C., Ejnisman, B., Santos, M. B., et al. (2018). Modulation of isometric quadriceps strength in soccer players with transcranial direct current stimulation: a crossover study. *J. Strength Cond. Res.* 32, 1336–1341. doi: 10.1519/jsc.0000000000001985

Verburgh, L., Scherder, E. J. A., van Lange, P. A. M., and Oosterlaan, J. (2016). The key to success in elite athletes? Explicit and implicit motor learning in youth elite and non-elite soccer players. *J. Sports Sci.* 34, 1782–1790. doi: 10.1080/02640414.2015.1137344

Verissimo, I. S., Barradas, I. M., Santos, T. T., Miranda, P. C., and Ferreira, H. A. (2016). "Effects of prefrontal anodal transcranial direct current stimulation on working-memory and reaction time," in *2016 38th Annual International Conference of the IEEE Engineering in Medicine and Biology Society (EMBC)*, Orlando, FL: IEEE, 2016, 1790–1793. doi: 10.1109/EMBC.2016.7591065

Vitor-Costa, M., Okuno, N. M., Bortolotti, H., Bertollo, M., Boggio, P. S., Fregni, F., et al. (2015). Improving cycling performance: transcranial direct current stimulation increases time to exhaustion in cycling. *PLoS One* 10:e0144916. doi: 10.1371/journal.pone.0144916

Vollmann, H., Ragert, P., Conde, V., Villringer, A., Classen, J., Witte, O. W., et al. (2014). Instrument specific use-dependent plasticity shapes the anatomical properties of the corpus callosum: a comparison between musicians and non-musicians. *Front. Behav. Neurosci.* 8:245. doi: 10.3389/fnbeh.2014.00245

Voss, M. W., Prakash, R. S., Erickson, K. I., Basak, C., Chaddock, L., Kim, J. S., et al. (2010). Plasticity of brain networks in a randomized intervention trial of exercise training in older adults. *Front. Aging Neurosci.* 2:32. doi: 10.3389/fnagi.2010.00032

Wessel, K., Zeffiro, T., Toro, C., and Hallett, M. (1997). Self-paced versus metronome-paced finger movements. A positron emission tomography study. *J. Neuroimaging.* 7, 145–151. doi: 10.1111/jon199773145

Yandell, K. M., and Spirduso, W. W. (1981). Sex and athletic status as factors in reaction latency and movement time. *Res. Q. Exerc. Sport* 52, 495–504. doi: 10.1080/02701367.1981.10607895

Conflict of Interest Statement: The authors declare that the research was conducted in the absence of any commercial or financial relationships that could be construed as a potential conflict of interest.

frontiers in Human Neuroscience

ORIGINAL RESEARCH
published: 04 June 2019
doi: 10.3389/fnhum.2019.00185

Age, Height, and Sex on Motor Evoked Potentials: Translational Data From a Large Italian Cohort in a Clinical Environment

Mariagiovanna Cantone[1], Giuseppe Lanza[2,3], Luisa Vinciguerra[4], Valentina Puglisi[4], Riccardo Ricceri[5], Francesco Fisicaro[6], Carla Vagli[6], Rita Bella[6], Raffaele Ferri[3], Giovanni Pennisi[2], Vincenzo Di Lazzaro[7] and Manuela Pennisi[8]*

[1] Department of Neurology, Sant'Elia Hospital, ASP Caltanissetta, Caltanissetta, Italy, [2] Department of Surgery and Medical-Surgical Specialties, University of Catania, Catania, Italy, [3] Department of Neurology IC, Oasi Research Institute – IRCCS, Troina, Italy, [4] Department of Neurology and Stroke Unit, IRCCS Centro Neurolesi Bonino Pulejo, Messina, Italy, [5] Department of Internal Medicine, Sant'Anna Hospital, AUSL Reggio Emilia, Castelnovo ne' Monti, Italy, [6] Department of Medical and Surgical Sciences and Advanced Technologies, University of Catania, Catania, Italy, [7] Research Unit of Neurology, Neurophysiology and Neurobiology, Università Campus Bio-Medico, Rome, Italy, [8] Department of Biomedical and Biotechnological Sciences, University of Catania, Catania, Italy

Introduction: Motor evoked potentials (MEPs) to transcranial magnetic stimulation (TMS) are known to be susceptible to several sources of variability. However, conflicting evidences on individual characteristics in relatively small sample sizes have been reported. We investigated the effect of age, height, and sex on MEPs of the motor cortex and spinal roots in a large cohort.

Methods: A total of 587 subjects clinically and neuroradiologically intact were included. MEPs were recorded during mild tonic contraction through a circular coil applied over the "hot spot" of the first dorsal interosseous and tibialis anterior muscles (TAs), bilaterally. Central motor conduction time (CMCT) was estimated as the difference between MEP cortical latency and the peripheral motor conduction time (PMCT) by cervical or lumbar magnetic stimulation. Peak-to-peak MEP amplitude to cortical stimulation and right-to-left difference of each parameter were also measured.

Results: After Bonferroni correction, general linear (multiple) regression analysis showed that both MEP cortical latency and PMCT at four limbs positively correlated with age and height. At lower limbs, an independent effect of sex on the same measures was also observed (with females showing smaller values than males). CMCT correlated with both age (negatively) and height (positively) when analyzed by a single regression; however, with a multiple regression analysis this significance disappeared, due to the correction for the multicollinearity within the dataset.

Conclusion: Physical individual features need to be considered for a more accurate and meaningful MEPs interpretation. Both in clinical practice and in research setting, patients and controls should be matched for age, height, and sex.

Keywords: motor evoked potentials, transcranial magnetic stimulation, physical variables, reference values, central motor conduction time, translational neurophysiology

OPEN ACCESS

Edited by:
Shozo Tobimatsu, Kyushu University, Japan

Reviewed by:
Hideyuki Matsumoto, Mitsui Memorial Hospital, Japan
Yuichiro Shirota, The University of Tokyo Hospital, Japan

****Correspondence:***
Giuseppe Lanza
giuseppe.lanza1@unict.it;
glanza@oasi.en.it

Received: *13 April 2019*
Accepted: *20 May 2019*
Published: *04 June 2019*

Citation:
Cantone M, Lanza G, Vinciguerra L, Puglisi V, Ricceri R, Fisicaro F, Vagli C, Bella R, Ferri R, Pennisi G, Di Lazzaro V and Pennisi M (2019) Age, Height, and Sex on Motor Evoked Potentials: Translational Data From a Large Italian Cohort in a Clinical Environment. Front. Hum. Neurosci. 13:185. doi: 10.3389/fnhum.2019.00185

INTRODUCTION

Transcranial magnetic stimulation is widely employed in daily clinical practice to non-invasively estimate *in vivo* and in real time the excitability of the M1 and the conductivity along the cortico-spinal tract. Moreover, the analysis of MEPs, produced contralaterally to the stimulated cortex, has recently attracting interest also in the assessment of synaptic plasticity and network connectivity, both in normal subjects and in patients with several neuropsychiatric disorders (Bella et al., 2011, 2013, 2016; Pennisi et al., 2015, 2016; Cantone et al., 2017; Lanza et al., 2017a), including systemic diseases involving the CNS (Pennisi et al., 2014; Bella et al., 2015). Briefly, TMS produces a rapid high-intensity pulse which passes unattenuated through the scalp (Hallett, 2007; Rossini and Rossi, 2007). When TMS is applied over M1, the cortex is activated through an electromagnetic induction, the impulses are transmitted along the cortico-spinal tract and peripheral nerves, so that a MEP can be recorded from a skeletal muscle using standard EMG surface electrodes. Translationally, MEPs provide a direct, objective, and painless assessment of the motor system (Hallett, 1996), including the excitability of the excitatory and inhibitory circuits, the integrity of central conduction pathways, and the functioning of transcallosal connections of motor cortices (Lanza et al., 2013).

Differentiating between altered MEP responses resulting from a central or peripheral nerve pathology and concomitantly excluding the sources of variability not related to neural dysfunction, is of paramount importance in clinical practice (Lanza et al., 2017b). Therefore, the reliable identification of normal or abnormal MEPs requires a comprehensive characterization in appropriate populations. Based on previous studies, some physical variables (i.e., age, height, and sex) all showed to affect MEPs (Chu, 1989; Booth et al., 1991; Ghezzi et al., 1991; Furby et al., 1992; van der Kamp et al., 1996; Mills and Nithi, 1997), although the samples studied are relatively small and conflicting evidences on the relationship between MEPs and individual characteristics have been reported. Additionally, most studies concentrated on the 20–50 years age range, and no conclusive description of reference values of upper and lower limb over different ranges of age (especially in older adults (Matamala et al., 2013) in a substantial sample of male and female subjects is available. Finally, several technical and procedural factors (such as the characteristics of the stimulator, the coil design, and other experimental conditions) make it difficult to obtain normative data and to compare those established by different laboratories.

To date, the relationship between MEPs and source of variability is not fully understood. If, in the same laboratory and under the same experimental conditions, a relationship between physical variables and MEPs is found, then, accounting for these factors through proper scaling of MEP parameters would allow for a more accurate recording and meaningful interpretation. Till now, however, no previously published study has systematically addressed these variables at the same time together. Correlating MEP cortical latencies with CMCT and height was suggested as an approach for standardizing MEPs response (Booth et al., 1991), although normal values and age- or height-adjusted latencies were not reported. About the influence that gender might have on conduction velocity, MEPs cortical latencies were found to be longer in males than in females (Mills and Nithi, 1997), albeit the possible confounding effect of height (in terms of longer conduction pathway in males) was not adequately addressed. Therefore, a systematic investigation of the effect of height on MEP cortical latency and CMCT between sexes and across different age groups is also warranted.

In the present study, diagnostic TMS data from a large cohort of subjects clinically and neuroradiologically intact are provided. Then, we assessed the relationship between MEPs and some physical variables (age, height, and sex) in order to identify the factors that are likely to affect motor responses. Given the physiological age-related slowing of the conduction velocity and the different length-dependent velocities between upper and lower limb, we hypothesized that both age and height would positively correlate with MEP cortical latency and PMCT. For the same reasons, we also expected a negative correlation between MEPs amplitudes and age, especially for lower limbs. When subjects' height is considered, we hypothesized that the adjusted latencies should demonstrate minimal interindividual variability.

MATERIALS AND METHODS

Participants

A total of 587 consecutive subjects ranging from 18 to 87 years in age (41.1% males) and from 145 to 197 cm in height were retrospectively included from the TMS Lab of the University of Catania (Italy), from March 2008 to November 2018. According to the inclusion criteria, none of them had motor deficit or history of central and peripheral motor or neuromuscular disorder based on a preliminary interview, a specific medical questionnaire, and a full neurological examination. All subjects had normal mobility and were able to engage in tasks of daily life without assistance, even the most elderly. Any CNS pathology was also ruled out by brain and spinal magnetic resonance imaging. Therefore, all participants eventually included were neurologically intact.

Based on previous TMS studies (Livingston et al., 2010, 2013; Matamala et al., 2013; Cueva et al., 2016), subjects were excluded if they had: history or presence of epilepsy, moderate-to-severe traumatic head injury, previous cranial or spinal surgery, stroke or chronic cerebrovascular diseases, chronic pain syndrome, peripheral neuropathies or other neurological or neuromuscular disorders; current or previous psychiatric diseases; any acute, advanced, or chronic not compensated medical illness (including diabetes, hypothyroidism, and neoplasm); alcohol or drug abuse; implanted electrical biomedical devices (i.e., pacemaker), pregnancy at the time of testing, or any other contraindication to TMS (Rossi et al., 2009); current treatment with neuroactive drugs or any other medication able to affect cortical excitability

Abbreviations: CCCT, cortico-conus motor conduction time; CMCT, central motor conduction time; CNS, central nervous system; EMG, electromyography; F, female; FDI, first dorsal interosseous muscle; M, male; M1, primary motor cortex; MEPs, motor evoked potentials; n, number of subjects; PMCT, peripheral motor conduction time; SD, standard deviation; TA, tibialis anterior muscle; TMS, transcranial magnetic stimulation.

(Paulus et al., 2008; Ziemann et al., 2015). Out of 587, 482 were out-patients, mainly referred by general practitioners or other specialists for non-specific clinical complaints in order to rule out the possibility of an underlying neurological condition. The remaining 105 were in-patients admitted because of subjective motor symptoms without clinical, radiological, and neurophysiological correlates.

Height was measured with a cloth tape measure with the subject standing in the anatomical position (barefoot, with heels together, arms at the side, legs straight, shoulders relaxed, and head in the horizontal plane). Measurement was recorded to the nearest 0.1 cm.

This study was carried out in accordance with the recommendations of the guidelines of the International Federation of Clinical Neurophysiology Committee for the diagnostic use of TMS (Ziemann et al., 2015). The protocol was approved by the Ethics Committee of the "Azienda Ospedaliero Universitaria Policlinico-Vittorio Emanuele" of Catania, Italy. All subjects gave written informed consent in accordance with the Declaration of Helsinki of 1964 and its later amendments.

Instrumentations and Technical Considerations

A high-power monopulse biphasic electromagnetic stimulator MagStim 220 (The Magstim Co., Ltd., Whitland, Dyfed, United Kingdom) capable of generating a maximal output of 2.0 Tesla, with a maximum duration of <1 ms and a rise time of 100 μs, was used to evoke motor responses. Magnetic pulse intensity was expressed as a percentage of the maximal stimulator output (100%). The capacitor was connected to a 90 mm circular coil (inner diameter of 5 cm), routinely employed for diagnostic TMS. Since the round coil stimulates a larger cortical volume, the positioning over the target region is easier than with the focal "figure-of-eight" shaped coil. The large round coil also results in a better depth penetration, which is advantageous for TMS of M1 leg area. Finally, the round coil is less susceptible to the unavoidable minimal changes in the coil position (Groppa et al., 2012; Rossini et al., 2015).

Coil was applied with the handle pointing backward and held tangentially flat on the scalp, with its center positioned over Cz (according to the international EEG 10–20 system) for recording from the FDI and over Fz for recording from the TA. For TMS of the right hemisphere, the current direction within the circular coil was clockwise, so that the induced cortical current was perpendicular to the cortex in posterior-anterior direction, and vice versa for the left hemisphere, as recommended (Wassermann et al., 2008). After the location was identified, the coil position was slightly adapted until the best excitation point ("hot spot") was accomplished. Once the position was defined, the outer rim of the coil was marked with a dermographic pen on the scalp to enable the examiner to maintain a constant position.

All motor responses were obtained at 80% of the maximum stimulator output, based on the evidence that threshold stimulation for a 2.0 Tesla magnetic stimulator is about 50–65% of the maximal output (Amassian et al., 1989; Alexeeva et al., 1998; Garry et al., 2004). In such a way, a visible contraction of the target muscle was constantly observed after each stimulation. We also verified that MEP cortical latency did not further shorten and amplitude did not further increase by incrementing the intensity above 80%. This implies that the intensity used was sufficiently high to excite the fast-conducting cortico-spinal neurons (Groppa et al., 2012).

Motor responses were amplified and filtered (bandwidth 3-3,000 Hz) using a 2-channel Medelec Synergy system (Oxford Instruments Medical, Inc., United Kingdom), with an amplification factor of the screen of 1 mV/division unit during the MEP recording. The temporal resolution of the screen (sweep) was 5 ms/division unit, in such a way that the TMS artifact, the beginning and the end of MEP were always clearly visible.

Subject Preparation

A detailed explanation of the exam was preliminarily provided to each subject. In preparation for placement of the recording electrodes and to decrease cutaneous impedances, the skin was gently abraded with fine-grade sandpaper and cleaned with an isopropyl alcohol pad. MEPs were recorded via standard surface EMG silver/silver chloride cup electrodes (9 mm diameter), filled with electrode jelly and applied on FDI and TA contralaterally to the side of stimulation, in a conventional belly tendon montage. For upper limbs, the recording (active) electrode was placed over the mid-point of the FDI belly, the reference electrode distally at the metacarpal-phalangeal joint of the index finger, and the ground electrode on the radial surface of wrist; for lower limbs, the recording (active) electrode was placed over the mid-point of TA belly, the reference electrode 3–4 cm distally over the muscle tendon, and the ground electrode over the patella. The FDI muscle, commonly examined using TMS, was selected because it can be easily contracted and recorded compared to other hand muscles. Based on the fact that evoking MEPs in the lower limbs is usually more difficult than in the upper limbs, we used the TA muscle for a number of reasons: it has a more pronounced representation than most of the other leg muscles; it has a relatively low excitation threshold; its MEPs have a larger amplitude compared to other leg muscles (Petersen et al., 2003); differently from the foot muscles, it is usually not wasted in elderly patients (Claus, 1990). Electrode impedance was constantly kept <10 KOhms, as recommended (Groppa et al., 2012).

Side-to-side difference was also considered, with "right" and "left" referred to the recording side of the target muscle. Trials containing any type of artifact were removed. Similarly, we have excluded trials contaminated by EMG activity at rest (indicating a non-relaxed muscle), as well as the "active" trials (during contraction) with excessive EMG voluntary activity that made a reliable recognition of the onset of MEP cortical latency difficult or doubtful.

All data were collected on a dedicated PC and stored for off-line analysis. Subjects were seated in a comfortable armchair, in a quiet environment, and asked to keep their hands and legs as relaxed as possible. All exams were conducted in the same laboratory and experimental conditions (including room temperature), at the same time of the day (approximately

9:00–11:30 am) and by the same trained operators. All measurements were made by a senior operator (GL) and finally checked and approved by the Lab head (GP).

TMS and Spinal Magnetic Stimulation

First, a reference MEP to TMS in the relaxed muscle was obtained. Then, subjects were asked to produce a small transient tonic contraction of the target muscle (about 10–20% of the subject's maximum voluntary contraction, just enough to overcome gravity), in order to obtain MEPs with higher amplitude and shorter latency compared to the reference response. Contracted MEPs, indeed, are mediated by the large and fast-propagating α-motoneuron pools and reflect a fast-propagating system from the cortex to the muscle (Rossini et al., 2015). Since active contraction potentiates and stabilizes MEPs (Boroojerdi et al., 1999; Sohn and Hallett, 2004), five trials were sufficient to confirm their reproducibility (Rossini and Caramia, 1992). Muscle contraction was kept constant by using a strain gauge and with the help of a continuous auditory and visual EMG activity monitoring, as recommended (Fritz et al., 1997). The acoustic feedback also allowed to monitor the level of muscular activity and to check for complete relaxation (Rossini et al., 2015).

Motor evoked potential cortical latency was calculated as the time interval from the TMS artifact to the first negative deflection of the muscular response from EMG baseline (Rossini et al., 2015). The MEP with the shortest latency was considered for CMCT calculation, according to international guidelines. Similarly, since diagnostic TMS estimates the cortico-motor response with maximal amplitude, only the trial with the largest amplitude was used for MEP size analysis. Amplitude was measured from the maximal negative to maximal positive deflection of the selected MEP (peak-to-peak amplitude) (Groppa et al., 2012). MEP amplitude represents the final pathway of spatial and temporal summation of several descending volleys activating the α-motoneurons, thus reliably reflecting the excitation state of the cortico-spinal cells, the pyramidal tract, the peripheral motor nerve, and the target muscle (Rossini et al., 2015).

Peripheral stimulation of the motor roots was carried out in all subjects to determine PMCT. MEPs to cervical or lumbar stimulation are presumably elicited by a direct ventral root excitation (Mills and Murray, 1986) and have been shown to display similar latencies when either magnetic or electric stimuli are applied (Caramia et al., 1989). In order to stimulate magnetically the spinal roots and facilitate foraminal stimulation, subjects were requested to slightly bend the neck or the trunk forward. The center of the coil was placed posteriorly over the 7th cervical (for upper limbs) and 4th lumbar (for lower limbs) spinous process. In some cases, the coil was slightly shifted laterally to the same side of the target muscle to define the location where maximum responses could be obtained, or slightly moved vertically up and down to determine the most effective level for stimulation. In any case, coil location and orientation were such that the maximal induced current flowed horizontally in the tissue toward the midline from the ipsilateral side of the muscle (Mills et al., 1993). Unlike stimulation of M1, facilitation is not needed for spinal stimulation (Claus, 1990), and, therefore, subjects were recorded at rest. PMCT was calculated as the time interval from the TMS artifact to the first negative spike from EMG baseline. To ensure reliability, two reproducible responses were recorded and averaged (Rossini et al., 2015).

Central motor conduction time was defined as the conduction time from motor cortical neurons to spinal motor neurons, thus reflecting the conductivity along the cortico-spinal tract (from the upper to the lower motor neuron). CMCT was estimated by subtracting the peripheral (cervical or lumbar) PMCT from the shortest MEP cortical latency (Rossini et al., 1985a,b, 1987, 1994; Ugawa et al., 1994): CMCT = MEP cortical latency – PMCT. CMCT is measured with the target muscle active, thereby giving the shortest latency from the cortex to the muscle. In this situation, the spinal motoneuron pool is close to the firing threshold and there is the greatest opportunity for the earliest descending cortico-spinal volley to induce a discharge (Chen et al., 2008).

Statistical Analysis

We first assessed the normality of the distribution of each variable under consideration in the whole group of subjects by mean of the Kolmogorov–Smirnov and the Lilliefors tests for normality. We then checked for possible simultaneous effects of age, height, and sex (independent factors) on the variables under consideration (dependent variables) by means of the General Regression Models module offered by the commercially available software STATISTICA v.6 (2001), StatSoft Inc., (this software was also used for all other statistical tests carried out in this study). For each study variable, three partial correlation coefficients were obtained, one for each independent factor, together with its statistical significance. Because of the large number of partial correlation coefficients obtained, we only considered as being significant the p-values that continued to be <0.05 after the Bonferroni correction (Bland and Altman, 1995). Due to the high number of subjects included, also small correlation values tend to be significant; however, following the Cohen's (Cohen, 1988) indications, we considered correlations 0.10, 0.30, and 0.50 as corresponding to small, medium, and large sizes, respectively, and considered only correlations ≥ 0.30 for further analysis. After this step, we computed descriptive statistics for all variables in the whole group (mean, standard deviation, mean $\pm$ 1.96 SD, and 95% confidence interval). For variables showing a moderate-to-large partial correlation coefficient with age and/or height and/or sex, subgroup specific scatterplots were obtained.

RESULTS

Descriptive Results

Both TMS and spinal root stimulations were well tolerated and no side-effect or significant discomfort was reported during or after the exam. As shown in **Figure 1**, no skewed distribution of age and height was present in the sample. Similarly, in the whole sample of subjects, the difference in height between males and females was not statistically significant, whereas, as expected, there was a decline in the mean height in both sexes

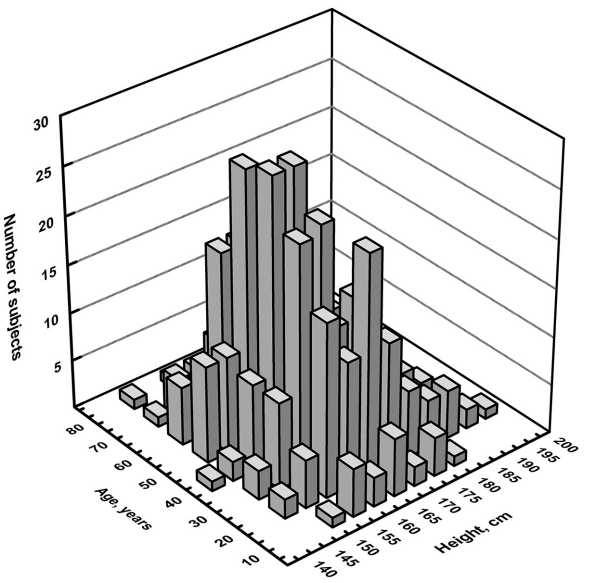

FIGURE 1 | Three-dimensional histogram of the distribution of the number of subjects per age and height.

TABLE 1 | Demographic features of the whole group of participants and of the age subgroups.

		n	Mean	SD
Age ≥ 18 < 35 years	F	91	26.8	4.83
	M	63	25.8	4.86
Age ≥ 35 < 50 years	F	138	41.7	4.05
	M	68	42.2	4.02
Age ≥ 50 < 65 years	F	83	55.8	3.64
	M	71	57.1	4.35
Age ≥ 65 years	F	34	70.6	6.32
	M	39	69.7	4.12
All	F	346	44.0	14.23
	M	241	46.7	16.05
Total		587	45.1	15.05

n, number of subjects; SD, standard deviation; F, female; M, male.

as age increased. In all subjects, motor responses during active contraction of FDI and TA were always obtained and recorded. Although MEPs from the lower limbs were usually more difficult to elicit than those recorded from the hand (Barker et al., 1987), we did not experience significant difficulty.

Table 1 summarizes the demographic features of all participants and the age subgroups. Mean value ± SD and the 95% confidence intervals for each measure, in the whole sample and split by muscle and side, are summarized in **Table 2**. The upper and lower limits were derived by determining the cut-off scores of 1.96 SD above and below the mean value, although these represented unadjusted latencies (not correlated for age, height, and sex). **Table 3** shows descriptive statistics of MEP cortical latency and PMCT computed separately for each age group.

TABLE 2 | Descriptive statistics of all variables studied.

	Mean ± SD	Mean ± 1.96 SD	95% confidence interval
Right FDI			
MEP amplitude, mV	7.9 ± 3.21	1.6/14.2	2.8/15.1
*MEP cortical latency, ms**	19.5 ± 1.45	16.7/22.4	16.9/22.5
*PMCT, ms**	13.6 ± 1.31	11.0/16.2	11.2/16.2
*CMCT, ms**	5.9 ± 0.89	4.2/7.7	4.3/7.6
Left FDI			
MEP amplitude, mV	7.6 ± 3.09	1.6/13.7	3.0/14.6
*MEP cortical latency, ms**	19.4 ± 1.45	16.6/22.2	17.0/22.5
*PMCT, ms**	13.5 ± 1.32	10.9/16.1	11.2/16.0
*CMCT, ms**	5.9 ± 0.87	4.2/7.6	4.2/7.6
Right-Left difference			
MEP amplitude, mV	0.26 ± 2.23	−4.1/4.6	−4.0/4.9
MEP cortical latency, ms	0.12 ± 0.69	−1.2/1.5	−1.3/1.5
PMCT, ms	0.09 ± 0.62	−1.1/1.3	−1.3/1.3
CMCT, ms	0.026 ± 0.75	−1.4/1.5	−1.5/1.5
Right TA			
MEP amplitude, mV	5.5 ± 2.30	1.0/10.0	2.0/10.4
*MEP cortical latency, ms**	26.5 ± 2.21	22.2/30.9	22.7/31.2
*PMCT, ms**	12.7 ± 1.43	9.8/15.5	10.2/15.8
*CMCT, ms**	13.9 ± 1.64	10.7/17.1	10.9/17.1
Left TA			
Amplitude, mV	5.3 ± 2.17	1.1/9.6	1.9/10.0
*MEP cortical latency, ms**	26.5 ± 2.20	22.2/30.8	22.7/31.0
*PMCT, ms**	12.6 ± 1.46	9.7/15.4	10.1/15.9
*CMCT, ms**	13.9 ± 1.69	10.6/17.2	10.8/17.2
Right-Left difference			
MEP amplitude, mV	0.18 ± 2.02	−3.8/4.1	−4.0/4.5
MEP cortical latency, ms	0.07 ± 1.94	−3.7/3.9	−4.4/4.1
PMCT, ms	0.07 ± 1.23	−2.3/2.5	−2.7/2.7
CMCT, ms	0.0002 ± 1.59	−3.1/3.1	−3.5/3.0

Subgroup-specific graphs in **Figures 2–10; SD, standard deviation; FDI, first dorsal interosseous muscle; TA, tibialis anterior muscle; MEP, motor evoked potential; PMCT, peripheral motor conduction time; CMCT, central motor conduction time.*

Correlation Results

The multiple linear regression analysis of the correlation between age, height, and sex, and all the TMS measures is shown in **Table 4**. Subgroup-specific graphs for MEP cortical latency and PMCT at the four limbs are shown in **Figures 2–9**, which illustrate their correlation with height, for each muscle in each age subgroup, further subdivided by sex. **Figure 10** shows the correlation between height and CMCT from right or left FDI and TA in participants, divided by sex.

A small non-significant correlation size was observed between MEP amplitude in the upper limbs and all the physical variables considered. In the lower limbs, a statistically significant correlation, but with a small-to-medium correlation size that did not resist to Bonferroni correction, was observed between MEPs amplitude and sex.

Motor evoked potential cortical latency at the four limbs correlated with age (medium-to-large correlation size for the

TABLE 3 | Descriptive statistics of the MEP cortical latency and PMCT values computed separately for each age group.

	Mean	SD	Mean ± 1.96 SD	95% confidence interval
Age ≥ 18 < 35 years				
Right FDI MEP cortical latency, ms	19.2	1.43	16.4/22.0	16.5/21.9
Right FDI PMCT, ms	13.1	1.26	10.6/15.6	10.6/15.9
Left FDI MEP cortical latency, ms	19.1	1.41	16.3/21.8	16.4/22.0
Left FDI PMCT, ms	13.1	1.25	10.6/15.5	10.8/15.8
Right TA MEP cortical latency, ms	26.0	2.41	21.3/30.7	22.4/31.4
Right TA PMCT, ms	12.2	1.38	9.5/14.9	9.9/15.4
Left TA MEP cortical latency, ms	25.9	2.33	21.4/30.5	22.0/30.1
Left TA PMCT, ms	12.1	1.27	9.6/14.6	10.0/14.9
Age ≥ 35 < 50 years				
Right FDI MEP cortical latency, ms	19.5	1.40	16.8/22.2	17.1/22.5
Right FDI PMCT, ms	13.6	1.21	11.2/16.0	11.7/16.2
Left FDI MEP cortical latency, ms	19.3	1.38	16.6/22.0	17.1/22.4
Left FDI PMCT, ms	13.4	1.27	10.9/15.9	11.3/15.9
Right TA MEP cortical latency, ms	26.4	1.95	22.5/30.2	22.9/30.5
Right TA PMCT, ms	12.6	1.38	9.9/15.3	10.4/15.6
Left TA MEP cortical latency, ms	26.4	2.07	22.4/30.5	23.0/31.0
Left TA PMCT, ms	12.7	1.47	9.8/15.6	10.3/15.8
Age ≥ 50 < 65 years				
Right FDI MEP cortical latency, ms	19.7	1.39	17.0/22.4	17.4/22.8
Right FDI PMCT, ms	13.9	1.27	11.4/16.4	11.5/16.2
Left FDI MEP cortical latency, ms	19.6	1.42	16.8/22.4	17.2/22.7
Left FDI PMCT, ms	13.8	1.23	11.4/16.2	11.5/16.0
Right TA MEP cortical latency, ms	27.0	2.26	22.5/31.4	23.0/31.5
Right TA PMCT, ms	12.9	1.46	10.0/15.8	10.2/16.0
Left TA MEP cortical latency, ms	26.7	2.15	22.5/30.9	23.1/31.2
Left TA PMCT, ms	12.8	1.57	9.7/15.8	10.1/16.3
Age ≥ 65 years				
Right FDI MEP cortical latency, ms	20.0	1.59	16.9/23.1	16.9/23.1
Right FDI PMCT, ms	14.2	1.35	11.5/16.8	11.9/17.0
Left FDI MEP cortical latency, ms	19.9	1.56	16.9/23.0	17.0/23.3
Left FDI PMCT, ms	14.2	1.37	11.5/16.8	11.4/16.9
Right TA MEP cortical latency, ms	27.3	2.06	23.2/31.3	22.6/31.3
Right TA PMCT, ms	13.1	1.34	10.5/15.7	10.3/16.3
Left TA MEP cortical latency, ms	27.2	2.13	23.1/31.4	22.7/31.6
Left TA PMCT, ms	12.9	1.30	10.4/15.5	10.1/15.3

*Subgroup-specific graphs for all these parameters in **Figures 2–10**; S.D, standard deviation; FDI, first dorsal interosseous muscle; TA, tibialis anterior muscle; MEP, motor evoked potential; PMCT, peripheral motor conduction time.*

left FDI and right TA; small-to-medium for the other limbs) and height (medium-to-large correlation size for the upper limbs and right TA, small-to-medium for the contralateral side). At the upper limbs, a significant correlation that passed the Bonferroni correction was observed between MEP cortical latency and sex (shorter in women), although with a small-to-medium correlation size. No correlation was evident between MEP cortical latency and sex at the lower limbs.

Peripheral motor conduction time at the four limbs positively correlated with age and height (medium-to-large correlation size for both FDI and right TA; small-to-medium for the contralateral muscle). At the upper limbs, PMCT correlated with sex, being shorter in women (medium-to-large correlation size for the left FDI; small-to-medium for the contralateral muscle), with a statistically significant difference, even after correction, bilaterally. A small non-significant correlation size was found with gender for the lower limbs.

Central motor conduction time correlated with both age and height when analyzed by a single regression. In particular, age negatively correlated (with small correlation coefficients) with CMCT from the upper limbs (right: $r = -0.108$, $p = 0.009$; left: $r = -0.100$, $p = 0.015$); height positively correlated (with small correlation coefficients) with CMCT from the upper limbs (right: $r = 0.110$, $p = 0.008$; left: $r = 0.094$, $p = 0.024$), while the correlation from the lower limbs appeared to be small-to-medium (right: $r = 0.304$, $p < 0.001$; left: $r = 0.173$, $p < 0.001$). However, when analyzed by multiple regression these significances disappeared, due to the correction for the multicollinearity within the dataset.

Regarding the difference between right and left side, a small non-significant correlation size was found for all TMS measures and the physical variables here considered at the four limbs. A statistically significant small-to-medium correlation size was evident for MEP cortical latency at the lower limbs, although it was not confirmed after Bonferroni correction.

DISCUSSION

Main Findings

The main finding of this study is that individual features need to be considered for accurate MEP evaluation and meaningful interpretation. In particular, when reference values of MEP cortical latency and PMCT are used, the correlation with age, height and, to a lesser extent, sex must be taken into consideration. This approach will account for the unwanted variability associated with demographic and physical variables and allows for appropriate and reliable comparisons of MEPs, especially in studies with heterogeneous groups of participants. Accounting for the variability of MEP responses is imperative to demonstrate or confirm a clinical picture possibly due to a central nerve pathology and not to technical artifact, selection bias, or methodological error.

More in detail, we found a positive correlation of age and height with MEP cortical latency at the four limbs, supporting previous studies showing similar results (Booth et al., 1991). One of the underlying mechanisms is probably owing to the fact that age- and length-dependent changes affect the cervical and lumbo-sacral pools of spinal motoneurons differently (Tomlinson and Irving, 1977). Indeed, there is a progressive temporal dispersion of descending impulses with a less synchronized effect on the foot α-motoneurons (Rossini, 1988; Rossini and Caramia, 1988; Rossini et al., 1992). The cervical cord also receives much more cortico-spinal fibers per unit of muscle mass than the lumbo-sacral cord (Rossini, 1988; Rossini and Caramia, 1988; Rossini et al., 1992). Such physiological factors might thus influence the observed changes along the motor pathway. Moreover, MEP cortical latency have been shown to be different in males and

TABLE 4 | General linear (multiple) regression analysis of the correlation between age, height, and sex and all the variables studied.

	Age		Height		Sex	
	partial correlation	***p* < ***	**partial correlation**	***p* < ***	**partial correlation**	***p* < ***
Right FDI						
MEP amplitude, mV	−0.112		0.060		−0.069	
*MEP cortical latency, ms**	0.284	0.000001	**0.394**	0.000001	−0.212	0.000012
*PMCT, ms**	**0.383**	0.000001	**0.381**	0.000001	−0.281	0.000001
CMCT, ms	−0.075		0.099		0.044	
Left FDI						
MEP amplitude, mV	−0.129		0.073		−0.099	
*MEP cortical latency, ms**	**0.301**	0.000001	**0.415**	0.000001	−0.243	0.000001
*PMCT, ms**	**0.397**	0.000001	**0.405**	0.000001	**−0.324**	0.000001
CMCT, ms	−0.068		0.092		0.052	
Right-Left difference						
MEP amplitude, mV	0.015		−0.014		0.037	
MEP cortical latency, ms	−0.015		−0.018		0.041	
PMCT, ms	−0.004		−0.024		0.058	
CMCT, ms	−0.010		0.010		−0.008	
Right TA						
MEP amplitude, mV	−0.089		−0.086		−0.220	0.000004
*MEP cortical latency, ms**	**0.317**	0.000001	**0.433**	0.000001	−0.097	
*PMCT, ms**	**0.323**	0.000001	**0.404**	0.000001	−0.023	
CMCT, ms	0.119		0.206	0.000025	−0.094	
Left TA						
MEP amplitude, mV	−0.010		−0.038		−0.153	0.0095
*MEP cortical latency, ms**	0.231	0.0000008	0.265	0.000001	−0.062	
*PMCT, ms**	0.253	0.000001	0.274	0.000001	0.002	
CMCT, ms	0.075		0.101		−0.077	
Right-Left difference						
MEP amplitude, mV	−0.088		−0.055		−0.084	
MEP cortical latency, ms	0.063		0.159	0.00012	−0.026	
PMCT, ms	0.048		0.121		−0.025	
CMCT, ms	0.038		0.098		−0.011	

*Correlations with medium-to-large size (≥0.30) are indicated in bold lettering. *, Significant after bonferroni correction (non-significant p-values are not shown); FDI, first dorsal interosseous muscle; TA, tibialis anterior muscle; MEP, motor evoked potential; PMCT, peripheral motor conduction time; CMCT, central motor conduction time.*

females, with longer latencies in the former (Livingston et al., 2010). This result may be explained by the different average height between genders (Toleikis et al., 1991), thus explaining the differences of MEP cortical latency involving upper/lower limbs and males/females (Toleikis et al., 1991). However, in our study we found an additional independent effect of sex that might be based on other features, different from height (i.e., nerve diameter), although with our data we cannot speculate further on this point.

The present study also confirms those investigating the effect of aging and height on PMCT (Mayer, 1963; Kimura et al., 1975; Dorfman and Bosley, 1979; Matsumoto et al., 2012). Prior reports have demonstrated the importance of age-related and length-dependent peripheral nerve changes, such as progressive fiber loss and segmental demyelination (Lascelles and Thomas, 1966; Swallow, 1966; Rivner et al., 2001). In this context, it is worth to highlight that, unlike standing height (which decreases progressively with aging), knee height remains relatively stable during adulthood, making this measurement a good alternative for calculating stature, especially in older adults (Chumlea et al., 1985; Lera et al., 2005).

It is noteworthy that, although amplitude of the motor response is known to be subject to several physiological influences, we did not observe significant correlation of MEP size with any physical variable, except for a small-to-medium correlation with sex at the lower limbs. However, this finding was not observed for the upper limbs, likely reflecting the gender-specific regional fat distribution and its effects on electrophysiological recording. As in EMG studies, indeed, most gender differences in nerve conduction velocity are largely explained by height, whereas differences in amplitude can be due to body composition and fat distribution (Robinson et al., 1993; Buschbacher, 1998).

Regarding CMCT, it is known that in adults it does not significantly correlate with age (Claus, 1990; Eisen and Shtybel, 1990; Mano et al., 1992; Mills and Nithi, 1997). Conversely, based on the different length of the motor pathway, a relationship between CMCT and height can be expected.

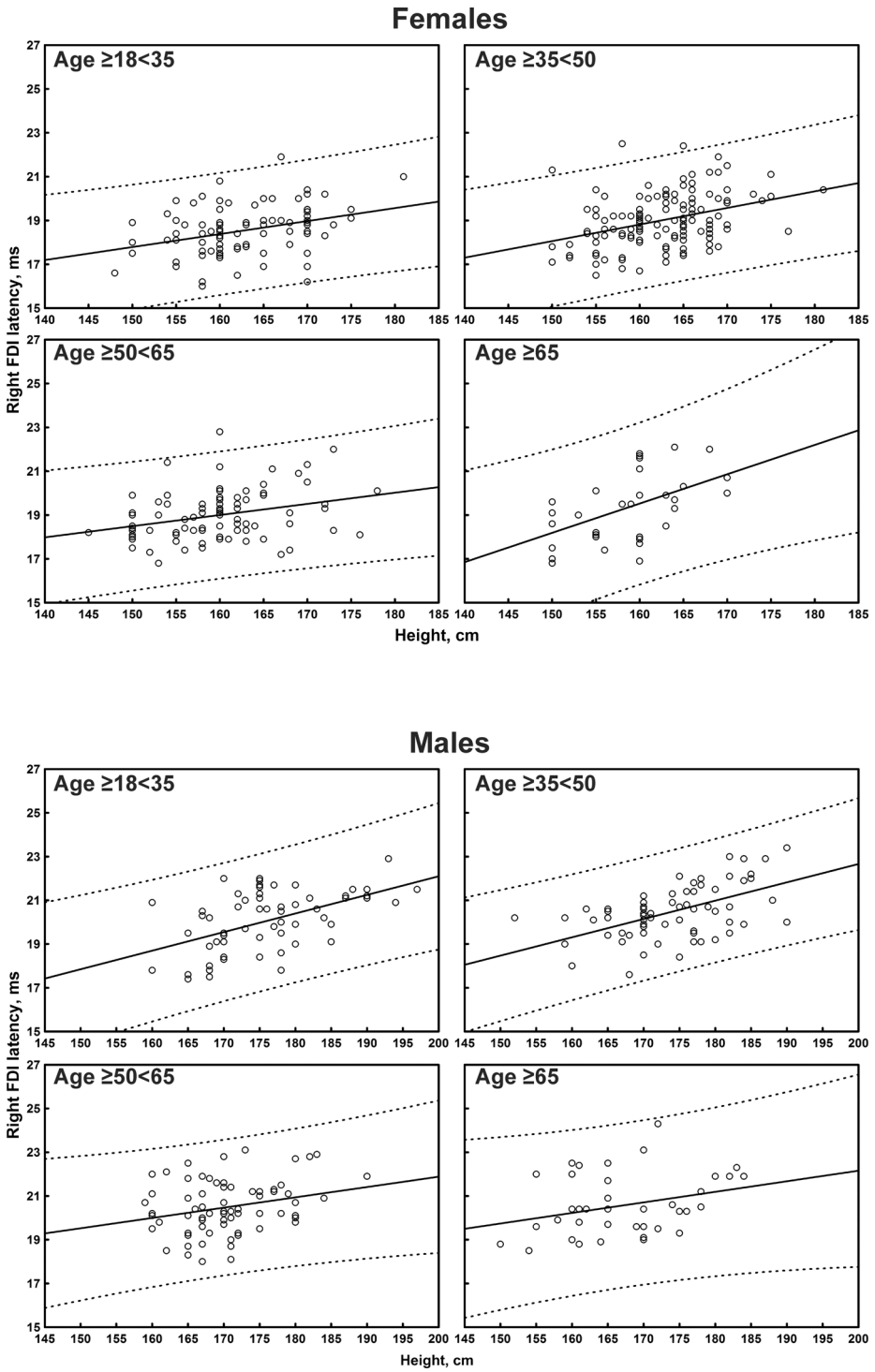

FIGURE 2 | Correlation between age and right first dorsal interosseous muscle (FDI) cortical latency of the motor evoked potentials (MEPs) in each age subgroup of participants, divided by sex. The continuous line is the regression line while the two dashed lines represent the limits of the area within which the 95% of points are expected.

In particular, since the conduction distance from M1 to the cervical segment is shorter than the lumbar segment, many studies found that CMCT to the upper limb muscles had no or only a weak correlation with height, whereas CMCT to lumbar segments was correlated with height (Rossini et al., 1987, 2015; Chu, 1989; Claus, 1990; Ghezzi et al., 1991;

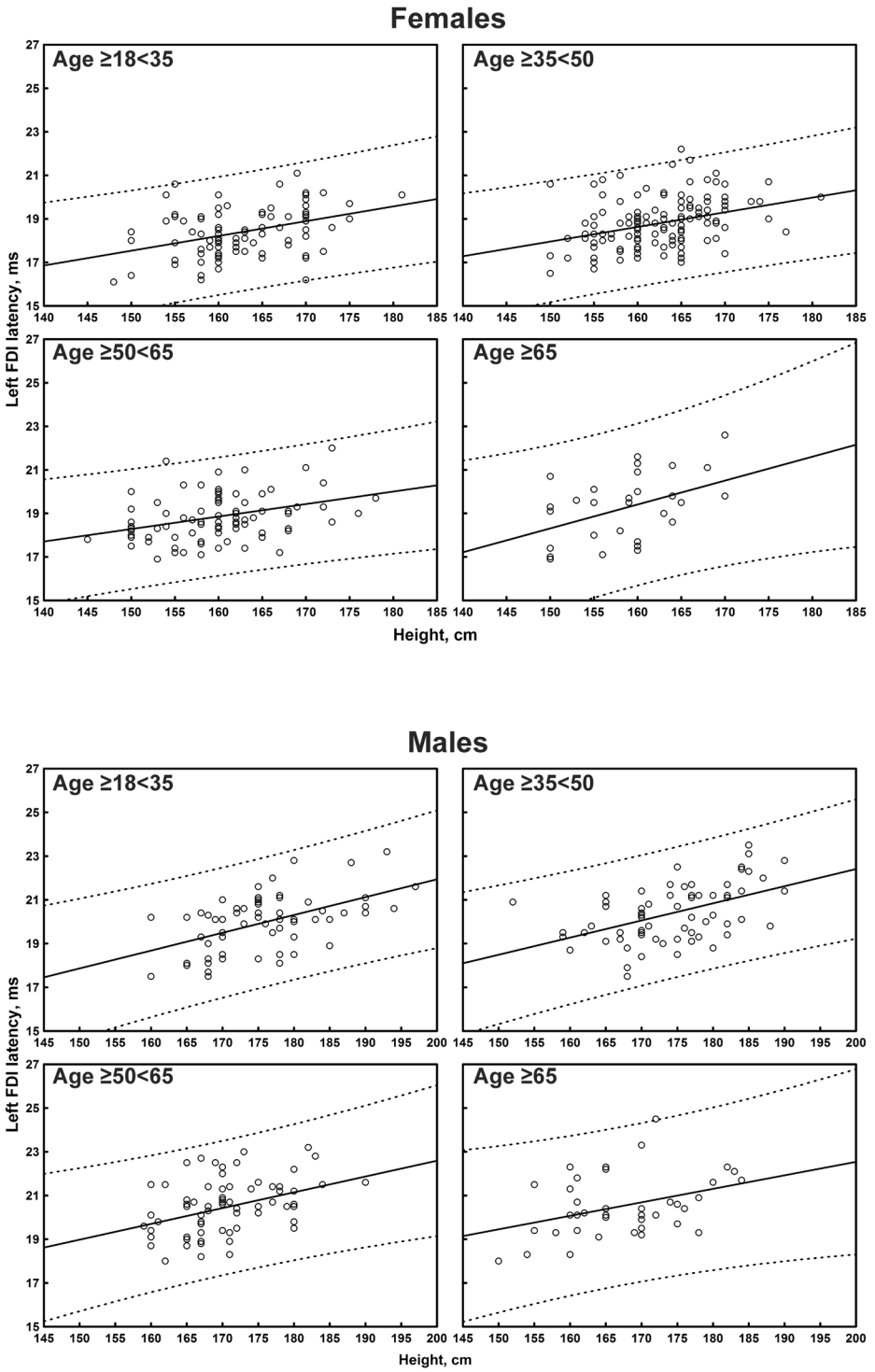

FIGURE 3 | Correlation between age and left first dorsal interosseous muscle (FDI) cortical latency of the motor evoked potentials (MEPs) in each age subgroup of participants, divided by sex. The continuous line is the regression line while the two dashed lines represent the limits of the area within which the 95% of points are expected.

Ravnborg and Dahl, 1991; Toleikis et al., 1991; Furby et al., 1992; Wochnik-Dyjas et al., 1997; Groppa et al., 2012; Udupa and Chen, 2013), without the influence from supraspinal sections (Claus, 1990). Formulae for calculating the upper limit of normal CMCT taking height into account have also been proposed (Claus, 1990).

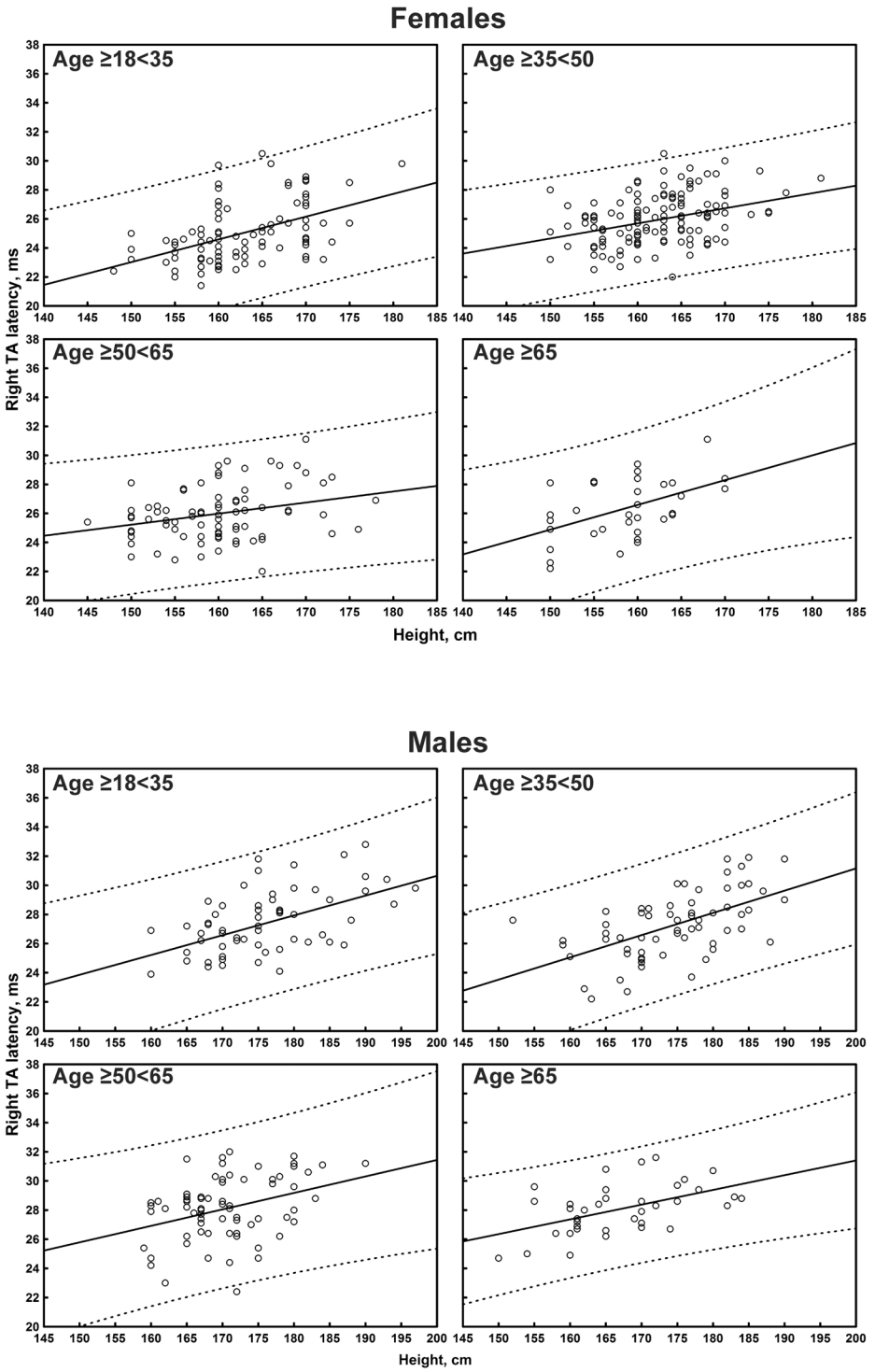

FIGURE 4 | Correlation between age and right tibialis anterior muscle (TA) cortical latency of the motor evoked potentials (MEPs) in each age subgroup of participants, divided by sex. The continuous line is the regression line while the two dashed lines represent the limits of the area within which the 95% of points are expected.

Also in our study, CMCT appeared to be correlated with both age (negatively) and height (positively) when analyzed by a single regression; however, with a multiple regression analysis this significance disappeared, due to the correction for the multicollinearity within the dataset. The use of a multiple regression analysis, indeed, may probably explain the lack of a

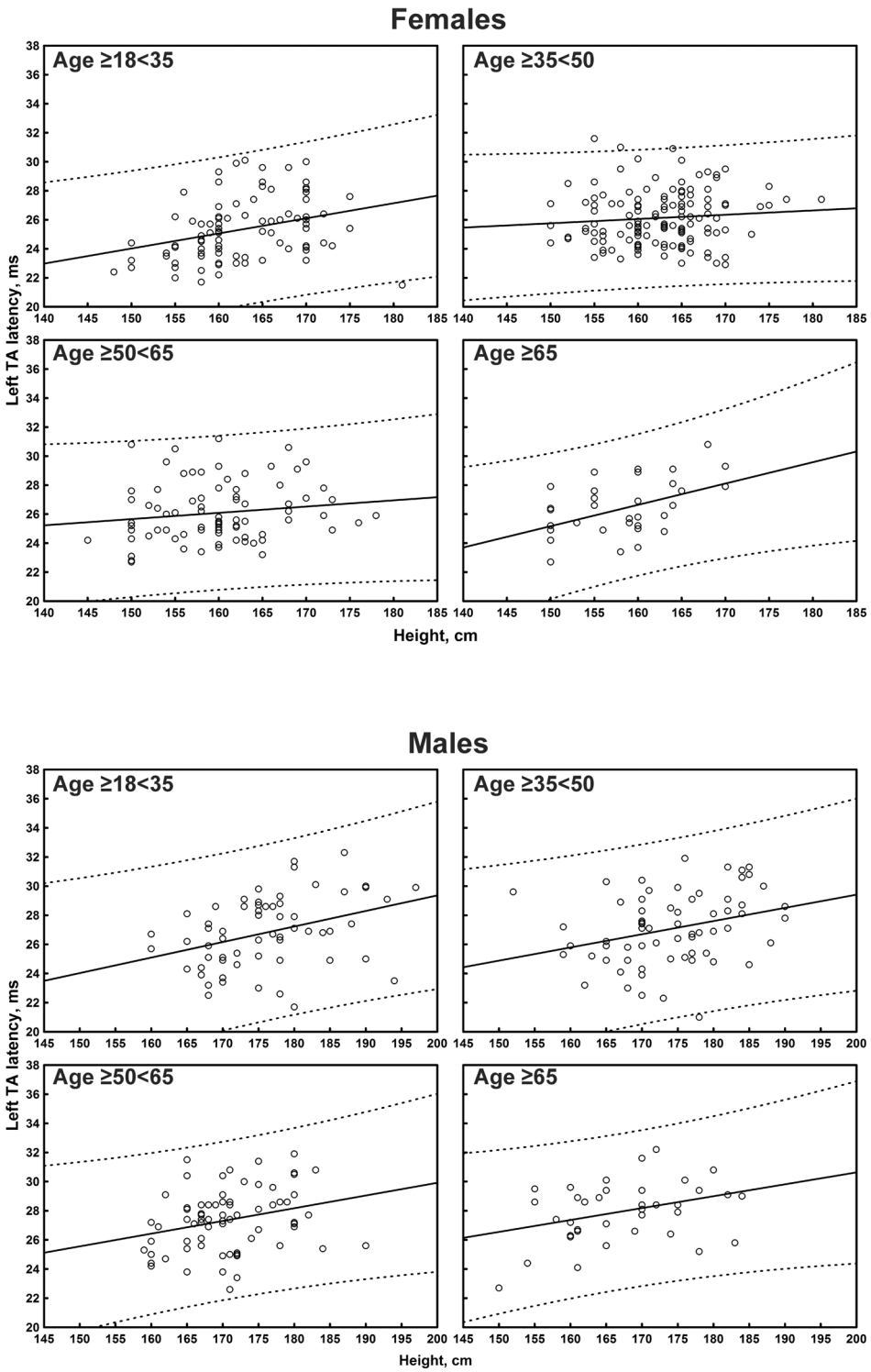

FIGURE 5 | Correlation between age and left tibialis anterior muscle (TA) cortical latency of the motor evoked potentials (MEPs) in each age subgroup of participants, divided by sex. The continuous line is the regression line while the two dashed lines represent the limits of the area within which the 95% of points are expected.

significant effect of height on conventional CMCT. Indeed, any height-related difference in intrathecal peripheral component is relatively small when compared with the differences in the more distal peripheral tract. However, even if our study suggests that height-related effects are small and non-statistically significant in these neurologically intact subjects, this might not be true in those

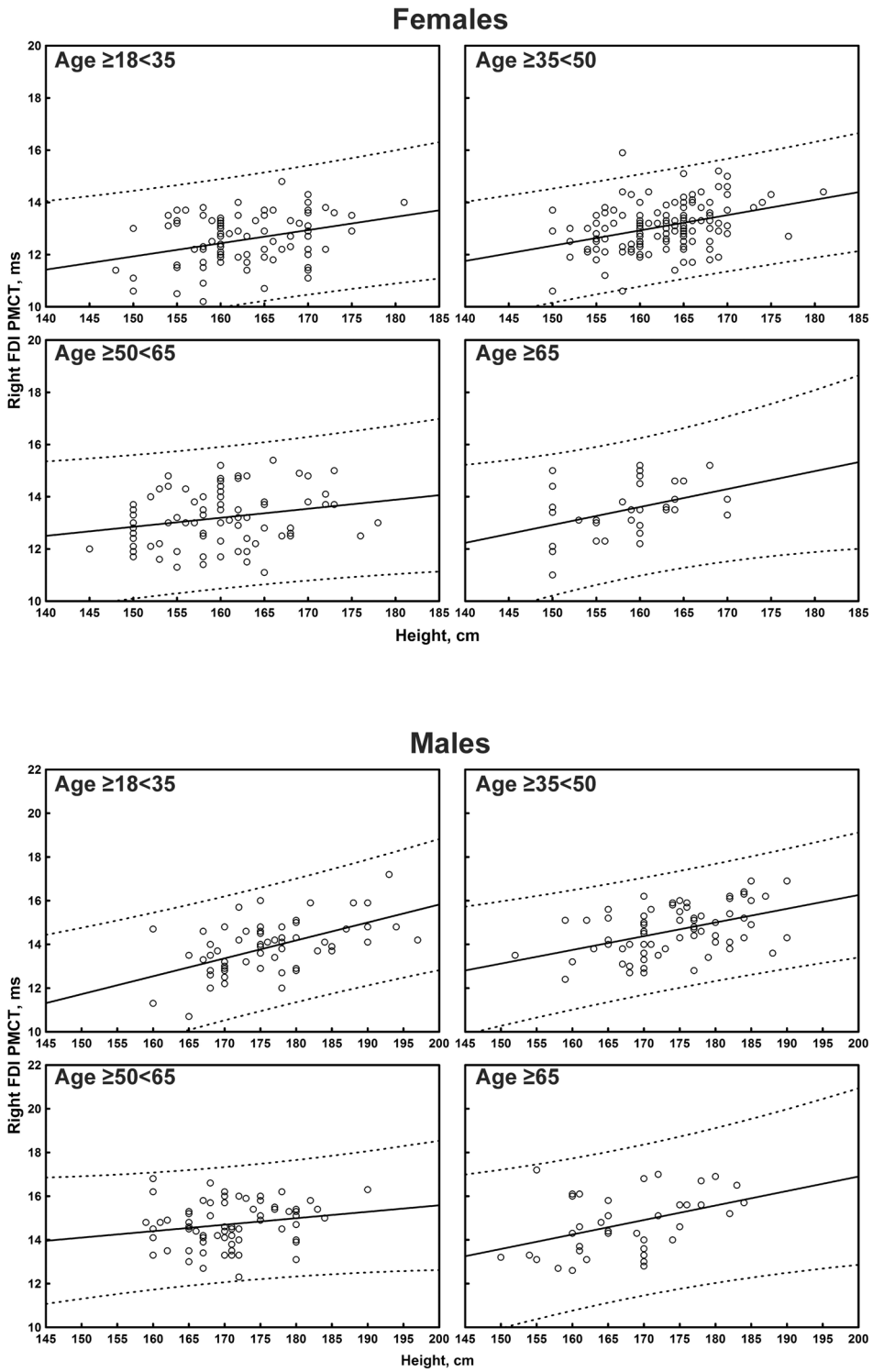

FIGURE 6 | Correlation between age and right first dorsal interosseous muscle (FDI) peripheral motor conduction time (PMCT) in each age subgroup of participants, divided by sex. The continuous line is the regression line while the two dashed lines represent the limits of the area within which the 95% of points are expected.

with specific diseases, such as cauda equina disorders or severe peripheral neuropathy. In these cases, indeed, the evaluation of CMCT by means of paravertebral magnetic stimulation might not be sufficient to differentiate a cortico-spinal tract involvement from an intrathecal peripheral involvement. In pathological conditions, therefore, the effect of height becomes much more

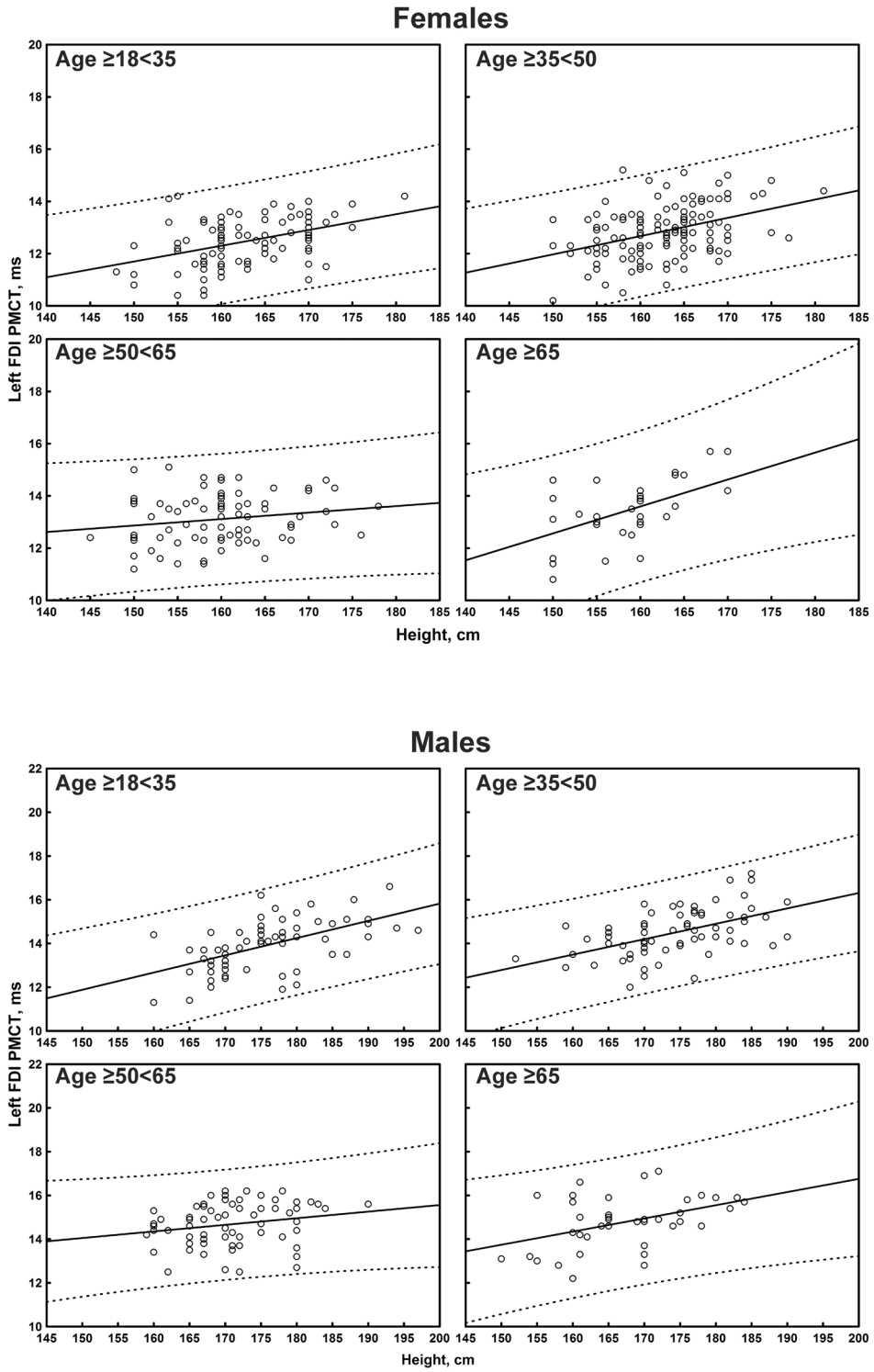

FIGURE 7 | Correlation between age and left first dorsal interosseous muscle (FDI) peripheral motor conduction time (PMCT) in each age subgroup of participants, divided by sex. The continuous line is the regression line while the two dashed lines represent the limits of the area within which the 95% of points are expected.

pronounced and an evaluation of CMCT with the F-wave method is mandatory. An alternative technique is the use of a modified coil, termed MATS (magnetic augmented translumbosacral stimulation), that activates the spinal roots at the conus medullaris level, thus making it possible to evaluate the CCCT for leg muscles (Matsumoto et al., 2010). Interestingly, using this

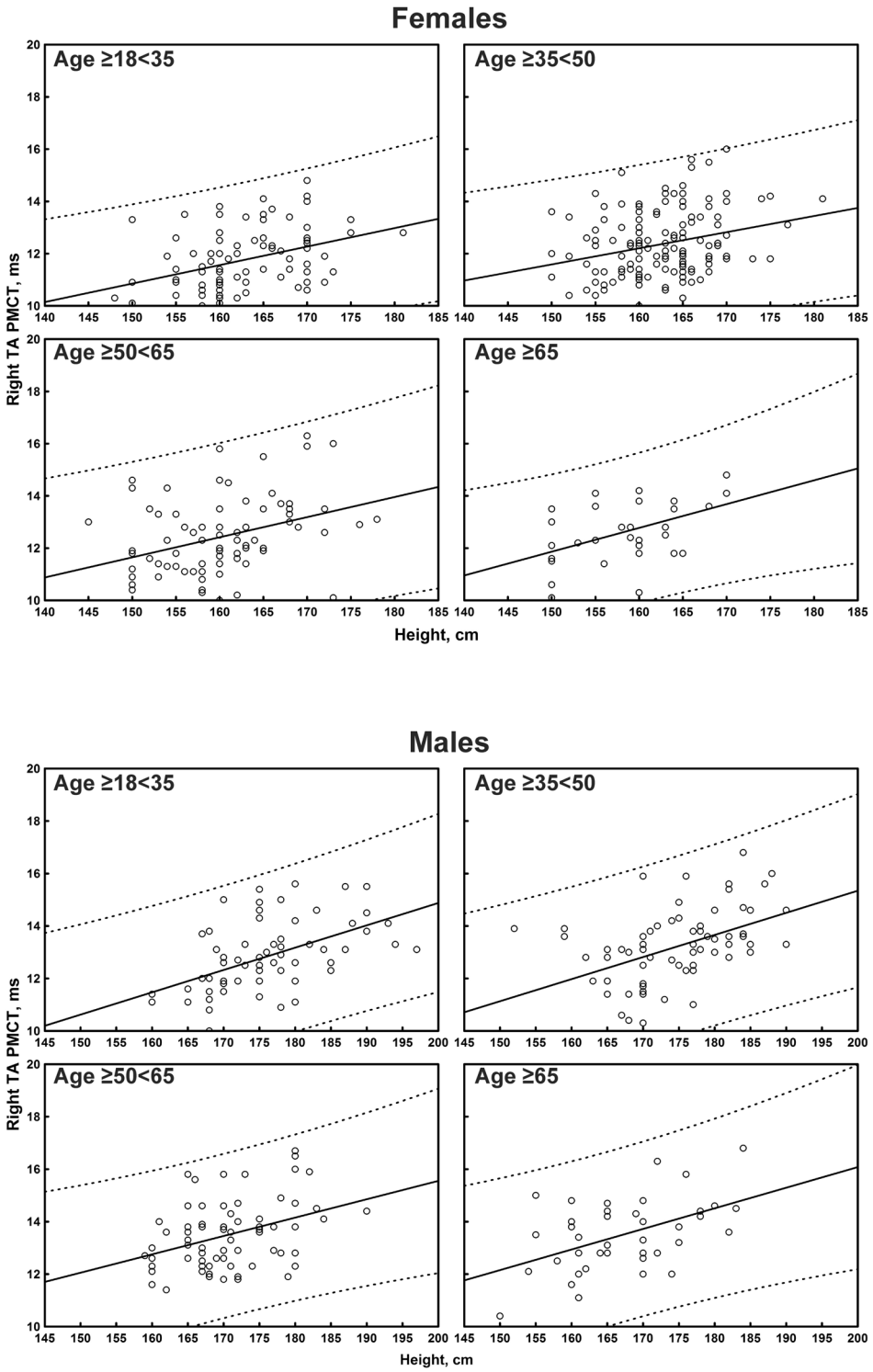

FIGURE 8 | Correlation between age and right tibialis anterior muscle (TA) peripheral motor conduction time (PMCT) in each age subgroup of participants, divided by sex. The continuous line is the regression line while the two dashed lines represent the limits of the area within which the 95% of points are expected.

coil in a sample of 51 Asian healthy volunteers, Matsumoto and coworkers showed that while there was a correlation between conventional CMCT and height, no correlation was present when the CCCT was considered (Matsumoto et al., 2010). However, unlike the present work, a multiple regression analysis was not performed (Matsumoto et al., 2010).

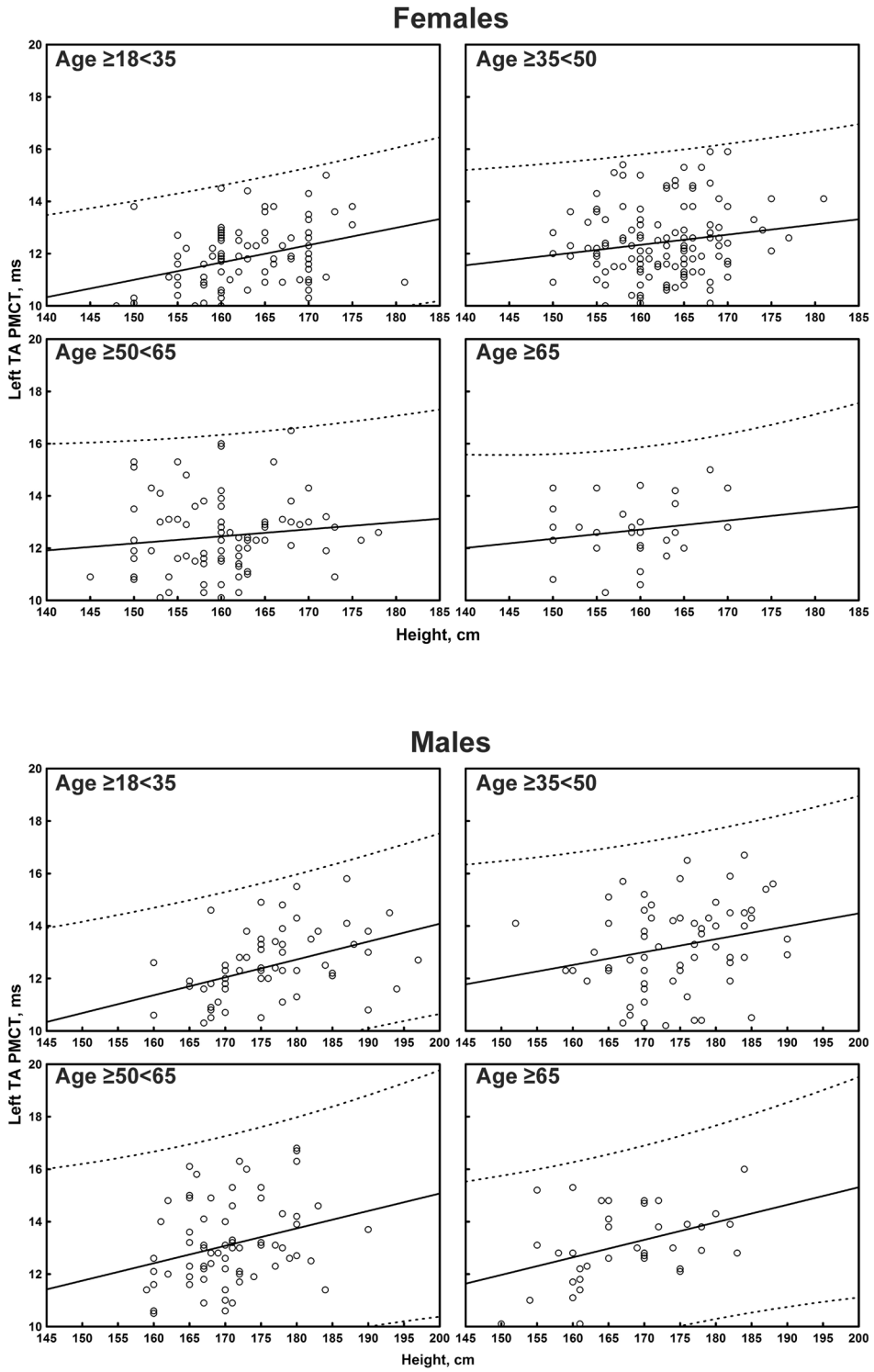

FIGURE 9 | Correlation between age and left tibialis anterior muscle (TA) peripheral motor conduction time (PMCT) in each age subgroup of participants, divided by sex. The continuous line is the regression line while the two dashed lines represent the limits of the area within which the 95% of points are expected.

Overall, this matter remains still controversial, with some investigators showing that CMCT was independent of both height and age (Ugawa et al., 1989; Booth et al., 1991; Mano et al., 1992; Heald et al., 1993) and others demonstrating the opposite (Chu, 1989; Eisen and Shtybel, 1990; Furby et al., 1992) (for a recent comprehensive review,

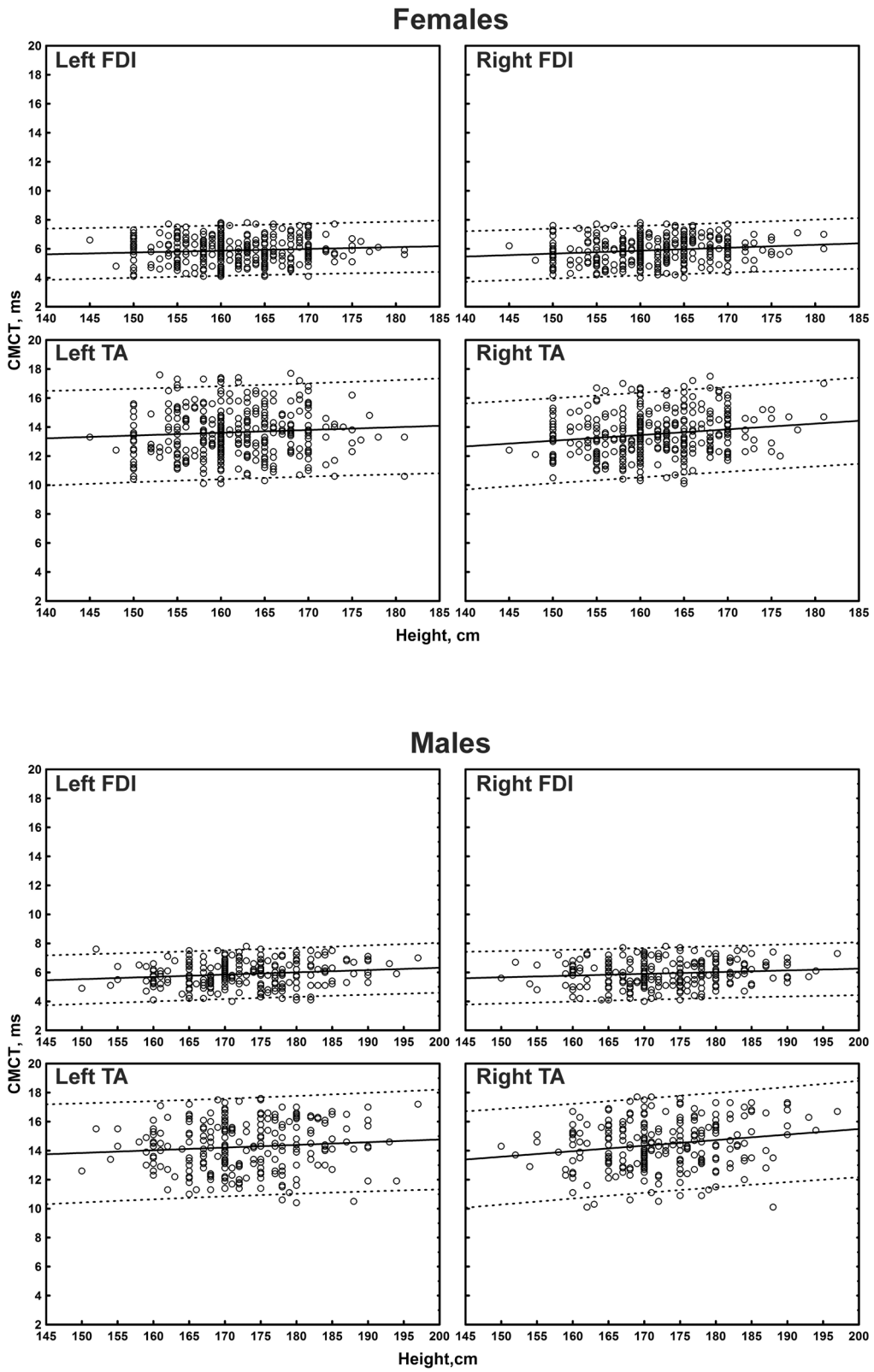

FIGURE 10 | Correlation between height and right or left first dorsal interosseous muscle (FDI) and right or left tibialis anterior muscle (TA) central motor conduction time (CMCT) in participants, divided by sex. The continuous line is the regression line while the two dashed lines represent the limits of the area within which the 95% of points are expected.

see Rossini et al., 2015). The reasons for such discrepant results remain unclear, although a reasonable explanation may be attributed to the different methods used across the studies and the demographic characteristics of the subjects. Notably, as mentioned, most of the previous reports adopted a simple regression analysis that, however, seems to be insufficient to analyze the effects of all physical variables on MEPs features. Conversely, a combined regression analysis provides a better prediction than each variable alone, as also demonstrated by studies using somatosensory (Allison et al., 1983; Chu, 1986) and visual evoked potentials (Celesia et al., 1987).

Finally, we did not find correlation between CMCT and sex or right-to-left difference (Claus, 1990; Toleikis et al., 1991; Furby et al., 1992; Mills and Nithi, 1997), in agreement with previously published reports (Eisen and Shtybel, 1990; Mills and Nithi, 1997), except for two. Chu (1989) compared two subgroups of female and male subjects with a homogenous height and found a gender difference in the leg CMCT, but not at the upper limbs. The other study reported a CMCT to the lower limbs marginally shorter in women than men, even controlling for differences in age and height (Tobimatsu et al., 1998).

Clinical Implications

As a general rule, laboratory environment, technical set up, stimulation and recording protocols, and measurement procedures need to be all standardized to allow a proper comparison within and across subjects. For instance, TMS data are influenced by the intensity and the time course of the magnetic field, the pulse configuration, and the relative threshold of each volley to the direction of the induced current flow in the cortex. The shape of the stimulation coil is also important because it influences the spatial distribution of the magnetic field (Di Lazzaro et al., 2003, 2004).

For clinical examination, cut-off values that separate normal and abnormal measurements should be available in every laboratory, for each muscle and adjusted for age, height, and sex. The measurement should be judged as abnormal when a given value deviates 2 SD (or, more conservatively, 2.5) from the mean of the data obtained from the control group. A right-left comparison is also recommended, especially to detect subtle abnormality on one side. While often difficult, it is important to build up a set of control data that match the specific population to study, since sensitivity and specificity of measurements may be insufficient if this is not done.

Strengths and Limitations

The recruitment of a large and homogenous sample, including elderly subjects, is the main strength of this study. Additionally, to the best of our knowledge, this is the largest "real-world" TMS study. As known, this type of studies allow the inclusion of a considerable number of subjects with a wide range of demographic features, thus realistically mimicking real-life practice settings (Zhang et al., 2019). Nonetheless, several limitations must also be acknowledged.

(i) Given that the study was conducted within a clinical environment, the sample could not be represented by healthy volunteers but by subjects (almost all out-patients) who, however, did not have any clinical and radiological evidence of a motor system disorder.

(ii) The sample of subjects was retrieved from a database containing all the TMS records collected in the Lab. Therefore, as in all retrospective studies, a selection bias cannot be entirely excluded, although the subjects were consecutive and carefully screened. In particular, the analysis of data was performed independently by two of the authors (MC and MP) and any discrepancy was discussed and resolved among all the authors to ensure consensus, as recommended (Makady et al., 2017).

(iii) The most precise estimation of the MEP size is through the amplitude ratio (the ratio between the maximal transcranially evoked MEP amplitude and the maximal distally evoked compound motor action potential). Moreover, to describe the stimulus-response characteristics, one should record MEPs over a wide range of intensity levels, both at rest and during contraction. However, even this if helpful in research to minimize the inter-trial and inter-subject variability, such a detailed assessment is not feasible in a routine clinical setting for diagnostic purposes (Groppa et al., 2012).

(iv) Central motor conduction time was not calculated by stimulating the peripheral nerve and eliciting the F-waves, but by magnetically stimulating the motor roots at their exit foramina (Mills and Murray, 1986) where the depolarizing threshold is the lowest (Rossini et al., 1987). This method overestimates the CMCT because the conduction time in proximal root segment between spinal cord and exit foramen is included. Moreover, with this method, spinal roots are not necessarily excited simultaneously (Claus, 1990). Nevertheless, unlike the F-wave technique, the method used here is applicable to most muscles (including TA) and is less painful (Chen et al., 2008). Moreover, as known, the electrical root stimulation only gives information on a relatively small sample of α-motoneurons and related motor axons (Groppa et al., 2012). Additionally, because conduction in the intraspinal part of the peripheral motor axons contribute to the central rather than the peripheral conduction time, the F-wave method can falsely increase CMCT in patients with nerve root lesions (Claus, 1990; Groppa et al., 2012). Finally, if F-wave persistence is low (normal for particular muscles, such as TA), the recorded F-wave sequence may not sample the fastest axons, thus producing a spuriously short CMCT (Rossini et al., 2015). Therefore, given that both approaches have pros and cons and that there is no optimal technique for all occasions (Rossini et al., 2015), many laboratories (including ours) prefer foraminal electromagnetic stimulation for routine diagnostic exams.

(v) An estimation of the peripheral nerve conduction velocity would have been useful to rule out a peripheral nervous system disease, although this goes beyond a routine TMS exam. Nevertheless, all subjects recruited did not have any sign or history of peripheral nerve pathology.

(vi) Limb length was not measured. This might result in some misinterpretations: for instance, MEP cortical latency can be prolonged in comparison to the contralateral limb as a result of pathological processes involving the cortico-motor pathway rather than explained by a subject's longer limb. A previous study showed that when MEP cortical latencies were adjusted to an individual's upper extremity length, no significant differences between limbs were observed (Livingston et al., 2010). Anyhow, we did not find correlations between side-to-side difference and any physical variable.

(vii) Finally, the timing of testing during the menstrual cycle and its potential effect on MEPs was not considered (Smith et al., 1999, 2002), although a conclusive remark on the relationship between TMS and hormonal status has not been firmly established.

Notwithstanding the mentioned limitations, in this large sample of subjects, age, height, and, sex were all important in defining and comparing MEPs. In particular, in order to construct MEPs normograms, age and body height had to be considered in the definition of the physiological range of MEP cortical latency and PMCT. Together with clinical, imaging, and other electrophysiological findings, CMCT can be considered as a reliable diagnostic and possibly prognostic translational marker of cortico-spinal conductivity in healthy subjects and in patients with neurological disorders.

CONCLUSION

The relationship between TMS measures and individual features needs to be clearly defined. The ability of TMS to discriminate between a pathology affecting the motor system and a bias from external variables is mandatory in both clinical practice and research setting. In this scenario, an optimal interpretation of MEPs will be possible only by a comprehensive understanding of the relationship between the motor responses and these variables. Here, a considerable amount of TMS data over a more than a decade of daily clinical activity is provided.

DATA AVAILABILITY

All relevant data are contained within the manuscript.

AUTHOR CONTRIBUTIONS

MC, GL, and MP conceived the study. RB, GP, and VDL designed and coordinated the study. GL, LV, and VP drafted the manuscript. RR, FF, and CV dealt with the clinical and neuroradiological assessment. MC, RR, and RF organized the database. RF performed the statistical analysis. LV, VP, FF, and RB reviewed the literature and wrote sections of the manuscript. CV, GP, VDL, and MP critically reviewed and finalized the manuscript. All authors contributed to manuscript revision, read, and approved the submitted version.

REFERENCES

Alexeeva, N., Broton, J. G., and Calancie, B. (1998). Latency of changes in spinal motoneuron excitability evoked by transcranial magnetic brain stimulation in spinal cord injured individuals. *Electroencephalogr. Clin. Neurophysiol.* 109, 297–303. doi: 10.1016/s0924-980x(98)00021-6

Allison, T., Wood, C. C., and Goff, W. R. (1983). Brain stem auditory, pattern-reversal visual, and short-latency somatosensory evoked potentials: latencies in relation to age, sex, and brain and body size. *Electroencephalogr. Clin. Neurophysiol.* 55, 619–636. doi: 10.1016/0013-4694(83)90272-9

Amassian, V. E., Cracco, R. Q., and Maccabee, P. J. (1989). Focal stimulation of human cerebral cortex with the magnetic coil: a comparison with electrical stimulation. *Electroencephalogr. Clin. Neurophysiol.* 74, 401–416. doi: 10.1016/0168-5597(89)90029-4

Barker, A. T., Freeston, I. L., Jalinous, R., and Jarratt, J. A. (1987). Magnetic stimulation of the human brain and peripheral nervous system: an introduction and the results of an initial clinical evaluation. *Neurosurgery* 20, 100–109.

Bella, R., Cantone, M., Lanza, G., Ferri, R., Vinciguerra, L., Puglisi, V., et al. (2016). Cholinergic circuitry functioning in patients with vascular cognitive impairment–no dementia. *Brain Stimul.* 9, 225–233. doi: 10.1016/j.brs.2015.09.013

Bella, R., Ferri, R., Cantone, M., Pennisi, M., Lanza, G., Malaguarnera, G., et al. (2011). Motor cortex excitability in vascular depression. *Int. J. Psychophysiol.* 82, 248–253. doi: 10.1016/j.ijpsycho.2011.09.006

Bella, R., Ferri, R., Lanza, G., Cantone, M., Pennisi, M., Puglisi, V., et al. (2013). TMS follow-up study in patients with vascular cognitive impairment-no dementia. *Neurosci. Lett.* 534, 155–159. doi: 10.1016/j.neulet.2012.12.017

Bella, R., Lanza, G., Cantone, M., Giuffrida, S., Puglisi, V., Vinciguerra, L., et al. (2015). Effect of a gluten-free diet on cortical excitability in adults with celiac disease. *PLoS One* 10:e0129218. doi: 10.1371/journal.pone.0129218

Bland, J. M., and Altman, D. G. (1995). Multiple significance tests: the bonferroni method. *BMJ* 310:170. doi: 10.1136/bmj.310.6973.170

Booth, K. R., Streletz, L. J., Raab, V. E., Kerrigan, J. J., Alaimo, M. A., and Herbison, G. J. (1991). Motor evoked potentials and central motor conduction: studies of transcranial magnetic stimulation with recording from the leg. *Electroencephalogr. Clin. Neurophysiol.* 81, 57–62. doi: 10.1016/0168-5597(91)90104-6

Boroojerdi, B., Foltys, H., Krings, T., Spetzger, U., Thron, A., and Töpper, R. (1999). Localization of the motor hand area using transcranial magnetic stimulation and functional magnetic resonance imaging. *Clin. Neurophysiol.* 110, 699–704. doi: 10.1016/s1388-2457(98)00027-3

Buschbacher, R. M. (1998). Body mass index effect on common nerve conduction study measurements. *Muscle Nerve* 21, 1398–1404. doi: 10.1002/(sici)1097-4598(199811)21:11<1398::aid-mus6>3.0.co;2-4

Cantone, M., Bramanti, A., Lanza, G., Pennisi, M., Bramanti, P., Pennisi, G., et al. (2017). Cortical plasticity in depression. *ASN Neuro.* 9, doi: 10.1177/1759091417711512

Caramia, M. D., Pardal, A. M., Zarola, F., and Rossini, P. M. (1989). Electric vs magnetic trans-cranial stimulation of the brain in healthy humans: a comparative study of central motor tracts "conductivity" and "excitability.". *Brain Res.* 479, 98–104. doi: 10.1016/0006-8993(89)91339-5

Celesia, G. G., Kaufman, D., and Cone, S. (1987). Effects of age and sex on pattern electroretinograms and visual evoked potentials. *Electroencephalogr. Clin. Neurophysiol.* 68, 161–171. doi: 10.1016/0168-5597(87)90023-2

Chen, R., Cros, D., Curra, A., Di Lazzaro, V., Lefaucheur, J.-P., Magistris, M. R., et al. (2008). The clinical diagnostic utility of transcranial magnetic stimulation: report of an IFCN committee. *Clin. Neurophysiol.* 119, 504–532. doi: 10.1016/j.clinph.2007.10.014

Chu, N. S. (1986). Somatosensory evoked potentials: correlations with height. *Electroencephalogr. Clin. Neurophysiol.* 65, 169–176. doi: 10.1016/0168-5597(86)90051-1

Chu, N.-S. (1989). Motor evoked potentials with magnetic stimulation: correlations with height. *Electroencephalogr. Clin. Neurophysiol.* 74, 481–485. doi: 10.1016/0168-5597(89)90039-7

Chumlea, W. C., Roche, A. F., and Steinbaugh, M. L. (1985). Estimating stature from knee height for persons 60 to 90 years of age. *J. Am. Geriatr. Soc.* 33, 116–120. doi: 10.1111/j.1532-5415.1985.tb02276.x

Claus, D. (1990). Central motor conduction: method and normal results. *Muscle Nerve* 13, 1125–1132. doi: 10.1002/mus.880131207

Cohen, J. (1988). *Statistical Power Analysis for the Behavioral Sciences*, 2nd Edn. Hillsdale, N.J: Erlbaum Associates.

Cueva, A. S., Galhardoni, R., Cury, R. G., Parravano, D. C., Correa, G., Araujo, H., et al. (2016). Normative data of cortical excitability measurements obtained by transcranial magnetic stimulation in healthy subjects. *Neurophysiol. Clin.* 46, 43–51. doi: 10.1016/j.neucli.2015.12.003

Di Lazzaro, V., Oliviero, A., Pilato, F., Mazzone, P., Insola, A., Ranieri, F., et al. (2003). Corticospinal volleys evoked by transcranial stimulation of the brain in conscious humans. *Neurol. Res.* 25, 143–150. doi: 10.1179/016164103101201292

Di Lazzaro, V., Pilato, F., Oliviero, A., Saturno, E., Dileone, M., and Tonali, P. A. (2004). Role of motor evoked potentials in diagnosis of cauda equina and lumbosacral cord lesions. *Neurology* 63, 2266–2271. doi: 10.1212/01.wnl.0000147296.97980.ca

Dorfman, L. J., and Bosley, T. M. (1979). Age-related changes in peripheral and central nerve conduction in man. *Neurology* 29, 38–44.

Eisen, A. A., and Shtybel, W. (1990). AAEM minimonograph #35: clinical experience with transcranial magnetic stimulation. *Muscle Nerve* 13, 995–1011. doi: 10.1002/mus.880131102

Fritz, C., Braune, H. J., Pylatiuk, C., and Pohl, M. (1997). Silent period following transcranial magnetic stimulation: a study of intra- and inter-examiner reliability. *Electroencephalogr. Clin. Neurophysiol.* 105, 235–240. doi: 10.1016/S0924-980X(97)96675-3

Furby, A., Bourriez, J. L., Jacquesson, J. M., Mounier-Vehier, F., and Guieu, J. D. (1992). Motor evoked potentials to magnetic stimulation: technical considerations and normative data from 50 subjects. *J. Neurol.* 239, 152–156. doi: 10.1007/BF00833916

Garry, M. I., Kamen, G., and Nordstrom, M. A. (2004). Hemispheric differences in the relationship between corticomotor excitability changes following a fine-motor task and motor learning. *J. Neurophysiol.* 91, 1570–1578. doi: 10.1152/jn.00595.2003

Ghezzi, A., Callea, L., Zaffaroni, M., Zibetti, A., and Montanini, R. (1991). Study of central and peripheral motor conduction in normal subjects. *Acta Neurol. Scand.* 84, 503–506. doi: 10.1111/j.1600-0404.1991.tb05003.x

Groppa, S., Oliviero, A., Eisen, A., Quartarone, A., Cohen, L. G., Mall, V., et al. (2012). A practical guide to diagnostic transcranial magnetic stimulation: report of an IFCN committee. *Clin. Neurophysiol.* 123, 858–882. doi: 10.1016/j.clinph.2012.01.010

Hallett, M. (1996). Transcranial magnetic stimulation: a useful tool for clinical neurophysiology. *Ann. Neurol.* 40, 344–345. doi: 10.1002/ana.410400303

Hallett, M. (2007). Transcranial magnetic stimulation: a primer. *Neuron* 55, 187–199. doi: 10.1016/j.neuron.2007.06.026

Heald, A., Bates, D., Cartlidge, N. E., French, J. M., and Miller, S. (1993). Longitudinal study of central motor conduction time following stroke. 1. Natural history of central motor conduction. *Brain* 116(Pt 6), 1355–1370. doi: 10.1093/brain/116.6.1355

Kimura, J., Bosch, P., and Lindsay, G. M. (1975). F-wave conduction velocity in the central segment of the peroneal and tibial nerves. *Arch Phys. Med. Rehabil.* 56, 492–497.

Lanza, G., Bella, R., Giuffrida, S., Cantone, M., Pennisi, G., Spampinato, C., et al. (2013). Preserved transcallosal inhibition to transcranial magnetic stimulation in nondemented elderly patients with leukoaraiosis. *Biomed. Res. Int.* 2013:351680. doi: 10.1155/2013/351680

Lanza, G., Bramanti, P., Cantone, M., Pennisi, M., Pennisi, G., and Bella, R. (2017a). Vascular cognitive impairment through the looking glass of transcranial magnetic stimulation. *Behav. Neurol.* 2017:1421326. doi: 10.1155/2017/1421326

Lanza, G., Kosac, A., Trajkovic, G., and Whittaker, R. G. (2017b). Nerve conduction studies as a measure of disease progression: objectivity or illusion? *J. Neuromuscul. Dis.* 4, 209–215. doi: 10.3233/JND-170243

Lascelles, R. G., and Thomas, P. K. (1966). Changes due to age in internodal length in the sural nerve in man. *J. Neurol. Neurosurg. Psychiatry* 29, 40–44. doi: 10.1136/jnnp.29.1.40

Lera, L., Luis Santos, J., García, C., Arroyo, P., and Albala, C. (2005). Predictive equations for stature in the elderly: a study in three latin american cities. *Ann. Hum. Biol.* 32, 773–781. doi: 10.1080/03014460500421304

Livingston, S. C., Friedlander, D. L., Gibson, B. C., and Melvin, J. R. (2013). Motor evoked potential response latencies demonstrate moderate correlations with height and limb length in healthy young adults. *Neurodiagn J.* 53, 63–78.

Livingston, S. C., Goodkin, H. P., and Ingersoll, C. D. (2010). The influence of gender, hand dominance, and upper extremity length on motor evoked potentials. *J. Clin. Monit. Comput.* 24, 427–436. doi: 10.1007/s10877-010-9267-8

Makady, A., de Boer, A., Hillege, H., Klungel, O., and Goettsch, W. (2017). (on behalf of GetReal Work Package 1). what is real-world data? a review of definitions based on literature and stakeholder interviews. *Value Health* 20, 858–865. doi: 10.1016/j.jval.2017.03.008

Mano, Y., Nakamuro, T., Ikoma, K., Sugata, T., Morimoto, S., Takayanagi, T., et al. (1992). Central motor conductivity in aged people. *Intern. Med.* 31, 1084–1087. doi: 10.2169/internalmedicine.31.1084

Matamala, J. M., Núñez, C., Lera, L., Verdugo, R. J., Sánchez, H., Albala, C., et al. (2013). Motor evoked potentials by transcranial magnetic stimulation in healthy elderly people. *Somatosens Mot. Res.* 30, 201–205. doi: 10.3109/08990220.2013.796922

Matsumoto, H., Hanajima, R., Shirota, Y., Hamada, M., Terao, Y., Ohminami, S., et al. (2010). Cortico-conus motor conduction time (CCCT) for leg muscles. *Clin. Neurophysiol.* 121, 1930–1933. doi: 10.1016/j.clinph.2010.04.014

Matsumoto, H., Konoma, Y., Shimizu, T., Okabe, S., Shirota, Y., Hanajima, R., et al. (2012). Aging influences central motor conduction less than peripheral motor conduction: a transcranial magnetic stimulation study. *Muscle Nerve* 46, 926–931. doi: 10.1002/mus.23430

Mayer, R. F. (1963). Nerve conduction studies in man. *Neurology* 13, 1021–1030.

Mills, K. R., McLeod, C., Sheffy, J., and Loh, L. (1993). The optimal current direction for excitation of human cervical motor roots with a double coil magnetic stimulator. *Electroencephalogr. Clin. Neurophysiol.* 89, 138–144. doi: 10.1016/0168-5597(93)90096-8

Mills, K. R., and Murray, N. M. (1986). Electrical stimulation over the human vertebral column: which neural elements are excited? *Electroencephalogr. Clin. Neurophysiol.* 63, 582–589. doi: 10.1016/0013-4694(86)90145-8

Mills, K. R., and Nithi, K. A. (1997). Corticomotor threshold to magnetic stimulation: normal values and repeatability. *Muscle Nerve* 20, 570–576. doi: 10.1002/(sici)1097-4598(199705)20:5<570::aid-mus5>3.3.co;2-f

Paulus, W., Classen, J., Cohen, L. G., Large, C. H., Di Lazzaro, V., Nitsche, M., et al. (2008). State of the art: pharmacologic effects on cortical excitability measures tested by transcranial magnetic stimulation. *Brain Stimul.* 1, 151–163. doi: 10.1016/j.brs.2008.06.002

Pennisi, G., Bella, R., and Lanza, G. (2015). Motor cortex plasticity in subcortical ischemic vascular dementia: what can TMS say? *Clin. Neurophysiol.* 126, 851–852. doi: 10.1016/j.clinph.2014.09.001

Pennisi, G., Lanza, G., Giuffrida, S., Vinciguerra, L., Puglisi, V., Cantone, M., et al. (2014). Excitability of the motor cortex in de novo patients with celiac disease. *PLoS One* 9:e102790. doi: 10.1371/journal.pone.0102790

Pennisi, M., Lanza, G., Cantone, M., Ricceri, R., Spampinato, C., Pennisi, G., et al. (2016). Correlation between motor cortex excitability changes and cognitive impairment in vascular depression: pathophysiological insights from a longitudinal TMS study. *Neural. Plast* 2016:8154969. doi: 10.1155/2016/8154969

Petersen, N. T., Pyndt, H. S., and Nielsen, J. B. (2003). Investigating human motor control by transcranial magnetic stimulation. *Exp. Brain Res.* 152, 1–16. doi: 10.1007/s00221-003-1537-y

Ravnborg, M., and Dahl, K. (1991). Examination of central and peripheral motor pathways by standardized magnetic stimulation. *Acta Neurol. Scand.* 84, 491–497. doi: 10.1111/j.1600-0404.1991.tb05001.x

Rivner, M. H., Swift, T. R., and Malik, K. (2001). Influence of age and height on nerve conduction. *Muscle Nerve* 24, 1134–1141. doi: 10.1002/mus.1124

Robinson, L. R., Rubner, D. E., Wahl, P. W., Fujimoto, W. Y., and Stolov, W. C. (1993). Influences of height and gender on normal nerve conduction studies. *Arch Phys. Med. Rehabil.* 74, 1134–1138.

Rossi, S., Hallett, M., Rossini, P. M., and Pascual-Leone, A. (2009). Safety, ethical considerations, and application guidelines for the use of transcranial magnetic

stimulation in clinical practice and research. *Clin. Neurophysiol.* 120, 2008–2039. doi: 10.1016/j.clinph.2009.08.016

Rossini, P. M. (1988). The anatomic and physiologic bases of motor-evoked potentials. *Neurol. Clin.* 6, 751–769. doi: 10.1016/s0733-8619(18)30841-7

Rossini, P. M., Barker, A. T., Berardelli, A., Caramia, M. D., Caruso, G., Cracco, R. Q., et al. (1994). Non-invasive electrical and magnetic stimulation of the brain, spinal cord and roots: basic principles and procedures for routine clinical application. Report of an IFCN committee. *Electroencephalogr. Clin. Neurophysiol.* 91, 79–92. doi: 10.1016/0013-4694(94)90029-9

Rossini, P. M., Burke, D., Chen, R., Cohen, L. G., Daskalakis, Z., Di Iorio, R., et al. (2015). Non-invasive electrical and magnetic stimulation of the brain, spinal cord, roots and peripheral nerves: basic principles and procedures for routine clinical and research application. An updated report from an I.F.C.N. Committee. *Clin. Neurophysiol.* 126, 1071–1107. doi: 10.1016/j.clinph.2015.02.001

Rossini, P. M., and Caramia, M. (eds) (1988). "Methodological and physiological considerations on the electric or magnetic transcranial stimulation," in *Noninvasive Stimulation of Brain and Spinal Cord: Fundamentals and Clinical Applications*, (New York, NY: Alan R Liss), 37–65.

Rossini, P. M., and Caramia, M. D. (1992). Central conduction studies and magnetic stimulation. *Curr. Opin. Neurol. Neurosurg.* 5, 697–703.

Rossini, P. M., Caramia, M. D., and Zarola, F. (1987). Mechanisms of nervous propagation along central motor pathways: noninvasive evaluation in healthy subjects and in patients with neurological disease. *Neurosurgery* 20, 183–191.

Rossini, P. M., Desiato, M. T., and Caramia, M. D. (1992). Age-related changes of motor evoked potentials in healthy humans: non-invasive evaluation of central and peripheral motor tracts excitability and conductivity. *Brain Res.* 593, 14–19. doi: 10.1016/0006-8993(92)91256-E

Rossini, P. M., Di Stefano, E., and Stanzione, P. (1985a). Nerve impulse propagation along central and peripheral fast conducting motor and sensory pathways in man. *Electroencephalogr. Clin. Neurophysiol.* 60, 320–334. doi: 10.1016/0013-4694(85)90006-9

Rossini, P. M., Marciani, M. G., Caramia, M., Roma, V., and Zarola, F. (1985b). Nervous propagation along "central" motor pathways in intact man: characteristics of motor responses to "bifocal" and "unifocal" spine and scalp non-invasive stimulation. *Electroencephalogr. Clin. Neurophysiol.* 61, 272–286. doi: 10.1016/0013-4694(85)91094-6

Rossini, P. M., and Rossi, S. (2007). Transcranial magnetic stimulation: diagnostic, therapeutic, and research potential. *Neurology* 68, 484–488. doi: 10.1212/01.wnl.0000250268.13789.b2

Smith, M. J., Adams, L. F., Schmidt, P. J., Rubinow, D. R., and Wassermann, E. M. (2002). Effects of ovarian hormones on human cortical excitability. *Ann. Neurol.* 51, 599–603. doi: 10.1002/ana.10180

Smith, M. J., Keel, J. C., Greenberg, B. D., Adams, L. F., Schmidt, P. J., Rubinow, D. A., et al. (1999). Menstrual cycle effects on cortical excitability. *Neurology* 53, 2069–2072.

Sohn, Y. H., and Hallett, M. (2004). Surround inhibition in human motor system. *Exp. Brain Res.* 158, 397–404. doi: 10.1007/s00221-004-1909-y

Swallow, M. (1966). Fibre size and content of the anterior tibial nerve of the foot. *J. Neurol. Neurosurg. Psychiatry* 29, 205–213. doi: 10.1136/jnnp.29.3.205

Tobimatsu, S., Sun, S.-J., Fukui, R., and Kato, M. (1998). Effects of sex, height and age on motor evoked potentials with magnetic stimulation. *J. Neurol.* 245, 256–261. doi: 10.1007/s004150050215

Toleikis, J. R., Sloan, T. B., and Ronai, A. K. (1991). Optimal transcranial magnetic stimulation sites for the assessment of motor function. *Electroencephalogr. Clin. Neurophysiol.* 81, 443–449. doi: 10.1016/0013-4694(91)90006-p

Tomlinson, B. E., and Irving, D. (1977). The numbers of limb motor neurons in the human lumbosacral cord throughout life. *J. Neurol. Sci.* 34, 213–219. doi: 10.1016/0022-510x(77)90069-7

Udupa, K., and Chen, R. (2013). Central motor conduction time. *Handb Clin Neurol* 116, 375–386. doi: 10.1016/B978-0-444-53497-2.00031-0

Ugawa, Y., Rothwell, J. C., Day, B. L., Thompson, P. D., and Marsden, C. D. (1989). Magnetic stimulation over the spinal enlargements. *J. Neurol. Neurosurg. Psychiatry* 52, 1025–1032. doi: 10.1136/jnnp.52.9.1025

Ugawa, Y., Uesaka, Y., Terao, Y., Hanajima, R., and Kanazawa, I. (1994). Magnetic stimulation of corticospinal pathways at the foramen magnum level in humans. *Ann. Neurol.* 36, 618–624. doi: 10.1002/ana.410360410

van der Kamp, W., Zwinderman, A. H., Ferrari, M. D., and van Dijk, J. G. (1996). Cortical excitability and response variability of transcranial magnetic stimulation. *J. Clin. Neurophysiol.* 13, 164–171. doi: 10.1097/00004691-199603000-00007

Wassermann, E. M., Epstein, C. M., and Ziemann, U. (2008). *The Oxford Handbook of Transcranial Stimulation*. Oxford: Oxford University Press.

Wochnik-Dyjas, D., Głazowski, C., and Niewiadomska, M. (1997). Segmental conduction times in the motor nervous system. *Electromyogr. Clin. Neurophysiol.* 37, 155–167.

Zhang, T., Zhu, J., Xu, L., Tang, X., Cui, H., Wei, Y., et al. (2019). Add-on rTMS for the acute treatment of depressive symptoms is probably more effective in adolescents than in adults: evidence from real-world clinical practice. *Brain Stimul.* 12, 103–109. doi: 10.1016/j.brs.2018.09.007

Ziemann, U., Reis, J., Schwenkreis, P., Rosanova, M., Strafella, A., Badawy, R., et al. (2015). TMS and drugs revisited 2014. *Clin. Neurophysiol.* 126, 1847–1868. doi: 10.1016/j.clinph.2014.08.028

Conflict of Interest Statement: The authors declare that the research was conducted in the absence of any commercial or financial relationships that could be construed as a potential conflict of interest.

frontiers in Human Neuroscience

ORIGINAL RESEARCH
published: 12 June 2019
doi: 10.3389/fnhum.2019.00173

EEG Microstates Analysis in Young Adults With Autism Spectrum Disorder During Resting-State

David F. D'Croz-Baron[1], Mary Baker[1], Christoph M. Michel[2] and Tanja Karp[3]*

[1] Autumn's Dawn Neuroimaging, Cognition, and Engineering Laboratory, Department of Electrical and Computer Engineering, Texas Tech University, Lubbock, TX, United States, [2] Functional Brain Mapping Laboratory, Department of Basic Neuroscience, Faculty of Medicine, University of Geneva, Geneva, Switzerland, [3] Department of Electrical and Computer Engineering, Texas Tech University, Lubbock, TX, United States

Electroencephalography (EEG) is a useful tool to inspect the brain activity in resting state and allows to characterize spontaneous brain activity that is not detected when a subject is cognitively engaged. Moreover, taking advantage of the high time resolution in EEG, it is possible to perform fast topographical reference-free analysis, since different scalp potential fields correspond to changes in the underlying sources within the brain. In this study, the spontaneous EEG resting state (eyes closed) was compared between 10 young adults ages 18–30 years with autism spectrum disorder (ASD) and 13 neurotypical controls. A microstate analysis was applied, focusing on four temporal parameters: mean duration, the frequency of occurrence, the ratio of time coverage, and the global explained variance (GEV). Using data that were acquired from a 65-channel EEG system, six resting-state topographies that best describe the dataset across all subjects were identified by running a two-step cluster analysis labeled as microstate classes A–F. The results indicated that microstates B and E displayed statistically significant differences between both groups among the temporal parameters evaluated. Classes B, D, E, and F were consistently more present in ASD, and class C in controls. The combination of these findings with the putative functional significance of the different classes suggests that during resting state, the ASD group was more focused on visual scene reconstruction, while the control group was more engaged with self-memory retrieval. Furthermore, from a connectivity perspective, the resting-state networks that have been previously associated with each microstate class overlap the brain regions implicated in impaired social communication and repetitive behaviors that characterize ASD.

Keywords: EEG microstates, autism spectrum disorder, resting state, topographical analysis, electroencephalography

OPEN ACCESS

Edited by:
Filippo Brighina, University of Palermo, Italy

Reviewed by:
Stavros I. Dimitriadis, Cardiff University School of Medicine, United Kingdom
Antonio Ivano Triggiani, University of Foggia, Italy

****Correspondence:***
David F. D'Croz-Baron
david.dcroz-baron@ttu.edu

Received: *24 February 2019*
Accepted: *13 May 2019*
Published: *12 June 2019*

Citation:
D'Croz-Baron DF, Baker M, Michel CM and Karp T (2019) EEG Microstates Analysis in Young Adults With Autism Spectrum Disorder During Resting-State. Front. Hum. Neurosci. 13:173. doi: 10.3389/fnhum.2019.00173

INTRODUCTION

Autism spectrum disorder (ASD) is a developmental disorder that has an onset in early life and is characterized by repetitive behaviors, restricted interests, and impaired social communication (American Psychiatric Association, 2013). According to the United States Center for Disease Control and Prevention (CDC), the diagnosis of autism at age 2 is reliable, and about 1 in

59 children was diagnosed with ASD (Centers for Disease Control and Prevention, Autism Spectrum Disorder [ASD], 2018). Attempts to enhance social communication and maintain healthy and productive social interactions in individuals with ASD have motivated different studies, which assist in providing data that enables researchers to model the autistic brain (Billeci et al., 2013; Mash et al., 2018). Several approaches to evaluate and inspect the brain networks have been taken, including investigating resting-state and task-oriented electroencephalography (EEG).

Resting-state EEG is used to determine the brain activity when an explicit task is not being performed (Biswal, 2012); specifically, it may detect abnormalities that are not identified using evoked potentials (Fox, 2010; Wang et al., 2013). In the present study, the resting-state spontaneous EEG activity of ASD and neurotypical individuals (controls) young adults is analyzed.

EEG microstates analysis is a well-established technique used to study the resting state of the human brain based on the topography of the electric potentials over the electrode array. The principles of this method are described by Lehman and collaborators (Lehmann et al., 1987), who observed that a specific configuration of a global scalp map (or brain state), produced by the electric field measured via multichannel EEG, remains stable for around 80–120 ms and then switches to a new brain state belonging to a limited number of dominant quasi-stable scalp map set, which were defined considering only the electrode localization of the extreme potentials (maximal and minimal), ignoring polarity inversion. The spatial cluster was introduced in the microstate analysis by Pascual-Marqui et al. (1995), where the whole scalp topography (or scalp map) is considered, instead of using only the position of the extreme potentials as in (Lehmann et al., 1987). In this approach, a group of several scalp topographies with a high spatial correlation independent of polarity are clustered into one representative topography (template map, spatial map, or cluster) that best describes the variance within this group (Pascual-Marqui et al., 1995; Michel and Koenig, 2018). The microstates are then defined by fitting the set of template maps back to the temporal data also ignoring polarity inversion.

The microstate technique offers a collection of parameters with physiological relevance that have been widely used in the last 30 years to display variations across behavioral states, personality types, and neuropsychiatric disorders (Koenig et al., 2002; Khanna et al., 2015; Michel and Koenig, 2018), which make it a suitable tool to evaluate the dissimilarities in these parameters between ASD and control subjects. Indeed, a recent study (Jia and Yu, 2019) applied the microstate analysis among the two groups in resting state (combining eyes-open and eyes-closed conditions), finding significant differences and indicating that this technique may offer some intuitions into the intrinsic activities in the autistic brain. However, the limitations stated by the authors are the large age range, involving different periods of development such as middle childhood and adolescence, and a single analysis for the combined conditions. Therefore, the goal of the current study was to compare the EEG resting-state microstates (eyes-closed condition) between neurotypicals and ASD in the early adulthood, concentrating the analysis on the four well-established temporal parameters: (1) the mean duration, (2) frequency of occurrence, (3) the fraction of total time covered, and (4) the global explained variance (GEV).

MATERIALS AND METHODS

Participants and Data Acquisition

The data set used in this analysis was obtained in a previous study. The experimental design and procedures, recording techniques, and participant data are described in more detail in Hames et al. (2016). Briefly, the EEG study had the participation of 16 neurotypical individuals (controls) and 15 autistic subjects (ASD) between the ages of 18 and 30 years. One subject in the ASD group is ambidextrous, and another from the same group is left-handed. The experiment was approved by the Human Subjects Internal Review Board at Texas Tech University, with written informed consent from all participants, in accordance with the Declaration of Helsinki. The study presented by Hames et al. (2016) consists of two sessions of different sensory tasks and one resting state (eyes closed). In this work, only the latter is considered for the EEG microstate analysis.

During the EEG resting-state recording, subjects were sitting in a comfortable upright position in a soundproof and electrical-shielded room. Participants were asked to stay as calm as possible, keeping their eyes closed for a time varying between 2 and 4 min. The EEG was acquired with a 65-channel monopolar EGI Hydrocel Geodesic Sensor using a sampling rate of 500 Hz (Electrical Geodesics Inc., Eugene, United States) with a vertex reference.

EEG Data Processing

The preprocessing is carried out using a combination of MATLAB R2017b (The MathWorks) and the free academic software Cartool[1] (Brunet et al., 2011). Microstate analysis is performed using only Cartool.

Preprocessing

The EEG data were band-pass filtered with half-power cutoff frequencies of 1 and 50 Hz applying a fourth-order non-causal Butterworth filter. The data were then visually inspected to detect and mark artifacts and bad epochs manually. Independent component analysis (ICA) was employed to identify and reject components associated with oculomotor activity and electrocardiography (ECG), as explained in Jung et al. (2000) and Makeig et al. (1996), corresponding to their waveform and topography. Only subjects with a number of samples greater than 20 times the number of channels squared (to obtain reliable decompositions) (Delorme and Makeig, 2004), after the visual inspection was performed, were considered in the ICA stage, reducing the number of participants to 13 neurotypicals and 10 ASD. The data were then down-sampled by a factor of 4 to 125 Hz to reduce computational time.

Cartool's built-in spatial filtering function, which is based on the XYZ electrode coordinates (obtained from the manufacturer),

[1]https://sites.google.com/site/cartoolcommunity/

was used to smooth the EEG signals and topographies for the posterior analysis. Finally, segments of ± 0.5 s around peaks with amplitudes above 100 μV, which are more associated with artifactual components rather than neural activity, were excluded from further analysis.

Microstate Analysis

In general, microstate analysis consists of finding the set of the most dominant spatial maps (or template maps) from the different scalp topographies in the time domain, and then, the posterior labeling of the EEG data based on these dominant template maps. Therefore, after preprocessing the data, the stages involved in the microstate analysis are (1) segmentation of EEG data to find the most representative template maps, which correspond to the different classes, and (2) fitting these classes back to the EEG data to compute the temporal parameters and statistics. **Figure 1** describes both stages with detailed steps.

In this work, the segmentation stage was carried out by running a two-step spatial cluster analysis, illustrated in **Figures 1A–G**, based on a modified version of the classical k-means algorithm (Pascual-Marqui et al., 1995), with the first step being run at the individual level (for each participant separately) (see **Figures 1A–E**) and the second step across all subjects (see **Figures 1F,G**; Murray et al., 2008; Tomescu et al., 2014; Gschwind et al., 2016). Although additional techniques are available to compute the segmentation stage (Poulsen et al., 2018; Von Wegner et al., 2018), a recent study reported that the underlying dynamics of the EEG signal seem to be independent of the initial clustering algorithm (Von Wegner et al., 2017, 2018).

To find each subject's most dominant template maps, the global field power (GFP) was calculated for each sample time according to Equation (1), where N is the number of sensors in each scalp map, u_i is the voltage at a specific electrode, and $\bar{u}$ is the average voltage of the electrodes at the respective sample time.

$$GFP = \sqrt{\frac{\sum_{i=1}^{N} (u_i - \bar{u})^2}{N}} \quad (1)$$

The GFP is a reference-free measure that represents the field strength at a global level (Lehmann and Skrandies, 1980). The local peaks of the artifact-free GFP curve represent moments of high global neuronal synchronization (Skrandies, 2007) and the scalp topographies around them remain stable, maximizing the signal-to-noise ratio (SNR) (Koenig et al., 2002; Michel et al., 2009; Michel and Koenig, 2018). The scalp maps at sample times with a local GFP maximum (see **Figure 1C**) were submitted to a spatial k-means clustering algorithm to determine a subject's most dominant template maps ignoring polarity inversion (see **Figure 1E**). The number of the dominant clusters was selected by a meta-criterion method described by Custo et al. (2017), which applies the information of seven different criteria from the literature.

To accomplish the second step in the two-step spatial cluster analysis, the dominant template maps for all subjects (ASD and controls) were submitted together to a spatial k-means group-cluster analysis to find the most representative maps across subjects, also denoted as classes. The number of classes was selected also ignoring polarity inversion based on the same meta-criterion as in step 1, resulting in the six microstate classes shown in **Figure 1G**.

Once the microstate classes were identified, they were fitted back to the individual EEG data in the temporal domain to define the microstates, as follows: each time frame (or sample point) of the original data was labeled with one microstate, considering the highest spatial correlation between the instantaneous scalp topography and every microstate class (winner-takes-all) (Murray et al., 2008; Michel and Koenig, 2018), but only if its correlation was above 0.5. In the fitting process, other temporal smoothing parameters such as strength 10 on a window half-size 3 [Besag factor $\lambda = 10$ and $b = 3$ in (Pascual-Marqui et al., 1995)] were applied to avoid interruptions in the EEG sequence associated with the same microstate. The microstate sequence is displayed color-coded in **Figure 1H**, and it is used, for every subject, to compute the different temporal parameters and the statistical analysis.

Temporal Parameters and Statistical Analysis

The six microstate classes (A, B, C, D, E, and F) were computed considering the cluster analysis throughout all subjects to be able to compare the statistics between the ASD and controls, calculating the following temporal parameters for each class and every participant:

- Mean duration: This refers to the average duration, in milliseconds, that a microstate class is continuously presented.
- Frequency of occurrence: This indicates how often a microstate class is present per time interval and independent of the duration and is computed by taking the number of segments labeled with a microstate class divided by the total duration in seconds of the analyzed EEG.
- Fraction of time covered: This represents the proportion of the total time a microstate is present during the whole time considered for analysis.
- GEV: This parameter gives a metric of how well the selected template maps describe the whole dataset, calculated for a specific microstate class by summing the squared spatial correlations between the microstate specific template map and its corresponding labeled scalp maps at each time weighted by the GFP using Equation (2) (Murray et al., 2008) as follows: $GFP_u\,(t)$ is the GFP of the EEG data assigned to microstate class u at the labeled time t, and C_{u,T_t} corresponds to the spatial correlation previously described.

$$GEV_u = \frac{\sum_{t=1}^{t\ max} \left(GFP_u\,(t) \cdot C_{u,T_t}\right)^2}{\sum_{t=1}^{t\ max} \left(GFP_u^2\,(t)\right)} \quad (2)$$

The statistical analysis was performed using R version 3.4.3 (The R Foundation for Statistical Computing, 2017). Separate *post hoc* two-tailed Mann–Whitney–Wilcoxon tests

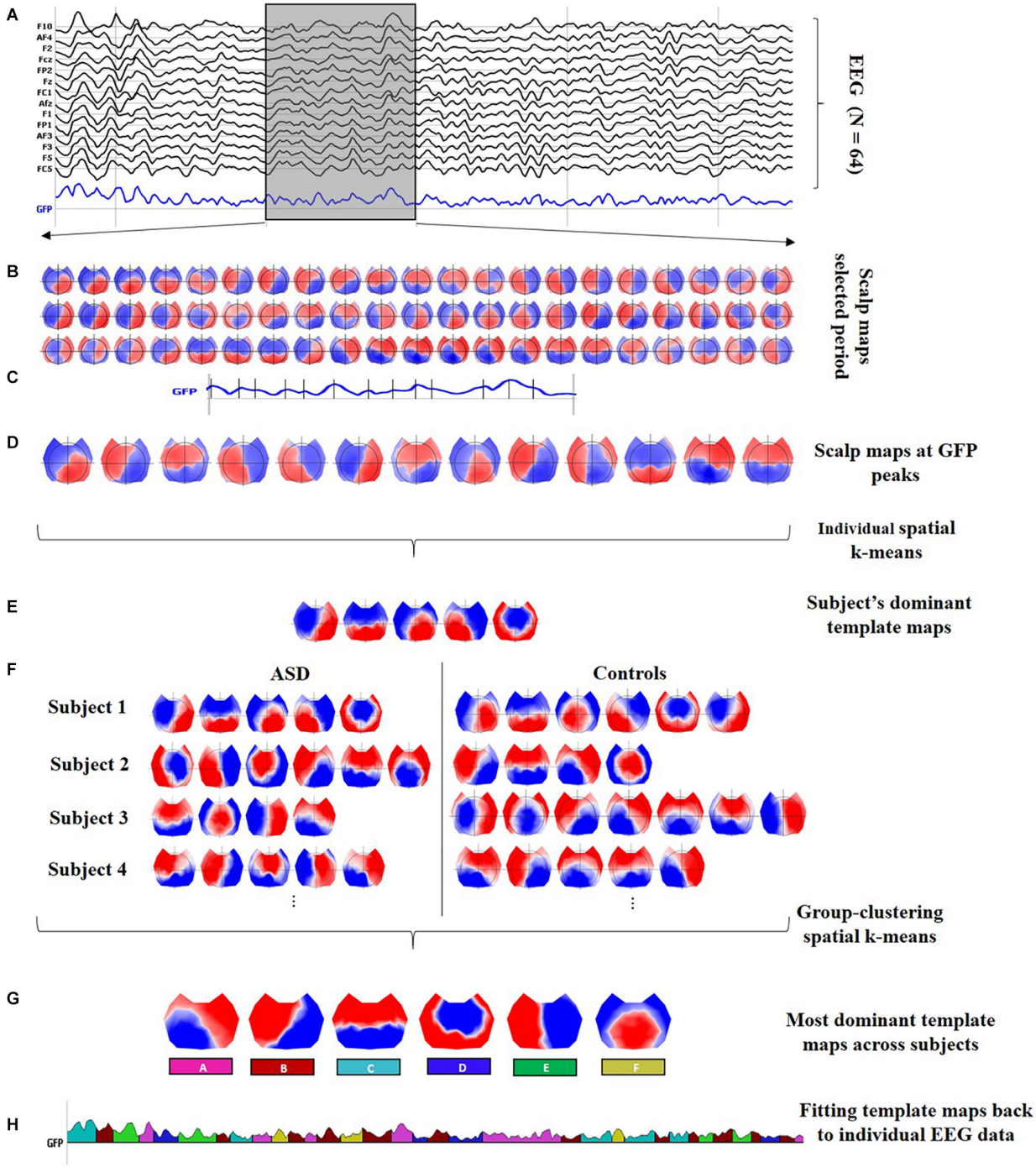

FIGURE 1 | Microstate analysis. **(A)** Preprocessed EEG recordings down-sampled at 125 Hz, illustrating 2 s of data for one subject (vertical gray lines represent intervals of 0.5 s). Black curves correspond to 14 out of the *N* = 64 channels; the blue curve shows the global field power (GFP). Moreover, a 0.5-s interval is highlighted in the gray shaded area to display a zoom-in of the topographical data. **(B)** Sixty-three scalp maps from the 0.5-s interval, i.e., one per time frame. **(C)** Identification of the local peaks, displayed as vertical black lines, at the GFP curve within the 0.5-s interval. **(D)** The scalp maps corresponding to the local GFP peaks were submitted to a spatial k-means cluster analysis. **(E)** The most dominant template maps for the subject were selected based on the meta-criterion. **(F)** Steps **(A)** to **(E)** were repeated at individual level to obtain the set of the most dominant spatial maps for every subject. The individual sets with the dominant spatial maps for all subjects were submitted together to a group clustering analysis. **(G)** The six classes are the most dominant template maps after the group clustering spatial k-means across all subjects. The number of clusters was selected based on the meta-criterion. **(H)** A microstate sequence for the same subject as in **(A)**. The six classes are fitted back to the original EEG data of every subject, labeling each time frame with only one microstate, which is selected considering the highest spatial correlation between the scalp topography and every class (winner-takes-all). The microstate sequence is used, for every subject, to extract the temporal parameters and statistical analysis.

were conducted pairwise between the two groups for each microstate class in every temporal parameter to identify statistically significant differences. Subsequently, the results were corrected for multiple comparisons by applying the false discovery rate (FDR), setting the significance at a 5% level ($\alpha = 0.05$).

RESULTS

The first step in the two-step spatial cluster analysis identified between four and seven template maps, selected by the meta-criterion method, for each subject as illustrated in **Figure 1F**. The second step (group cluster) was firstly performed for each group separately to compare the different topographies. Based on the meta-criterion, the number of clusters that best described the dataset was seven for controls and six for ASD. Similarly, when the grand-clustering was run across all subjects, the best number of dominant maps was six. **Figure 2A** illustrates the GEV as a function of the number of maps when the group-cluster analysis was implemented only in autistics (blue curve), controls (red curve), and all subjects (black curve). As illustrated, considering the same number of maps, until eight, the GEV was slightly higher for the neurotypicals. **Figure 2B** depicts the six template maps that described more than 80% of the global variance in all three cases, following the same three approaches, i.e., all subjects (top row), only ASD (middle row), and controls (bottom row).

Since the resulting template maps showed high similarity regardless of the approach, the selected temporal parameters are computed using the same six topographies obtained from all subjects for both groups to enable direct comparisons. Separate two-tailed Mann–Whitney–Wilcoxon tests were performed pairwise between ASD and controls for each microstate class in every temporal parameter to identify statistically significant differences and then corrected for multiple comparisons by applying the FDR.

Table 1 is divided into four major sections to illustrate the results of the microstate analysis. Each division, containing four rows, is labeled with the respective temporal parameter, summarizing the mean values and the standard deviation of every microstate class (the six columns) for the ASD and control groups in the first and second row, respectively; the p-value (pairwise) and the corrected p-value for multiple comparisons are displayed in the third and fourth row, respectively. The statistically significant differences ($p < 0.05$) in the last two rows are marked with an asterisk. It was observed that microstate classes B, C, and E exhibited significant group differences in some of the temporal parameters after the pairwise comparison, but only classes B and E demonstrated statistical significance at a 5% level after the correction for multiple comparisons.

- Microstate class A did not exhibit significant differences in any of the four temporal parameters (p-pairwise > 0.7; p-corrected > 0.7). However, it was the only class in which the parameters did not display a consistently increased presence in a specific group.
- Microstate class B illustrated a consistently higher presence in ASD, showing statistically significant differences, before or after correction for multiple comparisons, in the frequency of occurrence (p-pairwise = 0.008; p-corrected = 0.030), ratio of time coverage (p-pairwise = 0.021; p-corrected = 0.063), and GEV (p-pairwise = 0.018; p-corrected = 0.054).
- Microstate C was the only class that displayed a consistently higher presence in controls, showing statistically significant differences, before or after correction for multiple comparisons, in the main duration (p-pairwise = 0.026; p-corrected = 0.156), ratio of time coverage (p-pairwise = 0.042; p-corrected = 0.084), and GEV (p-pairwise = 0.049; p-corrected = 0.098). Furthermore, class C was systematically the most dominant in each group.
- Microstate class D exhibited a consistently increased presence in ASD, but without statistically significant differences (p-pairwise > 0.13; p-corrected > 0.26).
- Microstate class E displayed an increased presence in ASD, showing statistically significant differences, before or after correction for multiple comparisons, in the frequency of occurrence (p-pairwise = 0.010; p-corrected = 0.030), ratio of time coverage

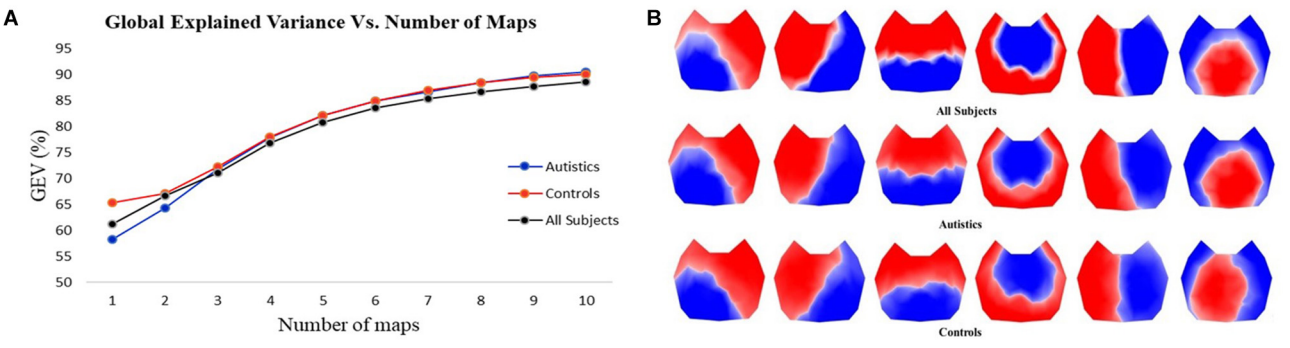

FIGURE 2 | (A) GEV vs. number of template maps using three different approaches in the cluster analysis: considering only autistics (blue curve), only controls (red curve), and all subjects (black curve). **(B)** Template topographies of the six classes of microstates using three approaches: all subjects (top row), autistics (middle row), and controls (bottom row).

TABLE 1 | Temporal parameters in the microstate analysis of the ASD and control groups.

	Microstate classes					
	Class A	**Class B**	**Class C**	**Class D**	**Class E**	**Class F**
Mean duration [milliseconds]						
ASD (mean ± SD)	76.29 ± 6.08	80.60 ± 4.45	87.16 ± 8.67	77.59 ± 6.94	74.26 ± 5.21	75.17 ± 6.23
Controls (mean ± SD)	78.79 ± 6.54	76.40 ± 7.70	103.35 ± 19.40	74.71 ± 11.76	71.87 ± 10.89	74.18 ± 7.29
P-value (pairwise)	0.738	0.077	0.026*	0.410	0.115	0.446
Corrected *P*-value	0.738	0.230	0.156	0.535	0.230	0.535
Freq. of occurrence [counts/second]						
ASD (mean ± SD)	1.73 ± 0.36	2.10 ± 0.41	2.24 ± 0.47	1.81 ± 0.38	1.33 ± 0.38	1.58 ± 0.46
Controls (mean ± SD)	1.71 ± 0.43	1.60 ± 0.40	2.54 ± 0.60	1.50 ± 0.64	1.01 ± 0.60	1.49 ± 0.47
P-value (pairwise)	0.927	0.008*	0.186	0.131	0.010*	0.522
Corrected *P*-value	0.927	0.030*	0.279	0.262	0.030*	0.626
Ratio of time coverage						
ASD (mean ± SD)	0.152 ± 0.043	0.196 ± 0.046	0.232 ± 0.075	0.162 ± 0.046	0.111 ± 0.038	0.138 ± 0.049
Controls (mean ± SD)	0.157 ± 0.050	0.142 ± 0.044	0.345 ± 0.137	0.136 ± 0.083	0.088 ± 0.082	0.128 ± 0.053
P-value (pairwise)	0.976	0.021*	0.042*	0.208	0.008*	0.446
Corrected *P*-value	0.976	0.063	0.084	0.312	0.048*	0.535
Global explained variance (GEV)						
ASD (mean ± SD)	0.077 ± 0.029	0.102 ± 0.035	0.156 ± 0.076	0.078 ± 0.024	0.055 ± 0.027	0.060 ± 0.026
Controls (mean ± SD)	0.081 ± 0.040	0.064 ± 0.026	0.274 ± 0.140	0.061 ± 0.044	0.038 ± 0.038	0.055 ± 0.029
P-value (pairwise)	0.976	0.018*	0.049*	0.131	0.010*	0.483
Corrected *P*-value	0.976	0.054	0.098	0.197	0.054	0.580

The p-value (pairwise) row corresponds to the result of the pairwise post-hoc Mann–Whitney–Wilcoxon tests. The corrected p-value row was obtained by applying the false discovery rate (FDR) correction for multiple comparisons. Statistically significant differences ($p < 0.05$) after the tests are marked with an asterisk.

(p-pairwise = 0.008; p-corrected = 0.048), and GEV (p-pairwise = 0.010; p-corrected = 0.054). Furthermore, class E was systematically the least dominant in each group.

- Microstate class F illustrated a consistently higher presence in ASD, but without statistically significant differences (p-pairwise > 0.44; p-corrected > 0.53).

DISCUSSION

In this study, we applied the microstate analysis to investigate the differences in four temporal parameters (mean duration, frequency of occurrence, time coverage, and GEV) between 10 autistic and 13 neurotypical young adults in resting state (eyes closed) data. We found that the EEG microstates lasted, on average, for around 75–105 ms, which is in line with the duration reported by different literature reviews (Khanna et al., 2015; Michel and Koenig, 2018).

The two-step cluster analysis combined with the meta-criterion revealed that six template maps best described the entire dataset explaining ∼83% of the global variance. Among these six topographies, it is possible to match the first four maps with the canonical microstates reported in different literature reviews (Khanna et al., 2015; Michel and Koenig, 2018) (classes A, B, C, and D); the other two maps also correspond to classes E and F reported in Bréchet et al. (2019) and Custo et al. (2017). Moreover, considering the four canonical topographies, ∼76% of the global variance is explained. Although predetermining the number of microstates, e.g., to four for the four canonical maps, has shown stable topography maps and is useful to compare or complement results across different studies, we believe that there is not a correct fixed number of classes, and it has been recommended that the number of clusters should be determined specifically for every dataset, based on the explained global variance and functionality, which depends on the conditions within the experiments (Michel and Koenig, 2018).

For the temporal parameters analyzed, microstates C and E were systematically the most and least dominant classes, respectively, during the eyes-closed resting-state analysis. Furthermore, classes B, C, and E exhibited significant group differences in some of the parameters after the pairwise comparison, but only B and E demonstrated statistical significance at a 5% level after the correction for multiple comparisons. However, note that the FDR correction might yield to conservative results, and therefore, the physiological relevance of microstate C is also considered.

Although microstate A did not exhibit any statistically significant difference, interestingly, it was the only class in which the temporal parameters did not display a consistently higher occurrence in a specific group, that is, despite having an increased frequency of occurrence in ASD, the mean duration, GEV, and time coverage were higher in the controls. These results are in line with the study conducted by Jia and Yu (2019), but

the authors reported a significant difference in this class. This discrepancy might be mainly due to the key differences between the two studies: age range and the combination of eyes-open and eyes-closed conditions incorporated Jia and Yu (2019). However, according to Tomescu et al. (2018), the development of microstate class A across age does not reveal a statistically significant difference in neurotypical subjects; still, this has not been explored in ASD yet.

Microstate class B displayed a systematically higher presence in the ASD group, being consistent with the results reported in Jia and Yu (2019). Specifically, it illustrated a significant higher frequency of occurrence than the control group. However, the ratio of time coverage and GEV also exhibited statistically significant differences between both groups after the Mann–Whitney–Wilcoxon pairwise tests (see **Table 1**). Microstate B has been related to the visual network in resting-state (Britz et al., 2010) and verbal processing (Milz et al., 2016). Consequently, the increased frequency of occurrence and time coverage in the ASD might be due to their enhanced inter-network connectivity reported in Morgan et al. (2019). Particularly, the authors reported a significant increased functional connectivity between the language (LAN) and visual (VIS) networks in resting-state fMRI, which is associated with the communication impairment that characterizes ASD. Moreover, a recent study (Bréchet et al., 2019) associates this class with the *scene-reconstruction subsystem*. Therefore, the combination of these findings with the higher presence of this class observed in the ASD group in this work indicates that autistics were more engaged with visual scene-reconstruction memories during resting state.

Microstate class C has a systematically larger occurrence in the temporal parameters for both groups, and it is expected to decrease during visualization (Milz et al., 2016). Additionally, it was the only class that exhibited a higher presence for all the temporal parameters in the control group. However, the significant differences obtained by applying the Mann–Whitney–Wilcoxon pairwise tests in the mean duration, frequency of occurrence, and GEV were not significant at the 5% level after the FDR correction. According to some authors (Michel and Koenig, 2018), microstate class C reflects a portion of the default mode network (DMN), a network where the brain areas involved decrease their activity during attention-demanding tasks (Raichle et al., 2001; Raichle, 2015). This hypothesis is consistent with the observations made by Custo et al. (2017) where the underlying sources associated with microstate C overlap a portion of the DMN, and the significant reduction observed in math conditions (Bréchet et al., 2019) and visualization (Milz et al., 2016) when compared to resting state. The higher presence of microstate class C in the control group might be addressed from the functional perspective. Some studies have found a hypo-connectivity in the posteromedial cortex in ASD (Lynch et al., 2013; Bi et al., 2018), and more importantly, the connectivity within the DMN not only helps in differentiating between ASD and neurotypicals (Assaf et al., 2010; Yao et al., 2016; Morgan et al., 2019) but also might explain the ASD social impairment due to the decreased functional connectivity between the precuneus and medial prefrontal cortex/anterior cingulate cortex (Assaf et al., 2010; Yao et al., 2016), which are regions associated with the resting-state networks in microstate class C (Britz et al., 2010).

A recent study (Bréchet et al., 2019) investigated the resting state compared to conditions of cognitive tasks involving self-related memories (memory condition) and arithmetic calculations (math condition). The study reported that compared to resting state, there is a significant reduction in the incidence of microstate C for the math condition, and no statistically significant difference in the presence of microstate C for memory conditions. Hence, the increased presence of class C in the control group could also imply that the neurotypicals were more focused on self-memory retrieval during the resting state.

Microstate class E was systematically the least dominant in the four temporal parameters analyzed, showing a significant difference between both groups in the frequency of occurrence and time coverage. Very few studies have reported the microstate E presence (Custo et al., 2017; Serrano et al., 2018; Wei et al., 2018; Bréchet et al., 2019), and its functional significance has not been explored. However, the brain regions associated with microstate E reported in Bréchet et al. (2019) and Custo et al. (2017) include the anterior cingulate cortex (ACC), which is also a brain area implicated, among others, in the repetitive behaviors in ASD (Amaral et al., 2008).

The EEG microstates analysis technique is applied over a broad frequency band. The presence and interpretation of microstate classes within narrower frequency bands and the relationship of these states to EEG rhythms, while outside of the scope of the research presented here, are an important topic and a worthy focus of future research to evaluate the impact on the different temporal parameters.

CONCLUSION

The main purpose of this study was to compare the EEG resting state between neurotypicals and ASD young adults applying microstate analysis, focusing on the analysis of mean duration, the frequency of occurrence, the ratio of time coverage, and the GEV. The grand-cluster analysis revealed that across all subjects, six template maps best described the complete dataset with ∼83% of the global variance. We suggest that unless a study is aimed to compare or complement previous reports, the number of microstates classes should be selected for each dataset individually, considering the explained global variance and the significance of the classes, depending on the conditions within the experiment.

We performed this study considering resting state only, finding important differences between both groups, and these results should be contemplated as a reference for further assessments comparing the different classes and both groups under task-oriented experiments. Specifically, (1) since microstate class C was the only one that exhibited a consistently increased incidence in controls, it would be interesting to quantify the decreasing presence compared to the ASD group once the subjects start being cognitively engaged, and (2) evaluate if microstate class E is still present under certain types of tasks.

DATA AVAILABILITY

The datasets generated for this study are available on request to the corresponding author.

ETHICS STATEMENT

The experiment was approved by the Human Subjects Internal Review Board at Texas Tech University. All subjects gave written informed consent in accordance with the Declaration of Helsinki.

AUTHOR CONTRIBUTIONS

DD-B and MB contributed to the conception of the study. MB provided the database and provided expertise on autism. DD-B conducted the pre-processing of the data, ran the microstates analysis and statistical tests, and wrote the initial draft of the manuscript. TK provided expertise on digital signal processing and reviewed the pre-processing stage and statistical analysis. MB and CM provided expertise on EEG signal analysis. DD-B and CM provided the functional significance of the microstates. MB, CM, and TK critically revised the different drafts, providing valuable feedback in all of them. All authors contributed to the interpretation of the results and manuscript revision, and read and approved the submitted version.

FUNDING

This research was funded in part by a private donor grant from Allen and Linnie Howard.

ACKNOWLEDGMENTS

We would like to acknowledge and thank the Howards for their generous contribution.

REFERENCES

Amaral, D. G., Schumann, C. M., and Nordahl, C. W. (2008). Neuroanatomy of autism. *Trends Neurosci.* 31, 137–145. doi: 10.1016/j.tins.2007.12.005

American Psychiatric Association (2013). *Diagnostic and Statistical Manual of Mental Disorders*, 5th edn. Washington, DC: APA.

Assaf, M., Jagannathan, K., Calhoun, V. D., Miller, L., Stevens, M. C., Sahl, R., et al. (2010). NeuroImage abnormal functional connectivity of default mode sub-networks in autism spectrum disorder patients. *Neuroimage* 53, 247–256. doi: 10.1016/j.neuroimage.2010.05.067

Bi, X., Zhao, J., Xu, Q., Sun, Q., and Wang, Z. (2018). Abnormal functional connectivity of resting state network detection based on linear ICA analysis in autism spectrum disorder. *Front. Physiol.* 9:475. doi: 10.3389/fphys.2018.00475

Billeci, L., Sicca, F., Maharatna, K., Apicella, F., Narzisi, A., Campatelli, G., et al. (2013). On the application of quantitative eeg for characterizing autistic brain: a systematic review. *Front. Hum. Neurosci.* 7:442. doi: 10.3389/fnhum.2013.00442

Biswal, B. B. (2012). Resting state fMRI: a personal history. *Neuroimage* 62, 938–944. doi: 10.1016/j.neuroimage.2012.01.090

Bréchet, L., Bunet, D., Birot, G., Gruetter, R., and Michel, C. M. (2019). NeuroImage capturing the spatiotemporal dynamics of self-generated, task-initiated thoughts with EEG and fMRI. *Neuroimage* 194, 82–92. doi: 10.1016/j.neuroimage.2019.03.029

Britz, J., Van DeVille, D., and Michel, C. M. (2010). BOLD correlates of EEG topography reveal rapid resting-state network dynamics. *Neuroimage* 52, 1162–1170. doi: 10.1016/j.neuroimage.2010.02.052

Brunet, D., Murray, M. M., and Michel, C. M. (2011). Spatiotemporal analysis of multichannel EEG: CARTOOL. *Comput. Intel. Neurosci.* 2011:813870. doi: 10.1155/2011/813870

Centers for Disease Control and Prevention, Autism Spectrum Disorder [ASD] (2018). *Data & Statistics on Autism Spectrum Disorder*. Available at: https://www.cdc.gov/ncbddd/autism/data.html (accessed October 18, 2018).

Custo, A., Ville, D., Van De Wells, W. M., Tomescu, M. I., Brunet, D., et al. (2017). Electroencephalographic resting-state networks. *Brain Connect.* 7, 671–682. doi: 10.1089/brain.2016.0476

Delorme, A., and Makeig, S. (2004). EEGLAB: an open sorce toolbox for analysis of single-trail EEG dynamics including independent component anlaysis. *J. Neurosci. Methods* 134, 9–21. doi: 10.1016/j.jneumeth.2003.10.009

Fox, M. D. (2010). Clinical applications of resting state functional connectivity. *Front. Syst. Neurosci.* 4:19. doi: 10.3389/fnsys.2010.00019

Gschwind, M., Hardmeier, M., Van De Ville, D., Tomescu, M. I., Penner, I. K., Naegelin, Y., et al. (2016). Fluctuations of spontaneous EEG topographies predict disease state in relapsing-remitting multiple sclerosis. *NeuroImage Clin.* 12, 466–477. doi: 10.1016/j.nicl.2016.08.008

Hames, E. C., Murphy, B., Rajmohan, R., Anderson, R. C., Baker, M., Zupancic, S., et al. (2016). Visual, auditory, and cross modal sensory processing in adults with autism: an EEG power and BOLD fMRI investigation. *Front. Hum. Neurosci.* 10:167. doi: 10.3389/fnhum.2016.00167

Jia, H., and Yu, D. (2019). Aberrant intrinsic brain activity in patients with autism spectrum disorder: insights from EEG microstates. *Brain Topogr.* 32, 295–303. doi: 10.1007/s10548-018-0685-0

Jung, T.-P., Makeig, S., Humphries, C., Lee, T., McKeown, M. J., Iragui, I., et al. (2000). Removing electroencephalographic aretfacts by blind source seperation. *Psychophysiology* 37, 163–178. doi: 10.1111/1469-8986.3720163

Khanna, A., Pascual-Leone, A., Michel, C. M., and Farzan, F. (2015). Microstates in resting-state EEG: current status and future directions. *Neurosci. Biobehav. Rev.* 49, 105–113. doi: 10.1016/j.neubiorev.2014.12.010

Koenig, T., Prichep, L., Lehmann, D., Sosa, P. V., Braeker, E., Kleinlogel, H., et al. (2002). Millisecond by millisecond, year by year: normative EEG microstates and developmental stages. *Neuroimage* 16, 41–48. doi: 10.1006/nimg.2002.1070

Lehmann, D., Ozaki, H., and Pal, I. (1987). EEG alpha map series: brain micro-states by space-oriented adaptive segmentation. *Electroencephalogr. Clin. Neurophysiol.* 67, 271–288. doi: 10.1016/0013-4694(87)90025-3

Lehmann, D., and Skrandies, W. (1980). Reference-free identification of components of checkerboard-evoked multichannel potential fields. *Electroencephalogr. Clin. Neurophysiol.* 48, 609–621. doi: 10.1016/0013-4694(80)90419-8

Lynch, C. J., Uddin, L. Q., Supekar, K., Khouzam, A., Phillips, J., and Menon, V. (2013). Default mode network in childhood autism: Posteromedial cortex heterogeneity and relationship with social deficits. *Biol. Psychiatry* 74, 212–219. doi: 10.1016/j.biopsych.2012.12.013

Makeig, S., Bell, J., Jung, T.-P., and Sejnowski, T. J. (1996). Independent component analysis of electroencephalographic data. *Adv. Neural Inf. Process. Syst.* 8, 145–151. doi: 10.1109/ICOSP.2002.1180091

Mash, L. E., Reiter, M. A., Linke, A. C., Townsend, J., and Müller, R. A. (2018). Multimodal approaches to functional connectivity in autism spectrum disorders: an integrative perspective. *Dev. Neurobiol.* 78, 456–473. doi: 10.1002/dneu.22570

Michel, C. M., and Koenig, T. (2018). EEG microstates as a tool for studying the temporal dynamics of whole-brain neuronal networks: a review. *Neuroimage* 180, 577–593. doi: 10.1016/j.neuroimage.2017.11.062

Michel, C. M., Koenig, T., Brandeis, D., Gianotti, L. R. R., and Wackermann, J. (2009). *Electrical Neuroimaging*. Cambridge: Cambridge University Press.

Milz, P., Faber, P. L., Lehmann, D., Koenig, T., Kochi, K., and Pascual-Marqui, R. D. (2016). The functional significance of EEG microstates-associations with

modalities of thinking. *Neuroimage* 125, 643–656. doi: 10.1016/j.neuroimage.2015.08.023

Morgan, B. R., Ibrahim, G. M., Vogan, V. M., Leung, R. C., Lee, W., and Taylor, M. J. (2019). Characterization of autism spectrum disorder across the age span by intrinsic network patterns. *Brain Topogr.* 32, 461–471. doi: 10.1007/s10548-019-00697-w

Murray, M. M., Brunet, D., and Michel, C. M. (2008). Topographic ERP analyses: a step-by-step tutorial review. *Brain Topogr.* 20, 249–264. doi: 10.1007/s10548-008-0054-5

Pascual-Marqui, R. D., Michel, C. M., and Lehmann, D. (1995). Segmentation of brain electrical activity into microstates: model estimation and validation. *Biomed. Eng. IEEE Trans.* 42, 658–665. doi: 10.1109/10.391164

Poulsen, A. T., Pedroni, A., Langer, N., and Hansen, L. K. (2018). Microstate EEGlab toolbox: an introductory guide. *bioRxiv*

Raichle, M. E. (2015). The Brain's default mode network. *Annu. Rev. Neurosci.* 38, 433–447. doi: 10.1146/annurev-neuro-071013-014030

Raichle, M. E., MacLeod, A., Snyder, A. Z., Powers, W. J., Gusnard, D. A., and Shulman, G. L. (2001). A default mode of brain function. *Proc. Natl. Acad. Sci. U.S.A.* 98, 676–682. doi: 10.1073/pnas.98.2.676

Serrano, J. I., Dolores, M., Cortés, V., Mendes, N., Arroyo, A., Andreo, J., et al. (2018). EEG microstates change in response to increase in dopaminergic stimulation in typical parkinson's disease patients. *Front. Neurosci.* 12:714. doi: 10.3389/fnins.2018.00714

Skrandies, W. (2007). The effect of stimulation frequency and retinal stimulus location on visual evoked potential topography. *Brain Topogr.* 20, 15–20. doi: 10.1007/s10548-007-0026-1

The R Foundation for Statistical Computing (2017). *The R Foundation for Statistical Computing*. Available at: https://cran.r-project.org/ (accessed January 18, 2019).

Tomescu, M. I., Rihs, T. A., Becker, R., Britz, J., Custo, A., Grouiller, F., et al. (2014). Deviant dynamics of EEG resting state pattern in 22q11. 2 deletion syndrome adolescents: a vulnerability marker of schizophrenia *Schizophr. Res.* 157, 175–181. doi: 10.1016/j.schres.2014.05.036

Tomescu, M. I., Rihs, T. A., Rochas, V., Hardmeier, M., Britz, J., Allali, G., et al. (2018). From swing to cane: Sex differences of EEG resting-state temporal patterns during maturation and aging. *Dev. Cogn. Neurosci.* 31, 58–66. doi: 10.1016/j.dcn.2018.04.011

Von Wegner, F., Knaut, P., and Laufs, H. (2018). EEG microstate sequences from different clustering algorithms are information-theoretically invariant. *Front. Comput. Neurosci.* 12:70. doi: 10.3389/fncom.2018.00070

Von Wegner, F., Tagliazucchi, E., and Laufs, H. (2017). NeuroImage Information-theoretical analysis of resting state EEG microstate sequences - non-Markovianity, non-stationarity and periodicities. *Neuroimage* 158, 99–111. doi: 10.1016/j.neuroimage.2017.06.062

Wang, J., Barstein, J., Ethridge, L. E., Mosconi, M. W., Takarae, Y., and Sweeney, J. A. (2013). Resting state EEG abnormalities in autism spectrum disorders. *J. Neurodev. Disord.* 5:24. doi: 10.1186/1866-1955-5-24

Wei, Y., Ramautar, J. R., Colombo, M. A., and Lindert, B. H. W. (2018). EEG Microstates indicate heightened somatic awareness in insomnia: toward objective assessment of subjective mental content. *Front. Psychiatry* 9:395. doi: 10.3389/fpsyt.2018.00395

Yao, Z., Hu, B., Xie, Y., Zheng, F., Liu, G., Chen, X., et al. (2016). Resting-state time-varying analysis reveals aberrant variations of functional connectivity in autism. *Front. Hum. Neurosci.* 10:463. doi: 10.3389/fnhum.2016.00463

Conflict of Interest Statement: The authors declare that the research was conducted in the absence of any commercial or financial relationships that could be construed as a potential conflict of interest.

frontiers in Human Neuroscience

ORIGINAL RESEARCH
published: 14 June 2019
doi: 10.3389/fnhum.2019.00203

Characterizing and Predicting Autism Spectrum Disorder by Performing Resting-State Functional Network Community Pattern Analysis

*Yuqing Song, Thomas Martial Epalle and Hu Lu**

School of Computer Science and Telecommunication Engineering, Jiangsu University, Zhenjiang, China

Growing evidence indicates that autism spectrum disorder (ASD) is a neuropsychological disconnection syndrome that can be analyzed using various complex network metrics used as pathology biomarkers. Recently, community detection and analysis rooted in the complex network and graph theories have been introduced to investigate the changes in resting-state functional network community structure under neurological pathologies. However, the potential of hidden patterns in the modular organization of networks derived from resting-state functional magnetic resonance imaging to predict brain pathology has never been investigated. In this study, we present a novel analysis technique to identify alterations in community patterns in functional networks under ASD. In addition, we design machine learning classifiers to predict the clinical class of patients with ASD and controls by using only community pattern quality metrics as features. Analyses conducted on six publicly available datasets from 235 subjects, including patients with ASD and age-matched controls revealed that the modular structure is significantly disturbed in patients with ASD. Machine learning algorithms showed that the predictive power of our five metrics is relatively high (∼85.16% peak accuracy for in-site data and ∼75.00% peak accuracy for multisite data). These results lend further credence to the dysconnectivity theory of this pathology.

Keywords: autism spectrum disorder, resting-state connectivity analysis, community detection, machine learning, linear discriminant analysis

OPEN ACCESS

Edited by:
Tzipi Horowitz-Kraus,
Technion Israel Institute of Technology, Israel

Reviewed by:
Mingrui Xia,
Beijing Normal University, China
Weidong Cai,
Stanford University, United States
Nicha C. Dvornek,
Yale University, United States

****Correspondence:***
Hu Lu
luhu@ujs.edu.cn

Received: *20 November 2018*
Accepted: *29 May 2019*
Published: *14 June 2019*

Citation:
Song Y, Epalle TM and Lu H (2019) Characterizing and Predicting Autism Spectrum Disorder by Performing Resting-State Functional Network Community Pattern Analysis. Front. Hum. Neurosci. 13:203. doi: 10.3389/fnhum.2019.00203

1. INTRODUCTION

The study of the human brain often confronts problems arising from the brain's inherent complexity (Bullmore and Sporns, 2009). To overcome this challenge, complex network analysis methods have been extensively used in neurosciences, where the human brain is typically modeled as a network or graph whose nodes represent brain regions and edges represent the anatomical or functional interactions among them (De Vico Fallani et al., 2014). Network representation has been a promising computational model to capture the brain's topological organization as well as its dynamics (Rubinov and Sporns, 2010). Studies in this area have revealed that the human brain has a scale-free small-world topology (Eguíluz et al., 2005) with modular fragmentation and highly connected hubs (Meunier et al., 2010; Nicolini et al., 2017).

One problem eliciting interest in the analysis of resting-state functional brain networks by using complex network methods is community detection (Fortunato, 2010), which can be described as

the unsupervised discovery of subgroups of brain regions that are typically activated together and densely connected (van den Heuvel et al., 2008; Shen et al., 2010). Several studies have shown that this modular structure of the functional network reflects the anatomical and functional segregation of the human brain, with the presence of hub nodes or regions sharing numerous inter-community edges. Recent studies have suggested that community hubs are highly vulnerable to the effects of brain disorders, resulting in an altered community structure observed in several neuropsychiatric pathologies (Nicolini et al., 2017).

Previous studies using complex networks methods to the study of neurological disorders aimed to characterize the differences between normal and pathological brains. Graph theoretical metrics illustrated alterations in the resting-state functional connectome under specific neurological pathologies, including trauma (van der Horn et al., 2017), amnestic mild cognitive impairment (Chen et al., 2012), Alzheimer's disease (Supekar et al., 2008), epilepsy (Ponten et al., 2007), attention deficit/hyperactivity disorder(ADHD) (Wang et al., 2009; Ahmadlou and Adeli, 2011), and autism spectrum disorder (ASD) (Zhou et al., 2014). In addition, machine learning techniques using different types of features have been increasingly used not only to detect pathology-related alterations but also to make individual subject predictions of brain disorders (Arbabshirani et al., 2017).

ASD is typically characterized by deficits in social interaction and communication, rigid and stereotypical behaviors, and abnormal sensory processing (Rapin and Tuchman, 2008). This neurological disorder has been classified as a dysconnectivity syndrome manifesting as the disruption or abnormal integration of brain regions evidenced by changes in network properties used as diagnostic markers (Hull et al., 2016). In the task of automatically detecting ASD by using resting-state functional MRI (rsfMRI) data, different types of features, including independent component analysis (ICA) (Uddin et al., 2011) and functional connectivity among regions of interest (ROIs) (Iidaka, 2015; Plitt et al., 2015), have been used in conjunction with various machine learning algorithms, such as logistic regression, random forest, and neural network algorithms.

In this study, we compared the resting-state functional community patterns of patients with ASD and controls at the group and individual level to gain a detailed understanding of the relationship between impaired connectivity and this brain pathology. We also reconstructed the communities of each ROI and used a permutation test based on the Rand index to detect the brain regions whose community structures differ significantly between patients with ASD and controls.

In previous studies applying network community pattern analysis to research brain disorders, modularity (a complex network metric) has emerged as a *de facto* standard to quantify the alterations in the distribution of inter-community vs. intra-community edges under a specific brain disorder. Despite the increasing popularity of this single metric in community detection approaches, one common drawback of single indices is their low sensitivity and specificity (Stam and van Straaten, 2012). Autism being a complex disorder, the underlying neural phenomenon could be better captured by combined community patterns indices beyond the individual capability of single metrics. Here, we used modularity as well as other descriptive community pattern metrics drawn from the complex networks literature that have not been previously used for analysing the community structure of resting-state functional connectivity networks built from neuroimaging data. By using experimental data from 235 subjects in six publicly available datasets and validation data from 214 subjects in six additional datasets, we showed that these five community pattern metrics alone can serve as efficient single-subject predictors of autism.

2. MATERIALS AND METHODS

2.1. Datasets

Experimental data were selected from the Autism Brain Imaging Data Exchange (ABIDE), a large multisite, publicly available repository of resting-state fMRI scans, forming part of the 1000 Functional Connectomes Project (Di Martino et al., 2014). The data were downloaded from five sites: Stanford University (STA), University of Leuven Sample 1 (LV1), University of Leuven Sample 2 (LV2), Olin Institute of Living at Hartford Hospital (OLI), University of Pittsburgh, School of Medicine (PIT), and California Institute of Technology (CAL). The imaging data included technical scan parameters as well as phenotypic information of each individual. Demographic information about participants in each dataset is shown in **Table 1**; **Table S1** provides the technical details of the scans. As part of the professional and ethical protocol of the 1000 Functional Connectomes Project, all datasets have been anonymized, and no protected health information was included. Despite the availability of phenotypic information, this study did not use any of this medical or biological information to analyse group differences or predict the clinical class of individual participants.

2.2. Descriptive Community Pattern Metrics

In the last decade, community detection has become a prolific research area in complex networks and pattern recognition (Pons and Latapy, 2006; Fortunato, 2010; Epalle and Liu, 2016), with many application domains, such as social network mining (Girvan and Newman, 2002), graph visualization (Bastian et al., 2009), compression (Hernández and Navarro, 2012),

TABLE 1 | Datasets.

	ASD		Control		Age($\bar{x} \pm \sigma$)	Total
Dataset	**M/F**	**Age**	**M/F**	**Age**		***N* = 235**
STA	16/4	7.5–12.9	16/4	7.8–12.4	9.9 ± 1.5	$n = 40$
LV1	15/0	18–32	14/0	18–32	22.5 ± 3.5	$n = 29$
LV2	12/3	12.1–16.8	15/5	12.2–16.9	14.16 ± 1.42	$n = 35$
OLI	17/3	11–24	14/2	10–23	16.8 ± 3.4	$n = 36$
PIT	26/4	9.3–35.2	23/4	9.4–33.2	18.9 ± 6.8	$n = 57$
CAL	15/4	17.5–45.1	15/4	17–56.2	28.15 ± 0.41	$n = 38$

M, male; F, female; $\bar{x}$, mean; σ, standard deviation.

parallel computing (Ngonmang et al., 2012), and recommender systems (Liben-Nowell and Kleinberg, 2007). In neuroscience, community detection has been applied as an important step in resolving more complex problems, such as localizing network alterations in specific brain disorder (Lerman-Sinkoff and Barch, 2016). In this subsection, we introduce the basic mathematical notations for community detection and review modularity as well as four other metrics used to describe community structure in graphs.

A network or graph $G = (V, E)$ is composed of a set of nodes V and a set of edges E. In this study, the nodes V, representing brain regions, are labeled $1, 2, 3..., N$, with $N = 90$. If an edge (x, y) is in E, then node x is connected to node y. If G is undirected and unweighted, the adjacency matrix A of G is the matrix of 0s and 1s such, that $A_{xy} = 1$ if and only if $(x, y) \in E$. Community detection, being a clustering of G, can be defined as a partition of V into the sets $V_1, ..., V_K$ such that $V_1 \cup ... \cup V_K = V$, and $V_i \cap V_j = \emptyset$ for any $i \neq j$, with none of the V_i being empty. The sets $V_1, ...V_K$ are called communities or clusters. Any partition $\mathbf{V} = \{V_1, ..., V_K\}$ is a community structure or community pattern of a network with $K = |\mathbf{V}|$ communities.

Community patterns are commonly described in terms of quality functions, which depend on both the graph G and the partition $\mathbf{V}$ and whose optimization is typically believed to yield the best community pattern. However, these metrics can be considered as descriptive of a network's modular organization, rather than true performance metrics, because they do not provide strict quantitative criteria for more and less optimal partitioning (Steinhaeuser and Chawla, 2010).

In this study, we investigated the community organization of resting-state functional brain networks in ASD by using the following descriptive metrics:

2.2.1. Modularity

Modularity (Q) is the most popular community characterization metric in the literature. In a network $G = (V, E)$ and a partition $\mathbf{V} = \{V_1, ..., V_K\}$, the edges of G can be grouped into community bridge sets B_{ij} as follows: $(x, y) \in B_{kl}$ if and only if $x \in V_k$ and $y \in V_l$. In particular, we note $B_k^i = B_{kk}$ as the set of internal edges of V_k having all their ends in the same community; we note $B_k^e = \cup_{k \neq l} B_{kl}$ as the set of external edges of V_k having one end in V_k and the other in $\mathbf{V} - V_k$. By using these notations, a network's modularity is defined as

$$Q(G, \mathbf{V}) = \sum_{k=1}^{K} \left(\frac{2|B_k^i|}{2m} - (\frac{m_k}{2m})^2 \right), \quad (1)$$

where $m_k = \sum_{x \in V_k} \sum_{y \in V} A_{xy}$ is the total degree of community V_k and m the total number of edges in the network.

The four other community pattern metrics which were first introduced in (Mitalidis et al., 2014) have so far received little attention from the scientific community probably because they were proposed after the publication of two authoritative review articles on complex network measures of brain connectivity (Bullmore and Sporns, 2009); (Rubinov and Sporns, 2010).

2.2.2. Global Density

The global density community quality function (not to be confused with the popular density metric) is defined as

$$Q_{GD}(G, \mathbf{V}) = \frac{1}{2}[Q_{GD}^i(G, V) + 1 - Q_{GD}^e(G, V)], \quad (2)$$

where

$$Q_{GD}^i(G, \mathbf{V}) = \frac{\sum_{k=1}^{K} \sum_{x \in V_k} \sum_{y \in V_k} A_{xy}}{\sum_{k=1}^{K} |V_k|^2}$$

represents the global internal density and

$$Q_{GD}^e(G, \mathbf{V}) = \frac{\sum_{k=1}^{K} \sum_{x \in V_k} \sum_{y \in V - V_k} A_{xy}}{\sum_{k=1}^{K} |V_k| * |V - V_k|}$$

represents the global external density. This formula assumes that $A_{xx} = 1$ for all $x \in V$, and all other edges are counted twice. $Q_{GD}(G, \mathbf{V})$ takes values in [0,1], where the value 1 is assigned only to graphs with perfect community structure.

2.2.3. Local Density

The local density quality function is defined as

$$Q_{LD}(G, \mathbf{V}) = \sum_{k=1}^{K} \frac{|V_k|}{2|V|} * [q^i(V_k, G) + 1 - q^e(V_k, G)], \quad (3)$$

where the local inner and outer densities are, respectively, defined as

$$q^i(V_k, G) = \frac{\sum_{x \in V_k} \sum_{y \in V_k} A_{xy}}{|V_k|^2}$$

and

$$q^e(V_k, G) = \frac{\sum_{x \in V_k} \sum_{y \in V - V_k} A_{xy}}{|V_k| * |V - V_k|}.$$

Q_{LD} is defined slightly differently than is Q_{GD}, but both are based on the idea of communities being formed by subsets of nodes that are more densely connected with each other than externally. Q_{LD} also takes values in [0,1].

2.2.4. Distance-Based Metric

The distance-based community quality function is defined as

$$Q_{DB}(G, \mathbf{V}) = \frac{1}{|V|^2} ||A_G - A_V||, \quad (4)$$

where $||B|| = \sum_{x \in V} \sum_{y \in V} |B_{xy}|$ is a matrix norm, A_G is the adjacency matrix of G, and $A_{V_{xy}} = 1$ if x, y belongs to the same cluster (under V), whereas $A_{V_{xy}} = 0$ if x, y belongs to different clusters (under V). Q_{DB} takes values in [0,1], but unlike with the other metrics, the value 0 is obtained for graphs exhibiting a perfect community structure.

2.2.5. Node Membership Metric

The node membership community quality function is defined as follows:

$$Q_{NM}(G, \mathbf{V}) = \frac{1}{2|V|} \sum_{x \in V} [\mu(x, V[x]) + 1 - \mu(x, V - V[x])]. \quad (5)$$

$V[x]$ indicates the cluster to which x belongs and node membership is defined by

$$\mu(x, U) = \frac{1}{|U|} \sum_{y \in U} A_{xy}.$$

Hence, $\mu(x, U) = 1$ if and only if x is connected to every $y \in U$ and $\mu(x, U) = 0$ if and only if x is connected to no $y \in U$; for intermediate situations, we obtain $\mu(x, U) \in]0, 1[$.

Brain's functional connectivity networks are known to be fundamentally modular. The neuronal regions within a community cluster have strong interconnections among themselves and weak interdependencies with neuronal regions outside the cluster. Modularity, global density, local density, distance-based, and node membership metrics try to quantify the quality of assignment of regional nodes into cohesive subgroups or neural functions. All these metrics take values between 0 and 1. A low value of the distance-based metric and a high value of the four other metrics indicate that connections between regions within community clusters are dense, and connections between regions in different community clusters are sparse. An advantage of these five community pattern metrics is that they can all be computed based solely on the connectivity of the graph. **Figure 1** provides an illustration of how these metrics are computed for a particular community partitioning of the popular Zachary Karate's club network (Zachary, 1977).

Several prior studies have investigated the modular structure of resting-state structural and functional connectivity networks derived from MRI in autistic patients compared to healthy individuals. For instance, Rudie and coauthors used the Louvain algorithm (Blondel et al., 2008) to partition the brain into functional subsystems (Rudie et al., 2013). They performed additional analyses with small-world metrics, including the clustering coefficient, the characteristic path length, and modularity, to discover that children and adolescents with autism display reduction in network modularity. In another differential study, the authors used the Louvain method to partition functional brain networks into various subnetworks, and the Scale Inclusivity metric to estimate the within and between group similarity of community structures. Their main finding was that ASD is characterized with atypical connectivity in the ventro-temporal-limbic subnetworks that may underlie social impairments in ASD (Glerean et al., 2016). In a similar study, Keown et al. (2017) showed that functional subnetworks are globally atypical in ASD, together with reduced network integration and increased dispersion. Altogether, these findings suggest an aberrant reorganization of community structure in ASD, globally characterized by a reduction in modularity in persons having autism. These pioneering results provide an important indication that community patterns might be good neuromarkers for discriminating between ASD patients and healthy controls. In this study, we verified the hypothesis that the values of $Q, Q_{GD}, Q_{LD}, Q_{DB}$, and Q_{NM} are significantly altered under ASD, 0,0,1which would indicate greater evidence of an altered community organization. In addition, we tested the hypothesis that these metrics can be used as features for predicting the clinical class of a particular participant.

The mathematical formulation of each of these metrics combines both the ideas of both functional integration and segregation, and they are used in this study to capture and reflect the imbalance between intra- and inter-cluster connections in autism. Using these five metrics together provides different indicators that map the brain's functional community patterns and helps highlight significant changes between health and disease states that can be leveraged by machine learning classifiers.

2.2.6. Comparing Community Patterns

In this study, we used the Rand index for comparing pairs of community patterns (Rand, 1971; Steinhaeuser and Chawla, 2010). The Rand index is a statistical metric based on the community assignment of each pair of nodes and measures the degree of agreement between two community patterns **U** and **R**; it is computed using the following parameters:

- a: the number of pairs of nodes assigned to the same community according to both **U** and **R**
- b: the number of pairs of nodes assigned to the same community according to **U** but different communities according to **R**
- c: the number of pairs of nodes assigned to the same community according to **R** but different communities according to **U**
- d: the number of pairs of nodes placed in different communities according to both **U** and **R**

The sum $a + d$ is the number of agreements between the two community patterns, whereas $b + c$ is the number of disagreements. The Rand index between **U** and **R** is defined as

$$Rand(\mathbf{U}, \mathbf{R}) = \frac{a + d}{\binom{N}{2}}. \quad (6)$$

2.3. Preprocessing Parameters

The rsfMRI data listed in **Table 1** were preprocessed in the conventional order to facilitate comparison across the six datasets (Waheed et al., 2016). The data were preprocessed using the following software tools: MRIcron, SPM12, DPABI V2.3170105 (Yan et al., 2016), and DPARSFA V4.3170105 (Yan and Zang, 2010). The first 10 volumes of each series were discarded for signal equilibrium. Slice timing was performed to correct images for the acquisition time delay between slices of each volume, followed by head motion correction by using a six-parameter (rigid body) spatial transformation. Next, the images were normalized to the Montreal Neurological Institute EPI template and resampled into 3-mm isotropic voxels. The resulting signals were successively smoothed using a 4 mm FWHM Gaussian kernel, detrended, and band-pass filtered by

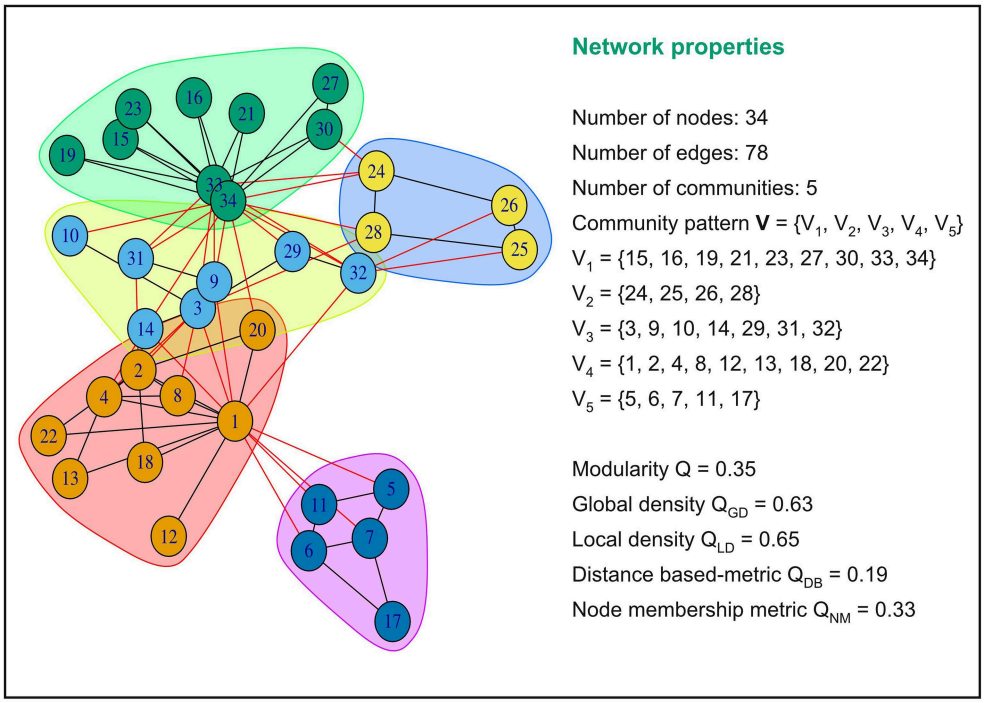

FIGURE 1 | Examples of values of modularity, global density, local density, distance based and node membership metric for a specific community partition of the popular Zachary Karate's Club network.This network partition is composed of five communities or modules. Intra-community connections are colored in black and inter-community connections in red. The five community pattern measures yielded different values for this graph partition.

using the frequency interval of 0.027–0.073 Hz (this interval was reported to be more reliable when the global signal is not regressed Liang et al., 2012). The normalized images were finally mapped with the Automated Anatomical Labeling atlas (AAL) to obtain 90 ROIs representing functional network nodes (Tzourio-Mazoyer et al., 2002). After preprocessing each dataset separately, we merged the time-series extracted from each site to form a multisite cohort.

2.4. Group-Level Analysis of Community Structures

To analyse group-level community patterns, first, we computed the correlation matrix for each participant from time-series data, by taking the average Pearson's correlation between all pairs of ROIs for each dataset. Next, we constructed the average correlation matrix (average brain network) for each diagnostic group. Third, these average networks were binarized using different threshold values ranging from 0.1 to 0.9. Finally, community detection was performed for each threshold value and compared between the two diagnostic groups.

Generating graphs at different sparsity levels has the advantage of allowing comparison between different graph representations at different levels of correlation. Community structures were detected using Newman's spectral modularity algorithm in the Matlab Community Detection Toolbox and visualized with BrainNet Viewer (Xia et al., 2013), a specialized Matlab toolbox for visualizing brain data. Many algorithms for community detection have been proposed, among which Newman's spectral modularity (Newman, 2006) and Infomap (Rossval and Bergstrom, 2008) have been extensively used in neuroscience studies. In this study, we used Newman's community detection algorithm because it rapidly optimizes the quality function (modularity) even with poor hardware performance, and is accurate. Community detection and evaluation were performed using the Community Detection Toolbox (ComDet) (Mitalidis et al., 2014) in Matlab. Visual inspection of networks across the datasets at different sparsities allowed the identification of general tendencies of group-level networks toward under- or overconnectivity.

2.5. Subject-Level Analysis

Community detection was also performed at the subject level and generated four sets of community patterns for sparsity thresholds ranging from 0.1 to 0.9. Community pattern metrics were computed for all participants in each site separately, and multisite data were generated by merging community pattern metrics computed for each site at each level of sparsity. We used a two-sample Kolmogorov-Smirnov test to assess the difference in the distribution of community quality metrics between the two diagnostic groups. This test was run on each individual dataset and on the multisite data independently. In addition, kernel density estimation (KDE) curves were plotted at each sparsity level to visualize the differences in community pattern metrics between the two clinical groups (Ledl, 2004). Additionally, a

pairwise correlation analysis was performed to visualize the distribution of data from patients with ASD and controls for each value of the binarization threshold.

The differences in community partition quality indexes, although important, do not indicate how community composition or node assignments differ between the two diagnostic groups. To this end, the Rand index between each pair of individuals was computed within each clinical group according to Equation (6). The Rand index was also extended to test for group differences in each dataset and in the multisite data. Intuitively, in case of a significant group difference, the mean within-group pairwise similarity should be higher than the mean between-group pairwise similarity. Because this cannot be tested directly, a non-parametric test comparing the average within-group Rand index in the original data with that in permuted data with randomized group membership was performed. *P*-values were computed based on the number of times the within-group Rand index on the permuted data was greater than that on the original data, divided by the total number of permutations ($n = 50{,}000$).

To locate the brain regions that could be responsible for the difference in the Rand index between the two clinical groups, we performed another statistical test proposed by Alexander-Bloch et al. (2012). This test was implemented only on multisite data. For each network node X, the other 89 nodes were relabeled to indicate whether they are in the same module as X. These labels were subsequently compared across participants. In terms of node X's functional community, the similarity of two participants was quantified using the Rand index. Similar to the previous test, the pairwise similarity metric was used to test for nodal group difference through a permutation of group labels. The true within-group mean Rand index was computed for all within-group subject-by-subject ROI pairs. Subsequently, the labels were shuffled 10,000 times and the average permuted within-group Rand index was computed and compared with that of the real data to generate a *p*-value. Thus, for each binarization threshold, a set of 90 p-values was generated to indicate whether each ROI's community assignment was more similar across participants in the same original group than across those in randomly permuted groups.

2.6. Automatic Prediction of a Participant's Class

The spatial distribution of data as visualized in the subject-level analysis prompted us to verify whether the five community features (modularity, global density, local density, distance-based, and node membership) could serve as reliable predictors of ASD. Therefore, the following classification algorithms were implemented using Scikit-Learn in a Python environment: logistic regression (LR), linear discriminant analysis (LDA), k-nearest neighbors (KNN), classification and regression trees (CART), naive Bayes (NB), and support vector machines (SVM).

Given that LDA which yielded the best ASD classification accuracy with community quality metrics as features is rather often used as a supervised feature extraction method, we briefly recall the classification process using LDA. LDA classifier is derived from a probabilistic model which models, for each class or diagnostic group k, the class conditional distribution of the data $P(D|y = k)$. Predictions can then be obtained by applying Bayes' rule:

$$P(y = k|D) = \frac{P(D|y = k)P(y = k)}{P(D)} = \frac{P(D|y = k)P(y = k)}{\sum_{l\in\{0,1\}} P(D|y = l)P(y = l)} \tag{7}$$

and we select the class k which maximizes this conditional probability. More specifically, $P(D|y)$ is modeled as a multivariate Gaussian distribution with density:

$$P(D|y = k) = \frac{1}{(2\pi)^{p/2}|\Sigma|^{1/2}} exp\left(-\frac{1}{2}(D - \mu_k)^t \Sigma^{-1}(D - \mu_k)\right) \tag{8}$$

where p is the number of features, $\mu_k \in \mathbb{R}^p$ the class mean vector, and $\Sigma = cov[D]$ the $p \times p$ covariance matrix. To use this model as a classifier, we estimate the class priors $P(y = k)$, the class means μ_k and the covariance matrix Σ from the training data (Hastie et al., 2009).

To estimate the performance of each classifier, LOO-cross-validation was used to evaluate the performance of these algorithms on each dataset at each sparsity threshold and a 10-fold cross validation was applied to multisite data at each sparsity level. The performance of each of these classifiers was reported in terms of accuracy, precision, and recall.

In order to rank community quality metrics based on their ASD predictive ability, we employed recursive feature elimination (RFE) on our best classifiers (Guyon et al., 2002). RFE is performed by recursively removing predictors and building a classification model based on those predictors that remain. It uses classification accuracy to identify predictors and (combination of predictors) that contribute the most to predicting the diagnostic group. RFE algorithm outputs a score between 0 and 1 for each predictor, and the larger the score, the more important the predictor.

2.7. Robustness of Community Features to Methodological Variation

Because of concerns about the effect of specific preprocessing parameters, we tested the robustness of the predictive power of the five community structure metric using a different validation dataset preprocessed with several methodological perturbations. To this end, we formed a separated multisite validation dataset composed of six additional sites, totalizing in 214 participants (ASD = 97, CTR = 117). These data were downloaded from the preprocessed version of ABIDE repository (Craddock et al., 2013). Our validation cohorts included data from the following imaging centers: Carnegie Mellon University (CMU, ASD = 14, CTR = 13), Kennedy Krieger Institute (KKI, ASD = 20, CTR = 28), Oregon Health and Science University (OHSU, ASD = 12, CTR = 14), Social Brain Laboratory (SBL, ASD = 15, CTR = 15), San Diego State University (SDS, ASD = 14 , CTR = 22) and Trinity Center for Health Sciences (TRI, ASD = 22, CTR = 25). Participant demographic information is provided

in **Table S3** and imaging acquisition parameters are summarized in **Table S4**. The downloaded imaging data derivatives were previously preprocessed using the DPARSF pipeline. The preprocessing treatments included the removal of the first ten volumes, slice timing and motion correction. Nuisance variable regression was carried out using 24 motion parameters and low-frequency drifts. Imaging signals were then band-pass filtered with a frequency range of 0.01 Hz to 0.1 Hz, without global signal correction, registered to Montreal Neuroimaging Institute template using DARTEL (Ashburner, 2007), and smoothed using a 6-mm FWHM Gaussian Kernel. The mean time courses for regions of interest were extracted for each subject based on the CC200 functional atlas which comprises 200 ROIs (Craddock et al., 2012). Functional connectomes for each participant were constructed as described previously, and community pattern metrics were computed for different network sparsity levels ($0.1 \leq T \leq 0.9$). We retrained KNN and LDA classifiers with features extracted for each value of the binarization threshold. Just as previously, A 10-fold cross-validation scheme was employed to evaluate these additional classifiers.

3. RESULTS

3.1. Variations in Community Patterns

3.1.1. Difference in Overall Network Structure

Visual inspection of community patterns in the group-averaged networks at all sparsity levels revealed no significant difference in the number of community clusters between patients with ASD and controls. Another important observation was an overall similarity in topological cluster organization between the brains of patients with ASD and those of controls. However, at higher sparsities, over- and underactivation of some communities in the average networks of ASD cohorts was gradually observed. Notably, overall underconnectivity was found in ASD cohorts in LV1, LV2, PIT, and CAL data (**Figure 2**), and resting-state group network overconnectivity was observed in the OLI and STA datasets (**Figure 3**).

To further investigate the extent to which community structures of task-free functional connectivity were altered in ASD, we computed the five descriptive community pattern metrics and generated plots of their average and standard deviation in patients with ASD and controls (**Figure 4**). *P*-values for mean group differences were estimated using the two-sample Kolmogorov-Smirnov test. The *p*-values obtained were subsequently FDR-corrected for multiple comparisons. Our five metrics are different ways of capturing the intuition that nodes within the same cluster should be more densely connected with each other than the rest of the network; however, they vary in their mathematical formulations. Communities were isolated through modularity maximization, and modularity was used in addition to the other four metrics to compare the resulting community patterns. **Figure 4** shows that the mean difference between patients with ASD and controls is significant at several sparsities. For example, modularity is significantly higher for the ASD class in STA and CAL, whereas it remains significantly lower in OLI. The spread of the metrics around their averages also differs between the two clinical classes. Compared with the control group, in the ASD class we observed a greater spread of the values of the metrics in STA, LV1, and LV2,and a smaller one in OLI, PIT, and CAL, possibly reflecting subtypes of ASD.

Multisite data at $T = 0.5$ exhibited significant differences in modularity, distance-based and node membership metrics, with an overall increase in modularity and node membership, and a decrease in the three other metrics for the ASD group (**Figure 5**). This increase in modularity suggests that there are relatively fewer connections between clusters and more connections within clusters in patients with ASD. However, the relationship between community quality metrics and under- and overconnectivity remains unclear because a decrease in modularity was associated with underconnectivity in CAL, but with overconnectivity in STA.

3.1.2. Differences in Community Composition

While the community pattern quality metrics revealed differences in the structure of resting-state functional networks, we still needed to quantify the degree of similarity of node assignment to clusters within each clinical group. To this end, Rand index similarity was computed between the ASD and control groups in the datasets (**Table 2**). The Rand index showed a high level of agreement and further confirmed the overall visual similarity of network structures observed (across binarization thresholds: mean Rand index = 0.82, standard deviation = 0.14). However, the Rand index permutation testing on individual subject network partitions revealed that, for some levels of sparsity, the within-group similarity of community structures of pairs of participants in the same diagnostic group is higher than would be expected if the group difference was not significant (**Table 3**). Moreover, this difference was also significant for multisite data ($p = 0.033$).

3.1.3. Investigating Group Differences by Using Subject-Level Analysis

The methods used in the group-level analysis enabled qualitative and quantitative characterization of the difference between the two clinical groups. However, they do not allow the estimation of the degree of variability of community structural metrics within a clinical group compared with that across groups. Visualizing the inter-subject variability inside and across the two groups was possible using KDE plots combined with scatter plots displaying the organization of data from both clinical groups with respect to each pair of features (see **Figures 6**, **7** and **Figures S1**–**S4**). Although group-level analyses revealed similar patterns in the ASD and control groups, KDE showed important perturbations in the distribution of community quality metrics in all datasets and across sparsity densities. Moreover, the spatial organization displayed via feature pairing plots revealed an interesting tendency of the data from members of each of the two groups to cluster together. These two-dimensional visualizations provided an encouraging basis for applying machine learning algorithms to predict the class of a particular participant by using community structure metrics as features.

A rigorous regional permutation test of community assignments adapted from Alexander-Bloch et al. (2012) was applied to multisite data and found several regions

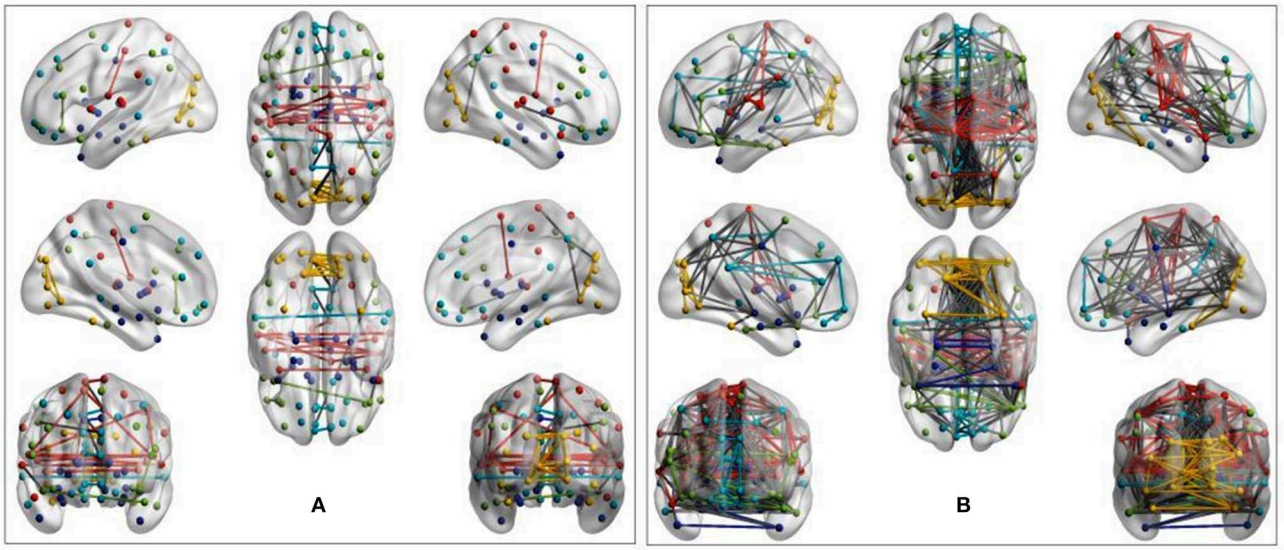

FIGURE 2 | Group-average network community pattern for the LV2 dataset at sparsity threshold $T = 0.8$. ROIs are defined according to the AAL90 brain atlas and colored based on community assignments by Newman's spectral algorithm. **(A)** ASD cohort. **(B)** Control cohort. The group-level community pattern showed an overall reduction of connectivity in the brains of patients with ASD. Underconnectivity was also observed in LV1, CAL, and PIT.

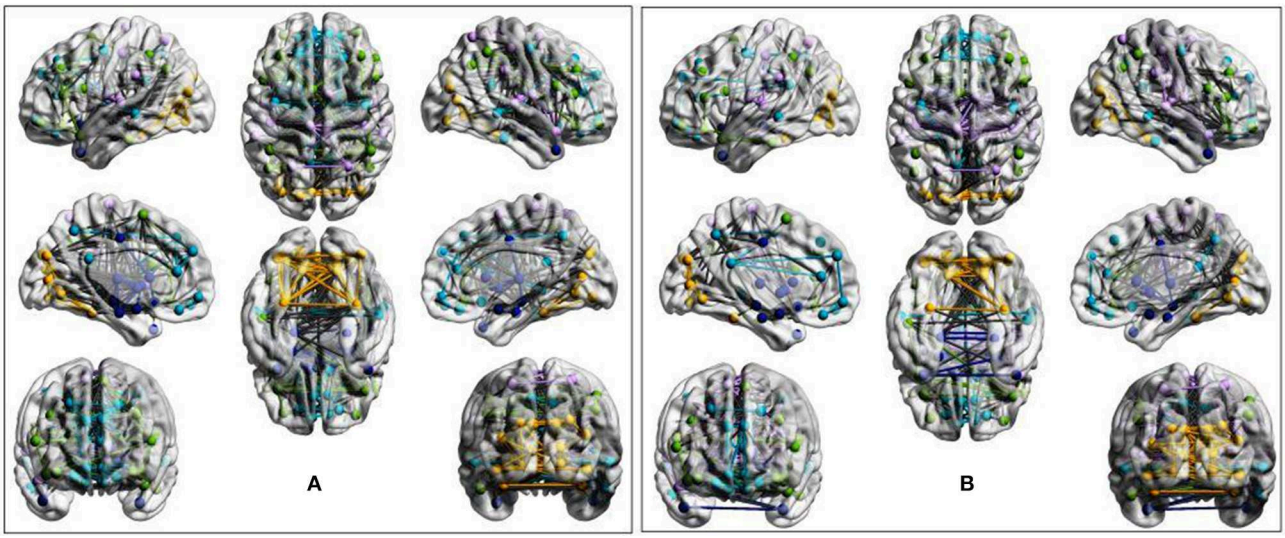

FIGURE 3 | Evidence of overactivation in the community colored in yellow observed in the average STA dataset network at the sparsity threshold $T = 0.4$, despite the community pattern showing an overall preservation of network morphology. **(A)** ASD cohort. **(B)** Control cohort. ROIs are defined according to the AAL90 atlas and colored on the basis of community assignment by using the Newman's spectral algorithm. At this density level, group-average network overconnectivity was also observed in the OLI dataset.

with functional community structure assignments differing significantly between the two clinical populations (see **Table 4** and **Figure 8**). There was variability across groups in the community assignment of ROIs across all network sparsity levels. Full details of the test results are presented in **Table S2**.

3.2. Single Subject Clinical Group Prediction

As previously mentioned in this document, six classification algorithms were implemented by using Scikit-learn in a Python environment to investigate whether the community structure quality metrics of the participant's resting-state functional connectivity networks alone could predict the clinical group of a particular participant. Among the classification algorithms, LDA and KNN yielded the best results with the LOO-cross-validation test; the performances of these two algorithms are reported in **Table 5**. LDA achieved peak accuracy ranging from 74.86% (CAL) to 85.16% (STA). KNN obtained a range of peak accuracy from 68.42% (PIT) to 76.12% (STA). However, these results were obtained at different network sparsity levels. We merged all the five community pattern features computed for each sparsity level,

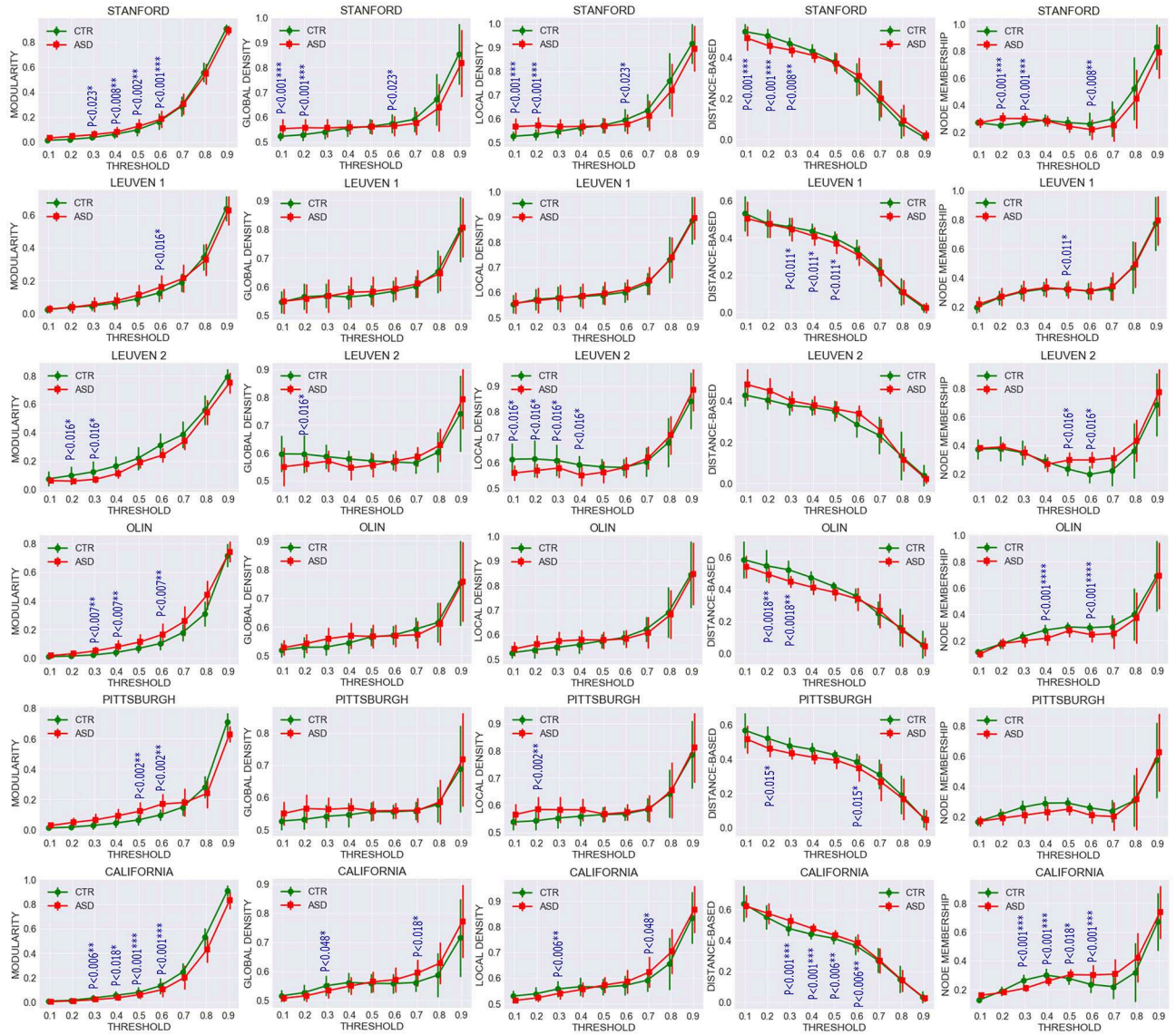

FIGURE 4 | Comparing average and standard deviation of community pattern quality metrics between patients with ASD and controls for the full range of thresholds. Community quality metrics were computed for each participant, and plots were created based on the average for patients with ASD and controls. Each row represents a dataset and each column one metric. Group statistical differences were analyzed using the two-sample Kolmogorov-Smirnov test. Only significant FDR-corrected *p*-values are reported ($p < 0.05$).

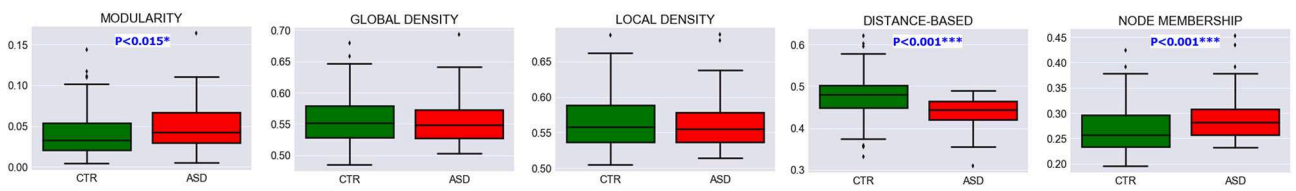

FIGURE 5 | Evidence of community pattern alteration in ASD. Box plots reveal group differences in terms of community quality indexes at $T = 0.5$ in pooled data across experimental sites . *P*-values were generated with the two-sample Kolmogorov-Smirnov test and subsequently FDR-corrected.

retrained the classifiers and performed a 10-fold cross-validation test. Multisite data yielded peak accuracy at $T = 0.5$ (65.66% for KNN and 74.86% for LDA). Compared with recent autism classification studies, this study obtained a relatively high classification accuracy with the lowest number of predictors (**Table 6**).

3.3. Feature Importance

To determine which community pattern features were most predictive, we performed Recursive Feature Elimination (RFE) on in-site as well as multisite data with stratified-10-fold cross-validation. This procedure used our LDA model to rank the five community pattern metrics according to their predictive performance during the classification process. For CAL, LV1, LV2, and PIT, the order of feature importance are global density, node membership, local density, modularity and distance-based metric, starting from the most important feature. For OLI and STA, important features are global density, node membership, local density, distance-based metric, modularity and node memebership. RFE on multisite data showed that local density was the most important predictor (score = 0.95), followed by global density (score = 0.75) and node membership (score = 0.5). Modularity and distance-based metric were the less predictive features with a score of 0.25 and 0.10, respectively.

3.4. Robustness to Methodological Variation

Finally, we examined how community pattern metrics would perform on novel datasets and under a different set of preprocessing parameters, including the head motion correction parameter, the smoothing parameter, the bandpass filtering frequency range and the ROI parcellation atlas. Our validation cohorts were used for this purpose. Group-level analyses of community structure for validation datasets are summarized in **Tables S5**, **S6**. Subject-level analyses of community quality metrics are recapitulated in **Figures S5–S11**. Single validation sites obtained peak classification accuracy of 68.12% for CMU (T = 0.3), 76.23% for KKI (T = 0.6), 82.02% for OHSU (T = 0.4), 71.09% for SBL (T = 0.7), 80.73% for SDSU (T = 0.3) and 72.58% for TRINITY (T = 0.8), using LDA and leave-one-out cross-validation method. Again, classification accuracies obtained on in-site data using KKN were consistently lower than those obtained with LDA. For multisite classification on the whole validation set, the highest classification obtained is 75.04% (T = 0.4) obtained with LDA and 10-fold cross-validation (see **Table 7** for full classification results on the whole validation dataset). Taken together, these results suggest that the discriminative capability of community patterns metrics used in this study is relatively well-preserved on novel datasets and under alternative preprocessing choices. However, the range of filtering thresholds values that yielded peak classification accuracy differs considerably between experimental and validation data. Furthermore, the most important features differs sightly from those obtained with experimental data. RFE applied on the whole validation dataset revealed global density was most discriminative (score = 0.90), followed by local density, node membership, modularity and distance-based metric that obtained predictive scores of 0.80, 0.70, 0.30, and 0.08, respectively.

TABLE 2 | Rand Index values measuring the degree of agreement of community structures between control and ASD groups in real data.

T	STA	LV1	LV2	OLI	PIT	CAL
0.1	0.69	0.64	0.76	0.84	0.97	1
0.2	0.62	0.53	0.69	0.71	0.68	0.89
0.3	0.55	0.68	0.6	0.83	0.65	0.65
0.4	0.77	0.77	0.74	0.71	0.75	0.56
0.5	0.89	0.74	0.72	0.82	0.83	0.77
0.6	0.92	0.86	0.84	0.85	0.87	0.76
0.7	0.99	0.95	0.89	0.95	0.92	0.9
0.8	1	1	0.95	0.99	0.99	0.97
0.9	1	1	0.95	1	1	1
$\bar{x}$	0.82	0.8	0.79	0.86	0.85	0.83
σ	0.17	0.17	0.12	0.11	0.13	0.16

T, sparsity threshold; $\bar{x}$, mean; σ, standard deviation.

4. DISCUSSION

This study addressed two separate but closely related problems: the characterization of differences in the resting-state functional network community patterns between patients with ASD and age-matched controls and the single-subject prediction of this same neurological disorder. We repeated the same analyses on six experimental datasets originating from different sites and including participants of different ages, obtained using different imaging acquisition parameters. We also applied this same analysis pipeline on a multisite cohort formed by merging experimental data from the six sites. We used

TABLE 3 | Rand index permutation testing revealed significant differences between ASD and CTR network community structures.

Dataset	Mean within-CTR	Mean within-ASD	Mean of all within-group pairings in real data	Mean of all Within-group pairings with permuted labels	*P*-value real > permuted data
STA (T = 0.4)	0.557	0.548	0.552	0.547	0.017
LV1 (T = 0.3)	0.549	0.551	0.550	0.540	0.032
LV2 (T = 0.3)	0.562	0.536	0.549	0.544	0.019
OLI (T = 0.4)	0.555	0.558	0.557	0.551	0.046
PIT (T = 0.4)	0.541	0.550	0.546	0.541	0.027
CAL (T = 0.4)	0.569	0.564	0.565	0.558	0.001
Multisite (T = 0.5)	0.565	0.557	0.563	0.557	0.033

P-values for mean group differences were estimated using a permutation test with n = 50,000 permutations.

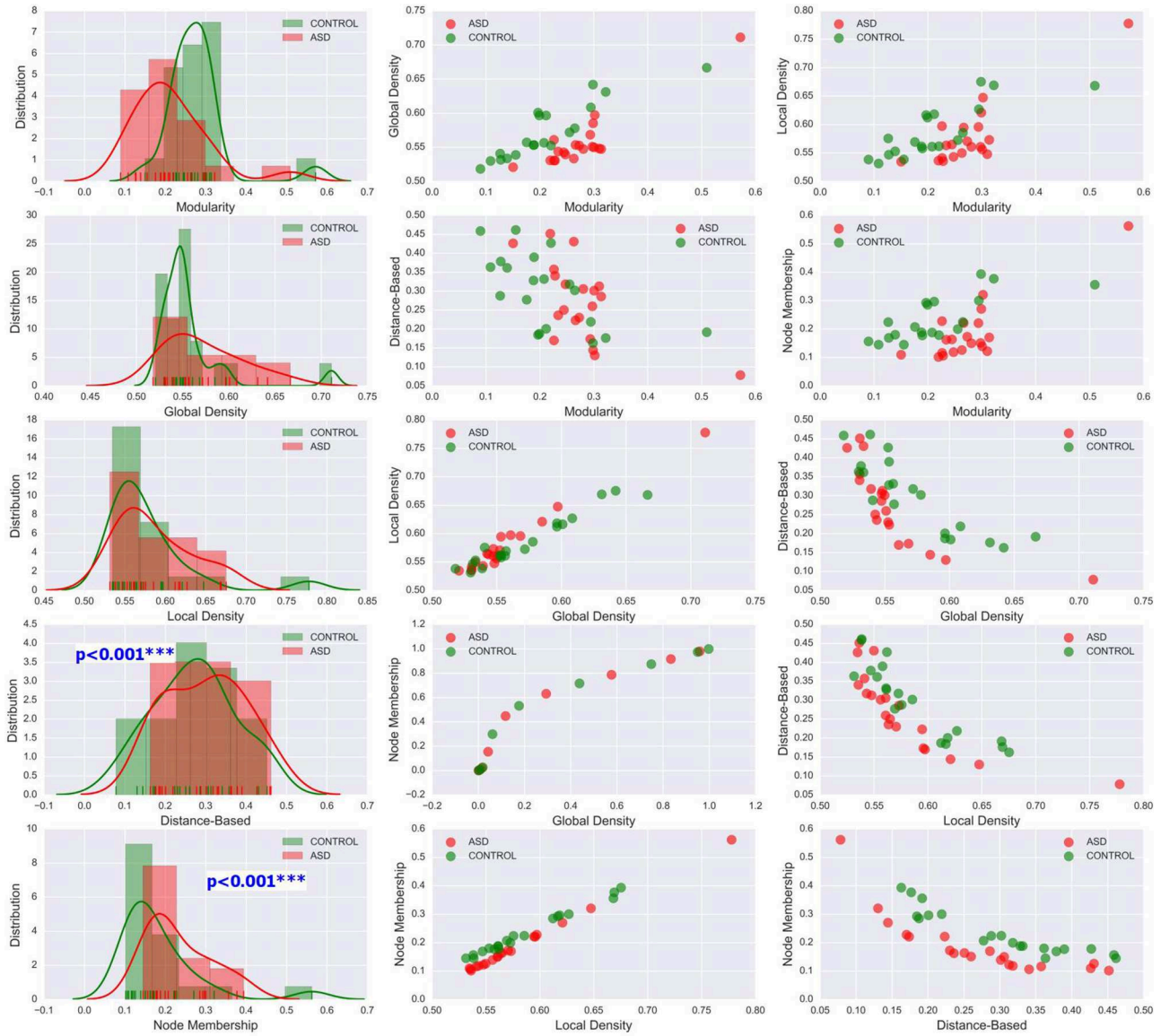

FIGURE 6 | Left column: KDE plots of variations in the five community pattern metrics across subjects and clinical groups in the CAL dataset at threshold $T = 0.4$ with a Gaussian kernel bandwidth of 0.02. These plots show significant differences in the distribution of community structure metrics between the two groups. Middle and right column: organization of ASD and control group data visualized by scatter plots of all pairs of community pattern metrics.

five community pattern comparison metrics to reach more robust conclusions. The major findings of our investigation are as follows: (1) Underconnectivity in the networks from patients with ASD compared with controls was found in four of the six datasets (LV1, LV2, CAL, and PIT) and overconnectivity was observed in two (STA and OLI); (2) statistical analyses provided strong evidence for alterations in functional community patterns in ASD, as determined using community quality indexes; (3) group-averaged networks from patients with ASD and controls exhibited a high level of Rand index similarity; however, testing of an individual's community structures revealed significant differences in cluster composition between the two classes; (4) the differences in community assignments was driven by specific regional nodes, most of which are known to be impaired in ASD; (5) community quality metrics yielded a minimum of 79% peak classification accuracy for experimental datasets, and 76% for validation datasets. Classification accuracy was lower for multisite data (74.86% for experimental data and 75.04 for validation data). The originality of our findings stems from the use of four complex network metrics that have not been previously used to analyse the functional modular organization of the human brain using neuroimaging data. To the best of our knowledge, this study is the first to reveal that the modular organization metrics

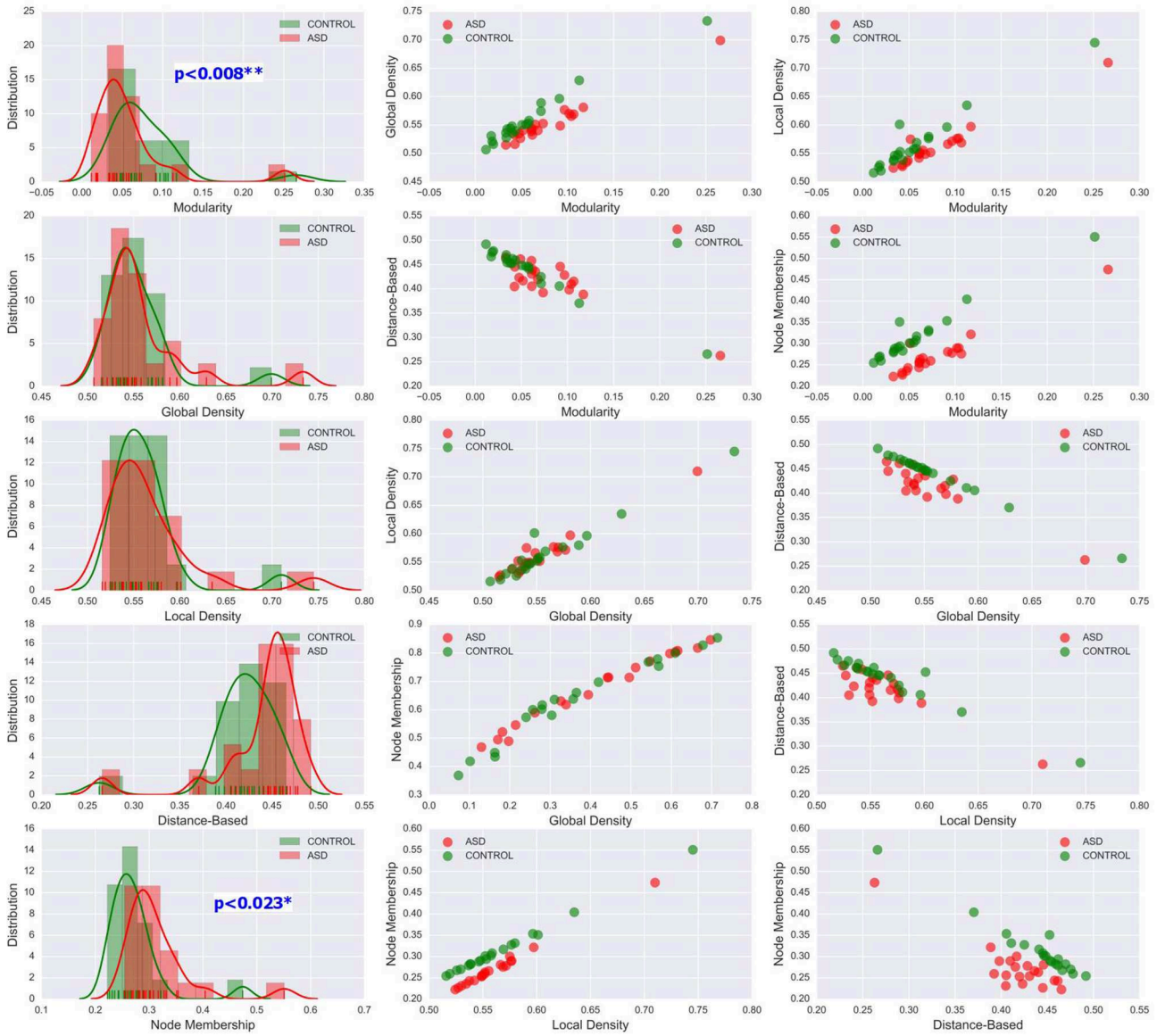

FIGURE 7 | Left column: KDE plots of variations in the five community pattern metrics across subjects and clinical groups in the STA dataset at threshold $T = 0.4$ with a Gaussian kernel bandwidth of 0.02. These plots show significant differences in the distribution of community structure metrics between the two groups. Middle and right column: organization of ASD and control group data visualized by scatter plots of all pairs of community pattern metrics.

alone are used to design individual subject predictive models of neurological disorders.

Our five metrics are derived from the concept of community structures in complex networks. While the notion of community structure has not been explicitly defined, community quality metrics formalize the intuition that while nodes in a community are densely interconnected, they are only sparsely connected to the rest of the network. Many quality functions have been proposed to formalize this intuition, which may suggest that none of them is completely satisfactory. This justifies the use of five metrics in this study to investigate community patterns in ASD. Although the five metrics are formalizations of the same intuition, they vary considerably in their mathematical formulations. Modularity Q is the fraction of the edges that fall within the given clusters or communities minus the expected fraction if connections were distributed randomly. Global density Q_{GD} is the average of global inner density and global outer antidensity. Global inner density is the sum of all within-cluster connections over all communities, divided by the number of all possible internal edges; global outer antidensity is evaluated as one minus the number of edges between the given clusters divided by the number of all possible bridge connections. Local density Q_{LD} is the average of a cluster's (local) inner densities and its (local) outer antidensities

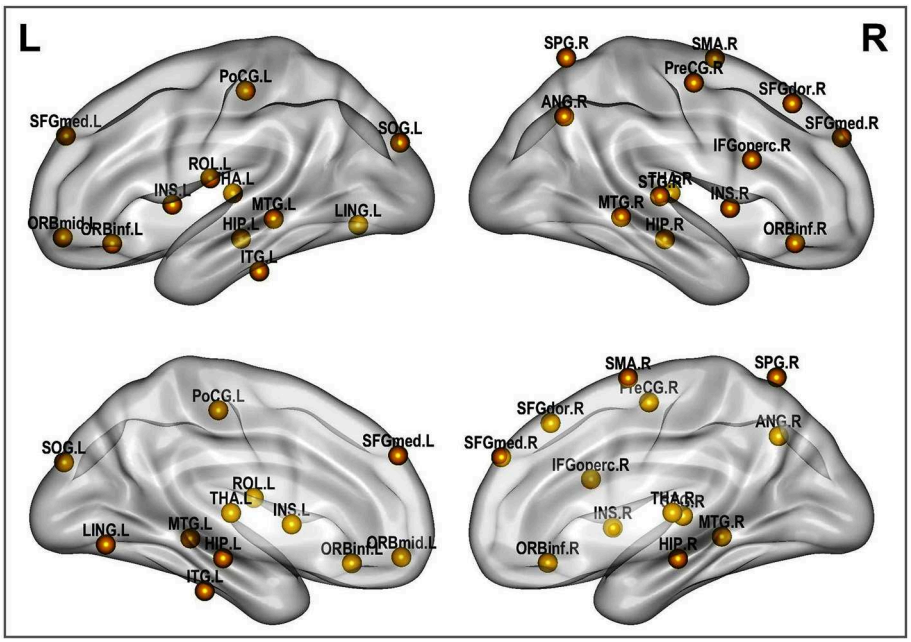

FIGURE 8 | Altered brain regions in autism as revealed by ROI community assignment test. This test was conducted on pooled data across experimental sites.

weighted by a term proportionate to the cluster's size (to ensure that small dense clusters do not influence the total clustering quality disproportionately). Q_{DB} tries to formalize the theoretical hypothesis of perfect community structure stipulating that any two nodes within the same community are connected and any two nodes in different communities are not connected. The node membership quality function computes the average (over all nodes of the graph) of a statistic that measures the likelihood of each node to belong to his assigned cluster and not other clusters. We can see that each of these metrics summarizing whole-brain connectivity with a single statistic captures a specific aspect of the quality of functional community structures. Considering that all these five measures of functional segregation are highly sensitive to every single connection and every meaningful grouping of connections in the graph, they provide a robust method for comparing connectivity between normal and pathological individuals. Nevertheless, although both underconnectivity and overconnectivity were discovered in our datasets, any potential relationship between these two potential subtypes of autism and functional community patterns remains unclear. This diversity in findings may be explained by the multifaceted manners in which ASD manifests across individuals.

With respect to functional connectivity differences between the ASD and control groups, our results are in agreement with previous findings and support the dysconnectivity theory of autism. Early studies on functional connectivity at rest in autism tended to support the underconnectivity theory, whereas a few recent studies have reported either over connectivity or evidence for both (Hull et al., 2016). However, most of these studies have focused only on specific ROIs or resting-state networks; few have addressed connectivity differences at the whole-brain level by using community detection and analysis over multiple datasets, as was done in the present study. While statistical testing revealed significant differences in the network structure and community composition, a test at the node level indicated that this difference was caused by several brain regions. These brain regions include the insula, thalamus, hippocampus, lingual gyrus, middle temporal gyrus and other functional areas that are known to be impaired in autism (Nielsen et al., 2013; Chen et al., 2016; Wang et al., 2017; Heinsfeld et al., 2018).

As shown in **Table 6**, descriptive community pattern metrics yielded over 79% accuracy on all of the individual datasets. Moreover, they yielded a maximum accuracy of 75.04% on a different multisite validation dataset (**Table 7**), thus proving to be robust, viable predictors of autism. While comparing accuracies across studies is not always straightforward, depending as they do on additional parameters such as the number of participants recorded and the preprocessing pipeline used, there is evidence that our classification significantly outperforms, even at the group level, recent approaches that used fine-scaled pairwise correlations on single-site data. Furthermore, our classification was achieved with the lowest number of features.

Despite the encouraging prediction performance obtained in this study, we do not advocate these metrics as potential ASD clinical biomarkers. One of their limitations for this purpose is that those network indexes are not complete invariants, in the sense that non-equivalent graph structures can yield the same values in those metrics. While this limitation is somewhat alleviated in this work by the use of several measures, they nevertheless fall short of neuromarker standards (Plitt et al.,

TABLE 4 | Regions displaying high disagreement between ASD and control group for community cluster assignment.

Label	Region	Hemi	Coordinates		
			x	y	z
2	Precental gyrus	R	41.37	−8.21	52.09
4	Superior frontal gyrus, dorsolateral	R	21.9	31.12	43.82
9	Middle frontal gyrus, orbital part	L	−30.65	50.43	−9.62
12	Inferior frontal gyrus, opercular part	R	50.2	14.98	21.41
15	Inferior frontal gyrus, orbital part	L	−35.98	30.71	−12.11
16	Inferior frontal gyrus, orbital part	R	41.22	32.23	−11.91
17	Rolandic operculum	L	−47.16	−8.48	13.95
20	Supplementary motor area	R	8.62	0.17	61.85
23	Superior frontal gyrus, medial	L	−4.8	49.17	30.89
24	Superior frontal gyrus, medial	R	9.1	50.84	30.22
29	Insula	L	−35.13	6.65	3.44
30	Insula	R	39.02	6.25	2.08
37	Hippocampus	L	−25.03	−20.74	−10.13
38	Hippocampus	R	29.23	−19.78	−10.33
47	Lingual gyrus	L	−14.62	−67.56	−4.63
49	Superior occipital gyrus	L	−16.54	−84.26	28.17
57	Postcentral gyrus	L	−42.46	−22.63	48.92
60	Superior parietal gyrus	R	26.11	−59.18	62.06
66	Angular gyrus	R	45.51	−59.98	38.63
77	Thalamus	L	−10.85	−17.56	7.98
78	Thalamus	R	13	−17.55	8.09
82	Superior temporal gyrus	R	58.15	−21.78	6.8
85	Middle temporal gyrus	L	−55.52	−33.8	−2.2
86	Middle temporal gyrus	R	57.47	−37.23	−1.47
89	Inferior temporal gyrus	L	−49.77	−28.05	−23.17

This test was performed on merged data across experimental sites. Hemi, hemisphere; L, left; R, right. These regions can be visualized in ***Figure 8****.*

TABLE 5 | Classification performance on our data cohorts by using the five community pattern descriptors as features with KNN and LDA algorithms.

Algorithm	KNN			LDA		
Dataset	**Accuracy**	**Precision**	**Recall**	**Accuracy**	**Precision**	**Recall**
STA (T=0.2)	76.12	74.48	72.91	85.16	84.25	83.95
LV1 (T = 0.3)	70.31	66.83	61.00	82.77	80.10	81.89
LV2 (T = 0.3)	69.69	48.17	51.67	81.33	80.79	80.29
OLI (T = 0.4)	74.44	77.58	72.01	80.28	79.08	80.04
PIT (T = 0.3)	68.42	57.50	52.49	79.59	78.03	78.77
CAL (T =0.6)	72.00	73.33	71.21	83.35	82.92	83.01
Multisite(T = 0.5)	65.66	59.00	59.00	74.86	76.07	71.67

T, Threshold; KNN, K-nearest neighbor; LDA, linear discriminant analysis. We only report the sparsity thresholds that yielded the highest classification accuracy.

2015). Another major limitation is their great dependence on network filtering threshold for which there is no objective selection criterion. That said, community quality patterns remain a valuable tool for investigating network connectivity disruptions in ASD pathology and anticipating the polarity of a particular participant before using the recommended diagnostic methods. Further research may provide a solid basis for their clinical application in the future. Autism spectrum encompasses several neurological disorders and manifests itself through a wide range of symptoms and different characteristics. The way the brain's architecture breaks down under the effects of autism is subtle and complex. A single metric, modularity, for example, is not enough to capture all the changes in brain structure across the spectrum. The use of several structural metrics is, therefore, more appropriate to capture and identify this disease.

Classifiers designed based on features extracted from ABIDE rsfMRI data typically perform better on single-site data than multisite data. Decreased accuracy in multisite data could be attributed to ASD subtypes or other heterogeneities across the ABIDE sites (Di Martino et al., 2014). Different studies employed different approaches for utilizing multisite data for ASD classification in the literature. One approach is to learn biomarkers of neurological status and perform separate classification at individual sites and then combine the results in a meta-analysis (Chen et al., 2016). Another approach consists of treating multisite data as a single, homogeneous dataset (Nielsen et al., 2013). These two approaches were used in this study to assess the viability of functional network community pattern metrics as predictors of ASD. While these two approaches fail to account for the variability that has been proven to be significant between sites, their use in this study provides preliminary evidence for community quality metrics as potential predictors of autism. Recent approaches for combining imaging data from multiple sites leverage similarity across sites while accounting for individual site differences through a joint optimization (Wang et al., 2017; Heinsfeld et al., 2018). While these novel approaches yield better classification accuracy in multisite studies, they may not be suited for studies that extract imaging features based on global connectivity indexes.

In this study, community detection was performed by optimizing the modularity quality function. Then the community quality indexes were calculated based on the found community structures. Given the results for feature importance, it is interesting to see that modularity is one of the least important predictive features for the ASD classifiers. One might then suspect that optimizing some of the other quality functions might lead to communities that yield better discrimination between persons with ASD and typical controls. In this work, the modularity maximization algorithm was chosen for community identification mostly because of its good performance on functional brain networks in previous studies. We cannot, therefore, rule out the fact that the predictive power of the other quality measures is a consequence of using modularity for the original clustering. Using an alternative graph clustering algorithm such as Infomap (Rossval and Bergstrom, 2008) to perform the original clustering could be useful for verifying this hypothesis. In addition, it would be interesting to conduct a comparative study where the initial community detection is performed by optimizing each of the other quality functions and then computing and using all the metrics as features for classification. This, however, is beyond the scope of this paper.

TABLE 6 | Comparing our classification results with recent works.

Types of features	# of features	Classifier	# of subjects (ASD, CTR, Total)	Peak accuracy %	References
Functional connectivity	26,393,745	Thresholding	(40, 40, 80)	79.0	Anderson et al., 2011
ICA components	10	Linear Regression	(20, 20, 40)	78.0	Uddin et al., 2011
Functional connectivity among 7266 ROIs	26,400,000	General Linear Model	(447, 517, 964)	60	Nielsen et al., 2013
Functional connectivity among 220 ROIs	24,090	Random Forest	(126, 126, 252)	91	Chen et al., 2015
Functional connectivity among 90 ROIs	4005	Probabilistic Neural Network	(312, 328, 640)	90	Iidaka, 2015
Functional connectivity	Variable	Support Vector Machine	(59, 89, 148)	76.7	Plitt et al., 2015
Functional connectivity among 84 ROIs	7,056	Support Vector Classification	(468, 403, 871)	67	Abraham et al., 2017
Functional connectivity among ROIs	600	Deep neural network	(505, 530, 1035)	70	Heinsfeld et al., 2018
HOG and personal characteristic data	47	Support Vector Machine	(538, 573, 1111)	65	Ghiassian et al., 2016
ROIs HMMs likelihoods	114	SVM	(121, 171, 292)	75.86	Jun et al., 2019
Time series	90	LSTM	(529, 571, 1100)	68.5	Dvornek et al., 2017
Community metrics from 90-ROI networks	5	Linear Discriminant Analysis	(117, 118, 235)	74.86	This work

HOG, Histogram of Oriented Gradients; LSTM, Long Short-Term Memory network; HMM, Hidden Markov Models.

TABLE 7 | Classification performance on the entire validation set by using the five community pattern descriptors as features with KNN and LDA algorithms.

Threshold	KNN			LDA		
	Accuracy	Precision	Recall	Accuracy	Precision	Recall
0.1	58.25	59.23	59.27	65.14	64.34	64.89
0.2	55.69	56.61	61.55	68.85	68.15	68.18
0.3	65.95	64.29	64.07	69	70.15	71.58
0.4	65.97	66.13	64.13	75.04	73.16	74.28
0.5	66.16	67.81	64.51	72.49	71.44	72.77
0.6	64.33	62.45	63.18	71.16	70.98	69.14
0.7	64.17	65.3	64.41	67.24	66.88	65.69
0.8	58.09	54.75	56.85	65.55	65.11	63.13
0.9	55.75	55.78	54.07	66.82	67.12	66.33

KNN, K-nearest neighbor; LDA, linear discriminant analysis.

One limitation of the classification framework proposed in this study, and graph-based approaches in general, is that the classification results are very dependent on thresholding parameter T. Graph screening is a major and most recurring issue for the binarization of functional brain networks. In this study, we performed a systematic analysis of functional brain networks for increasing threshold values ranging from 0.1 to 0.9, as there is no objective criterion for determining an interval of thresholds for which community quality metrics would remain relatively stable. Our classification results on single and multisite data show that, broadly, threshold values falling between 0.3 and 0.6 yielded the best classification accuracies (see **Tables 5**, **7**). This suggests that brain networks that are either too densely connected or too sparse are not good choices for reaching "optimal" classification accuracy on new data. Still, finding a general rule for choosing the best network filtering threshold remains a challenging endeavor De Vico Fallani et al. (2014). A potential good workaround solution to the threshold problem could be to perform community detection and compute metrics directly from unfiltered networks. A drawback of this solution could be the challenge of defining and interpreting communities in the context of signed networks with positive and negative connections.

Other limitations of this study include the fact that the same spatial normalization template was used for all participants despite age differences in the experimental populations. Detection of regional distortions could probably be more accurate by using multiple brain templates adapted to different age ranges. Also, many subjects with ASD were on medication at the time of scanning, and it cannot be ruled out that treatments could influence resting-state functional connectivity community patterns in these individuals. Third, community detection was performed on unweighted networks, ignoring the potential significance of the information carried by edge weights. Finally, we used values of Pearson's correlation coefficient as node weights before binarization; however, different correlation metrics may yield different graph representations of the same datasets and yield different characterizations of functional connectivity differences in ASD. Further studies are necessary to investigate community pattern differences in ASD by using weighted network representation. Further studies are also warranted to determine the effects of different correlation metrics and other network construction techniques on resting-state functional network community patterns.

5. CONCLUSION

We propose a framework to characterize and discriminate patients with autism spectrum disorder from normal control subjects. Our approach is based on graph-based feature extraction. A combination of five well-selected community pattern quality indexes was used as features for classification. In addition, various statistical tests were applied to evaluate the overall network topology and community composition in ASD at the group as well as subject levels. Results for functional connectivity difference between autistic patients and normal

subjects were consistent with existing studies, revealing both patterns of underconnectivity and overconnectivity. In particular, we demonstrated that the modular structure is significantly disturbed in patients with ASD. More importantly, we showed that the discriminative power of the modular structure as captured by the selected metrics is comparatively high, lending further credence to the dysconnectivity theory of this condition, for which network connectivity patterns are increasingly being considered as potential biomarkers.

AUTHOR CONTRIBUTIONS

All authors have made a substantial contribution to this work and approved it for publication. In particular, YS and TE designed the experimental framework, implemented computer code and drafted the manuscript and HL revised the manuscript.

FUNDING

This study was supported by the National Natural Science Foundation of China (Project No. 61572239).

ACKNOWLEDGMENTS

The authors thank Xinghao Huang for his assistance with DPARSFA and SPM, and all those who are actively working to share neuroimaging data through ABIDE.

SUPPLEMENTARY MATERIAL

The Supplementary Material for this article can be found online at: https://www.frontiersin.org/articles/10.3389/fnhum.2019.00203/full#supplementary-material

REFERENCES

Abraham, A., Milham, M. P., Martino, A. D., Craddock, R. C., Samaras, D., Thirion, B., et al. (2017). Deriving reproducible biomarkers from multi-site resting-state data: an autism-based example. *NeuroImage* 147(Suppl. C), 736–745. doi: 10.1016/j.neuroimage.2016.10.045

Ahmadlou, M., and Adeli, H. (2011). Functional community analysis of brain: a new approach for eeg-based investigation of the brain pathology. *NeuroImage* 58, 401–408. doi: 10.1016/j.neuroimage.2011.04.070

Alexander-Bloch, A., Lambiotte, R., Roberts, B., Giedd, J., Gogtay, N., and Bullmore, E. (2012). The discovery of population differences in network community structure: new methods and applications to brain functional networks in schizophrenia. *NeuroImage* 59, 3889–3900. doi: 10.1016/j.neuroimage.2011.11.035

Anderson, J. S., Nielsen, J. A., Froehlich, A. L., DuBray, M. B., Druzgal, T. J., Cariello, A. N., et al. (2011). Functional connectivity magnetic resonance imaging classification of autism. *Brain* 134, 3742–3754. doi: 10.1093/brain/awr263

Arbabshirani, M. R., Plis, S., Sui, J., and Calhoun, V. D. (2017). Single subject prediction of brain disorders in neuroimaging: promises and pitfalls. *NeuroImage* 145(Pt B), 137–165. doi: 10.1016/j.neuroimage.2016.02.079

Ashburner, J. (2007). A fast diffeomorphic image registration algorithm. *NeuroImage* 38, 95–113. doi: 10.1016/j.neuroimage.2007.07.007

Bastian, M., Heymann, S., and Jacomy, M. (2009). "Gephi: an open source software for exploring and manipulating networks," in *International AAAI Conference on Web and Social Media*. Retrieved from https://www.aaai.org/ocs/index.php/ICWSM/09/paper/view/154/1009

Blondel, V., Guillaume, J.-L., Lambiotte, R., and Lefebvre, E. (2008). Fast unfolding of communities in large networks. *J. Stat. Mech. Theory Exp.* 2008, 10008–10020 doi: 10.1088/1742-5468/2008/10/P10008

Bullmore, E., and Sporns, O. (2009). Complex brain networks: graph theoretical analysis of structural and functional systems. *Nat. Rev. Neurosci.* 10, 186–198. doi: 10.1038/nrn2575

Chen, C. P., Keown, C. L., Jahedi, A., Nair, A., Pflieger, M. E., Bailey, B. A., et al. (2015). Diagnostic classification of intrinsic functional connectivity highlights somatosensory, default mode, and visual regions in autism. *NeuroImage* 8(Suppl. C), 238–245. doi: 10.1016/j.nicl.2015.04.002

Chen, G., Ward, B. D., Xie, C., Li, W., Chen, G., Goveas, J. S., et al. (2012). A clustering-based method to detect functional connectivity differences. *NeuroImage* 61, 56–61. doi: 10.1016/j.neuroimage.2012.02.064

Chen, H., Duan, X., Liu, F., Lu, F., Ma, X., Zhang, Y., et al. (2016). Multivariate classification of autism spectrum disorder using frequency-specific resting-state functional connectivity-a multi-center study. *Prog. Neuro-Psychopharmacol. Biol. Psychiatry* 64, 1–9. doi: 10.1016/j.pnpbp.2015.06.014

Craddock, C., Benhajali, Y., Chu, C., Chouinard, F., Evans, A., Jakab, A., et al. (2013). The neuro bureau preprocessing initiative: open sharing of preprocessed neuroimaging data and derivatives. *Front Neuroinformatics*. doi: 10.3389/conf.fninf.2013.09.00041

Craddock, R. C., James, G., Holtzheimer, P. E. III., Hu, X. P., and Mayberg, H. S. (2012). A whole brain fmri atlas generated via spatially constrained spectral clustering. *Hum. Brain Mapp.* 33, 1914–1928. doi: 10.1002/hbm.21333

De Vico Fallani, F., Richiardi, J., Chavez, M., and Achard, S. (2014). Graph analysis of functional brain networks: practical issues in translational neuroscience. *Philos. Trans. R. Soc. Lond. B Biol. Sci.* 369:20130521. doi: 10.1098/rstb.2013.0521

Di Martino, A., Yan, C.-G., and Li, Q. (2014). The autism brain imaging data exchange: towards a large-scale evaluation of the intrinsic brain architecture in autism. *Mol. Psychiatry* 19, 659–667. doi: 10.1038/mp.2013.78

Dvornek, N. C., Ventola, P., Pelphrey, K. A., and Duncan, J. S. (2017). "Identifying autism from resting-state fmri using long short-term memory networks," in *Machine Learning in Medical Imaging*, eds Q. Wang, Y. Shi, H.-I. Suk, and K. Suzuki (Cham: Springer International Publishing), 362–370.

Eguíluz, V. M., Chialvo, D. R., Cecchi, G. A., Baliki, M., and Apkarian, A. V. (2005). Scale-free brain functional networks. *Phys. Rev. Lett.* 94:018102. doi: 10.1103/PhysRevLett.94.018102

Epalle, T. E., and Liu, H. (2016). "Optimization and evaluation of a random walks-based community detection algorithm," in *2016 12th International Conference on Natural Computation, Fuzzy Systems and Knowledge Discovery (ICNC-FSKD)* (Changsha), 1222–1228.

Fortunato, S. (2010). Community detection in graphs. *Phys. Rep.* 486, 75–174. doi: 10.1016/j.physrep.2009.11.002

Ghiassian, S., Greiner, R., Jin, P., and Brown, M. R. G. (2016). Using functional or structural magnetic resonance images and personal characteristic data to identify adhd and autism. *PLoS ONE* 11:e0166934. doi: 10.1371/journal.pone.0166934

Girvan, M., and Newman, M. E. (2002). Community structure in social and biological networks. *Proc. Natl. Acad. Sci. U.S.A.* 99, 7821–7826. doi: 10.1073/pnas.122653799

Glerean, E., Pan, R. K., Salmi, J., Kujala, R., Lahnakoski, J. M., Roine, U., et al. (2016). Reorganization of functionally connected brain subnetworks in high-functioning autism. *Hum. Brain Mapp.* 37, 1066–1079. doi: 10.1002/hbm.23084

Guyon, I., Weston, J., Barnhill, S., and Vapnik, V. (2002). Gene selection for cancer classification using support vector machines. *Mach. Learn.* 46, 389–422. doi: 10.1023/A:1012487302797

Hastie, T., Tibshirani, R., and Friedman, J. (2009). *The Elements of Statistical Learning, Second Edition: Data Mining, Inference, and Prediction*. New York, NY: Springer Series in Statistics. Springer.

Heinsfeld, A. S., Franco, A. R., Craddock, R. C., Buchweitz, A., and Meneguzzi, F. (2018). Identification of autism spectrum disorder using deep learning

and the abide dataset. *NeuroImage* 17, 16–23. doi: 10.1016/j.nicl.2017.08.017

Hernández, C., and Navarro, G. (2012). *Compressed Representation of Web and Social Networks via Dense Subgraphs*. Berlin; Heidelberg: Springer Berlin Heidelberg.

Hull, J. V., Dokovna, L. B., Jacokes, Z. J., Torgerson, C. M., Irimia, A., and Van Horn, J. D. (2016). Resting-state functional connectivity in autism spectrum disorders: a review. *Front. Psychiatry* 7:205. doi: 10.3389/fpsyt.2016.00205

Iidaka, T. (2015). Resting state functional magnetic resonance imaging and neural network classified autism and control. *Cortex* 63, 55–67. doi: 10.1016/j.cortex.2014.08.011

Jun, E., Kang, E., Choi, J., and Suk, H.-I. (2019). Modeling regional dynamics in low-frequency fluctuation and its application to autism spectrum disorder diagnosis. *NeuroImage* 184, 669–686. doi: 10.1016/j.neuroimage.2018.09.043

Keown, C. L., Datko, M. C., Chen, C. P., Maximo, J. O., Jahedi, A., and Müller, R.-A. (2017). Network organization is globally atypical in autism: a graph theory study of intrinsic functional connectivity. *Biol. Psychiatry* 2, 66–75. doi: 10.1016/j.bpsc.2016.07.008

Ledl, T. (2004). Kernel density estimation: theory and application in discriminant analysis. *Aust. J. Stat.* 33, 267–279. doi: 10.17713/ajs.v33i3.441

Lerman-Sinkoff, D. B., and Barch, D. M. (2016). Network community structure alterations in adult schizophrenia: identification and localization of alterations. *Neuroimage* 10, 96–106. doi: 10.1016/j.nicl.2015.11.011

Liang, X., Wang, J., Yan, C., Shu, N., Xu, K., Gong, G., et al. (2012). Effects of different correlation metrics and preprocessing factors on small-world brain functional networks: a resting-state functional MRI study. *PLoS ONE* 7:e32766. doi: 10.1371/journal.pone.0032766

Liben-Nowell, D., and Kleinberg, J. (2007). The link-prediction problem for social networks. *J. Am. Soc. Inform. Sci. Technol.* 58, 1019–1031. doi: 10.1002/asi.20591

Meunier, D., Lambiotte, R., and Bullmore, E. (2010). Modular and hierarchically modular organization of brain networks. *Front. Neurosci.* 4:200. doi: 10.3389/fnins.2010.00200

Mitalidis, M., Kehagias, A., Gevezes, T., and Pitsoulis, L. (2014). *Manual for the Community Detection Toolbox v. 0.9*.

Newman, M. (2006). Modularity and community structure in networks. *Proc. Natl. Acad. Sci. U.S.A.* 103, 8577–8582. doi: 10.1073/pnas.0601602103

Ngonmang, B., Tchuente, M., and Viennet, E. (2012). Local community identification in social networks. *Parall. Process. Lett.* 22. doi: 10.1142/S012962641240004X

Nicolini, C., Bordier, C., and Bifone, A. (2017). Community detection in weighted brain connectivity networks beyond the resolution limit. *NeuroImage* 146, 28–39. doi: 10.1016/j.neuroimage.2016.11.026

Nielsen, J. A., Zielinski, B. A., Fletcher, P. T., Alexander, A. L., Lange, N., Bigler, E. D., et al. (2013). Multisite functional connectivity mri classification of autism: abide results. *Front. Hum. Neurosci.* 7:599. doi: 10.3389/fnhum.2013.00599

Plitt, M., Barnes, K. A., and Martin, A. (2015). Functional connectivity classification of autism identifies highly predictive brain features but falls short of biomarker standards. *NeuroImage* 7, 359–366. doi: 10.1016/j.nicl.2014.12.013

Pons, P., and Latapy, M. (2006). Computing communities in large networks using random walks. *J. Graph Algorith. Appl.* 10, 191–218. doi: 10.7155/jgaa.00124

Ponten, S., Bartolomei, F., and Stam, C. (2007). Small-world networks and epilepsy: graph theoretical analysis of intracerebrally recorded mesial temporal lobe seizures. *Clin. Neurophysiol.* 118, 918–927. doi: 10.1016/j.clinph.2006.12.002

Rand, W. (1971). Objective criteria for the evaluation of clustering methods. *J. Am. Stat. Assoc.* 66, 846–850. doi: 10.1080/01621459.1971.10482356

Rapin, I., and Tuchman, R. F. (2008). Autism: definition, neurobiology, screening, diagnosis. *Pediatr. Clin. North Am.* 55, 1129–1146. doi: 10.1016/j.pcl.2008.07.005

Rossval, M., and Bergstrom, C. (2008). Maps of random walks on complex networks reveal community structure. *Proc. Natl. Acad. Sci. U.S.A.* 105, 1118–1123. doi: 10.1073/pnas.0706851105

Rubinov, M., and Sporns, O. (2010). Complex network measures of brain connectivity: uses and interpretations. *NeuroImage* 52, 1059–1069. doi: 10.1016/j.neuroimage.2009.10.003

Rudie, J., Brown, J., Beck-Pancer, D., Hernandez, L., Dennis, E., Thompson, P., et al. (2013). Altered functional and structural brain network organization in autism. *NeuroImage* 2, 79–94. doi: 10.1016/j.nicl.2012.11.006

Shen, X., Papademetris, X., and Constable, R. (2010). Graph-theory based parcellation of functional subunits in the brain from resting-state fMRI data. *NeuroImage* 50, 1027–1035. doi: 10.1016/j.neuroimage.2009.12.119

Stam, C. J., and van Straaten, E. C. (2012). The organization of physiological brain networks. *Clin. Neurophysiol.* 123, 1067–1087. doi: 10.1016/j.clinph.2012.01.011

Steinhaeuser, K., and Chawla, N. V. (2010). Identifying and evaluating community structure in complex networks. *Patt. Recogn. Lett.* 31, 413–421. doi: 10.1016/j.patrec.2009.11.001

Supekar, K., Menon, V., Rubin, D., Musen, M., and Greicius, M. D. (2008). Network analysis of intrinsic functional brain connectivity in alzheimer's disease. *PLoS Comput. Biol.* 4:e1000100. doi: 10.1371/journal.pcbi.1000100

Tzourio-Mazoyer, N., Landeau, B., Papathanassiou, D., Crivello, F., Etard, O., Delcroix, N., et al. (2002). Automated anatomical labeling of activations in {SPM} using a macroscopic anatomical parcellation of the {MNI} {MRI} single-subject brain. *NeuroImage* 15, 273–289. doi: 10.1006/nimg.2001.0978

Uddin, L. Q., Menon, V., Young, C. B., Ryali, S., Chen, T., Khouzam, A., et al. (2011). Multivariate searchlight classification of structural magnetic resonance imaging in children and adolescents with autism. *Biol. Psychiatry* 70, 833–841. doi: 10.1016/j.biopsych.2011.07.014

van den Heuvel, M., Mandl, R., and Hulshoff Pol, H. (2008). Normalized cut group clustering of resting-state fMRI data. *PLoS ONE* 3:e2001. doi: 10.1371/journal.pone.0002001

van der Horn, H. J., Liemburg, E. J., Scheenen, M. E., de Koning, M. E., Spikman, J. M., and van der Naalt, J. (2017). Graph analysis of functional brain networks in patients with mild traumatic brain injury. *PLoS ONE* 12:e0171031. doi: 10.1371/journal.pone.0171031

Waheed, S. H., Mirbagheri, S., Agarwal, S., Kamali, A., Yahyavi-Firouz-Abadi, N., Chaudhry, A., et al. (2016). Reporting of resting-state functional magnetic resonance imaging preprocessing methodologies. *Brain Connect.* 6, 663–668. doi: 10.1089/brain.2016.0446

Wang, J., Wang, Q., Peng, J., Nie, D., Zhao, F., Kim, M., et al. (2017). Multi-task diagnosis for autism spectrum disorders using multi-modality features: a multi-center study. *Hum. Brain Mapp.* 38, 3081–3097. doi: 10.1002/hbm.23575

Wang, L., Zhu, C., He, Y., Zang, Y., Cao, Q., Zhang, H., et al. (2009). Altered small-world brain functional networks in children with attention-deficit/hyperactivity disorder. *Hum. Brain Mapp.* 30, 638–649. doi: 10.1002/hbm.20530

Xia, M., Wang, J., and He, Y. (2013). Brainnet viewer: a network visualization tool for human brain connectomics. *PLoS ONE* 8:e68910. doi: 10.1371/journal.pone.0068910

Yan, C., Wang, X., Zuo, X., and Zang, Y. (2016). Dpabi: data processing and analysis for (resting-state) brain imaging. *Neuroinformatics* 14, 339–351. doi: 10.1007/s12021-016-9299-4

Yan, C., and Zang, Y. (2010). Dparsf: a matlab toolbox for 'pipeline' data analysis of resting-state fMRI. *Front. Syst. Neurosci.* 4:13. doi: 10.3389/fnsys.2010.00013

Zachary, W. W. (1977). An information flow model for conflict and fission in small groups. *J. Anthropol. Res.* 33, 452–473. doi: 10.1086/jar.33.4.3629752

Zhou, Y., Yu, F., and Duong, T. (2014). Multiparametric MRI characterization and prediction in autism spectrum disorder using graph theory and machine learning. *PLoS ONE* 9:e90405. doi: 10.1371/journal.pone.0090405

Conflict of Interest Statement: The authors declare that the research was conducted in the absence of any commercial or financial relationships that could be construed as a potential conflict of interest.

frontiers in Human Neuroscience

ORIGINAL RESEARCH
published: 14 January 2020
doi: 10.3389/fnhum.2019.00464

Neuroinflammation and White Matter Alterations in Obesity Assessed by Diffusion Basis Spectrum Imaging

*Amjad Samara[1], Tatianna Murphy[1], Jeremy Strain[2], Jerrel Rutlin[1], Peng Sun[3], Olga Neyman[1], Nitya Sreevalsan[1], Joshua S. Shimony[3], Beau M. Ances[2], Sheng-Kwei Song[3], Tamara Hershey[1,2,3,4] and Sarah A. Eisenstein[1,3]**

[1] Department of Psychiatry, Washington University School of Medicine, St. Louis, MO, United States, [2] Department of Neurology, Washington University School of Medicine, St. Louis, MO, United States, [3] Mallinckrodt Institute of Radiology, Washington University School of Medicine, St. Louis, MO, United States, [4] Department of Psychological & Brain Sciences, Washington University School of Medicine, St. Louis, MO, United States

Human obesity is associated with low-grade chronic systemic inflammation, alterations in brain structure and function, and cognitive impairment. Rodent models of obesity show that high-calorie diets cause brain inflammation (neuroinflammation) in multiple regions, including the hippocampus, and impairments in hippocampal-dependent memory tasks. To determine if similar effects exist in humans with obesity, we applied Diffusion Basis Spectrum Imaging (DBSI) to evaluate neuroinflammation and axonal integrity. We examined diffusion-weighted magnetic resonance imaging (MRI) data in two independent cohorts of obese and non-obese individuals (Cohort 1: 25 obese/21 non-obese; Cohort 2: 18 obese/41 non-obese). We applied Tract-based Spatial Statistics (TBSS) to allow whole-brain white matter (WM) analyses and compare DBSI-derived isotropic and anisotropic diffusion measures between the obese and non-obese groups. In both cohorts, the obese group had significantly greater DBSI-derived restricted fraction (DBSI-RF; an indicator of neuroinflammation-related cellularity), and significantly lower DBSI-derived fiber fraction (DBSI-FF; an indicator of apparent axonal density) in several WM tracts (all corrected $p < 0.05$). Moreover, using region of interest analyses, average DBSI-RF and DBSI-FF values in the hippocampus were significantly greater and lower, respectively, in obese relative to non-obese individuals (Cohort 1: $p = 0.045$; Cohort 2: $p = 0.008$). Hippocampal DBSI-FF and DBSI-RF and amygdalar DBSI-FF metrics related to cognitive performance in Cohort 2. In conclusion, these findings suggest that greater neuroinflammation-related cellularity and lower apparent axonal density are associated with human obesity and cognitive performance. Future studies are warranted to determine a potential role for neuroinflammation in obesity-related cognitive impairment.

Keywords: obesity, white matter, neuroinflammation, diffusion tensor imaging, diffusion basis spectrum imaging

OPEN ACCESS

Edited by:
Dieter J. Meyerhoff, University of California, San Francisco, United States

Reviewed by:
Natalie M. Zahr, Stanford University, United States
Mohammed Hankir, Leipzig University, Germany

***Correspondence:**
Sarah A. Eisenstein
seisens@wustl.edu

Specialty section:
This article was submitted to Brain Imaging and Stimulation, a section of the journal Frontiers in Human Neuroscience

Received: *10 October 2019*
Accepted: *18 December 2019*
Published: *14 January 2020*

Citation:
Samara A, Murphy T, Strain J, Rutlin J, Sun P, Neyman O, Sreevalsan N, Shimony JS, Ances BM, Song S-K, Hershey T and Eisenstein SA (2020) Neuroinflammation and White Matter Alterations in Obesity Assessed by Diffusion Basis Spectrum Imaging. Front. Hum. Neurosci. 13:464. doi: 10.3389/fnhum.2019.00464

Abbreviations: AD, axial diffusivity; BBB, blood-brain barrier; BMI, body mass index; CNS, central nervous system; CSF, cerebrospinal fluid; DBSI, Diffusion basis spectrum imaging; DTI, diffusion tensor imaging; FA, fractional anisotropy; FF, fiber fraction; GLM, general linear model; HF, hindered fraction; ICV, intra-cranial volume; MRI, magnetic resonance imaging; MS, multiple sclerosis; PET, positron emission tomography; RD, radial diffusivity; RF, restricted fraction; ROI, region of interest analysis; TBSS, tract-based spatial statistics; TFCE, Threshold-Free Cluster Enhancement; TSPO, translocator protein; WM, white matter.

INTRODUCTION

Obesity is a rapidly growing epidemic around the world. According to the World Health Organization, in 2016 more than 1.9 billion adults were overweight and 650 million (about 9% of the world population) were obese ($\geq$30 kg/m^2) (WHO, 2018). Obesity is associated with comorbidities including type 2 diabetes, hypertension, heart disease, and cancer (Haslam and James, 2005). In addition, obesity is linked to cognitive deficits and is a risk factor for Alzheimer's disease (Miller and Spencer, 2014; Walker and Harrison, 2015; Alford et al., 2018). These latter features have raised the question of how obesity and its comorbidities may influence brain function and structure. Neuroimaging studies have found both structural and functional abnormalities in obesity, but the mechanisms underlying these differences are not well understood (Devoto et al., 2018; van Galen et al., 2018; Garcia-Garcia et al., 2019). One potential mechanism for brain structural and functional findings is brain inflammation (neuroinflammation), but this has not been explored thoroughly in humans (Guillemot-Legris and Muccioli, 2017).

Obesity is a disease of low-grade chronic systemic inflammation that affects many body organs (Gregor and Hotamisligil, 2011). Also, evidence from rodent models shows that obesity causes neuroinflammation (Guillemot-Legris et al., 2016). Similarly, in humans with obesity, postmortem brain examination shows evidence of gliosis and abnormal microglia activation in the hypothalamus and altered mRNA expression of inflammatory markers in frontal cortex suggestive of neuroinflammation (Baufeld et al., 2016; Lauridsen et al., 2017). Hypercaloric diet induces breakdown of the BBB, allowing pro-inflammatory cytokines to enter the CNS (Guillemot-Legris et al., 2016; Stranahan et al., 2016; Guillemot-Legris and Muccioli, 2017) and promotes peripheral macrophage infiltration to the brain (Stranahan et al., 2016), which subsequently contributes, among other factors such as increased peripheral free fatty acid circulation (O'Brien et al., 2017), to obesity-associated neuroinflammation. Intriguingly, hippocampal neuroinflammation causes deficits in memory tasks in rodent models of obesity (Pistell et al., 2010; Beilharz et al., 2016; Cope et al., 2018). In humans, higher adiposity is generally associated with poorer cognitive performance in a variety of measures, yet the underlying mechanism is not entirely understood (Wright et al., 2016; Gameiro et al., 2017; Tsai et al., 2017). Taken together, it is reasonable to hypothesize that obesity-related neuroinflammation impacts the function and structure of the human brain and could be an underlying mechanism of obesity-associated cognitive impairment.

Evaluation of obesity-associated neuroinflammation in humans via imaging is technically challenging and there are few research studies in this area. Measuring specific processes related to neuroinflammation (e.g., microglial activation) with neuroimaging is possible via PET with radiotracers (e.g., TSPO radiotracer) (Vivash and O'Brien, 2016; Alam et al., 2017). However, these PET radiotracers vary in specificity, and some individuals (~34% of Caucasians) have genotypes that confer very low to mixed binding affinity for TSPO ligands (Owen et al., 2012). Other research groups utilized MRI-based techniques to evaluate obesity-associated neuroinflammation. For example, alterations in T2-weighted MRI signal intensity (an indicator of gliosis) in the hypothalamus have been found in obese individuals (Thaler et al., 2012; Schur et al., 2015; Kreutzer et al., 2017). Also, plasma fibrinogen, a driver of inflammation, has been related to alterations in diffusivity characteristics of extra-hypothalamic brain regions including orbitofrontal cortex and amygdala in overweight and obese individuals (Cazettes et al., 2011). Interestingly, a recent study has also shown sex-specific effects of central adiposity and systemic inflammatory markers on limbic system microstructure (Metzler-Baddeley et al., 2019).

At the same time, a large number of neuroimaging studies have focused on the impact of obesity on WM microstructure using standard DTI modeling (Kullmann et al., 2015; Alfaro et al., 2018). DTI models a single diffusion tensor within an image voxel, to derive the standard diffusion tensor metrics (AD, RD, FA). Using this standard model, several studies have found that individuals with higher BMI have lower FA in many WM tracts (Marks et al., 2011; Mueller et al., 2011; Stanek et al., 2011; Verstynen et al., 2012; Karlsson et al., 2013; Xu et al., 2013; Lou et al., 2014; Bolzenius et al., 2015; He et al., 2015; Kullmann et al., 2015; Kullmann et al., 2016; Mazza et al., 2017; Papageorgiou et al., 2017; Alfaro et al., 2018) and mixed effects on AD and RD (Mueller et al., 2011; Xu et al., 2013; Kullmann et al., 2016; Mazza et al., 2017; Papageorgiou et al., 2017). In the healthy brain or disease conditions with limited edema and inflammation, lower FA and AD reflects impaired overall WM integrity and axonal injury, respectively, while greater RD reflects myelin damage (Wheeler-Kingshott and Cercignani, 2009; Winklewski et al., 2018). However, neuroinflammation-related processes such as cellularity and edema may confound standard DTI modeling, lead to mixed effects on AD and RD, and decrease the sensitivity and specificity to detect WM microstructural alterations (Winklewski et al., 2018).

In recent years, a novel data-driven DBSI (Wang et al., 2011; Wang et al., 2014) approach has been developed that shows sensitivity to both neuroinflammation and WM microstructural alterations. DBSI resolves intra-voxel partial volume effects arising from anisotropic and isotropic diffusion signals, and models both simultaneously to obtain the best estimation of anisotropic and isotropic diffusion tensors. Anisotropic tensor components modeled by DBSI consider water diffusion of WM tracts within the image voxel, deriving the rate of water diffusion parallel to the axon (DBSI-axial diffusivity or DBSI-AD) and perpendicular to the axon (DBSI-radial diffusivity or DBSI-RD) or fiber-tract specific diffusion anisotropy (DBSI-fractional anisotropy or DBSI-FA) reflecting the integrity of axon bundles. DBSI-derived fiber fraction (DBSI-FF) indicates axonal density. Simultaneously, DBSI models restricted isotropic diffusion into DBSI-restricted fraction (DBSI-RF; an indicator of resident and neuroinflammation-related cellularity) and non-restricted diffusion into DBSI-hindered fraction (DBSI-HF; an indicator of tissue edema). DBSI-derived isotropic measures (DBSI-RF and DBSI-HF) are sensitive to inflammation-related cellularity and tissue edema, respectively (Cross and Song, 2017),

and both are present in neuroinflammation (Frohman et al., 2006; Stamatovic et al., 2006). Validation studies of DBSI in animal models have shown that this method can differentiate axonal injury, demyelination, and neuroinflammation in white and gray matter (Wang et al., 2014; Cross and Song, 2017; Zhan et al., 2018). In humans, DBSI has been used to detect indicators of neuroinflammation in MS (Chiang et al., 2014), cervical spondylotic myelopathy (Murphy et al., 2016), traumatic spinal cord injury (Sun et al., 2017), HIV (Strain et al., 2017), and Alzheimer's disease (Wang et al., 2019). Importantly, when neuroinflammation is present, DBSI can provide further insight into WM microstructural integrity (Wang et al., 2011; Chiang et al., 2014; Wang et al., 2014; Wang et al., 2015; Murphy et al., 2016; Cross and Song, 2017; Lin et al., 2017; Strain et al., 2017; Sun et al., 2017; Shirani et al., 2018; Zhan et al., 2018; Lin et al., 2019).

The goal of the current study was to apply DBSI in humans to evaluate the presence of neuroinflammation and provide further insight into WM microstructural integrity in obesity. DBSI-derived metrics may also help resolve some of the conflicting findings from the DTI literature in obesity (Kullmann et al., 2015). We hypothesized that obese individuals would have greater DBSI-RF (an indicator of increased neuroinflammation-related cellularity), greater DBSI-HF (an indicator of increased edema), and lower DBSI-FF (an indicator of decreased apparent axonal density) compared to non-obese individuals. We tested these hypotheses in a cohort of obese and non-obese individuals recruited specifically for a study of brain alterations in obesity (Cohort 1). We then examined a more heterogeneous convenience sample to confirm the presence of similar patterns related to BMI status (Cohort 2). Since obese individuals show impaired cognitive function relative to non-obese individuals (Wright et al., 2016; Gameiro et al., 2017; Tsai et al., 2017), hippocampal neuroinflammation causes impairment on memory tasks in rodent models of obesity (Pistell et al., 2010; Beilharz et al., 2016; Cope et al., 2018), and the hippocampus and amygdala operate together to form emotion-associated memory (Yang and Wang, 2017), we selected the hippocampus and amygdala to perform region of interest (ROI) analyses and explored the presence of similar alterations in these regions and their relation to cognitive performance.

MATERIALS AND METHODS

Participants

In both cohorts, obesity was defined as $\geq$30 kg/m^2. Non-obesity was defined as $\leq$25 kg/m^2. All studies were approved by the Washington University School of Medicine Human Research Protection Office and were carried out in accordance with the principles expressed in the Declaration of Helsinki. All participants gave written, informed consent prior to participation.

Cohort 1: Healthy obese and non-obese adults were recruited through an online research participant database at Washington University, advertisements, and word of mouth for a neuroimaging study on obesity. All participants were assessed for the presence of diabetes with an oral glucose tolerance test and excluded from further participation if glucose or hemoglobin A1c levels met American Diabetes Association criteria for Type 2 diabetes (American Diabetes Association, 2016). Participants were also assessed with a detailed history, including neurological and physical examinations, psychiatric interviews using the Structured Interview for DSM-IV-TR Axis I Disorders (SCID) (First et al., 2002), and routine blood tests. Volunteers were excluded for history of medical problems as well as other significant neurological, cerebrovascular, cardiovascular, or psychiatric diagnosis (DSM-IV Axis I disorders except for specific phobias), head trauma, any current or recent dopaminergic drug use (e.g., stimulants, agonists, bupropion, neuroleptics or metoclopramide), current heavy alcohol use (males $>$ 2 drinks per day, females $>$ 1 drink per day) or illicit drug use, history of substance abuse or dependence, and IQ $<$ 80 as measured by the Wechsler Abbreviated Scale of Intelligence (WASI) (Wechsler, 1999). Data from individuals in this sample have been reported previously (Eisenstein et al., 2013; Eisenstein et al., 2015a,b; Pepino et al., 2016).

Cohort 2: Healthy obese and non-obese adults were recruited through an online research database at Washington University and flyers to be a control group for ongoing studies. Exclusion criteria included self-reported diabetic medication use or unknown diabetic medication status, current or past history of confounding neurological disorders, depression as assessed by the Beck Depression Inventory II (BDI-II) (Beck et al., 1996), current alcohol or substance abuse, head injury with loss of consciousness greater than 30 min, claustrophobia or seizures, and fewer than 8 years of education. Data from some individuals in this sample have been reported previously (Strain et al., 2017).

BMI Measures

Body mass index was calculated as kg/m^2 in both cohorts. Cohort 1: Height and weight measurements were taken by a trained nurse. Cohort 2: Height and weight were self-reported by participants.

Neuropsychological Performance

As described previously (Strain et al., 2017), individuals in Cohort 2 completed a cognitive test battery that included executive function, verbal and visuospatial learning and memory, and psychomotor speed. These included the Wechsler Adult Intelligence Scale III [WAIS-III including digit span, digit symbol, symbol search, and letter number sequencing subtests (Wechsler, 1997)]; Trail-making Test Parts A and B (Reitan, 1958); Multilingual Aphasia Examination verbal fluency subtest (Benton and Hamsher, 1976); F-A-S test (Spreen and Benton, 1977); animal (category) fluency (Goodglass and Kaplan, 1972); Delis-Kaplan Executive Function System [D-KEFS including Color-Word Interference Task (Delis et al., 2001)]; Hopkins Verbal Learning Test (HVLT) learning and recall (Brandt, 1991); Brief Visuospatial Memory Test-Revised (BVMT-R) (Benedict, 1997); Grooved Peg Board (Baser and Ruff, 1987); and finger-tapping test (FTT) (Schmitt, 2013). The Wide Range Achievement Test 3 (WRAT3) (Snelbaker et al., 2001) was also administered.

MRI Acquisition

Cohort 1: Magnetic resonance imaging scanning was performed on a Siemens Trio 3T scanner with a 20 channel head coil. Structural magnetic resonance T1-weighted anatomical images were obtained using a 3-D MPRAGE sequence [sagittal orientation, repetition time (TR) = 2400 ms, echo time (TE) = 3.16 ms, inversion time (TI) = 1000 ms, voxel resolution = 1 × 1 × 1 mm^3, frames = 176, flip angle = 8°, FOV = 256 × 256 mm]. We acquired two echo planar DTI sequences, of similar phase encoding direction, with 27 volumes each (transverse orientation, 2 × 2 × 2 mm^3 voxels, TR = 12,300 ms, TE = 108 ms, flip angle = 90°, 25 directions, *b*-values ranging from 0 to 1400 s/$mm^{2,}$ and two non-diffusion weighted images).

Cohort 2: Magnetic resonance imaging scanning was performed on the same Siemens Trio 3T scanner with a 12 channel head coil. Structural magnetic resonance T1-weighted anatomical images were obtained using the 3-D MPRAGE sequence described for Cohort 1. Two sequential diffusion-weighted scans, of similar phase encoding direction, were obtained (transverse orientation, 2 × 2 × 2 mm^3 voxels, TR = 9,900 ms, TE = 102 ms, flip angle = 90°, 23 directions, *b*-values ranging from 0 to 1400 s/mm^2, and one non-diffusion weighted image).

Image Preprocessing and DTI Processing

For both cohorts, all DTI volumes were manually inspected to exclude the presence of large artifacts. FMRIB Software Library (FSL) (Smith et al., 2004) was used to perform all preprocessing steps and fit the DTI diffusion tensor model at each imaging voxel. Non-brain tissue was removed using FSL BET (brain extraction tool) (Smith, 2002), followed by motion and eddy-current distortions correction. Field maps were not acquired as part of these studies and thus corrections for susceptibility-induced distortions were not performed. For DTI analyses, FSL DTIFIT tool was used to compute diffusivities from fitting the diffusion tensor model and to generate DTI-FA (DTI-fractional anisotropy), DTI-MD (DTI-mean diffusivity), DTI-RD (DTI-radial diffusivity), and DTI-AD (DTI-axial diffusivity) volumes for each subject. DTI-derived image volumes for each participant were subsequently processed through the TBSS (Smith et al., 2006) pipeline to allow for whole-brain WM voxel-wise analyses as described below.

Since head motion during MRI scans is positively related to and shares genetic factors with BMI (Hodgson et al., 2017), and because registration-based correction methods do not exclude the effects of head motion entirely, we also computed motion parameters as described by Yendiki et al. (2014). These motion parameters include average volume-by-volume translation, average volume-by-volume rotation, percentage of slices with signal drop-out, and signal drop-out severity. In order to obtain these motion measures, we completed the image correction and quality assessment steps of the TRACULA pipeline (TRActs Constrained by UnderLying Anatomy), without running the WM pathways reconstruction steps (Yendiki et al., 2011). TRACULA-derived average volume-by-volume translation and average volume-by-volume rotation were included as regressors in subsequent voxel-wise and statistical analyses. The readout of percentage of slices with signal drop-out and signal drop-out severity were 0 and 1, respectively, for every participant in both cohorts.

DBSI Processing

Diffusion basis spectrum imaging measures were calculated using in-house software scripted in MATLAB and Statistics Toolbox Release (2012), and as first described in Wang et al. (2011). Unlike conventional DTI modeling, DBSI modeling simultaneously differentiates and quantifies several intravoxel pathological processes (axonal injury/loss, axonal demyelination, neuroinflammation-related cellularity, and vasogenic edema) by assigning a dedicated diffusion tensor for each of these pathological processes. While DTI-derived FA quantifies the degree of anisotropy for the whole image voxel, DBSI estimates anisotropy of fiber tracts within the image voxel without being confounded by isotropic diffusion. The total diffusion signal (S_k) measured by DBSI includes both anisotropic (A_k) and isotropic (I_k) diffusion tensor components, and the weighted sum of these components is presented in Eq. 1.

$$S_k = \sum_{i=1}^{N_{Aniso}} f_i e^{-|\vec{b}_k|.\lambda_{\perp_i}} e^{-|\vec{b}_k|.(\lambda_{\parallel_i}-\lambda_{\perp_i}).\cos^2\Phi_{ik}} + \int_a^b f(D) e^{-|\vec{b}_k|D}\, dD \quad (k = 1, 2, 3, \ldots, k). \qquad (1)$$

Where S_k and $\vec{b}_k$ are the signal and *b*-value of the k^{th} diffusion gradient; N_{Aniso} is the number of anisotropic tensors, $\Phi_{ik}$is the angle between the principal direction of the i^{th} anisotropic tensor and the k^{th} diffusion gradient; $\lambda_{\parallel_i}$ and $\lambda_{\perp_i}$ are the AD and RD of the i^{th} anisotropic tensor, f_i is the signal intensity fraction for the i^{th} anisotropic tensor, and *a* and *b* are the isotropic diffusion spectrum $f(D)$ low and high diffusivity limits.

Moreover, DBSI assesses isotropic diffusion tensor signal distribution within the whole spectrum of apparent isotropic diffusivity (resulting from intracellular and sub-cellular structures, and edematous extracellular tissue). Through previous experimental analyses (Wang et al., 2011; Wang et al., 2015), we grossly grouped isotropic diffusion as restricted diffusion ($D \leq 0.3\ \mu m^2$/ms; a proxy measure of water diffusion in the intracellular compartment hence cellularity), and non-restricted isotropic diffusion ($D > 0.3\ \mu m^2$/ms; a proxy measure of water diffusion in the extracellular space). By solving the DBSI model, we obtain a group of anisotropic and isotropic metrics that include: DBSI-FA (indicates overall WM integrity), DBSI-AD (indicates axonal loss/injury), DBSI-RD (indicates myelin loss), DBSI-fiber fraction or DBSI-FF (indicates apparent axonal density), DBSI-RF ($D \leq 0.3\ \mu m^2$/ms; indicates inflammation-related cellularity), and DBSI-hindered fraction or DBSI-HF ($D > 0.3\ \mu m^2$/ms; indicates extracellular tissue edema). DBSI-derived image volumes for each subject were subsequently processed through the TBSS pipeline to allow for whole-brain WM voxel-wise analyses as described below.

TBSS and Voxel-Wise Analyses

Post-processing and voxel-wise analyses of DTI- and DBSI-derived metrics were completed with TBSS (Smith et al., 2006). DTI-FA images were used to create an average WM skeleton. First, all DTI-FA were slightly eroded and end slices were excluded to remove potential outliers from diffusion tensor fitting. Secondly, all images were non-linearly registered to FMRIB58-FA standard-space image as a target image. Aligned FA images were then averaged to create a mean FA image, and fed into the skeletonization step to create a WM skeleton using a threshold of FA > 0.2. Using the same transformation process, all DTI- and DBSI-derived images, for each subject, were projected onto the mean FA skeleton, which represents the center of WM tracts common to all subjects, and used to perform further voxel-wise and ROI analyses.

Finally, the FSL Randomize tool (Winkler et al., 2014) was applied to perform separate voxel-wise statistical analyses within each cohort, and determined which skeleton voxels were significantly different between obese and non-obese groups ($p < 0.05$, corrected for multiple comparisons). We used GLMs controlling for age, sex, and race. Also, to account for the effects of head motion, we also controlled for TRACULA-derived motion measures (volume-by-volume translation and rotation). The TFCE option was used in TBSS analysis to correct for family-wise error (Nichols and Holmes, 2002).

Hippocampal and Amygdalar ROI and WM Tracts Analyses

In both cohorts, total hippocampal and amygdalar volumes for each individual were computed using FreeSurfer 6.0 segmentation[1] of corresponding structural MRI images. Hippocampal and amygdalar volumes were corrected for total intracranial volumes (ICV) and compared between obese and non-obese groups. For all individuals, average DBSI-derived metrics (both anisotropic and isotropic) in the right and left hippocampus and amygdala were extracted using ROIs from the 50% thresholded Harvard-Oxford Subcortical Structural Atlas provided by the Harvard Center for Morphometric Analysis in FSL (Smith et al., 2004). Average hippocampal and amygdalar DBSI-metrics were compared between obese and non-obese groups in each cohort separately. Additionally, the JHU-ICBM-DTI-81 WM labels atlas was used to create masks to define WM ROIs for further analyses (Mori et al., 2008). To assess whether differences in DBSI metrics between obese and non-obese groups were spatially and qualitatively similar across cohorts, we computed the percentage of overlap between cohorts in all 48 WM tracts for significant differences in DBSI-RF, DBSI-FF, and DBSI-AD. Importantly, the hypothalamus was not included in our ROI analyses. In our experience, anatomical boundaries of the hypothalamus are not clearly visible on MRIs, making it difficult to be certain whether measures are not affected by partial volume effects. Therefore, we did not include this region in our analyses.

[1]https://surfer.nmr.mgh.harvard.edu/

Statistical Analyses

Differences in demographic, motion parameters, and hippocampal volume variables between non-obese and obese individuals were assessed with between-subjects Student's *t*-tests or, if data were not normally distributed, Mann–Whitney *U* tests. Differences in race and sex distributions between obese and non-obese groups were assessed with Chi-square tests. Voxel-wise analyses compared DTI- and DBSI-derived metrics between obese and non-obese groups within each cohort separately, using GLM controlling for age, sex, race, and TRACULA-derived motion parameters (volume-by-volume translation and rotation). Further voxelwise GLM analyses determined whether BMI related to DBSI metrics of interest within each group in both cohorts. For each GLM, the FSL statistical package Randomize (Winkler et al., 2014) was used to correct for multiple comparisons via a TFCE approach with a family-wise error rate derived from 5000 Monte Carlo permutations (Nichols and Holmes, 2002). Statistical significance was thresholded at corrected $p \leq 0.05$. Average hippocampal and amygdalar DTI- and DBSI-derived metrics were compared between obese and non-obese groups, within each cohort separately, using a multiple linear regression model with age, sex, race, average hippocampal or amgydalar volume, and motion parameters as covariates. Additionally, in Cohort 2, we used partial Pearson *r* correlations controlling for age to relate main DBSI outcomes in the hippocampus and amygdala with performance on cognitive tasks. It was not expected that these exploratory correlational analyses would survive multiple comparison correction [0.05/(19 tests $\times$ 2 brain regions) = 0.0013]. Differences in cognitive performance between obese and non-obese individuals in Cohort 2 were assessed with two-tailed between-subjects Student's *t*-tests.

RESULTS

Participants

Participant demographics and descriptive statistics for Cohort 1 and Cohort 2 are shown in **Table 1**.

Cohort 1: Twenty-five obese (BMI = 33.4–51 kg/m^2) and twenty-one non-obese (BMI = 18.6–25.9 kg/m^2) participants contributed DTI scans for analyses. Data from two individuals whose BMIs were 25.1 and 25.9 kg/m^2 were included as non-obese since they met criteria for normal percent body fat and other metabolic parameters. Obese participants were older than non-obese participants and had a larger proportion of African Americans compared to the non-obese group. Non-obese and obese groups did not differ in sex distribution or years of education.

Cohort 2: Eighteen obese (BMI = 30–43 kg/m^2) and forty-one non-obese (BMI = 18.5–25 kg/m^2) participants contributed DTI scans for analyses. Sex and race distributions differed between obese and non-obese groups such that there were higher proportions of females and African Americans in the obese group. Obese and non-obese groups did not differ in age or years of education.

TABLE 1 | Demographic data and TRACULA-derived motion parameters for obese and non-obese participants in Cohort 1 and Cohort 2.

Cohort 1	**Non-obese (*n* = 21)**	**Obese (*n* = 25)**	***p*-value**
Age (years) mean (S.D.)	28 (5.2)	31.6 (6.4)	0.05*
Sex (male/female)	5/16	4/21	0.51
Race	18 C/2 AA/1 H	13 C/12 AA	0.01**
Body mass index (kg/m^2) mean (S.D.)	22 (2.2)	40 (4.9)	<0.001***
Education level (years) mean (S.D.)	15.8 (1.49)	15.1 (1.82)	0.23
Volume-by-volume translation (mm) mean (S.D.)	0.96 (0.2)	1.1 (0.1)	0.03*
Volume-by-volume rotation (mm) mean (S.D.)	0.0039 (0.0007)	0.0043 (0.0007)	0.08
Cohort 2	**Non-obese (*n* = 41)**	**Obese (*n* = 18)**	***p*-value**
Age (years) mean (S.D.)	29.5 (14.4)	29.8 (12.9)	0.12
Sex (male/female)	25/16	3/15	0.002**
Race	23 C/16 AA/1 AS/1 BI	5 C/13 AA	0.03*
Body mass index (kg/m^2) mean (S.D.)	21.7 (1.7)	35.7 (4.3)	<0.001***
Education level (years) mean (S.D.)	13.2 (2.08)	13.3 (1.33)	0.55
Volume-by-volume translation (mm) mean (S.D.)	1.06 (0.1)	1.13 (0.13)	0.04*
Volume-by-volume rotation (mm) mean (S.D.)	0.0042 (0.001)	0.0048 (0.001)	0.09

**, **, ***, $p \leq 0.05, 0.01, 0.001$ relative to non-obese. Independent Student's t-test, Mann–Whitney U test, or Pearson Chi-Square test were used as appropriate. C, Caucasian; AA, African American; H, Hispanic; AS, Asian; BI, Bi-racial. S.D., standard deviation.*

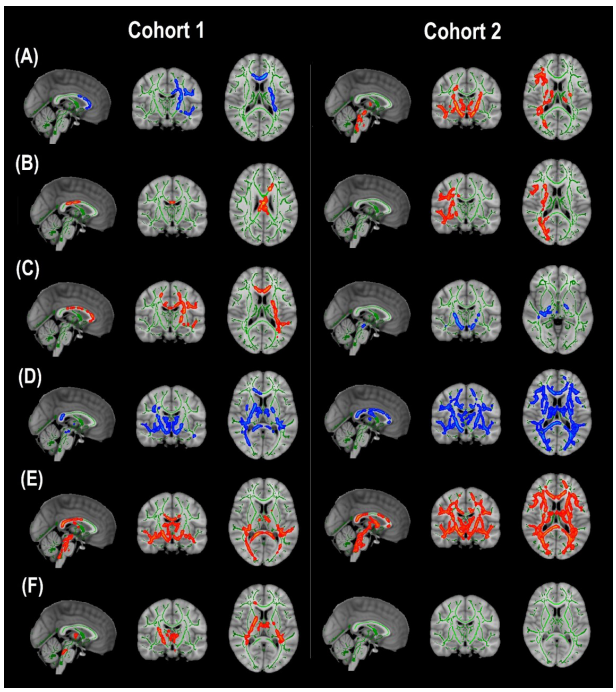

FIGURE 1 | Diffusion basis spectrum imaging-derived measures of white matter integrity and indicators of neuroinflammation in Cohort 1 and Cohort 2. **(A)** DBSI-derived fractional anisotropy. **(B)** DBSI-derived axial diffusivity. **(C)** DBSI-derived radial diffusivity. **(D)** DBSI-derived fiber fraction. **(E)** DBSI-derived restricted fraction. **(F)** DBSI-derived hindered fraction. *Green*, white matter skeleton; *red-yellow*, obese greater than non-obese group ($p < 0.05$, corrected); *blue-light blue*, obese lower than non-obese group ($p < 0.05$, corrected).

Motion Parameters

TRACULA-derived motion parameters for Cohort 1 and Cohort 2 are shown in **Table 1**. In both cohorts, the obese group required greater volume-by-volume translation for motion correction during the DTI scans. However, neither this measure nor volume-by-volume rotation related to BMI within non-obese ($r \leq 0.31$, $p \geq 0.18$) or obese ($r \leq 0.21$, $p \geq 0.40$) groups in either cohort.

Voxel-Wise Comparison of DBSI and DTI Metrics

Cohort 1: In TBSS analyses that covaried age, sex, race, and motion parameters, DBSI-FA was lower in obese compared to non-obese individuals, while DBSI-AD and RD were greater in obese compared to non-obese individuals (**Figures 1A–C**). DBSI-FF was lower in obese compared to non-obese individuals (**Figure 1D**) while DBSI-RF and DBSI-HF were greater in obese compared to non-obese individuals (**Figures 1E,F**). Lower DTI-FA and DTI-AD were observed in obese compared to non-obese individuals (**Figure 2A**). DTI-MD and DTI-RD were not significantly different between obese and non-obese individuals (data not shown).

Cohort 2: In TBSS analyses that covaried age, sex, race, and motion parameters, similar to Cohort 1, the obese group had lower DBSI-FF and greater DBSI-RF when compared to the non-obese group (**Figures 1D,E**). DBSI-FA and DBSI-AD were greater in the obese compared to the non-obese group while DBSI-RD was lower in the obese group compared to the non-obese group (**Figures 1A–C**). DBSI-HF did not differ between obese and non-obese groups. DTI-AD was lower in the obese compared to the non-obese group (**Figure 2B**). DTI-FA (**Figure 2B**), DTI-MD and DTI-RD were not significantly different between obese and non-obese individuals (data not shown).

For the group differences in DBSI-FF and DBSI-RF, we determined the degree to which WM tracts overlapped in both cohorts (**Figure 3**). Differences in DBSI-RF and DBSI-FF were observed in widespread WM tracts and the percentage of overlap between both cohorts in all 48 WM tracts are included in **Supplementary Table 1**, in which columns are sorted in descending order according to the number of voxels that overlap for DBSI-RF.

Voxelwise Correlations Between BMI and DBSI Metrics of Interest

Higher BMI related to greater voxelwise DBSI-RF in WM tracts within obese and non-obese groups in Cohort 1 but not within either group in Cohort 2. BMI did not relate to

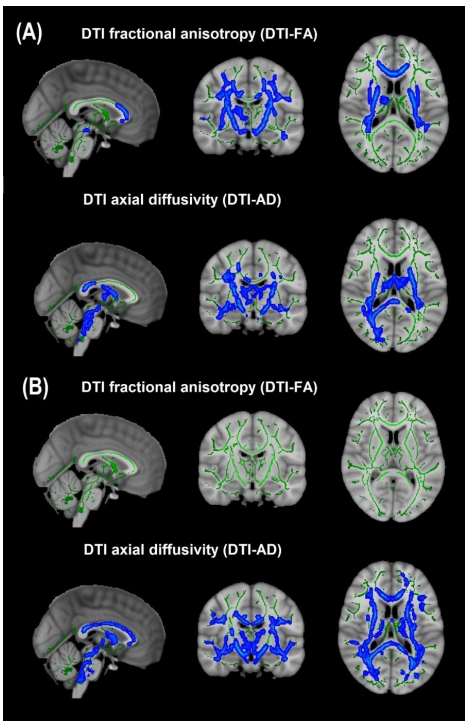

FIGURE 2 | Diffusion tensor imaging-derived measures of white matter integrity in Cohort 1 and Cohort 2. **(A)** Cohort 1: Obese individuals had lower white matter fractional anisotropy (FA) and axial diffusivity (AD) than non-obese individuals. **(B)** Cohort 2: Obese individuals had similar white matter FA but lower AD than non-obese individuals. *Green*, white matter skeleton; *blue-light blue*, obese lower than non-obese group ($p < 0.05$, corrected).

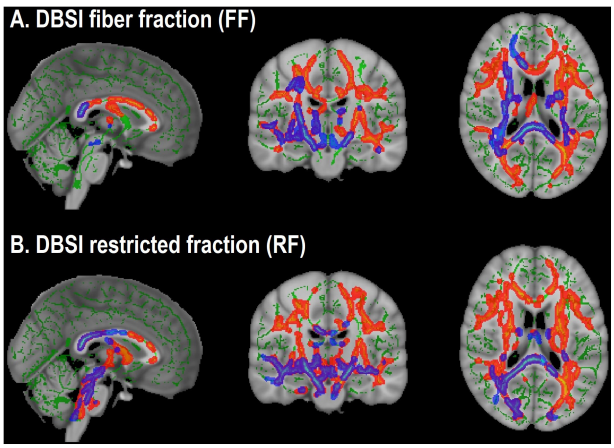

FIGURE 3 | Overlap in white matter tracts with significant differences between obese and non-obese groups in both cohorts (Cohort 1: *Blue-purple*; Cohort 2: *Red-yellow*). **(A)** Lower DBSI fiber fraction in obese compared to non-obese. **(B)** Greater DBSI restricted fraction in obese compared to non-obese.

voxelwise DBSI-FF in WM tracts in either group in either cohort (data not shown).

ROI Analyses of Hippocampal and Amygdalar DBSI Metrics

In both Cohort 1 and Cohort 2, we compared average hippocampal and amygdalar volumes and hippocampal and amygdalar DBSI-derived metrics (DBSI-FA, DBSI-AD, DBSI-RD, DBSI-FF, DBSI-RF, DBSI-HF) between obese and non-obese groups using multiple linear regression, covarying for age, sex, race, average hippocampal or amygdalar volumes, and motion measures (volume-by-volume translation and rotation) (**Figure 4** and **Tables 2**, **3**). In Cohort 1, hippocampal DBSI-RF was greater in the obese group when compared to the non-obese group (Cohen's *d* effect size = 1.03; 19.7% increase). Amygdalar DBSI metrics were not different between obese and non-obese groups in Cohort 1. In Cohort 2, hippocampal DBSI-AD and DBSI-RF were greater in the obese compared to the non-obese group (Cohen's *d* effect sizes = 0.59 and 0.70, 3.4% increase and 12.2% increase, respectively) and amygdalar DBSI-FF and DBSI-RF were lower and greater in the obese compared to the non-obese group, respectively (Cohen's *d* effect sizes = 1.2 for both comparisons, 8.3% decrease and 22% increase, respectively). Amygdalar volume was larger in obese relative to non-obese individuals in both cohorts. Hippocampal volumes and other DBSI-derived metrics were not different between obese and non-obese individuals in either cohort.

Cognitive Correlations With Hippocampal and Amygdalar DBSI-RF and DBSI-FF

Scores from cognitive measures acquired from Cohort 2 were correlated across obese and non-obese individuals with DBSI-RF and DBSI FF in the hippocampus and amygdala, controlling for age (**Figure 5**). Eighteen cognitive measures had enough data points to be included in these exploratory analyses. BVMT, WAIS-III digit span subtest and FTT for the non-dominant hand performances were not included due to insufficient data points (≥20 subjects did not have one or more of these data points). All other correlations between ROI DBSI-FF or DBSI-RF and cognitive measures were not significant ($p \geq 0.06$; data not shown). Also, we compared cognitive measure scores to assess between-group differences (data not shown). The obese group showed lower total recall (HVLT total recall, $p = 0.02$) and lower delayed verbal recall (HVLT delayed recall; $p = 0.007$), while no differences were observed in other cognitive measures ($p \geq 0.11$).

DISCUSSION

The findings of our current study indicate the presence of diffuse neuroinflammation (greater DBSI-RF) in several WM tracts and hippocampus in both cohorts and amygdala in Cohort 2 and lower apparent axonal density (DBSI-FF) in several WM tracts in both cohorts and amygdala in Cohort 2 in obese individuals as assessed by DBSI. Additionally, obese groups had consistently higher DBSI-AD when compared to non-obese groups, but DBSI-FA and DBSI-RD were inconsistent

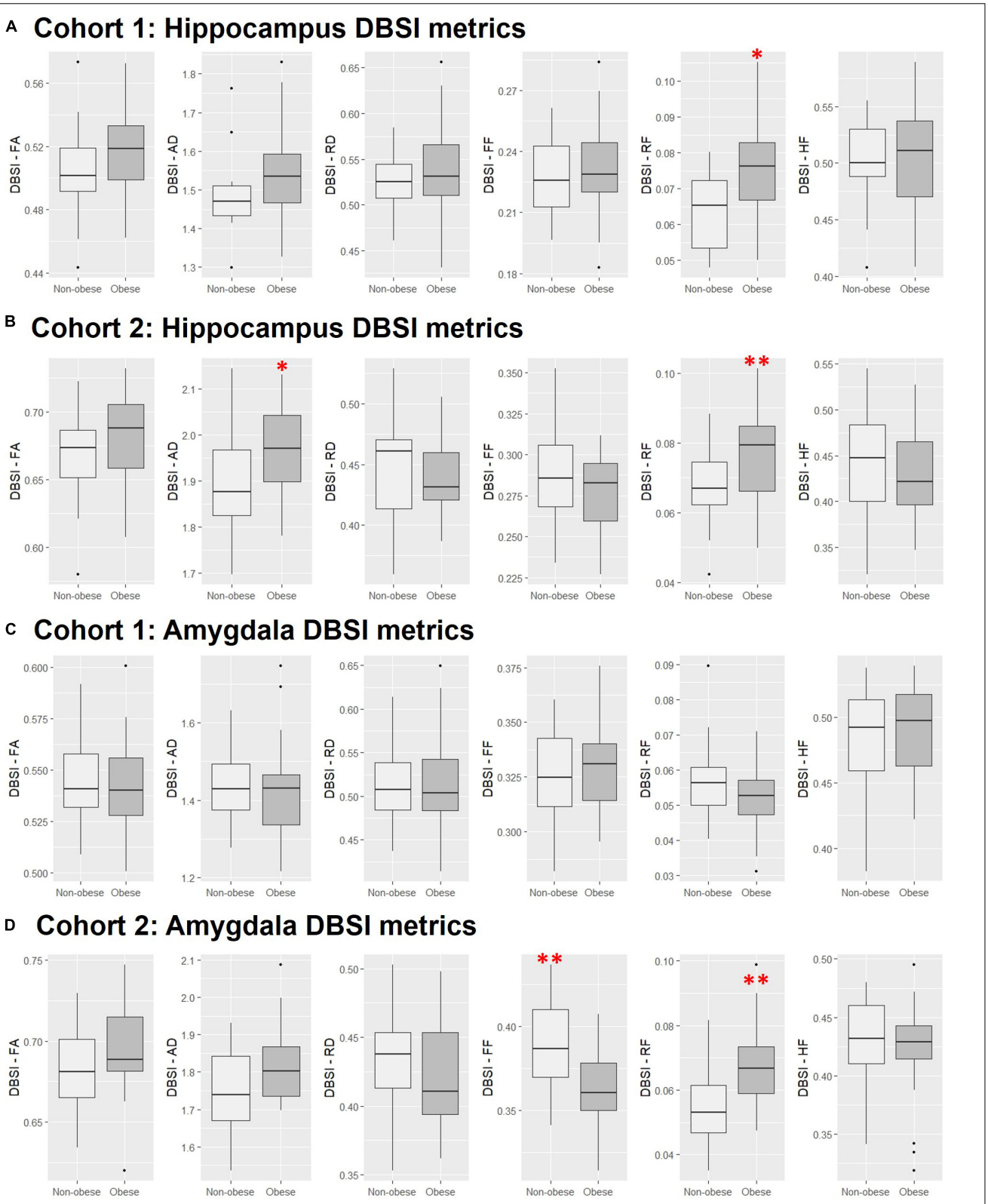

FIGURE 4 | Comparison of DBSI metrics in the hippocampus **(A,B)** and amygdala **(C,D)** between obese and non-obese groups in Cohort 1 and Cohort 2. FA, fractional anisotropy; AD, axial diffusivity; RD, radial diffusivity; FF, fiber fraction; HF, hindered fraction. Median, first and third quartiles, 1.5 × interquartile range shown. *, **, $p \leq 0.05$, 0.01, respectively.

TABLE 2 | Hippocampal DBSI metrics and volumes in obese and non-obese groups in Cohort 1 and Cohort 2.

	Cohort 1			Cohort 2		
	Obese	**Non-obese**	***p*-value**	**Obese**	**Non-obese**	***p*-value**
DBSI-FA	0.52 ± 0.03	0.5 ± 0.03	0.06	0.68 ± 0.03	0.67 ± 0.03	0.37
DBSI-AD	1.54 ± 0.11	1.48 ± 0.09	0.09	1.97 ± 0.1	1.9 ± 0.1	0.02*
DBSI-RD	0.54 ± 0.05	0.53 ± 0.03	0.35	0.44 ± 0.03	0.45 ± 0.04	0.67
DBSI-FF	0.23 ± 0.02	0.23 ± 0.02	0.37	0.28 ± 0.02	0.29 ± 0.03	0.22
DBSI-RF	0.08 ± 0.01	0.06 ± 0.01	0.045*	0.08 ± 0.01	0.07 ± 0.01	0.008*
DBSI-HF	0.51 ± 0.05	0.50 ± 0.04	0.35	0.43 ± 0.05	0.44 ± 0.06	0.54
Hippocampal volume (mm^3)	4203.2 ± 308	4009.2 ± 274	0.89	4358.8 ± 810	3856.1 ± 356	0.67

*Mean ± S.D. shown. DBSI metrics are unitless. *, **, ***, $p \leq 0.05, 0.01, 0.001$ relative to non-obese. DBSI, Diffusion Basis Spectrum Imaging; FA, fractional anisotropy; AD, axial diffusivity; RD, radial diffusivity; FF, fiber fraction; RF, restricted fraction; HF, hindered fraction.*

TABLE 3 | Amygdalar DBSI metrics and volumes in obese and non-obese groups in Cohort 1 and Cohort 2.

	Cohort 1			Cohort 2		
	Obese	**Non-obese**	***p*-value**	**Obese**	**Non-obese**	***p*-value**
DBSI-FA	0.54 ± 0.02	0.55 ± 0.02	0.3	0.7 ± 0.03	0.68 ± 0.02	0.41
DBSI-AD	1.43 ± 0.12	1.44 ± 0.09	0.61	1.83 ± 0.11	1.75 ± 0.11	0.31
DBSI-RD	0.51 ± 0.06	0.51 ± 0.04	0.26	0.42 ± 0.04	0.43 ± 0.03	0.16
DBSI-FF	0.33 ± 0.02	0.33 ± 0.02	0.27	0.36 ± 0.02	0.39 ± 0.03	<0.001***
DBSI-RF	0.05 ± 0.01	0.06 ± 0.01	0.33	0.07 ± 0.01	0.05 ± 0.01	<0.001***
DBSI-HF	0.49 ± 0.04	0.49 ± 0.04	0.28	0.42 ± 0.05	0.43 ± 0.03	0.78
Amygdala volume (mm^3)	1746.04 ± 157	1669.41 ± 116	0.07	1802.5 ± 338	1575.7 ± 117	0.05*

*Mean ± S.D. shown. DBSI metrics are unitless. *, **, ***, $p \leq 0.05, 0.01, 0.001$ relative to non-obese. DBSI, diffusion basis spectrum imaging; FA, fractional anisotropy; AD, axial diffusivity; RD, radial diffusivity; FF, fiber fraction; RF, restricted fraction; HF, hindered fraction.*

across cohorts (lower DBSI-FA and greater DBSI-RD in Cohort 1; greater DBSI-FA and lower DBSI-RD in Cohort 2). These findings might also indicate that neuroinflammation-related processes (cellular infiltration and tissue edema) could have confounded DTI-derived metrics. Exploratory analyses showed correlations between hippocampal and amygdalar DBSI-RF or DBSI-FF and some cognitive variables in Cohort 2.

Comparison Between DTI and DBSI Findings in Obesity

Diffusion tensor imaging has been extensively used to evaluate WM microstructure changes associated with obesity. Consistently, lower DTI-FA has been observed in obese compared to non-obese groups (Kullmann et al., 2015), while DTI-AD and DTI-RD alterations have been mixed (Mueller et al., 2011; Xu et al., 2013; Kullmann et al., 2016; Mazza et al., 2017; Papageorgiou et al., 2017). In our study, in several WM tracts, DTI-AD was lower in obese groups in both cohorts, DTI-FA was lower in the obese group in Cohort 1, while DTI-RD was not different between groups in either cohort. Using the traditional interpretation of DTI results, these findings indicate impaired overall WM integrity and axonal injury in the obese groups. Because DTI models both intra-axonal and extra-axonal water diffusion, cellularity associated with obesity might lead to decreased diffusion in all directions, resulting in the observed decrease in DTI-AD even without the presence of axonal injury. When isotropic diffusion was accounted for in the DBSI modeling, DBSI-AD was slightly greater in the obese groups in both cohorts, which could indicate increased water diffusion parallel to the axons in the extracellular compartment as a result of increased tissue edema. The presence of tissue edema could also contribute to the lower apparent axonal density (lower DBSI-FF) in the obese groups. These findings indicate that neuroinflammation-related processes (cellular infiltration and tissue edema) could have confounded DTI-derived metrics. This notion was previously suggested by some authors and demonstrated by histopathological studies in animal models of neuroinflammatory diseases (Wang et al., 2014; Cross and Song, 2017; Winklewski et al., 2018; Zhan et al., 2018).

The inconsistent differences in DBSI-FA and DBSI-RD (lower DBSI-FA and greater DBSI-RD in Cohort 1; greater DBSI-FA and lower DBSI-RD in Cohort 2) could also support the hypothesis that different biological processes may underlie obesity-related WM microstructure alterations (Haley et al., 2018). In each cohort, the pattern of change in DBSI-FA, DBSI-AD, and DBSI-RD might represent a different stage of WM reorganization post-injury. This hypothesis has been used to explain the bi-directional changes in DTI-FA in other conditions (e.g., a rodent model of traumatic brain injury) (Harris et al., 2016). In the case of obesity, the underlying mechanism could be an ongoing process of WM structural reorganization (demyelination/remyelination, loss of long WM tracts, axon

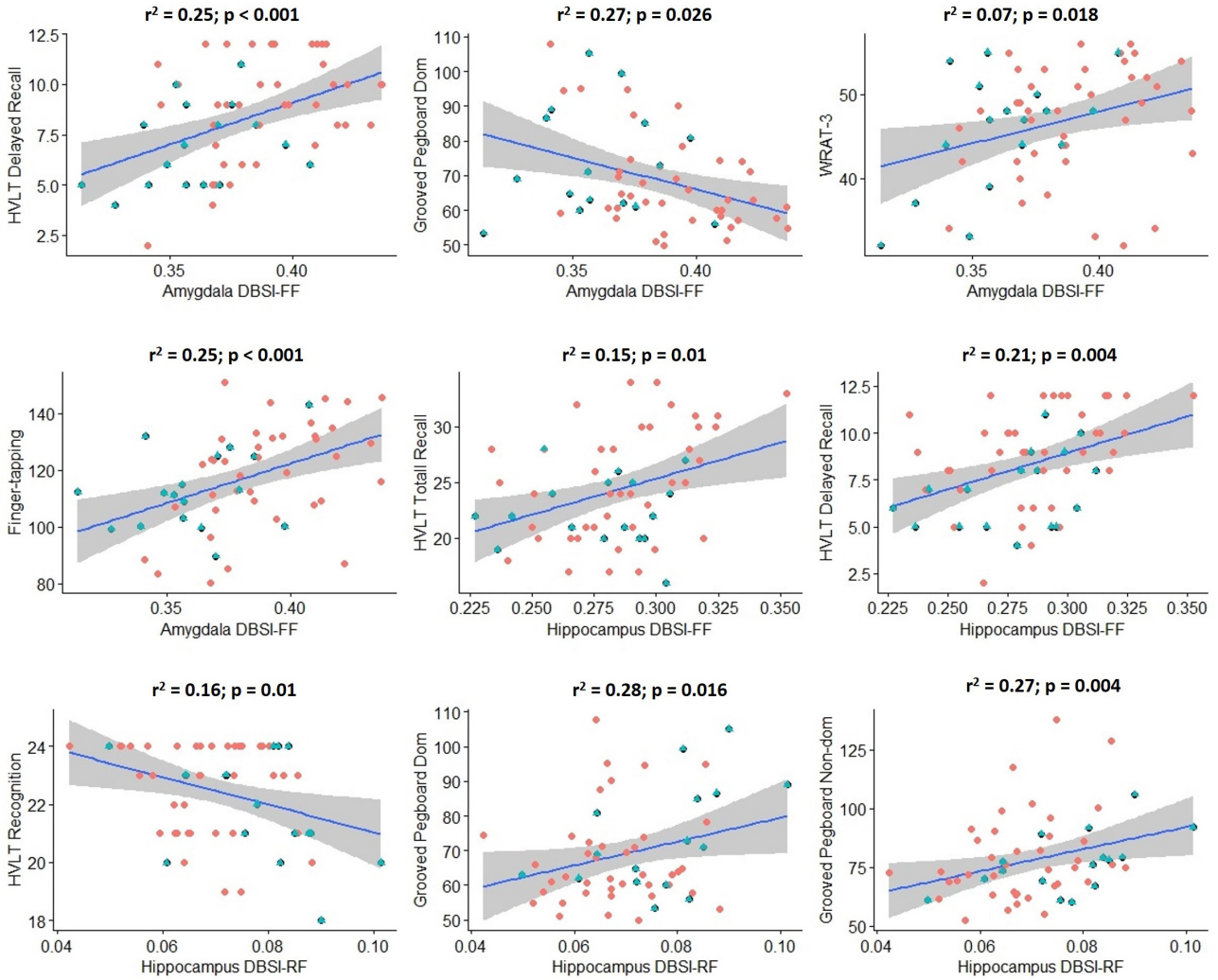

FIGURE 5 | Significant correlations between hippocampus/amygdala DBSI fiber fraction and DBSI restricted fraction with performance in key measures of cognition in Cohort 2 (blue: obese; red: non-obese). Shaded area surrounding regression lines are 95% confidence intervals). DBSI-FF, fiber fraction; DBSI-RF, restricted fraction; HVLT, Hopkins Verbal Learning Test; WRAT-3, Wide Range Achievement Test 3; Dom, dominant; Non-dom, Non-dominant.

sprouting) associated with persistent neuroinflammatory process. Nevertheless, although this hypothesis is a plausible explanation for the inconsistent diffusivity differences observed in our study, these differences might also be due to between-cohort differences in hardware used, such as head coils, and DTI acquisition parameters or participant characteristics due to sample selection criteria. As mentioned above, while DTI data from Cohort 2 participants were primarily selected from a convenience sample comprising the HIV- control group of an HIV neuroimaging study, Cohort 1 participants were selected specifically for a study of brain alterations in obesity unconfounded by current or past co-morbid disease. Therefore, more stringent screening for diabetes, mental illness, substance and alcohol abuse, and IQ/education was performed in Cohort 1 relative to Cohort 2. We excluded individuals with diabetes in order to study neuroinflammation in obesity *per se*, unconfounded by hyperglycemia and insulin resistance, factors already linked to neuroinflammation (Pugazhenthi et al., 2017). More rigorous experimental designs are necessary to confirm the validity of these hypotheses and to determine what non-BMI factors relate to DBSI measures.

Histopathological Abnormalities Associated With Neuroinflammation in Obesity

In obese groups, greater DBSI-RF in WM tracts and hippocampus presumably reflect an increase in CNS resident inflammatory cells. Significant increases in glial fibrillary acidic protein (GFAP) immunoreactive astrocytes were observed in the hippocampus and frontal and parietal cortices in rodent models of obesity (Tomassoni et al., 2013). Evidence of increased gliosis was observed in the mediobasal hypothalamus of living obese humans assessed by MRI (Thaler et al., 2012; Schur et al., 2015),

which related to greater post-mortem GFAP staining intensity (Schur et al., 2015). Peripheral inflammation as indicated by plasma fibrinogen related to alterations in DTI-measured apparent diffusivity in the amygdala (Cazettes et al., 2011). In several rodent studies, obesity-induced microglia activation and other types of neuroinflammation were frequently observed in hypothalamus, hippocampus, amygdala, and other brain regions (Erion et al., 2014; Tucsek et al., 2014; Guillemot-Legris and Muccioli, 2017). Obesity-related microglial activation in rodents mediates the relationship between synaptic dysfunction and cognitive deficits, which are blocked by inhibition of microglial activation (Erion et al., 2014; Cope et al., 2018). Reversal of obesity-related macrophage infiltration into leaky BBB improves obesity-associated cognitive dysfunction (Stranahan et al., 2016). Since DBSI doesn't distinguish different cell types, it would be necessary to perform validation studies, e.g., correlation of DBSI-derived metrics with histopathological measures of neuroinflammation in rodent models of obesity and in human postmortem brain, to confirm that these altered properties truly reflect neuroinflammation and detect which cell types are responsible for the observed changes in DBSI-RF in our study.

Interestingly, in Cohort 1, DBSI-HF was greater in obese compared to non-obese individuals. DBSI-HF models non-restricted water diffusion in the extracellular compartment and reflects tissue edema in acute neuroinflammatory conditions (Wang et al., 2011; Wang et al., 2014; Zhan et al., 2018). In the case of possible chronic neuroinflammation in disease states such as obesity, histopathological evaluation is needed to determine the mechanism that underlies greater DBSI-HF.

Neuroinflammation, Axonal Density, and Cognitive Performance

In the current study, we showed that DBSI-RF, an indicator of neuroinflammation, and DBSI-FF, an indicator of axonal density, in hippocampus and amygdala related to cognitive performance in some measures. These results are in line with studies in which impaired performance on memory tasks is induced by hippocampal neuroinflammation in rodents with diet-induced obesity (Pistell et al., 2010; Beilharz et al., 2016; Cope et al., 2018) and the observed association between plasma fibrinogen and water diffusion in the amygdala in obese and overweight individuals (Cazettes et al., 2011). The current results suggest altered water diffusivity in the brain, and perhaps neuroinflammation, may relate to altered cognitive performance. However, these data should be considered preliminary since analyses were exploratory and not corrected for multiple comparisons. Future studies may determine whether putative neuroinflammation modulates the relationship between BMI and cognitive performance.

Limitations and Future Directions

The primary strength of the current study is the replication of the findings that DBSI-RF, a putative marker of neuroinflammation, and DBSI-FF, a marker of axonal density, are greater and lower, respectively, in obese than non-obese individuals in two independent cohorts. The main weakness of this study is that data were not available to link DBSI metrics to alterations in inflammation-related behavior or proinflammatory cytokines in plasma or CSF. Without histopathological validation, though plausible, it remains speculative that the DBSI-measured alterations truly reflect neuroinflammation. Previous studies showed that DBSI-RF is associated with activated microglia and astrogliosis in several neuroinflammatory conditions (Wang et al., 2011; Chiang et al., 2014; Wang et al., 2014) but this has not been examined in obesity. Interestingly, the regions of increased DBSI-RF and decreased DBSI-FF in obese individuals in Cohort 1, from a study designed to test for differences in the brain due to obesity unconfounded by other health issues, falls almost entirely within the regions of the findings from obese individuals in Cohort 2, a convenience sample, as described above. Lack of convergent findings for some DBSI anisotropic metrics could be due to variations in stage of WM reorganization and differences between cohorts including participant characteristics and DTI sequence parameters, as discussed above. A third weakness is that age, sex and race distributions differed between obese and non-obese individuals in one or both cohorts. There are age, sex, and racial differences in adiposity and associated traits including systemic inflammation severity due to physiological, social and psychological factors (Thorand et al., 2006; Stepanikova et al., 2017a,b). While we controlled for age, sex and race in our data analyses, we cannot rule out the possibility that differences between groups in these factors contributed to our results. Clearly, age, sex, and race should be included in future studies as variables of primary interest with sufficient sample size to power these studies. DTI sequence parameters were slightly different between cohorts, which prevented us from combining data across cohorts. Future studies should be prospective in nature, include larger sample sizes and obtain complimentary measures of neuroinflammation using PET with radiotracers specific for activated microglia, plasma and CSF inflammatory marker levels, and measures of cognitive function. Also, studies of animal models of obesity would allow for histopathological validation of DBSI metrics.

CONCLUSION

In two independent cohorts, we showed that a DBSI-derived indicator of neuroinflammation is greater and axonal density is lower in obese compared to non-obese humans. In addition, the discrepancies between DBSI- and DTI-derived anisotropic metrics demonstrate the limitations of DTI when applied to disease states that may be accompanied by neuroinflammation. Additionally, these findings highlight the significance of applying multi-component models of diffusion imaging in these populations. Future studies are warranted to determine whether high-calorie diet-induced neuroinflammation occurs in ROIs outside hippocampus, amygdala, and hypothalamus and its potential role in obesity-associated impairment in behaviors thought to be regulated by these regions. Finally, the results of the current study indicate that putative neuroinflammation

and associated cognitive impairment occurs even in obese individuals without diabetes. Given the evidence implicating diabetes in the development of neuroinflammation and cognitive impairment (Pugazhenthi et al., 2017), it will be important to assess relationships between metabolic markers, cognition, and MRI-derived neuroinflammation metrics in individuals who do and do not develop insulin resistance over time. Also, further histopathological studies in postmortem brain are necessary to confirm that the altered DBSI properties we observed in obese humans truly reflect neuroinflammatory processes.

DATA AVAILABILITY STATEMENT

The datasets generated and used to perform analyses for this study are available upon a request to the corresponding author.

ETHICS STATEMENT

All studies were approved by the Washington University School of Medicine Human Research Protection Office and were carried out in accordance with the principles expressed in the Declaration of Helsinki.

AUTHOR CONTRIBUTIONS

TH, NS, and SE contributed to the conception of the study. NS, JS, PS, JSS, BA, S-KS, TH, and SE provided the imaging datasets and the expertise in neuroimaging. AS, TM, JR, ON, NS, and SE conducted pre-processing, neuroimaging, and statistical analysis. AS, TM, and SE wrote the initial draft of the manuscript. All authors critically revised the manuscript, contributed to the interpretation of the results, and approved the final version.

FUNDING

The studies presented in this work were conducted using the Center for Clinical Imaging Research (CCIR) located at the Washington University Medical Center. This research was funded by the National Institutes of Health (grant numbers R01 DK-085575, 2T32HL007456-26, R01NR01449, R01NR015738, and P30 DK020579 to the Washington University Diabetes Research Center), National Institute on Drug Abuse (grant number 5T32DA007261-27), Clinical and Translational Science Awards (CTSA) Program (grant number UL1 RR024992), and Washington University Summer Undergraduate Research Award (SURA). Support was also provided by the Eunice Kennedy Shriver National Institute of Child Health and Human Development of the National Institutes of Health to the Intellectual and Developmental Disabilities Research Center at Washington University NIH U54 HD087011. The funders had no role in study design, data collection and analysis, decision to publish, or preparation of the manuscript.

SUPPLEMENTARY MATERIAL

The Supplementary Material for this article can be found online at: https://www.frontiersin.org/articles/10.3389/fnhum.2019.00464/full#supplementary-material

REFERENCES

Alam, M. M., Lee, J., and Lee, S. Y. (2017). Recent progress in the development of TSPO PET ligands for neuroinflammation imaging in Neurological Diseases. *Nucl. Med. Mol. Imaging* 51, 283–296. doi: 10.1007/s13139-017-0475-8

Alfaro, F. J., Gavrieli, A., Saade-Lemus, P., Lioutas, V. A., Upadhyay, J., and Novak, V. (2018). White matter microstructure and cognitive decline in metabolic syndrome: a review of diffusion tensor imaging. *Metabolism* 78, 52–68. doi: 10.1016/j.metabol.2017.08.009

Alford, S., Patel, D., Perakakis, N., and Mantzoros, C. S. (2018). Obesity as a risk factor for Alzheimer's disease: weighing the evidence. *Obes. Rev.* 19, 269–280. doi: 10.1111/obr.12629

American Diabetes Association (2016). 2. Classification and diagnosis of Diabetes. *Diabetes Care* 39, S13–S22.

Baser, C. A., and Ruff, R. M. (1987). Construct validity of the San Diego neuropsychological test battery. *Arch. Clin. Neuropsychol.* 2, 13–32. doi: 10.1016/0887-6177(87)90031-x

Baufeld, C., Osterloh, A., Prokop, S., Miller, K. R., and Heppner, F. L. (2016). High-fat diet-induced brain region-specific phenotypic spectrum of CNS resident microglia. *Acta Neuropathol.* 132, 361–375. doi: 10.1007/s00401-016-1595-4

Beck, A. T., Steer, R. A., and Brown, G. K. (1996). *Manual for The Beck Depression Inventory-II*. San Antonio, TX: Psychological Corporation.

Beilharz, J. E., Maniam, J., and Morris, M. J. (2016). Short-term exposure to a diet high in fat and sugar, or liquid sugar, selectively impairs hippocampal-dependent memory, with differential impacts on inflammation. *Behav. Brain Res.* 306, 1–7. doi: 10.1016/j.bbr.2016.03.018

Benedict, R. H. B. (1997). *Brief Visuospatial Memory Test - Revised: Professional Manual*. Lutz, FL: Psychological Assessment Resources, Inc.

Benton, A. L., and Hamsher, K. (1976). *Multilingual Aphasia Examination: Manual of Instruction*. Iowa City, IA: University of Iowa.

Bolzenius, J. D., Laidlaw, D. H., Cabeen, R. P., Conturo, T. E., Mcmichael, A. R., Lane, E. M., et al. (2015). Brain structure and cognitive correlates of body mass index in healthy older adults. *Behav. Brain Res.* 278, 342–347. doi: 10.1016/j.bbr.2014.10.010

Brandt, J. (1991). The Hopkins verbal learning test: development of a new memory test with six equivalent forms. *Clin. Neuropsychol.* 5, 125–142. doi: 10.1080/13854049108403297

Cazettes, F., Cohen, J. I., Yau, P. L., Talbot, H., and Convit, A. (2011). Obesity-mediated inflammation may damage the brain circuit that regulates food intake. *Brain Res.* 1373, 101–109. doi: 10.1016/j.brainres.2010.12.008

Chiang, C. W., Wang, Y., Sun, P., Lin, T. H., Trinkaus, K., Cross, A. H., et al. (2014). Quantifying white matter tract diffusion parameters in the presence of increased extra-fiber cellularity and vasogenic edema. *Neuroimage* 101, 310–319. doi: 10.1016/j.neuroimage.2014.06.064

Cope, E. C., Lamarca, E. A., Monari, P. K., Olson, L. B., Martinez, S., Zych, A. D., et al. (2018). Microglia play an active role in obesity-associated cognitive decline. *J. Neurosci.* 38, 8889–8904. doi: 10.1523/JNEUROSCI.0789-18.2018

Cross, A. H., and Song, S. K. (2017). A new imaging modality to non-invasively assess multiple sclerosis pathology. *J. Neuroimmunol.* 304, 81–85. doi: 10.1016/j.jneuroim.2016.10.002

Delis, D. C., Kaplan, E., and Kramer, J. H. (2001). *Delis-Kaplan Executive Function System (D-KEFS)*. San Antonio, TX: The Psychological Corporation.

Devoto, F., Zapparoli, L., Bonandrini, R., Berlingeri, M., Ferrulli, A., Luzi, L., et al. (2018). Hungry brains: A meta-analytical review of brain activation imaging studies on food perception and appetite in obese individuals. *Neurosci. Biobehav. Rev.* 94, 271–285. doi: 10.1016/j.neubiorev.2018.07.017

Eisenstein, S. A., Antenor-Dorsey, J. A., Gredysa, D. M., Koller, J. M., Bihun, E. C., Ranck, S. A., et al. (2013). A comparison of D2 receptor specific binding in obese and normal-weight individuals using PET with (N-[(11)C]methyl)benperidol. *Synapse* 67, 748–756. doi: 10.1002/syn.21680

Eisenstein, S. A., Bischoff, A. N., Gredysa, D. M., Antenor-Dorsey, J. A., Koller, J. M., Al-Lozi, A., et al. (2015a). Emotional eating phenotype is associated with central dopamine D2 receptor binding independent of body mass index. *Sci. Rep.* 5:11283. doi: 10.1038/srep11283

Eisenstein, S. A., Gredysa, D. M., Antenor-Dorsey, J. A., Green, L., Arbelaez, A. M., Koller, J. M., et al. (2015b). Insulin, central dopamine D2 receptors, and monetary reward discounting in obesity. *PLoS One* 10:e0133621. doi: 10.1371/journal.pone.0133621

Erion, J. R., Wosiski-Kuhn, M., Dey, A., Hao, S., Davis, C. L., Pollock, N. K., et al. (2014). Obesity elicits interleukin 1-mediated deficits in hippocampal synaptic plasticity. *J. Neurosci.* 34, 2618–2631. doi: 10.1523/JNEUROSCI.4200-13.2014

First, M. B., Spitzer, R. L., Gibbon, M., and Williams, J. B. W. (2002). *Structured Clinical Interview for DSM-IV-TR Axis I Disorders, Research Version, Patient Edition With Psychotic Screen (SCID-I/P W/ PSY SCREEN)*. New York,NY: New York State Psychiatric Institute.

Frohman, E. M., Racke, M. K., and Raine, C. S. (2006). Multiple sclerosis–the plaque and its pathogenesis. *N. Engl. J. Med.* 354, 942–955. doi: 10.1056/nejmra052130

Gameiro, F., Perea, M. V., Ladera, V., Rosa, B., and Garcia, R. (2017). Executive functioning in obese individuals waiting for clinical treatment. *Psicothema* 29, 61–66. doi: 10.7334/psicothema2016.202

Garcia-Garcia, I., Michaud, A., Dadar, M., Zeighami, Y., Neseliler, S., Collins, D. L., et al. (2019). Neuroanatomical differences in obesity: meta-analytic findings and their validation in an independent dataset. *Int. J. Obes.* 43, 943–951. doi: 10.1038/s41366-018-0164-4

Goodglass, H., and Kaplan, E. (1972). *The Assessment of Aphasia and Related Disorders*. Philadelphia,PA: Lea and Febiger.

Gregor, M. F., and Hotamisligil, G. S. (2011). Inflammatory mechanisms in obesity. *Annu. Rev. Immunol.* 29, 415–445. doi: 10.1146/annurev-immunol-031210-101322

Guillemot-Legris, O., Masquelier, J., Everard, A., Cani, P. D., Alhouayek, M., and Muccioli, G. G. (2016). High-fat diet feeding differentially affects the development of inflammation in the central nervous system. *J. Neuroinflammation* 13:206. doi: 10.1186/s12974-016-0666-8

Guillemot-Legris, O., and Muccioli, G. G. (2017). Obesity-induced neuroinflammation: beyond the hypothalamus. *Trends Neurosci.* 40, 237–253. doi: 10.1016/j.tins.2017.02.005

Haley, A. P., Oleson, S., Pasha, E., Birdsill, A., Kaur, S., Thompson, J., et al. (2018). Phenotypic heterogeneity of obesity-related brain vulnerability: one-size interventions will not fit all. *Ann. N. Y. Acad. Sci.* 1428, 89–102. doi: 10.1111/nyas.13673

Harris, N. G., Verley, D. R., Gutman, B. A., and Sutton, R. L. (2016). Bi-directional changes in fractional anisotropy after experiment TBI: Disorganization and reorganization? *Neuroimage* 133, 129–143. doi: 10.1016/j.neuroimage.2016.03.012

Haslam, D. W., and James, W. P. (2005). Obesity. *Lancet* 366, 1197–1209.

He, Q., Chen, C., Dong, Q., Xue, G., Chen, C., Lu, Z. L., et al. (2015). Gray and white matter structures in the midcingulate cortex region contribute to body mass index in Chinese young adults. *Brain Struct. Funct.* 220, 319–329. doi: 10.1007/s00429-013-0657-9

Hodgson, K., Poldrack, R. A., Curran, J. E., Knowles, E. E., Mathias, S., Goring, H. H. H., et al. (2017). Shared genetic factors influence head motion during MRI and body mass index. *Cereb. Cortex* 27, 5539–5546. doi: 10.1093/cercor/bhw321

Karlsson, H. K., Tuulari, J. J., Hirvonen, J., Lepomaki, V., Parkkola, R., Hiltunen, J., et al. (2013). Obesity is associated with white matter atrophy: a combined diffusion tensor imaging and voxel-based morphometric study. *Obesity* 21, 2530–2537. doi: 10.1002/oby.20386

Kreutzer, C., Peters, S., Schulte, D. M., Fangmann, D., Turk, K., Wolff, S., et al. (2017). Hypothalamic inflammation in human obesity is mediated by environmental and genetic factors. *Diabetes* 66, 2407–2415. doi: 10.2337/db17-0067

Kullmann, S., Callaghan, M. F., Heni, M., Weiskopf, N., Scheffler, K., Haring, H. U., et al. (2016). Specific white matter tissue microstructure changes associated with obesity. *Neuroimage* 125, 36–44. doi: 10.1016/j.neuroimage.2015.10.006

Kullmann, S., Schweizer, F., Veit, R., Fritsche, A., and Preissl, H. (2015). Compromised white matter integrity in obesity. *Obes. Rev.* 16, 273–281. doi: 10.1111/obr.12248

Lauridsen, J. K., Olesen, R. H., Vendelbo, J., Hyde, T. M., Kleinman, J. E., Bibby, B. M., et al. (2017). High BMI levels associate with reduced mRNA expression of IL10 and increased mRNA expression of iNOS (NOS2) in human frontal cortex. *Transl. Psychiatry* 7:e1044. doi: 10.1038/tp.2016.259

Lin, T. H., Chiang, C. W., Perez-Torres, C. J., Sun, P., Wallendorf, M., Schmidt, R. E., et al. (2017). Diffusion MRI quantifies early axonal loss in the presence of nerve swelling. *J. Neuroinflammation* 14:78. doi: 10.1186/s12974-017-0852-3

Lin, T. H., Sun, P., Hallman, M., Hwang, F. C., Wallendorf, M., Ray, W. Z., et al. (2019). Noninvasive quantification of axonal loss in the presence of tissue swelling in traumatic spinal cord injury mice. *J. Neurotrauma* 36, 2308–2315. doi: 10.1089/neu.2018.6016

Lou, B., Chen, M., Luo, X., and Dai, Y. (2014). Reduced right frontal fractional anisotropy correlated with early elevated plasma LDL levels in obese young adults. *PLoS One* 9:e108180. doi: 10.1371/journal.pone.0108180

Marks, B. L., Katz, L. M., Styner, M., and Smith, J. K. (2011). Aerobic fitness and obesity: relationship to cerebral white matter integrity in the brain of active and sedentary older adults. *Br. J. Sports Med.* 45, 1208–1215. doi: 10.1136/bjsm.2009.068114

MATLAB and Statistics Toolbox Release (2012). *MATLAB and Statistics Toolbox Release*, The MathWorks, Inc., Natick, MA. doi: 10.1136/bjsm.2009.068114

Mazza, E., Poletti, S., Bollettini, I., Locatelli, C., Falini, A., Colombo, C., et al. (2017). Body mass index associates with white matter microstructure in bipolar depression. *Bipolar Disord.* 19, 116–127. doi: 10.1111/bdi.12484

Metzler-Baddeley, C., Mole, J. P., Leonaviciute, E., Sims, R., Kidd, E. J., Ertefai, B., et al. (2019). Sex-specific effects of central adiposity and inflammatory markers on limbic microstructure. *Neuroimage* 189, 793–803. doi: 10.1016/j.neuroimage.2019.02.007

Miller, A. A., and Spencer, S. J. (2014). Obesity and neuroinflammation: a pathway to cognitive impairment. *Brain Behav. Immun.* 42, 10–21. doi: 10.1016/j.bbi.2014.04.001

Mori, S., Oishi, K., Jiang, H., Jiang, L., Li, X., Akhter, K., et al. (2008). Stereotaxic white matter atlas based on diffusion tensor imaging in an ICBM template. *Neuroimage* 40, 570–582. doi: 10.1016/j.neuroimage.2007.12.035

Mueller, K., Anwander, A., Moller, H. E., Horstmann, A., Lepsien, J., Busse, F., et al. (2011). Sex-dependent influences of obesity on cerebral white matter investigated by diffusion-tensor imaging. *PLoS One* 6:e18544. doi: 10.1371/journal.pone.0018544

Murphy, R. K., Sun, P., Xu, J., Wang, Y., Sullivan, S., Gamble, P., et al. (2016). Magnetic resonance imaging biomarker of axon loss reflects cervical spondylotic myelopathy severity. *Spine* 41, 751–756. doi: 10.1097/BRS.0000000000001337

Nichols, T. E., and Holmes, A. P. (2002). Nonparametric permutation tests for functional neuroimaging: a primer with examples. *Hum. Brain Mapp.* 15, 1–25. doi: 10.1002/hbm.1058

O'Brien, P. D., Hinder, L. M., Callaghan, B. C., and Feldman, E. L. (2017). Neurological consequences of obesity. *Lancet. Neurol.* 16, 465–477.

Owen, D. R., Yeo, A. J., Gunn, R. N., Song, K., Wadsworth, G., Lewis, A., et al. (2012). An 18-kDa translocator protein (TSPO) polymorphism explains differences in binding affinity of the PET radioligand PBR28. *J. Cereb. Blood Flow Metab.* 32, 1–5. doi: 10.1038/jcbfm.2011.147

Papageorgiou, I., Astrakas, L. G., Xydis, V., Alexiou, G. A., Bargiotas, P., Tzarouchi, L., et al. (2017). Abnormalities of brain neural circuits related to obesity: a diffusion tensor imaging study. *Magn. Reson. Imaging* 37, 116–121. doi: 10.1016/j.mri.2016.11.018

Pepino, M. Y., Eisenstein, S. A., Bischoff, A. N., Klein, S., Moerlein, S. M., Perlmutter, J. S., et al. (2016). Sweet dopamine: sucrose preferences relate differentially to striatal D2 receptor binding and age in obesity. *Diabetes* 65, 2618–2623. doi: 10.2337/db16-0407

Pistell, P. J., Morrison, C. D., Gupta, S., Knight, A. G., Keller, J. N., Ingram, D. K., et al. (2010). Cognitive impairment following high fat diet consumption is

associated with brain inflammation. *J. Neuroimmunol.* 219, 25–32. doi: 10.1016/j.jneuroim.2009.11.010

Pugazhenthi, S., Qin, L., and Reddy, P. H. (2017). Common neurodegenerative pathways in obesity, diabetes, and Alzheimer's disease. *Biochim. Biophys. Acta Mol. Basis Dis.* 1863, 1037–1045. doi: 10.1016/j.bbadis.2016.04.017

Reitan, R. (1958). Validity of the trail making test as an indicator of organic brain damage. *Percept. Mot. Skill.* 8, 271–276. doi: 10.2466/pms.1958.8.3.271

Schmitt, L. (2013). *Finger-Tapping Test*. New York, NY: Springer.

Schur, E. A., Melhorn, S. J., Oh, S. K., Lacy, J. M., Berkseth, K. E., Guyenet, S. J., et al. (2015). Radiologic evidence that hypothalamic gliosis is associated with obesity and insulin resistance in humans. *Obesity* 23, 2142–2148. doi: 10.1002/oby.21248

Shirani, A., Sun, P., Schmidt, R. E., Trinkaus, K., Naismith, R. T., Song, S. K., et al. (2018). Histopathological correlation of diffusion basis spectrum imaging metrics of a biopsy-proven inflammatory demyelinating brain lesion: a brief report. *Mult. Scler.* 25, 1937–1941. doi: 10.1177/1352458518786072

Smith, S. M. (2002). Fast robust automated brain extraction. *Hum. Brain Mapp.* 17, 143–155. doi: 10.1002/hbm.10062

Smith, S. M., Jenkinson, M., Johansen-Berg, H., Rueckert, D., Nichols, T. E., Mackay, C. E., et al. (2006). Tract-based spatial statistics: voxelwise analysis of multi-subject diffusion data. *Neuroimage* 31, 1487–1505. doi: 10.1016/j.neuroimage.2006.02.024

Smith, S. M., Jenkinson, M., Woolrich, M. W., Beckmann, C. F., Behrens, T. E., Johansen-Berg, H., et al. (2004). Advances in functional and structural MR image analysis and implementation as FSL. *Neuroimage* 23(Suppl. 1), S208–S219.

Snelbaker, A. J., Wilkinson, G. S., Robertson, G. J., and Glutting, J. J. (2001). *Wide Range Achievement Test 3 (wrat3)*. Boston, MA: Springer.

Spreen, O., and Benton, A. L. (1977). *Neurosensory Center Comprehensive Examination for Aphasia : Manual of directions. revised edition*. Victoria BC: University of Victoria.

Stamatovic, S. M., Dimitrijevic, O. B., Keep, R. F., and Andjelkovic, A. V. (2006). Inflammation and brain edema: new insights into the role of chemokines and their receptors. *Acta Neurochir. Suppl.* 96, 444–450. doi: 10.1007/3-211-30714-1_91

Stanek, K. M., Grieve, S. M., Brickman, A. M., Korgaonkar, M. S., Paul, R. H., Cohen, R. A., et al. (2011). Obesity is associated with reduced white matter integrity in otherwise healthy adults. *Obesity* 19, 500–504. doi: 10.1038/oby.2010.312

Stepanikova, I., Bateman, L. B., and Oates, G. R. (2017a). Systemic inflammation in midlife: race, socioeconomic status, and perceived discrimination. *Am. J. Prev. Med.* 52, S63–S76. doi: 10.1016/j.amepre.2016.09.026

Stepanikova, I., Oates, G. R., and Bateman, L. B. (2017b). Does one size fit all? The role of body mass index and waist circumference in systemic inflammation in midlife by race and gender. *Ethn. Health* 22, 169–183. doi: 10.1080/13557858.2016.1235681

Strain, J. F., Burdo, T. H., Song, S. K., Sun, P., El-Ghazzawy, O., Nelson, B., et al. (2017). Diffusion basis spectral imaging detects ongoing brain inflammation in virologically well-controlled HIV+ patients. *J. Acquir. Immune. Defi.c Syndr.* 76, 423–430. doi: 10.1097/QAI.0000000000001513

Stranahan, A. M., Hao, S., Dey, A., Yu, X., and Baban, B. (2016). Blood-brain barrier breakdown promotes macrophage infiltration and cognitive impairment in leptin receptor-deficient mice. *J. Cereb. Blood Flow Metab.* 36, 2108–2121. doi: 10.1177/0271678x16642233

Sun, P., Murphy, R. K., Gamble, P., George, A., Song, S. K., and Ray, W. Z. (2017). Diffusion assessment of cortical changes, induced by traumatic spinal cord injury. *Brain Sci.* 7:21. doi: 10.3390/brainsci7020021

Thaler, J. P., Yi, C. X., Schur, E. A., Guyenet, S. J., Hwang, B. H., Dietrich, M. O., et al. (2012). Obesity is associated with hypothalamic injury in rodents and humans. *J. Clin. Invest.* 122, 153–162. doi: 10.1172/JCI59660

Thorand, B., Baumert, J., Doring, A., Herder, C., Kolb, H., Rathmann, W., et al. (2006). Sex differences in the relation of body composition to markers of inflammation. *Atherosclerosis* 184, 216–224. doi: 10.1016/j.atherosclerosis.2005.04.011

Tomassoni, D., Nwankwo, I. E., Gabrielli, M. G., Bhatt, S., Muhammad, A. B., Lokhandwala, M. F., et al. (2013). Astrogliosis in the brain of obese Zucker rat: a model of metabolic syndrome. *Neurosci. Lett.* 543, 136–141. doi: 10.1016/j.neulet.2013.03.025

Tsai, C. L., Huang, T. H., and Tsai, M. C. (2017). Neurocognitive performances of visuospatial attention and the correlations with metabolic and inflammatory biomarkers in adults with obesity. *Exp. Physiol.* 102, 1683–1699. doi: 10.1113/EP086624

Tucsek, Z., Toth, P., Sosnowska, D., Gautam, T., Mitschelen, M., Koller, A., et al. (2014). Obesity in aging exacerbates blood-brain barrier disruption, neuroinflammation, and oxidative stress in the mouse hippocampus: effects on expression of genes involved in beta-amyloid generation and Alzheimer's disease. *J. Gerontol. A Biol. Sci. Med. Sci.* 69, 1212–1226. doi: 10.1093/gerona/glt177

van Galen, K. A., Ter Horst, K. W., Booij, J., La Fleur, S. E., and Serlie, M. J. (2018). The role of central dopamine and serotonin in human obesity: lessons learned from molecular neuroimaging studies. *Metabolism* 85, 325–339. doi: 10.1016/j.metabol.2017.09.007

Verstynen, T. D., Weinstein, A. M., Schneider, W. W., Jakicic, J. M., Rofey, D. L., and Erickson, K. I. (2012). Increased body mass index is associated with a global and distributed decrease in white matter microstructural integrity. *Psychosom. Med.* 74, 682–690. doi: 10.1097/PSY.0b013e318261909c

Vivash, L., and O'Brien, T. J. (2016). Imaging microglial activation with TSPO PET: lighting up Neurologic Diseases? *J. Nucl. Med.* 57, 165–168. doi: 10.2967/jnumed.114.141713

Walker, J. M., and Harrison, F. E. (2015). Shared neuropathological characteristics of obesity, Type 2 diabetes and Alzheimer's Disease: impacts on cognitive decline. *Nutrients* 7, 7332–7357. doi: 10.3390/nu7095341

Wang, Q., Wang, Y., Liu, J., Sutphen, C. L., Cruchaga, C., Blazey, T., et al. (2019). Quantification of white matter cellularity and damage in preclinical and early symptomatic Alzheimer's disease. *Neuroimage Clin.* 22:101767. doi: 10.1016/j.nicl.2019.101767

Wang, X., Cusick, M. F., Wang, Y., Sun, P., Libbey, J. E., Trinkaus, K., et al. (2014). Diffusion basis spectrum imaging detects and distinguishes coexisting subclinical inflammation, demyelination and axonal injury in experimental autoimmune encephalomyelitis mice. *NMR Biomed.* 27, 843–852. doi: 10.1002/nbm.3129

Wang, Y., Sun, P., Wang, Q., Trinkaus, K., Schmidt, R. E., Naismith, R. T., et al. (2015). Differentiation and quantification of inflammation, demyelination and axon injury or loss in multiple sclerosis. *Brain* 138, 1223–1238. doi: 10.1093/brain/awv046

Wang, Y., Wang, Q., Haldar, J. P., Yeh, F. C., Xie, M., Sun, P., et al. (2011). Quantification of increased cellularity during inflammatory demyelination. *Brain* 134, 3590–3601. doi: 10.1093/brain/awr307

Wechsler, D. (1997). *Wechsler Adult Intelligence Scale III/Wechsler Memory Scale Third Edition Technical Manual*, San Antonio, TX: The Psychological Corporation.

Wechsler, D. (1999). *Wechsler Abbreviated Scale of Intelligence (WASI)*, San Antonio, TX: Harcourt Assessment.

Wheeler-Kingshott, C. A., and Cercignani, M. (2009). About "axial" and "radial" diffusivities. *Magn. Reson. Med.* 61, 1255–1260. doi: 10.1002/mrm.21965

WHO (2018). *Obesity and Overwieght*. Available at: https://www.who.int/en/news-room/fact-sheets/detail/obesity-and-overweight (Accessed March 1, 2018)

Winkler, A. M., Ridgway, G. R., Webster, M. A., Smith, S. M., and Nichols, T. E. (2014). Permutation inference for the general linear model. *Neuroimage* 92, 381–397. doi: 10.1016/j.neuroimage.2014.01.060

Winklewski, P. J., Sabisz, A., Naumczyk, P., Jodzio, K., Szurowska, E., and Szarmach, A. (2018). Understanding the physiopathology behind axial and radial diffusivity changes-what do we know? *Front. Neurol.* 9:92. doi: 10.3389/fneur.2018.00092

Wright, R. S., Cole, A. P., Ali, M. K., Skinner, J., Whitfield, K. E., and Mwendwa, D. T. (2016). Examining the influence of measures of adiposity on cognitive function in middle age and Older African Americans. *Arch. Clin. Neuropsychol.* 31, 23–28. doi: 10.1093/arclin/acv086

Xu, J., Li, Y., Lin, H., Sinha, R., and Potenza, M. N. (2013). Body mass index correlates negatively with white matter integrity in the fornix and corpus callosum: a diffusion tensor imaging study. *Hum. Brain Mapp.* 34, 1044–1052. doi: 10.1002/hbm.21491

Yang, Y., and Wang, J. Z. (2017). From structure to behavior in basolateral amygdala-hippocampus circuits. *Front. Neural. Circuits* 11:86. doi: 10.3389/fncir.2017.00086

Yendiki, A., Koldewyn, K., Kakunoori, S., Kanwisher, N., and Fischl, B. (2014). Spurious group differences due to head motion in a diffusion MRI study. *Neuroimage* 88, 79–90. doi: 10.1016/j.neuroimage.2013.11.027

Yendiki, A., Panneck, P., Srinivasan, P., Stevens, A., Zollei, L., Augustinack, J., et al. (2011). Automated probabilistic reconstruction of white-matter pathways in health and disease using an atlas of the underlying anatomy. *Front. Neuroinform.* 5:23. doi: 10.3389/fninf.2011.00023

Zhan, J., Lin, T. H., Libbey, J. E., Sun, P., Ye, Z., Song, C., et al. (2018). Diffusion basis spectrum and diffusion tensor imaging detect hippocampal inflammation and dendritic injury in a virus-induced mouse model of epilepsy. *Front. Neurosci.* 12:77. doi: 10.3389/fnins.2018.00077

Conflict of Interest: The authors declare that the research was conducted in the absence of any commercial or financial relationships that could be construed as a potential conflict of interest.

frontiers in Human Neuroscience

ORIGINAL RESEARCH
published: 06 February 2020
doi: 10.3389/fnhum.2020.00019

Real-Time Eye-to-Eye Contact Is Associated With Cross-Brain Neural Coupling in Angular Gyrus

*J. Adam Noah[1], Xian Zhang[1], Swethasri Dravida[2], Yumie Ono[3], Adam Naples[4], James C. McPartland[4] and Joy Hirsch[1,5,6,7]**

[1]Brain Function Laboratory, Department of Psychiatry, Yale School of Medicine, New Haven, CT, United States, [2]Interdepartmental Neuroscience Program, Yale School of Medicine, New Haven, CT, United States, [3]Department of Electronics and Bioinformatics, School of Science and Technology, Meiji University, Kawasaki, Japan, [4]Yale Child Study Center, Yale School of Medicine, New Haven, CT, United States, [5]Department of Neuroscience, Yale School of Medicine, New Haven, CT, United States, [6]Department of Comparative Medicine, Yale School of Medicine, New Haven, CT, United States, [7]Department of Medical Physics and Biomedical Engineering, University College London, London, United Kingdom

Direct eye contact between two individuals is a salient social behavior known to initiate and promote interpersonal interaction. However, the neural processes that underlie these live interactive behaviors and eye-to-eye contact are not well understood. The Dynamic Neural Coupling Hypothesis presents a general theoretical framework proposing that shared interactive behaviors are represented by cross-brain signal coherence. Using functional near-infrared spectroscopy (fNIRS) adapted for hyper scanning, we tested this hypothesis specifically for neural mechanisms associated with eye-to-eye gaze between human participants compared to similar direct eye-gaze at a dynamic video of a face and predicted that the coherence of neural signals between the two participants during reciprocal eye-to-eye contact would be greater than coherence observed during direct eye-gaze at a dynamic video for those signals originating in social and face processing systems. Consistent with this prediction cross-brain coherence was increased for signals within the angular gyrus (AG) during eye-to-eye contact relative to direct eye-gaze at a dynamic face video ($p < 0.01$). Further, activity in the right temporal-parietal junction (TPJ) was increased in the real eye-to-eye condition ($p < 0.05$, FDR corrected). Together, these findings advance a functional and mechanistic understanding of the AG and cross-brain neural coupling associated with real-time eye-to-eye contact.

Keywords: eye-to-eye contact, temporoparietal junction, two-person neuroscience, live dyadic interactions, fNIRS, hyperscanning, neural coupling, neural coherence

OPEN ACCESS

Edited by:
Felix Scholkmann, University Hospital Zürich, Switzerland

Reviewed by:
Hiroki C. Tanabe, Nagoya University, Japan
Sabrina Brigadoi, University of Padova, Italy
Felipe Orihuela-Espina, National Institute of Astrophysics, Optics and Electronics, Mexico

****Correspondence:***
Joy Hirsch
joy.hirsch@yale.edu

Specialty section:
This article was submitted to Brain Imaging and Stimulation, a section of the journal Frontiers in Human Neuroscience

Received: *01 July 2019*
Accepted: *17 January 2020*
Published: *06 February 2020*

Citation:
Noah JA, Zhang X, Dravida S, Ono Y, Naples A, McPartland JC and Hirsch J (2020) Real-Time Eye-to-Eye Contact Is Associated With Cross-Brain Neural Coupling in Angular Gyrus. Front. Hum. Neurosci. 14:19. doi: 10.3389/fnhum.2020.00019

INTRODUCTION

Eye contact is a fundamental component of face-to-face communications and important in a number of developmental disorders including autism and psychiatric conditions (Pelphrey et al., 2005; Nation and Penny, 2008; Schneier et al., 2009; Senju and Johnson, 2009; McPartland et al., 2011; Jones and Klin, 2013). However, the neural mechanisms underlying direct eye-to-eye contact and its specific role in communication and social interaction are active areas of research. Technical developments in functional near-infrared spectroscopy (fNIRS) now enable broad acquisition of brain signals acquired simultaneously on two individuals under naturalistic conditions. Previous hyper scanning investigations of real (person-to-person) eye-to-eye contact compared with

simultaneously viewing static face pictures using this technology have confirmed an association with language systems in the brain suggesting a link between eye contact and left hemisphere non-verbal communication systems (Hirsch et al., 2017). Other studies have shown roles for the inferior frontal gyrus, medial frontal gyrus, and occipito-temporal cortex involved in cross-brain interactions during up-regulation of attention and direct eye gaze (Lachat et al., 2012; Koike et al., 2016, 2019). In this study, we build on these advances to examine localized coherence responses of interacting dyads during real eye-to-eye contact, in contrast, to gaze at dynamic face videos. This is in contrast to previous work that focused on static photographs (Hirsch et al., 2017). We hypothesized that neural systems associated with socialization (Carter and Huettel, 2013) and dynamic face tracking (Pitcher et al., 2011a) would be associated with face and eye processing and that cross-brain coherence of neural responses would entrain face and social mechanisms between interacting pairs.

The perception of a dynamic face requires many complex factors to be interpreted in real-time to facilitate socialization and communication (Lachat et al., 2012; Koike et al., 2016, 2019; Chang and Tsao, 2017). Eye-to-eye contact is a dynamic and interactive behavior in which face cues are reciprocally exchanged and activity within neural networks specialized for facial recognition, dynamic motion, emotion, and socialization are expected to play a fundamental role. These networks include the temporal-parietal junction (TPJ), fusiform face area, occipital face area, and the posterior superior temporal sulcus (pSTS; George et al., 2001; Hooker et al., 2003; Mosconi et al., 2005; Pelphrey et al., 2005; Sorger et al., 2007; Saito et al., 2010; Cavallo et al., 2015). Additional anterior temporal gyrus and prefrontal lobe structures have also been shown to play a role in these interactions including the inferior and medial frontal gyri (Duchaine and Yovel, 2015). Neural activity specific to perception of faces has been observed in the inferior occipital and fusiform gyri, while perception of dynamic eye gaze has been associated with higher processing areas in the superior temporal sulci and TPJ (Haxby et al., 2000; Hoffman and Haxby, 2000; Pitcher et al., 2011a; Sato et al., 2016). While these areas have been shown to be involved in static and dynamic facial processing, the mechanism of information exchange and regulation of circuits that upregulate attentional mechanisms related to real and dynamic eye-to-eye contact between partners in social interaction is not well understood. Previous studies have explored the role of eye movement behaviors including blinking and attention regulation in a social circuit that is more active in joint attention tasks compared to simple eye gaze or during randomized video sequences (Lachat et al., 2012; Koike et al., 2016, 2019). Specifically, it was shown that neural synchrony across subjects was correlated with eye-blink synchronization (Koike et al., 2016) and that differences in alpha and mu oscillations in joint attention vs. no joint attention tasks suggested an increase in attention related to the social interaction (Lachat et al., 2012). The significance of these findings related to understanding the exchange of information in face-to-face interaction is enhanced by the relevance of eye contact behavior and social interaction difficulties that are characteristic of autism spectrum disorders (ASD), social anxiety, and schizophrenia (Schneier et al., 2009; Senju and Johnson, 2009; Tso et al., 2012).

The Dynamic Neural Coupling Hypothesis predicts that cross-brain coherence, calculated on residual, non-task related signals, represents a specific class of interactive functions characterized by exchange of rapid social information (Hasson and Frith, 2016). Evidence for coherence between neural circuits across partners has been observed during coordinated button pressing (Funane et al., 2011; Dikker et al., 2014); coordinated singing and humming (Osaka et al., 2014, 2015); gestural communication (Schippers et al., 2010); cooperative memory tasks (Dommer et al., 2012); and face-to-face unstructured dialogue (Jiang et al., 2012). Cross-brain coherence has also been previously shown to increase during live face-to-face interactions between dyads engaged in poker competitions in contrast to human-to-computer partners (Piva et al., 2017) in which cross-brain coherence specific to the human-to-human condition was observed between the angular gyrus (AG; a part of the TPJ) and occipito-temporal area, including the lateral aspect of the occipital and temporal lobes. This finding suggests a functional role for AG and face processing areas in coherent social interaction associated with face and eye processing and motivates the current investigation. It has been argued that increased neural synchrony or cross-brain coherence may represent changes in neural activity in the perceptual system of one brain which is coupled to the motor output system of another (Jacob, 2009; Dumas et al., 2010; Schippers et al., 2010; Koike et al., 2016).

Here, the specific neural responses across dyads while making eye contact were compared to when each subject alone interacted with a pre-recorded video of the face of a partner. In the case of the real partner, we hypothesize that detection of dynamic stimuli, such as facial expressions and eye movements known to occur in the real face condition, will elicit neural activity that is not present when subjects perform the same task with a pre-recorded video sequence of a dynamic face. Specifically, we predict increased cross-brain coherence of signals originating from areas of the cortex associated with visual and social functions.

MATERIALS AND METHODS

Participants

Thirty healthy adults (15 pairs; 75% female; mean age 27.1 ± 8.5 years; 100% right-handed; Oldfield, 1971) participated in the study. All participants provided written informed consent in accordance with guidelines approved by the Yale University Human Investigation Committee (HIC #1501015178) and were reimbursed for participation. Dyads were not acquainted prior to the experiment and were assigned in order of recruitment.

Stimuli and Procedures

Each dyad participated in two tasks in which they were seated 140 cm across a table from each other. In both tasks, dyads alternated their gaze between the eyes of their partner and two small Light Emitting Diodes (LEDs) 10° to the left and to the right of their partner (**Figure 1**). In one condition, the partner was a real participant (**Figure 1A**), and in the other

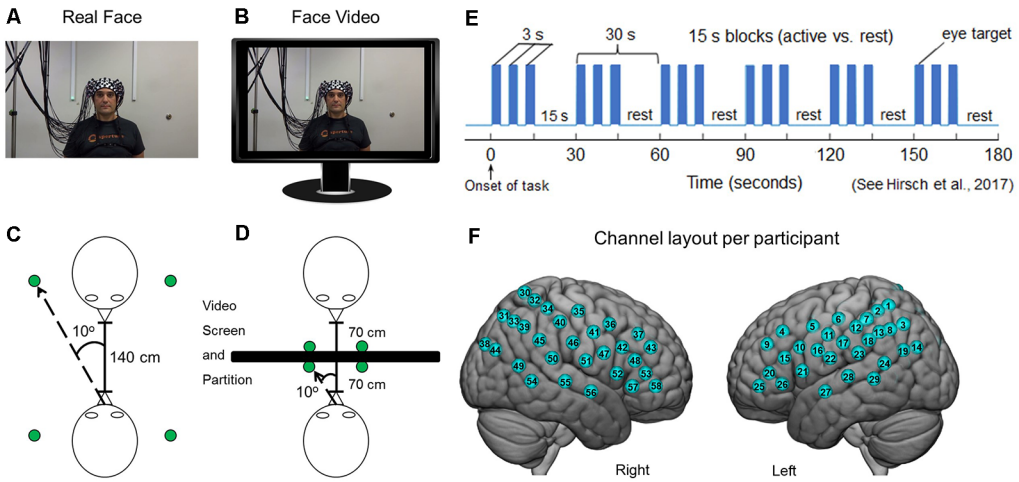

FIGURE 1 | Experimental conditions. **(A)** Subjects were set up with 58 functional near-infrared spectroscopy (fNIRS) channels distributed bilaterally on the heads of both participants, who were seated across from each other so that each individual in a dyad could see the face of their partner. A small green Light Emitting Diode (LED) indicator lights located to either side of their partner indicated rest gaze targets. **(B)** Twenty-four-inch 16 × 9 monitors were placed between subjects and a size-calibrated, pre-recorded face video was presented in the same field of view as the live interaction. **(C)** Diagrammatic representation of dyadic interaction. Subjects were 140 cm apart from each other and the LED indicator lights placed 10° to the left and right of the face. **(D)** In the face-video condition, a partition was placed between subjects and monitors were arranged in the field of view of both partners. The face and LED sizes and positions were calibrated to subtend the same visual angles in both conditions. **(E)** Time course of the experimental paradigm. The entire duration of the run was 3 min and was repeated twice each for both the live interaction and the video face interaction. During the 3-min interaction, participants alternated between 15-s task and rest periods. In the task period, participants looked either directly at the eyes of their partner or at the left or right LED that was lit. During the rest period, subjects looked only at the lighted LED. The task was modified from one that has been used previously (Hirsch et al., 2017). **(F)** Optical channel layout for both hemispheres of each participant. The median locations of each channel are shown in **Supplementary Table S1**. Written informed consent was obtained from the individual for the publication of the images shown in panels **(A,B)**.

condition, the "partner" was a pre-rendered video of a person performing the same task (**Figure 1B**). In both conditions, dyad partners performed all tasks concurrently. The order of runs was randomly sequenced between viewing their real partner directly or viewing a visual-angle corrected video partner on a 24-inch 16 × 9 computer monitor placed back-to-back between subjects, including a partition to assure that dyads could not see their real partner during video conditions (**Figures 1C,D**). The face and distance of the video stimuli were calibrated to subtend identical degrees of visual angle in the field of view of the subjects and the timing and range of motion of eye movements between partners was the same in both tasks. A version of the time-series (**Figure 1E**) and experimental details are similar to a prior study (Hirsch et al., 2017). At the start of each task, an auditory cue prompted participants to gaze at the eyes of their real or recorded partner. Subsequent auditory tones alternatingly cued eye gaze between eyes or LED according to the protocol time series. The 15-s active task period alternated with a 15 s rest/baseline period. The task period consisted of three 6 s cycles in which gaze alternated on eyes for 3 s and on a lighted LED to either the right or left (alternating) of the subject for 3 s for each of three events. The time series was performed in the same way for all runs. The order of runs was counterbalanced across pairs of subjects. During the 15 s rest/baseline period, participants focused on the lighted LED, as in the case of the 3 s periods that separated the eye contact and gaze events. The 15 s activity epoch with alternating eye contact events was processed as a single block.

Signal Acquisition and Channel Localization

Functional NIRS signal acquisition, optode localization, and signal processing, including global mean removal, were similar to methods described previously (Noah et al., 2015, 2017; Zhang et al., 2016, 2017; Piva et al., 2017; Dravida et al., 2018; Hirsch et al., 2018) and are summarized below. To assure that all participants provided recordable hemodynamic signals using fNIRS prior to participation in this experiment, subjects who demonstrated a significant fNIRS signal ($p < 0.05$) in the left motor cortex for both OxyHb and deOxyHb signals were eligible to participate in the present study. This technique assured that viable signals were recordable on all subjects.

Hemodynamic signals were acquired using three wavelengths of light, and an 80 fiber multichannel, continuous-wave fNIRS system (LABNIRS, Shimadzu Corporation, Kyoto, Japan). Each participant was fitted with an optode cap with predefined channel distances. Three sizes of caps were used based on the circumference of the heads of subjects. Large caps had a 60 cm circumference. Medium caps were 56.5 cm and small caps were 54.5 cm. Optode distances of 3 cm were designed for the 60 cm cap layout but were scaled equally to smaller caps. A lighted fiber-optic probe (Daiso, Hiroshima, Japan) was used to remove all hair from the optode channel prior to optode placement. Optodes consisting of 40 emitters and 40 detectors were arranged in a custom matrix, providing a total of 54 acquisition channels per subject. The specific layout

with the coverage of the optode channels is shown in **Figure 1F** and the mean channel coordinates and locations are detailed in **Supplementary Table S1**. For consistency, placement of the most anterior channel of the optode holder cap was centered 1 cm above nasion. To assure acceptable signal-to-noise ratios, resistance was measured for each channel prior to recording, and adjustments were made for each channel until all recording optodes were calibrated and able to sense known quantities of light from each laser wavelength (Tachibana et al., 2011; Ono et al., 2014; Noah et al., 2015).

Anatomical locations of optodes in relation to standard head landmarks were determined for each participant using a Patriot 3D Digitizer (Polhemus, Colchester, VT, USA; Okamoto and Dan, 2005; Singh et al., 2005; Eggebrecht et al., 2012, 2014; Ferradal et al., 2014). Montreal Neurological Institute (MNI) coordinates (Mazziotta et al., 2001) for each channel were obtained using NIRS-SPM software (Ye et al., 2009), and the corresponding anatomical locations of each channel shown in **Figure 1F** was determined and detailed in **Supplementary Table S1**, which lists the group median MNI coordinates and anatomical regions with probability estimates for each of the channels.

Signal Processing

Shimadzu LABNIRS systems utilize laser diodes at three wavelengths of light (780 nm, 805 nm, 830 nm). Raw optical density variations were translated into changes in relative chromophore concentrations using a modified Beer-Lambert equation (Hazeki and Tamura, 1988; Matcher et al., 1995; Hoshi, 2003). Signals were recorded at 30 Hz. Baseline drift was removed using wavelet detrending provided in NIRS-SPM (Ye et al., 2009). Global components attributable to blood pressure and other systemic effects (Tachtsidis and Scholkmann, 2016) were removed using a principal component analysis (PCA) spatial, global-mean filter (Zhang et al., 2016, 2017) prior to general linear model (GLM) analysis. Comparisons between conditions were based on GLM procedures using the NIRS-SPM software package. Event epochs within the time series (**Figure 1E**) were convolved with the hemodynamic response function provided from SPM8 (Penny et al., 2011) and were fit to the data, providing individual "beta values" for each participant across conditions. Group results based on these "beta values" were rendered on a standard MNI brain template (**Figure 3**). All analyses were performed on both Oxy- and deOxyHb signals (see **Figure 3**).

Region of Interest: Temporal-Parietal Junction (TPJ)

Real-face and face-video conditions were compared using TPJ as a region of interest. The mask for the region was determined using Neurosynth (Yarkoni et al., 2011) and created through a meta-search performed for the term "TPJ." Ninety-two results were found containing a total of 3,460 clusters. The mask was thresholded using a z-score of 6.3, and conditions were compared within this mask in the right hemisphere. To evaluate activity in the ROI determined in Neurosynth, each participant's channel locations were first converted into MNI space (Dravida et al., 2018). Once in normalized space, a median beta value was determined within the mask and within a 1.8 cm depth from the cortical surface to use for subsequent analysis (Hirsch et al., 2018).

Cross-Brain Coherence: Network of Interest

Cross-brain synchrony (coherence) was evaluated using wavelet analysis (Torrence and Compo, 1998; Cui et al., 2012) in the MATLAB 2018A Wavelet Toolbox. The wavelet kernel was a complex Gaussian provided by MATLAB. The number of octaves was four, and the range of frequencies was 0.4–0.025 Hz. The number of voices per octave was also four, and, therefore, 16 scales were used for which the wavelength difference was 2.5 s. Methodological details and validation of this technique have been previously described (Hirsch et al., 2017, 2018). Cross-brain coherence between dyads was measured between homologous pairs of brain regions using the combined Oxy- and deOxyHb signals. Individual channels were grouped into anatomical regions based on shared anatomy, which served to optimize signal-to-noise ratios. Grouping was achieved by identification of 14 bilateral ROIs from the acquired channels including: (1) AG (BA 39); (2) dorsolateral prefrontal cortex (BA 9); (3) dorsolateral prefrontal cortex (BA 46); (4) pars triangularis, BA 45; (5) supramarginal gyrus (SMG; BA 40); (6) middle temporal gyrus (MTG; BA 21); (7) superior temporal gyrus (STG; BA 22); (8) somatosensory cortex (BA 1, 2, and 3); (9) somatosensory association cortex (BA 7); (10) pre-motor and supplementary motor cortex (BA 6); (11) subcentral area (BA 43); (12) inferior frontal gyrus (BA 47); (13) visual cortex (Area V3, BA 19); and (14) frontal eye fields (BA 8). Signals acquired from predefined anatomical regions were decomposed into a range of temporal frequencies that were correlated across two brains for each dyad. This technique effectively removes the task regressor as is conventional for Psychophysiological Interaction (PPI) analysis (Friston et al., 1997). Here, we apply the decomposed "residual signal" to investigate effects other than the main task-induced effect. For example, cross-brain coherence of multiple signal components (wavelets) is thought to provide an indication of dynamic coupling processes rather than task-specific processes, which are coupled by virtue of the coordinated task. Coherence during eye-gaze was compared for face-to-face gaze and video-face gaze conditions. This analysis was also applied to shuffled dyads (random pairs). If the effects were due to social exchanges of salient cues, then the effects would be expected to disappear when partners were mixed (shuffled).

RESULTS

Figures 2A,B show cross-brain coherence (y-axis) and wavelet period in seconds (x-axis) for real and shuffled partners respectively comparing the eye-to-eye and face-video conditions. Red traces and shading indicate the mean ± SD in the live partner eye-to-eye condition, and blue traces indicate the face-video condition. An increase in coherence across live partners making direct eye-to-eye contact was observed in

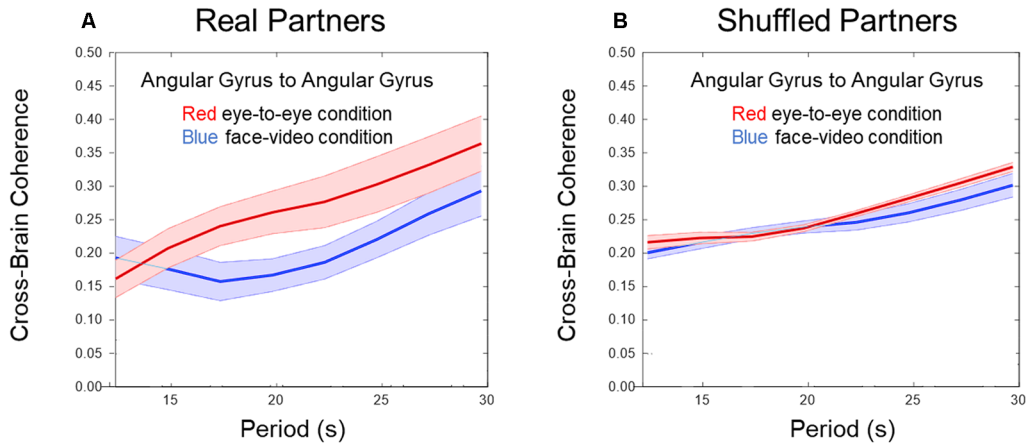

FIGURE 2 | Cross-brain coherence. **(A)** Angular gyrus (AG) cross-brain coherence between paired dyads during direct eye-to-eye contact (red trace) shows increased coherence in the combined DeOxy+OxyHb signals for periods between 15 and 25 s compared to the face video condition (blue trace; p 0.01, N = 15 pairs). **(B)** Shuffled dyads do not show differences in cross-brain synchrony in the AG when comparing face-to-face or video face interactions.

the AG between partners for temporal periods (wavelengths) between 15 and 25 s ($p < 0.01$). **Figure 2B** shows no difference in coherence between conditions when partners are shuffled, i.e., computationally paired with "partners" other than the real partner with whom he/she performed the task concurrently. Wavelet coherence was calculated for homologous regions. To further confirm the coherence results, we performed a permutation test between the 15 pairs of subjects and the two conditions. For this permutation test, we flipped the condition (face-to-face and video) for half the subjects and performed a t-test between the new mixed "conditions". This procedure was repeated 1,000 times. The results of this permutation test showed 3.7% of trials produced type 1 error (rejection of the null hypothesis when it is really true) with similar significance as our result.

Averaged event-triggered responses for Oxy- and deOxyHb signals for the two conditions are shown in **Figure 3**. The top row shows the average localized responses for the real face-to-face task and the bottom row shows responses for the video gaze task. The black circle on the right hemisphere diagrammatically represents the TPJ. The hemodynamic responses with relative increases in OxyHb and decreases in deOxyHb can be seen in this region for the eye-to-eye condition compared to the video condition.

GLM comparisons are shown on brain renderings in **Figure 4** for both the deOxyHb (**Figure 4A**) and the OxyHb (**Figure 4B**) signals (N = 30). Functional activity on the right hemisphere cortical surface for the eye-to-eye (left) and face-video (right) conditions are shown vs. rest ($p \leq 0.05$, FDR-corrected). Findings are similar for both Oxy- and deOxyHb signals, and the deOxyHb signal is described in detail below because the deOxyHb signal is considered most similar to the blood oxygen level-dependent (BOLD) signal acquired by functional magnetic resonance imaging (fMRI; Strangman et al., 2002; Kirilina et al., 2012; Dravida et al., 2018). In the eye-to-eye vs. rest condition, a single cluster of activity was found including the STG, MTG, AG, and SMG with a peak MNI coordinate of 68, −46, 18, T = 4.67 and a p-value of 0.00003 (FDR-corrected, $p \leq 0.05$). In the eye-to-video vs. rest condition, a single cluster of activity was found overlapping the right tertiary visual cortex and AG with a peak MNI coordinate of 48, −74, 18, T = 3.26 and a p-value of 0.0014.

A region of interest analysis based on the right TPJ (**Figure 5A**) was used to compare average signal strength (beta values) for the two conditions and two signals (**Figure 5B**). The real-eye > rest signals were greater than the video-gaze > rest for the deOxyHb signals. Average beta values in the ROI (paired t-test) yields a T statistic of $3.237 \pm 1.63e^{-04}$ ($p \leq 0.05$; **Figure 5B**, deOxyHb, left panel). OxyHb signals show a similar trend.

DISCUSSION

Increased cross-brain coherence between signals in the AG in the real eye-to-eye condition suggests that interactive and reciprocal behaviors between partners during eye contact increase activity in neural circuits associated with AG, a component of the TPJ. These results were specific only for eye-to-eye interactions (compared to watching a face video) and only occurred between interacting dyads (results on shuffled pairs showed no coherence). Increased coherence only in the live face-to-face task provides support for the hypothesis that reciprocal eye-contact dynamics between partners influences or modulates social network activity. A similar mechanism has been proposed by Tanabe and colleagues, suggesting an integrative role of the right STS in gaze processing, which has also been shown to be altered when individuals with autism interact with typically-developing subjects (Saito et al., 2010; Tanabe et al., 2012).

Both GLM (**Figure 4**) and ROI (**Figure 5**) results of the present study support and extend previous findings regarding the role of the TPJ in social interaction by demonstrating increased TPJ responses specific to dynamic face and eye contact in a live interaction. Real-time face-to-face interaction

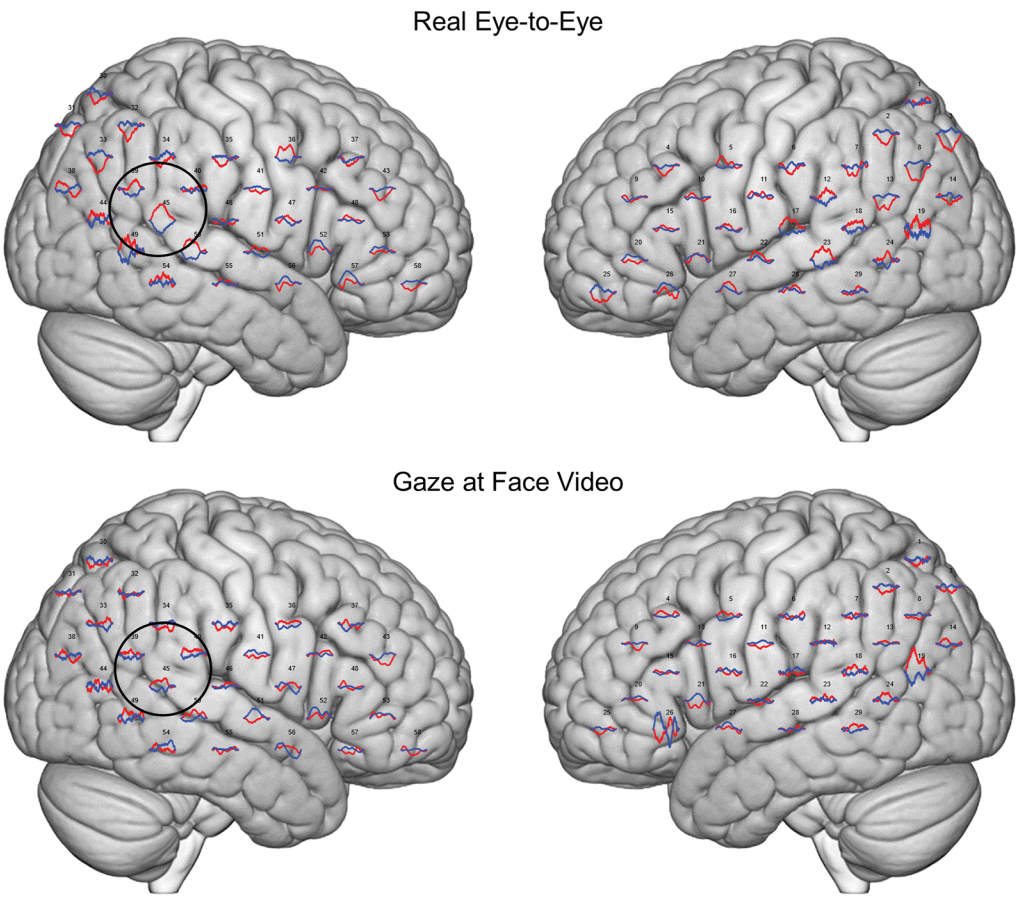

FIGURE 3 | Event-triggered responses. Brain renders indicate event-triggered averaged eye-to-eye responses (top) compared to gaze at face video responses (bottom). Red traces represent group averaged OxyHb responses and blue traces represent deOxyHb responses. The circle represents a diagrammatic representation of the TPJ region of interest for the OxyHb signal (top) and deOxyHb (bottom) signal.

in a direct eye-gaze task activates this area to a greater extent during eye-to-eye contact with a live partner compared to the same task in a dynamic video face interaction with a pre-recorded video partner. The increased activity in the TPJ for the live condition that is not observed in the video condition supports the theoretical framework proposed in the Interactive Brain Hypothesis (De Jaegher et al., 2016), which purports that live interaction between individuals engages neural functions not engaged during similar tasks performed alone, i.e., without interaction. The increased activity in the right TPJ during the real eye task is consistent with sensitivity to social interaction in that region and suggests that these neural circuits reflect ecologically valid social activity highlighting the importance of two-person paradigms (Schilbach et al., 2013).

These findings advance a framework for interpersonal interaction that is linked to reciprocally shared dynamic content. We suggest that eye contact mediates information transfer between dynamic face and social areas across the brains of interacting dyads. The right-lateralized TPJ has been referred to as the hub of human socialization (Carter and Huettel, 2013) and shares overlapping functional responses to stimuli associated with visual discrimination of human or biological motion. For example, lateral temporal regions of the brain have been shown to display specialized responses to the motion of humans and objects (Beauchamp et al., 2002). The pSTS specifically responds more to human motion than object motion, and lateral temporal regions respond to the movement of humans and objects more than ventral temporal areas, which respond to static human and object stimuli. Lateral regions of superior temporal sulcus display specific responses to dynamic or moving faces in addition to motion of the whole body (Avidan et al., 2005). More recently, it has been suggested that the pSTS processes specific information regarding the dynamic aspects of faces, including movements of eye, mouth and head (Pitcher et al., 2011a,b). These findings advance our understanding of

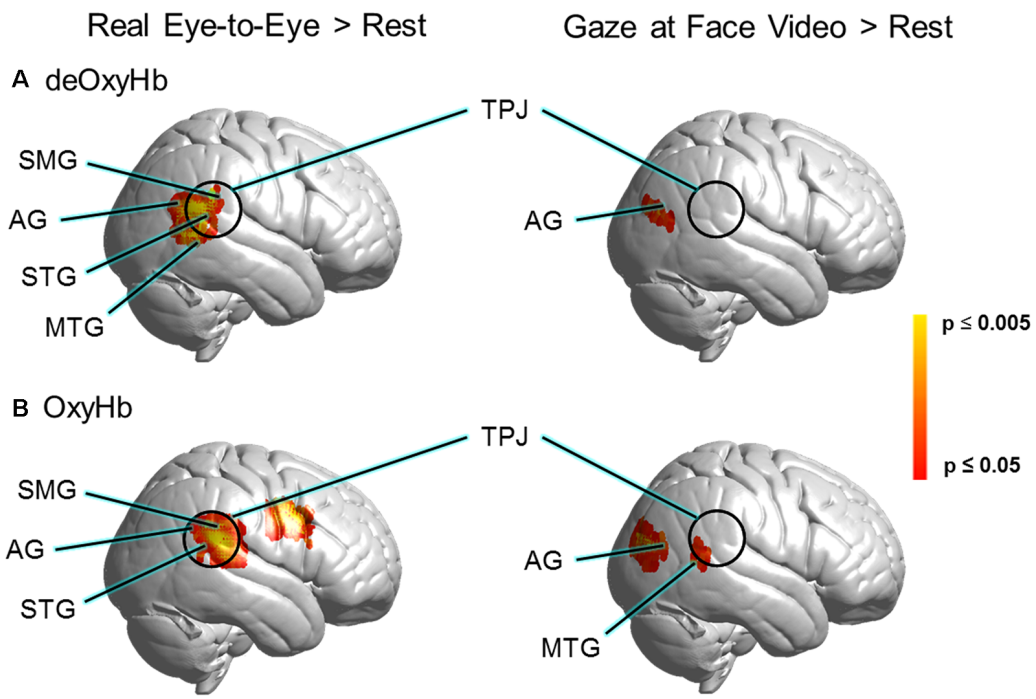

FIGURE 4 | GLM responses for **(A)** deOxyHb and **(B)** OxyHb signals. The left column shows results for real eye-to-eye > rest. The right column shows results for gaze at face video > rest, respectively. GLM results for real eye-to-eye > rest (left column) show a cluster of activity located centrally in the right-lateralized TPJ region of interest, including the SMG, AG, middle temporal gyrus (MTG), and the STG (p 0.05, FDR-corrected, N = 30). Face video > rest fails to provide evidence for activity in the TPJ.

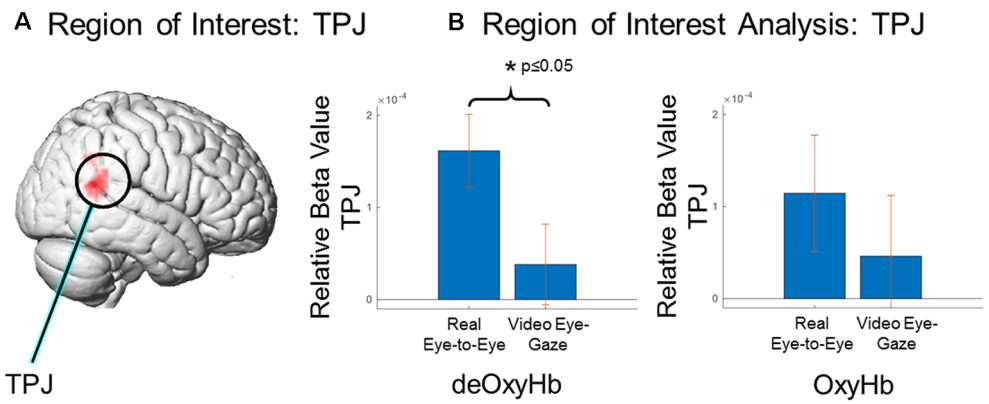

FIGURE 5 | Region of interest comparison of signal strength (beta values) for eye-to-eye gaze at a real face and a pre-rendered dynamic face video. **(A)** Region of interest within the right TPJ as determined by Neurosynth (neurosynth.org). **(B)** Region of interest analysis: TPJ, Comparison of deOxyHb (left) and OxyHb (right) responses. The left bar in each graph shows results for real eye-to-eye > rest and the right bar in each shows results for gaze at face video > rest. ROI comparisons demonstrate the increased sensitivity of the deOxyHb signal (left) compared to the spatially-filtered OxyHb signal (right). However, both signals provide consistent and congruent findings.

information transfer across individuals in the case of dynamic eye contact with cross-brain networks related to social interactions.

There are limitations to the interpretation of the results of this study. While the ROI analysis in this study showed activities specific to eye-to-eye interaction in the TPJ, other masks in additional ROIs were not investigated including the inferior and medial frontal gyri. These areas may also play a role in social attention. It is also possible that the mindset

of individuals was not identical in both eye-to-eye and face video conditions. Differences in mindsets when looking at a live face and a video of a face may have provided additional social information and contributed to the increased activity in the TPJ. The spatial resolution of fNIRS (approximately 3 cm) does not allow discrimination of small anatomical differences in functional activity between gyri and sulci in similar locations, such as the STG vs. the neighboring sulci. Even with this limitation the results of this study show activity and connectivity specific to the superficial cortex, including the pSTS and the TPJ, during live interaction. Due to the optical methods of fNIRS, signals may contain systemic effects that originate from cardiovascular rather than neural sources (Tachtsidis and Scholkmann, 2016). Recent techniques that employ spatial filtering and short channel separation to remove these artifacts have been developed (Gagnon et al., 2014; Goodwin et al., 2014; Zhang et al., 2016, 2017). Here, when the spatial filtering technique was employed (Zhang et al., 2016, 2017) we found that the deOxyHb signals in the ROI analysis showed a significant difference between groups, and the OxyHb signals revealed a similar trend. Although event-triggered average results indicated localized concordance of Oxy- and deOxyHb signals associated with neural processing, the additional variance in the OxyHb signal (seen in the error bars in **Figure 5**) may have contributed to the lack of a significant difference, although a consistent trend is observed between the two signals. fNIRS has a penetration limit into the superficial gray matter of the cortex of around 2 cm. While we have access to the superficial face and eye areas on the occipital face area and TPJ, this limitation does not allow us to record from deeper structures involved in face processing, such as the medial structures of the fusiform face area. All reported findings are restricted to these superficial regions. Activities and coherence are also limited to temporal resolutions associated with hemodynamic responses. Future experiments could include methodologies that employ electroencephalography (EEG) and double density fNIRS to further investigate the relation of hemodynamic and electrocortical signals.

In conclusion, the findings of this experiment show increased task-related activity in the right TPJ in pairs of subjects that view each other face-to-face in real-time compared to when they perform an identical task with a pre-recorded video of a dynamic face. Further, increased coherence of signals in the AG (part of the TPJ) of both partners in the face-to-face condition suggests a link between eye-contact behavior and neural mechanisms of social interaction.

DATA AVAILABILITY STATEMENT

The datasets analyzed for this study will be made available upon request at fmri.org.

ETHICS STATEMENT

The studies involving human participants were reviewed and approved by Yale Human Research Protection Program, Yale University. The patients/participants provided their written informed consent to participate in this study.

AUTHOR CONTRIBUTIONS

JN, XZ, SD, and JH designed and performed the experiment, analyzed the data, and wrote the manuscript. AN and JM assisted with experimental design. YO assisted with planning, data acquisition, and analysis.

FUNDING

This research was partially supported by the National Institute of Mental Health of the National Institutes of Health under award numbers 1R01MH111629 (PIs JH and JM); R01MH107513 (PI JH); 1R01MH119430 (PI JH); NIH Medical Scientist Training Program Training Grant T32GM007205 (SD); NRSA 1F30MH116626 (PI SD); and the Japan Society for the Promotion of Science (JSPS) Grants in Aid for Scientific Research (KAKENHI), JP15H03515 and JP16K01520 (PI YO). The content is solely the responsibility of the authors and does not necessarily represent the official views of the National Institutes of Health. All data reported in this article are available upon request from the corresponding author.

SUPPLEMENTARY MATERIAL

The Supplementary Material for this article can be found online at: https://www.frontiersin.org/articles/10.3389/fnhum.2020.00019/full#supplementary-material.

REFERENCES

Avidan, G., Hasson, U., Malach, R., and Behrmann, M. (2005). Detailed exploration of face-related processing in congenital prosopagnosia: 2. Functional neuroimaging findings. *J. Cogn. Neurosci.* 17, 1150–1167. doi: 10.1162/0898929054475145

Beauchamp, M. S., Lee, K. E., Haxby, J. V., and Martin, A. (2002). Parallel visual motion processing streams for manipulable objects and human movements. *Neuron* 34, 149–159. doi: 10.1016/s0896-6273(02)00642-6

Carter, R. M., and Huettel, S. A. (2013). A nexus model of the temporal-parietal junction. *Trends Cogn. Sci.* 17, 328–336. doi: 10.1016/j.tics.2013.05.007

Cavallo, A., Lungu, O., Becchio, C., Ansuini, C., Rustichini, A., and Fadiga, L. (2015). When gaze opens the channel for communication: integrative role of IFG and MPFC. *NeuroImage* 119, 63–69. doi: 10.1016/j.neuroimage.2015.06.025

Chang, L., and Tsao, D. Y. (2017). The code for facial identity in the primate brain. *Cell* 169, 1013.e14–1028.e14. doi: 10.1016/j.cell.2017.05.011

Cui, X., Bryant, D. M., and Reiss, A. L. (2012). NIRS-based hyperscanning reveals increased interpersonal coherence in superior frontal cortex during cooperation. *Neuroimage* 59, 2430–2437. doi: 10.1016/j.neuroimage.2011.09.003

De Jaegher, H., Di Paolo, E., and Adolphs, R. (2016). What does the interactive brain hypothesis mean for social neuroscience? A dialogue. *Philos. Trans. R. Soc. B Biol. Sci.* 371:20150379. doi: 10.1098/rstb.2015.0379

Dikker, S., Silbert, L. J., Hasson, U., and Zevin, J. D. (2014). On the same wavelength: predictable language enhances speaker-listener brain-to-brain synchrony in posterior superior temporal gyrus. *J. Neurosci.* 34, 6267–6272. doi: 10.1523/JNEUROSCI.3796-13.2014

Dommer, L., Jäger, N., Scholkmann, F., Wolf, M., and Holper, L. (2012). Between-brain coherence during joint n-back task performance: a two-person

functional near-infrared spectroscopy study. *Behav. Brain Res.* 234, 212–222. doi: 10.1016/j.bbr.2012.06.024

Dravida, S., Noah, J. A., Zhang, X., and Hirsch, J. (2018). Comparison of oxyhemoglobin and deoxyhemoglobin signal reliability with and without global mean removal for digit manipulation motor tasks. *Neurophotonics* 5:011006. doi: 10.1117/1.nph.5.1.011006

Duchaine, B., and Yovel, G. (2015). A revised neural framework for face processing. *Annu. Rev. Vis. Sci.* 1, 393–416. doi: 10.1146/annurev-vision-082114-035518

Dumas, G., Nadel, J., Soussignan, R., Martinerie, J., and Garnero, L. (2010). Inter-brain synchronization during social interaction. *PLoS One* 5:e12166. doi: 10.1371/journal.pone.0012166

Eggebrecht, A. T., Ferradal, S. L., Robichaux-Viehoever, A., Hassanpour, M. S., Dehghani, H., Snyder, A. Z., et al. (2014). Mapping distributed brain function and networks with diffuse optical tomography. *Nat. Photonics* 8, 448–454. doi: 10.1038/nphoton.2014.107

Eggebrecht, A. T., White, B. R., Ferradal, S. L., Chen, C., Zhan, Y., Snyder, A. Z., et al. (2012). A quantitative spatial comparison of high-density diffuse optical tomography and fMRI cortical mapping. *NeuroImage* 61, 1120–1128. doi: 10.1016/j.neuroimage.2012.01.124

Ferradal, S. L., Eggebrecht, A. T., Hassanpour, M., Snyder, A. Z., and Culver, J. P. (2014). Atlas-based head modeling and spatial normalization for high-density diffuse optical tomography: *in vivo* validation against fMRI. *NeuroImage* 85, 117–126. doi: 10.1016/j.neuroimage.2013.03.069

Funane, T., Kiguchi, M., Atsumori, H., Sato, H., Kubota, K., and Koizumi, H. (2011). Synchronous activity of two people's prefrontal cortices during a cooperative task measured by simultaneous near-infrared spectroscopy. *J. Biomed. Opt.* 16:077011. doi: 10.1117/1.3602853

Friston, K. J., Buechel, C., Fink, G. R., Morris, J., Rolls, E., and Dolan, R. J. (1997). Psychophysiological and modulatory interactions in neuroimaging. *Neuroimage* 6, 218–229. doi: 10.1006/nimg.1997.0291

Gagnon, L., Yücel, M. A., Boas, D. A., and Cooper, R. J. (2014). Further improvement in reducing superficial contamination in NIRS using double short separation measurements. *NeuroImage* 85, 127–135. doi: 10.1016/j.neuroimage.2013.01.073

George, N., Driver, J., and Dolan, R. J. (2001). Seen gaze-direction modulates fusiform activity and its coupling with other brain areas during face processing. *NeuroImage* 13, 1102–1112. doi: 10.1006/nimg.2001.0769

Goodwin, J. R., Gaudet, C. R., and Berger, A. J. (2014). Short-channel functional near-infrared spectroscopy regressions improve when source-detector separation is reduced. *Neurophotonics* 1:015002. doi: 10.1117/1.nph.1.1.015002

Hasson, U., and Frith, C. D. (2016). Mirroring and beyond: coupled dynamics as a generalized framework for modelling social interactions. *Philos. Trans. R. Soc. Lond. B Biol. Sci.* 371:20150366. doi: 10.1098/rstb.2015.0366

Haxby, J. V., Hoffman, E. A., and Gobbini, M. I. (2000). The distributed human neural system for face perception. *Trends Cogn. Sci.* 4, 223–233. doi: 10.1016/s1364-6613(00)01482-0

Hazeki, O., and Tamura, M. (1988). Quantitative analysis of hemoglobin oxygenation state of rat brain *in situ* by near-infrared spectrophotometry. *J. Appl. Physiol.* 64, 796–802. doi: 10.1152/jappl.1988.64.2.796

Hirsch, J., Adam Noah, J., Zhang, X., Dravida, S., and Ono, Y. (2018). A cross-brain neural mechanism for human-to-human verbal communication. *Soc. Cogn. Affect. Neurosci.* 13, 907–920. doi: 10.1093/scan/nsy070

Hirsch, J., Zhang, X., Noah, J. A., and Ono, Y. (2017). Frontal temporal and parietal systems synchronize within and across brains during live eye-to-eye contact. *NeuroImage* 157, 314–330. doi: 10.1016/j.neuroimage.2017.06.018

Hoffman, E. A., and Haxby, J. V. (2000). Distinct representations of eye gaze and identity in the distributed human neural system for face perception. *Nat. Neurosci.* 3, 80–84. doi: 10.1038/71152

Hooker, C. I., Paller, K. A., Gitelman, D. R., Parrish, T. B., Mesulam, M.-M., and Reber, P. J. (2003). Brain networks for analyzing eye gaze. *Cogn. Brain Res.* 17, 406–418. doi: 10.1016/s0926-6410(03)00143-5

Hoshi, Y. (2003). Functional near-infrared optical imaging: utility and limitations in human brain mapping. *Psychophysiology* 40, 511–520. doi: 10.1111/1469-8986.00053

Jacob, P. (2009). The tuning-fork model of human social cognition: a critique. *Conscious. Cogn.* 18, 229–243. doi: 10.1016/j.concog.2008.05.002

Jiang, J., Dai, B., Peng, D., Zhu, C., Liu, L., and Lu, C. (2012). Neural synchronization during face-to-face communication. *J. Neurosci.* 32, 16064–16069. doi: 10.1523/JNEUROSCI.2926-12.2012

Jones, W., and Klin, A. (2013). Attention to eyes is present but in decline in 2-6-month-old infants later diagnosed with autism. *Nature* 504, 427–431. doi: 10.1038/nature12715

Kirilina, E., Jelzow, A., Heine, A., Niessing, M., Wabnitz, H., Brühl, R., et al. (2012). The physiological origin of task-evoked systemic artefacts in functional near infrared spectroscopy. *NeuroImage* 61, 70–81. doi: 10.1016/j.neuroimage.2012.02.074

Koike, T., Sumiya, M., Nakagawa, E., Okazaki, S., and Sadato, N. (2019). What makes eye contact special? Neural substrates of on-line mutual eye-gaze: a hyperscanning fMRI study. *eNeuro* 6:ENEURO.0284-18.2019. doi: 10.1523/eneuro.0284-18.2019

Koike, T., Tanabe, H. C., Okazaki, S., Nakagawa, E., Sasaki, A. T., Shimada, K., et al. (2016). Neural substrates of shared attention as social memory: a hyperscanning functional magnetic resonance imaging study. *NeuroImage* 125, 401–412. doi: 10.1016/j.neuroimage.2015.09.076

Lachat, F., Hugueville, L., Lemaréchal, J. D., Conty, L., and George, N. (2012). Oscillatory brain correlates of live joint attention: a dual-EEG study. *Front. Hum. Neurosci.* 6:156. doi: 10.3389/fnhum.2012.00156

Matcher, S. J., Elwell, C. E., Cooper, C. E., Cope, M., and Delpy, D. T. (1995). Performance comparison of several published tissue near-infrared spectroscopy algorithms. *Anal. Biochem.* 227, 54–68. doi: 10.1006/abio.1995.1252

Mazziotta, J., Toga, A., Evans, A., Fox, P., Lancaster, J., Zilles, K., et al. (2001). A probabilistic atlas and reference system for the human brain: international consortium for brain mapping (ICBM). *Philos. Trans. R. Soc. B Biol. Sci.* 356, 1293–1322. doi: 10.1098/rstb.2001.0915

McPartland, J. C., Webb, S. J., Keehn, B., and Dawson, G. (2011). Patterns of visual attention to faces and objects in autism spectrum disorder. *J. Autism Dev. Disord.* 41, 148–157. doi: 10.1007/s10803-010-1033-8

Mosconi, M. W., Mack, P. B., McCarthy, G., and Pelphrey, K. A. (2005). Taking an "intentional stance" on eye-gaze shifts: a functional neuroimaging study of social perception in children. *NeuroImage* 27, 247–252. doi: 10.1016/j.neuroimage.2005.03.027

Nation, K., and Penny, S. (2008). Sensitivity to eye gaze in autism: is it normal? Is it automatic? Is it social? *Dev. Psychopathol.* 20, 79–97. doi: 10.1017/s0954579408000047

Noah, J. A., Dravida, S., Zhang, X., Yahil, S., and Hirsch, J. (2017). Neural correlates of conflict between gestures and words: a domain-specific role for a temporal-parietal complex. *PLoS One* 12:e0173525. doi: 10.1371/journal.pone.0173525

Noah, J. A., Ono, Y., Nomoto, Y., Shimada, S., Tachibana, A., Zhang, X., et al. (2015). fMRI validation of fNIRS measurements during a naturalistic task. *J. Vis. Exp.* 100:e52116. doi: 10.3791/52116

Okamoto, M., and Dan, I. (2005). Automated cortical projection of head-surface locations for transcranial functional brain mapping. *NeuroImage* 26, 18–28. doi: 10.1016/j.neuroimage.2005.01.018

Oldfield, R. C. (1971). The assessment and analysis of handedness: the Edinburgh inventory. *Neuropsychologia* 9, 97–113. doi: 10.1016/0028-3932(71)90067-4

Ono, Y., Nomoto, Y., Tanaka, S., Sato, K., Shimada, S., Tachibana, A., et al. (2014). Frontotemporal oxyhemoglobin dynamics predict performance accuracy of dance simulation gameplay: temporal characteristics of top-down and bottom-up cortical activities. *NeuroImage* 85, 461–470. doi: 10.1016/j.neuroimage.2013.05.071

Osaka, N., Minamoto, T., Yaoi, K., Azuma, M., and Osaka, M. (2014). Neural synchronization during cooperated humming: a hyperscanning study using fNIRS. *Proc. Soc. Behav. Sci.* 126, 241–243. doi: 10.1016/j.sbspro.2014.02.395

Osaka, N., Minamoto, T., Yaoi, K., Azuma, M., Shimada, Y. M., and Osaka, M. (2015). How two brains make one synchronized mind in the inferior frontal cortex: fNIRS-based hyperscanning during cooperative singing. *Front. Psychol.* 6:1811. doi: 10.3389/fpsyg.2015.01811

Pelphrey, K. A., Morris, J. P., and McCarthy, G. (2005). Neural basis of eye gaze processing deficits in autism. *Brain* 128, 1038–1048. doi: 10.1093/brain/awh404

Penny, W. D., Friston, K. J., Ashburner, J. T., Kiebel, S. J., and Nichols, T. E. (2011). *Statistical Parametric Mapping: The Analysis of Functional Brain Images.* London: Elsevier/Academic Press.

Pitcher, D., Dilks, D. D., Saxe, R. R., Triantafyllou, C., and Kanwisher, N. (2011a). Differential selectivity for dynamic versus static information in face-selective cortical regions. *NeuroImage* 56, 2356–2363. doi: 10.1016/j.neuroimage.2011.03.067

Pitcher, D., Walsh, V., and Duchaine, B. (2011b). The role of the occipital face area in the cortical face perception network. *Exp. Brain Res.* 209, 481–493. doi: 10.1007/s00221-011-2579-1

Piva, M., Zhang, X., Noah, J. A., Chang, S. W., and Hirsch, J. (2017). Distributed neural activity patterns during human-to-human competition. *Front. Hum. Neurosci.* 11:571. doi: 10.3389/fnhum.2017.00571

Saito, D. N., Tanabe, H. C., Izuma, K., Hayashi, M. J., Morito, Y., Komeda, H., et al. (2010). "Stay tuned": inter-individual neural synchronization during mutual gaze and joint attention. *Front. Integr. Neurosci.* 4:127. doi: 10.3389/fnint.2010.00127

Sato, W., Kochiyama, T., Uono, S., and Toichi, M. (2016). Neural mechanisms underlying conscious and unconscious attentional shifts triggered by eye gaze. *NeuroImage* 124, 118–126. doi: 10.1016/j.neuroimage.2015.08.061

Schilbach, L., Timmermans, B., Reddy, V., Costall, A., Bente, G., Schlicht, T., et al. (2013). Toward a second-person neuroscience. *Behav. Brain Sci.* 36, 393–414. doi: 10.1017/S0140525X12000660

Schippers, M. B., Roebroeck, A., Renken, R., Nanetti, L., and Keysers, C. (2010). Mapping the information flow from one brain to another during gestural communication. *Proc. Natl. Acad. Sci. U S A* 107, 9388–9393. doi: 10.1073/pnas.1001791107

Schneier, F. R., Kent, J. M., Star, A., and Hirsch, J. (2009). Neural circuitry of submissive behavior in social anxiety disorder: a preliminary study of response to direct eye gaze. *Psychiatry Res.* 173, 248–250. doi: 10.1016/j.pscychresns.2008.06.004

Senju, A., and Johnson, M. H. (2009). Atypical eye contact in autism: models, mechanisms and development. *Neurosci. Biobehav. Rev.* 33, 1204–1214. doi: 10.1016/j.neubiorev.2009.06.001

Singh, A. K., Okamoto, M., Dan, H., Jurcak, V., and Dan, I. (2005). Spatial registration of multichannel multi-subject fNIRS data to MNI space without MRI. *NeuroImage* 27, 842–851. doi: 10.1016/j.neuroimage.2005.05.019

Sorger, B., Goebel, R., Schiltz, C., and Rossion, B. (2007). Understanding the functional neuroanatomy of acquired prosopagnosia. *NeuroImage* 35, 836–852. doi: 10.1016/j.neuroimage.2006.09.051

Strangman, G., Culver, J. P., Thompson, J. H., and Boas, D. A. (2002). A quantitative comparison of simultaneous BOLD fMRI and NIRS recordings during functional brain activation. *NeuroImage* 17, 719–731. doi: 10.1006/nimg.2002.1227

Tachibana, A., Noah, J. A., Bronner, S., Ono, Y., and Onozuka, M. (2011). Parietal and temporal activity during a multimodal dance video game: an fNIRS study. *Neurosci. Lett.* 503, 125–130. doi: 10.1016/j.neulet.2011.08.023

Tachtsidis, I., and Scholkmann, F. (2016). False positives and false negatives in functional near-infrared spectroscopy: issues, challenges, and the way forward. *Neurophotonics* 3:031405. doi: 10.1117/1.NPh.3.3.031405

Tanabe, H. C., Kosaka, H., Saito, D. N., Koike, T., Hayashi, M. J., Izuma, K., et al. (2012). Hard to "tune in": neural mechanisms of live face-to-face interaction with high-functioning autistic spectrum disorder. *Front. Hum. Neurosci.* 6:268. doi: 10.3389/fnhum.2012.00268

Torrence, C., and Compo, G. P. (1998). A practical guide to wavelet analysis. Bulletin of the American Meteorological society. 79, 61–78.

Tso, I. F., Mui, M. L., Taylor, S. F., and Deldin, P. J. (2012). Eye-contact perception in schizophrenia: relationship with symptoms and socioemotional functioning. *J. Abnorm. Psychol.* 121, 616–627. doi: 10.1037/a0026596

Yarkoni, T., Poldrack, R. A., Nichols, T. E., Van Essen, D. C., and Wager, T. D. (2011). Large-scale automated synthesis of human functional neuroimaging data. *Nat. Methods* 8, 665–670. doi: 10.1038/nmeth.1635

Ye, J. C., Tak, S., Jang, K. E., Jung, J., and Jang, J. (2009). NIRS-SPM: statistical parametric mapping for near-infrared spectroscopy. *NeuroImage* 44, 428–447. doi: 10.1016/j.neuroimage.2008.08.036

Zhang, X., Noah, J. A., Dravida, S., and Hirsch, J. (2017). Signal processing of functional NIRS data acquired during overt speaking. *Neurophotonics* 4:041409. doi: 10.1117/1.nph.4.4.041409

Zhang, X., Noah, J. A., and Hirsch, J. (2016). Separation of the global and local components in functional near-infrared spectroscopy signals using principal component spatial filtering. *Neurophotonics* 3:015004. doi: 10.1117/1.nph.3.1.015004

Conflict of Interest: The authors declare that the research was conducted in the absence of any commercial or financial relationships that could be construed as a potential conflict of interest.

frontiers in Human Neuroscience

ORIGINAL RESEARCH
published: 28 February 2020
doi: 10.3389/fnhum.2020.00052

Transcranial Focused Ultrasound to the Right Prefrontal Cortex Improves Mood and Alters Functional Connectivity in Humans

Joseph L. Sanguinetti[1,2,3], Stuart Hameroff[1,2,4], Ezra E. Smith[1,5], Tomokazu Sato[6†], Chris M. W. Daft[7], William J. Tyler[8] and John J. B. Allen[1]*

[1] Department of Psychology, University of Arizona, Tucson, AZ, United States, [2] Center for Consciousness Studies, University of Arizona, Tucson, AZ, United States, [3] Department of Psychology, The University of New Mexico, Albuquerque, NM, United States, [4] Department of Anesthesiology, University of Arizona, Tucson, AZ, United States, [5] New York State Psychiatric Institute, New York, NY, United States, [6] The Division of Biology and Biological Engineering, California Institute of Technology, Pasadena, CA, United States, [7] River Sonic Solutions LLC, San Francisco, CA, United States, [8] School of Biological and Health Systems Engineering, Arizona State University, Tempe, AZ, United States

OPEN ACCESS

Edited by:
Seiki Konishi, Juntendo University, Japan

Reviewed by:
Martin Monti, University of California, Los Angeles, United States
Kentaro Miyamoto, University of Oxford, United Kingdom

***Correspondence:**
Joseph L. Sanguinetti
sanguine@email.arizona.edu

†Present address:
Tomokazu Sato, Computer Solutions LLC, Eagan, MN, United States

Specialty section:
This article was submitted to Brain Imaging and Stimulation, a section of the journal Frontiers in Human Neuroscience

Received: *27 August 2019*
Accepted: *04 February 2020*
Published: *28 February 2020*

Citation:
Sanguinetti JL, Hameroff S, Smith EE, Sato T, Daft CMW, Tyler WJ and Allen JJB (2020) Transcranial Focused Ultrasound to the Right Prefrontal Cortex Improves Mood and Alters Functional Connectivity in Humans. Front. Hum. Neurosci. 14:52. doi: 10.3389/fnhum.2020.00052

Transcranial focused ultrasound (tFUS) is an emerging method for non-invasive neuromodulation akin to transcranial magnetic stimulation (TMS) and transcranial direct current stimulation (tDCS). tFUS offers several advantages over electromagnetic methods including high spatial resolution and the ability to reach deep brain targets. Here we describe two experiments assessing whether tFUS could modulate mood in healthy human volunteers by targeting the right inferior frontal gyrus (rIFG), an area implicated in mood and emotional regulation. In a randomized, placebo-controlled, double-blind study, participants received 30 s of 500 kHz tFUS or a placebo control. Visual Analog Mood Scales (VAMS) assessed mood four times within an hour (baseline and three times after tFUS). Participants who received tFUS reported an overall increase in Global Affect (GA), an aggregate score from the VAMS scale, indicating a positive shift in mood. Experiment 2 examined resting-state functional (FC) connectivity using functional magnetic resonance imaging (fMRI) following 2 min of 500 kHz tFUS at the rIFG. As in Experiment 1, tFUS enhanced self-reported mood states and also decreased FC in resting state networks related to emotion and mood regulation. These results suggest that tFUS can be used to modulate mood and emotional regulation networks in the prefrontal cortex.

Keywords: transcranial focused ultrasound, neuromodulation, mood, functional connectivity, brain stimulation

INTRODUCTION

Transcranial focused ultrasound (tFUS) is an emerging tool for non-invasive neuromodulation that transmits low-intensity ultrasound through the skull to temporarily and safely modulate regional brain activity (Tyler, 2011). Ultrasound neuromodulation offers advantages over transcranial magnetic stimulation (TMS) and transcranial direct current stimulation (tDCS), such as better spatial resolution and the ability to reach deep targets in the brain (Fini and Tyler, 2017). tFUS reversibly modulates neuronal activity in rats (Tufail et al., 2010; Kim et al., 2014), sheep

(Lee et al., 2016c), pigs (Dallapiazza et al., 2017), and monkeys (Downs et al., 2016). In humans, tFUS has temporarily altered activity in somatosensory (Lee et al., 2016a), visual (Lee et al., 2016b), and thalamic brain regions (Legon et al., 2018). Researchers are interested in clinical applications of tFUS, including the treatment of psychiatric and neurological disease (Bystritsky and Korb, 2015; Monti et al., 2016). The current experiments investigated whether tFUS could modulate mood in healthy participants by sonicating a region in the prefrontal cortex implicated in emotional regulation, thereby uncovering a target for future therapeutic interventions (Experiment 1). The second experiment used resting-state functional magnetic resonance imaging (fMRI) to investigate FC changes after sonication of the prefrontal cortex to demonstrate that tFUS modulates brain function in networks related to emotional processing and mood.

The prefrontal cortex plays a vital role in emotion and mood regulation (Phan et al., 2002; Coan and Allen, 2004; Ochsner and Gross, 2005; Price and Drevets, 2012). Hemispheric asymmetries in prefrontal activity are thought to contribute to emotional processing (Coan and Allen, 2004; Davidson, 2004; Craig, 2005), and dysfunctions in these networks are related to mood disorders like depression (Stewart et al., 2014) and bipolar disorder (Kerestes et al., 2012). Higher levels of left frontal activity are correlated with more approach motivation (Phillips et al., 2008) and positive mood (Fitzgerald et al., 2008), whereas higher levels of right frontal activity are associated with more withdrawal motivation, negative mood (Hauptman et al., 2008), and increased risk for anxiety and depression (Rempel-Clower, 2007). Currently, TMS and tDCS interventions target lateralized frontal cortex to enhance emotional control in healthy participants or to treat negative mood states in depression (George et al., 2000) and bipolar disorder (Michael and Erfurth, 2004).

In addition to TMS and tDCS, tFUS shows promise as a neuromodulation technique for altering mood states. In a pilot experiment testing the effects of ultrasound neuromodulation on patients, Hameroff et al. (2013) used a clinical ultrasound device at eight megahertz and found that 15 s of sonication of the prefrontal cortex enhanced mood in chronic pain patients, which lasted up to 40 min. Although this experiment suggests that ultrasound neuromodulation could be useful as a therapeutic tool to modulate mood states, the results must be interpreted with caution due to methodological limitations. First, the researchers delivered ultrasound to the prefrontal cortex contralateral to the side that patients reported the most significant pain. In other words, the location where the ultrasound transducer was placed was not uniform across patients. Second, Hameroff and colleagues used an unfocused ultrasound beam applied to the temporal window of the skull, likely sonicating frontal, temporal, and prefrontal cortices. The lack of control of stimulation location makes it impossible to determine whether the unfocused ultrasound affected mood directly, by stimulating a substrate of mood, or indirectly, by modulating other networks, such as those involved in pain perception (i.e., reducing pain perception may lead to more positive mood states). tFUS can untangle these issues by directly targeting brain regions involved in mood and emotional regulation.

One major advantage of tFUS relative to the other neuromodulation techniques like TMS and tDCS is that tFUS has a higher spatial resolution relative to the others. In tFUS applications, the ultrasound beam can be focused at virtually any depth through the human skull to target distinct cortical areas with millimeter resolution (Kubanek, 2018). Lee et al. (2015) showed that tFUS targeting the primary somatosensory cortex produced sonication-specific tactile sensations and somatosensory evoked potentials. Another study further demonstrated the high spatial specificity of tFUS by targeting the primary or secondary sensory cortices with a dual-transducer apparatus, which elicited tactile sensations correlated with the targeted cortical area (Lee et al., 2016a). Sonication of a sub-region of the thalamus with tFUS modulates somatosensory evoked potentials in healthy volunteers, exhibiting the deep focal ability and superior spatial resolution of tFUS (Legon et al., 2018). These experiments suggest that tFUS offers a unique modality for non-invasive modulation of region-specific brain function, and could be a useful method for exploring the effects of ultrasound neuromodulation on emotional regulation centers in the prefrontal cortex.

The goal of the current study was to use tFUS to modulate mood by targeting the right ventrolateral prefrontal cortex (rVLPFC), one of the major areas in the prefrontal cortex for emotional control and mood regulation (Sang and Hamann, 2007), and in particular the regulation and suppression of negative emotions (Ochsner and Gross, 2005; Goldin et al., 2008; Wager et al., 2008). Increased activity of rVLPFC is associated with less negative emotional experience when participants view aversive stimuli (Wager et al., 2008), and symptoms of depression inversely correlate with rVLPFC activity (Drevets et al., 2008). Several experiments show that modulation of the rVLPFC can alter the subjective experience of emotions. For instance, the application of anodal tDCS over the rVLPFC reduces negative feelings in social isolation video games (Riva et al., 2012, 2015a,b) and reduces emotional reactions to negative video clips, even when participants are not explicitly told to suppress negative emotion (Vergallito et al., 2018). Thus, the rVLPFC can serve as a target to enhance control over the emotional experience, which may lead to more positive mood states. Given the focal specificity of tFUS, we chose to target a specific region in rVLPFC, the right inferior frontal gyrus (rIFG; BA 35). The rIFG is a central hub for inhibition and cognitive control (Aron et al., 2014) and has been demonstrated to promote control over emotional processing (Chiu et al., 2008). We predicted that tFUS to the rIFG, using pulse parameters previously shown by Hameroff et al. (2013) to modulate mood in chronic pain patients, would enhance mood in healthy volunteers (Experiment 1). Experiment 2 used resting-state fMRI FC analysis to determine whether tFUS to the rIFG temporarily altered networks associated with mood and emotional regulation. These results would support the notion that the rVLPFC (specifically the rIFG) is involved in processing mood states and would serve as the foundation for future research investigating therapeutic applications of tFUS for mood-related disorders.

EXPERIMENT 1

Methods

Participants

The Institutional Review Board of the University of Arizona approved the experimental protocol. From an introductory-level psychology class, 51 volunteers (27 female, mean age 19.7 years) participated and received class credit. All participants signed an informed consent document. Participants had no history of epilepsy, severe neurological problems, or psychiatric history, and were medication free and not pregnant. All participants were right-handed. Participants were randomly assigned to either the tFUS-Active ($n = 25$) or Placebo condition ($n = 26$). We removed data from three participants due to technical malfunction of the computer that collected mood responses, yielding a final sample of 48 participants (tFUS-Active $n = 24$; Placebo $n = 24$).

Experimental Design and Procedures

The experiment was conducted in a small private room at the University of Arizona and occurred between 10 AM and 5 PM. During the consent process, we told participants that the purpose of the study was to test the effects of ultrasound on mood, but we did not specify whether they should expect to feel better or worse after sonication (i.e., after receiving ultrasound). The experimenters followed a structured protocol that would minimize the chance that interaction could prejudice the volunteers about mood changes during the consent or experimental procedures. Participants remained seated throughout the experiment. They were instructed to remain seated during the procedures and to respond as honestly and accurately as they could on the mood questionnaires. Participants were not allowed to use any electronic devices (e.g., cellular phones) during the experiment and were asked to sit quietly until they received instructions. The researchers did not engage in conversation with the participants and only answered questions if the participants asked.

After providing consent, the researcher marked the participants head at a location directly above the rVLPFC: the F8 electrode location [International 10/20 EEG placement system; Klem et al. (1999)]. The J&J psychophysiology system recorded the electrocardiogram (ECG), with bipolar electrodes situated under a wrist strap on the arms, and a strap was placed around the upper abdomen, on the outside of the shirt, to measure respiration. Average heart rate, heart-rate variability (HRV), and respiratory sinus arrhythmia (RSA) were derived. These cardiovascular psychophysiological measures (average heart rate, HRV, and RSA) did not vary as a function of tFUS condition and are therefore not discussed further.

Measurements occurred at four-time points within a 1-h time frame: Once during a baseline period before tFUS (Baseline), 10 min after tFUS (Post-10), 20 min after tFUS (Post-20), and 30 min after tFUS (Post-30). At the start of each of the four data recording assessments, participants sat quietly for 5 min (for the ECG baseline), after which they rated their subjective mood states by filling out a Visual Analog Mood Scale (VAMS; Ahearn, 1997; Nyenhuis, 1997) on a computer (Marsh-Richard et al., 2009). The VAMS is composed of eight questions related to mood and arousal. Participants rated their answer on a scale ranging from 0 to 10. The categories were Happy, Calm, Sad, Tense, Alert, Sleepy, Effort, and Weary. From these categories, we calculated a metric for Global Affect (GA; feelings and mood) and another for Global Vigor [GV; alertness and vigilance (Monk, 1989)]. An increase in the GA rating would indicate an overall positive increase in affective state (happiness, calmness, and reverse-keyed sadness and tenseness). An increase in GV would indicate an overall increase in arousal (alert, reverse keyed weariness, effort, and sleepiness). These measures were the primary dependent variables.

The custom ultrasound system had two modes: stimulation and placebo. The researcher entered a unique five-digit code for each session that would select the mode; the experimenter was blinded to code-condition assignments. Stimulation mode emitted the ultrasound parameters outlined below, and the placebo mode emitted no ultrasound. The device had an LED screen with a timer count-down on it to notify the researcher when 10 min had passed. The screen looked the same for stimulation and placebo modes. Therefore, the researchers and participants were blind to the condition. An offsite researcher (TS), who had no contact with the participants or experimenters, created the randomization codes.

Safety

The use of ultrasound, or any source of energy on tissue, requires consideration of significant bioeffects. The effects of ultrasound on living tissue have been well-studied (Dalecki, 2004; O'Brien, 2007; ter Haar, 2007; Church et al., 2008). High-intensity ultrasound can cause tissue heating and cavitation, or small potentially damaging bubbles (usually > 600 W/cm^2; Wu and Nyborg, 2008). In order to avoid deleterious effects on tissue, the FDA guidelines specify that global maximum acoustic output of ultrasound should be below 720 mW/cm^2, measured as spatial peak temporal average (I_{spta}), and a peak average of 190 mW/cm^2, measured as spatial peak pulse average (I_{sppa}; Barnett et al., 2000). Decades of animal and human research, as well as thousands of hours of incident-free clinical use, provide evidence that ultrasound at these levels is safe and biological effects are reversible, including effects on the human brain (Tufail et al., 2010; Yoo et al., 2011; Mueller et al., 2014; Downs et al., 2016; Legon et al., 2018, 2012).

Focused Ultrasound Waveform

A custom focused ultrasound system generated ultrasound pulses (Neurotrek, Inc., Boston, MA, United States) emitted with a single element transducer (500 kHz, with a two-part lens focused at 30 mm; Blatek, Inc., Pittsburg, PA, United States). The resultant tFUS waveform had the following characteristics: acoustic frequency was 0.5 MHz, pulse duration was 65 μs, pulse repetition period was 23 ms, pulse repetition frequency was 40 Hz, duty cycle was 0.26%, and stimulus duration was 30 s. We chose these parameters on the waveforms used previously to enhance mood states in chronic pain patients (Hameroff et al., 2013) with a diagnostic ultrasound system. The parameters were matched as best as possible given the differences between a

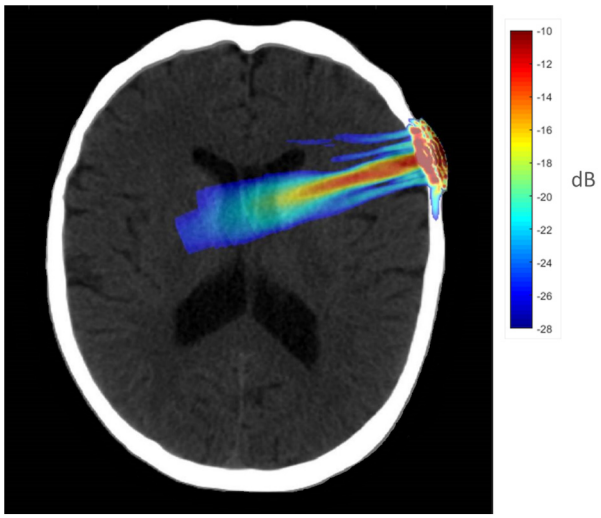

FIGURE 1 | Acoustic simulation model on a representative CT scan of a male patient. The transducer was positioned over the F8 EEG electrode location on the scalp which centers over the rIFG. Hotter colors (red, yellow) indicate more intense sonication, cooler colors (blue, green) indicate less intense sonication.

single-element focused custom ultrasound system and a phase-array diagnostic ultrasound system. A calibrated hydrophone measured the acoustic intensity (Onda, HN-500, Sunnyvale, CA, United States) by mounting the hydrophone on a three-axis stage positioning system and submerging the ultrasound transducer in a water tank with degassed water. At the center of the emitted ultrasound beam, the peak rarefactional pressure was 1.27 MPa, the mechanical index was 1.79, I_{sppa} was 54 W/cm^2, and I_{spta} was 130 mW/cm^2. Note, these measurements were taken in water alone (without skull) and therefore represented the energy delivered before transcutaneous and transcranial attenuation. All intensity levels were well below FDA guidelines. When measuring single-channel 500 kHz ultrasound beam characteristics in free water through a human skull, about 70–80% of the intensity is absorbed (Legon et al., 2018). Thus, I_{sppa} delivered to brain tissue, attenuated by the skull, would be unlikely to exceed 16.2 W/cm^2.

To better understand the tFUS properties of the focal beam, a head model was created using the K-Wave (Treeby and Cox, 2010) toolbox in MATLAB. A CT scan (randomly chosen from the R.I.R.E. project)[1] was used to construct the acoustic model of the head. The ultrasound field reported above was entered into the model and projected into the brain assuming the transducer was placed perpendicular to the scalp over F8 (the EEG location centered over the rIFG). The speed of sound entered was 1,550 m/s, and the brain density was 1030 kg/m^3. Acoustic simulations were performed with the k-Wave MATLAB toolbox on an archival CT scan to estimate the effects of an individual skull on the ultrasound beam properties targeting the rIFG. **Figure 1** displays the simulated ultrasound wave propagation through the skull at the location of F8. In this model, the skull reduced the intracranial max acoustic pressure by 53%.

[1]http://www.insight-journal.org/rire

Post-experiment Questions

At the end of the experiment, the blinded experimenter queried the participants about their subjective sensations when the transducer was on their head. They were asked to report any sounds they heard from the transducer on their head and were also asked to report any sensations they felt while the transducer was on their head.

Statistical Analysis

The dependent variables were GA and GV for the VAMS. We conducted a 4 × 2 repeated measures ANOVA for GA, and separately for GV, with Time of Assessment (Baseline, Post-10, Post-20, and Post-30 assessments) as the within-subjects' variable and Stimulation (tFUS-Active; Placebo) as the between subjects. Planned comparisons were performed when appropriate.

Results

Post-experiment Questions

A total of 15 out of 24 participants in the tFUS-Active condition reporting hearing some form of "buzzing, clicking or vibrating" when the transducer was on their head, and zero of 24 participants in the Placebo condition reported hearing any form or sound from the transducer. Additionally, 10 of 24 participants in the tFUS-Active condition reported feeling some sensation from the transducer (3 "pulsing," 5 "buzzing," and 2 "pressure"); 7 out of 24 participants in the Placebo condition reported feeling some sensation from the transducer (3 "pulsing," 3 "pressure," and 1 "warm"). We analyzed the difference in mood reports for participants in the tFUS-Active condition who reported hearing a sound to those who did not ("Sound Report") to ensure that hearing a sound did not influence the results below. Mauchly's Test of Sphericity indicated that the assumption of sphericity was violated, $\chi^2(5) = 16.112$, $p = 0.007$, and thus Greenhouse–Geisser corrections were used, with the original degrees of freedom reported. There was a significant main effect of Time, $F(3, 66) = 7.536$, $p = 0.002$, and there was not a significant interaction between Time of Assessment and Sound Report, $F(3, 66) = 0.591$, $p = 0.556$, indicating that hearing the sound from the transducer did not influence mood reports.

Visual Analog Mood Scales

For GA, Mauchly's Test of Sphericity indicated that the assumption of sphericity was violated, $\chi^2(2) = 19.220$, $p = 0.002$, and thus Greenhouse–Geisser corrections were used, with the original degrees of freedom reported. There was a significant main effect of Time, $F(3, 138) = 4.208$, $p = 0.013$, $\eta^2_{\partial} = 0.084$. There was a significant interaction between Stimulation and Time of Assessment, $F(3, 138) = 3.817$, $p = 0.019$, $\eta_{\partial}{}^2 = 0.077$. Pairwise comparisons were used to compare each Time of Assessment time-point relative to Baseline (within stimulation conditions; Bonferroni corrected). For participants receiving tFUS-Active, relative to Baseline ($M = 67.22$; SD = 13.74), GA was not significantly higher at the Post-10 condition ($M = 71.97$; SD = 12.05), $p = 0.173$, but was significant at Post-20 ($M = 75.36$;

TABLE 1 | Global Affect scores for Experiment 1.

	Global Affect			
	Baseline	**Post-10**	**Post-20**	**Post-30**
tFUS-Active				
Mean	67.22	71.97	75.36*	75.49*
SD	13.74	12.05	11.71	10.99
Placebo				
Mean	70.79	67.70	70.28	71.16
SD	13.16	16.00	13.60	11.99

Significant differences ($p < 0.05$) relative to Baseline are indicated by an asterisk.

TABLE 2 | Global Vigor scores for Experiment 1.

	Global Vigor			
	Baseline	**Post-10**	**Post-20**	**Post-30**
tFUS-Active				
Mean	47.57	47.35	55.41	57.08
SD	14.27	12.57	16.74	17.72
Placebo				
Mean	53.44	48.53	56.7	57.89
SD	14.33	16.64	16.93	16.74

No significant differences were found relative to Baseline.

SD = 11.71), $p = 0.014$, and Post-30 ($M = 75.49$; SD = 10.99), $p = 0.006$ (**Table 1**). No time points differed from baseline for those in the Placebo condition. Individual participant scores for GA and scores for the questions that comprise GA can be found in the **Supplementary Material**.

There was no difference in the baseline GA scores between tFUS-Active and Placebo conditions, $p > 0.05$, demonstrating that the groups did not differ in mood reports at the beginning of the experiment.

For GV, Mauchly's Test of Sphericity again indicated that the assumption of sphericity was violated, $\chi^2(2) = 33.915$, p = 0.001, and thus Greenhouse–Geisser corrections were used, with the original degrees of freedom reported. There was a main effect of time, $F(3, 138) = 8.794$, $p < 0.001$, $\eta_\partial^2 = 0.160$, as participants' tended to increase in GV over the experiment (**Table 2**). There was not a significant interaction between Stimulation and Time of Assessment, $F(3, 138) = 0.620$, $p = 0.537$, $\eta_\partial^2 = 0.013$ (**Table 2**).

The results from Experiment 1 suggest that 30-s exposures of 500 kHz focused ultrasound targeting the rIFG can induce positive mood effects for up to 30 min. Next, we determined the extent to which tFUS modulated brain activity using fMRI.

EXPERIMENT 2

To determine whether tFUS altered brain activity, we recorded resting state fMRI before and 20 min after sonification with the same custom focused ultrasound system from Experiment 1. Resting-state FC analysis was conducted by seeding the rIFG to determine whether sonification altered connectivity patterns relative in the rIFG network. We also seeded major hubs in the Default Mode Network (DMN). The DMN is a highly interconnected network of brain areas that are active when participants are not focused on a task and are instead daydreaming or involved with self-referential processing. Researchers have proposed that the DMN is a fundamental part of the neuronal substrate of the self (Gusnard et al., 2001). In mood disorders like depression, there is enhanced activity in the rIFG and hyper-connectivity in the DMN, which reflects the internal, ruminative nature of depression and the inability to regulate self-referential processes and emotion (Sheline et al., 2009; Kaiser et al., 2016). We hypothesized that 2 min of tFUS to the rIFG would alter connectivity patterns in the rIFG network. Additionally, we predicted that rIFG tFUS would alter connectivity in the DMN in a direction opposite to those patterns found in mood disorders. These results suggest that rIFG enhanced regulation of networks related to emotional processing (rIFG) and self-referential activity (DMN) may lead to altered mood states.

Methods

Participants

The Institutional Review Board of the University of Arizona approved the experiment. Nine volunteers (four females, mean age 19.2) participated. All participants signed an informed consent document. Participants had no history of epilepsy, severe neurological problems, or psychiatric history, and were medication free and not pregnant. All participants were right-handed.

Experimental Design and Procedures

After informed consent, participants filled out the VAMS scales (Baseline). Then, we collected 8 min of resting-state neuroimaging data. Participants were not given a task but were told to sit in the MRI scanner with their eyes open. Participants were then taken out of the MRI scanner and immediately received tFUS to the rIFG; they then sat quietly, without interacting with the researchers or anybody else for 10 min before completing the VAMS again; they sat for another 10 min before going back into the MRI scanner (20 min after sonication). After the scan, participants completed the VAMS scales outside the scanner (30 min after sonication). There were only three-time points for VAMS ratings: baseline, 10 min after sonication (Post-10), and 30 min after sonication (Post-30). There was no control condition. For the VAMS scale, we performed an ANOVA with Time as the factor with *post hoc* tests when appropriate. We used the same tFUS device and waveforms from Experiment 1, except the duty cycle increased to 0.5%, and the duration was 2 min. At the center of the emitted ultrasound beam, the peak rarefactional pressure, measured in water, was 1.26 MPa, the mechanical index was 1.79, I_{sppa} was 54 W/cm^2, and I_{spta} was 272 mW/cm^2.

fMRI Data Acquisition and Analysis

Functional images were acquired on a Siemens Skyra 3-Tesla scanner using EPI gradient echo sequence (TR = 1800 ms; TE = 25 ms; flip angle = 90; FOV = 192 mm; acquisition voxel size 3 mm × 3 mm × 3 mm). T1-weighted anatomical images were also acquired for registration of the functional

scans (MP-RAGE; TR was 2500 ms; TE was 4.35 ms; TI was 900 ms; flip angle was 8; FOV was 256 mm). Data pre-processing and analysis were performed using SPM8 (Welcome Trust Centre for Neuroimaging, University College London, United Kingdom) and the Functional Connectivity Toolbox (CONN; Whitfield-Gabrieli and Nieto-Castanon, 2012) in MATLAB (The MathWorks Inc., United States). Functional volumes underwent realignment and unwarping, slice-timing correction, structural segmentation, functional normalization, outlier detection, spatial smoothing (8 mm full width half maximum Gaussian kernel filter) and were normalized to the Montreal Neurological Institute (MNI) space using the normalized EPI template image (SPM) using CONN's "defaultMNI" pre-processing pipeline. Noise correction was performed in the CONN toolbox with the CompCor method (Behzadi et al., 2007).

We placed a seed at the tFUS target region (rIFG; BA 45; 58, 13, 6) to determine if network level changes occurred after sonication. We used the 10–20 International EEG coordinate system to place the transducer on the scalp at electrode location F8. We chose BA 45 as our RIO for the rIFG because F8 is correlated with BA 45 and is the most likely region sonicated with a transducer placed on F8 (Koessler et al., 2009). We also examined network-level changes in the DMN after sonication by placing seeds in the medial prefrontal cortex (BA10; 0, 48, −4) and posterior cingulate cortex (BA 31; −5, −51, 39). The DMN BA areas were chosen from the literature suggesting a link between those areas and mood disorder (increased DMN connectivity; e.g., Chen et al., 2015), mind wandering or mindfulness training (reduced DMN connectivity; e.g., Taylor et al., 2013). The seed-to-voxel analysis determined the connectivity of the specific seed regions outlined above with the whole brain and was carried out in CONN. White matter WM, cerebrospinal fluid, realignment parameters, motion artifacts, and physiological noise were taken as confounds and regressed out as implemented with the CompCor strategy (Behzadi et al., 2007). Heart rate and motion artifacts were taken as confounders. The whole-brain BOLD signal was also excluded to eliminate erroneous anti-correlations; the resulting data were bandpass filtered at 0.001 to 0.1 Hz. The temporal correlation between the BOLD signal from a given voxel to all other voxels in the brain was computed.

We computed differences in FC between networks before (pre) and after (post) tFUS with t-tests and Fisher's Z-transformed correlations in the second-level analysis. A first-level analysis used a general linear model (GLM) to determine significant resting-state connections at the individual level. We reported seed-to-voxel results with significant voxel wise thresholds exceeded at a level of $p < 0.001$ (uncorrected) and a cluster-level threshold of $p < 0.05$ FDR (corrected). Significant clusters (>10 voxels) are reported below.

Results

Visual Analog Mood Scales

For GA, Mauchly's Test of Sphericity indicated that the assumption of sphericity was violated, $\chi^2(2) = 8.891$, $p = 0.012$, and thus Greenhouse–Geisser corrections were used, with the original degrees of freedom reported. There was a main effect of time, $F(2, 16) = 4.908$, $p = 0.049$, $\eta_\partial^2 = 0.54$. GA ratings did not differ significantly between Baseline ($M = 81.44$, SD = 16.34) relative to Post-10 ($M = 84.44$; SD = 15.45), $p = 0.31$; however, mood significantly improved 30 min after stimulation, Post-30 ($M = 87.56$, SD = 14.89) relative to Baseline, $p = 0.044$ (**Table 3**).

TABLE 3 | Global Affect and Global Vigor scores for Experiment 2.

	Baseline	Post-10	Post-30
Global Affect			
Mean	81.44	84.44	87.56*
SD	16.34	15.45	14.89
Global Vigor			
Mean	75.83	78.06	82.5*
SD	13.22	13.56	13.57

Significant differences relative to Baseline are indicated by an asterisk. tFUS was active in both conditions.

For GV, the assumption of sphericity was not violated, $\chi^2(2) = 2.605$, $p = 0.272$. There was a main effect of time, $F(2, 16) = 5.439$, $p = 0.016$, $\eta_\partial^2 = 0.76$. On the GV scale, participants reported the same level of overall mental energy on baseline relative to Post-10, $p = 0.085$; however, participants reported an overall significant increase in mental vigor 30 min after sonication relative to baseline, $p = 0.028$ (**Table 3**).

fMRI Connectivity Results

Functional connectivity decreased after sonication within the rIFG network used in the seed-to-voxel analysis. Compared to the baseline, participants had significantly reduced connectivity between the rIFG and the subgenual cortex, orbitofrontal cortex, inferior prefrontal gyrus, dorsal anterior cingulate cortex, and entorhinal cortex (**Table 4** and **Figure 2**). The analysis revealed significant increases in connectivity between the rIFG and the premotor cortex (**Table 5** and **Figure 2**).

The DMN demonstrated decreased connectivity after sonication. For the MPFC seed, there was decreased connectivity with the premotor cortex, and ventral anterior cingulate cortex (**Table 4** and **Figure 3**) and increased connectivity with the superior temporal gyrus, insular cortex, primary auditory cortex, and subcentral area (**Table 5** and **Figure 3**). The PCC seed demonstrated decreased connectivity with the parahippocampal cortex, fusiform gyrus, perirhinal cortex, entorhinal cortex, and associative visual cortex (**Table 4** and **Figure 4**). **Figures 2**, **3** represent the regions of interest (seeds) and the corresponding locations of clusters of significant difference between pre- and post-sessions.

The results from Experiment 2 show that 2 min of tFUS targeting the rIFG modulated FC in a network related to the rIFG as well as the DMN 20 min after sonication. These results suggest that tFUS has effects on brain networks related to the area of sonication that lasts up to 20 min.

GENERAL DISCUSSION

Here we report two experiments that demonstrate for the first time that tFUS targeting the rIFG enhances mood, accompanied by changes in FC in networks related to emotional regulation.

TABLE 4 | Seed-to-voxel connectivity values for each seed region.

Reduced functional connectivity post-relative to pre for three seed regions							
Seed region	**Cluster coordinates**	**Cluster size**	**Cluster regions**	**BA**	**Voxels in regions**	**Coverage (%)**	**Cluster p value ($p < 0.05$ FDR)**
Inferior Frontal Gyrus	−06 + 28 − 24	548	(L) Subgenual cortex	25	101	17	0.001
			(R) Orbitofrontal cortex	11	83	3	
			(L) Inferior prefrontal gyrus	47	41	2	
			(L) Orbitofrontal cortex	11	32	1	
			(L) Dorsal anterior cingulate	32	17	1	
			(L) Posterior entorhinal cortex	28	12	2	
			(L) Anterior entorhinal cortex	34	12	2	
			(R) Subgenual cortex	25	4	1	
			Not assigned or <1% coverage		246		
Medial Prefrontal	−12 + 08 + 48	232	(L) Premotor cortex	6	96	1	0.008
			(L) Ventral anterior cingulate	24	66	4	
			(R) Premotor cortex	6	45	1	
			Not assigned or <1% coverage	–	25	–	
Posterior Cingulate	+20 − 40 − 10	263	(R) Parahippocampal cortex	36	97	13	0.002
			(R) Fusiform gyrus	37	47	3	
			(R) Associative visual cortex	19	26	1	
			(R) Perirhinal Cortex	35	18	5	
			(R) Posterior entorhinal cortex	28	7	1	
			Not assigned or <1% coverage	–	68	–	
	−34 − 88 + 28	145	(L) Associative visual cortex	19	105	2	0.033
			Not assigned or <1% coverage	–	40	–	

Reduced connectivity values are shown in this table, for the post-sonication scan relative to baseline.

In a double-blind, placebo-controlled experiment, participants reported a significant increase in mood 20 and 30 min after tFUS (Experiment 1). Experiment 2 replicated the positive mood effects of rIFG sonication and demonstrated FC changes in the rIFG network and the DMN after tFUS. Overall, we found an increase in connectivity between the rIFG and right middle frontal gyrus (rMFG) and decreased connectivity with left prefrontal and limbic areas. Regions within the DMN showed a general decrease in FC.

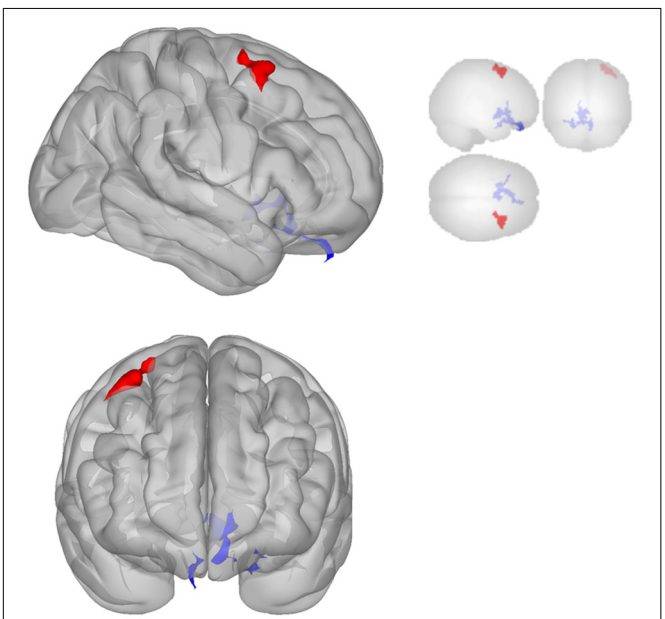

FIGURE 2 | Significant clusters for the rIFG seed-to-voxel analysis. Increased connectivity with rIFG is shown in red and decreased connectivity with rIFG in blue in the Post-scan relative to Baseline.

Previous research with ultrasound has demonstrated that ultrasound can modulate neural activity (see Introduction). Hameroff et al. (2013) found that a diagnostic ultrasound system altered mood in a population of chronic pain patients. We report, for the first time, that tFUS alters mood in healthy participants independent of clinical symptoms. The Hameroff et al. (2013) experiment did not control the location of stimulation, and the participants were chronic pain patients, some of whom were clinically depressed, complicating the interpretation of the result. Nonetheless, Hameroff et al. (2013) induced positive mood changes with 8 MHz stimulation (relative to placebo). In the Hameroff et al. (2013) study, patients reported a slight (but non-significant) decrease in pain. Thus, it is not clear if the elevation in mood was related to the reduction in pain in some participants, from ultrasound altering "mood circuits" in the brain, or a combination of both. By targeting the rIFG in a population of healthy participants with no clinical history or neurological or psychiatric disease, the current experiment is thus the first to demonstrate that tFUS of the rIFG can modulate mood.

The finding that tFUS focused on the rIFG resulted in improved self-reported mood can be understood in terms of the functions and connectivity of the rIFG. The rIFG plays a significant role in response inhibition and executive control

TABLE 5 | Seed-to-voxel connectivity values for each seed region.

Increased functional connectivity post-relative to pre by seed region							
Seed region	**Cluster coordinates**	**Cluster size**	**Cluster regions**	**BA**	**Voxels in region**	**Coverage (%)**	**Cluster p value ($p < 0.05$ FDR)**
Inferior Frontal Gyrus (BA 44)	+ 40 + 08 + 60	300	(R) Premotor cortex	6	253	3	0.001
			Not assigned or <1% coverage	–	47	–	
Medial Prefrontal (BA 10)	+ 52 − 6 − 4	220	(R) Superior temporal gyrus	22	98	4	0.008
			(R) Insular cortex	13	41	2	
			(R) Primary auditory cortex	41	39	6	
			(R) Subcentral area	43	12	4	
			Not assigned or <1% coverage	–	30	–	

Increased connectivity values are shown in this table, for the post-sonication scan relative to baseline.

(Aron et al., 2014). The rIFG is also involved in exerting cognitive control over emotion networks. For example, when participants are asked to voluntarily inhibit negative emotion during a task, or down-regulate emotion, rIFG is involved (Goldin et al., 2008) as it is generally with regulation of negative emotions (Ochsner and Gross, 2005; Sang and Hamann, 2007; Wager et al., 2008; Berkman and Lieberman, 2009; Parvaz et al., 2012; Touroutoglou et al., 2014). tDCS experiments targeting the same location we targeted in the current experiments have shown that modulation of that region enhances control over emotional experience, especially negative emotions (Riva et al., 2012, 2015b; Vergallito et al., 2018). Along with the middle frontal gyrus and limbic brain regions, the rIFG is part of an important mood regulation network that is related to mood disorders (Phillips et al., 2003). Patients with significant mood symptoms, including those with Parkinson's Disease, Bipolar Disorder, and Major Depressive Disorder (MDD) have altered connectivity in the rIFG network (Phillips et al., 2008). The results reported here support the notion that the rIFG is involved in a critical network that facilitates the overall regulation of mood states and is a promising target for therapeutic neuromodulation.

Experiment 2 found a significant increase in connectivity between the rIFG and the right middle frontal gyrus (rMFG) after sonication, which may have enhanced participants' ability to regulate emotional experience and mood during the experiment. Supporting the notion that the rIFG is involved in emotional regulation, research finds that the rIFG is hypoactivated in patients with mood disorders and increases activation

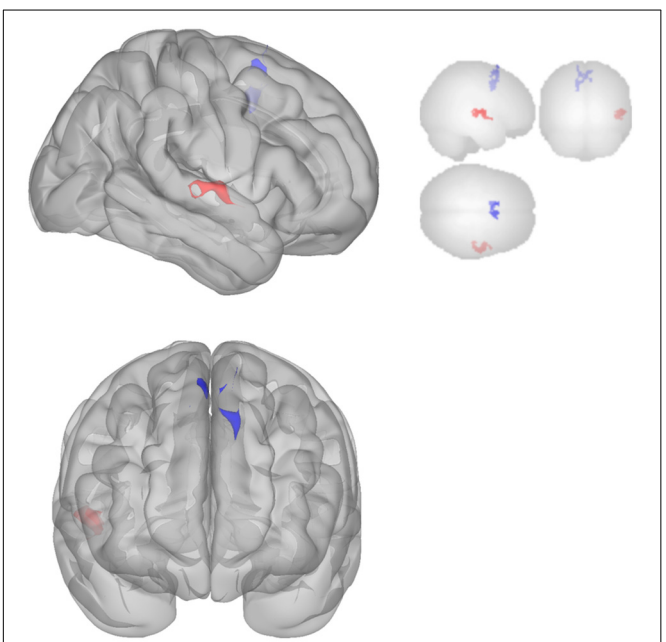

FIGURE 3 | Significant clusters for the medial prefrontal cortex (MPFC) seed-to-voxel analysis. Increased connectivity with MPFC is shown in red and decreased connectivity with MPFC in blue in the Post-scan relative to Baseline.

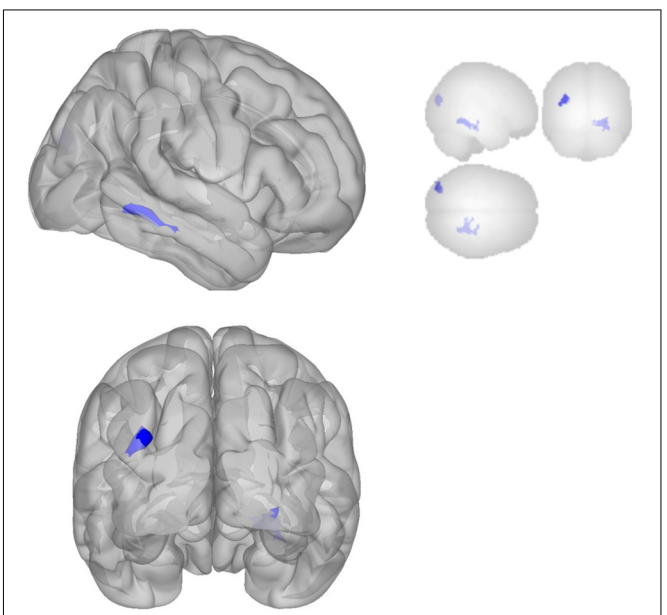

FIGURE 4 | Significant clusters for the medial posterior cingulate gyrus seed-to-voxel analysis. Increased connectivity with posterior cingulate gyrus is shown in red and decreased connectivity with posterior cingulate gyrus in blue in the Post-scan relative to Baseline.

after psychotherapy (Fitzgerald et al., 2008). The dorsolateral prefrontal cortex (DLPFC), in the MFG, has been linked to emotional regulation as well (Golkar et al., 2012). Female patients at high risk to develop MDD display decreased connectivity between the rIFG and the rMFG (Clasen et al., 2014). The rIFG-rMFG connectivity increases are suggestive of enhanced inter-region communication after sonication that may enable better regulation of emotional response to the challenges of the experimental setting.

There was also evidence of reduced connectivity between rIFG and left prefrontal and limbic areas. Indeed, left subgenual cortex (BA 25), dorsal anterior cingulate (BA 32), anterior entorhinal cortex (BA 34), left orbitofrontal cortex (BA 11), and left inferior prefrontal gyrus (BA 47), all showed decreased connectivity with the rIFG after sonication. These regions have demonstrated associations with affect and mood. The subgenual cortex (Lozano et al., 2010) is consistently associated with negative affect (Lindquist et al., 2016), and is a primary target of Deep Brain Stimulation for refractory depression. Dorsal anterior cingulate is involved in emotional reappraisal (Kalisch, 2009). The left orbitofrontal cortex (Rempel-Clower, 2007) and left inferior prefrontal gyrus (Ray and Zald, 2012) are involved in emotional regulation. Portions of the limbic system, including the entorhinal cortex, may be involved in mood disorders (Price and Drevets, 2012). The reduced connectivity of these many regions with the rIFG and increased connectivity of rIFG with rMFG, therefore, suggest a re-distribution or re-balancing of activity among a set of brain regions important for emotional experience and regulation.

Changes in connectivity within the DMN were also detected, which may relate to enhanced mood by reducing self-referential thinking and mind-wandering. In particular, the MPFC had reduced connectivity with the ventral anterior cingulate (BA 24), which is a major hub in the DMN (Greicius et al., 2003). The DMN is central to internal, self-referential thinking (Andrews-hanna et al., 2010); hyperconnectivity within the DMN is found for MDD (Kaiser et al., 2015). Alternatively, mindfulness training leads to a decrease in DMN activity, which correlates with positive health outcomes (Keng et al., 2011). Indeed, mind wandering relates to rumination (an essential feature of depression and anxiety), less happiness, and adverse health outcomes (Killingsworth and Gilbert, 2010). Thus, the decreased connectivity in the DMN may indicate a reduction in self-referential thinking and mind wandering, and a state characterized by being engaged in the present moment with the external environment rather than engaging in self-referential processing and rumination, all of which could lead to enhanced mood.

Decreases in the DMN network may also be related to enhanced cognitive control over emotional regulation during the experiment. Relative to the PCC seed, we found decreased connectivity for the right parahippocampal gyrus (BA 36), right temporal fusiform cortex (BA 37), right associative visual cortex (BA 19) and, perirhinal cortex (BA 35). PCC connectivity with parahippocampal gyrus and temporal cortex increases with sad mood induction in depressed patients and decreases in control participants (Renner et al., 2017). The observed changes in the DMN after negative mood induction in depressed patients may reflect an inability to exert cognitive control over emotional processing. Here, the opposite pattern was found, suggesting that the decreased connectivity supported greater cognitive control over emotional states during the experiment, which may have led to enhanced mood.

The effects of tFUS on mood in the current experiments indicate a lag between tFUS exposure and changes in functional brain activity, with effects peaking between 20 and 30 min (Hameroff et al., 2013; Sanguinetti et al., 2013). In experiments on rabbits and felines, respectively, modulatory effects of tFUS on visual evoked potentials lasted for several minutes (Yoo et al., 2011) and 30 min (Fry, 1957). These results suggest that the immediate physiological effects of tFUS may lead to reversible network-level changes over several minutes. The network-level changes could occur through membrane effects but are also consistent with ultrasound having immediate resonant effects on microtubules that result in delayed effects on synaptic plasticity. Assessing the time course of brain activity following tFUS, for example with EEG, could address more specifically how tFUS modulates brain activity and network dynamics, and how these, in turn, relate to mood and mental states.

The mechanisms by which tFUS modulates neuronal activity remains unknown, as is the mechanism by which neuronal activity results in phenomenal experience including mood. Several authors have proposed a mechanosensitivity hypothesis whereby ultrasound affects stretch-sensitive ion channels (Chapman et al., 1980), or lipid membranes surrounding them (Krasovitski et al., 2011), thus affecting membrane conductance (Tyler, 2011; Sassaroli and Vykhodtseva, 2016). Tyler (2011) suggested a "continuum mechanics hypothesis" in which ultrasound alters neuronal excitability through a combination of pressure/fluid/membrane actions involving stable cavitation, acoustic streaming, and fluid dynamics (radiation forces, shear stress, Bernoulli effects). Hameroff and others proposed that tFUS directly affects cytoskeletal microtubules inside neurons (and glia) (Hameroff et al., 2013) which may alter synaptic activity and function and lead to functional changes in brain processes (Hameroff and Penrose, 2014). Indeed, microtubules have been shown to have alternating current (AC) electron conductance resonances in the megahertz (Sahu et al., 2013) range. However, the mechanisms by which tFUS affects neural activity remain unknown, and more research is needed.

Limitations

The majority of recent human tFUS experiments have focused the sonication beam with MRI-based neuronavigation, which was unavailable for the present studies. Accordingly, we chose to use the 10–20 EEG system to aim the single-element transducer with a 30 mm focal depth beam. The 10–20 EEG system is considered accurate to 0.5-cm resolution (Chatrian et al., 2018) and our focal beam is on the order of millimeters; thus, we cannot validate precise targeting. With this limitation in mind, the experiments reported here demonstrate that tFUS navigated by EEG coordinates is useful to modulate mood in healthy volunteers. Indeed,

Legon et al. (2014) showed high spatial specificity with tFUS guided by EEG coordinates to stimulate the somatosensory cortex with at least centimeter resolution. These results could be significant for clinical applications where expensive and time-consuming neuronavigation is not feasible. Future experiments should directly compare the reliability of tFUS navigated by EEG coordinates to tFUS navigated by neuroimaging.

Some participants in the tFUS-Active condition reported hearing a sound when the transducer was on their head while none of the participants in the placebo condition reported hearing a sound. While an audible noise is not necessarily a cue for improved mood or active treatment, hearing a sound could have led participants to believe they were in the active condition thereby altering their mood. To rule out this possibility, we analyzed the changes in mood scores for participants in the active condition who reported hearing a sound to those who did not and found no significant difference in the scores. Furthermore, the difference scores for Post-30 (relative to Baseline) were 4.48 (SD = 9.10) for those who heard a sound and 13.99 (SD = 15.31) for those who did not. Although this difference was not significant, $p = 0.078$, this is the opposite pattern to what would be expected if hearing the sound from the transducer were to bias positive mood reports.

Experiments investigating tFUS in rodents have recently found that induced excitability changes in the brain can be, at least partially, due to an indirect effect of auditory stimulation, which was eliminated by removal of the cochlear fluid (Guo et al., 2018). Additionally, Sato et al. (2018) found that temporary chemical deafness could reduce the effects of tFUS on the brain. These studies show that important confounds can lead to brain activation through indirect pathways, but do not negate the notion that tFUS can also influence the brain directly. Experiments with organisms that lack auditory systems, like Xenopus oocyte (the "clawed frog"), show the effects of tFUS on neural activity (Kubanek et al., 2016), and ultrasound also influences neural activity and causes spike trains in slice preparations (Tyler et al., 2008). In humans, tFUS has produced tactile sensations (Lee et al., 2016a) and visual phosphenes (Lee et al., 2016b) with corresponding focal tissue activation that is hard to explain by activation through ascending auditory activation. Future experiments will need to better control unconscious and conscious auditory effects for ultrasound neuromodulation experiments on mood.

Future Research and Treatment

Overall, results from the experiments reported here and other recent tFUS studies motivate future investigations into the effects of ultrasound on brain function and cognitive disorders. Specifically, future studies should directly assess the impact of tFUS on experience, behavior, and brain network connectivity, with time-varying assessments in a sufficiently large sample to examine the potential mediational role of changes in network connectivity on mood and behavior. The positive findings reported here motivate testing tFUS in clinical populations with negative affect such as depression and anxiety disorders. Offering advantages over other non-invasive methods like TMS and tDCS, tFUS can be focused through the skull with millimeter precision or used in a wide beam to target large cortical areas. tFUS is relatively inexpensive, safe, and painless and can be used in an MRI or with EEG with little minimal signal interference. Additionally, other brain areas implicated in mood and emotional regulation, e.g., deep brain targets accessible until now only with invasive deep brain stimulation, can be targeted with tFUS. Therefore, tFUS holds excellent promise for the treatment of mental and cognitive disorders.

CONCLUSION

Transcranial focused ultrasound at 500 kHz targeting the rIFG for 30 s (Experiment 1) and 2 min (Experiment 2) increased self-reported mood in healthy participants as compared to baseline mood. Corresponding connectivity changes in networks relevant for emotion/mood regulation occurred 20 min after sonication in Experiment 2, demonstrating that tFUS could modulate functionally specific brain networks relevant for mood regulation. These results are in line with recent experiments suggesting that tFUS can modulate network connectivity (Folloni et al., 2019; Verhagen et al., 2019). These results are the first to demonstrate that tFUS can affect mood and cortical networks important for mood regulation, with effects that appear on the order of 20 min following tFUS delivery. Our results show that tFUS aimed at rIFG with a single element transducer can modulate prefrontal cortical activity and improve mood. The present findings suggest that tFUS could be a useful tool in the treatment of clinical disorders characterized by negative mood states, like depression and anxiety disorders and future studies are warranted.

DATA AVAILABILITY STATEMENT

The datasets generated for this study are available on request to the corresponding author.

ETHICS STATEMENT

The studies involving human participants were reviewed and approved by the Human Subjects Protection Program University of Arizona. The patients/participants provided their written informed consent to participate in this study.

AUTHOR CONTRIBUTIONS

JS, SH, TS, WT, and JA conceived and planned the experiments. TS created the blinding procedures. JS and ES carried out the experiments. CD planned and carried out the acoustic modeling. JS performed the mood analysis and functional connectivity analysis. JS, SH, ES, TS, WT, and JA contributed to the interpretation of the results. JS took the lead in writing the

manuscript. All authors provided critical feedback and helped to shape the research and manuscript.

FUNDING

This study received funding from Neurotrek, LLC. The funder was not involved in the study design, collection, analysis, interpretation of data, the writing of this article or the decision to submit it for publication. Funding was also provided by the Roger Penrose Institute, for partial salary support for JS and SH during manuscript preparation, and the Comprehensive Pain and Addiction Center, University of Arizona Health Sciences.

ACKNOWLEDGMENTS

We are deeply indebted to Russ Witte and the Experimental Ultrasound and Neuroimaging Lab at the University of Arizona, for their guidance on ultrasound parameters and the repeated use of the hydrophone.

SUPPLEMENTARY MATERIAL

The Supplementary Material for this article can be found online at: https://www.frontiersin.org/articles/10.3389/fnhum.2020.00052/full#supplementary-material

REFERENCES

Ahearn, E. P. E. (1997). The use of visual analog scales in mood disorders: a critical review. *J. Psychiatr. Res.* 31, 569–579. doi: 10.1016/S0022-3956(97)00029-0

Andrews-hanna, J. R., Reidler, J. S., Sepulcre, J., Poulin, R., and Buckner, R. L. (2010). Functional-anatomic fractionation of the brain's default network. *Neuron* 65, 550–562. doi: 10.1016/j.neuron.2010.02.005

Aron, A. R., Robbins, T. W., and Poldrack, R. A. (2014). Inhibition and the right inferior frontal cortex: one decade on. *Trends Cogn. Sci.* 18, 177–185. doi: 10.1016/j.tics.2013.12.003

Barnett, S. B., Ter Haar, G. R., Ziskin, M. C., Rott, H. D., Duck, F. A., and Maeda, K. (2000). International recommendations and guidelines for the safe use of diagnostic ultrasound in medicine. *Ultrasound Med. Biol.* 26, 355–366. doi: 10.1016/S0301-5629(00)00204-0

Behzadi, Y., Restom, K., Liau, J., and Liu, T. T. (2007). A component based noise correction method (CompCor) for BOLD and perfusion based fMRI. *Neuroimage* 37, 90–101. doi: 10.1016/j.neuroimage.2007.04.042

Berkman, E. T., and Lieberman, M. D. (2009). Using neuroscience to broaden emotion regulation: theoretical and methodological considerations. *Soc. Pers. Psychol. Compass* 3, 475–493. doi: 10.1111/j.1751-9004.2009.00186.x

Bystritsky, A., and Korb, A. S. (2015). A review of low-intensity transcranial focused ultrasound for clinical applications. *Curr. Behav. Neurosci. Rep.* 2, 60–66. doi: 10.1007/s40473-015-0039-0

Chapman, I. V., MacNally, N. A., and Tucker, S. (1980). Ultrasound-induced changes in rates of influx and efflux of potassium ions in rat thymocytes in vitro. *Ultrasound Med. Biol.* 6, 47–49. doi: 10.1016/0301-5629(80)90063-0

Chatrian, G. E., Lettich, E., and Nelson, P. L. (2018). Ten percent electrode system for topographic studies of spontaneous and evoked EEG activities. *Am. J. EEG Technol.* 25, 83–92. doi: 10.1080/00029238.1985.11080163

Chen, Y., Wang, C., Zhu, X., Tan, Y., and Zhong, Y. (2015). Aberrant connectivity within the default mode network in first-episode, treatment-naïve major depressive disorder. *J. Affect. Disord.* 183, 49–56. doi: 10.1016/j.jad.2015.04.052

Chiu, P. H., Holmes, A. J., and Pizzagalli, D. A. (2008). Dissociable recruitment of rostral anterior cingulate and inferior frontal cortex in emotional response inhibition. *Neuroimage* 42, 988–997. doi: 10.1016/j.neuroimage.2008.04.248

Church, C. C., Carstensen, E. L., Nyborg, W. L., Carson, P. L., Frizzell, L. A., and Bailey, M. R. (2008). The risk of exposure to diagnostic ultrasound in postnatal subjects: nonthermal mechanisms. *J. Ultrasound Med.* 27, 565–592. doi: 10.7863/jum.2008.27.4.565

Clasen, P. C., Beevers, C. G., Mumford, J. A., and Schnyer, D. M. (2014). Cognitive control network connectivity in adolescent women with and without a parental history of depression. *Dev. Cogn. Neurosci.* 7, 13–22. doi: 10.1016/j.dcn.2013.10.008

Coan, J. A., and Allen, J. J. (2004). Frontal EEG asymmetry as a moderator and mediator of emotion. *Biol. Psychol.* 67, 7–50. doi: 10.1016/j.biopsycho.2004.03.002

Craig, A. D. (2005). Forebrain emotional asymmetry: a neuroanatomical basis? *Trends Cogn. Sci.* 9, 566–571. doi: 10.1016/j.tics.2005.10.005

Dalecki, D. (2004). Mechanical bioeffects of ultrasound. *Ann. Rev. Biomed. Eng.* 6, 229–248. doi: 10.1146/annurev.bioeng.6.040803.140126

Dallapiazza, R. F., Timbie, K. F., Holmberg, S., Gatesman, J., Lopes, M. B., Price, R. J., et al. (2017). Noninvasive neuromodulation and thalamic mapping with low-intensity focused ultrasound. *J. Neurosurg.* 128, 875–884. doi: 10.3171/2016.11.JNS16976

Davidson, R. J. (2004). What does the prefrontal cortex "do" in affect: perspectives on frontal EEG asymmetry research. *Biol. Psychol.* 67, 219–233. doi: 10.1016/j.biopsycho.2004.03.008

Downs, M. E., Buch, A., Karakatsani, M. E., Teichert, T., Sierra, C., Chen, S., et al. (2016). Focused ultrasound enhances decision-making in monkeys. *BioRxiv* [Preprint], doi: 10.1101/041152

Drevets, W. C., Price, J. L., and Furey, M. L. (2008). Brain structural and functional abnormalities in mood disorders: implications for neurocircuitry models of depression. *Brain Struct. Funct.* 213, 93–118. doi: 10.1007/s00429-008-0189-x

Fini, M., and Tyler, W. J. (2017). Transcranial focused ultrasound: a new tool for non-invasive neuromodulation. *Intern. Rev. Psychiat.* 29, 168–177. doi: 10.1080/09540261.2017.1302924

Fitzgerald, P. B., Laird, A. R., Maller, J., and Daskalakis, Z. J. (2008). A meta-analytic study of changes in brain activation in depression. *Hum. Brain Mapp.* 29, 683–695. doi: 10.1002/hbm.20426.A

Folloni, D., Verhagen, L., Mars, R. B., Fouragnan, E., Constans, C., Aubry, J. F., et al. (2019). Manipulation of subcortical and deep cortical activity in the primate brain using transcranial focused ultrasound stimulation. *Neuron* 101, 1109–1116.e5. doi: 10.1016/j.neuron.2019.01.019

Fry, W. (1957). Use of intense ultrasound in neurological research. *Am. J. Phys. Med.* 37, 143–147. r

George, M. S., Nahas, Z., Molloy, M., Speer, A. M., Oliver, N. C., Li, X. B., et al. (2000). A controlled trial of daily left prefrontal cortex TMS for treating depression. *Biol. Psychiatr.* 48, 962–970. doi: 10.1016/S0006-3223(00)01048-9

Goldin, P. R., McRae, K., Ramel, W., and Gross, J. J. (2008). The neural bases of emotion regulation: reappraisal and suppression of negative emotion. *Biol. Psychiatr.* 63, 577–586. doi: 10.1016/j.biopsych.2007.05.031

Golkar, A., Lonsdorf, T. B., Olsson, A., Lindstrom, K. M., Berrebi, J., Fransson, P., et al. (2012). Distinct contributions of the dorsolateral prefrontal and orbitofrontal cortex during emotion regulation. *PLoS One* 7:48107. doi: 10.1371/journal.pone.0048107

Greicius, M. D., Krasnow, B., Reiss, A. L., and Menon, V. (2003). Functional connectivity in the resting brain: a network analysis of the default mode hypothesis. *Proc. Natl. Acad. Sci. U.S.A.* 100, 253–258. doi: 10.1073/pnas.0135058100

Guo, H., Hamilton, M., Offutt, S. J., Gloeckner, C. D., Li, T., Kim, Y., et al. (2018). Ultrasound produces extensive brain activation via a cochlear pathway. *Neuron* 98, 1020–1030.e4. doi: 10.1016/j.neuron.2018.04.036

Gusnard, D. A., Akbudak, E., Shulman, G. L., and Raichle, M. E. (2001). Medial prefrontal cortex and self-referential mental activity: relation to a default mode of brain function. *Proc. Natl. Acad. Sci. U.S.A.* 98, 4259–4264. doi: 10.1073/pnas.071043098

Hameroff, S., and Penrose, R. (2014). Consciousness in the universe a review of the ' Orch OR ' theory. *Phys. Life Rev.* 11, 39–78. doi: 10.1016/j.plrev.2013.08.002

Hameroff, S., Trakas, M., Duffield, C., Annabi, E., Gerace, M. B., Boyle, P., et al. (2013). Transcranial ultrasound (TUS) effects on mental states: a pilot study. *Brain Stimul.* 6, 409–415. doi: 10.1016/j.brs.2012.05.002

Hauptman, J. S., DeSalles, A. A., Espinoza, R., Sedrak, M., and Ishida, W. (2008). Potential surgical targets for deep brain stimulation in treatment-resistant depression. *Neurosurg. Focus* 25:E3. doi: 10.3171/FOC/2008/25/7/E3

Kaiser, R. H., Andrews-Hanna, J. R., Wager, T. D., and Pizzagalli, D. A. (2015). Large-scale network dysfunction in major depressive disorder: a meta-analysis of resting-state functional connectivity. *JAMA Psychiatry* 72, 603–611. doi: 10.1001/jamapsychiatry.2015.0071

Kaiser, R. H., Whitfield-Gabrieli, S., Dillon, D. G., Goer, F., Beltzer, M., Minkel, J., et al. (2016). Dynamic resting-state functional connectivity in major depression. *Neuropsychopharmacology* 41, 1822–1830. doi: 10.1038/npp.2015.352

Kalisch, R. (2009). The functional neuroanatomy of reappraisal: time matters. *Neurosci. Biobehav. Rev.* 33, 1215–1226. doi: 10.1016/j.neubiorev.2009.06.003

Keng, S. L., Smoski, M. J., and Robins, C. J. (2011). Effects of mindfulness on psychological health: a review of empirical studies. *Clin. Psychol. Rev.* 31, 1041–1056. doi: 10.1016/j.cpr.2011.04.006

Kerestes, R., Bhagwagar, Z., Nathan, P. J., Meda, S. A., Ladouceur, C. D., Maloney, K., et al. (2012). Prefrontal cortical response to emotional faces in individuals with major depressive disorder in remission. *Psychiatry Res. Neuroimag.* 202, 30–37. doi: 10.1016/j.pscychresns.2011.11.004

Killingsworth, M. A., and Gilbert, D. T. (2010). A wandering mind is an unhappy mind. *Science* 12:932. doi: 10.1126/science.1192439

Kim, H., Lee, S. D., Chiu, A., Yoo, S. S., and Park, S. (2014). Estimation of the spatial profile of neuromodulation and the temporal latency in motor responses induced by focused ultrasound brain stimulation. *Neuroreport* 25, 475–479. doi: 10.1097/WNR.0000000000000118

Klem, G. H., Lüders, H. O., Jasper, H. H., and Elger, C. (1999). The ten-twenty electrode system of the international federation. *Electroencephalogr. Clin. Neurophysiol.* 52, 3–6. r

Koessler, L., Maillard, L., Benhadid, A., Vignal, J. P., Felblinger, J., Vespignani, H., et al. (2009). Automated cortical projection of EEG sensors: anatomical correlation via the international 10-10 system. *Neuroimage* 46, 64–72. doi: 10.1016/j.neuroimage.2009.02.006

Krasovitski, B., Frenkel, V., Shoham, S., and Kimmel, E. (2011). Intramembrane cavitation as a unifying mechanism for ultrasound-induced bioeffects. *Proc. Natl. Acad. Sci. U.S.A.* 108, 3258–3263. doi: 10.1073/pnas.1015771108

Kubanek, J. (2018). Neuromodulation with transcranial focused ultrasound. *Neurosurg. Focus* 44:E14. doi: 10.3171/2017.11.FOCUS17621

Kubanek, J., Shi, J., Marsh, J., Chen, D., Deng, C., and Cui, J. (2016). Ultrasound modulates ion channel currents. *Sci. Rep.* 6, 1–14. doi: 10.1038/srep24170

Lee, W., Chung, Y. A., Jung, Y., Song, I.-U., and Yoo, S.-S. (2016a). Simultaneous acoustic stimulation of human primary and secondary somatosensory cortices using transcranial focused ultrasound. *BMC Neurosci.* 17:68. doi: 10.1186/s12868-016-0303-6

Lee, W., Kim, H.-C., Jung, Y., Chung, Y. A., Song, I.-U., Lee, J.-H., et al. (2016b). Transcranial focused ultrasound stimulation of human primary visual cortex. *Sci. Rep.* 6:34026. doi: 10.1038/srep34026

Lee, W., Kim, H., Jung, Y., Song, I.-U., Chung, Y. A., and Yoo, S.-S. (2015). Image-guided transcranial focused ultrasound stimulates human primary somatosensory cortex. *Sci. Rep.* 5:8743. doi: 10.1038/srep08743

Lee, W., Lee, S. D., Park, M. Y., Foley, L., Purcell-Estabrook, E., Kim, H., et al. (2016c). Image-guided focused ultrasound-mediated regional brain stimulation in sheep. *Ultrasound Med. Biol.* 42, 459–470. doi: 10.1016/j.ultrasmedbio.2015.10.001

Legon, W., Ai, L., Bansal, P., and Mueller, J. K. (2018). Neuromodulation with single-element transcranial focused ultrasound in human thalamus. *Hum. Brain Mapp* 39, 1995–2006. doi: 10.1002/hbm.23981

Legon, W., Rowlands, A., Opitz, A., Sato, T. F., and Tyler, W. J. (2012). Pulsed ultrasound differentially stimulates somatosensory circuits in humans as indicated by EEG and fMRI. *PLoS One* 7:e51177. doi: 10.1371/journal.pone.0051177

Legon, W., Sato, T. F., Opitz, A., Mueller, J., Barbour, A., Williams, A., et al. (2014). Transcranial focused ultrasound modulates the activity of primary somatosensory cortex in humans. *Nat. Neurosci.* 17, 322–329. doi: 10.1038/nn.3620

Lindquist, K. A., Satpute, A. B., Wager, T. D., Weber, J., and Barrett, L. F. (2016). The brain basis of positive and negative affect: evidence from a meta-analysis of the human neuroimaging literature. *Cereb. Cortex* 26, 1910–1922. doi: 10.1093/cercor/bhv001

Lozano, A. M., Mayberg, H. S., Craddock, R. C., and Kennedy, S. H. (2010). Stimulation for treatment- resistant depression. *J. Am. Psychiatry* 8, 583–591.

Marsh-Richard, D. M., Hatzis, E. S., Mathias, C. W., Venditti, N., and Dougherty, D. M. (2009). Adaptive Visual analog scales (AVAS): a modifiable software program for the creation, administration, and scoring of visual analog scales. *Behav. Res. Methods* 41, 99–106. doi: 10.3758/BRM.41.1.99

Michael, N., and Erfurth, A. (2004). Treatment of bipolar mania with right prefrontal rapid transcranial magnetic stimulation. *J. Affect. Disord.* 78, 253–257. doi: 10.1016/S0165-0327(02)00308-7

Monk, T. H. (1989). A visual analogue scale technique to measure global vigor and affect. *Psychiatry Res.* 27, 89–99. doi: 10.1016/0165-1781(89)90013-9

Monti, M. M., Schnakers, C., Korb, A. S., Bystritsky, A., and Vespa, P. M. (2016). Non-invasive ultrasonic thalamic stimulation in disorders of consciousness after severe brain injury: a first-in-man report. *Brain Stimul.* 9, 940–941. doi: 10.1016/j.brs.2016.07.008

Mueller, J., Legon, W., Opitz, A., Sato, T. F., and Tyler, W. J. (2014). Transcranial focused ultrasound modulates intrinsic and evoked EEG dynamics. *Brain Stimul.* 7, 900–908. doi: 10.1016/j.brs.2014.08.008

Nyenhuis, D. L. (1997). Standardization and validation of the standardization and validation of the visual analog mood scales. *Clin. Neuropsychol.* 11, 407–415. doi: 10.1080/13854049708400470

O'Brien, W. D. (2007). Ultrasound-biophysics mechanisms. *Prog. Biophys. Mol. Biol.* 93, 212–255. doi: 10.1016/j.pbiomolbio.2006.07.010

Ochsner, K. N., and Gross, J. J. (2005). The cognitive control of emotion. *Trends Cogn. Sci.* 9, 242–249. doi: 10.1016/j.tics.2005.03.010

Parvaz, M. A., MacNamara, A., Goldstein, R. Z., and Hajcak, G. (2012). Event-related induced frontal alpha as a marker of lateral prefrontal cortex activation during cognitive reappraisal. *Cogn. Affect. Behav. Neurosci.* 12, 730–740. doi: 10.3758/s13415-012-0107-9

Phan, K. L., Wager, T., Taylor, S. F., and Liberzon, I. (2002). Functional neuroanatomy of emotion: a meta-analysis of emotion activation studies in PET and fMRI. *Neuroimage* 16, 331–348. doi: 10.1006/nimg.2002.1087

Phillips, M. L., Drevets, W. C., Rauch, S. L., and Lane, R. (2003). Neurobiology of emotion perception I: the neural basis of normal emotion perception. *Biol. Psychiatry* 54, 504–514. doi: 10.1016/S0006-3223(03)00168-9

Phillips, M. L., Ladouceur, C. D., and Drevets, W. C. (2008). A neural model of voluntary and automatic emotion regulation: implications for understanding the pathophysiology and neurodevelopment of bipolar disorder. *Mol. Psychiatry* 13, 833–857. doi: 10.1038/mp.2008.65

Price, J. L., and Drevets, W. C. (2012). Neural circuits underlying the pathophysiology of mood disorders. *Trends Cogn. Sci.* 16, 61–71. doi: 10.1016/j.tics.2011.12.011

Ray, R. D., and Zald, D. H. (2012). Anatomical insights into the interaction of emotion and cognition in the prefrontal cortex. *Neurosci. Biobehav. Rev.* 36, 479–501. doi: 10.1016/j.neubiorev.2011.08.005

Rempel-Clower, N. L. (2007). Role of orbitofrontal cortex connections in emotion. *Ann. N. Y. Acad. Sci. U.S.A.* 1121, 72–86. doi: 10.1196/annals.1401.026

Renner, F., Siep, N., Arntz, A., van de Ven, V., Peeters, F. P. M. L., Quaedflieg, C. W. E. M., et al. (2017). Negative mood-induction modulates default mode network resting-state functional connectivity in chronic depression. *J. Affect. Disord.* 208, 590–596. doi: 10.1016/j.jad.2016.10.022

Riva, P., Romero Lauro, L. J., DeWall, C. N., and Bushman, B. J. (2012). Buffer the pain away: stimulating the right ventrolateral prefrontal cortex reduces pain following social exclusion. *Psychol. Sci.* 23, 1473–1475. doi: 10.1177/0956797612450894

Riva, P., Romero Lauro, L. J., DeWall, C. N., Chester, D. S., and Bushman, B. J. (2015a). Reducing aggressive responses to social exclusion using transcranial direct current stimulation. *Soc. Cogn. Affect. Neurosci.* 10, 352–356. doi: 10.1093/scan/nsu053

Riva, P., Romero Lauro, L. J., Vergallito, A., DeWall, C. N., and Bushman, B. J. (2015b). Electrified emotions: modulatory effects of transcranial direct stimulation on negative emotional reactions to social exclusion. *Soc. Neurosci.* 10, 46–54. doi: 10.1080/17470919.2014.946621

Sahu, S., Ghosh, S., Ghosh, B., Aswani, K., Hirata, K., Fujita, D., et al. (2013). Atomic water channel controlling remarkable properties of a single brain microtubule: correlating single protein to its supramolecular assembly. *Biosens. Bioelectron.* 47, 141–148. doi: 10.1016/j.bios.2013.02.050

Sang, H. K., and Hamann, S. (2007). Neural correlates of positive and negative emotion regulation. *J. Cogn. Neurosci.* 19, 776–798. doi: 10.1162/jocn.2007.19.5.776

Sanguinetti, J. L., Smith, E. E., Dieckman, L., Vanuk, J., Hameroff, S., and Allen, J. J. B. (2013). Transcranial ultrasound for brain stimulation: effects on mood. *Psychophysiology* 50:S46. r

Sassaroli, E., and Vykhodtseva, N. (2016). Acoustic neuromodulation from a basic science prospective. *J. Therap. Ultrasound* 4, 1–14. doi: 10.1186/s40349-016-0061-z

Sato, T., Shapiro, M. G., and Tsao, D. Y. (2018). Ultrasonic neuromodulation causes widespread cortical activation via an indirect auditory mechanism. *Neuron* 98, 1031–1041.e5. doi: 10.1016/j.neuron.2018.05.009

Sheline, Y. I., Barch, D. M., Price, J. L., Rundle, M. M., Vaishnavi, S. N., Snyder, A. Z., et al. (2009). The default mode network and self-referential processes in depression. *Proc. Natl. Acad. Sci. U.S.A.* 106, 1942–1947. doi: 10.1073/pnas.0812686106

Stewart, J. L., Coan, J. A., Towers, D. N., and Allen, J. J. B. (2014). Resting and task-elicited prefrontal EEG alpha asymmetry in depression: support for the capability model. *Psychophysiology* 51, 446–455. doi: 10.1111/psyp.12191

Taylor, V. A., Daneault, V., Grant, J., Scavone, G., Breton, E., Roffe-vidal, S., et al. (2013). Impact of meditation training on the default mode network during a restful state. *Soc. Cogn. Affect. Neurosci.* 8, 4–14. doi: 10.1093/scan/nsr087

ter Haar, G. (2007). Therapeutic applications of ultrasound. *Prog. Biophys. Mol. Biol.* 93, 111–129. doi: 10.1016/j.pbiomolbio.2006.07.005

Touroutoglou, A., Lindquist, K. A., Dickerson, B. C., and Barrett, L. F. (2014). Intrinsic connectivity in the human brain does not reveal networks for "basic" emotions. *Soc. Cogn. Affect. Neurosci.* 10, 1257–1265. doi: 10.1093/scan/nsv013

Treeby, B. E., and Cox, B. T. (2010). k-Wave: MATLAB toolbox for the simulation and reconstruction of photoacoustic wave fields. *J. Biomed. Opt.* 15:021314. doi: 10.1117/1.3360308

Tufail, Y., Matyushov, A., Baldwin, N., Tauchmann, M. L., Georges, J., Yoshihiro, A., et al. (2010). Transcranial pulsed ultrasound stimulates intact brain circuits. *Neuron* 66, 681–694. doi: 10.1016/j.neuron.2010.05.008

Tyler, W. J. (2011). Noninvasive neuromodulation with ultrasound? A continuum mechanics hypothesis. *Neuroscientist* 17, 25–36. doi: 10.1177/1073858409348066

Tyler, W. J., Tufail, Y., Finsterwald, M., Tauchmann, M. L., Olson, E. J., and Majestic, C. (2008). Remote excitation of neuronal circuits using low-intensity, low-frequency ultrasound. *PLoS One* 3:3511. doi: 10.1371/journal.pone.0003511

Vergallito, A., Riva, P., Pisoni, A., and Lauro, L. J. R. (2018). Modulation of negative emotions through anodal tDCS over the right ventrolateral prefrontal cortex. *Neuropsychologia* 119, 128–135. doi: 10.1016/j.neuropsychologia.2018.07.037

Verhagen, L., Gallea, C., Folloni, D., Constans, C., Jensen, D. E. A., Ahnine, H., et al. (2019). Offline impact of transcranial focused ultrasound on cortical activation in primates. *eLife* 8:e40541. doi: 10.7554/eLife.40541

Wager, T. D., Davidson, M. L., Hughes, B. L., Lindquist, M. A., and Ochsner, K. N. (2008). Prefrontal-subcortical pathways mediating successful emotion regulation. *Neuron* 59, 1037–1050. doi: 10.1016/j.neuron.2008.09.006

Whitfield-Gabrieli, S., and Nieto-Castanon, A. (2012). Conn: a functional connectivity toolbox for correlated and anticorrelated brain networks. *Brain Connect.* 2, 125–141. doi: 10.1089/brain.2012.0073

Wu, J., and Nyborg, W. L. (2008). Ultrasound, cavitation bubbles and their interaction with cells. *Adv. Drug Deliv. Rev.* 60, 1103–1116. doi: 10.1016/j.addr.2008.03.009

Yoo, S.-S., Bystritsky, A., Lee, J.-H., Zhang, Y., Fischer, K., Min, B.-K., et al. (2011). Focused ultrasound modulates region-specific brain activity. *Neuroimage* 56, 1267–1275. doi: 10.1016/j.neuroimage.2011.02.058

Conflict of Interest: The ultrasound device used in these studies was provided by WT, who is an equity holding founder of IST, LLC, a private neurotechnology company, and the inventor of issued and pending international and US patents covering systems and methods for ultrasonic and bioelectronic neuromodulation. CD was a principal of River Sonic Solutions LLC and is currently self-employed as an ultrasound expert consultant. TS and CD do not own patents or intellectual property, nor work for or own stock and financial interests in any company in the neuromodulation field.

The remaining authors declare that the research was conducted in the absence of any commercial or financial relationships that could be construed as a potential conflict of interest.

Frontiers in
Human Neuroscience

Bridges neuroscience and psychology to understand the human brain

The second most-cited journal in the field of psychology, that bridges research in psychology and neuroscience to advance our understanding of the human brain in both healthy and diseased states.

Discover the latest Research Topics

See more →

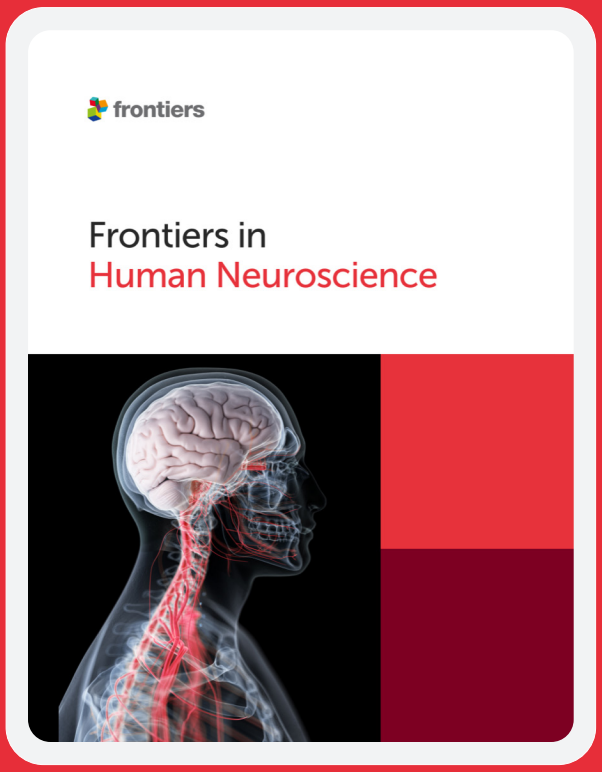

Frontiers

Avenue du Tribunal-Fédéral 34
1005 Lausanne, Switzerland
frontiersin.org

Contact us

+41 (0)21 510 17 00
frontiersin.org/about/contact